Thèse n° 7481

Stilling Basin Performance Downstream of Stepped Spillways

Présentée le 21 février 2020

à l'Ecole polytechnique fédérale de Lausanne
Faculté de l'environnement naturel, architectural et construit
Laboratoire de maintenance, construction et sécurité des ouvrages
Programme doctoral en génie civil et environnement

et à l'Instituto Superior Técnico (IST) da Universidade de Lisboa
Doutoramento em Engenharia civil

pour l'obtention du grade de Docteur ès Sciences

par

Ivan STOJNIC

Acceptée sur proposition du jury

Prof. A. J. Wüest, président du jury
Prof. E. Brühwiler, Prof. J. de Saldanha Gonçalves Matos, directeurs de thèse
Prof. R. Boes, rapporteur
Dr S. Erpicum, rapporteur
Prof. J. Eduardo de Barros Teixeira Borges, rapporteur

École
polytechnique
fédérale
de Lausanne

2020

Acknowledgements

This research was conducted in the frame of the H2Doc program, a joint doctoral initiative of IST and EPFL. This project is supported by “Fundação para a Ciência e a Tecnologia” (FCT) from Portugal [grant PD/BD/113621/2015] and by the Laboratory of Hydraulic Constructions (LCH) of EPFL, Switzerland.

I would like to acknowledge people who contributed to this research or supported me during this PhD.

First of all, I am deeply grateful to my thesis directors Prof. Jorge Matos and Prof. Anton Schleiss for giving me the opportunity to conduct this research. Their guidance, advices, trust and encouragements throughout the thesis was invaluable. I would also like to thank Prof. Eugen Brühwiler who kindly took over supervision in the last year of my thesis.

I would also like to express my deep sense of thankfulness to Prof. Michael Pfister. His expertise, remarkable knowledge in hydraulics, support and availability was precious for the outcome of this research project.

Helpful and fruitful discussions with Dr. Giovanni De Cesare (EPFL), Dr. Pedro Manso (EPFL), Prof. Mário Franca (IHE Delft, Netherlands), Prof. Antonio Cardoso (IST), Prof. Rui Ferreira (IST), Prof. Didia Covas (IST), Prof. António Pinheiro (IST) and Prof. Dubravka Pokrajac (University of Aberdeen, UK) are deeply acknowledged.

Furthermore, I would like to thank Prof. Robert Boes (ETH Zürich, Switzerland), Prof. João Teixeira Borges (IST) and Dr. Sébastien Erpicum (University of Liège; Belgium) for being part of the jury and Prof. Johny Wüest (EPFL) for accepting to be the president. All received comments significantly improved the quality of this work.

This PhD project would not be possible without technical assistance of the workshop and therefore I thank Cédric Bron, Michel Teuscher, Armin Krkic and Kosta Nikolov for their availability to continuously adjust and improve the physical model.

My special gratitude goes to Prof. Dejana Đorđević (University of Belgrade, Serbia) for encouraging me to do a PhD and for her continuous support during the last four years.

During my years at EPFL and IST, I had the pleasure to work with many wonderful colleagues and friends, whithout whom time spent in Lausanne and Lisbon woud have not been this great, namely: Alain, Aldo, Alex, Andris, Ana Clara, Ana Margarida, Ana Quaresma, Anil, Azin, Bruno, Severino, Carmelito, Caroline, Catarina, Chenfei, Christian, Clodii, Daniel, Davide, Dora, Elena, Federica, Felix, Fränz, Hannes, Irene, Jean-Noël, Jessica, João, Maria, Mariana,

Mona, Nicolas, Olga, Paloma, Pedram, Pierre, Ricardo, Sabine, Samuel, Sarita, Sebastián, Sebastian, Selim, Séverine, Shun, Stéphane, Zé Pedro and all the students and interns.

My family and friends across Balkans and around the world were always over supportive. Such trust kept me going through all the hardships and I am sincerely grateful to them for that. Last but not the least, I would like to thank my monkey, Christine Schärer, with all my heart for her incredible support throughout these last years.

Lausanne, 4 January 2020

I.S.

Abstract

Advances in dam construction techniques have significantly increased the number of implemented stepped spillways worldwide. A key hydraulic feature of a stepped chute, compared to a smooth chute, is the enhanced energy dissipation resulting in a reduced residual energy at the chute end. Nevertheless, stepped chutes provide only a partial energy dissipation, so that an adequate dissipation structure may be still required at the chute end. Stepped chute hydraulics was extensively investigated in the past decades. However, only a few studies focused on the hydraulics of stilling basins downstream of stepped chutes. As a result, design guidelines developed for stilling basins downstream of smooth chutes are still considered for stilling basins preceded by stepped chutes. As a stepped surface alters the flow structure of the approaching flow, such practice is questionable.

The present experimental research work aimed to examine the effect of stepped chute approach flows on the performance of a plain stilling basin. Physical modeling was conducted using a relatively large-scale experimental facility of a smooth or stepped chute with adjustable slope, terminating in a plain stilling basin. The experimental campaign included both smooth and stepped chute approaches, allowing direct comparison of the basin performance. The measuring campaign included collection of flow conditions at the chute end, dynamic bottom pressure and flow depths along the basin, and internal air-water flow properties of the hydraulic jump.

The results show a significant effect of stepped chute approach flows on the hydraulic characteristics of the stilling basin for the tested range of relative critical depths ($2.70 \leq h_c/s \leq 7.94$) and chute angles ($30° \leq \varphi \leq 50°$).

Using a novel analysis technique of acquired flow depths and bottom pressures along the basin, the present study demonstrates that normalized hydraulic jump lengths are up to 17% longer downstream of stepped chutes as compared to tested smooth chutes, and relative to values reported in the literature for smooth chute spillways. Consequently, the present results suggest that longer normalized stilling basin lengths are required downstream of stepped chutes. Considering some safety margin, a basin length of 7 times the tailwater depth is recommended.

The analysis of bottom pressures shows that the stepped chute approach flow pronounce extreme and fluctuating pressure coefficients within about one tailwater depth downstream of the chute end, as compared to smooth chute approach flows. The coefficients increase with increasing chute slope and extreme positive and negative pressure coefficients can reach up to

125% and 60% of the approach flow kinetic energy, respectively. These magnitudes are up to 3 times higher compared to observed magnitudes for smooth chute approach flows or relative to magnitudes reported in the literature for smooth chute spillways. However, this zone should not be endangered by cavitation damage as the measured bottom air concentration values are well above the recommended limits to avoid cavitation damage.

In conclusion, the present thesis demonstrates that stilling basin design guidelines developed for smooth chute approach flows are not applicable for stepped chute approach flows. Empirical formulae for predicting flow properties along the basin downstream of smooth and stepped chute approach flows, which can be used for the design of plain stilling basins, are proposed.

Keywords: Stepped spillway, Hydraulic jump, Stilling basin, Flow depths, Fluctuating bottom pressures, Air-water flow properties, Jump length, Roller length, Stilling basin length.

Zusammenfassung

Durch Fortschritte in der Dammbautechnik wurde die Anzahl errichteter Treppenschussrinnen weltweit erheblich erhöht. Ein wesentliches hydraulisches Merkmal der gestuften Schussrinne ist die im Vergleich zur glatten Schussrinne verbesserte Energiedissipation, die zu einer verringerten Endenergie am Fuss der Schussrinne führt. Trotzdem sorgen gestufte Schussrinnen nur für eine teilweise Energiedissipation, so dass am Ende der Schussrinne noch eine Dissipationsstruktur erforderlich ist.

Die Hydraulik von Treppenschussrinnen wurde in den letzten Jahrzehnten eingehend untersucht. Nur wenige Studien befassten sich jedoch mit der Hydraulik des Tossbeckens unterhalb von Treppenschussrinnen. Deswegen werden nach wie vor Konstruktionsrichtlinien, die für Tossbecken unterhalb glatter Schussrinnen entwickelt wurden, für Tossbecken unterhalb Treppenschussrinnen verwendet. Da die gestufte Oberfläche die Strömungsstruktur der sich nähernden Strömung erheblich verändert, ist eine solche Praxis höchst fragwürdig.

Die vorliegende experimentelle Forschungsarbeit zielte darauf ab, die Auswirkung einer Treppenschussrinne auf die hydraulische Leistung eines einfachen Beruhigungsbeckens zu untersuchen. Die physikalische Modellierung wurde mittels Verwendung einer Versuchsanlage mit einer glatten und einer abgestuften Schussrinne mit einstellbarer Neigung durchgeführt. Unterhalb dieser Schussrinne befand sich ein ebenes, horizontales Tossbecken. Die experimentellen Versuche umfassten sowohl glatte als auch gestufte Schussrinnen, wodurch ein direkter Vergleich der Leistung des Tossbeckens ermöglicht wurde. Die Messkampagne umfasste die Erfassung der Strömungsverhältnisse am Ende der Rinne, den dynamischen Bodendruck und die Abflussttiefen entlang des Tossbeckens, sowie die Luft-Wasser-Strömungseigenschaften im Becken.

Die Ergebnisse zeigen einen signifikanten Einfluss der Treppenschussrinnen auf die hydraulischen Eigenschaften des Tossbeckens für den untersuchten Bereich von relativen kritischen Abflusstiefen ($2.7 \leq h_c/s \leq 7.94$) und Rinnenneigungen ($30\,° \leq \varphi \leq 50°$).

Unter Verwendung einer neuartigen Analysetechnik der Fliesstiefen und Druckverteilung entlang des Tossbeckens wird gezeigt, dass die normalisierte hydraulische Länge des Wechselsprunges unterhalb Treppenschussrinnen im Vergleich zu den untersuchten glatten Schussrinnen bis zu 17% länger ist. Die vorliegenden Ergebnisse legen nahe, dass für Treppenschussrinnen, verglichen mit glatten Schussrinnen längere Tossbecken erstellt werden sollten. Es wird eine Beckenlänge empfohlen, die inklusive eines Sicherheitsfaktors das 7-fache der Unterwassertiefe beträgt.

Die Analyse der Druckverteilung im Tossbecken zeigte, dass eine gestufte Schussrinne im Vergleich zu glatten Schussrinnen extreme und schwankenden Druckkoeffizienten aufweisen. Die Druckkoeffizienten nehmen mit zunehmender Rinnenneigung zu und die relativen Über- und Unterdrücke können bis zu 125% bzw. 60% der kinetischen Energie der Zuflussströmung erreichen. Diese Beträge sind bis zu dreimal höher als die beobachteten Beträge für Zuflüsse in glatten Rinnen und relativ zu den in Fachliteratur angegebenen Beträgen für Überläufe mit glatter Rinne. Es wurde jedoch festgestellt, dass diese Zone nicht durch Kavitationsschäden gefährdet ist, da die gemessenen Werte der Luftkonzentration deutlich über den empfohlenen Grenzwerten liegen, um Kavitationsschäden zu vermeiden.

Zusammenfassend zeigt die vorliegende Arbeit, dass die Dimensionierungsrichtlinien für die Gestaltung von Schussrinnen und Tossbecken nicht für Treppenschussrinnen anwendbar sind. Es sind empirischer Formeln zur Bestimmung der Abflusstiefetiefe, des Bodendrucks und der Luft-Wasser-Strömungscharakteristik im Tossbecken, von sowohl glatten als auch gestuften Schussrinnen, entwickelt worden, die für die Dimensionierung von Tossbecken verwendet werden können.

Keywords: Treppenschussrinne, Wechselsprung, Tossbecken, Abflusstiefen, dynamische Bodendruckverteilung, Luft-Wasser Fliesseigenschaften, Wechselsprunglänge, Rollerlänge, Tossbeckenlänge.

Resumo

O desenvolvimento de técnicas de construção de barragens conduziu a um aumento significativo do número de descarregadores de cheias em degraus implementados no mundo. Uma característica hidráulica essencial de um descarregador em degraus, comparativamente a um descarregador com paramento convencional, liso, é o acréscimo de dissipação de energia, o que se traduz numa menor energia residual no pé do descarregador. No entanto, os descarregadores em degraus fornecem apenas uma dissipação parcial de energia, pelo que ainda se torna necessário dispor de uma estrutura de dissipação adequada na extremidade de jusante dos mesmos A hidráulica de descarregadores em degraus foi objeto de extensa investigação nas últimas décadas. No entanto, apenas alguns estudos foram dedicados à hidráulica de bacias de dissipação de energia a jusante de descarregadores em degraus. Desta forma, os critérios de dimensionamento desenvolvidos para bacias de dissipação de energia a jusante de descarregadores com paramento liso ainda são utilizados para bacias de dissipação precedidas de descarregadores em degraus. Como uma superfície em degraus altera a estrutura do escoamento à entrada da bacia, tal prática é questionável.

O presente trabalho de investigação experimental teve como objetivo estudar o efeito do escoamento de aproximação no desempenho de uma bacia de dissipação sem acessórios. A modelação física foi conduzida usando uma instalação experimental de relativamente grande dimensão, incluindo um descarregador com paramento liso ou em degraus, de declive ajustável, terminando numa bacia de dissipação de energia.

A campanha de ensaios experimentais incluiu condições de aproximação em descarregadores em degraus e com paramento liso, permitindo uma comparação direta do desempenho da bacia de dissipação. Incluiu também a aquisição das características do escoamento no final do descarregador, da pressão dinâmica na soleira da bacia de dissipação, das alturas de escoamento ao longo da bacia e a caracterização do escoamento de emulsão ar-água no ressalto hidráulico.

Os resultados evidenciam um efeito significativo das condições do escoamento de aproximação nas características hidráulicas da bacia de dissipação, para a gama analisada de alturas críticas adimensionalizadas ($2.7 \leq h_c/s \leq 7.94$) e ângulos do descarregador com a horizontal ($30° \leq \varphi \leq 50$).

Usando uma nova técnica de análise das alturas do escoamento e das pressões na soleira ao longo da bacia, o presente estudo demonstrou que os comprimentos adimensionalizados do ressalto hidráulico a jusante de descarregadores em degraus são até 17% superiores aos observados a jusante de descarregadores com paramento liso, bem como em relação a valores apresentados na literatura para este último tipo de descarregadores. Consequentemente, os resultados obtidos sugerem que devem ser dimensionadas bacias de maior comprimento relativo (adimensionalizado pela altura do escoamento a jusante do ressalto) a jusante de descarregadores em degraus, comparativamente a bacias precedidas por descarregadores com paramento liso. Considerando uma certa margem de segurança, recomenda-se um comprimento da bacia igual a sete vezes a altura do escoamento a jusante do ressalto.

A análise das flutuações de pressão evidencia que o escoamento de aproximação no descarregador em degraus conduz, numa extensão da ordem de grandeza da altura do escoamento a jusante do ressalto, a flutuações de pressão e a pressões extremas superiores às obtidas com escoamento de aproximação num descarregador com paramento liso. Observa-se que as magnitudes aumentam com o declive do descarregador, e as pressões extremas, positivas e negativas, podem atingir valores até 125% e 60% da energia cinética do escoamento de aproximação, respetivamente. Essas magnitudes são até três vezes superiores às observadas para escoamentos de aproximação no descarregador com paramento liso, ou em relação às magnitudes apresentadas na literatura para descarregadores com paramento liso. No entanto, esta zona não deverá estar sujeita a risco de erosão de cavitação, devido ao facto de se terem medido valores de concentração do ar junto do fundo consideravelmente superiores aos limites recomendados para evitar danos por erosão de cavitação.

Em conclusão, a presente tese demonstrou que os critérios de dimensionamento de bacias de dissipação desenvolvidos para escoamentos de aproximação em descarregadores com paramento liso não são aplicáveis para escoamentos de aproximação em descarregadores em degraus. Desenvolveram-se também fórmulas empíricas para estimar as características do escoamento ao longo da bacia a jusante de descarregadores com paramento liso e em degraus, que podem ser aplicadas no dimensionamento de bacias de dissipação sem acessórios.

Palavras-Chave: Descarregador de cheias em degraus; ressalto hidráulico; bacia de dissipação de energia; alturas do escoamento; pressões dinâmicas na soleira; características do escoamento de emulsão ar-água; comprimento do ressalto; comprimento do rolo; comprimento da bacia de dissipação de energia.

Contents

Acknowledgements **v**

Abstracts **vii**

List of figures **xvi**

List of tables **xxv**

List of Symbols **xxix**

Introduction **1**

1 Introduction **1**

1.1 Objectives 4

1.2 Structure of the report 5

2 State-of-the-art **7**

2.1 Overview on stepped chute hydraulics 7

2.1.1 Flow regimes 7

2.1.2 Definition of basic air-water flow terms 9

2.1.3 Skimming flow regime 11

2.2 Overview on hydraulic jumps and stilling basin flow 22

2.2.1 Classical hydraulic jumps 22

2.2.2 Forms and classification of hydraulic jumps 24

2.2.3 Sequent depth ratio 26

2.2.4 Free surface characteristics 27

2.2.5 Energy dissipation and jump efficiency 28

2.2.6 Length characteristics 28

2.2.7 Air-water flow properties 29

2.2.8 Bottom pressure characteristics 34

2.3 Standard stilling basins types 37

2.4 Overview of existing studies on stilling basin performance downstream of stepped chutes 38

2.5 Gaps in knowledge and specific research questions 44

3 Experimental setup 45
3.1 Experimental facility 45
3.1.1 Jet-box 46
3.1.2 Chute 46
3.1.3 Stilling basin 49
3.2 Instrumentation 50
3.2.1 Flowmeter 50
3.2.2 Fiber optical phase detection system 50
3.2.3 Pitot-Prandtl tube 52
3.2.4 Ultrasonic distance sensor 53
3.2.5 Pressure transducers 54
3.2.6 Acquisition card for pressure transmitters and US sensor 56
3.2.7 Chute trolley and automatic positioning system 57
3.2.8 Visual estimation of the roller end 58
3.3 Test program 59
3.4 Scale effects 60
3.5 Measuring procedure 62

4 Hydraulic performance of a plain stilling basin downstream of 30° sloping smooth and stepped chute 65
4.1 Overview 65
4.2 Test program and inflow conditions 66
4.3 Visual observations 69
4.4 Free surface characteristics of the hydraulic jump 71
4.4.1 Mean flow depths 71
4.4.2 Roller length 73
4.4.3 Flow depth fluctuations and jump length 73
4.5 Bottom pressure characteristics 75
4.5.1 Statistical analysis and jump length 75
4.5.2 Streamwise distribution of mean pressure 77
4.5.3 Streamwise distribution of pressure fluctuations 80
4.5.4 Streamwise distribution of extreme pressures 81
4.5.5 Frequency domain analysis 82
4.5.6 Streamwise PSD development with smooth chute approach flows 82
4.5.7 Streamwise PSD development with stepped chute approach flows 83
4.6 Conclusions 85

5 Air-water flow properties of a plain stilling basin for 30° sloping smooth and stepped chute approach flows 89
5.1 Overview 89
5.2 Test program and inflow conditions 90
5.3 Air concentration distribution 90
5.3.1 Smooth versus stepped chute approach flows 93

5.3.2 Streamwise development of maximum C_{max} and minimum C_{min} air concentration . . . 94
5.3.3 Streamwise bottom air concentration . . . 96
5.3.4 Streamwise development of the mean air concentrations . . . 99
5.3.5 Effect of 30° inclined approach flows on air concentration distribution in hydraulic jumps . . . 99
5.4 Air-phase frequency . . . 101
5.5 Vertical distribution of air-water flow velocity . . . 105
5.6 Characteristic flow depths . . . 111
5.7 Conclusions . . . 113

6 Effect of chute slope on the performance of a plain stilling basin downstream of smooth and stepped chutes 117
6.1 Overview . . . 117
6.2 Test program and approach flow conditions . . . 117
6.2.1 50° sloping smooth chute . . . 119
6.2.2 50° sloping stepped chute . . . 120
6.3 Free surface characteristics . . . 122
6.3.1 Mean flow depths . . . 122
6.3.2 Roller length . . . 124
6.3.3 Flow depth fluctuations and jump length . . . 125
6.4 Bottom pressure characteristics . . . 128
6.4.1 Jump length . . . 128
6.4.2 Streamwise distribution of mean pressure . . . 130
6.4.3 Streamwise distribution of pressure fluctuation . . . 134
6.4.4 Streamwise distribution of extreme pressures . . . 137
6.4.5 Frequency domain analysis . . . 139
6.5 Air-water flow properties . . . 143
6.5.1 Air concentration, air-phase frequency distributions and representative flow depths . . . 143
6.5.2 Vertical distribution of air-water flow velocity . . . 153
6.6 Conclusions . . . 157

7 Conclusions 161
7.1 Results . . . 162
7.2 Design recommendations . . . 166
7.3 Outlook . . . 166
7.4 Design example . . . 167
7.4.1 Approach flow conditions . . . 168
7.4.2 Tailwater depth . . . 170
7.4.3 Hydraulic jump, stilling basin and roller length . . . 170
7.4.4 Flow depth development and sidewall height . . . 171
7.4.5 Bottom pressure characteristics . . . 173

A Recorded tailwater depth, roller and jump lengths **177**

B Test-sheets **179**

Bibliography **254**

Curriculum Vitae **255**

List of Figures

1.1 Bajina Basta dam, Serbia. Spillway consisting of a gated ogee crest followed by a smooth chute with energy dissipation in a stilling basin. 1
1.2 Pedrógão dam, Portugal. 2
1.3 Paradise dam, Australia, 2013 flood event : (a) Stepped spillway in operation, (b) sideview of the damaged stilling basin (McDonald 2013) and (c) downstream view of the scour hole (McDonald 2013). 3

2.1 Flow regimes over a stepped chute (adapted from André (2004)). 8
2.2 Flow regime limits proposed by Chanson (2015b) as a function of dimensionless critical depth h_c/s and step configuration s/l. 9
2.3 Definition sketch of air-water flow properties over a stepped chute. 10
2.4 Definition scheme of skimming flow regime over a stepped chute. 12
2.5 Downstream view of φ=30° sloping stepped chute at LCH operating in skimming flow regime. 13
2.6 Darcy-Weisbach friction factor in skimming flow regime as a function of the relative cavity height $s \cos\varphi / D_H$ (Chanson 2015b). 19
2.7 Flow impact on the step edge (internal jet) for: (a) 19° sloping chute and (b) 55° sloping chute. Adapted from Takahashi and Ohtsu (2012). 21
2.8 Definition sketch of a classical hydraulic jump. 23
2.9 Hydraulic jump with a: (a) developed and (b) non-developed roller flow state. Adapted from Hager (1992). 24
2.10 Hydraulic jump forms based on approach Froude number F_1: (a) weak jump, (b) transition jump, (c) steady jump and (d) rough or choppy jump. Adapted from Peterka (1958). 25
2.11 Hydraulic jump forms based on its position within the spillway: (a) A jump type, (b) B jump type, (c) C jump type and (d) D jump type. Adapted from Khatsuria (2005). 25
2.12 Normalized jump length L_J/h_2 (Peterka 1958). 30
2.13 Approach flow condition types for classical hydraulic jumps. 30
2.14 Sketches of air entrainment mechanisms at the hydraulic jump toe with partially developed approach flows. Adapted from Wang (2014). 31
2.15 Air entrainment in hydraulic jumps with partially developed approach flow conditions. 32

2.16 Sketch of a typical (a) air concentration, (b) air-phase frequency and (c) velocity profile within hydraulic jump roller. 32

2.17 Air entrainment in hydraulic jump for: (a) undeveloped and partially developed approach flow conditions, and (b) fully developed approach flow condition. Adapted from Takahashi and Ohtsu (2017). 33

2.18 Sketch of the USBR (a) type II, (b) type III and (b) type IV stilling basin (Peterka 1958). 37

2.19 Upper Stillwater Dam, USA. 38

2.20 Siah-Bishe stepped spillway, Iran (Photo: Ivan Stojnic). 39

2.21 Folsom dam with auxiliary stepped spillway, USA. 40

2.22 Sideview photo of a USBR type III stilling basin downstream of a 53° sloping stepped chute at LNEC (Lisbon) in operation (Meireles et al. 2010). 42

3.1 Front view of the experimental facility. 45

3.2 Definition sketch with instrumentation and nomenclature. Note: FOP – Fiber optical probe, PPT – Pitot-Prandtl tube, US – Ultrasonic distance meter, and APS – Automatic positioning system. 46

3.3 The jetbox: (a) view from the side and (b) downstream view without front panel. 47

3.4 Stepped chute configuration: (a) downstream view (s=0.06 m and φ=50°), and (b) sideview of s=0.03 m high steps (φ=30°). 47

3.5 Smooth chute configuration: (a) downstream view without the grid (φ=50°), (b) downstream view with the grid (φ=30°). 48

3.6 (a) Closeup view of the grid and (b) pre-aeration setup. 49

3.7 Sideview of the stilling basin. 49

3.8 The fiber optical phase detection system: (a) sideview of the FOP used for chute measurements, (b) sideview of the FOP used for stilling basin measurements in operation, (c) opto-electronic module, oscilloscope and acquisition card, and (d) acquisition and treatment software ISO v2.9. 51

3.9 The Pitot-Prandtl tube: (a) view of the side and (b) sideview in operation with differential pressure transducer. 53

3.10 The ultrasonic distance sensor: (a) Closeup view of the sensor and (b) upstream view of the sensor in operation. 54

3.11 Ultrasonic distance sensor signal for Run 11 at x=0.2 m: (a) raw and (b) filtered. 55

3.12 (a) Pressure transmitter Keller series 25 (Switzerland) and (b) pressure calibrator Keller LPX (Switzerland). 55

3.13 The aqusition card and power supply units. 56

3.14 (a) Chute trolley and (b) Automatic positioning system (APS). 57

3.15 Visual estimation of the roller end. 58

4.1 Smooth chute flow characteristics seen in flow direction: (a) Run 8, (b) Run 6, and (c) Run 2. 67

4.2 Stepped chute flow characteristics seen from downstream for Run 10 (Table 4.1). 68

4.3 Air concentration profiles at the inflow section for (a) smooth (Runs 1-9), and (b) stepped chutes (Runs 10-15); (——) advective diffusion model of Chanson and Toombes (2002) with C1 from the tests. 68
4.4 Dimensionless velocity V/V_{90} profiles at the inflow section and comparison with Eq. (2.25), for (a) smooth (Runs 1-9), and (b) stepped chutes (Runs 10-15). . . . 69
4.5 Sideview photos of the stilling basin in operation (Run 9) showing: (a) flow structure (with injected dye), (b) "developed roller" state, and (c) "non-developed roller" state. Flow direction from left to right. 70
4.6 Streamwise mean flow depth η and standard deviation η' along the hydraulic jumps of Runs 7 (smooth chute) and 10 (stepped chute). 71
4.7 Comparison of measured sequent depth ratio h_2/h_1 [Runs 1-9: smooth chute; Runs 10-15: stepped chute] with Eq. (2.38). 72
4.8 Dimensionless flow depths Z along the hydraulic jump roller. Comparison of experimental data with Eq. (4.1; [Runs 1-9: smooth chute; Runs 10-15: stepped chute]. 73
4.9 (a) Dimensionless roller L_R/h_2 and jump L_J/h_2 lengths obtained from measurements ($L_{R,\eta}$ and $L_{J,\eta'}$) and visual observation ($L_{R,D}$), compared to jump length by Peterka (1958), and (b) comparison between measured and visually estimated roller lengths L_R/h_1 with Eq. (2.47) by Hager et al. (1990), and Eq. (4.2); [Runs 1-9: smooth chute; Runs 10-15: stepped chute]. 74
4.10 (a) Streamwise distribution of the flow depth coefficient $C_H{}'$ versus normalized streamwise coordinate x/h_2, and (b) comparison of $C_H{}'$ with the normalized coordinate as $X_J = x/L_{J,\eta'}$ and Eqs. (4.3) and (4.4); [Runs 1-9: smooth chute; Runs 10-15: stepped chute] 75
4.11 Streamwise distribution (Run 7, smooth chute) of (a) extreme maximum bottom pressure p_{max}, bottom pressure with 99.9% probability $p_{99.9}$, mean bottom p_m, bottom pressure with 0.1% probability $p_{0.1}$, extreme minimum bottom pressure p_{min} and mean flow depth η, and (b) fluctuating pressure p', skewness S and excess kurtosis K. 76
4.12 (a) Dimensionless jump lengths L_J/h_2 from pressure ($L_{J,SK}$ and $L_{J,p'}$) and flow depth ($L_{J,\eta'}$) against the inflow Froude number F_1, compared to the jump length of Peterka (1958), and (b) pressures: impact mean coefficient $C_P{}^{def}$, fluctuation coefficient $C_P{}'$, extreme maximum coefficient $C_P{}^{max}$ and extreme minimum coefficient $C_P{}^{min}$ at the jump toe against the inflow Froude number F_1. [Runs 1-9: smooth chute; Runs 10-15: stepped chute]. 77
4.13 Streamwise distribution of: (a) mean pressure coefficient P_m, comparison with dimensionless flow depth Z as a function of X_J and with Eq. (4.5), (b) pressure fluctuation coefficient $C_P{}'$, comparison with Eqs. (4.3), (4.4), (4.6) and (4.7), (c) maximum pressure coefficient $C_P{}^{max}$ and 99.9th percentile $C_P{}^{99.9}$, comparison with Eqs. (4.6) and (4.7), (d) minimum pressure coefficient $C_P{}^{min}$ and 0.1th percentile $C_P{}^{0.1}$, comparison with Eqs. (4.6) and (4.7), (e) skewness S, and (f) excess kurtosis K; [Runs 1-9: smooth chute; Runs 10-15: stepped chute]. 80

4.14 Power spectral densities of the pressure fluctuations at selected flow distances along the stilling basin invert, for (a-c) Run 8, and (d-f) Run 14. 84

5.1 Air concentration profiles along the stilling basin for: (a-b) Run 7 (smooth chute), and (c-d) Run 10 (stepped chute); (——) Eq. (5.1); (- - -) Eq. (5.2). 92

5.2 Streamwise variation of the dimensionless turbulent diffusivity in a: (a) shear region ${D_t}^s(V_1 h_1)^{-1}$ and (b) recirculation region ${D_t}^r(V_1 h_1)^{-1}$; [Runs 1-8: smooth chute, Runs 10-15: stepped chute]; (——) Wang and Chanson (2017). 93

5.3 Comparison between air concentration profiles in the stilling basin for Runs 2, 5 and 8 (smooth chute approach flows), and Runs 11 and 14 (stepped chute approach flows) at $x/L_{R,\eta}$= (a) 0.1, (b) 0.3, (c) 0.5, (d) 0.7, (e) 1.0 and (f) 1.2. . . 94

5.4 Streamwise development of: (a) maximum air concentration C_{max} and (b) minimum air concentration C_{min} along the advective diffusive zone; (——) Eqs. (5.3) and (5.4); [Runs 1-8: smooth chute, Runs 10-15: stepped chute]. 95

5.5 Streamwise development of the dimensionless vertical positions of maximum Z_{max} and minimum Z_{min} air concentration; (——) Eqs. (5.5) and (5.6); [Runs 1-8: smooth chute, Runs 10-15: stepped chute]. 96

5.6 Streamwise development of the bottom air concentration C_b verus normalized streamwise coordinate X_J, including bottom air concentration at the inflow section $C_{b,ce}$ ($X_J = -0.3$); (——) Eq. (5.7); (- - -) Eq. (5.8); [Runs 1-8: smooth chute, Runs 10-15: stepped chute]. 97

5.7 Sketch of air entrainment in hydraulic jumps with a: (a) horizontal approach flow, (b) smooth chute approach flow and (c) stepped chute approach flow. . . 98

5.8 Streamwise development of mean air concentration C_a compared to (——) Eq. (5.10); [Runs 1-8: smooth chute, Runs 10-15: stepped chute]. 99

5.9 Comparison of air concentration profiles for Run 14 (stepped chute, Table 4.1) at x/h_1=4.67, 9.35 and 14.02 (i.e. $x/L_{R,\eta}$= 0.1, 0.2 and 0.3) with those for: (a-b) PD approach flow for F_1=7.5 and R_1=1.4×10^5 at x/h_1=8.33 and x/h_1=12.5 (Wang 2014), (c-d) FD approach flow for F_1=7.2 and R_1=6.2×10^4 at x/h_1=9.1 and x/h_1=13.3 (Takahashi and Ohtsu 2017), (e-f) PA approach flow for F_1=5.49 and R_1=6.68×10^4 at x/h_1=4.86 and x/h_1=11.34 (Thandaveswara 1974). 100

5.10 Dimensionless vertical air-phase frequency Fh_1/V_1 profiles at the selected distances $x/L_{R,\eta}$ for: (a) Run 7 (smooth chute) and (b) Run 10 (stepped chute). . . 102

5.11 Streamwise development of dimensionless: (a) maximum air-phase frequency $F_{max}h_1/V_1$ and (b) secondary peak in air phase frequency $F_{sec}h_1/V_1$; [Runs 1-8: smooth chute, Runs 10-15: stepped chute]. 103

5.12 Streamwise development of dimensionless locations: (a) Z_{Fmax} and Z_{Fsec} versus normalized coordinate $x/L_{R,\eta}$ and (b) Z_{Fmax} versus normalized coordinate X_J; [Runs 1-8: smooth chute, Runs 10-15: stepped chute]. 103

5.13 Relationship between dimensionless locations Z_{Fmax} and Z_{Cmax} (full symbols), and Z_{Fsec} and Z_{min} (open symbols); [Runs 1-8: smooth chute, Runs 10-15: stepped chute]. 104

5.14 Dimensionless vertical velocity distributions V/V_1 along the stilling basin for: (a) Run 7 (smooth chute) and (b) Run 10 (stepped chute). 106

5.15 Dimensionless vertical velocity distributions $(V-V_{rec})/(V_{max}$-$V_{rec})$ within advective diffusive zone for: (a) smooth chute approach flows and (b) stepped chute approach flows; (- - -) Eq. (5.11); (——) Eq. (5.12) with M=10. 107

5.16 Streamwise development of dimensionless: (a) maximum velocity V_{max}/V_1 vs. normalized streamwise coordinate $x/L_{R,\eta}$, and (b) maximum velocity $(V_{max}-V_2)/(V_1-V_2)$ vs. normalized streamwise coordinate X_J and (c) elevation of maximum velocity Z_{Vmax} vs. normalized streamwise coordinate X_J; (——) Wang and Chanson (2017) and Eqs. (5.13) and (5.14); [Runs 1-8: smooth chute, Runs 10-15: stepped chute] 108

5.17 Relationship between dimensionless locations: (a) Z_{Vmax} and Z_{Fmax} and (b) Z_{V0} and Z_{max} (full symbols), and Z_{V0} and Z_{min} (open symbols); [Runs 1-8: smooth chute, Runs 10-15: stepped chute] 109

5.18 Streamwise development of dimensionless: (a) mean recirculation velocity normalized as $|V_{rec,a}|/V_1$, (b) mean recirculation velocity normalized as $(|V_{rec,a}|-V_2)/(V_1-V_2)$ and (c) elevation of flow reversal onset Z_{V0} along the stilling basin; (——) Eqs. (5.15) and (5.16); [Runs 1-8: smooth chute, Runs 10-15: stepped chute].110

5.19 (a) Streamwise development of the characteristic flow depths Z_{90} against normalized streamwise coordinate $x/L_{R,\eta}$ compared to Eq. (5.17) and (b) relationship between dimensionless flow depths Z recorded with US sensor and characteristic flow depths Z_{50}, Z_{70} and Z_{90}; [Runs 1-8: smooth chute, Runs 10-15: stepped chute]. 111

5.20 Streamwise development of the dimensionless equivalent clear water depths Z_{cw} along the stilling basin; (——) Eqs. (4.5) and (5.18); [Runs 1-8: smooth chute, Runs 10-15: stepped chute]. 112

6.1 50° sloping smooth chute flow characteristics seen in flow direction for: (a) Run 23, (b) Run 20, and (c) Run 17. 119

6.2 (a) Air concentration profiles at the inflow section for 50° smooth chute test runs (Runs 16-24, Table 6.1) and comparison with (——) advective diffusion model of Chanson and Toombes (2002) with C_1=0.16, 0.29 and 0.36, and (b) Dimensionless velocity V/V_{90} profiles at the inflow section for 50° smooth chute test runs (Runs 16-24, Table 6.1) and comparison with (——) Eq. (2.25). 120

6.3 (a) Air concentration profiles at the inflow section for 50° stepped chute test runs (Runs 25-30, Table 6.1) and comparison with (——) advective diffusion model of Chanson and Toombes (2002) with C_1=0.55 and 0.46, and (b) Dimensionless velocity V/V_{90} profiles at the inflow section for 50° stepped chute test runs (Runs 25-30, Table 6.1) and comparison with (——) Eq. (2.25). 121

6.4 50° stepped chute flow characteristics seen from downstream for Run 26 (Table 6.1). 121

6.5 Comparison between measured mean air concentration values C_1 at 50° stepped chute inflow section and quasi-uniform values C_u of Takahashi and Ohtsu (2012). Note: T&O stands for Takahashi and Ohtsu (2012). 122

6.6 Streamwise mean flow depths η along the stilling basin for Runs 7, 10, 22 and 25 (Table 6.1). $L_{R,\eta}$=roller length based on flow depth measurements; h_2=tailwater depth; x=streamwise coordinate starting at the intersection of chute (pseudo) bottom and stilling basin invert. 123

6.7 Sequent depth ratio h_2/h_1 as a function of approach Froude number F_1; (——) Eq. (2.38); [Runs 1-9: 30° smooth chute, Runs 10-15: 30° stepped chute, Runs 16-24: 50° smooth chute, Runs 25-30: 50° stepped chute]. 123

6.8 Dimensionless mean flow depths Z along the hydraulic jump roller for 30° and 50° sloping: (a) smooth chute and (b) stepped chute; (——) Eq. (4.1); [Runs 1-9: 30° smooth chute, Runs 10-15: 30° stepped chute, Runs 16-24: 50° smooth chute, Runs 25-30: 50° stepped chute]. 124

6.9 Roller lengths obtained from measurements $L_{R,\eta}$ and visual observation $L_{R,D}$ plotted against F_1 in dimensionless form as: (a) L_R/h_1 and (b) L_R/h_2; (——) Eq. (4.2); [Runs 1-9: 30° sloping smooth chute, Runs 10-15: 30° sloping stepped chute, Runs 16-24: 50° sloping smooth chute, Runs 25-30: 50° sloping stepped chute]. 125

6.10 Streamwise flow depth fluctuations η' along the stilling basin for Runs 7, 10, 22 and 25 (Table 6.1). 126

6.11 Dimensionless jump lengths $L_{J,\eta'}$ obtained from flow depth fluctuations η' as a function of inflow Froude number F_1, compared to jump length prediction of Peterka (1958); [Runs 1-9: 30° smooth chute, Runs 10-15: 30° stepped chute, Runs 16-24: 50° smooth chute, Runs 25-30: 50° stepped chute]. 126

6.12 Streamwise development of flow depth fluctuation coefficient $C_H{}'$ versus normalized streamwise coordinate $x/L_{J,\eta'}$ for: (a) 50° smooth and stepped chute test runs (b) 30° and 50° smooth and stepped chute test runs; (− − −) Eq. (4.3), (——) Eq. (4.4);; [Runs 1-9: 30° smooth chute, Runs 10-15: 30° stepped chute, Runs 16-24: 50° smooth chute, Runs 25-30: 50° stepped chute]. 127

6.13 Streamwise pressure distribution (Run 22, smooth chute, Table 6.1) of: (a) extreme maximum p_{max}, 99.9% probability $p_{99.9}$, mean p_m, 0.1% probability $p_{0.1}$, and extreme minimum pressure p_{min}, and (b) fluctuating pressure p', skewness S and kurtosis K. 128

6.14 Dimensionless jump lengths L_J/h_2 downstream of 30° and 50° smooth and stepped chutes from pressure ($L_{J,SK}$ and $L_{J,p'}$) and flow depth ($L_{J,\eta'}$) measurements against the inflow Froude number F_1; (− − −) Peterka (1958); [Runs 1-9: 30° smooth chute, Runs 10-15: 30° stepped chute, Runs 16-24: 50° smooth chute, Runs 25-30: 50° stepped chute]. 129

6.15 Streamwise distribution of: (a) mean pressure coefficient P_m, (b) pressure fluctuation coefficient $C_P{}'$, (c) maximum pressure coefficient $C_P{}^{max}$, (d) 99.9th percentile $C_P{}^{99.9}$, (e) minimum pressure coefficient $C_P{}^{min}$, (f) 0.1th percentile $C_P{}^{0.1}$, (g) skewness S, and (h) excess kurtosis K; (——) Eqs. (4.5), Eqs. (4.6) and (6.1); (– – –) Eqs. (4.3), (4.4), (6.2) and (6.3) ; [Runs 16-24: smooth chute; Runs 25-30: stepped chute]. 132

6.16 Streamwise distribution of mean pressure coefficients P_m downstream of 30° and 50° sloping: (a) smooth chute, and (b) stepped chute; [Runs 1-9: 30° smooth chute, Runs 10-15: 30° stepped chute, Runs 16-24: 50° smooth chute, Runs 25-30: 50° stepped chute]. 133

6.17 Mean pressure coefficients $C_P{}^{def}$ against inflow Froude number F_1; [Runs 1-9: 30° smooth chute, Runs 10-15: 30° stepped chute, Runs 16-24: 50° smooth chute, Runs 25-30: 50° stepped chute]. 134

6.18 Streamwise development of pressure fluctuation coefficient $C_P{}'$ for 30° and 50° sloping: (a) smooth chute, and (b) stepped chute; [Runs 1-9: 30° smooth chute, Runs 10-15: 30° stepped chute, Runs 16-24: 50° smooth chute, Runs 25-30: 50° stepped chute]. 135

6.19 Pressure fluctuation coefficients $C_P{}'$ at the flow deflection point and jump toe against inflow Froude number F_1; [Runs 1-9: 30° smooth chute, Runs 10-15: 30° stepped chute, Runs 16-24: 50° smooth chute, Runs 25-30: 50° stepped chute]. 136

6.20 Streamwise development of bottom pressure fluctuations p' for Run 24 (50° smooth chute) and Run 30 (50° stepped chute chute). 136

6.21 Streamwise development of extreme pressure coefficients: (a) $C_P{}^{max}$ for 30° and 50° smooth chutes, (b) $C_P{}^{max}$ for 30° and 50° stepped chutes, (c) $C_P{}^{min}$ for 30° and 50° smooth chutes, and (d) $C_P{}^{min}$ for 30° and 50° stepped chutes; [Runs 1-9: 30° smooth chute, Runs 10-15: 30° stepped chute, Runs 16-24: 50° smooth chute, Runs 25-30: 50° stepped chute]. 138

6.22 Extreme pressure coefficients: (a) $C_P{}^{max}$ and (b) $C_P{}^{min}$ at the flow deflection point and jump toe; [Runs 1-9: 30° smooth chute, Runs 10-15: 30° stepped chute, Runs 16-24: 50° smooth chute, Runs 25-30: 50° stepped chute]. 139

6.23 Power spectral densities of the pressure fluctuations at selected flow distances along the stilling basin invert, for (a-c) Run 20 (50° smooth chute), and (d-f) Run 29 (50° smooth chute). 141

6.24 Comparison of power spectral densities for 50° smooth (Run 20) and stepped chute (Run 29) approach flows at (a) flow deflection point, and (b) $X_J = 0.07$. . 142

6.25 Comparison of power spectral densities for 30° (Run 14) and 50° (Run 29) stepped chute approach flows at (a) flow deflection point, and (b) $X_J \approx 0.07$. 143

6.26 Air concentration profiles along the stilling basin for: (a-b) Run 22 (50° smooth chute), and (c-d) Run 25 (50° stepped chute); (——) Eq. 5.1; (- - -) Eq. 5.2. 144

6.27 Dimensionless vertical air-phase frequency Fh_1/V_1 profiles at the selected flow distances $x/L_{R,\eta}$ for: (a) Run 22 (50° smooth chute) and (b) Run 25 (50° stepped chute). 145

6.28 Streamwise variation of dimensionless turbulent diffusivity in a: (a) shear region ${D_t}^s$ and (b) recirculation region ${D_t}^r$; [Runs 1-9: 30° smooth chute, Runs 10-15: 30° stepped chute, Runs 16-24: 50° smooth chute, Runs 25-30: 50° stepped chute].145

6.29 Comparison between air concentration profiles in the stilling basin for Runs 16, 19 and 22 (smooth chute approach flows), and Runs 25 and 28 (stepped chute approach flows) at $x/L_{R,\eta}$=: (a) 0.1, (b) 0.3, (c) 0.5, (d) 0.7, (e) 1.0 and (f) 1.2. . . 146

6.30 Comparison between air concentration profiles in the stilling basin at distances $x/L_{R,\eta}$=0.1, 0.3 and 0.6 for 50° and 30°: (a-c) smooth chute approach flows (30° chutes: Run 1, 4, 7; 50° chutes:16, 19 and 22) and (d-f) stepped chute approach flows (30° chutes: Run 10, 13; 50° chutes: Run 25 and 28). 147

6.31 Streamwise development of (a) maximum air concentration C_{max} and (b) minimum air concentration C_{min}; [Runs 1-9: 30° smooth chute, Runs 10-15: 30° chute, Runs 16-24: 50° smooth chute, Runs 25-30: 50° stepped chute]. 148

6.32 Streamwise development of (a) dimensionless elevation of maximum air concentration Z_{max} and (b) dimensionless elevation of minimum air concentration Z_{min}; [Runs 1-9: 30° smooth chute, Runs 10-15: 30° stepped chute, Runs 16-24: 50° smooth chute, Runs 25-30: 50° stepped chute]. 149

6.33 Streamwise development of depth-averaged air concentration C_a; [Runs 1-9: 30° smooth chute, Runs 10-15: 30° stepped chute, Runs 16-24: 50° smooth chute, Runs 25-30: 50° stepped chute]. 149

6.34 Streamwise development of bottom air concentration C_b; [Runs 1-9: 30° smooth chute, Runs 10-15: 30° stepped chute, Runs 16-24: 50° smooth chute, Runs 25-30: 50° stepped chute]. 150

6.35 Streamwise development of (a) dimensionless maximum air-phase frequency $F_{max}h_1/V_1$, (b) dimensionless secondary air-phase frequency $F_{sec}h_1/V_1$, (c) dimensionless vertical position of maximum air-phase frequency Z_{Fmax}, (d) dimensionless vertical position of secondary air-phase frequency Z_{Fsec}; [Runs 1-9: 30° smooth chute, Runs 10-15: 30° stepped chute, Runs 16-24: 50° smooth chute, Runs 25-30: 50° stepped chute]. 152

6.36 Streamwise development of (a) dimensionless characteristic flow depth Z_{90} and (b) dimensionless clear-water depth Z_{cw}; [Runs 1-9: 30° smooth chute, Runs 10-15: 30° stepped chute, Runs 16-24: 50° smooth chute, Runs 25-30: 50° stepped chute] 153

6.37 Dimensionless vertical velocity distributions V/V_1 along the stilling basin for: (a) Run 22 (50° smooth chute) and (b) Run 25 (50° stepped chute). 154

6.38 Dimensionless vertical velocity distributions $(V - V_{rec})/(V_{max} - V_{rec})$ within advective diffusive zone for 50°: (a) smooth chute and (b) stepped chute approach flows; [Runs 16-24: 50° smooth chute, Runs 25-30: 50° stepped chute]. 155

6.39 Streamwise development of dimensionless: (a) maximum velocity $(V_{max} - V_2)/(V_2 - V_1)$, (b) elevation of maximum velocity Z_{Vmax}, (c) mean recirculation velocity $(|V_{rec,a}| - V_2)/(V_1 - V_2)$, and (d) elevation of flow reversal onset Z_{V0}; [Runs 1-9: 30° smooth chute, Runs 10-15: 30° stepped chute, Runs 16-24: 50° smooth chute, Runs 25-30: 50° stepped chute]. 156

7.1 General definition scheme of the design example. 167

7.2 Streamwise development of mean flow depth η and characteristic flow depth z_{90} along the stilling basin downstream of a: (a) stepped, and (b) smooth chute; q=12.5 m^2/s, $\varphi = 50°$ and $H_{dam} = 50$ m. 172

7.3 Streamwise development of bottom: (a) mean pressure p_m, extreme maximum pressure p_{max}, pressure with 99.9% probability p_{99}, extreme minimum pressure p_{min} and pressure with 0.1% probability $p_{0.1}$ for smooth chute, (b) mean pressure p_m, extreme maximum pressure p_{max}, pressure with 99.9% probability p_{99}, extreme minimum pressure p_{min} and pressure with 0.1% probability $p_{0.1}$ for stepped chute), (c) fluctuating pressure p' for smooth chute and (d) fluctuating pressure p' for stepped chute; q=12.5 m^2/s, $\varphi = 50°$ and $H_{dam} = 50$ m. 175

List of Tables

3.1 Position of the pressure transmitters at the stilling basin channel centerline (Figure 3.2). 55
3.2 Test program. SM=smooth chute, R=smooth chute roughened with grid; PA=smooth chute roughened with grid and pre-aeration, ST=stepped chute. 61
3.3 Criteria to minimize scale effects for air-water flows under Froude similitude. . 62

4.1 Test program for 30° sloping chutes. SM=smooth chute, R=smooth chute roughened with grid; PA=smooth chute roughened with grid and pre-aeration, ST=stepped chute. 66
4.2 Coefficients of Eq. (4.6). 82
4.3 Coefficients of Eq. (4.7). 82

5.1 Test program for air-water flow measurements for a stilling basin preceded by 30° sloping smooth and stepped chutes. SM=smooth chute, R=smooth chute roughened with grid; PA=smooth chute roughened with grid and pre-aeration, ST=stepped chute. 90

6.1 Test program for plain stilling basin preceded by 30° and 50° sloping chutes. SM=smooth chute; R=smooth chute roughened with grid; PA=smooth chute roughened with grid and pre-aeration; ST=stepped chute; *s*=step size. 118
6.2 Coefficients of Eq. (6.3). 139

A.1 Data of recorded tailwater depths h_2, roller lengths from flow depth measurements $L_{R,\eta}$ and visual observation $L_{R,D}$, jump lengths from flow depths $L_{J,\eta'}$ and pressure $L_{J,p'}$, and $L_{J,SK}$ measurements for plain stilling basin. 177

List of Symbols

Roman

a	coefficient	[-]
B	channel width	[m]
b	coefficient	[-]
c	coefficient	[-]
C	local air concentration	[-]
$C_H{}'$	flow depth fluctuation coefficient	[-]
C_{min}	minimum air concentration in the shear layer region	[-]
C_{max}	maximum air concentration in the shear layer region	[-]
$C_P{}'$	pressure fluctuation coefficient	[-]
$C_P{}^{def}$	mean pressure coefficient at deflection point	[-]
$C_P{}^{max}$	extreme maximum pressure coefficient	[-]
$C_P{}^{min}$	extreme minimum pressure coefficient	[-]
$C_P{}^{0.1}$	minimum pressure coefficient with 0.1% probability	[-]
$C_P{}^{99.9}$	maximum pressure coefficient with 99.9% probability	[-]
C_a	mean air concentration in the stilling basin	[-]
C_b	bottom air concentration	[-]
$C_{b,ce}$	bottom air concentration at the inflow section	[-]
C_{mean}	depth averaged air concentration	[-]
$C_{mean,i}$	depth averaged air concentration at the inception point	[-]
C_u	mean air concentration in quasi-uniform flow	[-]
C_1	mean air concentration at the inflow section	[-]
c	coefficient	[-]
D_a	apparent time-averaged diffusivity	[m^2/s]

D_h	hydraulic radius	[m]
D'	dimensionless turbulent diffusivity	[-]
D_t^s	turbulent diffusivity in the shear layer	[m^2/s]
D_t^r	turbulent diffusivity in the recirculating region	[m^2/s]
d	coefficient	[-]
E	specific energy	[m]
E_{res}	residual energy	[m]
e	coefficient	[-]
F_1	inflow clear water Froude number	[-]
F	air-phase frequency	[Hz]
F_{max}	maximum air-phase frequency	[Hz]
F_s	step height Froude number	[-]
F_{sec}	secondary peak of the air-phase frequency	[Hz]
f	frequency	[Hz]
f_D	Darcy-Weisbach friction factor	[-]
g	acceleration due to gravity	[m/s^2]
H_{dam}	dam height	[m]
H_k	kinetic energy at the inflow section	[m]
h_c	critical flow depth	[m]
h_{cw}	equivalent clear water flow depth	[m]
$h_{cw,i}$	equivalent clear water flow depth at the inception point	[m]
h_i	mixture flow depth at the inception point	[m]
h_{sw}	sidewall height	[m]
h_1	clear water depth at the inflow section	[m]
h_2	tailwater depth	[m]
h_{90}	mixture flow depth	[m]
I_1	inertial forces at section 1-1	[kg/(m s^2)]
I_2	inertial forces at section 2-2	[kg/(m s^2)]
j	coefficient	[-]
K	excess kurtosis	[-]
K'	integration constant	[-]

K''	integration constant	[-]
k	coefficient	[-]
k_s	concrete surface roughness	[m]
L_i	streamwise position of the inception point	[m]
L_J	hydraulic jump length	[m]
$L_{J,p'}$	hydraulic jump length obtained from streamwise distribution of pressure fluctuations	[m]
$L_{J,SK}$	hydraulic jump length obtained from streamwise distribution of skewness and excess kurtosis	[m]
$L_{J,\eta'}$	hydraulic jump length obtained from the streamwise distribution of flow depth fluctuations	[m]
L_R	roller length	[m]
$L_{R,D}$	visually observed roller length	[m]
$L_{R.\eta}$	roller length obtained from flow depth measurements	[m]
l	coefficient	[-]
M	coefficient	[-]
m	coefficient	[-]
N	coefficient	[-]
n	number of samples	[-]
P_m	mean pressure coefficient	[-]
P_{xx}	power spectral density	[m^2/Hz]
P_1	pressure force at section 1-1	[kg/(m s^2)]
P_2	pressure force at section 2-2	[kg/(m s^2)]
p_{def}	mean pressure at deflection point	[m]
p_i	pressure at a given instance	[m]
p_m	mean pressure	[m]
p_{min}	extreme maximum pressure	[m]
p_{max}	extreme minimum pressure	[m]
p_{vap}	vapor pressure	[m]
$p_{0.1}$	minimum pressure with 0.1% probability	[m]
$p_{99.9}$	maximum pressure with 99.9% probability	[m]
p'	pressure fluctuation	[m]

Q	discharge	[m^3/s]
Q_d	design discharge	[m^3/s]
q	unit discharge	[m^2/s]
q_d	design unit discharge	[m^2/s]
R^2	coefficient of determination	[-]
R_1	Reynolds number	[-]
r	coefficient	[-]
S	skewness	[-]
s	step height	[m]
V	local velocity	[m/s]
V_{max}	maximum velocity	[m/s]
V_{mean}	mean equivalent clear water flow velocity	[m/s]
V_{rec}	local recirculation velocity	[m/s]
$V_{rec,a}$	depth averaged recirculation velocity	[m/s]
V_1	clear water velocity at the inflow section	[m/s]
V_2	mean velocity in the tailwater	[m/s]
V_{90}	mixture velocity at $y(C{=}0.9)$	[m/s]
W_1	inflow clear water Weber number	[-]
w	coordinate parallel to the chute (pseudo) bottom starting at the intersection of chute (pseudo) bottom and stilling basin invert	[m]
X_J	dimensionless streamwise coordinate x/L_J	[-]
x	horizontal coordinate starting at the intersection of chute (pseudo) bottom and stilling basin invert	[m]
x_c	streamwise coordinate from the crest	[m]
y	vertical coordinate perpendicular to and starting at the chute (pseudo) bottom	[m]
y_{90}	characteristic flow depth up to $y(C{=}0.9)$	[m]
Z	dimensionless flow depth in the stilling basin	[-]
Z_{Cmax}	dimensionless elevation of the maximum air concentration	[-]
Z_{cw}	dimensionless equivalent clear water depth	[-]
Z_{Fmax}	dimensionless elevation the maximum air-phase frequency	[-]

Z_{Fsec}	dimensionless elevation of the secondary peak of the air-phase frequency	[-]
Z_{max}	dimensionless elevation of maximum air concentration	[-]
Z_{min}	dimensionless elevation of minimum air concentration	[-]
Z_{V0}	dimensionless elevation of flow reversal onset	[-]
Z_{50}	dimensionless characteristic flow depth z_{50}	[-]
Z_{70}	dimensionless characteristic flow depth z_{70}	[-]
Z_{90}	dimensionless characteristic flow depth z_{90}	[-]
z	vertical coordinate perpendicular to stilling basin invert	[m]
z_i	vertical distance between dam crest and inception point	[m]
z_{cw}	clear water depth	[m]
z_{Fmax}	vertical position of the maximum air-phase frequency	[m]
z_{Fsec}	vertical position of the secondary peak of the air-phase frequency	[m]
z_{max}	vertical position of the maximum air concentration	[m]
z_{min}	vertical position of the minimum air concentration	[m]
z_{Vmax}	vertical position of the maximum velocity	[m]
z_{V0}	vertical position of the flow reversal onset	[m]
$z_{0.5}$	vertical position in the stilling basin where $V{=}V_{max}/2$	[m]
z_{50}	characteristic flow depth defined up to $z(C{=}0.5)$	[m]
z_{70}	characteristic flow depth defined up to $z(C{=}0.7)$	[m]
z_{90}	characteristic flow depth defined up to $z(C{=}0.9)$	[m]
$z_{90,max}$	maximum characteristic flow depth defined up to $z(C{=}0.9)$	[m]

Greek

α	kinetic energy correction coefficient	[-]
δ_{bl}	turbulent boundary layer thickness	[m]
η	mean flow depth in the stilling basin	[m]
η_{max}	maximum mean flow depth in the stilling basin	[m]
η'	flow depth fluctuation in the stilling basin	[m]
Λ	jump efficiency	[-]
ν	water kinematic viscosity	[m^2/s]

ρ	water density	[kg/m^3]
σ	water surface tension	[kg/m^3]
φ	chute slope	[°]

1 Introduction

Dams are hydraulic structures built to create a reservoir, hydraulic head or water surface (Vischer and Hager 1998). All dams must be designed to safely discharge waters without jeopardizing the dam structure or surroundings. Therefore, every dam must have a flood releasing facility (i.e. spillway) which conveys floods from the reservoir to the downstream river and dissipates kinetic energy of the flow. A traditional spillway layout features a smooth chute, solely serving as a conveyor of floods, and a stilling basin in which kinetic energy of the flow is dissipated and safely released into the downstream river by means of a hydraulic jump (Figure 1.1).

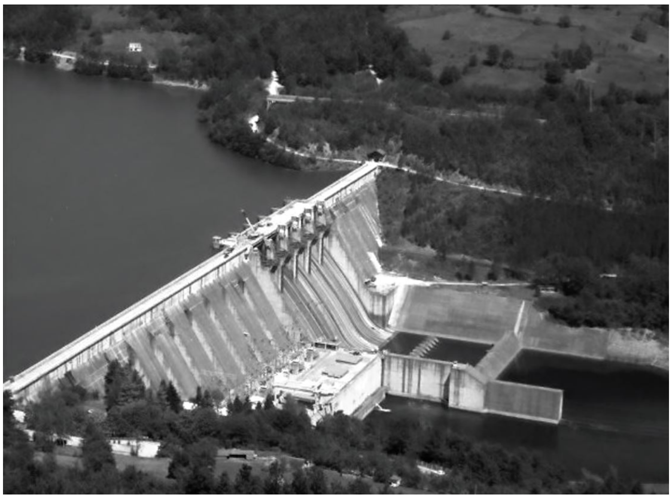

Figure 1.1 – Bajina Basta dam, Serbia. Spillway consisting of a gated ogee crest followed by a smooth chute with energy dissipation in a stilling basin.

A hydraulic jump is a rapidly varied hydraulic phenomenon, in which supercritical flow transforms into subcritical flow. Hydraulic jump with a marked roller is characterized by macro turbulence with large pressure and velocity pulsations, intensive air entrainment/detrainment, high rate of energy dissipation, spray and surface wave generation (Hager 1992; Chanson

2015b). Since its energy dissipation rate may reach up to 85% (Peterka 1958), hydraulic jumps i.e. stilling basins have been widely utilized as a measure for energy dissipation in spillway systems.

Stepped chutes (Figure 1.2) are one type of flood transporting facility at dams which has been used for more than 3000 years (Chanson 2015b). In the first half of 20th century the first standardized stilling basin types were developed. Stepped spillways built with masonry at dam abutments became outdated. However, in the last several decades, due to the advancements in RCC (Roller Compacted Concrete) construction technique, stepped spillways are frequently built directly on the downstream dam face. A key hydraulic feature of a stepped chute, compared to a smooth chute, is the enhanced energy dissipation resulting in a reduced residual energy at the chute end. However, even stepped chutes do not provide enough energy dissipation and an adequately designed dissipation structure is still required at the chute end.

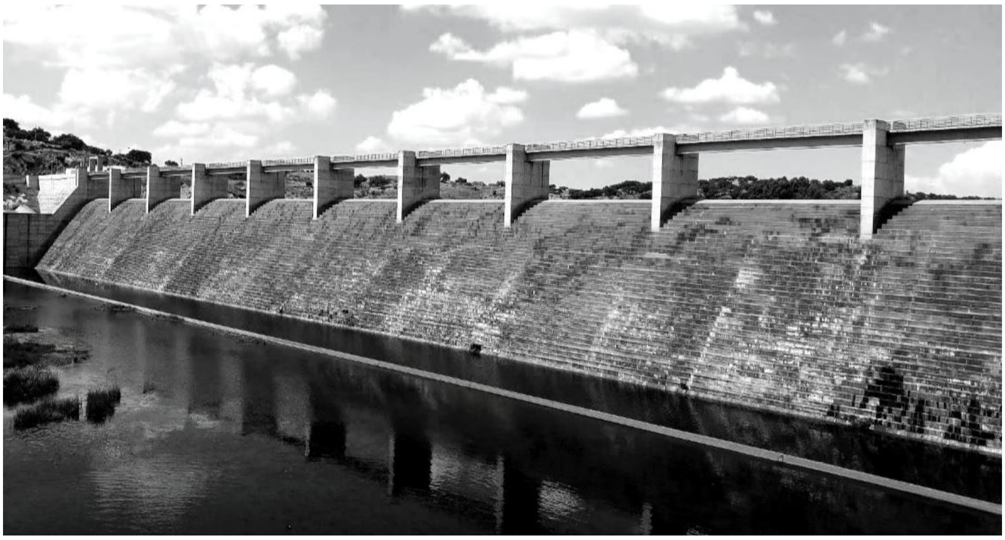

Figure 1.2 – Pedrógão dam, Portugal.

As example, the recent flood event at Paradise dam in Australia (Figure 1.3a) may be mentioned. The latter, commissioned in 2005, is a 37 m high RCC gravity dam equipped with a 315 m wide and 57° sloping stepped chute at its downstream face, followed by a 20 m long stilling basin with a 1 m high vertical end sill. In the beginning of 2013, the spillway operated for three months with peak unit discharge reaching some 54.3 m^2/s (equivalent to a flood return period of 180 years). The follow-up inspection revealed massive damages to the stilling basin apron (Figure 1.3b) with complete destruction of the end sill (Figure 1.3b). Pronounced downstream scouring occurred with local depths of 15 m below the apron elevation and progressing towards dam foundation (Figure 1.3c). A 7 tons end sill piece was found some 150 meters downstream of its original location (Bollaert et al. 2016; McDonald 2013).

Stepped chute hydraulics was extensively investigated, for example by Amador et al. (2006), Amador et al. (2009), Boes and Hager (2003a), Boes and Hager (2003b), Chamani and Rajaratnam (1999), Chanson and Toombes (2002), Chanson and Toombes (2004), Felder and Chanson (2016), Frizell (2006), Hunt and Kadavy (2014), Kramer and Chanson (2018), Matos et al. (2000), Meireles and Matos (2009) and Zhang and Chanson (2017) among others. These studies resulted in empirical and analytical relationships with which flow properties along the chute, such as air concentration, velocity, flow depth, pressure etc., can be reliably estimated. However, only a few studies focused on the hydraulic behavior of stilling basins in combination with stepped chutes (e.g. Meireles et al. 2005, Cardoso et al. 2007, Meireles et al. 2010, Bung et al 2012, Frizell and Svodoba 2012, Frizell et al. 2016, and Novakoski et al 2017a,b). Consequently, design guidelines developed for stilling basins below smooth chutes are still considered for stilling basins preceded by stepped chutes. As the stepped surface significantly alters the structure of the flow leading to higher turbulence levels, as compared to those of smooth chute spillways (Amador et al. 2006), such practice is questionable. Presently, there is still insufficient information available on the stilling basin performance downstream of stepped chutes.

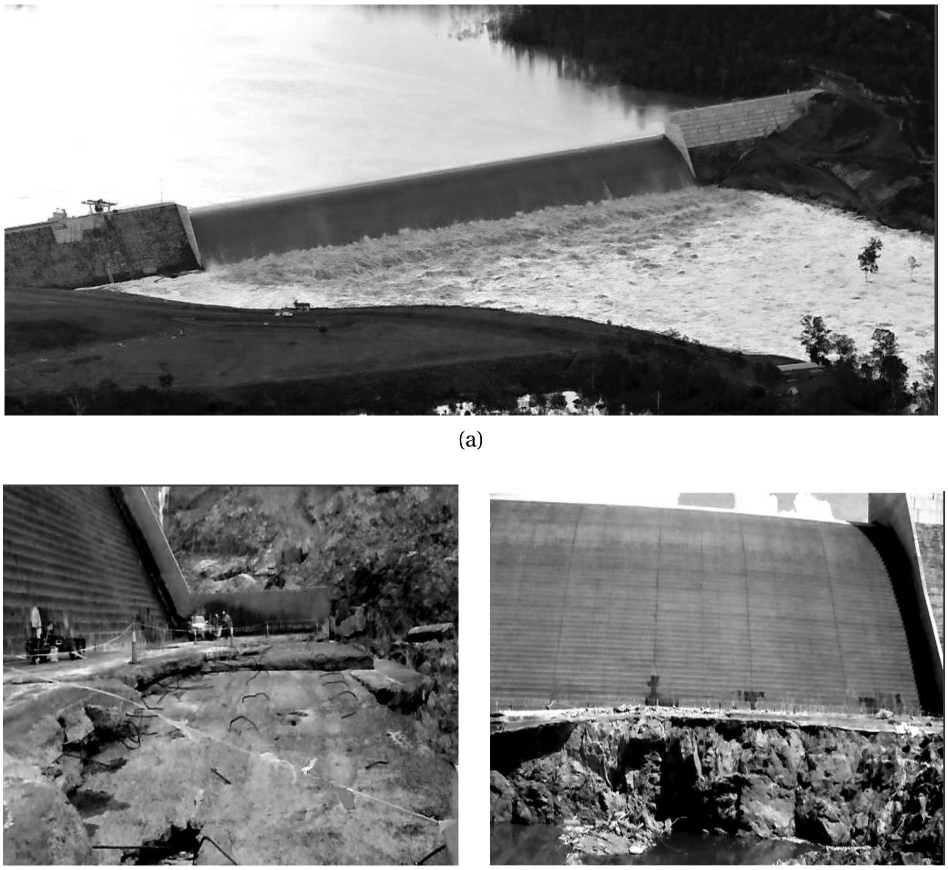

(a)

(b)

(c)

Figure 1.3 – Paradise dam, Australia, 2013 flood event : (a) Stepped spillway in operation (www.news-mail.com.au/news/sunwater-gives-answers-on-Paradise-Dam/1944448), (b) sideview of the damaged stilling basin (McDonald 2013) and (c) downstream view of the scour hole (McDonald 2013).

1.1 Objectives

The objective of this research project is to investigate the effect of stepped chute approach flows on the performance and hydraulic characteristics of a plain stilling basin (i.e. basin without appurtenances). The detailed main goals the present research project can be summarized as:

- Investigate the effect of stepped chute approach flows on the hydraulic characteristics of the stilling basin,
- Define the length of necessary bottom protection, i.e. the stilling basin length,
- Describe dynamic bottom pressure characteristics relevant for the assessment of the hydrodynamic loading,
- Describe free surface development and define required tailwater depth to maintain the hydraulic jump within the stilling basin perimeter,
- Describe air-water flow properties of the hydraulic jump,
- Investigate the effect of aerated inflows,
- Investigate the effect of chute slope, and
- Give practical recommendations for the design of the stilling basins downstream of stepped chutes.

To achieve these goals, a comprehensive experimental campaign was performed to measure parameters relevant for assessment of the stilling basin performance, such as approach flow conditions, flow depths, dynamic bottom pressures and air-water flow properties of the hydraulic jump. The experimental campaign included both smooth and stepped chute approaches, allowing direct comparison of the stilling basin performance. To address the influence of aerated inflows, approach flow aeration for smooth chute test runs was varied. Moreover, the chute slope was varied to study its effect on the performance and flow characteristics of the stilling basin.

1.2 Structure of the report

This thesis report is divided into seven chapters:

- *Chapter 1* introduces the general problematic and gap of knowledge in the hydraulic performance of stilling basins downstream of stepped chutes,
- *Chapter 2* presents literature review on stepped chute and stilling basin hydraulics. Furthermore, an overview of existing studies on stilling basin performance downstream of stepped chutes is presented,
- *Chapter 3* describes the experimental facility and instrumentation used in the present study. In addition, the experimental campaign and measurement procedure are detailed,
- *Chapter 4* focuses on the effect of 30° sloping stepped chute approach flows on the performance and flow characteristics of a plain stilling basin,
- *Chapter 5* presents the air-water flow properties of a plain stilling basin preceded by 30° sloping smooth and stepped chutes,
- *Chapter 6* addresses the effect of chute slope on the performance and flow characteristics of a plain stilling basin,
- *Chapter 7* summarizes the key findings with design recommendations and presents an outline for the future work on stilling basins downstream of stepped chutes. Moreover a practical design example of a plain stilling basin downstream of a smooth and stepped chute is presented.

Finally, the *Appendices* provide supplementary experimental data and test sheets of experimental runs. Chapters 4 to 6 have been prepared as publications for reviewed scientific journals.

2 State-of-the-art

The state of the art is divided into five main parts. The first part gives a brief overview of the *stepped chute* hydraulics, focusing on the characteristics relative to the present study. The second part describes flow features of *hydraulic jumps and stilling basins.* The third part briefly describes *standard stilling basin types.* The fourth part gives an overview of existing studies on the *stilling basin performance downstream of stepped chutes.* Finally, in the fifth part, the *gaps in knowledge* and *specific research questions* are detailed.

2.1 Overview on stepped chute hydraulics

Since the introduction of the RCC construction technique the number of built stepped spillways has notably increased. The first experimental studies on stepped spillways were conducted in the 1960s (Hager and Pfister 2013). In following decades, numerous experimental studies were performed (e.g. Tozzi 1992, Chanson 1994, Boes 2000c, Matos 2000, Matos et al. 2001, Toombes 2002, Boes and Hager 2003b, André 2004, Gonzales 2005, Amador et al. 2006, Frizell 2006, Bung 2011, Pfister and Hager 2011, Meireles et al. 2012, Hunt and Kadavy 2013, and Kramer and Chanson 2018).These studies mainly focused on the two-phase flow features, aiming to provide better design guidelines in terms of: air entrainment, air concentrations, velocity distributions, flow depths, hydrodynamic pressure acting on the steps, flow resistance and energy dissipation. This subchapter gives a brief overview of, among others, the above mentioned studies and key findings relative to the present study.

2.1.1 Flow regimes

Flow over a stepped chute, depending upon discharge Q, can be divided into (Figure 2.1):

- nappe flow regime,
- transition flow regime,
- skimming flow regime.

The nappe flow regime occurs for low discharges where the flow drops from one step to the next one as a falling jet (Figure 2.1a) and can be divided in three subtypes (Essery and Horner 1978; Peyras et al. 1992): (1) isolated nappe flow with fully developed hydraulic jump, (2) isolated nappe flow with partially developed hydraulic jump and (3) partial nappe flow. The energy dissipation occurs mainly by jet breakup in the air, jet impact onto the step and formation of a hydraulic jump on the step (Chanson 2015b). Authoritative reviews on nappe flow regime can be found in: Horner (1969), Essery and Horner (1978), Chamani and Rajaratnam (1994), Rajaratnam and Chamani (1995), Toombes and Chanson (2000), Chanson (2002), Toombes (2002) and Chanson (2015b).

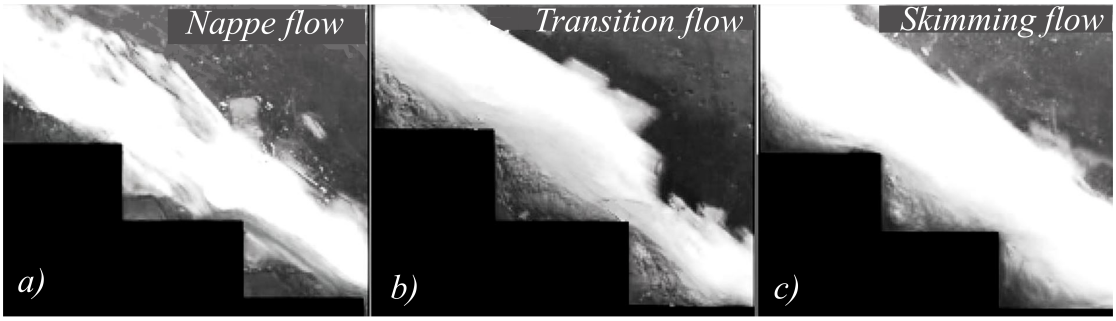

Figure 2.1 – Flow regimes over a stepped chute (adapted from André (2004)).

For intermediate discharges *the transition flow* regime can be observed (Figure 2.1b). The main features of the transition flow regime are intense splashing, strong hydrodynamic fluctuations and free-surface aeration. The transition flow regime is further characterized by flow instabilities and significant streamwise variations of flow properties at each step, thus it is recommend to avoid this regime for medium to high operating discharges (Chanson 2015b). For more information on transition flow regime, reference may be made to Elviro and Mateos (1995), Ohtsu and Yasuda (1997), Chanson (2001), Matos (2001), Chanson (2002) and Chanson and Toombes (2004) .

For large discharges the *skimming flow regime* occurs, where flow over stepped chute skims over a pseudo bottom, formed by step edges, as a coherent stream (Figure 2.1c). In the step cavities, beneath the pseudo bottom, a secondary flow in form of three dimensional recirculating eddies are formed and maintained by the transfer of shear stress from the adjacent flow (Chanson 1997). Most of the kinetic energy is dissipated to maintain the cavity circulation (Chanson 2015b). In skimming flow regime, the direction of the main flow is mostly parallel to the pseudo-bottom, however a portion of the flow deflects and impacts the region near the step edge of the horizontal step face (Takahashi and Ohtsu 2012). As skimming flow regime occurs for relatively high discharges, most stepped chutes are designed to operate in skimming flow regime.

A large number of studies focused on defining the limits between the flow regimes, e.g. Rajaratnam and Chamani (1995), Yasuda and Ohtsu (1999), Chanson (2002), Boes and Hager (2003a), André (2004) and Chanson (2015b) . These studies showed that the onset of transition and skimming flow regime is mainly governed by the step configuration, i.e. step height s and length l and the unit discharge q represented as h_c/s, where h_c is the critical flow depth. The regime limits suggested by Chanson (2015b) are illustrated in Figure 2.2.

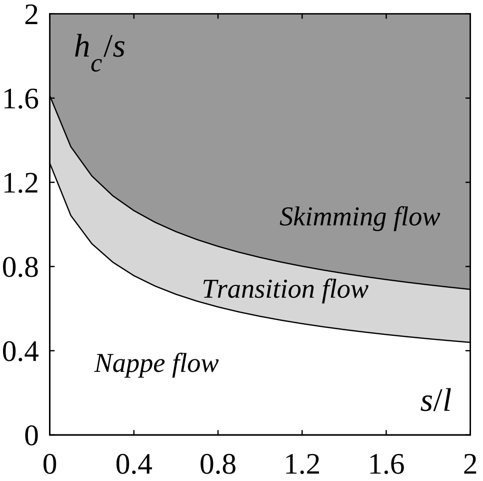

Figure 2.2 – Flow regime limits proposed by Chanson (2015b) as a function of dimensionless critical depth h_c/s and step configuration s/l.

2.1.2 Definition of basic air-water flow terms

Self-aerated flows are characterized by high rate of air entertainment giving it a white appearance typically known as "white waters". A schematic representation of the fully developed air-water flow structure down a stepped chute is shown on Figure 2.3. When studying self-aerated flows, the flow properties have to be characterized by taking into account the entrained air. The studies on air-water flows are typically performed with phase detection instruments giving, among others, local air concentration C and local air-water flow velocity V. The local air concentration is defined as the volume of air per unit volume of air and liquid. The measurements are typically performed between the bottom and the characteristic mixture flow depth y_{90} [m], where the local air concentration is C=0.9 (Figure 2.3), satisfying the continuity equation. The depth y_{90} is commonly defined as the location of the "free surface" (Straub and Anderson 1958; Wood 1983; Chanson 2002).

Using the measured air concentration and flow velocity profiles, following two-phase flow parameters, typically used to describe the self-aerated flows, can be obtained:

- The depth averaged air concentration C_{mean}, defined as:

$$C_{mean} = \int_0^{y_{90}} C\,dy \tag{2.1}$$

- The equivalent clear water flow depth h_{cw}, defined as:

$$h_{cw} = \int_0^{y_{90}} (1-C)\,dy = (1-C_{mean})\,y_{90} \tag{2.2}$$

- The mean equivalent clear water velocity V_{mean}, defined as:

$$V_{mean} = \frac{\int_0^{y_{90}} (1-C)\,V\,dy}{\int_0^{y_{90}} (1-C)\,dy} = \frac{q}{h_{cw}} \tag{2.3}$$

  where q is the water discharge per unit width.

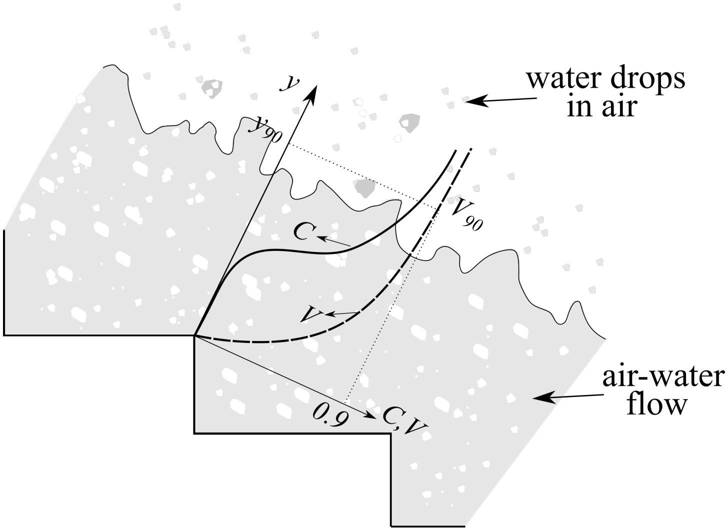

Figure 2.3 – Definition sketch of air-water flow properties over a stepped chute.

2.1.3 Skimming flow regime

Skimming flows over stepped chutes exhibit an appearance very similar to those of self-aerated flows over a smooth chute invert (Wood 1991; Chanson 1997). Four different developing flow regions are distinguished (Figure 2.4):

- non-aerated flow region
- partially developed aerated flow region
- fully developed aerated flow region
- quasi-uniform flow region.

At the upstream end, in the *non-aerated flow region*, flow is smooth and glassy and there is no air entrainment. A turbulent boundary layer develops from the crest along the chute. If the chute is long enough, the turbulent boundary layer reaches the flow surface and air is entrained from the surface into the flow (Wood 1991). The onset point of the flow self-aeration is usually called *inception point*. Downstream of the inception point, in the *partially developed aerated flow region*, air is rapidly entrained into the flow. In the *fully developed aerated flow region*, continuous flow aeration is observed and flow properties gradually vary. Far downstream, the flow tends to reach *quasi uniform flow* conditions, where flow properties are quasi invariant with distance.

Non aerated flow region and inception point

When water discharges from a reservoir over the ogee crest, its surface is smooth and glassy. Flow depth decreases streamwise due to flow acceleration. The turbulent boundary layer grows gradually from the dam crest and its thickness δ_{bl} development, similarly to the smooth chute flows, can be expressed as (Bauer 1953; Cain and Wood 1981; Chanson 2002):

$$\frac{\delta_{bl}}{x_c} = a\left(\frac{x_c}{k}\right)^{-b} \tag{2.4}$$

with x_c as the streamwise coordinate from the crest, $k = s\cos\varphi$ as the step roughness and a and b as coefficients. The growth of the turbulent boundary layer for stepped chute flows was, among others, studied by Tozzi (1992), Chanson (2002), Meireles and Matos (2009) and Meireles et al. (2012). These studies have demonstrated that the turbulent boundary layer develops roughly two to three times faster for stepped chute flows, as compared to the smooth chute flows, thus resulting in earlier self-aeration of the flow.

Near the dam crest the depth averaged air concentrations C_{mean} tends to zero (Pfister and Boes 2014). With the increasing distance from the dam crest the C_{mean} increases due to the free surface instabilities, leading to the entrapment of air (Meireles and Matos 2009; Meireles et al. 2012). Relations for streamwise development of mean air concentration and equivalent clear water depth in non aerated flow region were presented by Meireles et al. (2012).

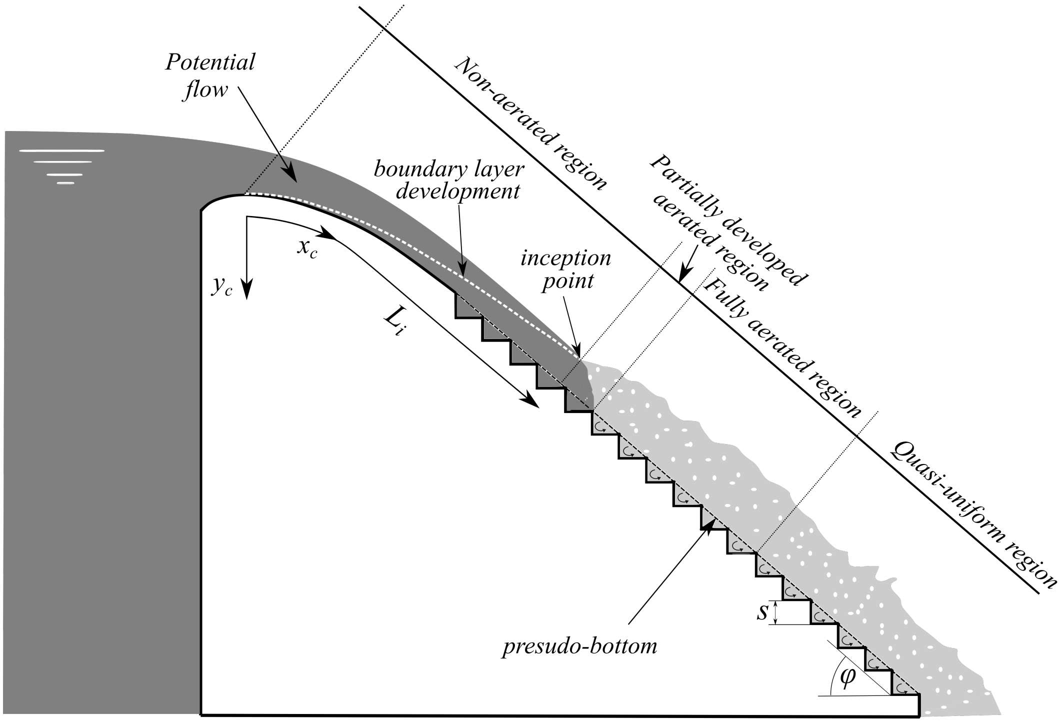
Potential flow
boundary layer development
Non-aerated region
Partially developed aerated region
Fully aerated region
Quasi-uniform region
inception point
x_c
y_c
L_i
s
φ
presudo-bottom

Figure 2.4 – Definition scheme of skimming flow regime over a stepped chute.

When the outer edge of the turbulent boundary layer reaches the free surface, the turbulent energy of the vortices are strong enough to overcome surface tension, and consequently free surface aeration takes place at the *inception point* (Figure 2.4 and 2.5).

In terms of stepped chute design the location of inception point is important, as it delimits the reach of the chute prone to cavitation damage. As such, numerous studies have been performed to determine its streamwise position L_i and flow properties such as mean air concentration $C_{mean,i}$, mixture flow depth h_i and equivalent clear water depth $h_{cw,i}$ (e.g. Chamani (2000), Matos et al. (2000), Chanson (2002), Boes and Hager (2003b), Chanson (2006) Gonzalez and Chanson (2007), André et al. (2008), Amador et al. (2009), Felder and Chanson (2009b), Bung (2011), Hunt and Kadavy (2011), Pfister and Hager (2011), Meireles et al. (2012) and Hunt and Kadavy (2013)). Due to the unsteadiness of the free surface and developing turbulent boundary layer, the location of inception point is constantly fluctuating in time (Pfister and Hager 2011).

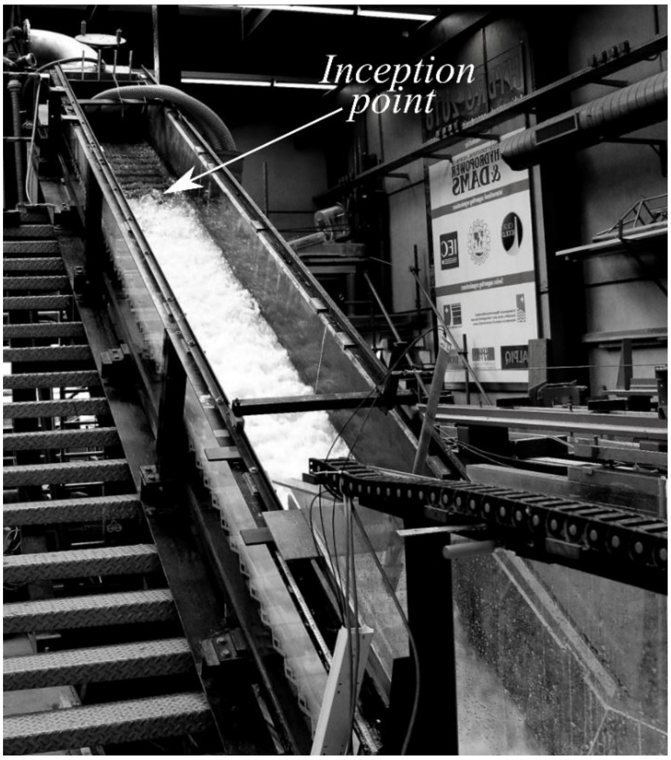

Figure 2.5 – Downstream view of φ=30° sloping stepped chute at LCH operating in skimming flow regime.

Several definitions and methods have been used to define its streamwise position (Meireles 2011):

- As the location where air is present across the flow depth including the step cavities,
- As the location with bottom air concentration C_b equal to 1%,
- As the location with depth averaged air concentration equal to 20%,
- As the location where the outer edge of turbulent boundary layer intersects the free surface.

Onset of air entrainment was found to be mainly dependent on: (1) step size s, (2) chute slope φ, (3) unit discharge q and (4) intake type (i.e. pressurized or free overflow). Large step heights, steep slopes and pressurized intakes tend to reduce the length to the inception point, whereas higher discharges tend to increase it (Chanson 2006; Matos and Meireles 2014). Empirical relations for predicting flow characteristics at the inception point were, among other, proposed by Matos et al. (2000), Chanson (2002), Boes and Hager (2003a), André et al. (2008), Amador et al. (2009) and Meireles et al. (2012).

Aerated flow regions

Downstream of the inception point, large quantities of air are entrained via the free surface. In the *partially developed aerated flow region*, rapid flow aeration is observed and thus flow properties charge very rapidly. The main features of this region are intense splashing, flow bulking and high air entrainment in the vicinity of the flow surface (Gonzalez 2005). Due to the turbulent nature of the flow, air is transported across the flow depth, and flow rapidly becomes fully aerated. In the *fully developed aerated flow* region, the mixture flow depth h_{90} and the mean air concentration C_{mean} tend to increase down the chute. Relations for streamwise development of C_{mean}, h_{90} and h_{cw} in partially and fully developed aerated flow regions was, among others, proposed by Boes (2000c), Matos (2000), Bung (2011), Pfister and Hager (2011) and Takahashi and Ohtsu (2014).

If the chute is long enough, the flow reaches quasi-equilibrium state, in which the flow properties such as mean air concentration, mean flow velocity and flow depths are quasi-invariant with distance. In this *quasi-uniform flow region*, it is assumed that the quantity of air transported in the flow is close to maximum, namely at the saturation air concentration (André 2004).

Several studies focused on defining the streamwise location at which the quasi uniform flow conditions are attained (e.g. Christodoulou (1999), Boes (2000a), Matos et al. (2001), Boes and Hager (2003a), Ohtsu et al. (2004), Bung (2011) and Pfister and Hager (2011)). Matos et al. (2001) used a dimensionless length to inception point $(x_c - L_i)/L_i$ and suggested that if $(x_c - L_i)/L_i$ is greater than 100, the quasi uniform flow conditions will be attained. According to Boes and Hager (2003a) the location of the quasi uniform region is attained at certain vertical distance from the dam crest $H_{dam,u}$, which is a function of the chute slope φ and critical flow depth h_c as:

$$\frac{H_{dam,u}}{h_c} \approx 24\left(\sin\varphi\right)^{2/3} \tag{2.5}$$

More recently, Bung (2011) and Pfister and Hager (2011) obtained that the distance to the quasi uniform flow region starts roughly at two to three times the distance to the inception point L_i.

The quasi-uniform flow is typically characterized by its mean air concentration C_u, characteristic flow depth $y_{90,u}$ and equivalent clear water depth $h_{cw,u}$. Boes (2000c) proposed two set of equations for predicting C_u for steeply sloped chutes:

$$C_u = 0.43 - 0.00234F_s \qquad \text{for } \varphi = 30° \tag{2.6}$$

$$C_u = 0.6 - 0.00611F_s \qquad \text{for } \varphi = 50° \tag{2.7}$$

with F_s as step height Froude number defined as:

$$F_s = \frac{q}{\sqrt{g \sin\varphi s^3}} \tag{2.8}$$

For 30° sloping stepped chutes André (2004) proposed:

$$C_u = 0.55 \left(\sin\varphi\right)^{-0.12} \qquad \text{for } F_s < 4 \tag{2.9}$$

$$C_u = 0.81 \left(\sin\varphi\right)^{0.81} \qquad \text{for } F_s > 4 \tag{2.10}$$

Takahashi and Ohtsu (2012) suggested an empirical relation as a function of chute slope φ and relative critical depth h_c/s, adapted from Wilhelms and Gulliver (2005) for smooth chute flows:

$$C_u = 0.073 + \left(\frac{6.9}{\varphi} - 0.12\right)\frac{s}{h_c} + 0.656\left(1 - \mathrm{e}^{-0.0356(\varphi-10.9)}\right) \tag{2.11}$$

with φ as the chute slope in degrees.

Multiple studies have demonstrated that the values of C_u for stepped chutes are very similar to those observed for quasi-uniform flows on smooth chutes (e.g. Matos (1999), Chanson (1994) and Boes and Hager (2003a)). Typically used expressions for predicting depth-averaged air concentration C_u for quasi-uniform smooth chute flows are listed below.

Hager (1991):

$$C_u = 0.75 \left(\sin\varphi\right)^{0.75} \tag{2.12}$$

Chanson (1994):

$$C_u = 0.9 \sin\varphi \tag{2.13}$$

Wilhelms and Gulliver (2005):

$$C_u = 0.073 + 0.656\left(1 - \mathrm{e}^{-0.0356(\varphi-10.9)}\right) \tag{2.14}$$

with φ as the chute slope in degrees.

For steeply sloped stepped chutes, i.e. 30°≤φ≤50°, Boes and Hager (2003b) proposed the following relations for predicting the characteristic flow depth $y_{90,u}$ and the equivalent clear water depth $h_{cw,u}$:

$$\frac{y_{90,u}}{s} = 0.5F_s^{-0.1\tan\varphi+0.5} \tag{2.15}$$

$$\frac{h_{cw,u}}{s} = 0.23F_s^{0.65} \tag{2.16}$$

Air concentration profiles

The air concentration distribution at the step edge perpendicular to the pseudo-bottom exhibits a smooth continuous S-shaped profile (Figure 2.3) very similar to that measured for high velocity smooth chute flows (Chanson 2002). For self-aerated smooth chute flows, Chanson (1997) proposed an analytical solution of the advection-diffusion equation for describing the air concentration profiles:

$$C = 1 - \tanh^2\left(K' - \frac{y}{2D'y_{90}}\right) \tag{2.17}$$

with D' as dimensionless turbulent diffusivity and K' as integration constant. The D' represents the ratio of the air bubble diffusion coefficient to the rise velocity component perpendicular to the flow direction multiplied by characteristic transverse dimension of the shear flow (Chanson 1997). Although Eq. (2.17) was originally developed for smooth chute quasi-uniform flow region, several researches showed that it is also applicable in gradually varied flow region over smooth chutes and gradually varied and quasi-uniform flow region over stepped chutes (Matos 2000; Chanson and Toombes 2001). Note that in case of stepped chutes, the Eq. (2.17) is only applicable at the step edges. Between the edges, air concentration are typically higher close to pseudo-bottom, as reported by Chanson and Toombes (2002). The dimensionless diffusivity D' and integration constant K' of Eq. (2.17) can be obtained with the following equations (Chanson 2002):

$$D' = \frac{0.848C_{mean} - 0.00302}{1 + 1.1375C_{mean} - 2.2925{C_{mean}}^2} \tag{2.18}$$

$$K' = \operatorname{atanh}\left(\sqrt{0.1}\right) + \frac{0.5}{D'} \tag{2.19}$$

An improved analytical solution of the advective diffusion equation was later introduced by Chanson and Toombes (2002):

$$C = 1 - \tanh^2\left(K'' - \frac{y}{2 D_0 y_{90}} + \frac{\left(y/y_{90} - 1/3\right)^3}{3 D_0}\right) \tag{2.20}$$

with K'' as integration constant and dimensionless turbulent diffusivity D' defined as:

$$D' = \frac{D_0}{1 - 2\left(y/y_{90} - 1/3\right)^2} \tag{2.21}$$

where D_0 is a function of the depth averaged air concentration C_{mean}. The parameters K'' and D_0 can be obtained from the following equations:

$$K'' = 0.32745015 + \frac{1}{2D_0} - \frac{8}{81 D_0} \tag{2.22}$$

$$C_{mean} = 0.7622\left(1.0434 - \mathrm{e}^{-3.614 D_0}\right) \tag{2.23}$$

Recently, Zhang and Chanson (2017) presented a new analytical solution of advective diffusion equation for the partially developed aerated flow region (Figure 2.4):

$$C = \frac{1}{2}\operatorname{erfc}\left(\frac{y_{50} - y}{2\sqrt{\frac{D_a (x - L_i)}{V_{mean}}}}\right) \tag{2.24}$$

with y_{50} as flow depth defined up to $y(C = 0.5)$ and D_a as apparent time-averaged diffusivity.

Velocity distribution

Velocity distribution in skimming flow regime (Figure 2.3), can be approximated by a power law equation as (Cain and Wood 1981; Chanson 2015b):

$$\frac{V}{V_{90}} = \left(\frac{y}{y_{90}}\right)^{1/N} \tag{2.25}$$

with V_{90} as the velocity at $y(C = 0.9)$ and N as constant. The exponent N was studied, among others, by: Amador et al. (2006), Meireles and Matos (2009), Bung (2011), Takahashi and Ohtsu (2012) and Meireles et al. (2012). These studies suggested that the exponent N mainly depends on: (1) chute angle φ and (2) relative step height s/h_c. For mildly sloped chutes, Bung

(2011) showed that the exponent N was mainly slope dependent and proposed the following empirical expression as a function of φ:

$$\frac{1}{N} = \frac{0.947}{(\cos\varphi)^{0.984}(\sin\varphi)^{0.078}} - 1 \tag{2.26}$$

For a wide range of chute slopes, covering both mildly and steeply sloping chutes, Takahashi and Ohtsu (2012) proposed the following relation for predicting N, as a function of φ and h_c:

$$N = 14\varphi^{-0.65}\frac{s}{h_c}\left(\frac{100s}{\varphi h_c} - 1\right) - 0.041\varphi + 6.27 \tag{2.27}$$

Overall, all conducted studies suggested that the exponent N decreases with the increasing chute slope φ. Typical values for steeply sloped chutes, i.e. φ>30°, are 3.5≤N≤6.5 (Amador et al. 2006; Meireles et al. 2012; Boes 2000a; Takahashi and Ohtsu 2012), whereas for mildly sloped chutes they can range between 4≤N≤14 (Meireles and Matos 2009; Takahashi and Ohtsu 2012; Bung 2011).

A slightly modified power law equation was introduced by Boes and Hager (2003b):

$$\frac{V}{V_{90}} = 1.05\left(\frac{y}{y_{90}}\right)^{1/4.3} \qquad \text{for } 0.04 \leq \frac{y}{y_{90}} \leq 0.8 \tag{2.28}$$

$$\frac{V}{V_{90}} = 1 \qquad \text{for } \frac{y}{y_{90}} > 0.8 \tag{2.29}$$

Similar equations were later obtained by André et al. (2005).

Friction factor and energy dissipation

The prominent feature of the stepped chutes, as compared to smooth chutes, is the enhanced energy dissipation along the chute resulting in a reduced residual energy at the chute end. As such, the Darcy-Weisbach friction factor f_D in the quasi-uniform flow region is defined as:

$$f_D = \frac{2g\sin\varphi D_h}{V_{mean}^2} \tag{2.30}$$

with D_h as hydraulic radius, was investigated in numerous studies (Matos 1999; Chanson et al. 2002; Boes and Hager 2003b; Ohtsu et al. 2004; Matos 2005; Amador et al. 2006; Chanson 2006; Felder and Chanson 2009a; Takahashi and Ohtsu 2012). These studies suggested that the friction factor f_D mainly depends on chute slope φ, relative step height s/h_c and intake type.

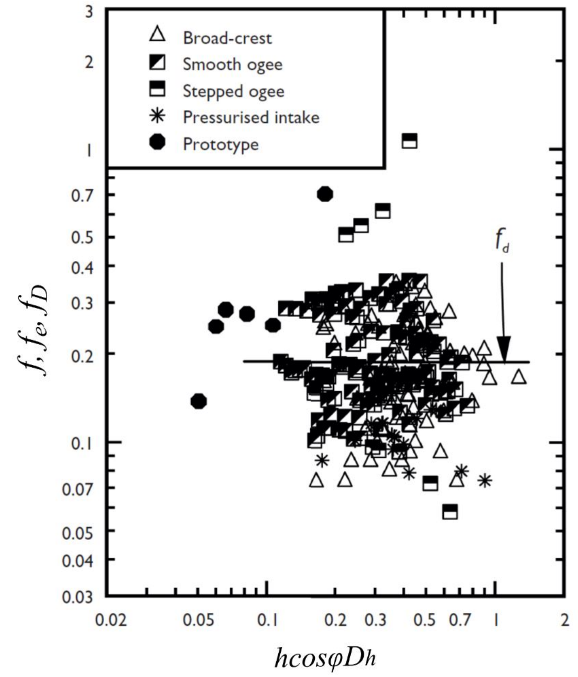

Figure 2.6 – Darcy-Weisbach friction factor in skimming flow regime as a function of the relative cavity height $s\cos\varphi/D_H$ (Chanson 2015b).

A wide range of f_D has been reported, as illustrated on Figure 2.6 where the re-analysis of flow resistance data in laboratory and prototype studies performed by Chanson (2015b) is shown. The data re-analysis indicated three dominant friction factor values, namely f_D=0.11, 0.17 and 0.30. The large data scatter can be contributed to (Boes and Hager 2003a; Matos 2005; Chanson 2015b): (1) usage of mixture flow depth in some of the studies, leading to the overestimation of f_D and (2) non quasi-uniform flow conditions in some of the studies. Matos and Meireles (2014) showed that the friction factor decreases along the chute and reaches quasi-constant values in the quasi uniform flow region.

The energy dissipation in skimming flow regime is mainly caused by (Chanson 2002; Felder and Chanson 2011): (1) vortical structures formed in the step cavities and (2) jet impact onto the step surface. At any given cross-section along the stepped chute, the specific energy can be expressed as (Chanson 2002):

$$E = h_{cw}\cos\varphi + \alpha\frac{V_{mean}^2}{2g} \tag{2.31}$$

with α as the kinetic energy correction coefficient taking into account the velocity and air concentration profiles perpendicular to the pseudo-bottom and defined as (Matos 1999):

$$\alpha = \frac{1}{V_{mean}^2} \frac{\int_0^{y_{90}} (1-C)\, V^3 dy}{\int_0^{y_{90}} (1-C)\, V dy} \tag{2.32}$$

For skimming flow regime, the typical values of the energy correction coefficient range between α=1.05-1.2 (Matos 1999; Boes and Hager 2003a; Meireles and Matos 2009; Meireles et al. 2012; Takahashi and Ohtsu 2012).

The procedures for estimating the residual energy E_{res} at the chute end was, among others, developed by Matos (2000), Boes and Hager (2003a), Takahashi and Ohtsu (2012) and Chanson (2015b). For stepped chutes, in which quasi-uniform flow conditions are not attained, Boes and Hager (2003a) suggested the following relation for residual energy estimation:

$$\frac{E_{res}}{E_{max}} = \exp\left[\left(-0.045\left(\frac{s\cos\varphi}{D_h}\right)^{0.1}\left(\sin\varphi\right)^{-0.8}\right)\frac{H_{max}}{h_c}\right] \tag{2.33}$$

with E_{max}=$H_{dam} + 1.5h_c$ as the maximum energy head above chute end, where H_{dam} is the dam height.

For quasi-uniform flow conditions, E_{res} can be estimated as a function of f_D (Chanson 2015b):

$$\frac{E_{res}}{E_{max}} = \frac{\left(\frac{f_D}{8\sin\varphi}\right)^{1/3} + 0.5\alpha\left(\frac{f_D}{8\sin\varphi}\right)^{-2/3}}{1.5 + \frac{H_{dam}}{s_c}} \tag{2.34}$$

Hydrodynamic pressure on steps

The knowledge of hydrodynamic pressures acting on the step faces is essential when it comes to the structural design of the stepped chutes. To this regards, numerous studies have been performed, for example by Sánchez-Juny et al. (2000), André (2004), Sánchez-Juny and Dolz (2005), Gomes et al. (2006), Sanchez-Juny et al. (2007), André and Schleiss (2008), Sánchez-Juny et al. (2008), Amador et al. (2009), Takahashi and Ohtsu (2012), Zhang et al. (2012), Frizell et al. (2013) and Chanson (2015a).

The hydrodynamic pressures on the *horizontal step face* are characterized by a distinctive S-shape type profile (Sanchez-Juny et al. 2007; Zhang et al. 2012; Takahashi and Ohtsu 2012). The maximum mean and extreme pressures take place at the downstream half of the step, where the step face is exposed to flow impact, i.e. the internal jet (Figure 2.7). On the other hand, the minimum mean and extreme pressures occur in the upstream half of the step, where the step face is subjected to the boundary layer separation induced by the recirculating eddies in the step cavities (Sánchez-Juny et al. 2000; Sanchez-Juny et al. 2007; André and Schleiss 2008; Amador et al. 2009). The pressure fluctuations exhibit similar pattern. According to Sánchez-Juny et al. (2000), André (2004), André and Schleiss (2008), Sánchez-Juny et al. (2008) and Amador et al. (2009), the absolute maximum pressures occur at approximately 70% of the step length from step corner. At this point the absolute maximum observed magnitudes are up to 7 and 5.5 times the step height for chute slopes of 51.2°and 30°, respectively (André 2004; Sanchez-Juny et al. 2007).

The hydrodynamic pressure distribution on the *vertical step face* was also found to exhibit a S-shape type profile. The maximum mean and extreme pressures occur at step corner, whereas minimum mean and extreme pressures take place close to the step edge (Sánchez-Juny et al. 2000; André 2004; Sánchez-Juny and Dolz 2005; Gomes et al. 2006; Sanchez-Juny et al. 2007; André and Schleiss 2008; Zhang et al. 2012). Due to the flow separation, the extreme negative pressures are more pronounced on the vertical step face, as compared to those of horizontal face. As such, the vertical step faces are more exposed to potential cavitation. The critical cavitation region was found to be in the vicinity of the inception point (Gomes et al. 2007; Amador et al. 2009).

The cavitation potential of stepped chutes were, among others, investigated by Gomes et al. (2006), Amador et al. (2009) and Frizell et al. (2013). By analyzing the extreme negative pressures at the inception point, Amador et al. (2009) suggested a limiting mean velocity of some 15 m/s or a unit discharge of q=15 m^2/s to avoid cavitation for 51.3° sloping stepped chutes.

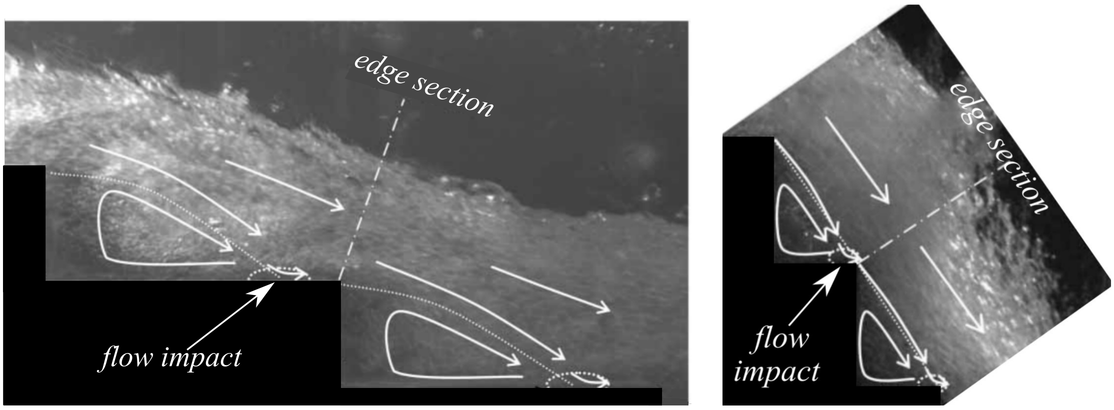

(a)

(b)

Figure 2.7 – Flow impact on the step edge (internal jet) for: (a) 19° sloping chute and (b) 55° sloping chute. Adapted from Takahashi and Ohtsu (2012).

2.2 Overview on hydraulic jumps and stilling basin flow

A hydraulic jump is a sudden and rapid transition from a high velocity flow into a slower motion in an open channel (Chanson 2015b). It essentially represents a transition from supercritical into a subcritical flow. The first description of this particular hydraulic phenomena was provided in the 16th century by Leonardo Da Vinci (Hager 1992). However, the experimental investigations on the hydraulic jumps only started in early 19th century with pioneering studies of Bidone (1820) and Bélanger (1828). In the following centuries numerous studies on various aspects of the hydraulic jumps were performed, and it is probably one of the most extensively investigated phenomena in hydraulic engineering.

In open channel flows, the occurrence of hydraulic jump is usually associated with depth discontinuity, slope change, sudden channel expansion or flow obstacles such as hydraulic structures. The main properties of the hydraulic jump include (Hager 1992; Vischer and Hager 1998):

- Macro turbulent flow,
- High pressure and velocity fluctuations in the body of jump,
- High air entrainment rate at the jump toe,
- Air detrainment along the jump,
- Intensive surface fluctuations, spray and sound,
- High energy dissipation due to turbulence production,
- Erosive potential and generation of tailwater waves.

Due to its flow properties, the hydraulic jumps have found a wide range of practical applications, such as energy dissipation in spillway structures, flow re-aeration in industrial plants, sludge mixing in water treatment plants or even for recreational purposes.

2.2.1 Classical hydraulic jumps

The hydraulic jump formed on a smooth, rectangular, prismatic and horizontal channel is often called a *classical hydraulic jump*. The flow pattern of the classical hydraulic jump can be considered as two-dimensional, apart from the boundary layers formed along the sidewalls (Hager 1992). Macroscopically, hydraulic jumps are characterized by supercritical approach flow depth h_1 with mean flow velocity V_1, subcritical flow depth h_2 with mean flow velocity V_2, roller length L_R and jump length L_J (Figure 2.8). Flow depths h_1 and h_2 are also known as sequent or conjugate flow depths. The approach flow depth h_1 and mean velocity V_1 together with gravitational acceleration g form a parameter, i.e. approach Froude number F_1, that defines the condition of the flow (Hager 1992):

$$F_1 = \frac{V_1}{\sqrt{g h_1}} \tag{2.35}$$

In general, the hydraulic jumps are characterized by two flow zones (Figure 2.8): a bottom jet flow (forward flow zone) in the lower part of the flow and a roller zone above (Hager 1992). In the forward flow zone, the approaching supercritical jet is considerably perturbed by the jump. Along the bottom, the flow is in the forward, streamwise direction. With increasing distance from the jump toe, the bottom jet flow starts to detach from the invert and forms a roller zone, in which the flow recirculates. Within the roller perimeter, the flow depths monotonically increase with increasing distance from the jump toe. Further downstream, the flow becomes smoother and a gradually varied open channel flow is attained in the tailwater zone, i.e. downstream of the jump end.

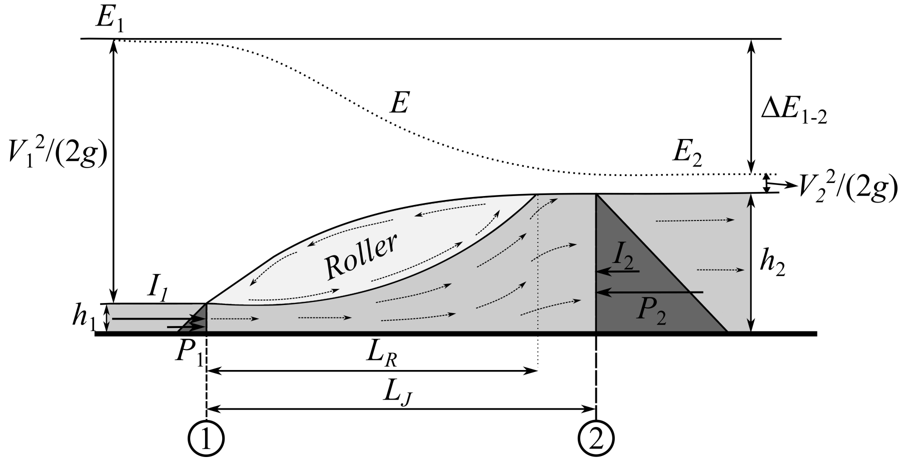

Figure 2.8 – Definition sketch of classical hydraulic jump.

Note that the previous description only reflects an idealized, time-averaged phenomena. In reality, the hydraulic jumps are characterized by heavy oscillations, free surface deformation and formation of surface waves. Hager et al. (1990) described two types of a classical hydraulic jump appearance, namely a developed and non-developed roller flow (Figure 2.9). The *developed roller flow* state is characterized by smooth and quasi-steady conditions (Figure 2.9a). The roller end can be clearly identified as typical boiling of the flow occurs. Further downstream, small surface waves are generated. On the other hand, the *non-developed roller flow* state is more dynamic and energetic (Figure 2.9b). A large scale bottom separation sporadically occurs in the forward flow zone leading to the deflection of the bottom jet flow towards the surface, sudden downstream shift of the jump toe and generation of heavy surface waves propagating towards the tailwater zone. The developed and non-developed roller flows are alternately formed, including the transitional states (Hager 1992).

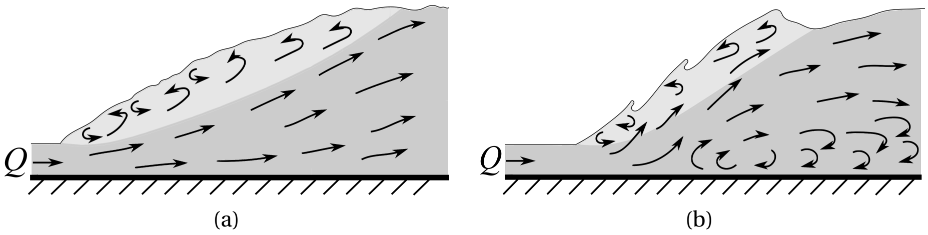

Figure 2.9 – Hydraulic jump with a: (a) developed and (b) non-developed roller flow state. Adapted from Hager (1992).

2.2.2 Forms and classification of hydraulic jumps

Hydraulic jumps can take many different forms and shapes. Based on the approach Froude number F_1, several jump types are distinguished (Peterka 1958; Hager 1992):

- *Weak* or *pre jump* for $1.7 \leq F_1 \leq 2.5$, characterized by a relatively smooth surface with a series of small rollers and fairly uniform velocity distribution (Figure 2.10a),
- *Transition jump* for $2.5 \leq F_1 \leq 4.5$, characterized by significant wave action caused by pronounced oscillations of the entering jet (Figure 2.10b),
- *Steady jump* for $4.5 \leq F_1 \leq 9$, characterized by well balanced flow conditions (Figure 2.10c),
- *Rough* or *choppy jump* for $F_1 > 9$, characterized by rough surface and significant wave action caused by pronounced jump toe oscillations (Figure 2.10d).

In terms of energy dissipation, *rough* jump type is the most effective. However, this jump form is most sensitive to tailwater variation and thus requires tailwater depths greater than conjugate depth in order maintain the jump within stilling basin perimeter (Peterka 1958). The best flow conditions are achieved with *steady jumps* and its performance can be further increased by placing additional energy dissipating elements such as chute or baffle blocks.

In case of spillway structures, hydraulic jumps are classified depending on its position within the spillway (Khatsuria 2005). Four different jump types can occur:

- *A jump* type, where the jump toe forms at the junction of the sloping chute and stilling basin invert (Figure 2.11a),
- *B jump* type, where the jump toe forms on the sloping chute and ends on the stilling basin invert (Figure 2.11b),
- *C jump* type, where the jump toe forms on the sloping chute and ends at the junction of the sloping chute and stilling basin invert (Figure 2.11c),
- *D jump*, where the hydraulic jump entirely forms on the sloping chute (Figure 2.11d).

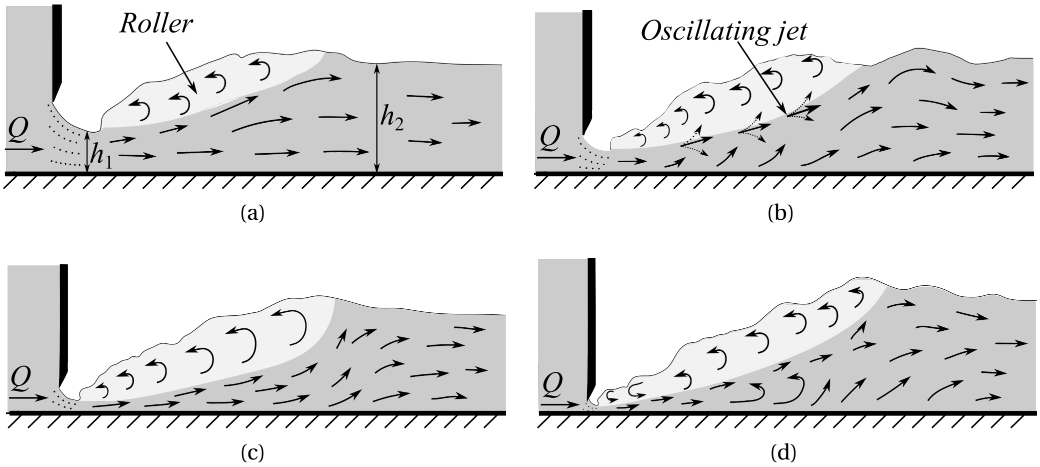

Figure 2.10 – Hydraulic jump forms based on approach Froude number F_1: (a) weak jump, (b) transition jump, (c) steady jump and (d) rough or choppy jump. Adapted from Peterka (1958).

Stilling basins are usually designed so that the hydraulic jump toe forms at the intersection of the chute bottom and the stilling basin invert, i.e. *A jump* type.

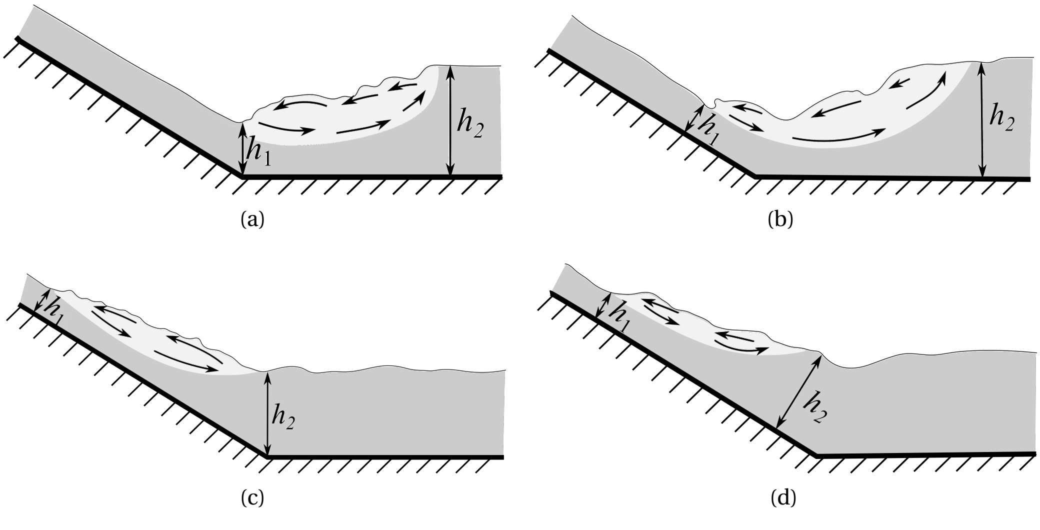

Figure 2.11 – Hydraulic jump forms based on its position within the spillway: (a) A jump type, (b) B jump type, (c) C jump type and (d) D jump type. Adapted from Khatsuria (2005).

Hydraulic jumps can be further classified based on the geometry of the channel in which they occur (e.g. trapezoidal, triangular, circular etc.), based on available tailwater depth (i.e. free jump and submerged jump) and if appurtenant structures like end sill or baffle blocks are used (i.e. forced and free jump).

2.2.3 Sequent depth ratio

Assuming hydrostatic pressure distribution with uniform velocity profiles at both ends of the hydraulic jumps, i.e. sections 1 and 2 in Figure 2.8, and negligible wall frictional forces, the momentum equation between cross sections 1 and 2 yields:

$$P_1 + I_1 = P_2 + I_2 \tag{2.36}$$

$$\frac{1}{2}\rho g B {h_1}^2 + \rho Q V_1 = \frac{1}{2}\rho g B {h_2}^2 + \rho Q V_2 \tag{2.37}$$

with P_1 and P_2 as pressure forces at sections 1 and 2, I_1 and I_2 as inertial forces at sections 1 and 2, and B as channel width. Dividing the Eq. (2.37) with $2/(\rho g B {h_1}^2)$ gives a well know Bèlanger's equation for sequent depth ratio (Chanson 2009a; Hager 1992):

$$\frac{h_2}{h_1} = 0.5\left(\sqrt{1 + 8{F_1}^2} - 1\right) \tag{2.38}$$

Peterka (1958) investigated the applicability of Bellanger's equation for smooth chute spillways covering a wide range of approach Froude numbers $2 \leq F_1 \leq 20$ and chute slopes $0 < \varphi < 51.3°$. An excellent agreement was reported over the entire range. They further stated that the Eq. (2.38) seemed to be applicable even if the approach flow enters the stilling basin at a significant angle with the horizontal.

An improved sequent depth ratio relation was later introduced by Hager and Bremen (1989), by incorporating wall frictional forces:

$$\frac{h_2}{h_1} = Y_o\left[1 - 3.25\left(\frac{h_1}{B}\right)\exp\left(\frac{F_1}{7}\right)\log(R_1)^{-3}\right] \tag{2.39}$$

where Y_o is defined as:

$$Y_o = \left(\frac{h_2}{h_1}\right)_o\left[1 - 0.7\exp\left(\frac{F_1}{8}\right)\log(R_1)^{-2.5}\right] \tag{2.40}$$

with $(h_2/h_1)_o$ as sequent depth ratio calculated using Eq. (2.38). The differences in sequent depth ratio calculated using Eq. (2.38) and Eq. (2.39) were found to be insignificant if $F_1 < 12$, $h_1/B < 0.1$ and $R_1 > 1.0 \times 10^5$, where $R_1 = q/\nu$ is the inflow Reynolds number with ν as kinematic viscosity.

2.2.4 Free surface characteristics

The highly turbulent nature of hydraulic jumps is visually reflected by its free surface (Hager 1992). The surface is characterized by large fluctuations, strong deformations, splashes and spray. For practical purposes, time-averaged free surface profiles are usually considered.

The mean surface profiles of hydraulic jumps were first measured by Bakhmeteff and Matzke (1936) and Moore (1943). Schröder (1963) first showed that the mean surface profiles of a hydraulic jump exibits a self-similar shape. Further early contributions encompass, among others, Henry (1950), Rajaratnam (1962b), Rajaratnam and Subramanya (1968), Ohtsu et al. (1990) and Hager (1993). In these studies, the flow depths were collected with a simple point gauge, and the empirical equations expressing the relationship between mean streamwise flow depths η, roller length L_R, sequent depths h_2 and h_1, and approach flow conditions were proposed. Hager (1993) obtained:

$$\frac{\eta - h_1}{h_2 - h_1} = \tanh\left(1.5\frac{x}{L_R}\right) \tag{2.41}$$

with x as the streamwise distance to the jump toe. Theoretical predictions of time-averaged surface profiles were developed by McCorquodale and Khalifa (1983), Madsen and Svendsen (1983) and Richard and Gavrilyuk (2013).

In recent years, the development of surface detection instrumentation allowed more precise and continuous measurements of the flow depths along the hydraulic jump. The surface dynamics were measured intrusively using wire gauges (e.g., Mouaze et al. (2005) and Murzyn et al. (2007)) and non-intrusively using ultrasonic sensors (e.g., Murzyn and Chanson (2009b), Chachereau and Chanson (2011a)), digital and high speed cameras (e.g., Long et al. (1991), Mouaze et al. (2005) and Zhang et al. (2013)) and LIDAR (Montano et al. (2018)). Apart of the mean flow depths, these recent studies also reported dynamic properties of the jump surface, such as flow depth fluctuations, characteristic frequencies, integral turbulent time and length scales, and jump toe oscillations.

Using the ultrasonic sensors, Chanson (2011) described the mean flow depth over the jump roller with a self-similar function:

$$\frac{\eta - h_1}{h_2 - h_1} = \left(\frac{x}{L_R}\right)^{0.441} \tag{2.42}$$

Similar equation was later obtained by Wang and Chanson (2015b) with the exponent of 0.537.

2.2.5 Energy dissipation and jump efficiency

Hydraulic jumps with a marked roller are characterized by high rate of energy dissipation, as illustrated in Figure 2.8. The dissipated energy $\Delta E_{1,2}$ between the cross-sections 1 and 2 (Figure 2.8) can be expressed as:

$$\Delta E_{1,2} = E_1 - E_2 = h_1 + \frac{q^2}{2g{h_1}^2} - h_2 - \frac{q^2}{2g{h_2}^2} = \frac{(h_2 - h_1)^3}{4h_1 h_2} \tag{2.43}$$

with E_1 and E_2 as the energy heads at sections 1 and 2, respectively (Figure 2.8). The efficiency of the jump Λ (i.e. relative energy dissipation) can be then formulated as:

$$\Lambda = \frac{E_{1,2}}{E_1} = 1 - \frac{\frac{h_2}{h_1} + \frac{{F_1}^2}{2\left(\frac{h_2}{h_1}\right)^2}}{1 + \frac{{F_1}^2}{2}} \tag{2.44}$$

For F_1>2 Eq. (2.44) can be simplified as (Hager and Sinniger 1985):

$$\Lambda = \left[1 - \frac{\sqrt{2}}{F_1}\right]^2 \tag{2.45}$$

Eqs. (2.44) and (2.45) indicate that the energy dissipation rate of the jump is directly proportional to the approach flow Froude number F_1. For example, the energy dissipation rate for hydraulic jumps with relatively low F_1, e.g. F_1<3, is below 28%, whereas for relatively high F_1, e.g. F_1>9, it exceeds 70%.

2.2.6 Length characteristics

The hydraulic jumps are usually characterized by two length parameters, namely jump L_J and roller length L_R. The jump length is difficult to determine or measure precisely thus it was often subject to visual observations (Peterka 1958; Hager 1992; Khatsuria 2005). The upstream extremity of the hydraulic jump is usually defined at the jump toe. Various definitions for the downstream extremity of the jump were proposed, such as (Peterka 1958; Hager 1992; Khatsuria 2005):

1. Cross section where the surface turbulence is diminished,
2. Cross section where deaeration of large bubbles is completed,
3. Cross section where gradually varied flow is retained,
4. Cross section where high-velocity jet begins to leave the floor,

5. Cross section immediately downstream of the roller,
6. Cross section where free surface is essentially levelled.

For practical purposes, the hydraulic jump length is usually considered as a distance where bottom riverbed protection is necessary. Based on a large set of experiments covering a wide range of approach Froude numbers F_1 and chute slopes φ, Peterka (1958) proposed a curve relating the normalized jump length L_J/h_2 with the approach Froude number F_1 (Figure 2.12). For $4<F_1<12$ the curve can be approximated as (Hager 1992):

$$L_J = 6h_2 \tag{2.46}$$

The second length characteristic, i.e. the roller length L_R, is usually defined as a distance between the jump toe and the surface stagnation point (Hager 1992). Hager et al. (1990) investigated the roller lengths of classical hydraulic jumps and proposed two relations for predicting normalized roller length L_R/h_1, as a function of the approach flow Froude number F_1 and the aspect ratio h_1/B:

$$\frac{L_R}{h_1} = -12 + 160\tanh\left(\frac{F_1}{20}\right) \qquad \text{for} \quad \frac{h_1}{B} < 0.1 \tag{2.47}$$

$$\frac{L_R}{h_1} = -12 + 100\tanh\left(\frac{F_1}{12.5}\right) \qquad \text{for} \quad 0.1 \leq \frac{h_1}{B} \leq 0.7 \tag{2.48}$$

In more recent studies, the roller lengths were usually obtained from the flow depth measurements and defined as a longitudinal distance from the jump toe over which mean flow depth increase monotonically (e.g, Murzyn et al. (2007), Murzyn and Chanson (2009b) and Wang and Chanson (2015b)). Based on reanalysis of data acquired by Murzyn et al. (2007), Murzyn and Chanson (2009b), Kucukali and Chanson (2008) and Wang (2014), Wang and Chanson (2017) presented a simple equation relating dimensionless roller length L_R/h_1 with the approach Froude number F_1:

$$\frac{L_R}{h_1} = 6\,(F_1 - 1) \tag{2.49}$$

2.2.7 Air-water flow properties

One of the most distinctive feature of hydraulic jumps is the intense air entrainment at the jump toe and rapid detrainment along its length. Rajaratnam (1962a) first performed successful air-water flow measurements in classical hydraulic jumps. The main findings of this study were that air concentration distribution strongly depends on the approach flow Froude number F_1 and the aeration length (i.e. the distance from the jump toe to the section

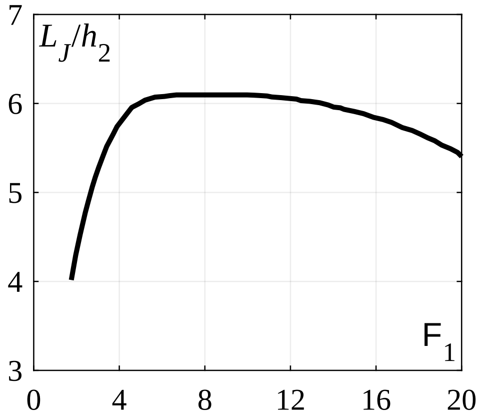

Figure 2.12 – Normalized jump length L_J/h_2 (Peterka 1958).

where mean air concentration is equal to zero) was larger than the corresponding jump length L_J. Leutheusser and Kartha (1972), Resch et al. (1974) and Thandaveswara (1974) revealed that approach flow conditions have a major effect on the air entrainment, momentum transfer and energy dissipation processes. These studies clearly demonstrated that the air bubble redistribution in the jump roller strongly depends on the inflow conditions. Four types of approach flow conditions and thus classical hydraulic jumps are distinguished (Figure 2.13):

- Hydraulic jump with *undeveloped* approach flow conditions (hereafter UD), in which the hydraulic jump toe forms at venna contracta,
- Hydraulic jump with *partially developed* approach flow conditions (hereafter PD), in which the approaching flow exhibits a developing turbulent boundary layer and a quasi-potential core above,
- Hydraulic jump with *fully developed* approach flow conditions (hereafter FD), in which turbulent boundary layer in the approaching flow expanded over entire flow depth,
- *Pre-aerated* hydraulic jumps (hereafter PA), with fully developed and aerated approach flow conditions.

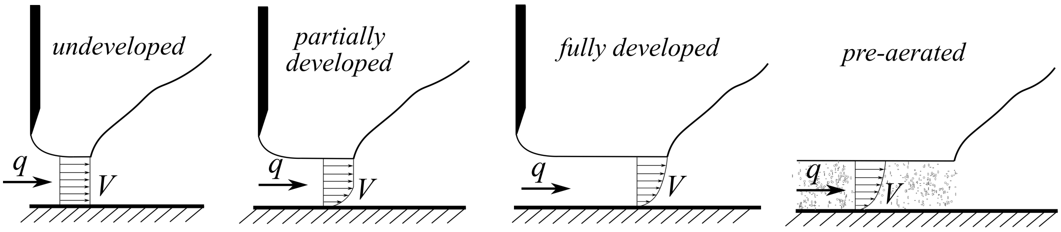

Figure 2.13 – Approach flow condition types for classical hydraulic jumps.

Recently, most studies focused on the hydraulic jumps generated with PD approach flows (Chachereau and Chanson 2011a; Chanson 1995, 2007, 2009b,a, 2010, 2011; Chanson and

Brattberg 2000; Chanson and Chachereau 2013; Chanson and Gualtieri 2008; Gualtieri and Chanson 2007; Kucukali and Chanson 2009; Murzyn et al. 2005, 2007; Murzyn and Chanson 2008, 2009a,b; Wang et al. 2014, 2015a,b; Wang and Chanson 2015a, 2017, 2019). The importance of inflow conditions in the characterization of internal flow features of the jump was further highlighted by Takahashi and Ohtsu (2017) and Montano and Felder (2018).

The air entrainment mechanisms in hydraulic jumps are complex and strongly depend on the approach flow conditions (Chanson 2009a; Takahashi and Ohtsu 2017). For hydraulic jumps with PD inflows, Chanson (2009b) described two main mechanism of air entertainment at the jump toe, namely: (1) formation of a moving air layer next to the free surface of the approaching flow intruding into the roller, due to air-water shear friction and (2) aspiration of the induction trumpet formed at the jump toe. These mechanisms are illustrated in Figure 2.14, where V_{air} is the air velocity above the approaching flow.

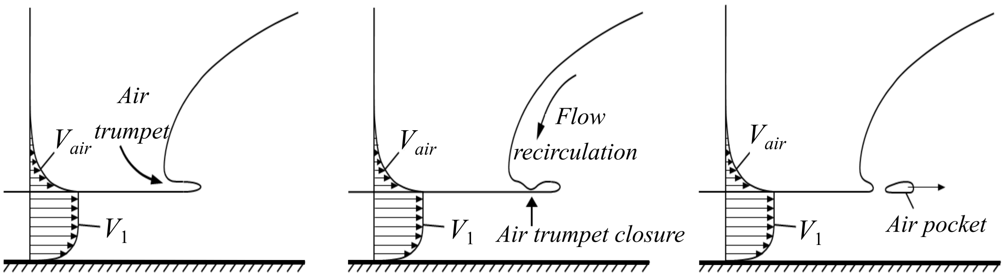

Figure 2.14 – Sketches of air entrainment mechanisms at the hydraulic jump toe with partially developed approach flows. Adapted from Wang (2014).

The trumpet acts as a ventilated cavity. The closure of the trumpet by reversed flow releases air pockets into the downstream shear flow. The air pockets are broken up into small air bubbles due to the high turbulent shear stresses (Figure 2.14). The air bubbles are then transported with vortical structures, formed at jump toe, and diffused into the flow (Figure 2.15). Apart from the jump toe, the air is also entrapped at the roller surface via macro turbulence. The air entrained at the jump toe and surface roller is gradually released into the atmosphere due to buoyancy.

A typical air concentration C and air-phase frequency F profile within hydraulic jump roller is sketched in Figures 2.16a and b (Chanson 1997). Two main flow regions are distinguished, namely a: (1) turbulent shear layer region in the lower part of the flow and (2) recirculation region above. The shear layer region is characterized by a bell-shape profile with the maximum air concentration C_{max} and air-phase frequency F_{max} located at the elevation z_{max} and z_{Fmax}, respectively. The z_{Fmax} is typically located below the z_{max} due to double diffusion processes, where air concentration and vorticity are diffused at a different rate and manner (Chanson 2010). The local minimum air concentration C_{min}, located at the elevation z_{min}, delimits the turbulent shear layer region and recirculation region. The air concentration and air

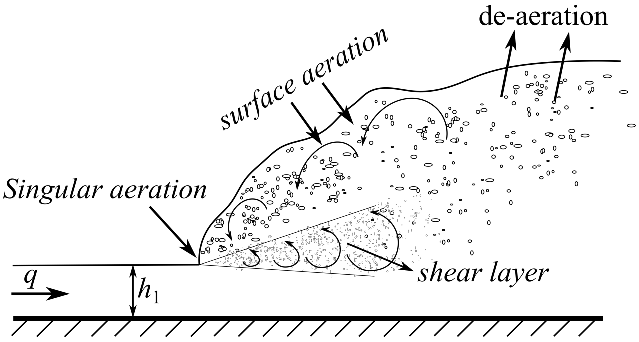
de-aeration
surface aeration
Singular aeration
shear layer
q
h1

Figure 2.15 – Air entrainment in hydraulic jumps with partially developed approach flow conditions.

phase frequency tend to decrease with increasing distance from the jump toe, as air bubbles and vorticity are diffused and dispersed into the flow. In the recirculation region, the air concentration distribution is characterized by a monotonic increase to unity (Chanson 1997), where air-phase frequency distribution exhibits a local maximum F_{sec} at the elevation z_{Fsec}.

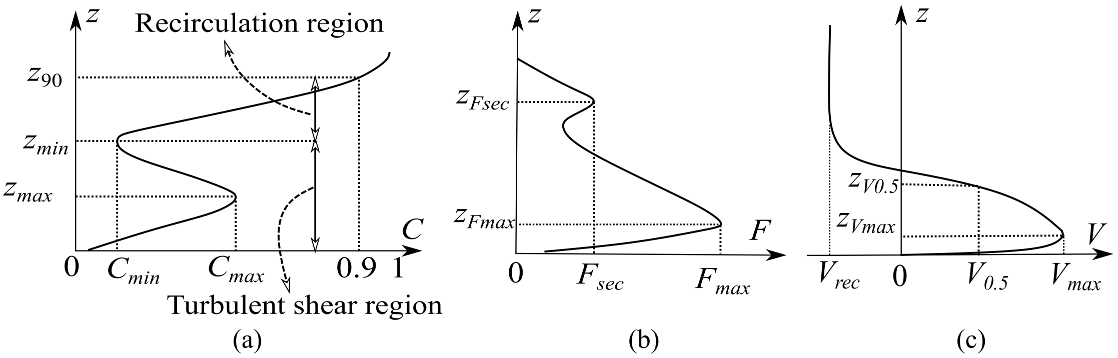
z
Recirculation region
z90
zmin
zmax
C
0
Cmin
Cmax
0.9
1
Turbulent shear region
(a)
z
zFsec
zFmax
F
0
Fsec
Fmax
(b)
z
zV0.5
zVmax
V
Vrec
0
V0.5
Vmax
(c)

Figure 2.16 – Sketch of a typical (a) air concentration, (b) air-phase frequency and (c) velocity profile within hydraulic jump roller.

For hydraulic jumps generated with PD inflows, Chanson (1995) proposed two analytical solutions of the advection-diffusion equation for air bubbles to describe the air concentration profiles:

$$C(z) = C_{max}\exp\left[\frac{\left(\frac{z-z_{max}}{h_1}\right)^2}{4\left(\frac{D_t^s}{V_1 h_1}\right)\left(\frac{x}{h_1}\right)}\right] \qquad \text{for } z < z_{min} \qquad (2.50)$$

$$C(z) = 0.5\left[1+\operatorname{erf}\left(\frac{\frac{z-z_{50}}{h_1}}{2\sqrt{\frac{D_t^r}{V_1 h_1}}\sqrt{\frac{x}{h_1}}}\right)\right] \qquad \text{for } z > z_{min} \qquad (2.51)$$

with z as vertical coordinate originating at the bottom, z_{50} as characteristic flow depth defined up to z(C=0.5), D_t^s as depth averaged turbulent diffusivity in the shear layer region, D_t^r as depth averaged turbulent diffusivity in the recirculation region. Wang and Chanson (2017) proposed the following relations for predicting the dimensionless turbulent diffusivity $D_t^s/(V_1 h_1)$ and $D_t^r/(V_1 h_1)$ for PD inflows:

$$\frac{D_t^s}{V_1 h_1} = 0.1\left[1 - \exp\left(-2.3\frac{x}{L_R}\right)\right] \tag{2.52}$$

$$\frac{D_t^r}{V_1 h_1} = 0.1\exp\left(-3.56\frac{x}{L_R}\right) \tag{2.53}$$

Eqs. (2.50) and (2.51) were successfully verified for UD and FD approach flow conditions (Takahashi and Ohtsu 2017; Montano and Felder 2018). However, the air concentration profiles for FD inflows typically exhibit higher air concentration values in the shear layer region, as compared to those for UD and PD inflow conditions. Takahashi and Ohtsu (2017) argued that this is due to higher free surface fluctuation magnitudes of the approaching flow with FD inflows, leading to entrainment of air entrapped in the approaching flow at the jump toe (Figure 2.17).

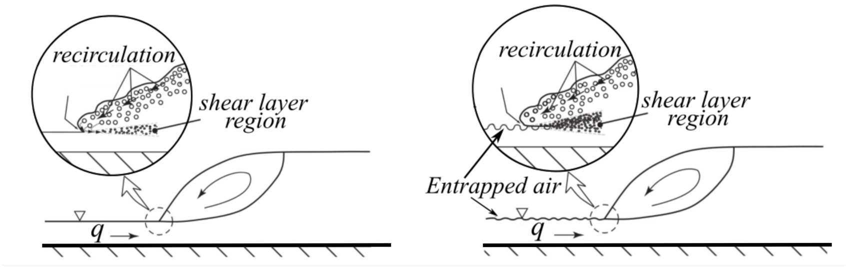

(a) (b)

Figure 2.17 – Air entrainment in hydraulic jump for: (a) undeveloped and partially developed approach flow conditions, and (b) fully developed approach flow condition. Adapted from Takahashi and Ohtsu (2017).

The velocity distribution in hydraulic jumps have been measured and investigated in several studies (e.g. Rajaratnam 1965, Ohtsu et al. 1990, Hager 1992, Chanson and Brattberg 2000, Murzyn and Chanson 2009a, and Chanson 2010). A typical vertical velocity profile of a hydraulic jump within the roller region is sketched in Figure 2.16c. The velocity field is characterized by a boundary layer flow, formed next to the channel invert, with a maximum velocity V_{max} located at the elevation z_{Vmax} and the flow reversal in the recirculation region with negative velocities V_{rec}. These profiles are somewhat analogues to the classical wall jet profiles, a feature first observed by Rajaratnam (1965) and later confirmed by Ohtsu et al. (1990) and Hager (1992). The velocity magnitudes decrease in the streamwise direction as a result of intense energy dissipation.

Chanson and Brattberg (2000) proposed the following relations for predicting the velocity distribution in hydraulic jumps with PD inflows, adapted from Ohtsu et al. (1990):

$$\frac{V}{V_{max}} = \left(\frac{z}{z_{Vmax}}\right)^{1/M} \qquad \text{for } \frac{z}{z_{Vmax}} < 1 \tag{2.54}$$

$$\frac{V - V_{rec,a}}{V_{max} - V_{rec,a}} = \exp\left[-0.5\left(1.765\left(\frac{z - z_{Vmax}}{z_{0.5}}\right)\right)^2\right] \qquad \text{for } \frac{z}{z_{Vmax}} > 1 \tag{2.55}$$

with $V_{rec,a}$ as depth averaged recirculation velocity, $z_{V0.5}$ as the vertical elevation where $V{=}V_{max}/2$ (Figure 2.16c) and M as a constant. Eqs. (2.54) and (2.55) were later successfully verified in numerous studies involving PD approach flow conditions, for example in Kucukali and Chanson (2008), Murzyn and Chanson (2009a), Chanson (2010), Chanson (2011), Zhang et al. (2013), Wang and Chanson (2015b) and Wang and Chanson (2019).

2.2.8 Bottom pressure characteristics

Research on bottom pressure characteristics of hydraulic jumps intensively started around 1960s, as the first instrumentation for dynamic pressure analysis became available. In addition, several reports of severe damages on spillway chutes and basins caused by extreme bottom pressures, such as the case of Karnafuli dam (Toso and Bowers 1988), spurred the research in this domain.

Since dynamic pressures are highly random in nature, they are usually treated with statistical parameters such as (Fiorotto and Rinaldo 1992b; Lopardo and Henning 1985; Toso and Bowers 1988; Pinheiro 1995; Khatsuria 2005):

- mean (time-averaged) pressure p_m,
- fluctuating pressure characterized by the standard deviation p',
- extreme maximum pressure p_{max},
- extreme pressure with 99.9% probability $p_{99.9}$,
- extreme minimum pressure p_{min},
- extreme pressure with 0.1% probability $p_{0.1}$,
- skewness S defined as $S = \sum\left(p_i - p_m\right)^3 / \left(n\left(p'\right)^3\right)$, where p_i is the pressure at given instance and n is number of samples,
- excess kurtosis K defined as $K = \sum\left(p_i - p_m\right)^4 / \left(n\left(p'\right)^4\right) - 3$

Pressure fluctuations and extreme pressures are typically analyzed using dimensionless pressure coefficients defined with respect to approach flow kinetic energy. They include:

- Pressure fluctuation coefficient C_P', defined as:

$$C_P{}' = \frac{p'}{\frac{\alpha V_1{}^2}{2g}} \tag{2.56}$$

- Extreme maximum pressure coefficient $C_P{}^{max}$ and that corresponding to 99.9th percentile $C_P{}^{99.9}$, defined as:

$$C_P{}^{max} = \frac{p_{max} - p_m}{\frac{\alpha V_1{}^2}{2g}} \tag{2.57}$$

$$C_P{}^{99.9} = \frac{p_{99.9} - p_m}{\frac{\alpha V_1{}^2}{2g}} \tag{2.58}$$

- Extreme minimum pressure coefficient $C_P{}^{min}$ and that corresponding to 0.1th percentile $C_P{}^{0.1}$, defined as:

$$C_P{}^{min} = \frac{p_m - p_{min}}{\frac{\alpha V_1{}^2}{2g}} \tag{2.59}$$

$$C_P{}^{0.1} = \frac{p_m - p_{0.1}}{\frac{\alpha V_1{}^2}{2g}} \tag{2.60}$$

Starting with a pioneering work of Vasiliev and Bukreyev (1967), numerous studies on dynamic pressure characteristics under hydraulic jump were performed (Bowers and Tsai 1969; Abdul Khader and Elango 1974; Bribesca and Mariles 1979; Akbari et al. 1982; Lopardo et al. 1982; Tullis and Rahmeyer 1982; Spoljaric 1984; Lopardo and Henning 1985; Toso and Bowers 1988; Fiorotto and Rinaldo 1992a,b; Khatsuria et al. 1992; Pinheiro 1995; Lopardo and Romagnoli 2009). In these studies, the dynamic bottom pressures characteristics were studied for a wide range of approach flow F_1, various approach flow conditions (i.e. undeveloped, partially developed, fully developed and pre-aerated, Figure 2.13), various submergence levels and different stilling basin types (i.e. simple stilling basin, USBR types II and III basins). The general conclusions of these studies can be summarize as:

- Approach flow conditions (i.e. undeveloped, partially developed and fully developed inflows) have a strong influence on the magnitude of C_P',
- The standard deviation of the pressure fluctuations decreases with developed approach

flow conditions,

- The maximum value of C_p' reaches about 0.07 for fully developed approach flow conditions and about 0.08 for undeveloped approach flow conditions,
- Correlation in the longitudinal direction is shorter (order of 2 to $4h_1$) than in the transverse direction (order of 8 to $10h_1$),
- Decrease of C_p' magnitudes are more pronounced for free hydraulic jumps in comparison to submerged jumps,
- Aerated approach flows tend to slightly reduce the magnitudes of C_P',
- Dominant frequency of pressure fluctuations range from 2 to 5 Hz,
- The extreme pressure coefficients $C_P{}^{max}$ and $C_P{}^{min}$ can reach up to 0.8-1.0 corresponding to 10-20 times the standard deviation,
- The maximum values of $C_P{}^{max}$ and $C_P{}^{min}$ for the jump formed at chute toe (i.e. *A jump type*, Figure 2.11a) are up to two times lower than for the jump formed on the chute slope (i.e. *B jump type*, Figure 2.11b),
- Values of $C_P{}^{max}$ and $C_P{}^{min}$ are not significantly higher for USBR type II and III, as compared to classical hydraulic jumps on plain stilling basins,
- Maximal values of $C_P{}^{max}$ and $C_P{}^{min}$ increase with sampling time. For sampling time over twelve hours, the maximal value is almost constant,
- Sidewall pressure fluctuations are significant and peak at one to two approach flow depth h_1 above the bottom,
- Magnitudes of extreme pressures with 0.1% probability can reach vapor pressure values in the initial region of hydraulic jump.

2.3 Standard stilling basins types

The first standardized stilling basins were introduced in 1930s. In the following decades many basin types have been developed. The most well known standardized stilling basin types are (Hager 1992; Chanson 2015b): USBR type (US Bureau of Reclamation), SAF basin (Saint Anthony Falls laboratory), PWD (Public Works Department) and WES (Waterways Experimental Station). These standardized basins have been tested both on scale models or in prototype conditions. For a range of operating conditions, the recommended design specifications may be directly applied without any additional model studies. In particular, the basins developed by the US Bureau of Reclamation have been widely used (Peterka 1958).

In the late 1950s USBR conducted a series of model studies on various stilling basin designs. These studies were performed on six different test flumes for a wide range of operating conditions. Based on model tests results and available prototype data, ten different energy dissipator designs have been developed and described in detail. These studies were published as Reclamation Engineering Monograph No. 25 “Hydraulic Design of Stilling Basins and Energy Dissipators” which is being used (where applicable) as a manual for the energy dissipator design. Among the well known USBR stilling basin types are type II (including chute blocks and an end sill, Figure 2.18a), type III (including chute blocks, baffle blocks and an end sill, Figure 2.18b), and type IV (including chute blocks and an optional end sill, Figure 2.18c).

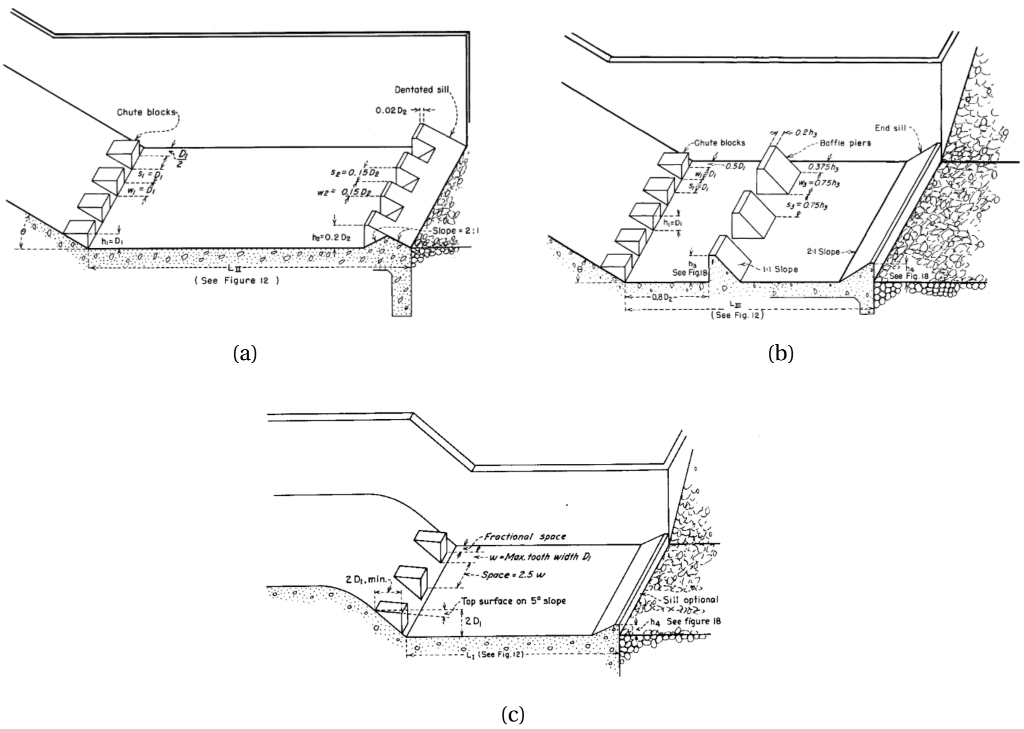
Chute blocks
Dentated sill
0.02 D_2
$\frac{D_1}{2}$
$s_1 = D_1$
$w_1 = D_1$
$s_2 = 0.15 D_2$
$w2 = 0.15 D_2$
$h_1 = D_1$
$h_2 = 0.2 D_2$
Slope = 2:1
θ
L_{II}
(See Figure 12)
Chute blocks
0.2h_3
Baffle piers
End sill
0.5D_1
$w_1 = D_1$
$s_1 = D_1$
0.375h_3
$w_3 = 0.75h_3$
$s_3 = 0.75h_3$
$h_1 = D_1$
h_3
See Fig.18
1:1 Slope
2:1 Slope
h_4
See Fig. 18
θ
0.8D_2
L_{III}
(See Fig. 12)
Fractional space
w = Max. tooth width D_1
Space = 2.5 w
2 D_1, min.
Top surface on 5° slope
2 D_1
Sill optional
h_4 See figure 18
L_I (See Fig. 12)

(a)

(b)

(c)

Figure 2.18 – Sketch of the USBR (a) type II, (b) type III and (b) type IV stilling basin (Peterka 1958).

2.4 Overview of existing studies on stilling basin performance downstream of stepped chutes

Although hydraulics of stepped chutes has been extensively investigated during the last three decades, only a few studies dealt with energy dissipation at their toe. At this moment, there is only a fragmentary information available on stilling basin performance downstream of stepped spillways. In the following, a brief overview of the studies concerning stilling basins downstream of stepped chutes is presented.

Houston (1987) conducted a model study of the stepped spillway and the dissipation structure of the upper Stillwater Dam (Figure 2.19). The investigation of the basin included sizing the stilling basin, measuring wave heights and impact pressure on stilling basin invert and testing debris-handling capability of the stilling basin. Stilling basin length was reduced to 10 m as a result of lower velocities at the toe of the stepped chute (when compared to the smooth invert approach).

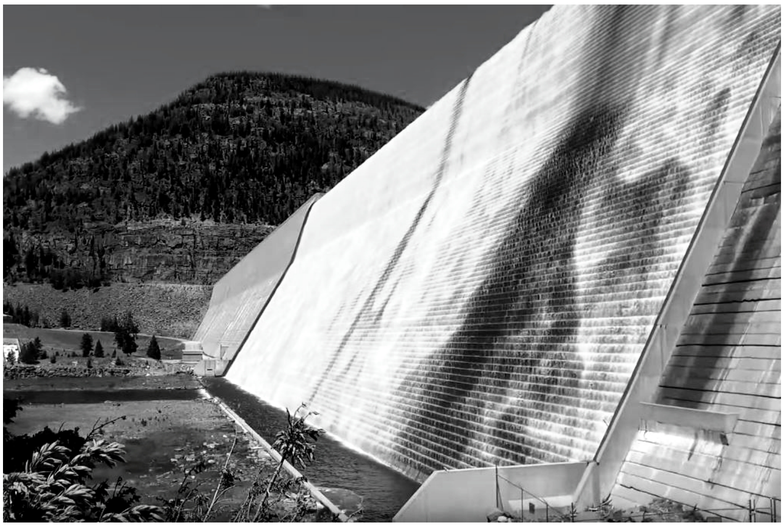

Figure 2.19 – Upper Stillwater Dam, USA. Photo from https://www.flickr.com/photos/gonzoshots/5903778121 .

Frizell (1990) investigated stilling basin with an end sill downstream of converging stepped spillway proposed for McClure Dam in USA. For designed unit discharge of 31 m^2/s, 53% of energy dissipation was recorded at the end of the converging stepped chute. The 40 m long stilling basin was tested with and without designed end sill. Removal of designed end sill produced poor flow conditions in the basin and thus basin with an end sill was adopted, which produced excellent flow conditions and energy dissipation.

Baumann et al. (2006) described two stepped spillways with stilling basins installed at the upper and lower reservoirs of the Siah-Bishe pumped-storage scheme in Iran (Figure 2.20). The arrangement was chosen mainly as a result of instabilities at the toe of the lower dam, requesting for an increased energy dissipation along the spillway and a thorough dissipation of the residual energy within the basin. Hydraulics was investigated and optimized using physical model tests with scale factors of 1:15 and 1:20. Rather small stilling basin lengths were sufficient.

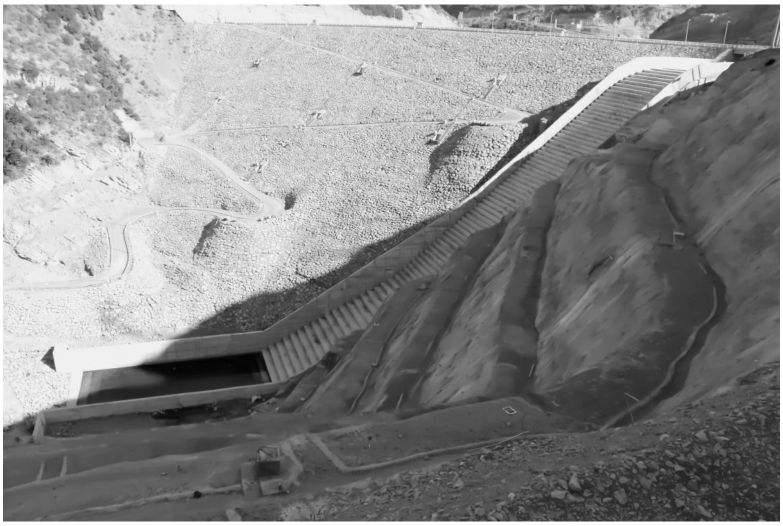

Figure 2.20 – Siah-Bishe stepped spillway, Iran (Photo: Ivan Stojnic).

Lueker et al. (2008) conducted a physical model study of the auxiliary stepped spillway of the Folsom Dam in California that was designed to operate under a unit design discharge of q=80 m^2/s and a maximum PMF value of q=163 m^2/s (Figure 2.21). The objectives of the study were, among others, to investigate the performance of the designed stilling basin for different flow conditions, measure the head loss over the stepped chute and the stilling basin, and determine if the stepped spillway or the stilling basin was prone to cavitation damages at discharges equal or less than the design flow. Initial 1:26 scale model included stepped chute and 52 m long stilling basin with a double row of 2.7 m high baffle blocks and a 1.4 m high end sill. The scale model tests showed that the designed basin was unable to keep the hydraulic jump within the basin limits under design flow conditions. Therefore, the basin length was increased up to 76 m, and the two baffle rows were replaced by one single row of seven 4.8 m tall baffle blocks and 4.5 m tall end sill. As as result, 80% energy dissipation was reported immediately downstream of modified stilling basin under the design flow condition, of which 55% was attributed to the stepped chute. Finally, low pressures zones were observed on baffle block sides and on the stilling basin invert, indicating cavitation risk for flow rates below and above the designed flow rate.

Frizell et al. (2009) discussed probable factors that could affect the design of standard stilling basins for stepped chutes. Based on reanalysis of Peterka (1958) type III basin data, i.e. with smooth chute spillways, they suggested that approaching chute angle affects stilling basin performance and that mildly sloped chute would require longer basins. As stated, this factor has a relatively small effect on the performance for smooth chute, however it was anticipated to have a more pronounced effect for stepped chutes. They further hypothesized that slope dependence for type III basins appears to be closely linked to the baffle blocks and inflow velocity distribution. For flatter slopes, streamline curvature is reduced resulting in a less abrupt transition and hence a localized reduction in energy dissipation. A comparison of the velocity profiles (obtained with numerical simulations) at the upstream end of the basin indicated the stepped spillway significantly decreased the average value and smoothed the velocity profile. Accordingly, this could reduce energy dissipation especially within the lower one-third of the water column thus reducing the impact of the baffle blocks in the overall performance of the stilling basin. In addition, reanalysis of Peterka's (1958) type II and type V data did not show any slope dependence, strengthening the idea that for a type III basin, the vertical distribution of velocity (i.e. energy) entering the basin is of more importance due to the effect of baffle blocks.

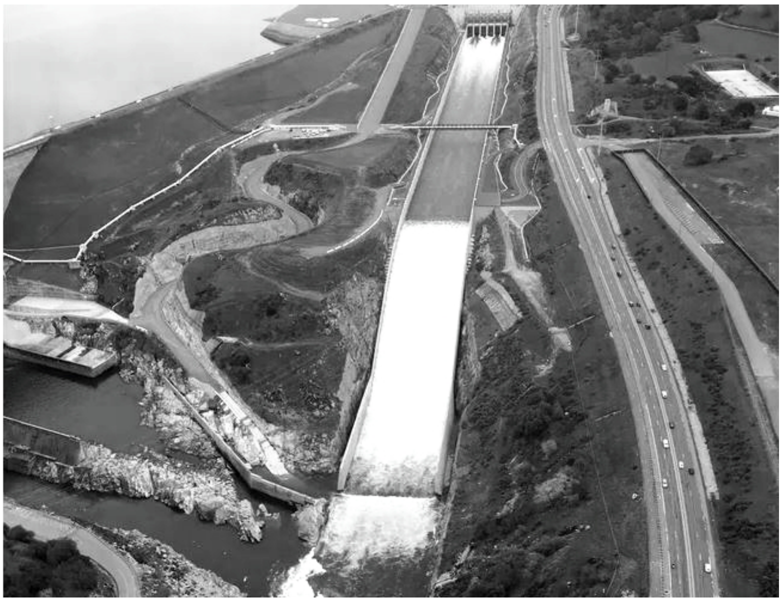

Figure 2.21 – Folsom dam with auxiliary stepped spillway, USA. Photo from https://kfbk.iheart.com/featured/cristina-mendonsa/content/2019-02-13 -making-room-for-the-pineapple-express/.

Several experimental studies on USBR simple stilling basin and modified III stilling basin performance downstream of stepped chutes were conducted at National Laboratory of Civil Engineering (LNEC) in Lisbon (Meireles et al. 2005; Cardoso et al. 2007; Meireles et al. 2010; Bung et al. 2012). The experimental facility featured 2.9 m high, 1.0 m wide stepped chute with a $\varphi = 53°$ bottom slope followed by a 5.0 m long, 1.0 m wide stilling basin. These studies mainly focused on mean invert pressures, length characteristics and flow depths. All studies were conducted for stepped chute operating in skimming flow regime with approach flow Froude number of about $F_1 = 8$, mean air concentration of about 60% and flow rates within 0.08 $\mathrm{m^2/s} \leq q \leq 0.2\ \mathrm{m^2/s}$. Flow depths and length characteristics were visually collected with rulers mounted on transparent sidewalls, whereas mean invert pressures were recorded in the basin centerline and 0.03 m apart from the centerline using piezometric pressure taps. Meireles et al. (2005) studied a simple stilling basin mainly focusing on mean invert pressures. Two different step heights were tested, namely s=0.04 and 0.08 m. Cardoso et al. (2007) investigated flow depths, length characteristics and mean invert pressures of a simple and USBR type III stilling basin. The USBR type III basin was designed following design guidelines of Peterka (1958) with an exception to the upstream end where the chute blocks were not mounted due to the stepped configuration of the approaching channel. Further to the study of Meireles et al. (2005), step height of s=0.02 m was additionally tested for simple stilling basin. A study of Meireles et al. (2010) mainly focused on the hydraulic characteristics of USBR type III stilling basin. Mean invert pressure and flow depth data for type III basin were recorded for s=0.04 m high steps. In addition, the effect of upstream chute blocks was evaluated. Due to the stepped spillway surface, the chute blocks were not installed in an inclined plane, as recommended by the USBR for smooth chutes. Instead, modified cubic blocks were mounted in the last step niche. Bung et al. (2012) extended the work previously conducted at LNEC by analyzing the influence of chute blocks and tailwater elevations on the performance of type III stilling basins. Three different arrangements of type III basin were tested: (1) without chute blocks, (2) modified cubic chute blocks used in Meireles et al. (2010) and (3) conventional chute block in combination with a filled step niche. All tests were performed for s=0.08 m high steps for five different tailwater elevations. The main results of the above mentioned studies can be summarized as:

- Mean invert pressure head of simple stilling basin increases with augmenting discharge (Meireles et al. 2005; Cardoso et al. 2007),
- For a given discharge, mean invert pressure heads in simple stilling basin were almost independent of the step height (Meireles et al. 2005; Cardoso et al. 2007),
- At the impact point of flow (i.e. immediately downstream of the stepped chute), the mean pressure head were significantly larger than those corresponding to hydrostatic pressure for both simple and USBR type III basin (Meireles et al. 2005; Cardoso et al. 2007; Meireles et al. 2010),
- Downstream of the impact region the mean invert pressure head becomes lower than the flow depth for USBR type III basin (Meireles et al. 2005; Cardoso et al. 2007; Meireles et al. 2010),
- Low pressure peak values were observed in the tap located immediately downstream of the baffle blocks, resulting in sub-atmospheric values for the largest discharges (Cardoso et al. 2007),

- A larger increase of the mean pressure head next to the baffle blocks and reduced jump length are observed for the type III basin (Cardoso et al. 2007),
- The conjugate depth of the type III basin was approximately 80% of that corresponding to simple stilling basin (Cardoso et al. 2007),
- The adjustment between flow depths along the type III basin and flow depths proposed by Peterka (1958) was acceptable (Meireles et al. 2010),
- Mean pressure head at the entrance of the type III basin downstream of stepped chute is considerably higher than those proposed by Peterka (1958) (Meireles et al. 2010),
- The hydraulic jump stabilizes faster (i.e. jump length is shorter) for type III basin compared to simple stilling basin downstream of stepped chute (Meireles et al. 2010),
- Chute blocks seem to be dispensable in USBR type III basin in combination with stepped spillways (Meireles et al. 2010; Bung et al. 2012),
- The maximum pressure at impingement is only discharge dependent with a value of approximately $3.8h_c$. Further downstream, a considerable influence of the tailwater elevation was found.

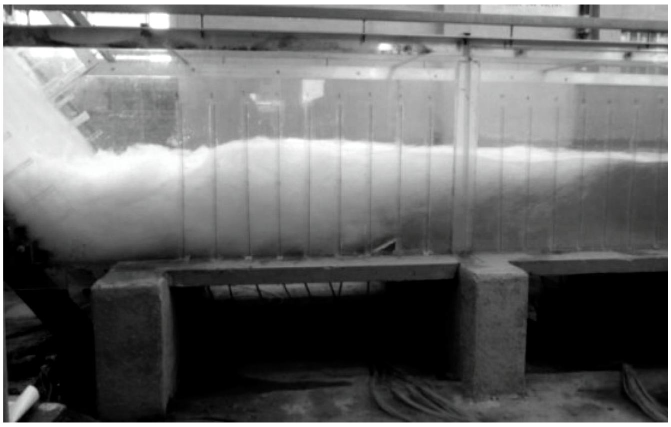

Figure 2.22 – Sideview photo of a USBR type III stilling basin downstream of a 53° sloping stepped chute at LNEC (Lisbon) in operation (Meireles et al. 2010).

Frizell and Svoboda (2012) and Frizell et al. (2016) studied the performance of USBR type III stilling basin downstream of smooth and stepped chute, mainly focusing on flow depths and length characteristics of the jump. Smooth and stepped chute were investigated with pseudo bottom angles of φ=14°, 26.5° and 51°. Water to the chute model was supplied via a jet-box with unit flow rates ranging within 0.25 $m^2/s \le q \le 0.62$ m ^{2}/s. At the downstream end of the chute, quasi-uniform flow conditions were attained and verified by air concentration measurements in several cross-sections close to the chute end. USBR type III basin was designed for a Froude number of F_1=8 with incoming depth of h_1=0.076 m. Two tailwater depths were tested, namely fully conjugated depth and sweep out conditions (i.e. minimum acceptable tailwater depth). Several parameters were measured, namely mean air concentration at the chute end, sequent depths and jump lengths. The main conclusion of the study was that the use of the equivalent clear-water parameters of stepped spillway flow allows a consistent application of the USBR design principles for a type III stilling basin. As stated, this observation was not justified physically, but pointing at flow depths measurement inaccuracy of the initial USBR study implementing unintentionally some reserve in the design principles. Acceptable stilling basin performance both in case of smooth and stepped chute was attained at sequent depth ratio 20% to 25% lower than the full sequent depth value. Furthermore, for Froude numbers F_1 ≤6, required tailwater depth was significantly lowered, to the point where the jump can be maintained solely by appurtenances. However, this finding cannot be generalized since the tested basin was designed for F_1=8.

Recently, Novakoski et al. (2017a,b) investigated bottom pressure characteristics of a simple stilling basin downstream of a 53° sloping stepped chute. Dynamic pressures were acquired, whereas the flow conditions at the chute toe were estimated based on the measurement of the subcritical depth of the hydraulic jump (positioned at the beginning of the straight section of the stilling basin), along with the application of Bélanger and continuity equations. Pronounced mean, fluctuating and extreme pressure magnitudes were reported at the closest point to the stepped chute. These were attributed to the abrupt flow deviation. Both roller and jump lengths were obtained, based on the location where the skewness coefficient reached its minimum value, or where the skewness coefficient showed a tendency to stabilize around zero, respectively. The longitudinal distribution of the skewness and kurtosis coefficients for a hydraulic jump formed downstream of a smooth or a stepped chute were found to be similar. The simultaneous analysis of both parameters lead to the conclusion that the pressure data at a given position within the hydraulic jump did not follow a normal probability density function.

Finally, Valero et al. (2016, 2018) numerically investigated USBR type III stilling basin performance downstream of stepped chute using a single fluid approach. The experimental set-up used in Frizell and Svoboda (2012) was entirely reproduced, and smooth and stepped chute configurations were compared. The performance of the stilling basin was evaluated under designed and adverse flow conditions. The results showed that stepped configuration cause higher decay of the maximum velocity within the basin. The influence of the baffle blocks was found to exceed other stilling basin elements. Accounting for both the effect of the stepped spillway and the adverse flow conditions, they concluded that the classical design of Peterka (1958), developed for smooth chute approach flows, could be improved.

2.5 Gaps in knowledge and specific research questions

In the past three decades, numerous studies on hydraulics of stepped chutes have been conducted. Flow features such as air entrainment, flow depths and energy dissipation have been successfully described and quantified. On the other hand, the hydraulic jump has been investigated for over two hundred years and is probably one of the most researched phenomena in hydraulics. However, overviewing the literature, only few studies dealt with stilling basins and associated flow features downstream of stepped chutes. The contribution of previous investigators gave some insights into the flow features of stilling basin flow downstream of stepped chute (e.g. mean invert pressures, flow depths, dynamic bottom pressures and length characteristics). However, most of these studies were limited to particular cases, for example Meireles et al. (2005), Cardoso et al. (2007), Meireles et al. (2010), Bung et al. (2012), Novakoski et al. (2017a) and Novakoski et al. (2017b) studied only one chute slope (i.e. φ =53°). Frizell et al. (2009) pointed out the importance and necessity of a systematic study to address the effect of the chute slope on the performance of the downstream stilling basin. So far, no systematic study has been conducted providing general design guidelines for stilling basins downstream of stepped chutes. Furthermore, most of the previous studies focused only on macro flow features of the hydraulic jumps (i.e. flow depths, length characteristics and mean invert pressures). Flow structure of a hydraulic jumps downstream of stepped spillways and internal air-water flow properties was not studied yet. As such, the knowledge of the stilling basin performance downstream of stepped chutes remains fragmented.

Based on the literature review and above presented gaps in knowledge, the specific research questions in the present study can be formulated as:

- What is the effect of smooth or stepped chute approach flows on the performance and hydraulic characteristics of a plain stilling basin?
- What is the effect of smooth or stepped chute approach flows on the dynamic bottom pressure characteristics?
- What is the effect of smooth or stepped chute approach flows on the air-water flow properties of the hydraulic jump?
- What is length of necessary bottom protection, i.e. stilling basin length?
- What is the effect of aerated inflows?

3 Experimental setup

3.1 Experimental facility

Experiments were conducted in the sectional spillway model at the *Laboratory of Hydraulic Constructions* (LCH) of the *Ecole Polytechnique Fédérale de Lausanne* (EPFL) in Switzerland. The experimental facility was previously used by André (2004), Ostad Mirza (2016) and Terrier (2006) to investigate stepped chute flows. The present facility consisted of three main parts (Figure 3.1): (a) jet-box, (b) chute and (c) stilling basin. The definition sketch with instrumentation and nomenclature is shown in Figure 3.2. In the following subchapters each part of the experimental facility and instrumentation will be detailed.

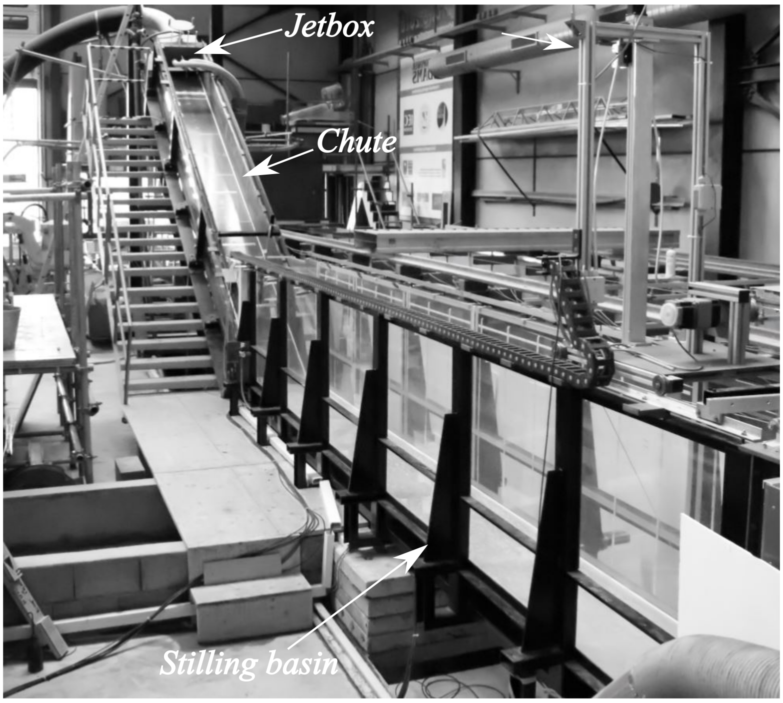

Figure 3.1 – Front view of the experimental facility.

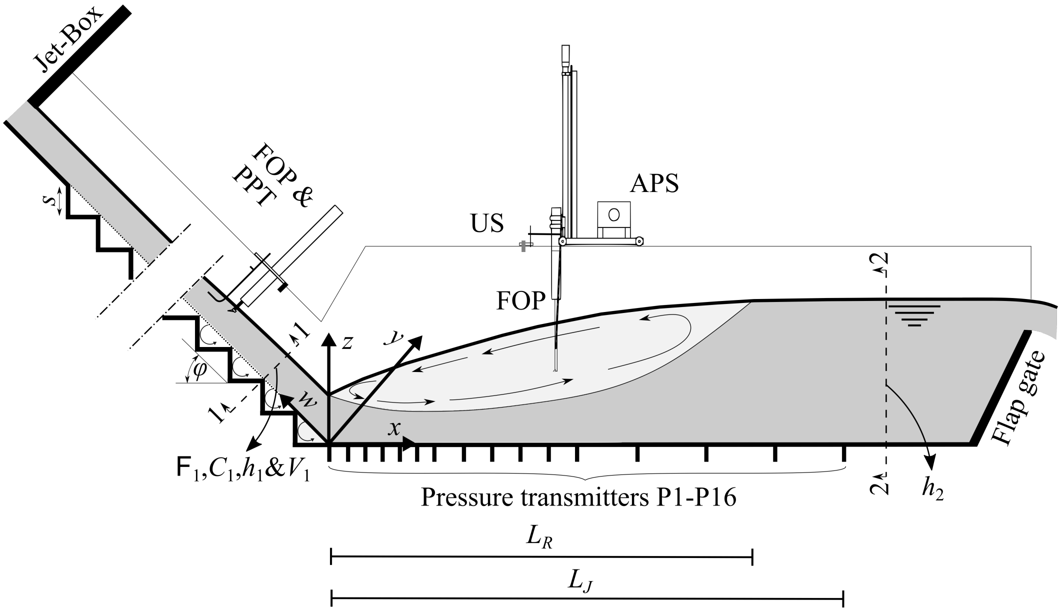

Figure 3.2 – Definition sketch with instrumentation and nomenclature. Note: FOP – Fiber optical probe, PPT – Pitot-Prandtl tube, US – Ultrasonic distance meter, and APS – Automatic positioning system.

3.1.1 Jet-box

The chute inlet consisted of a a jet-box (Figure 3.2 and 3.3), allowing generation of flows with variable conditions (Schwalt and Hager 1992). The jet-box transforms the pressurized pipe flow into a free surface flow. The pressurized flow is passed through five guiding walls inside the jetbox and twenty-two at exit (Figure 3.3b) a generating homogeneous flow distribution at the chute entrance. By using the jet-box, the flow at the chute entrance is already supercritical resulting in the shortening of the developing flow region and shifting the inception of air entertainment upstream, as compared to an uncontrolled ogee crest (Chanson 2006). Therefore, gradually varied or quasi-uniform flow conditions at the stepped chute end can be achieved with relatively short chute lengths. The jet-box opening can be varied within the range 0.015-0.113 m.

3.1.2 Chute

The chute channel was made out of 2 m long, rectangular and prismatic modules with the jetbox installed in the most upstream one (Figure 3.4a). The channel was 0.5 m wide and 0.6 m deep measured from the bottom. The chute slope φ was constant and adjustable. Two slopes were tested, namely φ=30° and φ=50° with 5.9 and 4.8 m long chutes, respectively.

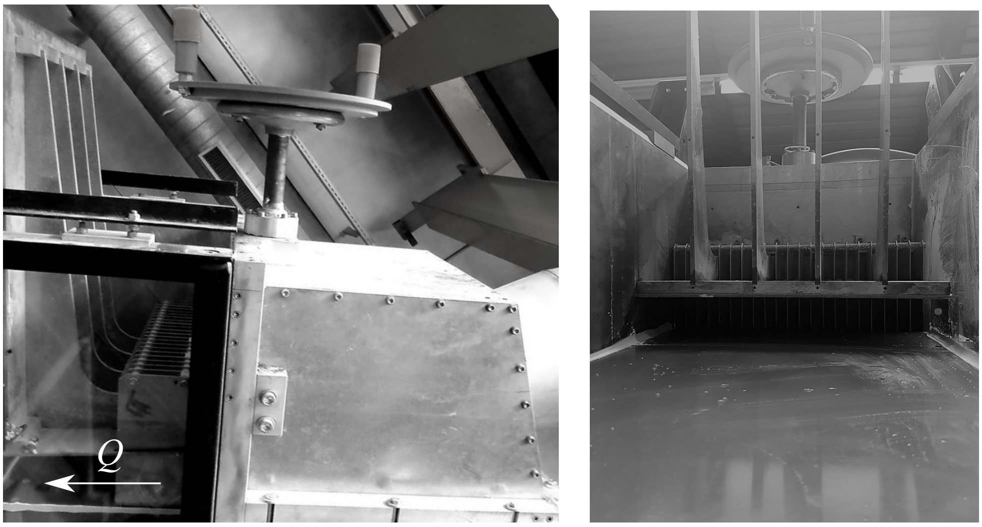

(a) (b)

Figure 3.3 – The jetbox: (a) view from the side and (b) downstream view without front panel.

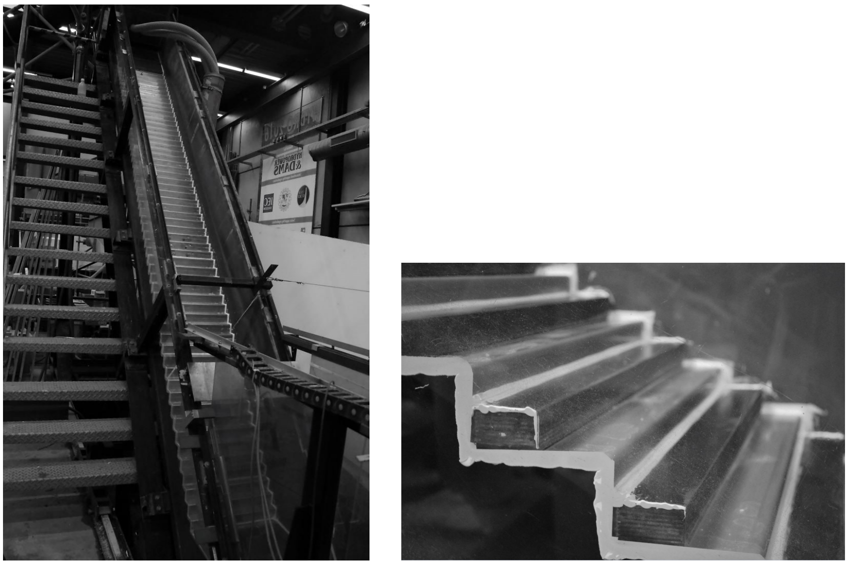

(a) (b)

Figure 3.4 – Stepped chute configuration: (a) downstream view (s=0.06 m and φ=50°), and (b) sideview of s=0.03 m high steps (φ=30°).

The channel sidewalls were made of aluminum plates on the right side and of glass on the left side (in the streamwise direction), allowing flow observation. The upstream reach of the chute channel (within 0.47 m downstream of the jet-box) was modeled with a smooth bottom (build in PVC) representing the final reach of the standard ogee crest (Figure 3.2 and 3.4a). Further downstream, the chute channel was equipped with steps made out of folded stainless-steel sheets with fold radius of 6.0 and 5.5 mm for 30° and 50° sloping chutes, respectively. The step height was constant along the chute and set to s=0.06 m. Smaller step height, i.e. s=0.03 m, was modelled by inserting rectangular wooden bars in the stainless-steel step cavities (Figure 3.4b). The total number of 0.06 m high steps was 45 and 56 for 30° and 50° sloping chutes, respectively. In case of smaller step height the latter numbers were doubled.

Smooth chute configuration was modelled by installing 10 mm thick PVC plates on top of the steps (Figure 3.5a). However, this configuration generated black-water flow at the chute end. Two means were applied to provoke aerated flow at the smooth chute end:

1. Placing a 4.0 m (φ = 30°) or 3.5 m (φ = 50°) long, 0.496 m wide and 0.0015 m thick metal grid with rectangular holes of 0.008 m spaced by 0.002 m on the smooth bottom (Figure 3.5b and 3.6a).

2. Pre-aerating the approach flow in combination with metal grid placed on the smooth bottom.

Pressurized air was introduced into the flow directly in the supply conduit of the jetbox, 15.0 m upstream of the its cross section by means of two air supply hoses provided by EPFL's infrastructure, each at roughly 8 bars of pressure (Figure 3.6b). In such a way homogeneous aerated flow was attained at the chute entrance.

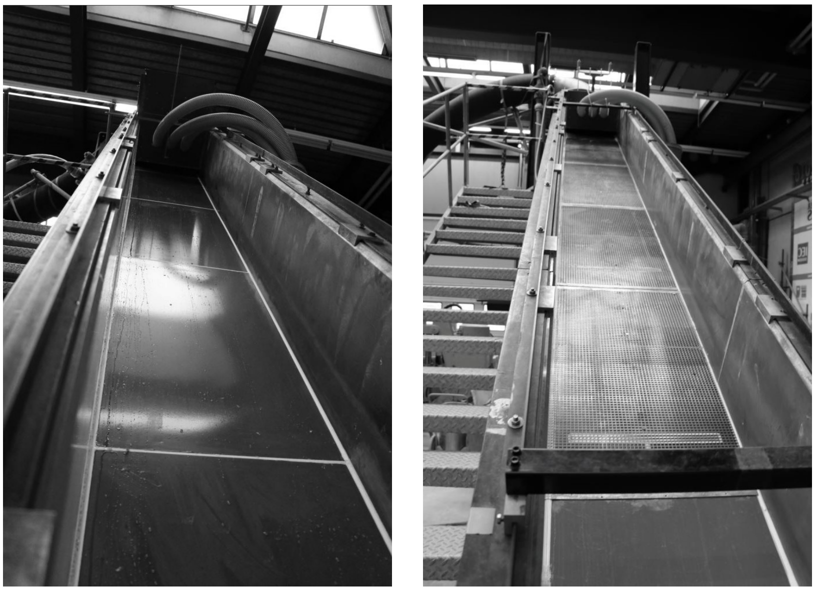

(a) (b)

Figure 3.5 – Smooth chute configuration: (a) downstream view without the grid (φ=50°), (b) downstream view with the grid (φ=30°).

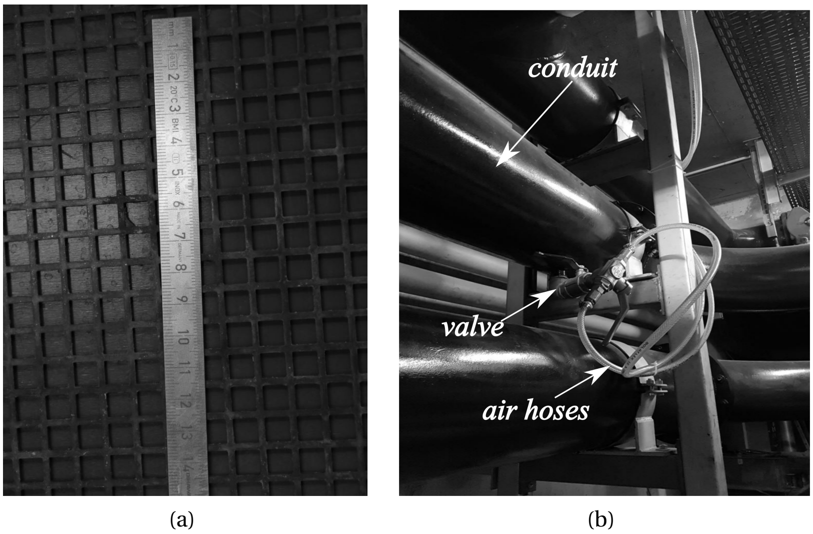

(a) (b)

Figure 3.6 – (a) Closeup view of the grid and (b) pre-aeration setup.

3.1.3 Stilling basin

The chute channel was followed by a 6.0 m (φ = 30°) or 6.5 m (φ = 50°) long and 0.5 m wide plain,horizontal and prismatic stilling basin channel (Figure 3.7). The stilling basin channel was built with 0.015 m thick aluminum plates as bottom, and transparent PMMA sidewalls for flow observation. A flap gate installed at the end of the stilling basin channel allowed the control of the tailwater depth (Figures 3.2 and 3.7).

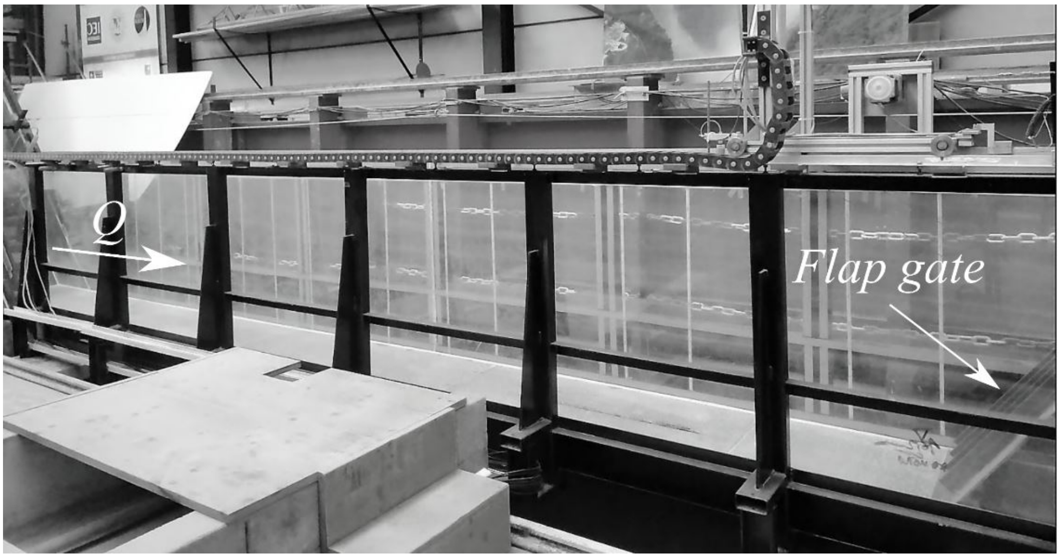

Figure 3.7 – Sideview of the stilling basin.

3.2 Instrumentation

3.2.1 Flowmeter

An electromagnetic flowmeter ABB FXE4000 (COPA-XE) (Switzerland) was used to measure the water discharge Q supplied to the experimental facility. The latter was installed on the supply conduit (DN300) of the jet-box. The flowmeter can measure up to Q_{max}=0.667 m^3/s with a measuring accuracy better than ±0.5% for flow rates above $0.07Q_{max}$. As such, the maximum errors for herein tested conditions were between ±0.005 and ±0.009 m^3/s. The flow meter was calibrated before the experimental campaign with an in-house made calibration system. The flow rate was acquired during the entire experiment via the command system of the laboratory. The acquisition frequency was set to 0.33 Hz.

3.2.2 Fiber optical phase detection system

Most of the research on high velocity air-water flows in hydraulic structures in past two decades was performed using phase detection systems with a: (a) conductivity and (b) fiber optical probe. In the present study, the two-phase flow measurements were conducted using a dual tip fiber optical phase detection system (RBI Instrumentation, France) (Figure 3.8). The latter was previously successfully used by Boes (2000c), André (2004), Kramer (2004), Pfister (2008), Ostad Mirza (2016) and Terrier (2006) for chute flows and by Murzyn et al. (2005) in hydraulic jumps. A comparative analysis between a conductivity and fiber optical phase detection system for stepped chute flows was performed by Felder and Pfister (2017) in the same experimental facility used in this study. The analysis indicated no major differences in basic air-water properties.

The fiber optical phase detection system comprises of four parts:

1. The fiber optical probe (hereafter FOP) made out of the optical fiber with a sapphire tip at its end of some 30 microns in diameter (Figure 3.8a and 3.8b). The measuring principle of the FOP relies on the discrete variation of the refraction index of the flow components (i.e. air and water). The sapphire tip acts as a Descartes prism thus, depending on the medium in contact, the light supplied through the optical fiber will be either reflected (water) or diffracted by the wall (air). By using a second optical fiber with the tip positioned at some streamwise distance behind the first one, the flow velocity can be deduced from the cross-correlation analysis of the two signals.
2. The opto-electronic module which acts as a source of infrared light supplied to the optical fiber and a receiver of the reflected infrared light (Figure 3.8c). The module is equipped with a photo-sensitive element which transforms the optic signal into an electric one. The resulting analog signal is amplified and shaped into a TTL signal with 0 V corresponding to the water and 5 V to air phase.The signal is visualized on the oscilloscope allowing signal adjustment onsite.

3. The acquisition card which receives the output TTL signal from the opto-electronic module and transmits it to the PC at the rate of 1 MHz, fixed by the manufacturer (Figure 3.8c).

4. The acquisition and treatment software "Interface Software for Optical probe" (ISO v2.09) in which the probe geometry and acquisition settings are defined and data post-processing is performed (Figure 3.8d). During acquisition, a series of .rbi files are generated, each containing the information on the measured air concentration, intefacial frequency (i.e. bubble number), interfacial velocity, interfacial area and Sauter diameter at the measuring location. The software is equipped with a synthetic analysis option allowing batch analysis of the generated .rbi files producing a single spreadsheet containing all results for a particular experimental run.

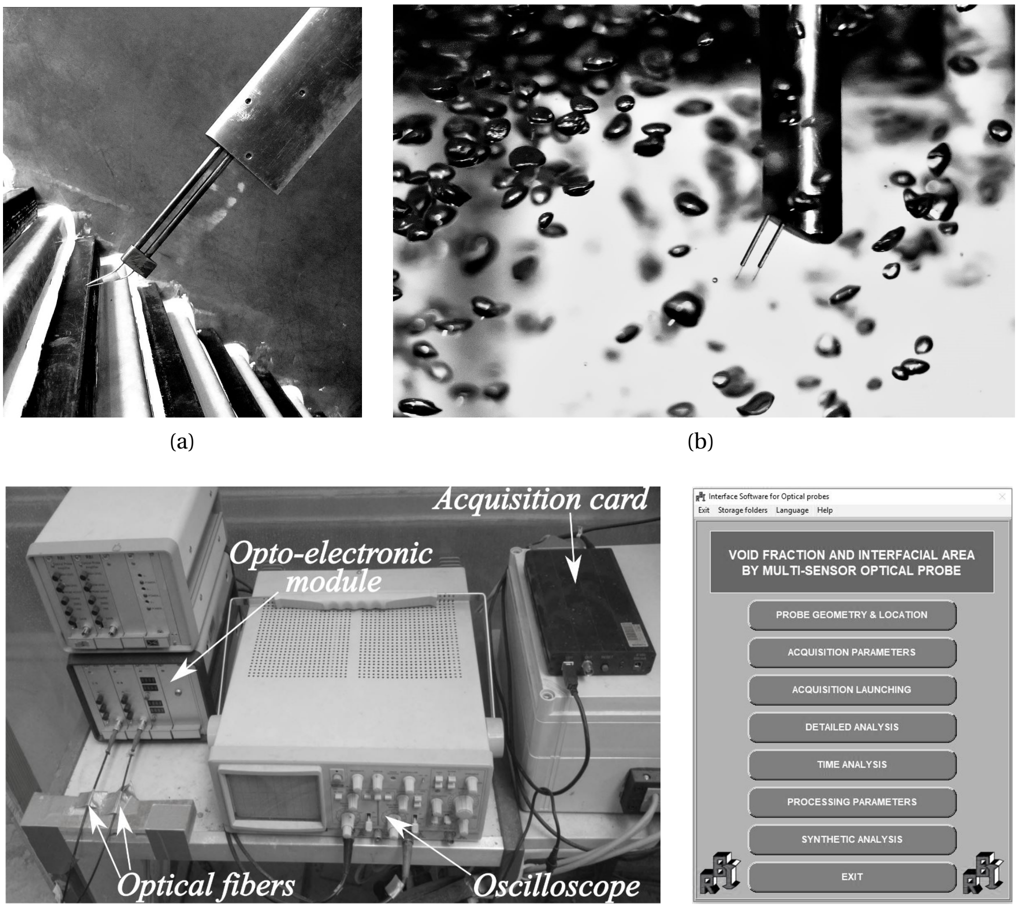
Acquisition card
Opto-electronic module
Optical fibers
Oscilloscope
Interface Software for Optical probes
Exit
Storage folders
Language
Help
VOID FRACTION AND INTERFACIAL AREA BY MULTI-SENSOR OPTICAL PROBE
PROBE GEOMETRY & LOCATION
ACQUISITION PARAMETERS
ACQUISITION LAUNCHING
DETAILED ANALYSIS
TIME ANALYSIS
PROCESSING PARAMETERS
SYNTHETIC ANALYSIS
EXIT

(a) (b)

(c) (d)

Figure 3.8 – The fiber optical phase detection system: (a) sideview of the FOP used for chute measurements, (b) sideview of the FOP used for stilling basin measurements in operation, (c) opto-electronic module, oscilloscope and acquisition card, and (d) acquisition and treatment software ISO v2.9.

A FOP design, previously used by Ostad Mirza (2016) and Terrier (2006), featuring a hydrodynamically shaped aluminum housing, optimized for chute flows was used for the chute end measurements (Figure 3.8a). The FOP had an in-line tip arrangement with streamwise tip distance of 1.2 mm. The tip distance was measured with a microscope of an accuracy below 0.001 mm. Air concentration and velocity profiles (some 15-20 points per profile) were measured at the chute centerline, perpendicular to the bottom/pseudo-bottom, in three sections close to chute end. More precisely, measurements were performed at the sections w= 0.260, 0.460 and 0.660 m for smooth chute configurations and at step edges 2, 3 and 4 (i.e. w= 0.240, 0.360 and 0.480 m) and 3, 4 and 5 (i.e. w=0.235, 0.313 and 0.391 m) for stepped chute configuration with φ=30° and φ=50° sloping chutes, respectively (see Figure 3.2 for axis definition). The FOP was placed on a chute trolley and positioned manually with an aid of Vernier scale of an accuracy below 0.1 mm. The sampling duration was 30 s with acquisition frequency of 1 MHz.

Air-water flow properties in the stilling basin were measured using an additional dual tip FOP (Figure 3.8b). The preliminary stilling basin measurements involved the same, previously described, FOP design (Figure 3.8a) and led to the severe damage of the probe tips. Thus a more robust FOP design incorporating a stainless-steel circular rod housing with shorter optical fiber and sapphire tip support channel was used for stilling basin measurements (Figure 3.8b). The FOP also had an in-line tip arrangement with a streamwise distance of 2.51 mm. The probe was mounted on the two axis automatic positioning system (hereafter APS, Figure 3.2) together with a wing shaped support structure shown on Figure 3.14b to minimize flow induced vibrations. The measurements were conducted at 15 equidistant sections along the stilling basin centerline ranging within 0.1≤ $x/L_{R,\eta}$ ≤1.5, where $L_{R,\eta}$ is the roller length derived from the flow depth measurements (reported in Appendix A). The air-water flow properties were collected perpendicular to the basin invert, including 40 points per section from 6 mm distance to the bottom up to the flow surface. Each point was measured for 45 s at an acquisition rate of 1 MHz.

3.2.3 Pitot-Prandtl tube

A Pitot-Prandtl tube (i.e. Pitot-static tube, hereafter PPT) with a classical design (Figure 3.9a) was used to measure mono-phase velocities in regions of low air content, where the phase detection probe could not reliably measure the flow velocity due to the insufficient number of entrained bubbles. The measurements were restricted to region with local air concentrations below C<0.03 as pressure readings can be adversely affected in highly aerated flows. The PPT consisted of an inner tube with 1 mm diameter and an outer tube with an external diameter of 3 mm with eight equally spaced 0.5 mm holes around its circumference, 24 mm from the tip. The PPT was connected to a differential pressure transducer Keller PD-33X (Switzerland) (Figure 3.9b). The pressure transducer had measuring range between 0-1 bar with an accuracy of pressure readings below 0.02 % at full scale. The pressures were sampled for 60 s with acquisition frequency of 30 Hz. The PPT was attached to the chute trolley and positioned manually using a Vernier scale of an accuracy better than 0.1 mm. The connection between the PPT and the pressure transducer was made using transparent rubber tubes allowing visual inspection of possible air bubbles entrained in the system (Figure 3.9b).

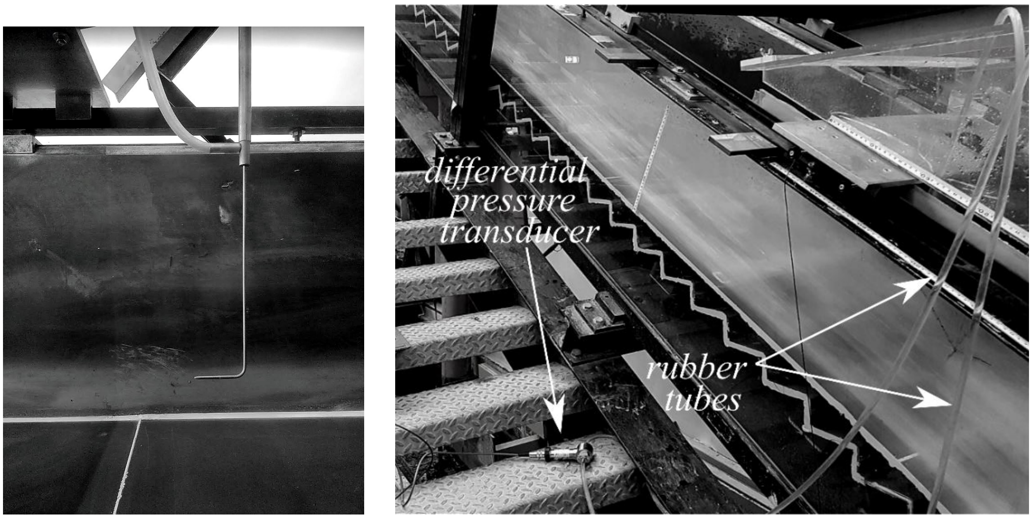

(a) (b)

Figure 3.9 – The Pitot-Prandtl tube: (a) view of the side and (b) sideview in operation with differential pressure transducer.

3.2.4 Ultrasonic distance sensor

The flow depths along the stilling basin were measured non-intrusively using an ultrasonic distance sensor (hereafter US sensor). The measuring principle of the US sensor relies on the emission of ultrasounds which reflects from the measured surface and are received by the sensor. Based on the time lag between the emitted and received ultrasound the distance between the sensor and the measuring surface can be derived. In the present study, US sensor Baumer UNAM 30U9103/S14 (Switzerland) with a measuring range of between 100-1000 mm and an accuracy below 0.5 mm was used (Figure 3.10). The response time of the sensor was below 80 ms. The sensor was attached to the APS (Figure 3.10, 3.2) with the sensor head placed parallel to the channel bottom. The flow depths were measured for roughly 328 s (4096 samples) at each measuring location with a sampling rate of 12.5 Hz. The flow depths were collected at 24 points along the stilling basin centerline for each experimental run ranging between $0.2<x<4.9$ m.

The US sensor was calibrated before the experimental campaign. In addition, before each experimental run, the sensor was tested for several levels by stacking plastic plates of known height on the stilling basin invert. In case of faulty readings, the sensor was re-calibrated.

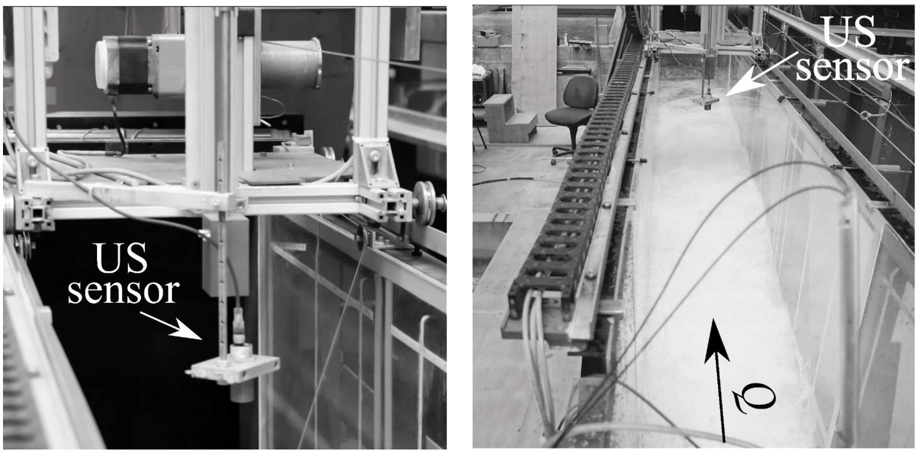

(a) (b)

Figure 3.10 – Ultrasonic distance sensor: (a) Closeup view of the sensor and (b) upstream view of the sensor in operation.

Using this measuring technique, intense surface fluctuation and splashes could result in outliers, as described by Murzyn and Chanson (2009b). The outliers are caused by:

- Severe surface deformation leading to the reflection of the ultrasound away from the sensor head,
- Foamy structure of the free surface, and
- Splashes and droplets coming into the contact with the sensitive part of the sensor

In the data post-processing, the meaningless data points were manually removed using a simple threshold technique. An example of a filtered signal is given in Figure 3.11.

3.2.5 Pressure transducers

The dynamic pressures along the stilling basin invert were measured using sixteen piezoresistive vented gauge pressure transmitters Keller series 25 (Switzerland) (Figure 3.12a). The pressure transmitters were of a flush diaphragm type. Measuring range of the pressure transmitters was ±1.0 bar with an accuracy below 0.1% at full scale. Pressures were acquired for roughly 393 s (393216 samples) at the sampling frequency of 1 kHz. Pressure transmitters were screwed directly into stilling basin invert and sealed with thread-locking fluid to ensure water tightness. The measuring cell of the transmitters was flushed with the invert, directly exposing it to the flow. The locations of pressure transducers are given in Table 1. For comparability, position of pressure transducers was kept the same in relation to the intersection of smooth chute bottom and stepped chute pseudo-bottom with the stilling basin invert (see Figure 3.2).

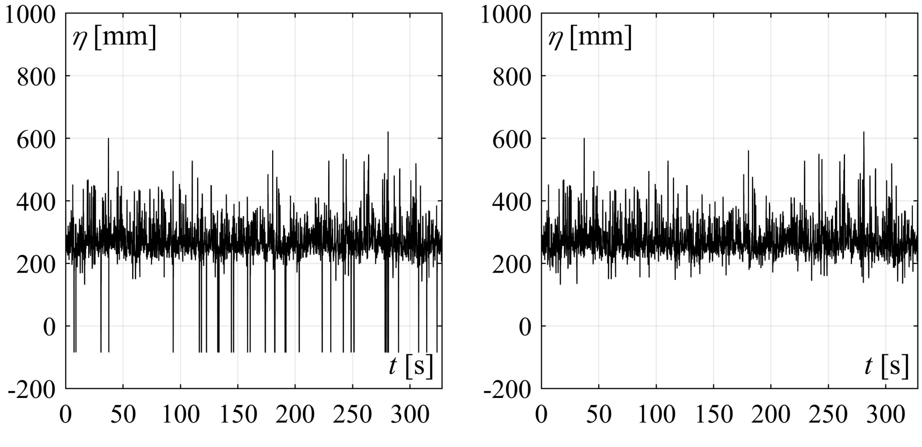

(a)

(b)

Figure 3.11 – Ultrasonic distance sensor signal for Run 11 at x=0.2 m: (a) raw and (b) filtered.

KELLER
25660

(a)

(b)

Figure 3.12 – (a) Pressure transmitter Keller series 25 (Switzerland) and (b) pressure calibrator Keller LPX (Switzerland).

Table 3.1 – Position of the pressure transmitters at the stilling basin channel centerline (Figure 3.2).

N^o	x [m]	N^o	x [m]
P1	0.010	P9	1.260
P2	0.135	P10	1.510
P3	0.260	P11	1.760
P4	0.385	P12	2.010
P5	0.510	P13	2.510
P6	0.635	P14	3.010
P7	0.760	P15	3.510
P8	1.010	P16	4.010

The transmitters were calibrated before the experimental campaign using a pressure calibrator Keller LPX (Switzerland) with a measuring range between -0.85 and 1.0 bar and accuracy below 0.05% at full scale (Figure 3.12b). In addition, the pressure readings from the pressure transmitters were checked before each experimental run with the following procedure:

- Pumps are launched and a very small flow rate is supplied to the model,
- The flap gate is raised achieving horizontal water surface in the stilling basin model (hydrostatic conditions),
- The water level and pressures along the stilling basin are simultaneously measured with the US sensor and pressure transmitters, respectively,
- The procedure is repeated for several levels by further raising the flap gate,
- The readings from the US sensor and pressure transducers are compared and, in case of faulty pressure readings, the pressure transducer(s) are re-calibrated with the pressure calibrator.

3.2.6 Acquisition card for pressure transmitters and US sensor

Signal from pressure transducers and US sensors were sampled with a high-speed acquisition system NI USB-6255 connected to a PC and controlled with a tailor made LabView® application (Figure 3.13). The sensors were powered with inhouse made power supply units. Simultaneous sampling was only performed for pressure sensors.

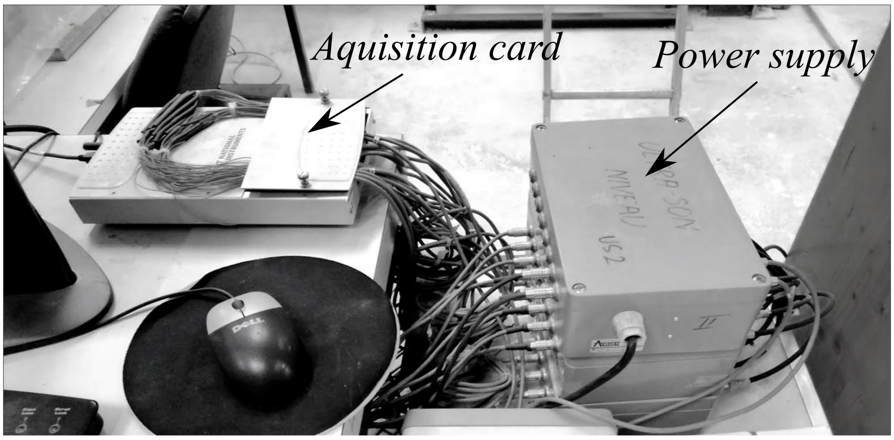

Figure 3.13 – The aqusition card and power supply units.

3.2.7 Chute trolley and automatic positioning system

The FOP and the PPT used for the chute measurements were mounted on a trolley placed at the chute end (Figure 3.14a). The trolley was positioned manually in the streamwise (w) and vertical (y) direction with an aid of Vernier scale placed on the rails and FOP or PPT probe of an accuracy below 0.1 mm.

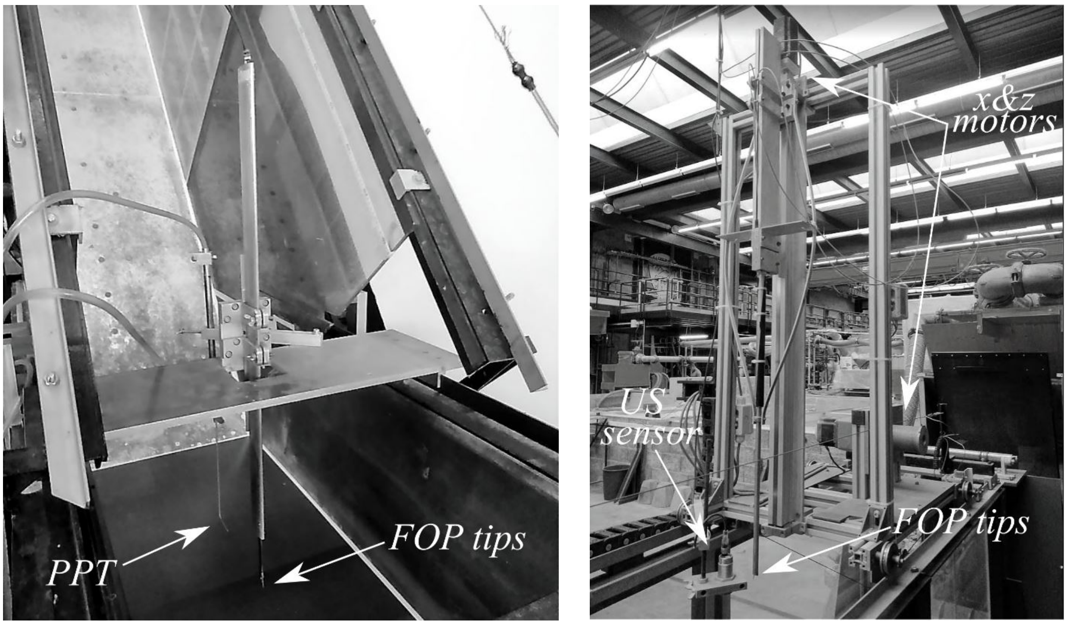

(a) (b)

Figure 3.14 – (a) Chute trolley and (b) Automatic positioning system (APS).

The flow depth and air-water flow measurements in the stilling basin were automatized by mounting the US sensor and FOP on the APS (Figure 3.2 and 3.14b). The system is motorized in the horizontal (streamwise, x) and vertical (z) direction. It can be positioned within $0<x<4.9$ m and $0.006<z<1.05$ m with an accuracy of 0.1 mm.

The APS was synchronized with acquisition cards used for air-water flow measurement (i.e. RBI system) and free surface measurement (i.e. NI USB-6255). A script, containing all commands for the positioning of the APS was generated before (during) each measuring campaign. When launched, the APS will move to the measuring location, specified in the script, stop and fire a trigger signal to the acquisition card commencing the measurement. During the measurement, the APS is paused. When the measurement is finished, the APS moves to the next specified location. At the end of the measuring campaign, the last vertical and horizontal position of the APS is measured to confirm then accuracy.

3.2.8 Visual estimation of the roller end

The end of the hydraulic jump roller was visually estimated using dye. The latter was supplied from the top of the stilling basin and the stagnation point of the flow was tracked, i.e. where no forward or backward movement prevails (Figure 3.15). Once identified, the streamwise position was measured through sidewall rulers. Due to the heavy oscillations of the flow, the procedure was repeated several times during the experimental run and an average value was taken in the analysis.

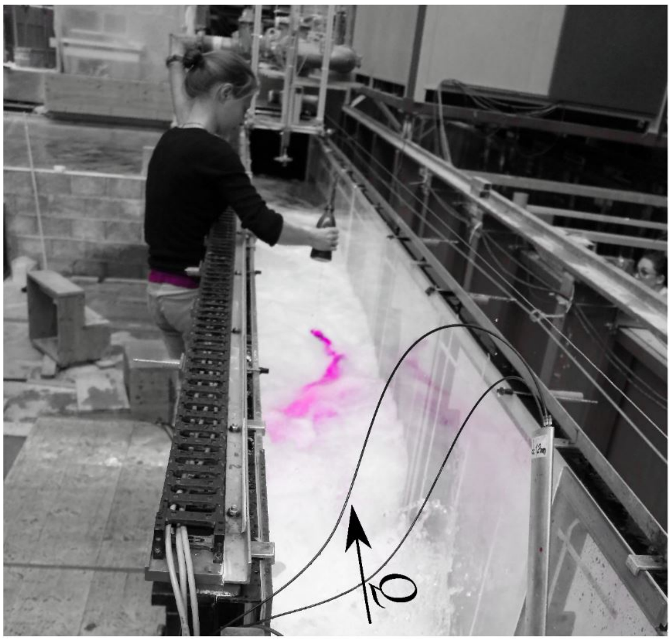

Figure 3.15 – Visual estimation of the roller end.

3.3 Test program

The experimental campaign included 30 test runs listed in Table 3.2. All experiments runs involved a plain stilling basin (i.e. basin without appurtenances).

The most downstream measured section at the chute end (i.e. w = 0.26 for smooth chutes or w = 0.26 and w = 0.235 for 30° and 50° sloping stepped chutes, respectively) was herein defined as an inflow section for the stilling basin analysis (section 1-1, Figure 3.2). Based on the measured air concentration profiles at the inflow section, the depth averaged air concentration C_1 was calculated using the Eq. (2.1). Then, the equivalent clear water parameters at the inflow section were deduced and used for the stilling basin analysis. They included (Table 3.2): (1) the inflow equivalent clear water depth h_1=(1-C_1)y_{90}, (2) the inflow mean velocity V_1=q/h_1, (3) the inflow Froude number F_1=$V_1/(h_1 g)^{0.5}$, (4) the inflow Reynolds number R_1=$V_1 h_1/\nu$ and (5) the inflow Weber number W_1=$(\rho V_1^2 h_1)/\sigma$, where ρ is the water density, ν is the kinematic viscosity of water and σ is the water surface tension.

In total 12 experimental runs with *stepped chute* approach flows were performed (ST in Table 3.2). Two chute slopes were tested, namely φ = 30° and 50°. The maximum tested chute slope of φ=50° is typical of RCC gravity dams. The second tested chute slope is more close to those typically found on the embankment dams. To assess the influence of the step size, two step size were tested, namely s = 0.03 and 0.06 m. RCC dams are built in layers with a typical thickness of 0.3 m. The spillway step height thus results from a single or multiple layers of the latter thickness. Considering the tested step size of s = 0.06, the geometrical scale with respect to prototype structures would be 1:5 and 1:15 for prototype steps of s = 0.3 m and s = 0.9 m, respectively.

The unit discharge for *stepped chute* approach flows was varied between 0.204 m^2/s≤ q ≤ 0.364 m^2/s, corresponding to the relative critical depth between 2.71 ≤ h_c/s ≤ 7.94 (Table 3.2). The unit discharge range was selected based on two criteria: (1) to minimize scale effects (discussed in the following sub-chapter) and (2) to achieve skimming flow regime on the stepped chute. The skimming flow conditions were selected as stepped spillways are typically designed to operate in this flow regime. Note that in the present facility transition flow regime occurs at around h_c/s < 0.8 and h_c/s < 1.0 for 30° and 50° sloping chute, respectively, considering criteria of Chanson (2015b) (Figure 2.2). The depth averaged air concentration at the inflow section was varied between 0.41 ≤ C_1 ≤ 0.42 and 0.46 ≤ C_1 ≤ 0.55 for 30° and 50° sloping stepped chutes, respectively (Table 3.2). Such a range of depth averaged air concentration corresponds to gradually varied or quasi-uniform flow conditions. Note that depth-averaged air concentration for quasi-uniform flow conditions for tested range of h_c/s are 0.41 ≤ C_u ≤ 0.44 and C_u ≈ 0.57 for 30° and 50° sloping chutes, respectively, according to Takahashi and Ohtsu (2012). The stepped chute approach flow conditions will be further detailed in the following chapters.

In addition, 18 experimental runs with *smooth chute* approach flows were performed, allowing direct comparison and assessment of the stilling basin performance downstream of smooth/stepped chutes (R+PA, R and SM in Table 3.2). The smooth chute test runs were performed for the same chute slopes, i.e. $\varphi = 30°$ and 50°, and similar range of unit discharges, i.e. $0.198\ \mathrm{m}^2/\mathrm{s} \le q \le 0.358\ \mathrm{m}^2/\mathrm{s}$ (Table 3.2). In order to address the influence of the aerated approach flows, flow aeration at the smooth chute end was systematically varied between $0.15 \le C_1 \le 0.32$ and $0.15 \le C_1 \le 0.37$ for 30° and 50° sloping smooth chutes, respectively. The minimum depth averaged air concentration at the inflow section of $C_1 \approx 0.15$ was achieved for smooth chute configuration without the grid of pre-aeration (SM in Table 3.2, Figure 3.5a). The higher flow aeration resulted from the roughened chute bottom (i.e. with placed grid, R in Table 3.2, Figure 3.5b) and the roughened chute bottom in combination with pre-aeration (R+PA in Table 3.2, Figure 3.6b). The approach flow conditions will be further detailed in following chapters. Test-sheets summarizing the main results of each experimental runs can be found in Appendix B.

3.4 Scale effects

In physical modeling of free surface flows, where gravity and inertia forces have a dominant effect, a Froude similitude is commonly applied (i.e. model and prototype Froude numbers must be equal). A true dynamic similarity is achieved only if Froude $Fr = h_{ref}/(ug)^{0.5}$, Reynolds $R_e = uh_{ref}/\nu$ and Weber $W_e = \rho u^2 h_{ref}/\sigma$ similitude, with h_{ref} as reference flow depth, u as characteristic velocity, ν as kinematic viscosity and σ as the surface tension, are simultaneously fulfilled, which is physically not possible in scale physical modeling. Applying Froude similitude and using the same fluids, two-phase flows cannot be modeled unless working at full scale (Felder and Chanson 2009b). The air transport in models is affected by scale effects because viscous forces represented by the Reynolds number R_e are underestimated, whereas surface tensions forces represented by W_e are overestimated (Chanson 2009c). Therefore, Froude similitude leads to higher detrainment rate since the bubbles are too large in the model (Kobus 1984). However, model families are used to study scale effects giving recommendations of minimal value of Reynolds R_e and Weber W_e number required to minimize the scale effects.

Several studies assessed the scale effects for air-water flows and various criteria to minimize scale effects were proposed. Table 3.3 summarizes the most related to stepped chute and hydraulic jump flows. Chanson and Gualtieri (2008) showed that bubble properties are more affected by scale effects than air concentration or velocities. Pfister and Chanson (2014) indicated that scale effects are expected to be small in terms of air concentration if $R_e > 2$ to 3×10^5 for $5 \le F_r \le 15$. Furthermore, they showed that if one limitation is considered, then the other is implicitly respected. If same fluids are used both in model and prototype, the Morton number becomes constant:

$$M_o = \frac{g\mu^4}{\rho\sigma^3} = \frac{W_e^6}{F_r {R_e}^4} \tag{3.1}$$

with μ as dynamic water viscosity.

Table 3.2 – Test program. SM=smooth chute, R=smooth chute roughened with grid; PA=smooth chute roughened with grid and pre-aeration, ST=stepped chute.

Test run	φ [°]	Chute Configuration	q [m^2/s]	h_c/s [-]	C_1 [-]	h_1 [m]	V_1 [m/s]	F_1 [-]	$R_1 \times 10^5$ [-]	W_1 [-]
1	30	R+PA	0.198	/	0.32	0.031	6.47	11.8	1.98	133
2	30	R+PA	0.277	/	0.32	0.038	7.22	11.8	2.77	166
3	30	R+PA	0.358	/	0.32	0.046	7.79	11.6	3.58	196
4	30	R	0.198	/	0.25	0.032	6.21	11.1	1.98	130
5	30	R	0.277	/	0.26	0.04	6.86	10.9	2.77	162
6	30	R	0.356	/	0.26	0.047	7.51	11.0	3.56	192
7	30	SM	0.198	/	0.16	0.029	6.95	13.1	1.98	137
8	30	SM	0.278	/	0.15	0.036	7.68	12.9	2.78	171
9	30	SM	0.356	/	0.15	0.042	8.38	13.0	3.56	202
		min	0.198	/	0.15	0.029	6.21	10.9	1.98	130
		max	0.358	/	0.32	0.047	8.38	13.1	3.58	202
10	30	ST s=0.06	0.204	2.70	0.42	0.048	4.24	6.2	2.04	109
11	30	ST s=0.06 m	0.284	3.36	0.42	0.058	4.91	6.5	2.84	138
12	30	ST s=0.06	0.362	3.95	0.41	0.068	5.35	6.6	3.62	163
13	30	ST s=0.03	0.204	5.40	0.41	0.047	4.34	6.4	2.04	110
14	30	ST s=0.03 m	0.282	6.70	0.41	0.056	5.07	6.9	2.82	140
15	30	ST s=0.03	0.364	7.94	0.41	0.066	5.54	6.9	3.64	166
		min	0.204	2.71	0.41	0.047	4.24	6.2	2.04	109
		max	0.364	7.94	0.42	0.068	5.54	6.9	3.64	166
16	50	R+PA	0.198	/	0.37	0.028	7.16	13.8	1.98	140
17	50	R+PA	0.280	/	0.36	0.036	7.88	13.4	2.80	174
18	50	R+PA	0.358	/	0.35	0.043	8.38	13.0	3.58	203
19	50	R	0.199	/	0.28	0.029	6.88	12.9	1.99	137
20	50	R	0.278	/	0.29	0.038	7.41	12.2	2.78	168
21	50	R	0.358	/	0.28	0.044	8.07	12.2	3.58	199
22	50	SM	0.199	/	0.16	0.026	7.61	15.0	1.99	144
23	50	SM	0.279	/	0.16	0.033	8.38	14.7	2.79	179
24	50	SM	0.356	/	0.15	0.040	8.99	14.4	3.56	210
		min	0.198	/	0.15	0.026	6.88	12.2	1.98	137
		max	0.358	/	0.37	0.044	8.99	15.0	3.58	210
25	50	ST s=0.06 m	0.205	2.71	0.55	0.041	4.95	7.8	2.05	118
26	50	ST s=0.06 m	0.284	3.36	0.53	0.051	5.52	7.8	2.84	147
27	50	ST s=0.06 m	0.364	3.97	0.50	0.061	5.96	7.7	3.64	173
28	50	ST s=0.03 m	0.205	5.41	0.50	0.040	5.10	8.1	2.05	120
29	50	ST s=0.03 m	0.284	6.73	0.48	0.050	5.71	8.2	2.84	149
30	50	ST s=0.03 m	0.364	7.94	0.46	0.060	6.08	7.9	3.64	174
		min	0.205	2.71	0.46	0.040	4.95	7.7	2.05	118
		max	0.364	7.94	0.55	0.061	6.08	8.2	3.64	174

As it can be seen from Eq. (3.1), the Morton number M_o gives a direct relation between Reynolds R_e and Weber W_e number for Froude similitude (Pfister and Chanson 2014).

For the tested flow conditions, considering criteria given in Table 3.3, the scale effects in terms of the air concentration and interfacial velocity are presumably small, given that tests included $R_1 \geq 1.98 \times 10^5$ (Table 3.2). The parameters related to the bubble characteristics, such as the air-phase frequency, are expected to be affected by scale effects (Chanson and Chachereau 2013; Pfister and Chanson 2014).

Table 3.3 – Criteria to minimize scale effects for air-water flows under Froude similitude.

Reference	Application	Characteristic	Criteria
Kobus (1984)	General	Air entrainment	R_e>1x10^5
Boes (2000b)	Stepped Chutess	Air concentration	R_e>1x10^5 W_e>100
Takahashi et al. (2005)	Stepped Chutes	Air concentration	R_e>4x10^4
Chanson and Gualtieri (2008)	Hydraulic Jumps	Air concentration	R_e>4x10^4
Murzyn and Chanson(2008)	Hydraulic Jumps	Air concentration	R_e>6x10^4
Chanson (2009c)	Hydraulic Structures	Bubble properties	R_e>5x10^5
Felder and Chanson (2009b)	Stepped Chutes	Bubble properties	R_e>1.3x10^5
Chanson and Chachereau (2013)	Hydraulic jumps	Air concentration	R_e>4x10^4
Pfister and Chanson (2014)	General	Air concentration	R_e>1.5-3.0 x10^5

3.5 Measuring procedure

Each experimental run performed herein followed the following measuring procedure:

1. A test-sheet is prepared including all test parameters, manual measurements and visual observations,
2. The physical model and instrumentation is visually inspected for any signs of malfunction,

3. The US sensor is tested for several levels and in case of faulty readings the sensor is re-calibrated,
4. Pumps are launched and a small discharge is supplied to the model. The pressure readings from the pressure transducers are checked and in case of faulty readings the pressure transducer(s) are re-calibrated,
5. The fiber optical probe's settings are checked and adapted if required,
6. The discharge is increased, the jet-box opening is adjusted and measured, and air is introduced into the supply conduit if required,
7. The toe of the hydraulic jump is pushed downstream away from the inflow section (by controlling the flap gate) to avoid any interference with the inflow conditions measurements,
8. When the stationary conditions are reached, the discharge acquisition is launched,
9. The inflow conditions are manually measured using FOP at three sections close to the chute end,
10. In case of low air content, the velocity measurements are complemented by PPT,
11. When the inflow condition measurements are completed, the jump toe is brought back to the intersection of the chute bottom and stilling basin invert (Figure 3.2),
12. The flow depths are measured along the stilling basin using the US sensor,
13. The bottom pressures are simultaneously measured with sixteen pressure transducers,
14. During the flow depth and pressure measurements, the roller end is visually measured several times,
15. The flow depths data is pre-processed and APS script is created for air-water flow measurements in the stilling basin,
16. The fiber optical probe's settings are readjusted,
17. The APS script is launched, commencing the air-water flow measurements,
18. During the measurements the model is regularly checked and the roller end is visually measured several times when the fiber optical probe does not interfere with the flow,
19. Photo and videos were taken,
20. When the air-water flow measurements are completed the last position of the APS is verified,
21. The model is turned off.

4 Hydraulic performance of a plain stilling basin downstream of 30° sloping smooth and stepped chute

4.1 Overview

This chapter investigates the effect of 30° sloping stepped chute approach flows on the hydraulic performance of a simple stilling basin. The experimental campaign included both smooth and stepped chute approaches, allowing the assessment of the stilling basin performance. Experiments were conducted under different discharges and step sizes. To asses the influence of the aerated inflows on the hydraulic characteristics of the stilling basin, smooth chute approach flow aeration was varied. The flow characteristics of the stilling basin are described, mainly focusing on flow depth, bottom pressure and length measurements.

The results show that the use of equivalent clear water parameters at the smooth or stepped chute end gives a correct prediction of the sequent depth ratio using the classical momentum principle, and thus the required tailwater depth to maintain the hydraulic jump within the stilling basin perimeter. Based on flow depth and pressure measurements, novel criteria for hydraulic jump length estimation is introduced. The jump length results show that up to 17% longer dimensionless stilling basin lengths are required after stepped chute approach flows, as compared to smooth chute approach flows and values reported in the literature. In the vicinity of the jump toe, pronounced extreme and fluctuating pressures are observed downstream of stepped chutes. The power spectrum analysis show pronounced spectral energy participation at high frequency ranges for stepped chute approach flows within the zone of pronounced pressure coefficients, indicating that the pronounced pressure coefficients are caused by the higher, step induced, turbulence levels of the incoming flow, as compared to smooth chute approach flows. The tested range of smooth chute approach flow aeration C_1 or stepped chute step size s is found not to affect the hydraulic characteristics of the stilling basin.

This chapter is based on the scientific article "Influence of smooth and stepped chute approach flow on the performance of a stilling basin" by Stojnic, I., Pfister, M., Matos, J., and Schleiss, A. J., under review in Journal of Hydraulic Engineering. The experimental work and the analyses presented hereafter are original and were performed by the author.

4.2 Test program and inflow conditions

Nine test runs with 30° sloping smooth and six with 30° sloping stepped chutes are considered in the present chapter (Table 4.1). The unit discharge q was constant during a particular run, and varied between $0.198\ \mathrm{m^2/s} \le q \le 0.364\ \mathrm{m^2/s}$ for different runs.

For the smooth chute, depth-averaged air concentration C_1 at the chute end was systematically varied between $0.15<C_1<0.32$ (Table 4.1). For the stepped chutes, a $C_1 \approx 0.41$ resulted. The inflow section for the hydraulic jump analysis (discussed in Chapter 3, Figure 3.2) was the most downstream measured section of the chute (i.e. w=0.26 m for smooth chutes, and w=0.24 m for stepped chutes).

Table 4.1 – Test program for 30° sloping chutes. SM=smooth chute, R=smooth chute roughened with grid; PA=smooth chute roughened with grid and pre-aeration, ST=stepped chute.

Test run	Chute Configuration	q [m^2/s]	C_1 [-]	h_1 [m]	V_1 [m/s]	α [-]	F_1 [-]	$R_1 \times 10^5$ [-]	W_1 [-]
1	R+PA	0.198	0.32	0.031	6.47	1.09	11.8	1.98	133
2	R+PA	0.277	0.32	0.038	7.22	1.08	11.8	2.77	166
3	R+PA	0.358	0.32	0.046	7.79	1.09	11.6	3.58	196
4	R	0.198	0.25	0.032	6.21	1.09	11.1	1.98	130
5	R	0.277	0.26	0.04	6.86	1.08	10.9	2.77	162
6	R	0.356	0.26	0.047	7.51	1.08	11.0	3.56	192
7	SM	0.198	0.16	0.029	6.95	1.08	13.1	1.98	137
8	SM	0.278	0.15	0.036	7.68	1.08	12.9	2.78	171
9	SM	0.356	0.15	0.042	8.38	1.08	13.0	3.56	202
	min	0.198	0.15	0.029	6.21	1.08	10.9	1.98	130
	max	0.358	0.32	0.047	8.38	1.09	13.1	3.58	202
10	ST s=0.06 m	0.204	0.42	0.048	4.24	1.18	6.2	2.04	109
11	ST s=0.06 m	0.284	0.42	0.058	4.91	1.18	6.5	2.84	138
12	ST s=0.06 m	0.362	0.41	0.068	5.35	1.18	6.6	3.62	163
13	ST s=0.03 m	0.204	0.41	0.047	4.34	1.19	6.4	2.04	110
14	ST s=0.03 m	0.282	0.41	0.056	5.07	1.19	6.9	2.82	140
15	ST s=0.06 m	0.364	0.41	0.066	5.54	1.18	6.9	3.64	166
	min	0.204	0.41	0.047	4.24	1.18	6.2	2.04	109
	max	0.364	0.42	0.068	5.54	1.19	6.9	3.64	166

Figure 4.1 shows the flow features for three characteristic C_1, whose air concentration profiles are shown in Figure 4.3a. The minimum value C_1≈0.15 was achieved for the *smooth chute* without grid or pre-aeration (Figure 4.1a). These profiles show almost no air below y/y_{90}<0.6 indicating that fully developed air entrainment did not occur down the chute. In the upper flow region (i.e. y/y_{90}>0.6), some air was measured due to surface instabilities. Roughening the smooth chute (by a grid, or by a grid combined with pre-aeration in the jet-box) led to an enhanced turbulent boundary layer resulting in earlier self-aeration of the flow (Figure 4.1b and 4.1c) with values of C_1≈0.25 to 0.32. The air concentration profiles show the typical S-shape profile from the advective diffusion model of Chanson and Toombes (2002). The dimensionless velocity V/V_{90} profiles, with V_{90} as velocity at $y(C=0.9)$, are shown on Figure 4.4a for all smooth chute runs (Runs 1-9). They are approximated with a power law equation, i.e. Eq. (2.25), with N=12.6 for a coefficient of determination of R^2=0.91.

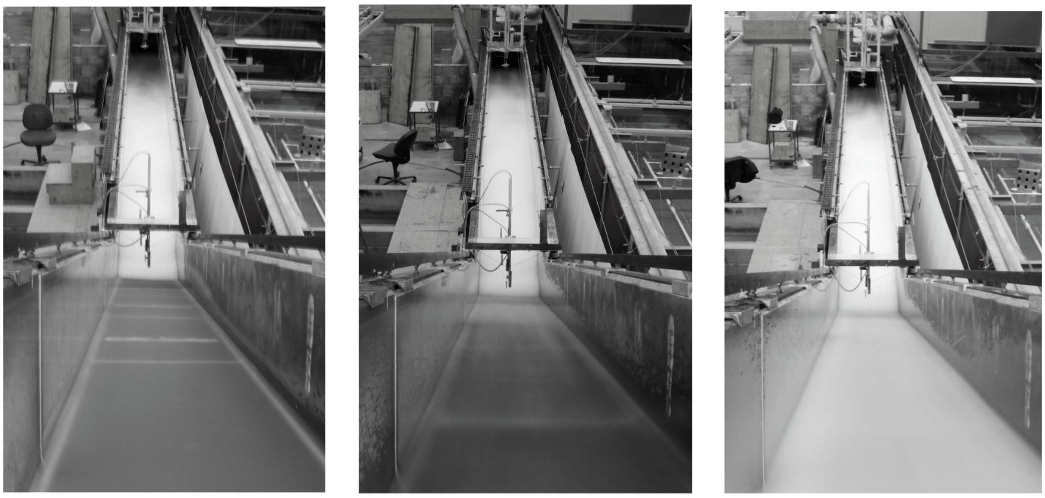
(a) (b) (c)

Figure 4.1 – Smooth chute flow characteristics seen in flow direction: (a) Run 8, (b) Run 6, and (c) Run 2.

The *stepped chute* tests were conducted with two step heights, namely s=0.03 and 0.06 m. For all tested discharges, corresponding to 2.6≤ h_c/s ≤7.9, skimming flow occurred. The air concentration profiles measured at the inflow section are shown in Figure 4.3b, whereas stepped chute flow characteristics seen from downstream is shown in Figure 4.2. The air concentration profiles (Figure 4.3b) are practically constant over distance suggesting that quasi-uniform flow conditions were attained. Measured values around C_1≈0.41 collapse with computed uniform flow values of 0.40≤C_u≤0.45 reported by Chanson (1994), Hager (1991), and Wilhelms and Gulliver (2005) for self-aerated flows on smooth chute of identical slope. The advective diffusion model (Chanson and Toombes 2002) well reproduce the concentration profiles (Figure 4.3b). Dimensionless velocity V/V_{90} profiles are shown in Figure 4.4b, approximated with Eq. (2.25) using N=5.5 and resulting in R^2=0.87.

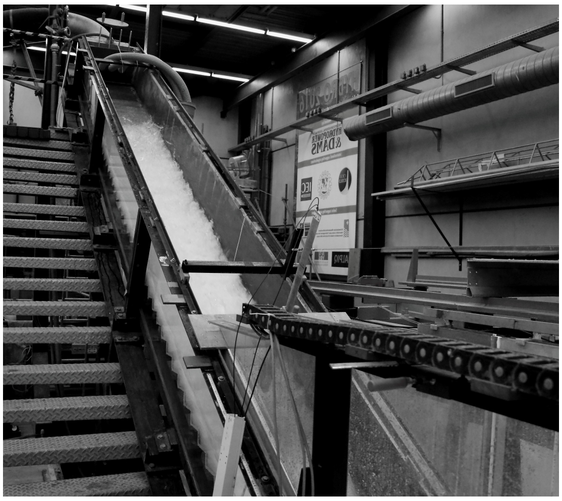

Figure 4.2 – Stepped chute flow characteristics seen from downstream for Run 10 (Table 4.1).

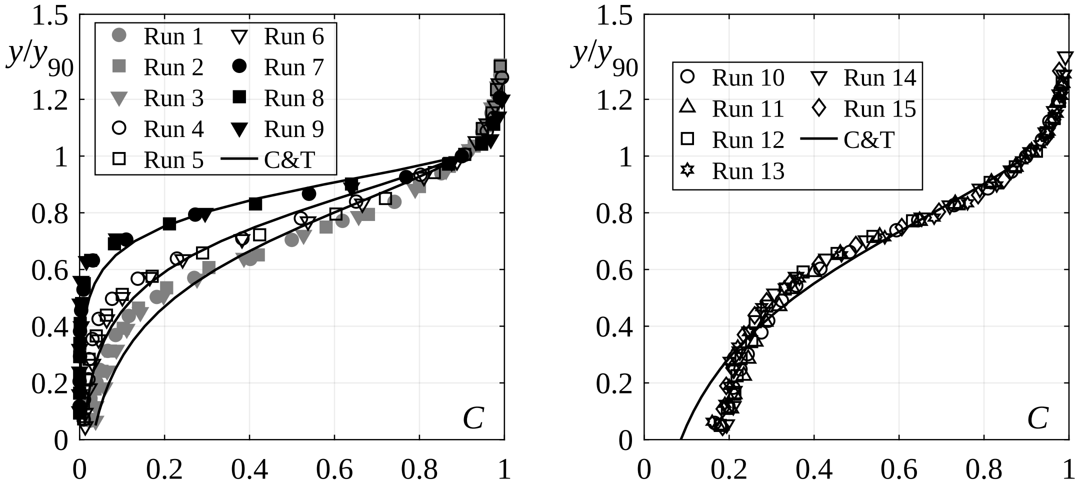

(a)

(b)

Figure 4.3 – Air concentration profiles at the inflow section for (a) smooth (Runs 1-9), and (b) stepped chutes (Runs 10-15); (——) advective diffusion model of Chanson and Toombes (2002) with C_1 from the tests.

As described in Chapter 3, the clear water parameters were derived from the air-water measurements conducted at the inflow section close to the chute end and used for the hydraulic jump analysis (Table 4.1), namely (1) the inflow equivalent clear water depth h_1, (2) the inflow mean water velocity V_1, (3) the inflow Froude number F_1, (4) the inflow Reynolds number R_1 and (5) the inflow Weber number W_1.

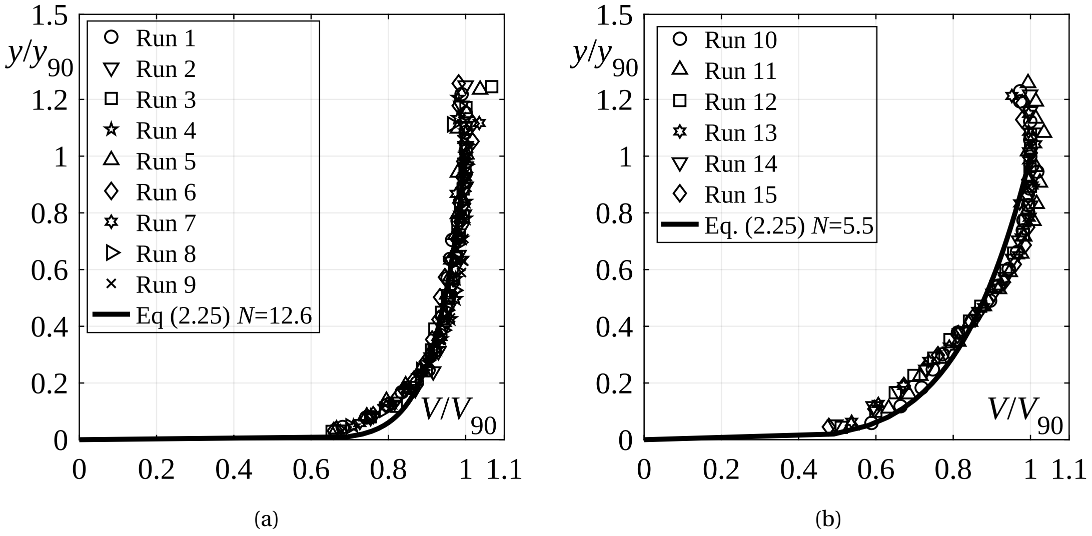

Figure 4.4 – Dimensionless velocity $V\,/\,V_{90}$ profiles at the inflow section and comparison with Eq. (2.25), for (a) smooth (Runs 1-9), and (b) stepped chutes (Runs 10-15).

4.3 Visual observations

Figure 4.5 shows a typical side view of the stilling basin in operation. A forward flow zone (bottom jet flow) and a surface roller are visible (Figure 4.5a). Vortices of different sizes and shapes were observed in the forward flow zone, growing in size with distance. The jump surface (i.e., the roller) was rough and characterized by strong pulsations, intense splashes and spray. The flow depth sharply increased from the jump toe towards the roller end, followed by a quasi-constant level in the tailwater zone.

Periodical bursts occurred in the upstream roller part, completely destabilizing the flow (Figure 4.5c). These led to more pronounced oscillations at the jump toe and to the generation of waves propagating towards the tailwater. As described by Hager (1992), the destabilization of the flow is caused by a sporadically deflection of the forward flow from the invert towards the surface leading to a “non-developed” roller (Figure 2.9). The above presented oscillations were observed for all experimental runs, however, they were less pronounced for stepped chutes as compared to smooth chutes.

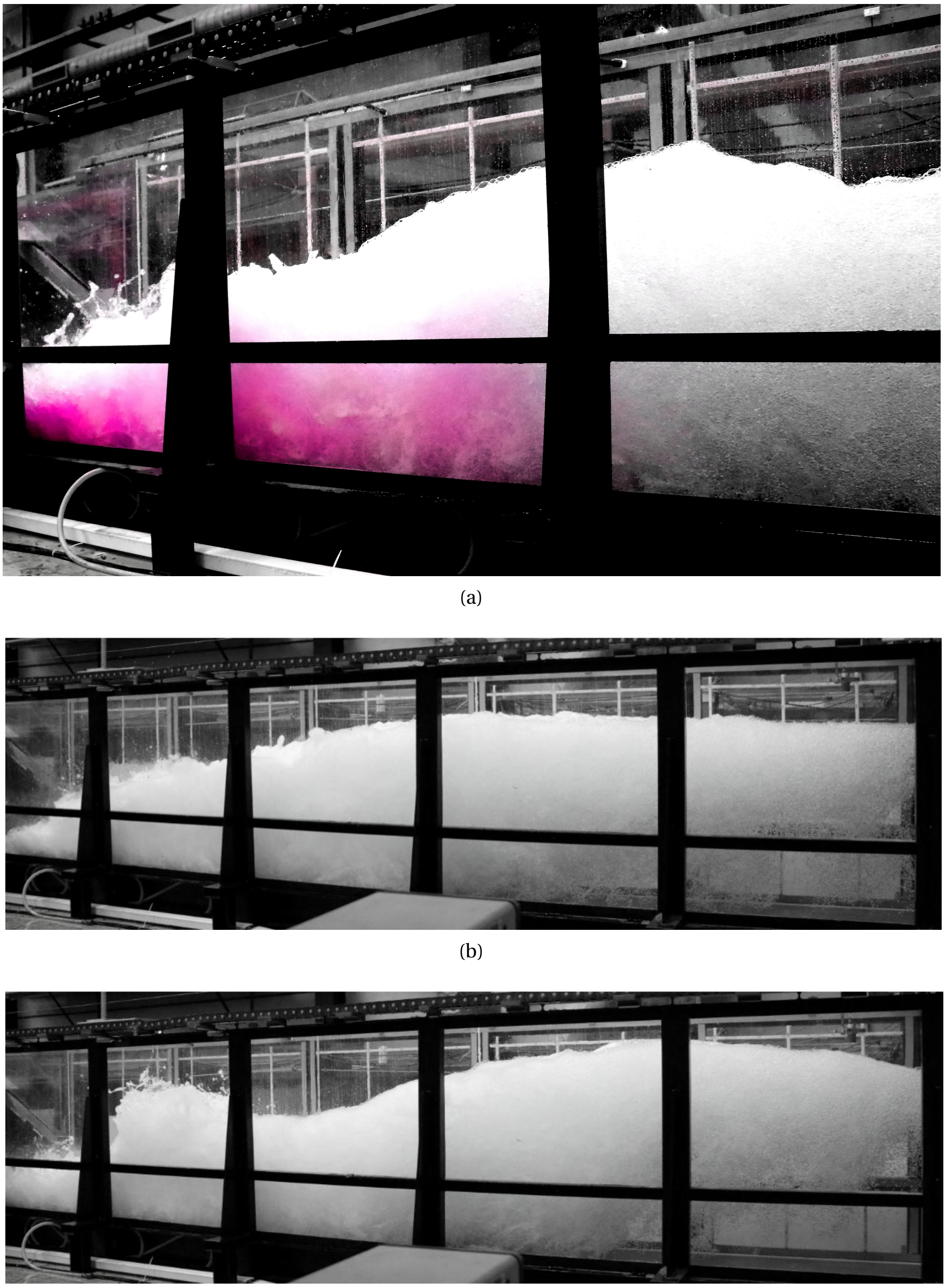

(a)

(b)

(c)

Figure 4.5 – Sideview photos of the stilling basin in operation (Run 9) showing: (a) flow structure (with injected dye), (b) “developed roller” state, and (c) “non-developed roller” state. Flow direction from left to right.

4.4 Free surface characteristics of the hydraulic jump

4.4.1 Mean flow depths

Figure 4.6 shows mean (time-averaged) flow depths η [m] as a representative example for smooth (Run 7) and stepped (Run 10) chute approach flow, respectively (Table 4.1) The profiles are characterized by a rapid and monotonic flow depth increase in flow direction at the jump toe. As expected, the reduced Froude number F_1 at the stepped chute end (as compared to that at the smooth chute end) led to lower flow depths for a quasi-similar discharge q.

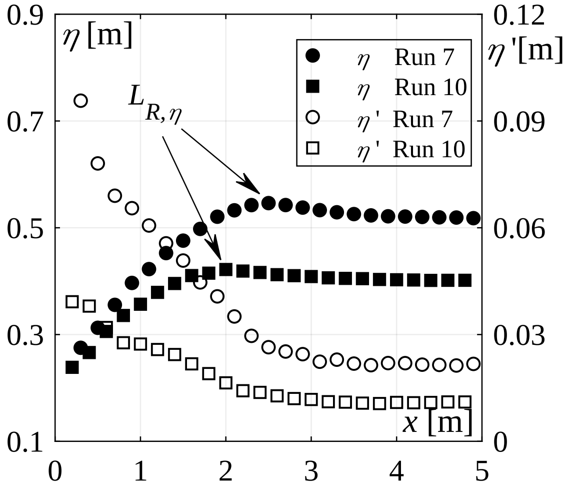

Figure 4.6 – Streamwise mean flow depth η and standard deviation η' along the hydraulic jumps of Runs 7 (smooth chute) and 10 (stepped chute).

Downstream of the surface roller reaching up to the maximum in Figure 4.6, the flow depths decrease due to intense de-aeration ultimately reaching quasi-constant depths in the tailwater. The comparison of the measured sequent depth ratio h_2/h_1 (where h_2 is the flow depth in the tailwater zone, i.e. last measuring point in the stilling basin) obtained from the momentum equation for a rectangular, prismatic and horizontal channel, i.e. Bélanger's equation Eq. (2.38), resulted in a good agreement (Figure 4.7). Accordingly, the sequent depth ratio is virtually independent of the step size or the approach flow aeration. Thus, the equivalent clear water parameters at the chute end correctly predicts the sequent depth ratio using Eq. (2.38). Although physically not sound, these results indicate that Eq. (2.38) is applicable even if the flow enters the stilling basin at an important angle relative to the horizontal (herein φ=30°). This was also observed by Peterka (1958) for smooth chute approach flows, who showed that Eq. (2.38) was applicable for a wide range of upstream chute slopes. The tailwater depth data are reported in Table A.1. Note that Figure 4.6 also shows the standard deviation η' of the fluctuating flow depths.

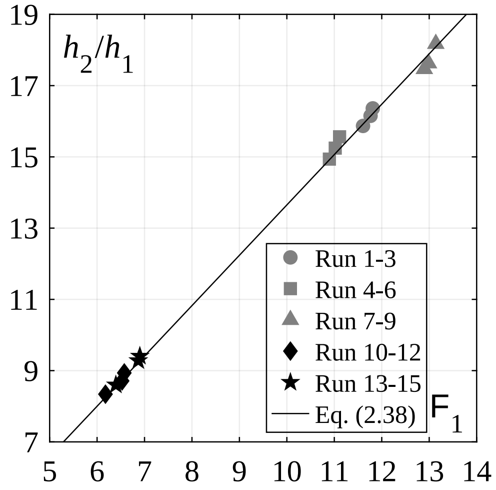

Figure 4.7 – Comparison of measured sequent depth ratio h_2/h_1 [Runs 1-9: smooth chute; Runs 10-15: stepped chute] with Eq. (2.38).

The dimensionless flow depths Z along the jump roller are described with a self-similar function (Chanson 2011; Wang and Chanson 2015a) as:

$$Z = \frac{\eta - h_1}{h_2 - h_1} = a\left(\frac{x}{L_{R,\eta}}\right)^b \tag{4.1}$$

where η is the mean flow depth, $L_{R,\eta}$ the roller (index R) length measured from the jump toe (i.e., x=0) to the surface maximum (Figure 4.6), and a and b are coefficients. The experimental data are plotted against the normalized streamwise coordinate $x/L_{R,\eta}$ and compared with Eq. (4.1) in Figure 4.8. Three sets of coefficients (1) a=1.07 and b=0.39, (2) a=1.07 and b=0.32 and (3) a=1.0 and b=0.441 (from Chanson (2011) for classical hydraulic jumps, i.e. jump formed with horizontal approach flow) are considered. It can be seen that the dimensionless flow depths Z after a stepped chute (Runs 10-15) are higher in magnitude within the first roller half, as compared to a smooth chute, which was attributed to the relatively higher approach flow depth with stepped chutes. No significant effect of the inflow aeration C_1 or of the step height s is observed. The coefficients of a=1.07 and b=0.39 for smooth and a=1.07 and b=0.32 for stepped chute approach flows results in coefficients of determination R^2=0.98 and R^2=0.99, respectively. The a and b values proposed by Chanson (2011) for classical hydraulic jumps consistently underestimate the herein measured flow depths. It has to be noted that Chanson's correlation implicitly suggests that the flow depth h_2 is equal to the flow depth at the roller end (i.e., a=1.0 in Eq. (4.1)), not being the case herein.

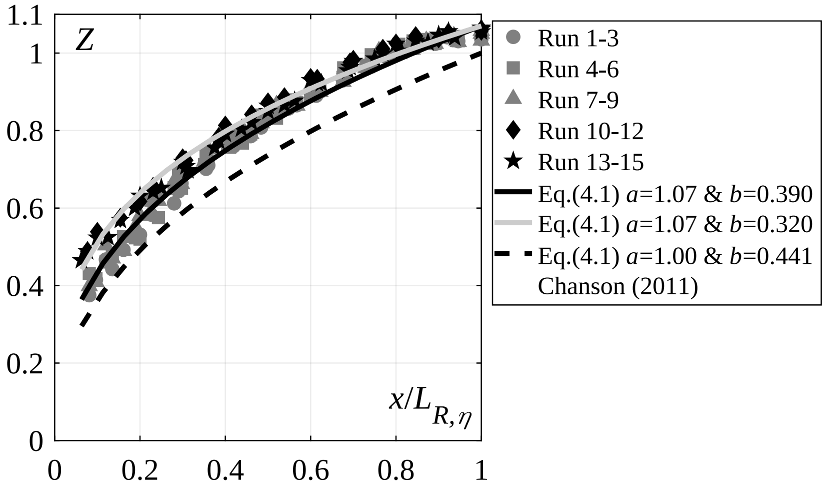

Figure 4.8 – Dimensionless flow depths Z along the hydraulic jump roller. Comparison of experimental data with Eq. (4.1); [Runs 1-9: smooth chute; Runs 10-15: stepped chute].

4.4.2 Roller length

Figure 4.9a shows the dimensionless roller lengths L_R/h_2 obtained from the flow depths measurement $L_{R,\eta}$ (Figure 4.6) and from visual observation $L_{R,D}$ (Figure 3.15), both plotted against F_1. The length data are reported in Table A.1. The measured length values $L_{R,\eta}/h_2$ (black symbols) appear to be independent of the approach flow aeration and chute characteristics with a typical value of $L_{R,\eta}/h_2 \approx 5.0$ for all runs (Figure 4.9a). The visually observed lengths $L_{R,D}$ (Figure 4.9a, open symbols) indicate consistently shorter values of $L_{R,D} \approx 4.6 h_2$. In Figure 4.9b, the roller length prediction of Hager et al. (1990), i.e. Eq. (2.47), is also added. A slight underestimation of 4% is found for visually estimated roller lengths $L_{R,D}$, whereas the measured roller lengths $L_{R,\eta}$ are underestimated by 13% as compared to Eq. (2.47). This can be explained by the different measurement techniques and definitions. Note that the visual roller length is estimated similarly as in Hager et al. (1990). The present data can be described with a slightly modified Eq. (2.47) (R^2=0.98):

$$\frac{L_R}{h_1} = c\big(-12 + 160\tanh(F_1/20)\big) \tag{4.2}$$

with c=1.04 and c=1.13 for $L_{R,D}$ and $L_{R,\eta}$, respectively (Figure 4.9b).

4.4.3 Flow depth fluctuations and jump length

The streamwise flow depth fluctuations η', corresponding to the standard deviation of the measurements, show a decrease in streamwise direction (Figure 4.6). Lower fluctuations are observed with stepped chute as compared to smooth chute approach flows. To study the streamwise development, the flow depth fluctuation coefficient $C_H{}'=\eta'/H_k$ is introduced, with

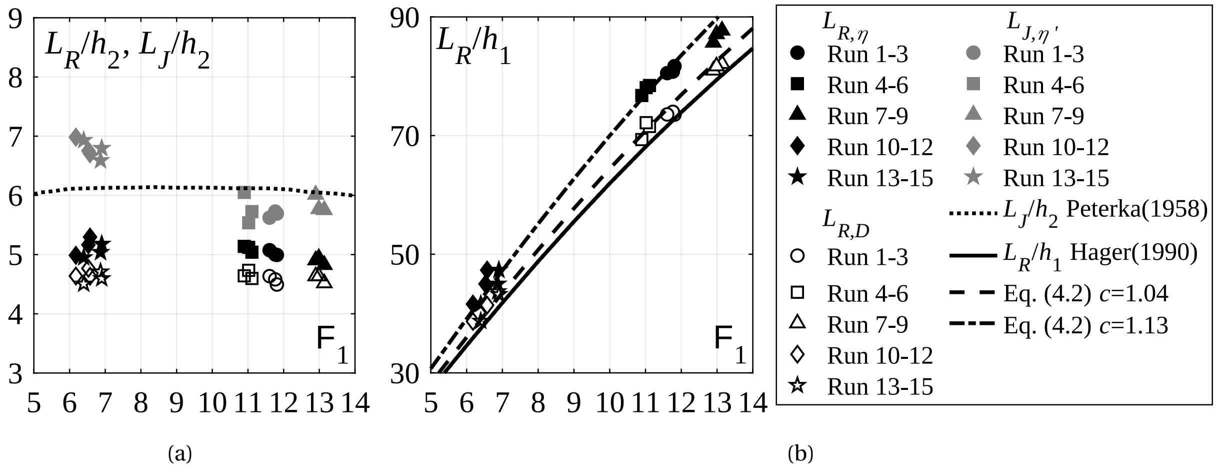

(a) (b)

Figure 4.9 – (a) Dimensionless roller L_R/h_2 and jump L_J/h_2 lengths obtained from measurements ($L_{R,\eta}$ and $L_{J,\eta'}$) and visual observation ($L_{R,D}$), compared to jump length by Peterka (1958), and (b) comparison between measured and visually estimated roller lengths L_R/h_1 with Eq. (2.47) by Hager et al. (1990), and Eq. (4.2); [Runs 1-9: smooth chute; Runs 10-15: stepped chute].

$H_k = \alpha V_1^2 (2g)^{-1}$ as kinetic head at the inflow section and α as kinetic energy correction coefficient (Table 4.1, Eq. (2.32)) from the air concentration and velocity profiles. The streamwise development of $C_H{}'$ is plotted in Figure 4.10a for all runs against the normalized streamwise coordinate x/h_2. Maximum fluctuations are observed near the jump toe for all runs, caused by the intense splashing. In the flow direction, the flow depth fluctuations then strongly reduce up to $x/h_2 \leq 6$, as the splashing reduced. Further downstream, a quasi-constant magnitude of $C_H{}'$=0.01 is reached in the tailwater region. Again, no significant effect of the approach flow aeration C_1 occurs.

However, one can observe from Figure 4.10a that the depth fluctuations require an increased distance x/h_2 after stepped chutes than after smooth chutes to decline, so that a longer hydraulic jump appears after stepped chutes. A hydraulic jump length based on the reduction of the flow depth turbulence is thus proposed. A hydraulic jump length $L_{J,\eta'}$ is defined as the distance between the jump toe and the location where the flow depth fluctuations η' are 1.1 times those measured in the tailwater zone. The jump length results are reported in Table A.1. The length of the hydraulic jump with smooth chute approach flow are $5.55 \leq L_{J,\eta'}/h_2 \leq 6.05$ with an overall average value of $L_{J,\eta'}=5.75h_2$. This is in agreement with literature values for smooth chute spillways (e.g. Peterka (1958), Figure 4.9a). However, hydraulic jumps with stepped chute approach flows consistently require longer stabilization lengths of $6.6 \leq L_{J,\eta'}/h_2 \leq 7$ with an overall average value of $L_{J,\eta'}=6.75h_2$.

Normalizing the streamwise coordinate with the hydraulic jump length $X_J = x/L_{J,\eta'}$ made reasonably collapse all $C_H{}'$ (Figure 4.10b). The streamwise development of $C_H{}'$ can be described as (R^2=0.59 and R^2=0.96):

$$C_H{}' = -0.059X_J + 0.042 \qquad 0< X_J \leq 0.25 \qquad (4.3)$$

$$C_H{}' = 1.009 - \tanh\left(2.8X_J\right)^{0.26X_J-0.028} \qquad X_J > 0.25 \qquad (4.4)$$

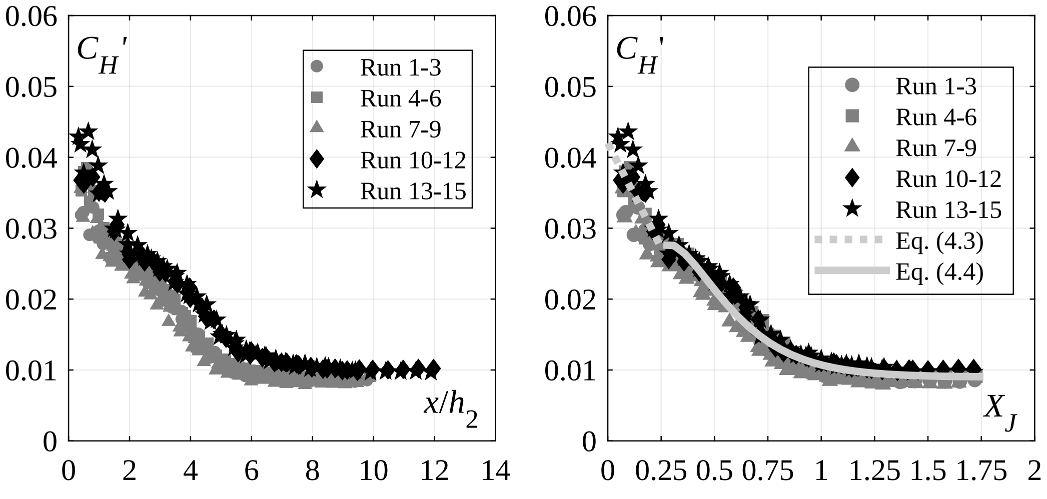

(a) (b)

Figure 4.10 – (a) Streamwise distribution of the flow depth coefficient $C_H{}'$ versus normalized streamwise coordinate x/h_2, and (b) comparison of $C_H{}'$ with the normalized coordinate as $X_J = x/L_{J,\eta'}$ and Eqs. (4.3) and (4.4); [Runs 1-9: smooth chute; Runs 10-15: stepped chute].

4.5 Bottom pressure characteristics

4.5.1 Statistical analysis and jump length

Knowledge of the hydrodynamic loads acting on the invert is essential for the design of stilling basins. As mentioned in Chapter 2, the dynamic pressures are highly random in nature and thus usually described with statistical methods (Khatsuria 2005). Based on instantaneous pressure measurements conducted at 16 positions (Table 3.1, Figure 3.2), the relevant pressure parameters were derived, namely (1) mean (time-averaged) pressure p_m, (2) fluctuating pressure characterized by standard deviation p', (3) extreme maximum pressure p_{max} and corresponding 99.9th percentile $p_{99.9}$, (4) extreme minimum pressure p_{min} and corresponding 0.1th percentile $p_{0.1}$, (5) skewness S, and (6) excess kurtosis K. A typical streamwise pressure distribution is shown on Figure 4.11 (Run 7, smooth chute approach flow).

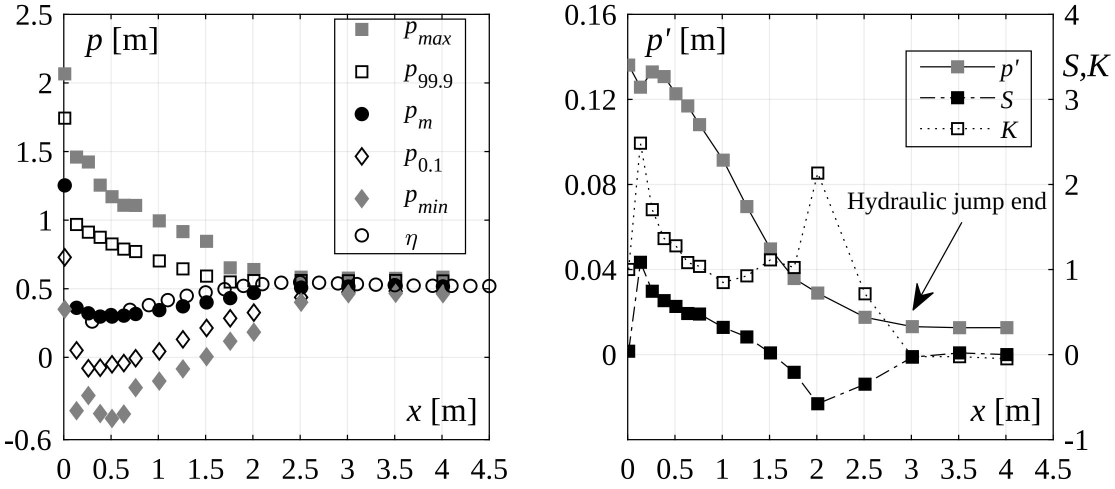

(a) (b)

Figure 4.11 – Streamwise distribution (Run 7, smooth chute) of (a) extreme maximum bottom pressure p_{max}, bottom pressure with 99.9% probability $p_{99.9}$, mean bottom p_m, bottom pressure with 0.1% probability $p_{0.1}$, extreme minimum bottom pressure p_{min} and mean flow depth η, and (b) fluctuating pressure p', skewness S and excess kurtosis K.

Figure 4.11 shows that the bottom pressures downstream of a hydraulic jump ($x \geq 3$ m) are quasi-hydrostatic. More precisely, the pressure fluctuations as well as extreme pressures are damped, and the probability density function is of Gaussian shape with values of $S\approx 0$ and $K\approx 0$. The hydraulic jump length with respect to the bottom pressures is defined as: (1) $L_{J,p'}$ distance from the jump toe to the section where pressure fluctuations p' are 1.1 times those measured in the tailwater zone, and (2) $L_{J,SK}$ as a distance from the jump toe to the section where the pressure distribution was Gaussian-shaped with values of $S\approx 0$ and $K\approx 0$. The jump length results are reported in Table A.1. These jump lengths are plotted as L_J/h_2 in Figure 4.12a, along with the jump lengths obtained via flow depth measurements $L_{J,\eta'}$ (Figure 4.9a). The pressure measurements indicate the same range of dimensionless jump lengths, confirming that hydraulic jumps initiated after stepped chutes require a greater normalized distance x/h_2 than that after a smooth chute. The overall values are L_J/h_2=5.7 and L_J/h_2=6.7 for smooth and stepped chute approach flows, respectively.

To describe the streamwise pressure distribution, the pressure coefficients introduced in Chapter 2 were derived, namely: (1) mean coefficient P_m=$(p_m - h_1)/(h_2 - h_1)$, (2) fluctuation coefficient $C_P{}'= p' H_k{}^{-1}$, (3) extreme maximum coefficient $C_P{}^{max}= (p_{max} - p_m) H_k{}^{-1}$ and that corresponding to 99.9th percentile $C_P{}^{99.9}= (p_{99.9} - p_m) H_k{}^{-1}$, (4) extreme minimum $C_P{}^{min}= (p_m - p_{min}) H_k{}^{-1}$ and that corresponding to 0.1th percentile $C_P{}^{0.1}= (p_m - p_{0.1}) H_k{}^{-1}$. The streamwise coefficients, skewness and kurtosis developments are plotted in Figure 4.13a to 4.13f, with a normalized streamwise coordinate $X_J = x/L_J$. An overall average value of the jump length is used, i.e. $L_J = 5.7 h_2$ and $L_J = 6.7 h_2$ for smooth and stepped chute approach flows, respectively.

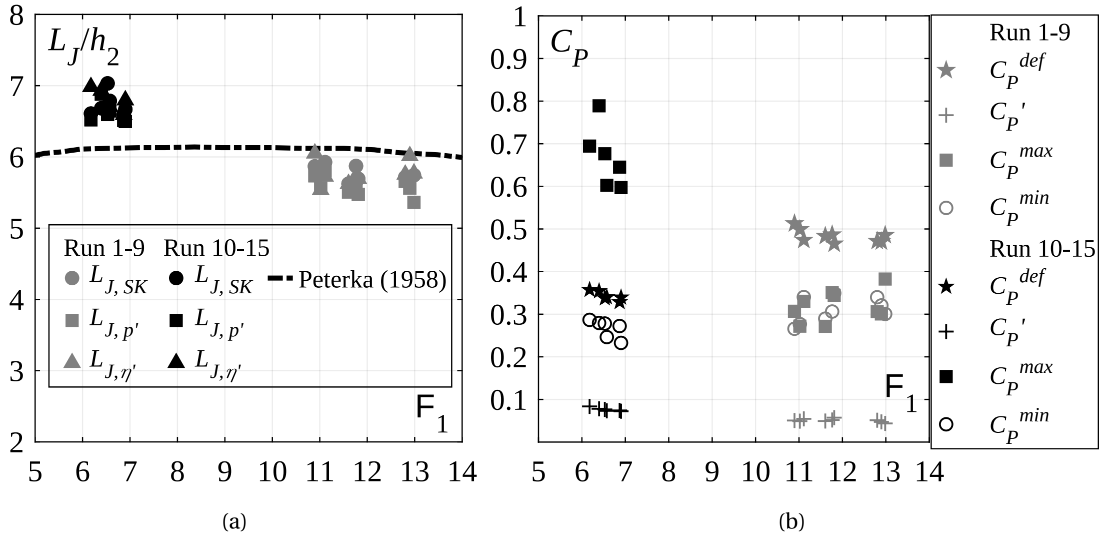

Figure 4.12 – (a) Dimensionless jump lengths L_J/h_2 from pressure ($L_{J,SK}$ and $L_{J,p'}$) and flow depth ($L_{J,\eta'}$) against the inflow Froude number F_1, compared to the jump length of Peterka (1958), and (b) pressures: impact mean coefficient $C_P{}^{def}$, fluctuation coefficient $C_P{}'$, extreme maximum coefficient $C_P{}^{max}$ and extreme minimum coefficient $C_P{}^{min}$ at the jump toe against the inflow Froude number F_1; [Runs 1-9: smooth chute; Runs 10-15: stepped chute].

4.5.2 Streamwise distribution of mean pressure

The streamwise dimensionless mean pressure coefficients P_m versus the normalized flow depth Z (Figure 4.13a), indicate the following flow zones:

I. *deflection zone* along $0 \leq X_J \leq 0.15$, being characterized by pronounced mean pressures due to the impact and curvature of the flow,

II. *transition zone* along $0.15 < X_J < 1$, where the mean pressures qualitatively follow the flow depths, and

III. *tailwater zone* along $X_J \geq 1$, where mean pressures are quasi-hydrostatic.

Maximum mean pressures are observed at the deflection point, i.e. at the jump toe $X_J \approx 0$ (Figure 4.13a). Up to 2.5 times higher dimensionless mean pressures P_m are observed after smooth chutes than that after stepped chutes. As the mean pressure at this location comes from the kinetic energy of the approaching flow, the mean pressure at the deflection point p_{def} is normalized with the kinetic energy of the approaching flow H_k. The resulting mean pressure coefficients at the deflection point $C_P{}^{def} = p_{def}/H_k$ are shown on Figure 4.12b. The mean pressures are, on average, 48% and 34% of the corresponding approach flow kinetic energy of smooth and stepped chutes, respectively. The higher magnitudes after smooth chutes can be explained with its lower approach flow depth, resulting in a more “concentrated” impact.

The relatively higher magnitudes of the skewness and kurtosis coefficients for stepped chute approach flows support this observation (Figure 4.13e and 4.13f). Downstream of the jump toe, the mean pressures decrease as the flow curvature weakens, reaching a local minimum at $X_J \approx 0.15$. The flow curvature generates an elevated skewness and kurtosis coefficients (Figure 4.13e and 4.13f).

Further downstream, in the transition zone, the flow curvature diminishes, the mean pressure increase with distance ultimately reaching quasi-hydrostatic magnitudes in the tailwater zone. The mean pressures in the transition zone are lower than the corresponding flow depths due to flow aeration. Downstream of the jump toe, the dimensionless mean pressure distribution is practically independent of the approach flow conditions, and is described as (R^2=0.97):

$$P_m = \tanh\left(3.1X_J\right)^{5.9X_J-0.14} \qquad 0.03 \leq X_J \leq 1.5 \qquad (4.5)$$

In the present experiments, the mean air concentration at the downstream chute end is practically constant for the stepped chute ($C_1 \approx 0.41$), whereas it ranged from $C_1 \approx 0.15$ to 0.32 for the smooth chute. In Pinheiro (1995), a slight reduction of the mean pressures were observed for tests conducted with forced aeration on a smooth chute (for $C_1 \approx 0.4$-0.5), in relation to those observed for upstream clear-water flow conditions ($C_1 \approx 0$). However, in the latter study, the change in C_1 was considerably higher, and the approach chute geometry and flow conditions were distinct to those analysed herein.

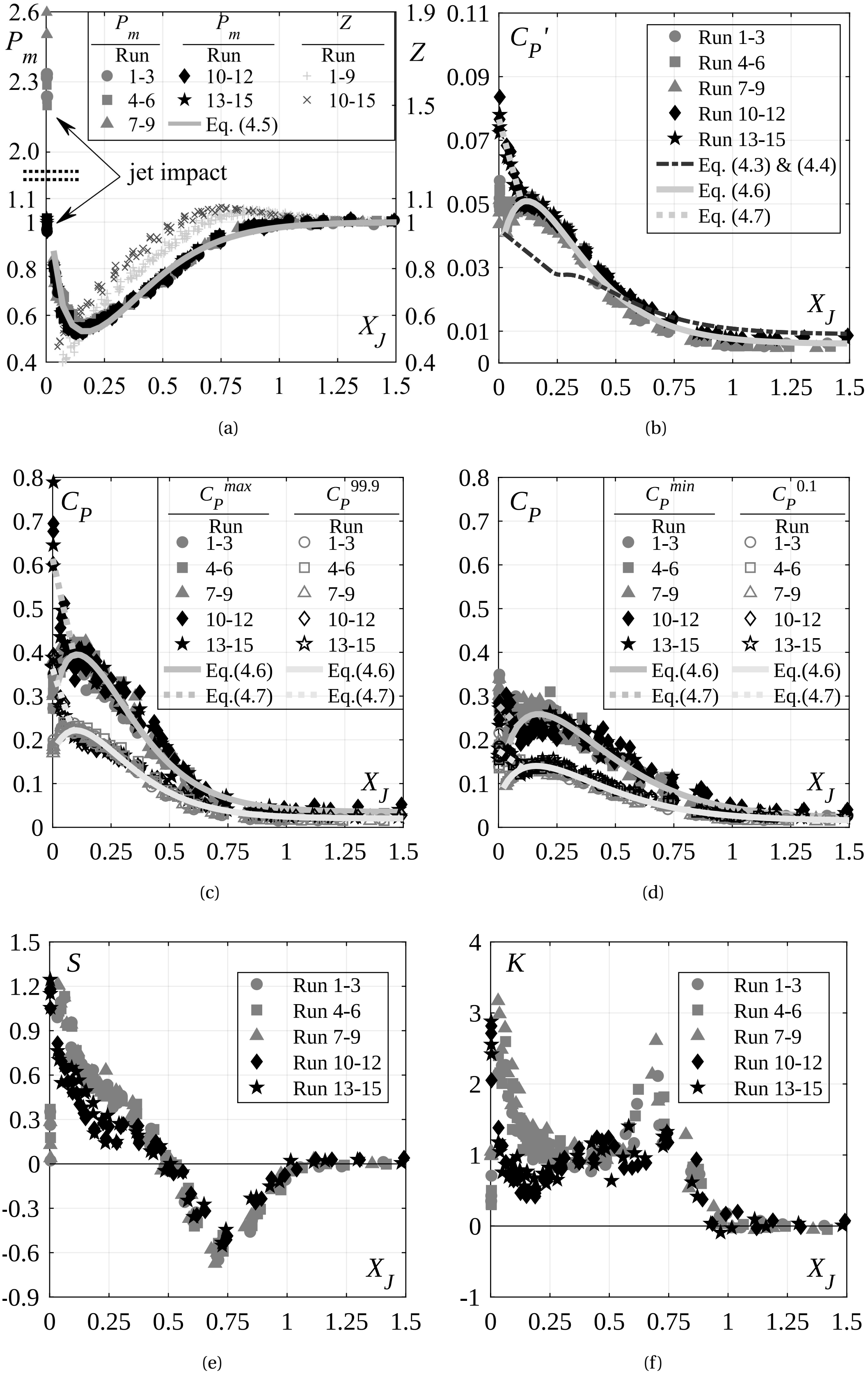
P_m
Z
P_m Run 1-3 4-6 7-9
P_m Run 10-12 13-15 Eq. (4.5)
Z Run 1-9 10-15
jet impact
X_J
2.6 2.3 2.0 1.1 1 0.8 0.6 0.4
1.9 1.5 1.1 1 0.8 0.6 0.4
C_P'
Run 1-3
Run 4-6
Run 7-9
Run 10-12
Run 13-15
Eq. (4.3) & (4.4)
Eq. (4.6)
Eq. (4.7)
0.11 0.09 0.07 0.05 0.03 0.01 0
C_P
C_P^{max} Run 1-3 4-6 7-9 10-12 13-15 Eq.(4.6) Eq.(4.7)
$C_P'^{99.9}$ Run 1-3 4-6 7-9 10-12 13-15 Eq.(4.6) Eq.(4.7)
C_P^{min} Run 1-3 4-6 7-9 10-12 13-15 Eq.(4.6) Eq.(4.7)
$C_P'^{0.1}$ Run 1-3 4-6 7-9 10-12 13-15 Eq.(4.6) Eq.(4.7)
0.8 0.7 0.6 0.5 0.4 0.3 0.2 0.1 0
S
1.5 1.2 0.9 0.6 0.3 0 -0.3 -0.6 -0.9
K
4 3 2 1 0 -1
0 0.25 0.5 0.75 1 1.25 1.5

(a)

(b)

(c)

(d)

(e)

(f)

Figure 4.13 – Streamwise distribution of: (a) mean pressure coefficient P_m, comparison with dimensionless flow depth Z as a function of X_J and with Eq. (4.5), (b) pressure fluctuation coefficient $C_P{}'$, comparison with Eqs. (4.3), (4.4), (4.6) and (4.7), (c) maximum pressure coefficient $C_P{}^{max}$ and 99.9th percentile $C_P{}^{99.9}$, comparison with Eqs. (4.6) and (4.7), (d) minimum pressure coefficient $C_P{}^{min}$ and 0.1th percentile $C_P{}^{0.1}$, comparison with Eqs. (4.6) and (4.7), (e) skewness S, and (f) excess kurtosis K; [Runs 1-9: smooth chute; Runs 10-15: stepped chute].

4.5.3 Streamwise distribution of pressure fluctuations

The *smooth chute* approach flows generate a typical streamwise pressure fluctuation $C_P{}'$ development (Figure 4.13b) downstream of the jump toe (Abdul Khader and Elango 1974; Akbari et al. 1982; Bukreev 1966; Fiorotto and Rinaldo 1992b,a; Lopardo et al. 1982; Lopardo and Henning 1985; Lopardo and Romagnoli 2009; Pinheiro 1995; Schiebe and Bowers 1971; Toso and Bowers 1988). An increase with a peak in the region of the maximum turbulence intensity is observed, followed by a monotonic decrease towards the quasi-constant values in the tailwater zone. The peak reaches up to $C_P{}'\approx0.05$ at $X_J\approx0.12$, in agreement with observations of Toso and Bowers (1988) considering a 30° sloping smooth chute. At the jump toe ($X_J=0$), the pressure fluctuations reach or exceed the observed magnitudes at $X_J\approx0.12$. The elevated fluctuations at the jump toe are attributed to the flow deflection. The streamwise pressure fluctuation development is practically independent of the inflow aeration C_1. In Pinheiro (1995), a reduction of the standard deviation of the pressure fluctuations was observed with forced aeration (for $C_1\approx0.4$-0.5) until approximately half of the jump length, compared to that obtained for upstream clear-water flow conditions.

Comparing the pressure fluctuation development, a clear effect of a stepped chute (black symbols) approach flow is visible. At the toe up to 50% higher magnitudes are observed, with values reaching up to $C_P{}'=0.084$ (Figure 4.12b and Figure 4.13b). Downstream of the toe, the fluctuation decrease in a linear manner up to $X_J\approx0.1$, beyond which the magnitudes coincide with those of smooth chute approach flow along the complete downstream basin reach. The fluctuations are virtually independent of the step height s.

At the first half of the jump ($X_J\leq0.5$), the pressure fluctuation coefficients $C_P{}'$ are higher compared to the related flow depth fluctuation coefficients $C_H{}'$ for all experimental runs (Figure 4.13b, Eqs. 4.3 and 4.4). At $X_J\approx0.5$, the pressure and surface fluctuations coincide, indicating that the influence of the highly turbulent bottom jet flow (Figure 4.5a) is reduced. The latter becomes evident when observing the streamwise skewness development (Figure 4.13e). These reach negative values at $0.5\leq X_J\leq1$ indicating detachment of the bottom jet flow (Lopardo et al. 1982). Thus, the pressure fluctuations are mostly induced by surface waves and oscillations. The skewness coefficient attained minimal values at $X_J\approx0.75$, within the zone of the roller end, followed by an increase towards the tailwater (jump end) where the probability density function is of Gaussian shape with $S\approx0$.

4.5.4 Streamwise distribution of extreme pressures

The extreme pressures (Figure 4.13c and 4.13d) reveal similar streamwise distributions as the previously described fluctuations. Downstream of the jump toe, the extreme coefficients for *smooth chute* approach flows increase, reaching up to $C_P{}^{max}$=0.42 and $C_P{}^{min}$=0.30 at X_J≈0.12 and X_J≈0.18, respectively. They are followed by a decrease towards quasi-constant magnitudes in the tailwater zone (Toso and Bowers 1988). At the jump toe, the extreme pressures are of the same order of magnitudes around $C_P{}^{max} \approx C_P{}^{min} \approx 0.30$, caused by the flow deflection (Figure 4.12b).

As for stepped chute approach flows, up to two times higher extreme maximum coefficients at the jump toe are observed, reaching $C_P{}^{max}$=0.8 (Figure 4.13c and Figure 4.12b). The extreme negative pressures $C_P{}^{min}$ are similar to those for smooth chute approach flows. Further downstream, extreme pressures decrease within X_J≤0.1, after which the magnitudes coincide with smooth chute approach flows.

Similar conclusions can be drawn for extreme pressure coefficients with 99.9% and 0.1% percentiles, but with typically two times lower magnitudes (Figure 4.13c and 4.13d).

The pronounced extreme and fluctuating pressures within the deflection zone were reported by Novakoski et al. (2017a,b) for a 50° sloping stepped chute, who attributed it to the absence of a curved transition between the stepped chute and the stilling basin invert. Herein, this seems not the case, as the present smooth chute configuration did not involve such a transition. Thus it may be concluded that the pronounced pressure magnitudes with stepped chute approach flows in the zone X_J≤0.1 are likely due to the higher, step induced, turbulence levels of the incoming flow, as compared to smooth chute approach flows.

The fluctuation and extreme pressure coefficients for smooth chute approach flow can be described as (Figure 4.13b to 4.13d):

$$C_P = d - \tanh\left(eX_J\right)^{jX_J+k} \qquad X_J \geq 0.03 \qquad (4.6)$$

where the coefficients d, e, j and k are listed in Table 4.2.

The same equation is used for stepped chute approach flow in range X_J≥0.1. The pronounced pressure coefficients with stepped chute approach flows are (Figure 4.13b to 4.13d):

$$C_P = mX_J + r \qquad X_J < 0.10 \qquad (4.7)$$

where the coefficients m and r are listed in Table 4.3.

Table 4.2 – Coefficients of Eq. (4.6).

Coefficient	d	e	j	k	R^2
$C_P{}'$	1.006	3.00	0.31	0.006	0.99
$C_P{}^{max}$	1.035	3.41	3.41	0.060	0.97
$C_P{}^{99.9}$	1.020	3.31	1.60	0.037	0.98
$C_P{}^{min}$	1.020	2.52	1.80	0.010	0.91
$C_P{}^{0.1}$	1.015	2.46	0.79	0.010	0.97

Table 4.3 – Coefficients of Eq. (4.7).

Coefficient	m	r	R^2
$C_P{}'$	-0.266	0.076	0.90
$C_P{}^{max}$	-2.400	0.604	0.75
$C_P{}^{99.9}$	-1.650	0.362	0.90
$C_P{}^{min}$	-0.560	0.278	0.42
$C_P{}^{0.1}$	-0.375	0.175	0.60

4.5.5 Frequency domain analysis

The pressure fluctuations were further analysed using a power spectral analysis. The power spectral densities (PSD) P_{xx} were computed for each time series using FFT based on the Welch periodogram method. Figure 4.14 shows the resulting spectral diagrams, for Run 8 (Figure 4.14a to 4.14c) and Run 14 (Figure 4.14d to 4.14f) being representative examples for smooth and stepped chute approach flows, respectively.

4.5.6 Streamwise PSD development with smooth chute approach flows

At the flow deflection point, i.e. $X_J \approx 0$, the PSD show a horizontal spectral energy content at the low frequency range (Figure 4.14a). Due to the flow deflection, kinetic energy of the flow is abruptly dissipated leading to a reduction of spectral energy within low frequencies at $X_J \approx 0.04$. Both locations are characterized by dominant frequency of some 11 Hz which is associated with generation of vortices induced by shear at the jump toe. Secondary frequencies are observed in the range of 0.5 to 0.8 Hz, as a result of jump toe oscillations and wave action. These frequencies are in line with studies on classical hydraulic jump, which identified dominant jump toe oscillation frequencies within 0.5 to 2 Hz (Chanson and Gualtieri 2008; Montano et al. 2018; Mossa and Tolve 1998; Murzyn and Chanson 2009b).

Within 0.04≤X_J≤0.11, the spectral energy increases at low frequencies, namely between 1 to 10 Hz. The inertial range of scales remains practically unaltered, indicating turbulent energy production and thus a rise of pressure fluctuations (Figure 4.14a). In turbulent flow, each frequency can be related to an eddy of a corresponding length (Monin and Yanglom 1975; Frisch 1995). The spread of frequencies that dominate the signal indicate the coalescence of vortical structures leading to the growth of the bottom jet flow (Figure 4.5a).

Further downstream, within 0.14≤X_J≤0.42 (Figure 4.14b and 4.14c), the spectral energy decreases at high frequencies due to the energy dissipation. Each PSD is characterized by a cluster of frequencies that dominate the signal, i.e. vortical structures of different sizes in the bottom jet flow, which shifts towards lower frequency ranges (1 to 6 Hz) in the streamwise direction due to the further coalescence of vortices and velocity reduction.

Figure 4.14c shows that at X_J=0.49 the bottom jet flow ceases to dominate the PSD. The dominant frequency is around 0.6 Hz, being in line with visually observed surface waves. This further supports previously made conclusions that at X_J≈0.50 the detachment of the bottom jet flow is prominent. Thus the influence of the bottom jet flow is diminished. In the downstream half of the hydraulic jump (Figure 4.14c), the influence of the bottom jet flow is further reduced with distance and the power of the signal mostly comes from the propagating surface waves.

In the tailwater zone at X_J≈1 the PSD is concentrated in a narrow frequency range of 0 to 1 Hz caused by the waves, thus confirming that the hydraulic jump ends at this point. Within the hydraulic jump perimeter, the inertial range of scales has a typical decay rate of $f^{-5/3}$ (Figure 4.14a to 4.14c), in line with the observation of Abdul Khader and Elango (1974) for classical hydraulic jumps.

Similar conclusions can be made for all experimental runs with smooth chute approach flows. Inflow aeration C_1 is found not to affect the PSDs. Typical dominant frequencies range between 1 to 12 Hz within the upstream half of the jump, whereas in the downstream half they are within 0.5 to 0.8 Hz.

4.5.7 Streamwise PSD development with stepped chute approach flows

Globally, the PSD evolution shows similar patterns with stepped chute approach flows but with lower energy and frequency range (as compared to smooth chutes, Figure 4.14d to 4.14f), due to the reduced Froude number F_1 at the chute end. However, a major effect of stepped chute approach flows on the PSDs is observed within the zone 0≤X_J≤0.11 (Figure 4.14d). The low frequency range exhibits similar pattern as the smooth chute approach flows. However, the pronounced participation of energy content at the high frequency range are observed. This is represented by the double-sloped spectral energy decay of the inertial range of the scales.

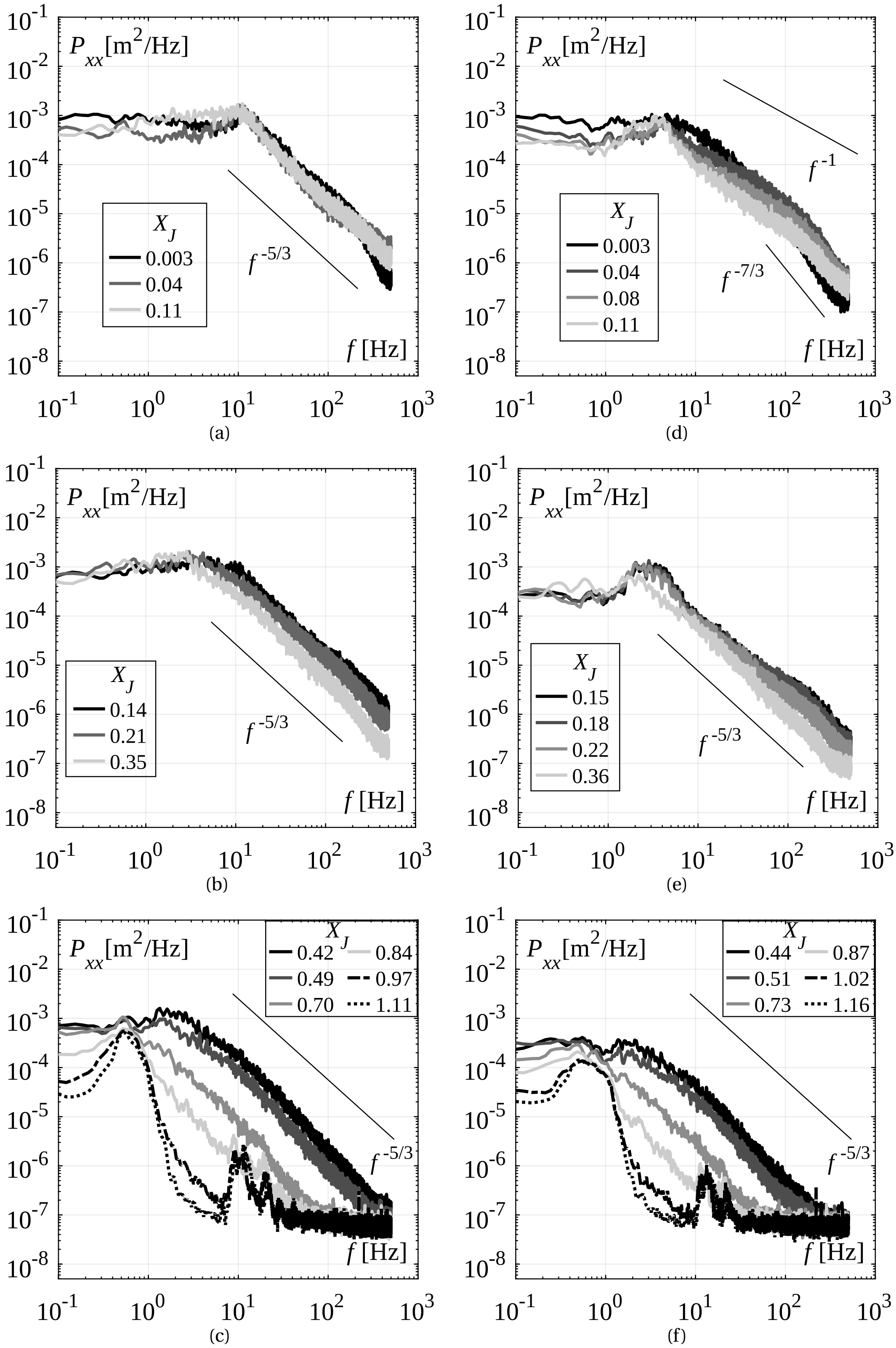

(a) (d) (b) (e) (c) (f)

Figure 4.14 – Power spectral densities of the pressure fluctuations at selected flow distances along the stilling basin invert, for (a-c) Run 8, and (d-f) Run 14.

At the flow deflection point, the energy decays at the rate of f^{-1}, within approximately 6-50 Hz, followed by a steeper decay slope of $f^{-7/3}$. Further downstream, similar behavior is observed at lower energy levels, however, the f^{-1} decay rate expands to some 100 Hz. The decay rate of f^{-1} indicates higher turbulence levels over a broader range of scales when compared to the $f^{-5/3}$ observed with smooth chute approach flows. Such a behavior can be caused by the higher turbulence levels of the incoming flow thus pronouncing the pressure fluctuations. Downstream of X_J=0.11(Figure 4.14e and 4.14f) the PSDs are similar to the ones obtained with smooth chute approach flows with a typical decay rate of $f^{-5/3}$. For other experimental runs involving stepped chute approach flows the same can be concluded. The step height s is found not to affect the PSDs. Typical dominant frequencies range between 1 to 6 Hz in the upstream half of the jump, and 0.4 to 0.8 Hz in the downstream half.

4.6 Conclusions

The present chapter investigates the effect of the approach flow on the performance of a plain stilling basin. Physical modelling was conducted using a large-scale facility with a 30° sloping smooth or stepped chute upstream of the basin. Experiments were performed for different discharges and step heights. To address the influence of aerated approach flows, flow aeration at the smooth chute end was varied.

The hydraulic characteristics of the hydraulic jump were described, focusing mainly on flow depth, bottom pressure, and length measurements. The following conclusions may be drawn:

- The use of equivalent clear water parameters at the smooth or stepped chute end lead to a correct prediction of the sequent jump depth ratio h_2/h_1 using the momentum principle. As such, the sequent depth ratio is virtually independent of the approach flow conditions, for identical F_1.
- The dimensionless surface roller length L_R/h_2 is practically independent of the approach flow conditions. Depending on the definition, the roller length can be estimated as L_R=4.6h_2 (stagnation point) or L_R=5.0h_2 (maximum flow depth). Alternatively, Eq. (4.2) can be used.
- The flow depths η along the jump roller are self-similar in shape following Eq. (4.1). Dimensionless flow depths Z downstream of stepped chutes are higher in magnitude within the first half of the roller, as compared to smooth chutes.
- The flow depth fluctuations η' decrease in the streamwise direction with the maximum magnitudes close to the jump toe caused by intense splashing of the flow. The streamwise development of flow depth fluctuation coefficient $C_H{}'$ along the hydraulic jump can be estimated with Eq. (4.3) and (4.4).
- Criteria for the hydraulic jump length L_J are proposed based on (1) $L_{J,\eta'}$ reduction of flow depth fluctuations η', (2) $L_{J,p'}$ reduction of bottom pressure fluctuations p' and (3)

$L_{J,SK}$ Gaussian-shaped pressure distribution with $S \approx 0$ and $K \approx 0$. The results show that the hydraulic jump initiated after stepped chutes require an increased distance, namely $L_J = 6.7h_2$, as compared to $L_J = 5.7h_2$ after smooth chutes.

- The streamwise bottom mean pressure p_m distribution along the stilling basin is characterized by pronounced magnitudes within $X_J \leq 0.15$ caused by the jet impact and flow curvature. The dimensionless mean pressure development P_m is independent of the approach flow conditions downstream of the jump toe and can be estimated with Eq. (4.5).

- Smooth chute approach flows exhibit typical bottom pressure fluctuation p' distribution downstream of the jump toe with maximum fluctuation coefficients of $C_P{}'$=0.05 at X_J=0.12. At the toe, pronounced magnitudes are observed, caused by the flow deflection, which tend to exceed the latter value. The streamwise distribution of extreme pressure coefficients $C_P{}^{max}$ and $C_P{}^{min}$ exhibit similar patterns. The maximum magnitudes downstream of the jump toe are $C_P{}^{max}$ =0.42 and $C_P{}^{min}$ =0.30 at $X_J \approx 0.12$ and $X_J \approx 0.18$, respectively. The coefficients are not influenced by inflow aeration.

- Stepped chute approach flows exhibit pronounce extreme and fluctuating pressure coefficients within $X_J \leq 0.1$, as compared to smooth chute approach flows. The pressure fluctuation coefficients are up to 50% higher at the jump toe. At the same location, up to two times higher extreme maximum coefficients are observed, reaching $C_P{}^{max}$=0.8, whereas the extreme minimum is of the same order of magnitude as with smooth chute approach flows. Further downstream, the pressure coefficients decrease in a linear manner and coincide with the smooth chute magnitudes at $X_J \geq 0.1$. The pressure coefficients are not influenced by the step size.

- Pressure coefficients with 99.9% $C_P{}^{99.9}$ and 0.1% $C_P{}^{0.1}$ probability exhibit similar streamwise development as the extreme pressures, but with typically two times lower magnitudes than the corresponding extreme maximum $C_P{}^{max}$ and minimum $C_P{}^{min}$ coefficients.

- The streamwise distribution of fluctuating and extreme pressure coefficients for smooth chute approach flows can be estimated with Eq. (4.6) for $X_J \geq 0.03$. The same equation can be used for stepped chute approach flow for $X_J \geq 0.1$. The pronounced magnitudes with stepped chute approach flow within $X_J < 0.1$ can be estimated with Eq. (4.7).

- The spectral analysis of the pressure fluctuations provided additional information on the flow features. Dominant frequencies are in range of 0.5-12 Hz and 0.4-6 Hz with smooth and stepped chute approach flows, respectively. Pronounced spectral energy participation at high frequency ranges is found for stepped chute approach flows within $0 < X_J \leq 0.11$, indicating that the pronounced pressure coefficients in this zone are likely caused by the higher, step induced, turbulence levels of the incoming flow, as compared to smooth chute approach flows.

- Finally, the present results suggest that longer dimensionless "classical" (plain) stilling basin lengths are required downstream of 30° sloping stepped chutes, as compared to the basins preceded by smooth chute invert approach. Considering some safety margin, a basin length of $7h_2$ is recommended. Furthermore, special care should be taken when designing stilling basin slabs in the zone $X_J \leq 0.1$, as stepped chute flows pronounce the fluctuating and extreme pressures compared to smooth chute approach flows.

5 Air-water flow properties of a plain stilling basin for 30° sloping smooth and stepped chute approach flows

5.1 Overview

This chapter investigates the effect of 30° sloping smooth and stepped chute approach flows on the internal flow characteristics of plain stilling basin. The experimental results on dynamic bottom pressure, flow depths and length characteristics presented in Chapter 4 are further expanded herein by analyzing air-water flow properties, collected in the same test runs.

The air water flow measurements indicate two main flow zones, namely advective diffusive zone along $0.1 \leq x/L_{R,\eta} \leq 0.8$ and air release zone along $x/L_{R,\eta} \geq 0.9$, irrespective of the approach flow conditions. The advection diffusion model of Chanson (1995) and modified wall jet expressions of Chanson (2010) describe well the measured air concentration and velocity profiles in the advective diffusive zone, respectively. The stepped chute approach flows show lower de-aeration rate along the stilling basin in terms of $x/L_{R,\eta}$, confirming the jump length measurements obtained from flow depth and bottom pressure characteristics. Pronounced bottom air concentration values within $X_J \leq 0.4$ are observed with stepped chute approach flows, as compared to smooth chute approach flows. The zone of cavitation damage protection, in terms of bottom air concentration, is longer for stepped chute approach flow and thus they are less endangered by cavitation damage, as compared to smooth chute approach flows. The maximum velocity decays in an exponential manner and is practically independent of the approach flows conditions. The tested range of smooth chute approach flow aeration C_1 or stepped chute step size s did not affect air-water flow properties of the hydraulic jump.

This chapter is based on the scientific article "Comparison of air-water flow in a classical stilling basin downstream of a smooth and stepped chute" by Stojnic, I., Pfister, M., Matos, J., and Schleiss, A. J., under review in International Journal of Multiphase Flow. The experimental work and the analyses presented hereafter are original and were performed by the author.

5.2 Test program and inflow conditions

The air-water flow properties for stilling basin preceded by 30° sloping smooth and stepped chutes were collected in the same test runs presented and analyzed in Chapter 4. The air-water flow measurements were not performed for highest tested discharges for smooth chute approach flows, i.e. $q \approx 0.357$ (Runs 3, 6 and 9, Table 4.1). For completeness, the test program involving air-water flow measurements analyzed in the present chapter is given in Table 5.1. Further information on the approach flow conditions can be found in Chapter 4.

Table 5.1 – Test program for air-water flow measurements for a stilling basin preceded by 30° sloping smooth and stepped chutes. SM=smooth chute, R=smooth chute roughened with grid; PA=smooth chute roughened with grid and pre-aeration, ST=stepped chute.

Test run	φ [°]	Chute Configuration	q [m^2/s]	h_c/s [-]	C_1 [-]	h_1 [m]	V_1 [m/s]	F_1 [-]	$R_1 \times 10^5$ [-]	W_1 [-]
1	30	R+PA	0.198	/	0.32	0.031	6.47	11.8	1.98	133
2	30	R+PA	0.277	/	0.32	0.038	7.22	11.8	2.77	166
4	30	R	0.198	/	0.25	0.032	6.21	11.1	1.98	130
5	30	R	0.277	/	0.26	0.04	6.86	10.9	2.77	162
7	30	SM	0.198	/	0.16	0.029	6.95	13.1	1.98	137
8	30	SM	0.278	/	0.15	0.036	7.68	12.9	2.78	171
		min	0.198	/	0.15	0.029	6.21	10.9	1.98	130
		max	0.358	/	0.32	0.047	8.38	13.1	3.58	202
10	30	ST s=0.06 m	0.204	2.70	0.42	0.048	4.24	6.2	2.04	109
11	30	ST s=0.06 m	0.284	3.36	0.42	0.058	4.91	6.5	2.84	138
12	30	ST s=0.06 m	0.362	3.95	0.41	0.068	5.35	6.6	3.62	163
13	30	ST s=0.03 m	0.204	5.40	0.41	0.047	4.34	6.4	2.04	110
14	30	ST s=0.03 m	0.282	6.70	0.41	0.056	5.07	6.9	2.82	140
15	30	ST s=0.03 m	0.364	7.94	0.41	0.066	5.54	6.9	3.64	166
		min	0.204	2.70	0.41	0.047	4.24	6.2	2.04	109
		max	0.364	7.94	0.42	0.068	5.54	6.9	3.64	166

5.3 Air concentration distribution

Figure 5.1 shows air concentration profiles measured along the stilling basin plotted against the dimensionless vertical coordinate $z/(h_2 - h_1)$ for Run 7 (Figure 5.1a and b) and Run 10 (Figure 5.1c and d), being representative examples for smooth and stepped chute approach flows, respectively. The air concentration profiles are arranged with a streamwise spacing of $0.2x/L_{R,\eta}$, starting from $0.1x/L_{R,\eta}$ in Figure 5.1a and c, and $0.2x/L_{R,\eta}$ in Figure 5.1b and d.

The air concentration profiles indicate two flow zones:

I *Advective diffusive zone* along $x/L_{R,\eta}$≤0.8, being characterized by two dominant flow regions, namely a: (1) turbulent shear layer region in the lower part of the flow, and (2) free surface recirculation region above.

II *Air release zone* along $x/L_{R,\eta}$≥0.9, being characterized by intense flow de-aeration due to buoyancy effects.

In the *advective diffusive zone*, the air concentration profiles exhibit a characteristic S-shape profile, similar to those reported for classical hydraulic jumps (Chanson 1995; Montano and Felder 2018; Resch et al. 1974; Takahashi and Ohtsu 2017; Thandaveswara 1974). The shear layer region is characterized by a rise of air concentration from the channel invert reaching a local maximum C_{max} at a vertical position from the bottom z_{max}, followed by a decrease with increasing z attaining a local minimum C_{min} at vertical position from the bottom z_{min}. The vertical position z_{min} marks a boundary between the shear layer region and the free surface recirculating region. The local maximum C_{max} and minimum C_{min} air concentrations decrease in the streamwise direction, whereas their vertical positions z_{max} and z_{min} increase, demonstrating the growth of the shear layer region. In the recirculation region, i.e. z>z_{min}, the air concentration increases rapidly to unity. In the *air release zone,* i.e. $x/L_{R,\eta}$≥0.9, the shear layer region disappears (Figure 5.1), irrespective of the approach flow conditions. Within 0.9≤$x/L_{R,\eta}$≤1.1, the air concentration profiles are characterized by a monotonic increase in C from the channel invert, which is associated with intense flow deaeration driven by buoyancy. Further downstream, in the tailwater, air is mostly present in the upper part of the flow.

In Figure 5.1, the air concentration profiles of the advective diffusive zone are further compared to the analytical solutions developed by Chanson (1995) :

$$C(z) = C_{max}\exp\left[\frac{\left(\frac{z-z_{max}}{h_1}\right)^2}{4\left(\frac{D_t^s}{V_1 h_1}\right)\left(\frac{x}{h_1}\right)}\right] \qquad \text{for } z < z_{min} \qquad (5.1)$$

$$C(z) = 0.5\left[1+\operatorname{erf}\left(\frac{\frac{z-z_{50}}{h_1}}{2\sqrt{\frac{D_t^r}{V_1 h_1}}\sqrt{\frac{x}{h_1}}}\right)\right] \qquad \text{for } z > z_{min} \qquad (5.2)$$

with ${D_t}^s$ and ${D_t}^r$ as depth averaged turbulent diffusivity in the shear layer and recirculating regions, respectively, and z_{50} as characteristic flow depth defined as $z(C{=}0.5)$. The experimental data show a good agreement with Eqs. (5.1) and (5.2), irrespective of the approach flow conditions (Figure 5.1).

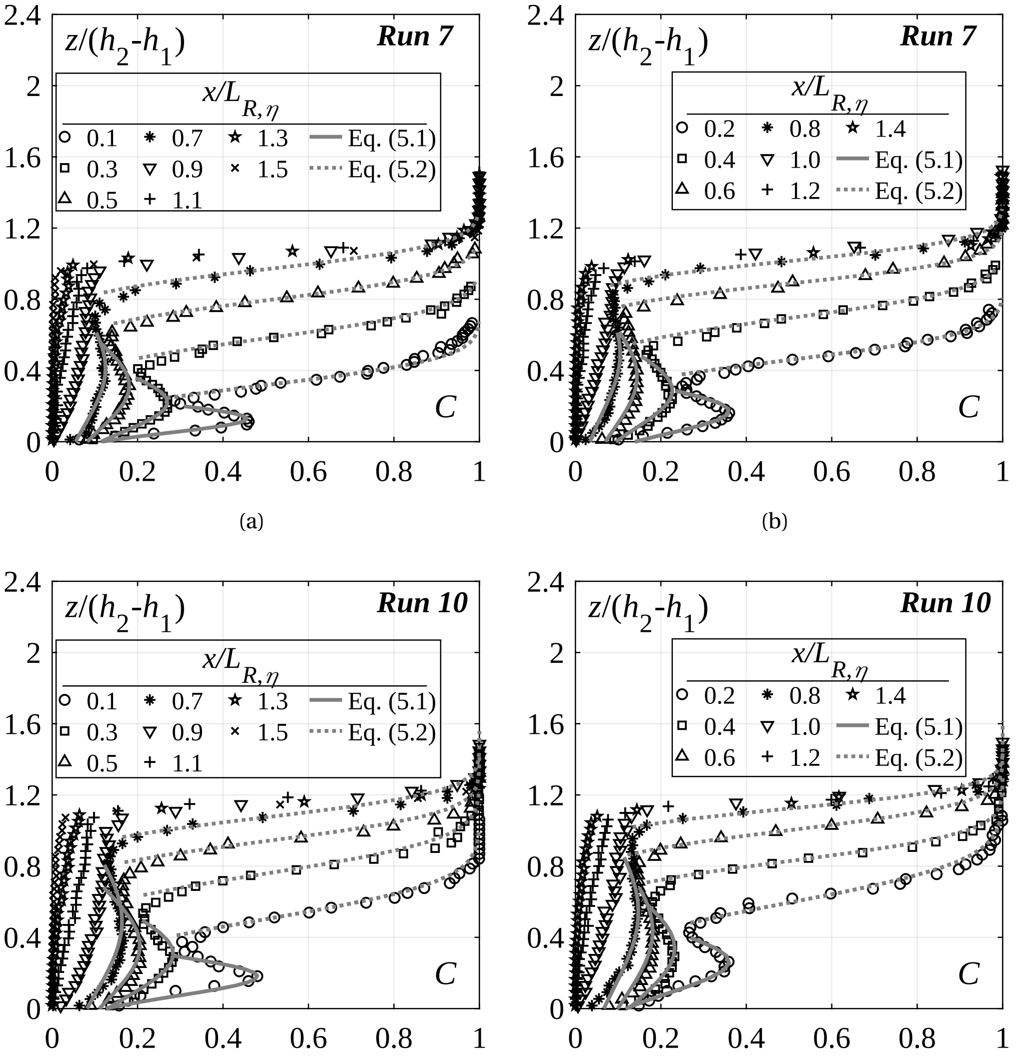

(a) (b)

(c) (d)

Figure 5.1 – Air concentration profiles along the stilling basin for: (a-b) Run 7 (smooth chute), and (c-d) Run 10 (stepped chute); (——) Eq. (5.1); (- - -) Eq. (5.2).

The depth averaged turbulent diffusivities ${D_t}^s$ and ${D_t}^r$ were deduced from the best fit of the air concentration distribution in the related flow region. The obtained diffusivities ${D_t}^s(V_1 h_1)^{-1}$ and ${D_t}^r(V_1 h_1)^{-1}$ are plotted against the normalized streamwise $x/L_{R,\eta}$ in Figure 5.2a and b, respectively, and compared to Wang and Chanson (2017) for classical hydraulic jumps with PD approach flows. The ${D_t}^s(V_1 h_1)^{-1}$ increase with increasing $x/L_{R,\eta}$, showing the broadening of the turbulent shear layer (Figure 5.2a). On the contrary, the dimensionless diffusivity ${D_t}^r(V_1 h_1)^{-1}$ decrease with increasing $x/L_{R,\eta}$, indicating flow de-aeration in the recirculating region and reduction of flow depth fluctuations (Figure 5.2b). No considerable effect of step size s for stepped chute approach flows or approach flow aeration C_1 for smooth chute approach flows on the values of ${D_t}^s(V_1 h_1)^{-1}$ and ${D_t}^r(V_1 h_1)^{-1}$ occurs. However, slightly higher values were observed downstream of smooth chutes (gray symbols), as compared to those downstream of stepped chutes (black symbols), which is linked to the difference in the approach Froude number F_1 (Figure 5.2). Wang and Chanson (2017) underestimates the herein obtained values of $D_t{}^s(V_1 h_1)^{-1}$ and $D_t{}^r(V_1 h_1)^{-1}$ (Figure 5.2). The comparatively higher values of $D_t{}^s(V_1 h_1)^{-1}$ shows that the herein measured air concentration distributions in the shear layer region exhibit a more "uniform" profile, as compared to those with partially developed approach flows, whereas higher $D_t{}^r(V_1 h_1)^{-1}$ values may indicate higher flow aeration in the recirculation region.

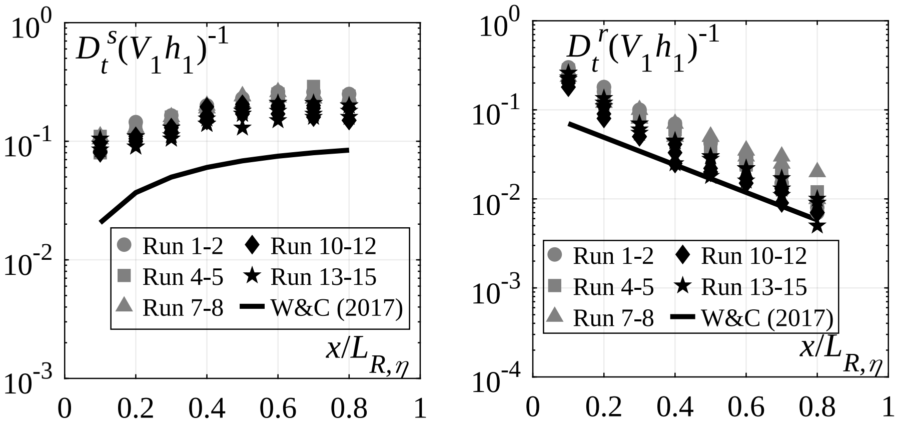

(a) (b)

Figure 5.2 – Streamwise variation of the dimensionless turbulent diffusivity in a: (a) shear region $D_t{}^s(V_1 h_1)^{-1}$ and (b) recirculation region $D_t{}^r(V_1 h_1)^{-1}$; [Runs 1-8: smooth chute, Runs 10-15: stepped chute]; (——) Wang and Chanson (2017).

5.3.1 Smooth versus stepped chute approach flows

Air concentration profiles in the stilling basin for smooth chute approach flow with various C_1 (Runs 2,5 and 8, Table 5.1) and stepped chute approach flow with different s (Runs 11 and 14, Table 5.1) are compared in Figure 5.3 at selected normalized distances $x/L_{R,\eta}$ for unit discharges of about $q \approx 0.280$ m^2/s. The vertical coordinate z was normalized with the characteristic flow depth z_{90} defined as $z(C=0.9)$.

Within $0.1 \leq x/L_{R,\eta} \leq 0.3$ (Figure 5.3 a and b) the dimensionless air concentration profiles are mostly independent of the approach flow conditions. The major differences occur close to the stilling basin bottom, where stepped chute approach flows induce significantly higher air concentration values, as compared to those for smooth chute approach flows. Moreover, stepped chute approach flows exhibit a slightly lower de-aeration rate in the shear layer region. Further downstream, within $0.4 \leq x/L_{R,\eta} \leq 0.8$ (Figure 5.3c and d), the air concentration profiles exhibit a similar shape, however, significantly higher air concentration values were observed in the shear layer region after stepped chutes (as compared to smooth chutes). Consequently, stepped chutes transport larger quantities of air towards the roller end and further downstream, i.e. $x/L_{R,\eta}\geq 1$ (Figure 5.9d and 5.9e). As the roller length $L_{R,\eta}$ is mostly independent of the approach flow conditions (Figure 4.9a), these results suggest longer hydraulic jump lengths L_J in terms of x/h_2 downstream of stepped chutes (compared to smooth chutes), thus being in line with jump length observations based on pressure and flow depth measurements (Figure 4.12a). Accordingly, no apparent effect of the approach flow aeration C_1 for smooth chute approach flows ($0.15 \leq C_1 \leq 0.32$) or relative step size s for stepped chute approach flows ($2.71 \leq h_c/s \leq 7.94$) on the air concentration distribution in the stilling basin occurred. The same conclusions were obtained for other test runs.

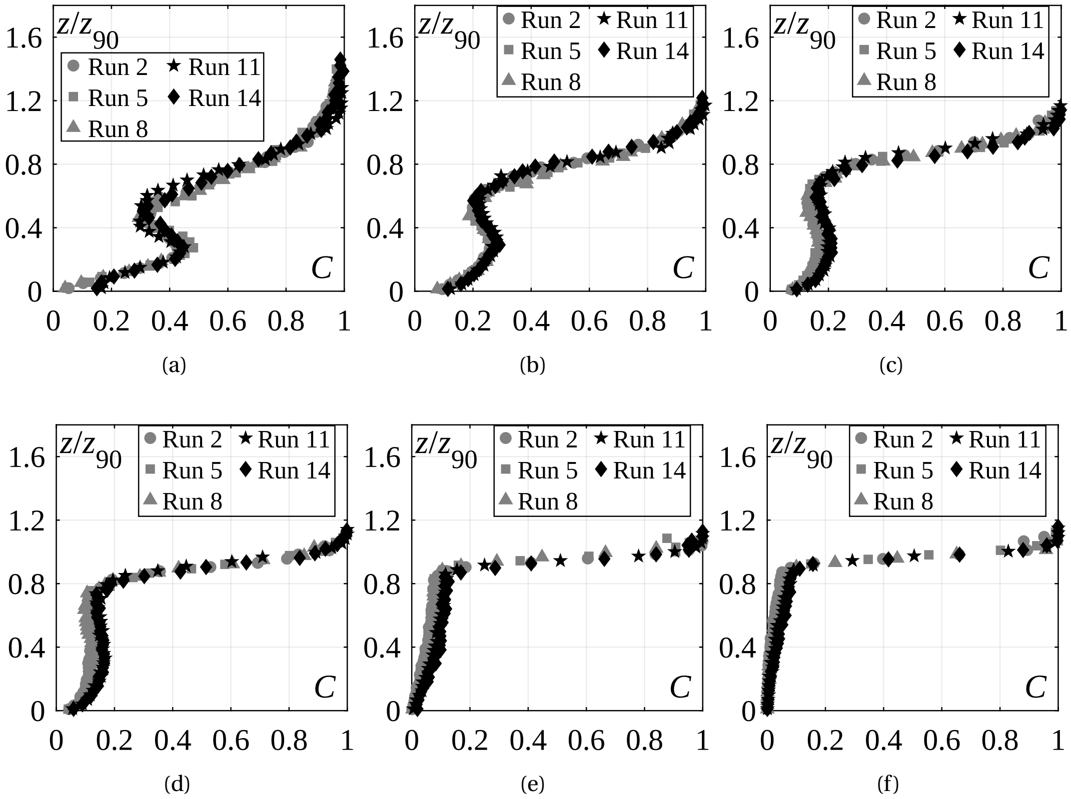

(a) (b) (c)

(d) (e) (f)

Figure 5.3 – Comparison between air concentration profiles in the stilling basin for Runs 2, 5 and 8 (smooth chute approach flows), and Runs 11 and 14 (stepped chute approach flows) at $x/L_{R,\eta}$= (a) 0.1, (b) 0.3, (c) 0.5, (d) 0.7, (e) 1.0 and (f) 1.2.

5.3.2 Streamwise development of maximum C_{max} and minimum C_{min} air concentration

The streamwise development of the maximum C_{max} and minimum C_{min} air concentration in the shear layer region is shown in Figure 5.4a and b, both plotted against the streamwise coordinate normalized with the hydraulic jump length $X_J = x/L_J$. An overall average value of the jump length is used, i.e. $L_J = 5.75h_2$ and $L_J = 6.7h_2$ for smooth and stepped chute approach, respectively. C_{max} is largest close to the jump toe, with values reaching C_{max}=0.48 (Figure

5.4a). With increasing distance, C_{max} decrease as the air bubbles diffuse and disperse in the flow (Wang et al. 2014). C_{min} exhibit a similar development as C_{max} but with lower air concentration values (Figure 5.4b). No considerable effect of approach flow conditions on the streamwise development of C_{max} and C_{min} occurs. The following formulae can be used to describe the development of C_{max} (R^2=0.99) and C_{min} (R^2=0.97) in the shear layer region (Figure 5.4):

$$C_{max} = 0.5\exp\left(-4X_J\right) + 0.09 \qquad 0.07 \le X_J \le 0.7 \tag{5.3}$$

$$C_{min} = 0.3\exp\left(-3.1X_J\right) + 0.07 \qquad 0.07 \le X_J \le 0.7 \tag{5.4}$$

Figure 5.5 shows the streamwise development of the dimensionless vertical position of

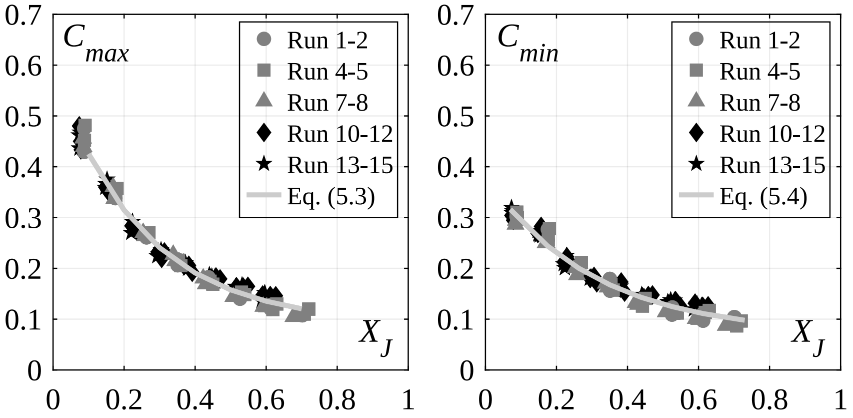

(a) (b)

Figure 5.4 – Streamwise development of: (a) maximum air concentration C_{max} and (b) minimum air concentration C_{min} along the advective diffusive zone; (——) Eqs. (5.3) and (5.4); [Runs 1-8: smooth chute, Runs 10-15: stepped chute].

the maximum Z_{max}=$(z_{max} - h_1)(h_2 - h_1)^{-1}$ and minimum Z_{min}=$(z_{min} - h_1)(h_2 - h_1)^{-1}$ air concentrations plotted against the normalized streamwise coordinate $x/L_{R,\eta}$. They linearly increase with increasing distance, indicating a linear spread of the turbulent shear region along the jump roller. The streamwise development of Z_{max} is mostly independent of the approach flow conditions and can be described as (Figure 5.5, R^2=0.96):

$$Z_{max} = 0.49\frac{x}{L_{R,\eta}} + 0.018 \qquad 0.1 \le \frac{x}{L_{R,\eta}} \le 0.8 \tag{5.5}$$

However, higher values of Z_{min} are consistently observed downstream of stepped chute flows within approximately 0.1≤$x/L_{R,\eta}$≤0.4, indicating a broader turbulent shear layer region, as compared to that after smooth chutes (Figure 5.5). This is in line with mean flow depth measurements conducted with an US sensor (Figure 4.8), and it is judged to be due to relatively higher approach flow depths downstream of stepped chutes. The development of Z_{min} can be described with (Figure 5.5):

$$Z_{min} = a\frac{x}{L_{R,\eta}} + b \qquad 0.1 \leq \frac{x}{L_{R,\eta}} \leq 0.8 \tag{5.6}$$

with a=0.91 and b=0.092 for smooth chute approach flows (R^2=0.99), and a=0.8 and b=0.17 for stepped chute approach flows (R^2=0.99).

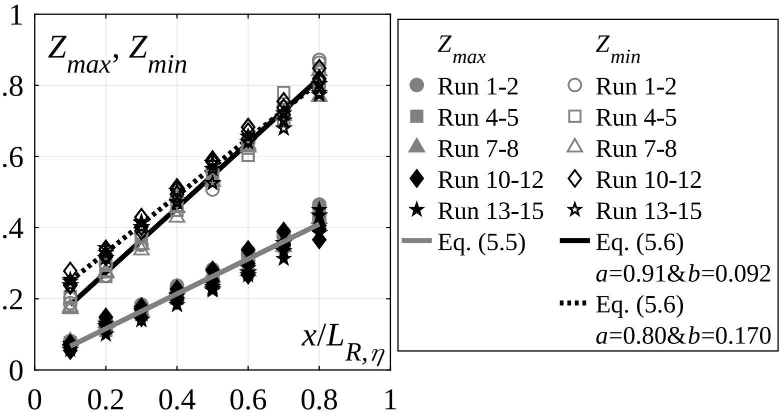

(a)

Figure 5.5 – Streamwise development of the dimensionless vertical positions of maximum Z_{max} and minimum Z_{min} air concentration; (——) Eqs. (5.5) and (5.6); [Runs 1-8: smooth chute, Runs 10-15: stepped chute].

5.3.3 Streamwise bottom air concentration

Flow aeration close to the bottom was often neglected due to very small concentrations C_b. Herein, all visual observations indicated significant presence of air close to the stilling basin bottom. The streamwise development of C_b (at some 6 mm from the basin invert) is shown in Figure 5.6, including the bottom air concentration measured at the inflow section $C_{b,ce}$ (section 1-1, Figure 3.2) at $X_J = -0.3$.

Hydraulic jumps generated after *smooth chutes* are characterized by a sharp initial rise in the bottom air concentration, reaching C_b=0.11 at X_J≈0.17 (gray symbols in Figure 5.6). Further downstrem, C_b values gradually decrease until X_J≈0.9, beyond which they tend to zero. A comparative analysis between the values measured at the inflow section, i.e. $C_{b,ce}$, with those of the section close to the jump toe, i.e. at X_J≈0.08, revealed no significant correlation, indicating that the development of the bottom air concentration C_b is not influenced by the approach flow aeration. This can be linked to the flow deviation at the jump toe (Figure 4.13a), i.e. at X_J=0, generating high pressures close to the invert and thus promoting de-aeration of the flow at the entrance of the basin.

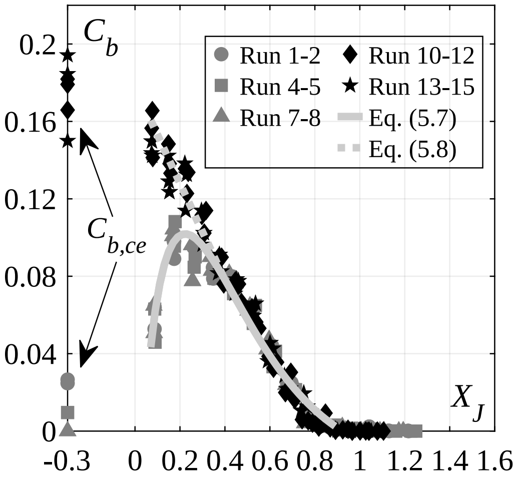

Figure 5.6 – Streamwise development of the bottom air concentration C_b verus normalized streamwise coordinate X_J, including bottom air concentration at the inflow section $C_{b,ce}$ ($X_J = -0.3$); (——) Eq. (5.7); (- - -) Eq. (5.8); [Runs 1-8: smooth chute, Runs 10-15: stepped chute].

The pronounced C_b values with smooth chute approach flows, as compared to classical hydraulic jumps, can be also explained by the presence of the flow deviation at the jump toe. As described by Chanson (2015b), the air bubbles in classical hydraulic jumps are mainly entrained at the impingement perimeter, at the beginning of the jump toe, and carried downstream by large scale vortices generated due to the shear of the flow (Figure 5.7a). Due to the flow deviation, chute inflows induce high curvature of the flow near the jump toe leading to a pronounced vorticity and thus mixing. The enhanced vorticity initiate air bubble transport close to the bottom in the upstream reach of the stilling basin, as illustrated on Figure 5.7b which reflects only an idealized, time-averaged flow field. In fact, the position of the jump toe and thus the inception point of the highly aerated vorticial structures is constantly fluctuating, leading to a sharp rise of C_b values within $x/L_{R,\eta}$≤0.2. Further downstream, i.e. $x/L_{R,\eta}$>0.2, the air bubbles close to the invert are transported by a high-velocity bottom-jet flow and tend to rise from the invert, partially due to boyency effects (flow depth increase) and partially due to the detachment of the bottom jet flow (Figure 4.13e), resulting in a reduction of the bottom air concentration.

The bottom air concentration development points out a clear effect of *stepped chute* approach flows that can be clearly observed (black symbols in Figure 5.6). In the vicinity of the jump toe, at X_J≈0.08, the values of the bottom air concentration are up to three times higher (as compared to those after smooth chutes) reaching C_b=0.16. Further downstream, the values of C_b decrease up to X_J≈0.4, beyond which they coincide with smooth chute approach flow values along the remaining downstream reach of the stilling basin. No considerable effect of step size s occurs.

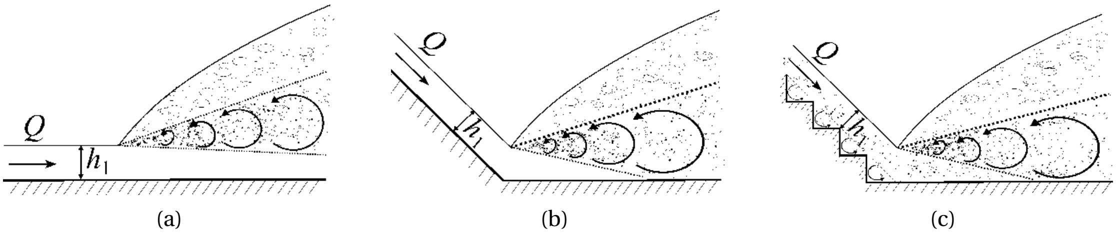

Figure 5.7 – Sketch of air entrainment in hydraulic jumps with a: (a) horizontal approach flow, (b) smooth chute approach flow and (c) stepped chute approach flow.

The pronounced bottom air concentration values downstream of *stepped chutes* (as compared to those after smooth chutes) within 0.08≤X_J≤0.4 can be explained by a combination of two factors: (1) higher flow aeration close to the bottom on the stepped chute end, i.e. higher $C_{b,ce}$ values (Figure 5.6), and (2) lower bottom mean pressure magnitudes at the flow deviation point (i.e. jump toe) downstream of stepped chutes (Figure 4.13a). Comparatively lower pressure magnitudes at the deviation point results in a lower de-aeration rate after stepped chutes. Consequently, large quantities of air are transported from the chute end into the region below the developing shear layer, as illustrated in Figure 5.7c, and advected downstream causing pronounced C_b values. Moreover, air bubbles as well as turbulence are transported from the stepped chute flow, resulting in pronounced extreme and fluctuating pressure coefficients within X_J≤0.1 (as compared to smooth chute flows) as shown in Chapter 4 (Figure 4.13b, c and d). The streamwise development of the bottom air concentration for *smooth chute* approach flow can be decribed as (Figure 5.6, R^2=0.95):

$$C_b = 0.98 - \tanh\left(2.4X_J\right)^{0.95X_J-0.03} \qquad 0.08 \leq X_J \leq 0.9 \qquad (5.7)$$

The same equation can be used for *stepped chute* approach flow in the range X_J ≥0.4. The pronounced bottom air concentrations with *stepped chute* approach flows can be approximated as (Figure 5.6, R^2=0.85):

$$C_b = -0.25X_J + 0.178 \qquad 0.08 \leq X_J \leq< 0.4 \qquad (5.8)$$

Based on Peterka (1958), Rasmussen (1956) and Russell and Sheehan (1974) a bottom air concentration C_b of about 5% to 8% is typically considered to be sufficient to avoid cavitation damage. Considering these limits, the present results suggest that plain stilling basins with smooth chute approach flows are expected to be exempted from cavitation damage within $0.1 \leq X_J \leq 0.5$ and $0.15 \leq X_J \leq 0.4$ for 5% and 8% bottom air concentration limit, respectively (Figure 5.6). On the other hand, stepped chute approach flows provide additional air and the plain stilling basins are expected to be protected from cavitation damage within 0≤X_J≤0.5 and 0≤X_J≤0.4 for 5% and 8% bottom air concentration limits, respectively (Figure 5.6).

5.3.4 Streamwise development of the mean air concentrations

Air concentrations along the jump are usually described with the mean (depth-averaged) air concentration C_a calculated as (Wood et al. 1983):

$$C_a = \frac{1}{z_{90}} \int_0^{z_{90}} C dz \tag{5.9}$$

Figure 5.8 shows the streamwise development of C_a for all test runs, plotted against the normalized streamwise coordinate X_J. As indicated by the air concentration profiles (Figure 5.3a), the air entrainment in a hydraulic jump is mostly independent of the approach flow conditions, with mean air concentration values of up to C_a=0.49 at $X_J \approx 0.08$. With increasing distance from the jump toe, a rapid flow deaeration is observed, ultimately attaining quasi constant values of $C_a \approx 0.05$ in the tailwater. They are described as (Figure 5.8, R^2=0.98):

$$C_a = 0.54 \exp\left(-1.84 X_J\right) \qquad 0.08 \leq X_J \leq 1.34 \tag{5.10}$$

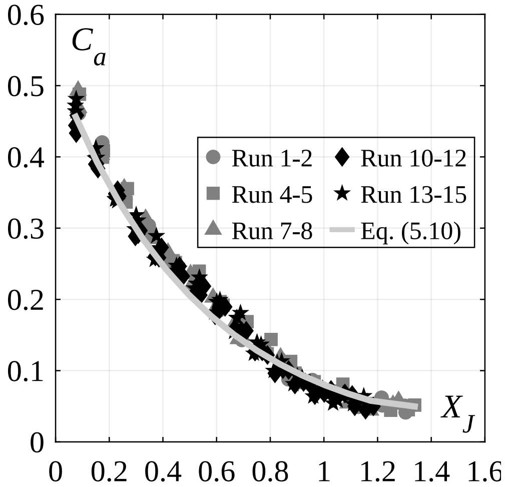

Figure 5.8 – Streamwise development of mean air concentration C_a compared to (——) Eq. (5.10); [Runs 1-8: smooth chute, Runs 10-15: stepped chute].

5.3.5 Effect of 30° inclined approach flows on air concentration distribution in hydraulic jumps

To illustrate the effect of chute (30° inclined) approach flows on the air concentration distribution in the hydraulic jump (as compared to horizontal approach flows), the herein measured air concentration profiles in the advective diffusive zone are compared to the air concentration profiles for classical hydraulic jumps with PD approach flows of Wang (2014), FD approach flows of Takahashi and Ohtsu (2017), and PA approach flow of Thandaveswara (1974) in Figure 5.9 a-b, c-d and e-f, respectively. The air concentration profiles are compared for similar approach flow Froude number F_1 and streamwise distance x/h_1, as the experimental data for classical hydraulic jumps were originally collected in terms of x/h_1. Furthermore, as air-water flow properties of classical hydraulic jumps were typically studied for lower ranges or F_1, Run 14 (stepped chute, Table 4.1) was selected for comparison.

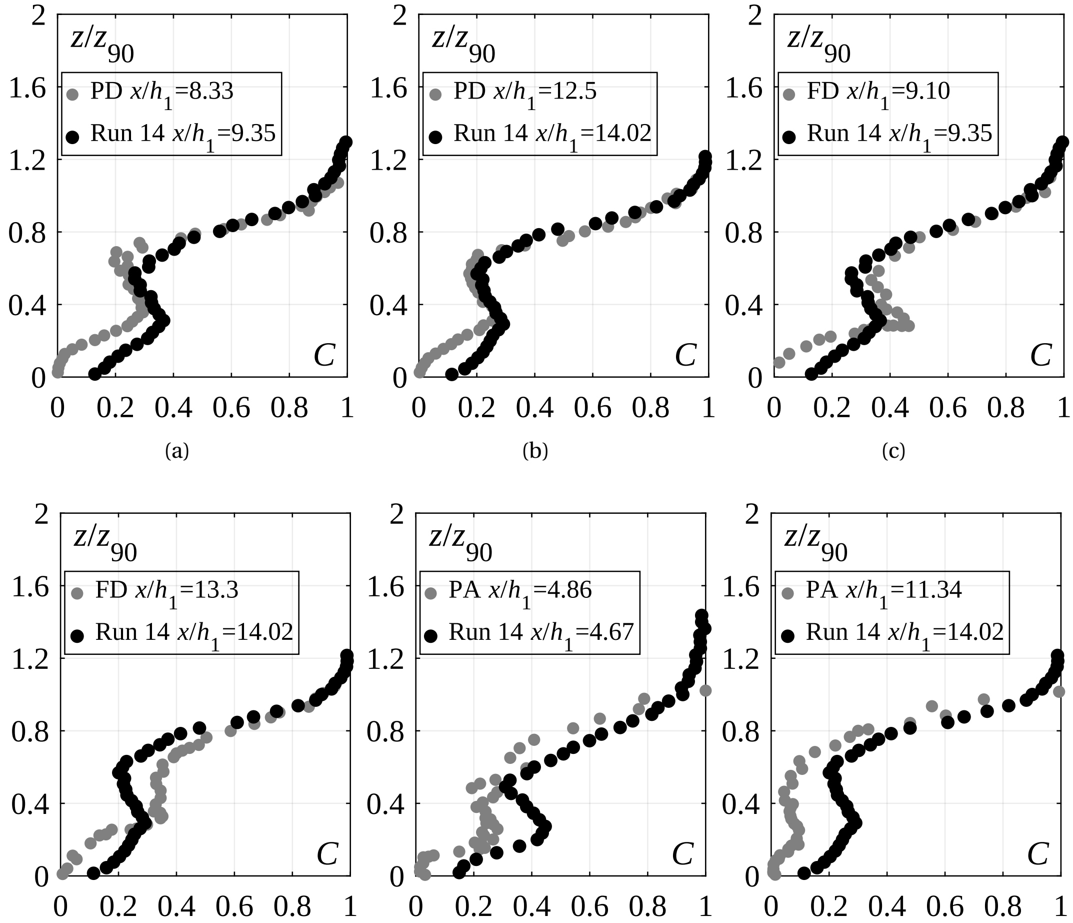

(a) (b) (c)

(d) (e) (f)

Figure 5.9 – Comparison of air concentration profiles for Run 14 (stepped chute, Table 4.1) at x/h_1=4.67, 9.35 and 14.02 (i.e. $x/L_{R,\eta}$= 0.1, 0.2 and 0.3) with those for: (a-b) PD approach flow for F_1=7.5 and R_1=1.4×10^5 at x/h_1=8.33 and x/h_1=12.5 (Wang 2014), (c-d) FD approach flow for F_1=7.2 and R_1=6.2×10^4 at x/h_1=9.1 and x/h_1=13.3 (Takahashi and Ohtsu 2017), (e-f) PA approach flow for F_1=5.49 and R_1=6.68×10^4 at x/h_1=4.86 and x/h_1=11.34 (Thandaveswara 1974).

Comparing the air concentration profiles, a clear effect of chute approach flows (black symbols) is visible. As indicated by the obtained values of dimensionless turbulent diffusivities in the shear layer region (Figure 5.2a), the air concentration profiles for chute approach flows exhibit a more “uniform” distribution in the shear layer region compared to those with PD approach flows (Figures 5.9a and b). The latter is even more pronounced when compared to profiles for FD approach flow conditions (Figures 5.9c and d). Therefore, inclined chute approach flows induce significantly higher air concentration values in the lower part of the shear layer region, i.e. $z < z_{max}$, as compared to PD and FD approach flows. In the upper part of the shear layer region, i.e. $z_{min} < z < z_{max}$, the air concentration values are mostly higher than those for PD approach flows (Figures 5.9a and b), whereas lower values are observed in comparison with FD approach flows (Figures 5.9c and d). In the recirculation region, i.e. $z > z_{min}$, the air concentration distribution for inclined chute approach flows is similar to those with PD and FD approach flows (Figures 5.9 a-d). As mentioned before, this “uniformity” of the air concentration profiles is attributed to the enhanced vorticity leading to the higher diffusion rate of the air bubbles across the shear layer region. Finally, inclined chute approach flows exhibit significantly higher air concentration values across the flow depth in comparison with the PA approach flow conditions (Figures 5.9 e-f).

5.4 Air-phase frequency

The air-phase frequency F was defined as the average number of air bubbles per unit time detected by the leading tip of the FOP. The F is proportional to the air-water interface area and inversely proportional to the bubble size for a given air concentration (Chanson 2011). Figure 5.10 shows a typical variation of dimensionless air-phase frequency Fh_1/V_1 profiles at the selected distances $x/L_{R,\eta}$, plotted against the normalized vertical coordinate $z/(h_2\text{-}h_1)$ for smooth chute (Run 7, Figure 5.10a) and stepped chute (Run 10, Figure 5.10b) approach flows, respectively.

In the *advective diffusive zone*, i.e. $0.1 \leq x/L_{R,\eta} \leq 0.8$, the profiles exhibit a distinctive shape, similar to those reported for classical hydraulic jumps formed with PD approach flows (e.g. Chanson 2010; Chanson and Brattberg 2000; Murzyn et al. 2005; Wang and Chanson 2015b). Each profile is characterized by a maximum air-phase frequency F_{max} located at a vertical position from the bottom z_{Fmax} in the lower part of the flow, and a secondary peak F_{sec} at vertical position from the bottom z_{Fsec} in the upper part of the flow. The magnitudes of F_{max} and F_{sec} decrease with increasing distance from the jump toe, whereas their vertical positions z_{Fmax} and z_{Fsec} increase.

Further downstream, in the air release zone (i.e. $x/L_{R,\eta} \geq 0.9$), the profiles first tend to transform into a more “uniform” distribution ($x/L_{R,\eta}$=1.0 in Figure 5.10), where the F_{max} and F_{sec} are of the same order of magnitude (note that F_{max} could be lower than F_{sec}), and then into a monotonically increasing profile ($x/L_{R,\eta}$=1.2 in Figure 5.10), where F_{max} disappears and only a single peak can be observed in the upper part of the flow, i.e. F_{sec}. This transformation is

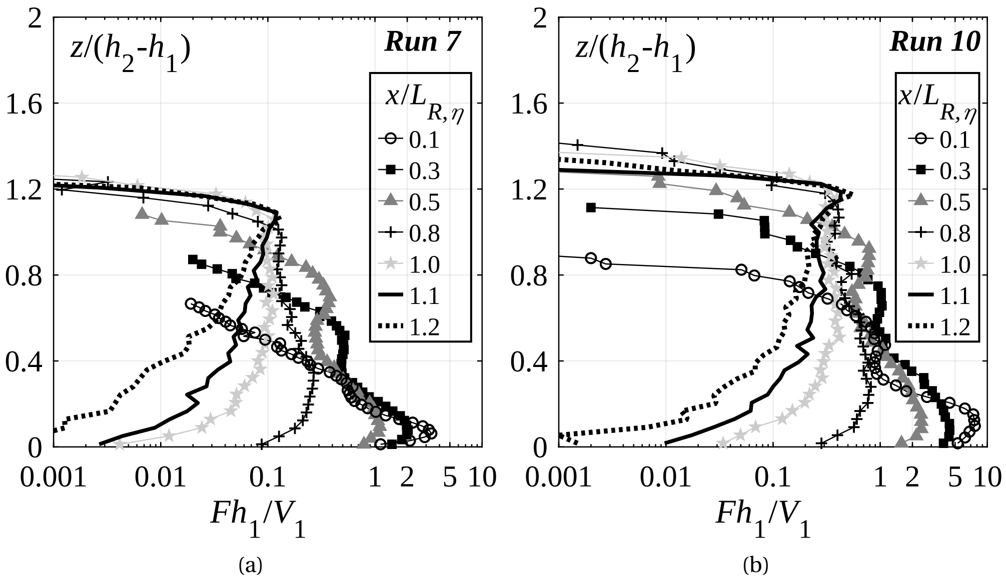

Figure 5.10 – Dimensionless vertical air-phase frequency Fh_1/V_1 profiles at the selected distances $x/L_{R,\eta}$ for: (a) Run 7 (smooth chute) and (b) Run 10 (stepped chute).

somewhat longer with stepped chute approach flows, i.e. $0.9 \leq x/L_{R,\eta} \leq 1.2$ (Figure 5.10b), as compared to smooth chute approach flows, i.e. $0.9 < x/L_{R,\eta} \leq 1.1$ (Figure 5.10a).

The streamwise development of the dimensionless characteristic frequencies $F_{max}h_1/V_1$ and $F_{sec}h_1/V_1$ are plotted in Figure 5.11a and b, respectively, against the normalized streamwise coordinate $x/L_{R,\eta}$. The development of their dimensionless vertical positions $Z_{Fmax}=z_{Fmax}/(h_2-h_1)$ and $Z_{Fsec}=(z_{Fsec}-h_1)/(h_2-h_1)$ are shown in Figure 5.12a.

$F_{max}h_1/V_1$ decreases in an exponential manner with increasing $x/L_{R,\eta}$ (Figure 5.11a). Its vertical position Z_{Fmax} exhibit a slight increase tendency within $0 < x/L_{R,\eta} \leq 0.6$, followed by a sharp increase towards the surface (Figure 5.12a). As the maximum air-phase frequency can be linked with a region of maximum shear stress (Chanson 2011), i.e. the high velocity bottom jet flow containing large scale vortices (Figure 4.5a), a sharp rise of Z_{Fmax} at $x/L_{R,\eta} \approx 0.6$ is associated with the detachment of the bottom jet flow. No apparent effect of approach flow aeration or step size on the development of Z_{Fmax} occurs. However, the bottom jet flow downstream of stepped chutes (black symbols) consistently required an increased normalized length $x/L_{R,\eta}$ to detach and reach the surface, as compared to smooth chute approach flows (gray symbols). This again demonstrates longer hydraulic jump lengths L_J (in terms of $x/L_{R,\eta}$) downstream of stepped chutes, as compared to smooth chutes. Normalizing the streamwise coordinate with the hydraulic jump length $X_J = x/L_J$, made reasonably collapse all Z_{Fmax} (Figure 5.12b). The approximate location of the herein observed detachment point, i.e. at $X_J \approx 0.5$ (Figure 5.12b), is in close agreement with the observations based on bottom pressure characteristics presented in Chapter 4. Therein, the skewness coefficients of the pressure readings reached negative values at $X_J \approx 0.5$ (Figure 4.13e).

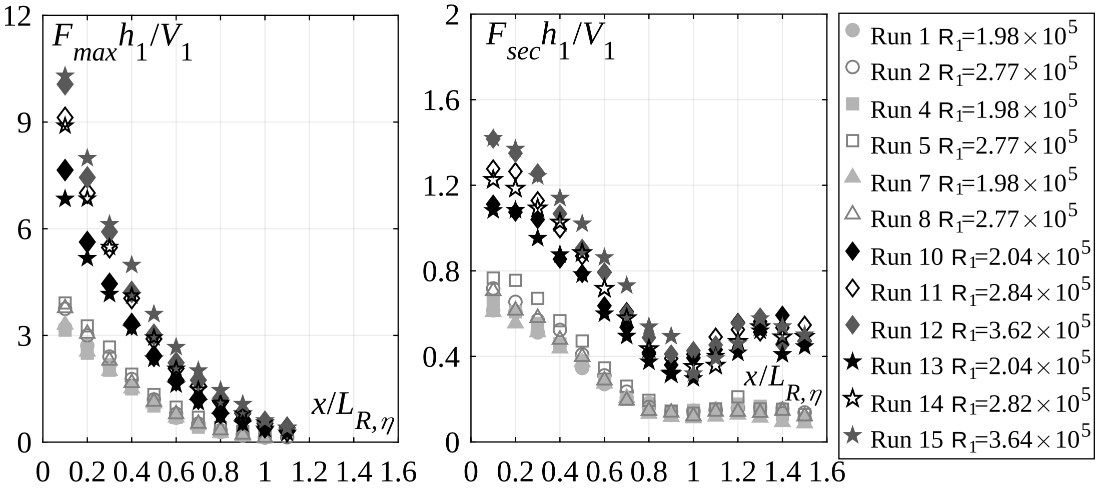

(a)

(b)

Figure 5.11 – Streamwise development of dimensionless: (a) maximum air-phase frequency $F_{max}h_1/V_1$ and (b) secondary peak in air phase frequency $F_{sec}h_1/V_1$; [Runs 1-8: smooth chute, Runs 10-15: stepped chute].

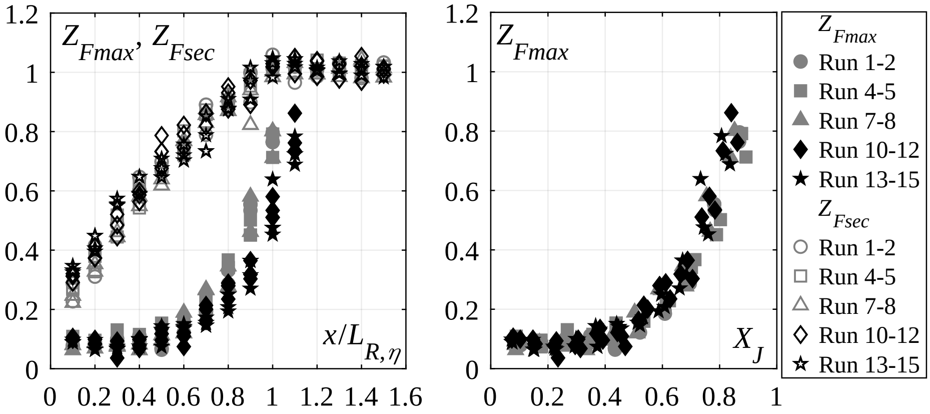

(a)

(b)

Figure 5.12 – Streamwise development of dimensionless locations: (a) Z_{Fmax} and Z_{Fsec} versus normalized coordinate $x/L_{R,\eta}$ and (b) Z_{Fmax} versus normalized coordinate X_J; [Runs 1-8: smooth chute, Runs 10-15: stepped chute].

The present results further show that at a given streamwise location in the advective diffusive zone, the locus of the F_{max} is consistently lower than the locus of the C_{max}, i.e. $z_{Fmax} < z_{max}$, in line with studies on classical hydraulic jumps with PD approach flows (e.g. Chanson (2011), Chanson and Brattberg (2000) and Wang et al. (2015a)). This is illustrated in Figure 5.13 where Z_{Fmax} is plotted as a function of Z_{Cmax}=$z_{max}/(h_2 - h_1)$. Chanson (2010) argued that the non-coincidence of the z_{Fmax} and z_{max} is caused by double diffusion processes where air bubbles and vorticity are diffused at the different rate and manner in the shear layer region.

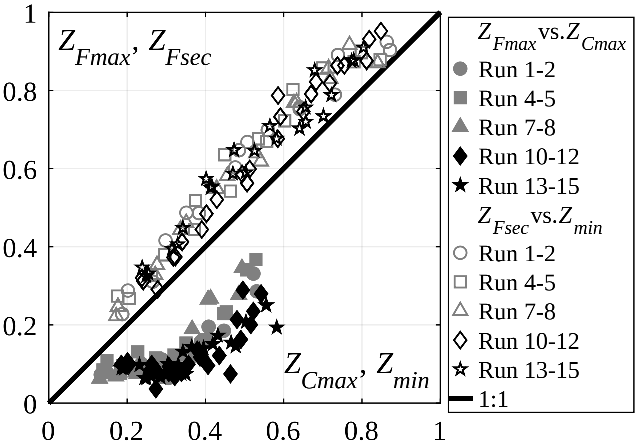

Figure 5.13 – Relationship between dimensionless locations Z_{Fmax} and Z_{Cmax} (full symbols), and Z_{Fsec} and Z_{min} (open symbols); [Runs 1-8: smooth chute, Runs 10-15: stepped chute].

The streamwise development of $F_{sec}h_1/V_1$ (Figure 5.11b) is characterized by a monotonic decrease, reaching minimum values in the vicinity of the roller end, i.e. for $x/L_{R,\eta}\approx1$. Further downstream, i.e. for $x/L_{R,\eta}\geq1$, $F_{sec}h_1/V_1$ increase reaching a local maximum at $x/L_{R,\eta}\approx1.2$ and $x/L_{R,\eta}\approx1.3$ for smooth and stepped approach flows, respectively, followed by a decrease until the end of the measuring reach. Its dimensionless vertical position Z_{Fsec} increase in the streamwise direction reaching maximum values at the roller end, i.e. $x/L_{R,\eta}\approx1$, beyond which it decreases towards quasi-constant tailwater magnitudes (Figure 5.12a). The latter qualitatively followed the surface profiles measured with the US sensor (Figure 4.6). In Figure 5.13, Z_{Fsec} is plotted as a function of Z_{min}, showing that the locus of F_{sec} is in the recirculation region, i.e. $Z_{Fsec}>z_{min}$. The air concentration values at Z_{Fsec} are typically between C=0.3 to 0.5, in line with observations of Wang (2014) for classical hydraulic jumps with PD inflows. Therefore, the F_{sec} is associated with the flow structure in the vicinity of the surface and is mainly governed by the surface fluctuations and air bubbles sizes in the in the upper (foamy) part of the flow. The streamwise reduction of $F_{sec}h_1/V_1$ within the roller length is thus attributed to the streamwise decrease of surface fluctuations (Figure 4.10b) and increase of air bubble sizes. On the other hand, the increase in magnitudes downstream of the roller end, i.e. $x/L_{R,\eta}\geq1$, is mainly driven by the detachment of the bottom jet flow. This results in the transport of smaller air bubbles from the shear layer region towards the foamy surface, pronouncing the magnitudes of the F_{sec}. This is further supported by the relative downstream shift of the streamwise position of the local maximum of $F_{sec}h_1/V_1$, in terms of $x/L_{R,\eta}$, for stepped chute approach flows as compared to smooth chute approach flows (Figure 5.11b).

Although the shape and the streamwise development of the air-phase frequency profiles is similar for all experimental runs, the magnitudes of Fh_1/V_1 are mainly affected by the: (1) approach flow Reynolds number R_1 and (2) stepped chute approach flows. This can be observed by comparing the values of $F_{max}h_1/V_1$ and $F_{sec}h_1/V_1$ for different runs (Figure 5.11). For example, at a given streamwise location $x/L_{R,\eta}$ for quasi-similar F_1 and 40% larger R_1 (i.e. $R_1 \approx 2.0 \times 10^5$ and 2.8×10^5), the values of $F_{max}h_1/V_1$ and $F_{sec}h_1/V_1$ increase up to 55% and 27%, respectively, indicating scale effects in terms of air phase frequencies. As stated by Chanson and Chachereau (2013) the dynamic similarity of air-phase frequencies in hydraulic jumps cannot be achieved with Froude similarity unless working at full geometric scale. On the other hand, for quasi similar R_1, the values of $F_{max}h_1/V_1$ and $F_{sec}h_1/V_1$ for stepped chute approach flows in the roller region are up to 3.5 and 3 times larger, respectively, as compared to those for smooth chute approach flows. As the air-phase frequency is inversely proportional to the air bubble size, this suggests smaller air bubble size distribution in the hydraulic jump with stepped chute approach flows (as compared to smooth chute approach flows).

5.5 Vertical distribution of air-water flow velocity

Air-water flow velocity V was deduced from cross-correlation analysis of the dual-tip FOP signals measured in the stilling basin. A typical streamwise development of dimensionless velocity profiles V/V_1 along the basin is shown in Figure 5.14a and b for smooth chute (Run 7) and stepped chute (Run 10) approach flow, respectively. At each measured section, the zero lines for the velocity origin are shown with dashed lines. The measured velocities were analyzed up to a characteristic flow depth z_{90} (continuous lines, Figure 5.14), as for $z > z_{90}$ the cross-correlation analysis often yielded meaningless flow velocities due to the intense and erratic splashing of the flow. No slip conditions are imposed at the channel invert, i.e. $V(z{=}0){=}0$.

The velocity distribution in the *advective diffusive zone*, i.e. $x/L_{R,\eta} \leq 0.8$, exhibit a self-similar shape resembling a wall jet flow, in line with studies on the classical hydraulic jump (e.g. Chanson and Brattberg (2000), Hager (1992), Murzyn and Chanson (2009a), Ohtsu et al. (1990), Rajaratnam (1965) and Wang and Chanson (2019)). A boundary layer flow is observed next to the stilling basin invert, where the velocity rapidly increase from zero to the maximum velocity V_{max} at a vertical position from the bottom z_{Vmax}. Above $z > z_{Vmax}$, the velocities decrease reaching negative recirculation velocities V_{rec} at vertical position from the bottom z_{V0}. Note that the transition between the positive and negative velocities is abrupt and no velocity data of $V{=}0$ is observed, as it presents a singularity in the FOP processing technique. The distribution of V_{rec} is quasi-uniform at a given streamwise position $x/L_{R,\eta}$. The flow reversal occurs within $0 < x/L_{R,\eta} \leq 0.8$, irrespective of the approach flow conditions. The velocity magnitudes tend to decrease with increasing distance from the jump toe, due to the intense energy dissipation.

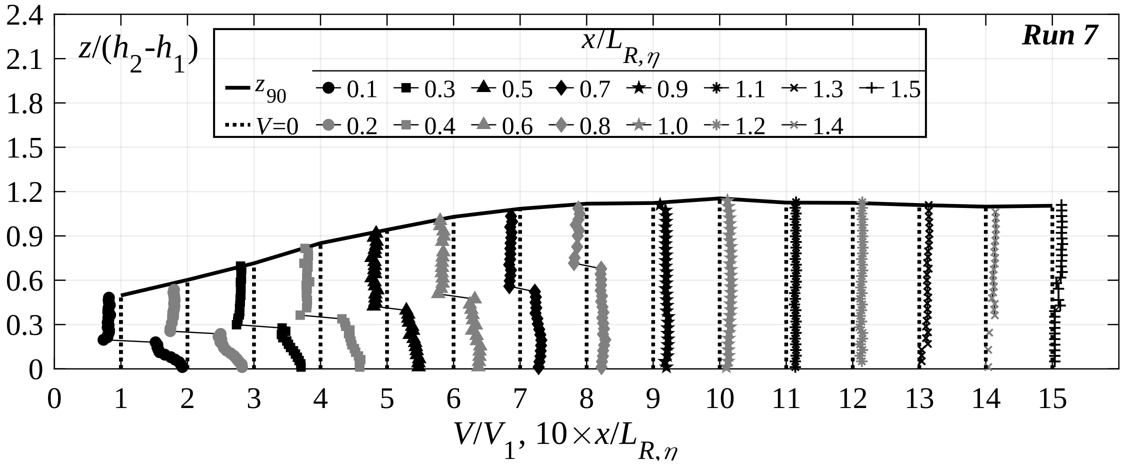

(a)

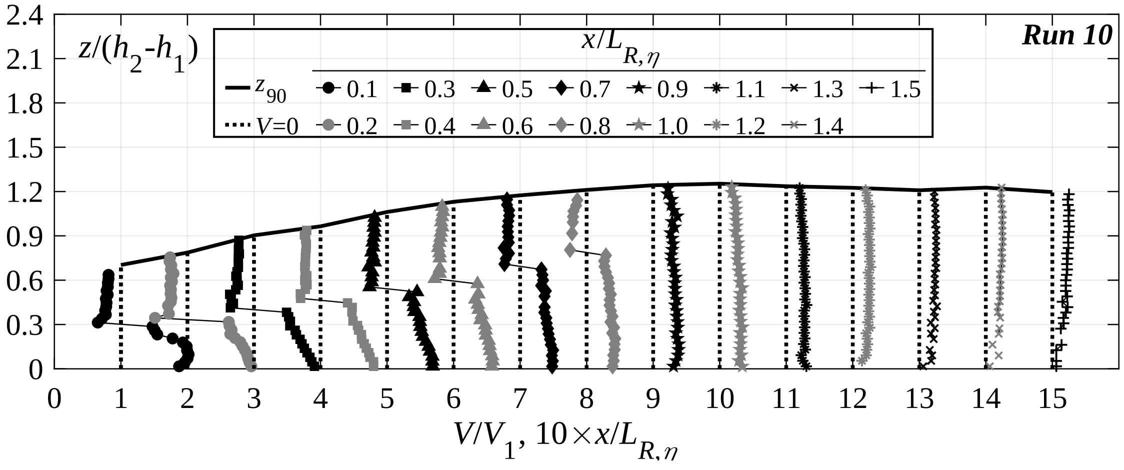

(b)

Figure 5.14 – Dimensionless vertical velocity distributions V/V_1 along the stilling basin for: (a) Run 7 (smooth chute) and (b) Run 10 (stepped chute).

In the *air release zone*, the flow reversal disappears, however, the velocity profiles still tend to exhibit a “wall jet” type profile within $0.9 \leq x/L_{R,\eta} \leq 1.0$, typically. Further downstream, the profiles first tend to transform into a more “uniform” distribution and then into, what appears to be, a fully developed open channel velocity distribution in the tailwater.

It has to be noted that velocities could not be reliably estimated in the lower part of the flow towards the end of the measuring reach, due to the low air concentration values. Moreover, the velocity magnitudes in the recirculating region should be taken with caution, due to the intrusive nature of measurement technique and flow direction.

For classical hydraulic jumps formed with PD approach flow conditions, Chanson (2010) proposed modified wall jet expressions, taking into account the flow reversal in the upper part of the flow:

$$\frac{V}{V_{max}} = \left(\frac{z}{z_{Vmax}}\right)^{1/M} \qquad \text{for } \frac{z}{z_{Vmax}} < 1 \tag{5.11}$$

$$\frac{V - V_{rec,a}}{V_{max} - V_{rec,a}} = \exp\left[-0.5\left(1.765\left(\frac{z - z_{Vmax}}{z_{0.5}}\right)\right)^2\right] \qquad \text{for } \frac{z}{z_{Vmax}} > 1 \tag{5.12}$$

with $V_{rec,a}$ as depth averaged recirculation velocity, $z_{0.5}$ as a vertical elevation where V=$V_{max}/2$ and M as a constant. The measured velocity profiles in the advective diffusive zone are compared with Eqs. (5.11) and (5.12) in Figures 5.15a and b for smooth and stepped chute approach flows, respectively. Despite some scatter, the measured velocity profiles are in an overall good agreement with those equations. The exponent M in Eq. (5.11) is typically between 8 to 12. Accordingly, no considerable effect of approach flow conditions on the shape of velocity profiles occurs.

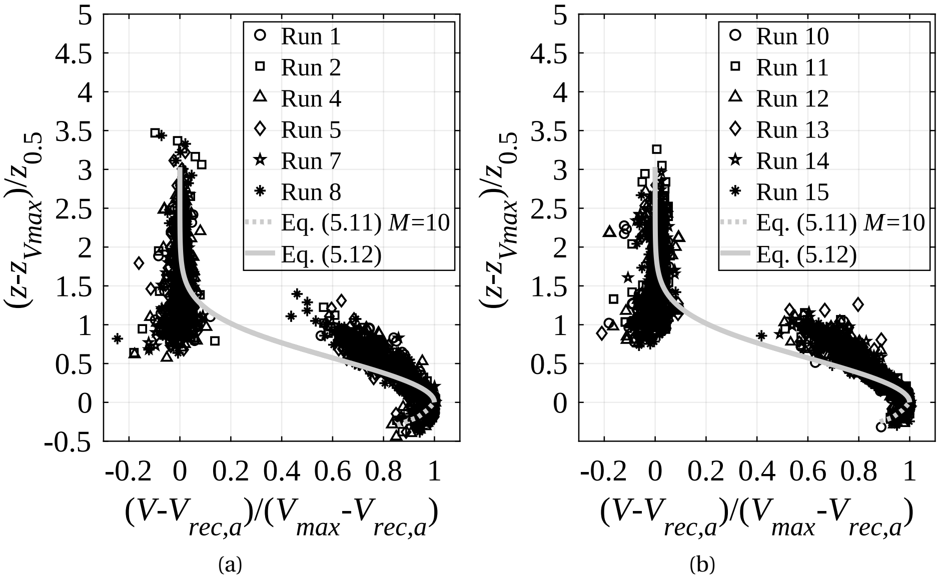

Figure 5.15 – Dimensionless vertical velocity distributions $(V - V_{rec})/(V_{max}$-$V_{rec})$ within advective diffusive zone for: (a) smooth chute approach flows and (b) stepped chute approach flows; (- - -) Eq. (5.11); (——) Eq. (5.12) with M=10.

Figure 5.16a shows the streamwise development of the dimensionless maximum velocity V_{max}/V_1, plotted against the normalized streamwise coordinate $x/L_{R,\eta}$ for all test runs, including maximum velocity decay prediction of Wang and Chanson (2017) for classical hydraulic jumps with PD inflows. The maximum velocities show a gradual streamwise decrease with increasing distance from the jump toe, reaching quasi constant values in the tailwater. As expected, the lower F_1 at the stepped chute end (as compared to that at the smooth chute end) leads to the higher quasi-constant values of V_{max}/V_1 in the tailwater. The herein measured decay of V_{max}/V_1 is qualitatively comparable to the velocity decay prediction of Wang and Chanson (2017). However, it has to be noted that their correlation does not consider the approach F_1. No significant effect of approach flow aeration C_1 for smooth chute approach flow or step size for stepped chute approach flows on the streamwise development of V_{max}/V_1 occurs. However, the maximum velocities downstream of stepped chutes (black symbols) require an increased distance $x/L_{R,\eta}$ to decline to the tailwater magnitudes, compared to those downstream of smooth chutes, showing that a longer hydraulic jump (in terms of $x/L_{R,\eta}$) formed after stepped chutes. To consider different approach F_1 and hydraulic jump length L_J, the maximum velocities are normalized as $(V_{max} - V_2)/(V_1 - V_2)$, where V_2=q/h_2 is mean flow velocity in the tailwater zone, and the streamwise coordinate with jump length $X_J = x/L_J$, resulting in a reasonable collapse of all maximum velocity data, as shown on Figure 5.16b. They can be described as (R^2=0.98):

$$\frac{V_{max} - V_2}{V_1 - V_2} = 1.1 - \tanh\left(2X_J\right)^{1.5} \qquad 0.08 \le X_J \le 1.34 \qquad (5.13)$$

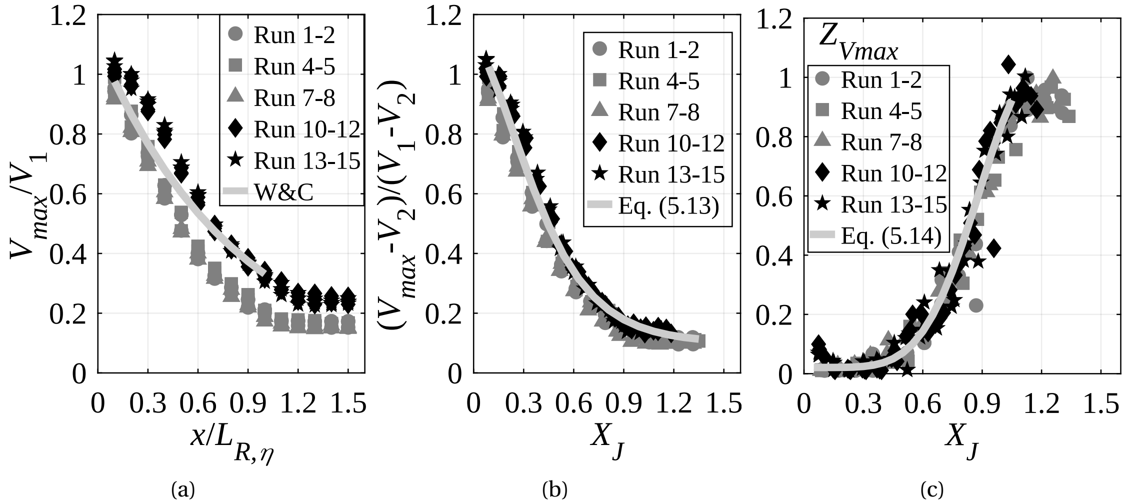

Figure 5.16 – Streamwise development of dimensionless: (a) maximum velocity V_{max}/V_1 vs. normalized streamwise coordinate $x/L_{R,\eta}$, and (b) maximum velocity $(V_{max} - V_2)/(V_1 - V_2)$ vs. normalized streamwise coordinate X_J and (c) elevation of maximum velocity Z_{Vmax} vs. normalized streamwise coordinate X_J; (——) Wang and Chanson (2017) and Eqs. (5.13) and (5.14); [Runs 1-8: smooth chute, Runs 10-15: stepped chute]

The streamwise development of the dimensionless vertical position of the maximum velocity Z_{Vmax} =$z_{Vmax}/(h_2 - h_1)$ is shown in Figure 5.16c as a function of X_J. Within 0<X_J<0.5, Z_{Vmax}

is close to the bottom and exhibit a minor increasing tendency in the streamwise direction. Close to the jump toe, i.e. X_J≈0.08, stepped chute approach flows induce slightly higher values of Z_{Vmax}, as compared to smooth chute approach flows, which is judged to be due to the different approach flow velocity distribution (Figure 4.4). At X_J≥0.5, Z_{Vmax} exhibit a sharp increase in the streamwise direction, ultimately attaining quasi-constant values close to the surface in the tailwater. The pronounced increase in Z_{Vmax} at X_J≈0.5, similarly to the development of Z_{Fmax} (Figure 5.12b), clearly demonstrates the detachment of the high velocity bottom jet flow. At a given streamwise location in the stilling basin, z_{Vmax} is mostly below the corresponding z_{Fmax}, as shown in Figure 5.17a, where Z_{Vmax} is plotted as a function of Z_{Fmax}.

Apart from the section close to the jump toe, i.e. X_J≈0.08, no considerable effect of approach flow conditions on the streamwise development of Z_{Vmax} occurs. They can be described as (R^2=0.94, Figure 5.16c):

$$Z_{Vmax} = 0.021 - \sin\left(1.33X_J\right)^{5.7+X_J} \qquad 0.08 \le X_J \le 1.1 \qquad (5.14)$$

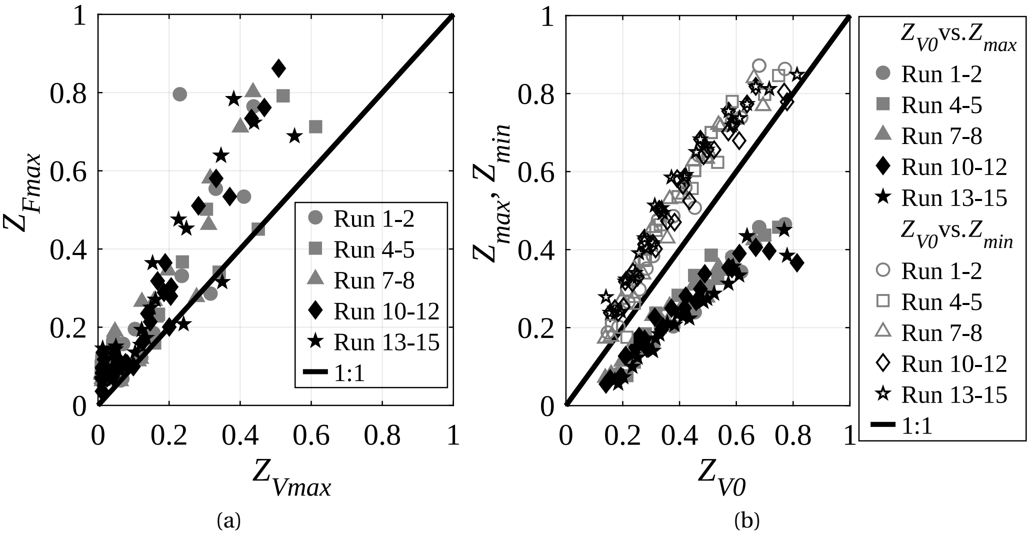

(a) (b)

Figure 5.17 – Relationship between dimensionless locations: (a) Z_{Vmax} and Z_{Fmax} and (b) Z_{V0} and Z_{max} (full symbols), and Z_{V0} and Z_{min} (open symbols); [Runs 1-8: smooth chute, Runs 10-15: stepped chute].

Figure 5.18a shows the streamwise development of the dimensionless absolute depth-averaged recirculation velocity $|V_{rec,a}|/V_1$ plotted against the normalized streamwise coordinate $x/L_{R,\eta}$. They are characterized by a slight streamwise increase within 0.1≤$x/L_{R,\eta}$≤0.2, followed by a gradual decrease towards the end of the advective diffusive zone, i.e. $x/L_{R,\eta}$=0.8, where the flow reversal disappears. Similarly to the dimensionless maximum velocity V_{max}/V_1, the $|V_{rec,a}|/V_1$ is dependent on the approach F_1, in line with observations of Wang and Chanson (2017) for classical hydraulic jumps with PD approach flows.

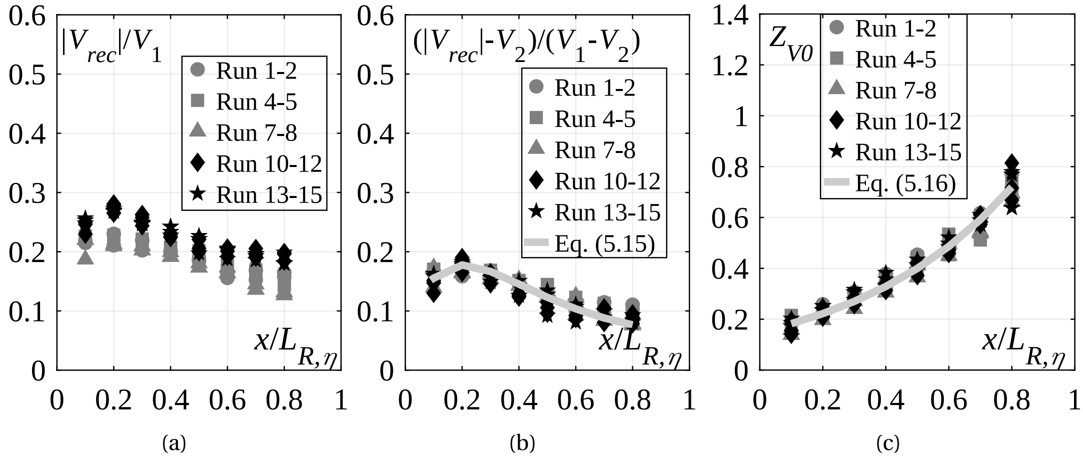

Figure 5.18 – Streamwise development of dimensionless: (a) mean recirculation velocity normalized as $|V_{rec,a}|/V_1$, (b) mean recirculation velocity normalized as $(|V_{rec,a}| - V_2)/(V_1 - V_2)$ and (c) elevation of flow reversal onset Z_{V0} along the stilling basin; (——) Eqs. (5.15) and (5.16); [Runs 1-8: smooth chute, Runs 10-15: stepped chute].

The herein measured range of $0.13 \le |V_{rec,a}|/V_1 \le 0.28$ is qualitatively comparable to the proposed range of Wang and Chanson (2017) of $0.26 \le |V_{rec,a}|/V_1 \le 0.36$ for $6 \le F_1 \le 10$. To consider different approach flow F_1, the recirculation velocities are normalized as $(|V_{rec,a}| - V_2)/(V_1 - V_2)$, resulting in a reasonable collapse of all recirculation velocity data along the advective diffusive zone (Figure 5.18b). They can be approximated as (R^2=0.84):

$$\frac{|V_{rec,a}| - V_2}{V_2 - V_1} = 1.05 - \tanh\left(2.54\frac{x}{L_{R,\eta}}\right)^{x/L_{R,\eta}-0.02} \qquad 0.1 \le \frac{x}{L_{R,\eta}} \le 0.8 \qquad (5.15)$$

The dimensionless elevation of the flow reversal onset $Z_{V0}=(z_{V0} - h_1)/(h_2 - h_1)$ increases exponentially along the advective diffusive zone (Figure 5.18c). It is consistently observed to be in the upper part of the shear layer region, i.e. $z_{max} < z_{V0} < z_{min}$, as illustrated in Figure 5.17b, where Z_{V0} is plotted as a function of both Z_{max} (full symbols) and Z_{min} (open symbols). The streamwise development of Z_{V0} is practically independent of the approach flow condition, and can be described as (Figure 5.18c, R^2=0.97):

$$Z_{V0} = 0.15\exp\left(1.96\frac{x}{L_{R,\eta}}\right) \qquad 0.1 \le \frac{x}{L_{R,\eta}} \le 0.8 \qquad (5.16)$$

5.6 Characteristic flow depths

Figure 5.19a shows the streamwise development of the dimensionless characteristic flow depths Z_{90}=$(z_{90}-h_1)/(h_2-h_1)$ along the stilling basin for all experimental runs. They increase in the streamwise direction and reach a maximum at the roller end, in line with the mean flow depth recordings of the US sensor (Figure 4.6). Further downstream, due to the intense flow de-aeration, Z_{90} decreases and reach quasi-constant values in the tailwater. It is visible that the dimensionless characteristic flow depths downstream of stepped chutes (compared to smooth chutes) are higher within $0.1 \le x/L_{R,\eta} \le 0.3$. As mentioned before, this is judged to be due to relatively higher approach flow depths after stepped chutes (Figure 4.8). The normalized characteristic flow depths $Z_9$0 along the jump roller are described with a self-similar function as (Figure 5.19a):

$$Z_{90} = 1.12\left(\frac{x}{L_{R,\eta}}\right)^{c} \qquad 0.1 \le \frac{x}{L_{R,\eta}} \le 1 \tag{5.17}$$

with c=0.36 and 0.30 for smooth (R^2=0.96) and stepped chute (R^2=0.98) approach flows, respectively.

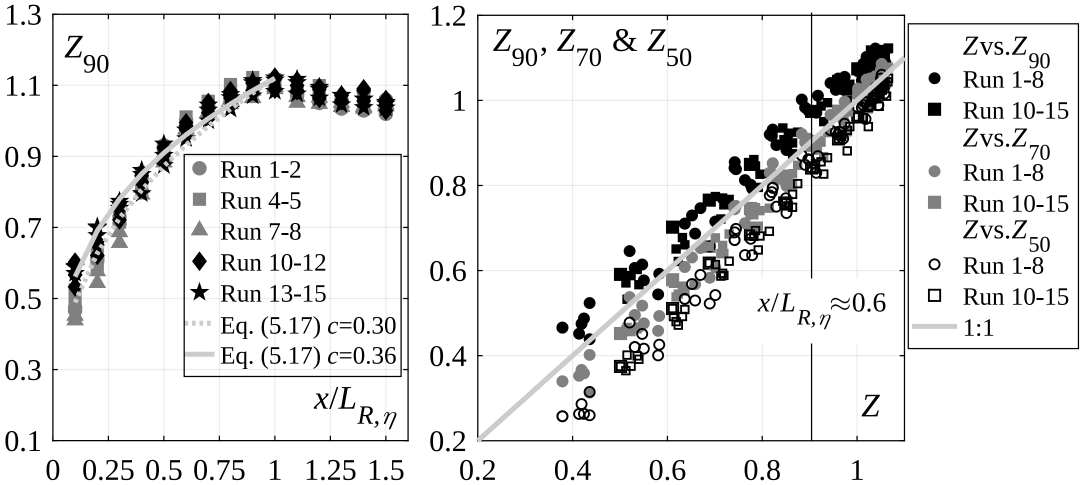

(a) (b)

Figure 5.19 – (a) Streamwise development of the characteristic flow depths Z_{90} against normalized streamwise coordinate $x/L_{R,\eta}$ compared to Eq. (5.17) and (b) relationship between dimensionless flow depths Z recorded with US sensor and characteristic flow depths Z_{50}, Z_{70} and Z_{90}; [Runs 1-8: smooth chute, Runs 10-15: stepped chute].

In Figure 5.19b the dimensionless mean flow depths Z=$(\eta-h_1)/(h_2-h_1)$ recorded with the US sensor within the roller region , i.e. $0.1 \le x/L_{R,\eta} \le 1.0$, are plotted as a function of the characteristic flow depths Z_{90}, Z_{70}=$(Z_{70}-h_1)/(h_2-h_1)$ and Z_{50}=$(Z_{50}-h_1)/(h_2-h_1)$, where Z_{70} is the characteristic flow depth defined up to $z(C$=0.7$)$. One can notice that within $0.1 \le x/L_{R,\eta} < 0.6$, the US sensor readings correspond to a range between$Z_{70} \leq Z \leq Z_{90}$. Further downstream, i.e. $x/L_{R,\eta} \geq 0.6$, this range tend to shift towards $Z_{50} \leq Z \leq Z_{70}$, which may be attributed to the significant reduction of the spray and water ejections. Identical results are obtained downstream of the roller end (not showed herein). These results are in close agreement with studies on classical hydraulic jumps (e.g. Chachereau and Chanson (2011b), Kucukali and Chanson (2008), Murzyn and Chanson (2009b) and Wang et al. (2014)), which observed ranges within $Z_{50} \leq Z \leq Z_{90}$.

The streamwise development of the dimensionless equivalent clear water depth $Z_{cw} = (z_{cw} - h_1)/(h_2 - h_1)$, with z_{cw}=$(1 - C_a) z_{90}$ as the equivalent clear water depth, is plotted on Figure 5.20 against the normalized streamwise coordinate X_J for all experimental runs, and compared with the dimensionless mean pressure P_m development prediction introduced in Chapter 4, i.e. Eq. (4.5). The development of Z_{cw} show a monotonic increase in the streamwise direction, attaining quasi-constant magnitudes in the tailwater. The equivalent clear water depths practically coincide with the measured mean pressures at $X_J \geq 0.5$. This again clearly demonstrates that the detachment of the bottom jet flow is prominent at $X_J \approx 0.5$ and that the mean pressure distribution is essentially "hydrostatic" at the bottom. As expected, stepped chute approach flows induce a slightly higher values of Z_{cw} approximately within $0.08 \leq X_J \leq 0.3$, as compared to those downstream of smooth chutes. However, these differences are practically negligible and the development of Z_{cw} for all experimental runs can be described as (Figure 5.20, R^2=0.99):

$$Z_{cw} = \tanh(3X_J)^{4.4X_J - 0.65} \qquad 0.08 \leq X_J \leq 1.34 \qquad (5.18)$$

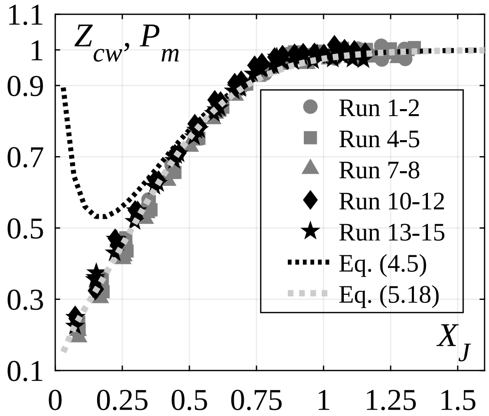

Figure 5.20 – Streamwise development of the dimensionless equivalent clear water depths Z_{cw} along the stilling basin; (- - -) Eqs. (4.5) and (5.18); [Runs 1-8: smooth chute, Runs 10-15: stepped chute].

5.7 Conclusions

The experimental results on bottom pressures, flow depths and length characteristics presented in Chapter 4 are further expanded in this chapter by analyzing the internal flow characteristics of the hydraulic jump collected in the same test runs, mainly focusing on the air concentration, air-phase frequency, velocity and air-water flow depths measurements. The following conclusions are drawn:

- The air-water flow measurements indicate two main flow zones, namely advective diffusive zone along $0.1 \leq x/L_{R,\eta} \leq 0.8$, and air release zone along $x/L_{R,\eta} \geq 0.9$.
- The advective diffusive zone is characterized by a shear layer region in the lower part of the flow, where air concentration profiles exhibit a typical bell shape type profile. The shear layer region linearly spreads across the advective diffusive zone. A recirculation region is observed above, where air concentrations monotonically and rapidly increase to unity. The advective diffusive zone is observed within $0.1 \leq x/L_{R,\eta} \leq 0.8$, irrespective of the approach flow conditions.
- In the air release zone within $0.9 \leq x/L_{R,\eta} \leq 1.0$, the air concentrations monotonically increase from the channel invert due to the intense flow de-aeration. Further downstream, in the tailwater, air is only present in the upper part of the flow.
- The advective diffusion model of Chanson (1995) for classical hydraulic jumps well reproduce the air concentration profiles in the advective diffusive zone. However, the obtained dimensionless turbulent diffusivities ${D_t}^s (V_1 h_1)^{-1}$ and ${D_t}^r (V_1 h_1)^{-1}$ are considerably higher than those reported for classical hydraulic jump with partially developed approach flows.
- Air concentration profiles are mostly independent of the approach flow conditions within $0.1 \leq x/L_{R,\eta} \leq 0.3$. The major differences are in the vicinity of the bottom, where significantly higher air concentration values are found after stepped chutes, as compared to those after smooth chutes. Moreover, smooth chute approach flows show a slightly higher de-aeration rate in the shear layer region. Further downstream, i.e. $x/L_{R,\eta} \geq 0.4$ smooth chute approach flows exhibit significantly higher de-aeration rate, confirming the jump length measurements presented in Chapter 4. The air concentration profiles are practically independent of the approach flow aeration C_1 for smooth chute approach flows ($0.16 \leq C_1 \leq 0.32$) or relative step size s for stepped chute approach flows ($2.70 \leq h_c/s \leq 7.94$).
- 30 ° inclined (chute) approach flows induce significantly higher flow aeration in the lower part of the shear layer region and close to the bottom, i.e. $z < z_{max}$, as compared to classical hydraulic jumps.
- Smooth chute approach flows are characterized by a sharp rise of the bottom air concentration with maximum values of C_b=0.11 at $X_J \approx 0.17$, followed by a gradual decrease

towards zero values at X_J≥0.9. The bottom air concentrations are not influenced by the approach flow aeration C_1 and can be estimated using Eq. (5.7).

- Stepped chute approach flows exhibit higher bottom air concentration values within X_J≤0.4, compared to smooth chute approach flow. The bottom air concentrations are up to three times higher in the vicinity of the toe, i.e. X_J ≈0.08, reaching values up to C_b=0.16. Further downstream, they decrease in a linear manner and coincide with smooth chute approach flow values at X_J≥0.4. The bottom air concentration is not influenced by the step size s and can be estimated using Eqs. (5.7) and (5.8).
- The present experimental results suggest that plain stilling basins with smooth chute approach flows are expected to be exempted from cavitation damage within $0.1 \leq X_J \leq 0.5$ and $0.15 \leq X_J \leq 0.4$ for 5% and 8% bottom air concentration limit to avoid cavitation damage, respectively. In these terms, stepped chute approach flows provide additional air and the plain stilling basins are expected to be protected from cavitation damage within 0≤X_J≤0.4 and 0≤X_J≤0.5 for 5% and 8% bottom air concentration limit, respectively.
- The air entrainment rate at the jump toe and de-aeration rate along the jump, described by depth-averaged air concentration C_a , is independent of the approach flow conditions, and can be estimated using Eq. (5.10).
- The air-phase frequency profiles in the advective diffusive zone exhibit a typical shape with a major peak F_{max} in the shear layer region and a secondary peak F_{sec} in recirculation region. Further downstream, in the air release zone, the profiles tend to transform into monotonically increasing profiles from the channel invert, where F_{max} disappears.
- The streamwise development of the dimensionless elevation of the maximum air-phase frequency Z_{Fmax} shows a slight increase tendency within 0.08 ≤X_J≤0.5, followed by a sharp increase towards the roller end, indicating the detachment of bottom jet flow, in line with bottom pressure measurements presented in Chapter 4.
- The magnitudes of air-phase frequency are mainly affected by stepped chute approach flows.
- Velocity profiles in the advective diffusive zone exhibit a self-similar shape including a high velocity boundary layer flow in the lower part of the flow and flow reversal in the upper part of the flow. The flow reversal is observed within 0.1≤$x/L_{R,\eta}$≤0.8 irrespective of the approach flow conditions. The modified wall jet expressions of Chanson (2010) describe well the velocity profiles in the advective diffusive region for both approach flow conditions.
- In the air release zone, within 0.9≤$x/L_{R,\eta}$≤1.0, the velocity profiles still tend to exhibit a wall jet type profile. Further downstream, towards the tailwater, they transform into an open channel flow velocity distribution.

- The maximum velocities V_{max} decays in an exponential manner and are practically independent of the approach flow conditions. They can be estimated using Eq. (5.13).

- The dimensionless elevations of the maximum velocity Z_{Vmax}, similarly to the development of Z_{Fmax}, show a sharp increase at X_J≈0.5, indicating the detachment of the bottom jet flow. They are practically independent of the approach flow conditions and can be estimated using Eq. (5.14).

- The streamwise development of depth averaged recirculation velocities $V_{rec,a}$ show a slight increase within $0.1 \leq x/L_{R,\eta} \leq 0.2$, followed by a gradual decrease towards the end of the advective diffusive zone, where flow reversal disappears. They can be estimated using Eq. (5.15).

- The characteristic flow depths z_{90} along the jump roller are self-similar in shape following Eq. (5.17). The mean flow depths η recorded with a US sensor corresponds to a range of characteristic flow depths between $z_{70} \leq \eta \leq z_{90}$ for $0.1 \leq x/L_{R,\eta} \leq 0.6$, and $z_{50} \leq \eta \leq z_{70}$ for $x/L_{R,\eta} \geq 0.6$.

- The development equivalent clear-water depth z_{cw} show a monotonic increase in the streamwise direction, reaching quasi-constant values in the tailwater zone. They coincide with the mean pressure heads p_m at X_J≈0.5, showing that the influence of the highly turbulent bottom jet flow is greatly diminished. The streamwise development of dimensionless equivalent clear-water depth Z_{cw} can be estimated using Eq. (5.18).

6 Effect of chute slope on the performance of a plain stilling basin downstream of smooth and stepped chutes

6.1 Overview

This chapter investigates and compares the effect of chute slope φ on the hydraulic behaviour of a plain stilling basin preceded by smooth and stepped chutes. For this, fifteen additional test runs with 50° sloping smooth and stepped chutes were performed. The experimental results are systematically compared to the results for the plain stilling basin preceded by 30° sloping smooth or stepped chutes, presented in Chapters 4 and 5.

The results show that the sequent depth ratio can be estimated with the momentum principle by using the clear water parameters at the chute end, irrespective of the chute slope (i.e. φ=30° or 50°). The normalized hydraulic jump lengths, deduced with criteria established in Chapter 4, are found to be independent of the chute slope. These results further strengthen the conclusions made in Chapter 4, that hydraulic jumps initiated after stepped chutes have longer dimensionless flow length L_J/h_2 as compared to smooth chute approach flows. Steeper chute slopes increase mean pressure coefficients within the flow deflection zone due to the stronger flow curvature. The pronounced extreme and fluctuating pressure coefficients observed with 30° sloping stepped chute approach flows magnifies with increasing chute slope. Air water flow properties are found to be mostly independent of the chute slope.

6.2 Test program and approach flow conditions

Table 6.1 shows the test program conducted for a plain stilling basin downstream of 30° and 50° sloping smooth and stepped chutes. Detailed information on the approach flow conditions for 30° sloping smooth and stepped chute configurations can be found in Chapter 4. In the following subchapters, approach flow conditions for 50° sloping smooth and stepped chutes will be detailed. Similarly to the 30° chutes, the equivalent clear water parameters were derived from the air-water flow measurements conducted at the most downstream measured section at the 50° sloping chute end (i.e., w=0.26 m for 50° smooth chutes and step edge 3 or w=0.235 m for 50° stepped chutes, Figure 3.2) and used for the hydraulic jump analysis.

Table 6.1 – Test program for plain stilling basin preceded by 30° and 50° sloping chutes. SM=smooth chute; R=smooth chute roughened with grid; PA=smooth chute roughened with grid and pre-aeration; ST=stepped chute; *s*=step size.

Test run	φ	Chute Configuration	q [m2/s]	h_c/s [-]	C_1 [-]	h_1 [m]	V_1 [m/s]	α [-]	F_1 [-]	$R_1 \times 10^5$ [-]	W_1 [-]
1	30	R+PA	0.198	/	0.32	0.031	6.47	1.09	11.8	1.98	133
2	30	R+PA	0.277	/	0.32	0.038	7.22	1.08	11.8	2.77	166
3	30	R+PA	0.358	/	0.32	0.046	7.79	1.09	11.6	3.58	196
4	30	R	0.198	/	0.25	0.032	6.21	1.09	11.1	1.98	130
5	30	R	0.277	/	0.26	0.04	6.86	1.08	10.9	2.77	162
6	30	R	0.356	/	0.26	0.047	7.51	1.08	11.0	3.56	192
7	30	SM	0.198	/	0.16	0.029	6.95	1.08	13.1	1.98	137
8	30	SM	0.278	/	0.15	0.036	7.68	1.08	12.9	2.78	171
9	30	SM	0.356	/	0.15	0.042	8.38	1.08	13.0	3.56	202
		min	0.198	/	0.15	0.029	6.21	1.08	10.9	1.98	130
		max	0.358	/	0.32	0.047	8.38	1.09	13.1	3.58	202
10	30	ST *s*=0.06 m	0.204	2.70	0.42	0.048	4.24	1.18	6.2	2.04	109
11	30	ST *s*=0.06 m	0.284	3.36	0.42	0.058	4.91	1.18	6.5	2.84	138
12	30	ST *s*=0.06 m	0.362	3.95	0.41	0.068	5.35	1.18	6.6	3.62	163
13	30	ST *s*=0.03 m	0.204	5.40	0.41	0.047	4.34	1.19	6.4	2.04	110
14	30	ST *s*=0.03 m	0.282	6.70	0.41	0.056	5.07	1.19	6.9	2.82	140
15	30	ST *s*=0.03 m	0.364	7.94	0.41	0.066	5.54	1.18	6.9	3.64	166
		min	0.204	2.70	0.41	0.047	4.24	1.18	6.2	2.04	109
		max	0.364	7.94	0.42	0.068	5.54	1.19	6.9	3.64	166
16	50	R+PA	0.198	/	0.37	0.028	7.16	1.08	13.8	1.98	140
17	50	R+PA	0.280	/	0.36	0.036	7.88	1.07	13.4	2.80	174
18	50	R+PA	0.358	/	0.35	0.043	8.38	1.07	13.0	3.58	203
19	50	R	0.199	/	0.28	0.029	6.88	1.08	12.9	1.99	137
20	50	R	0.278	/	0.29	0.038	7.41	1.07	12.2	2.78	168
21	50	R	0.358	/	0.28	0.044	8.07	1.08	12.2	3.58	199
22	50	SM	0.199	/	0.16	0.026	7.61	1.08	15.0	1.99	144
23	50	SM	0.279	/	0.16	0.033	8.38	1.09	14.7	2.79	179
24	50	SM	0.356	/	0.15	0.040	8.99	1.08	14.4	3.56	210
		min	0.198	/	0.15	0.026	6.88	1.07	12.2	1.98	137
		max	0.358	/	0.37	0.044	8.99	1.09	15.0	3.58	210
25	50	ST *s*=0.06 m	0.205	2.71	0.55	0.041	4.95	1.18	7.8	2.05	118
26	50	ST *s*=0.06 m	0.284	3.36	0.53	0.051	5.52	1.19	7.8	2.84	147
27	50	ST *s*=0.06 m	0.364	3.97	0.50	0.061	5.96	1.19	7.7	3.64	173
28	50	ST *s*=0.03 m	0.205	5.41	0.50	0.040	5.10	1.18	8.1	2.05	120
29	50	ST *s*=0.03 m	0.284	6.73	0.48	0.050	5.71	1.19	8.2	2.84	149
30	50	ST *s*=0.03 m	0.364	7.94	0.46	0.060	6.08	1.19	7.9	3.64	174
		min	0.205	2.71	0.46	0.040	4.95	1.18	7.7	2.05	118
		max	0.364	7.94	0.55	0.061	6.08	1.19	8.2	3.64	174

6.2.1 50° sloping smooth chute

The 50° sloping *smooth chute* test series was performed for unit discharge ranging between 0.198 $m^2/s \leq q \leq 0.358$ m^2/s. The depth-averaged air concentration C_1 at the chute end was systematically varied between $0.15 \leq C_1 \leq 0.37$ (Table 6.1). Figure 6.1 shows the flow features for three characteristic C_1, whose air concentration profiles measured at the inflow section are shown in Figure 6.2a. The minimal value of $0.15 \leq C_1 \leq 0.16$ (Runs 22, 23 and 24, Table 6.1) corresponds to a smooth chute configuration without a grid or pre-aeration in the jet-box, for which black water flow is observed at the chute end (Figure 6.1a). Similarly to the 30° smooth chute configuration (Runs 7, 8 and 9, Figure 4.3a, Table 6.1), the air concentration profiles at the inflow section show almost no presence of air below $y/y_{90}<0.6$ indicating that fully developed air entrainment did not occur down the chute (Figure 6.2a). Roughening the smooth chute bottom (by placing the grid) results in the inception of air entrainment upstream of the chute end (Figure 6.1b) with values of $0.28 \leq C_1 \leq 0.29$ (Runs 19, 20 and 21, Table 6.1). The inception point is observed to be more upstream, as compared to the 30° sloping chute runs roughened with grid (Runs 4, 5 and 6, Table 6.1). The maximum values of $0.35 \leq C_1 \leq 0.37$ (Runs 16, 17 and 18, Table 6.1) were achieved for roughened smooth chute bottom with pre-aeration in the jet-box (Figure 6.1c).

The air concentration profiles measured at the inflow section exhibit a typical S-shape profile and compare favorably with the advective diffusion model of Chanson and Toombes (2002) (Figure 6.2a). The dimensionless velocity V/V_{90} profiles measured at the inflow section are shown in Figure 6.2b for all 50° sloping smooth chute test runs. They tend to follow the power law equation, i.e. Eq. (2.25), with N=12.9 and a coefficient of determination of R^2=0.92. The velocity profiles are found to be similar with those measured for the 30° sloping smooth chute approach flows (Figure 4.4b), as indicated by the similar value of the exponent N (N=12.6 in case of 30° sloping smooth chutes).

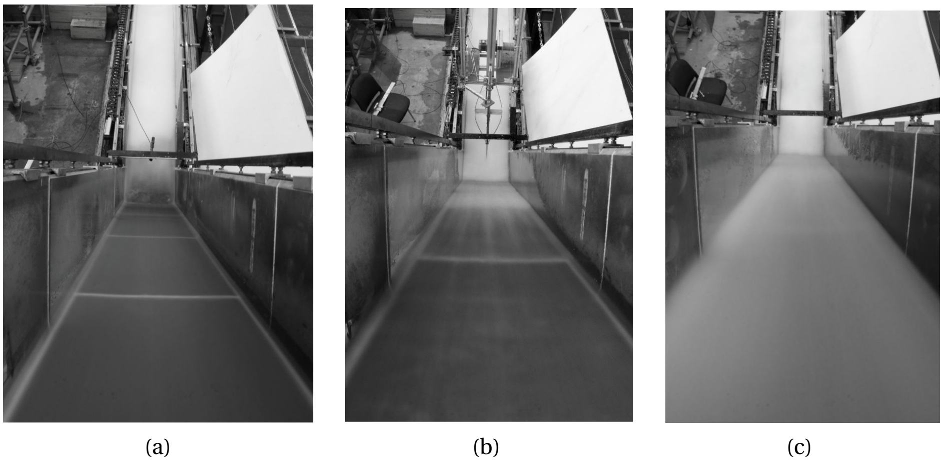
(a) (b) (c)

Figure 6.1 – 50° sloping smooth chute flow characteristics seen in flow direction for: (a) Run 23, (b) Run 20, and (c) Run 17.

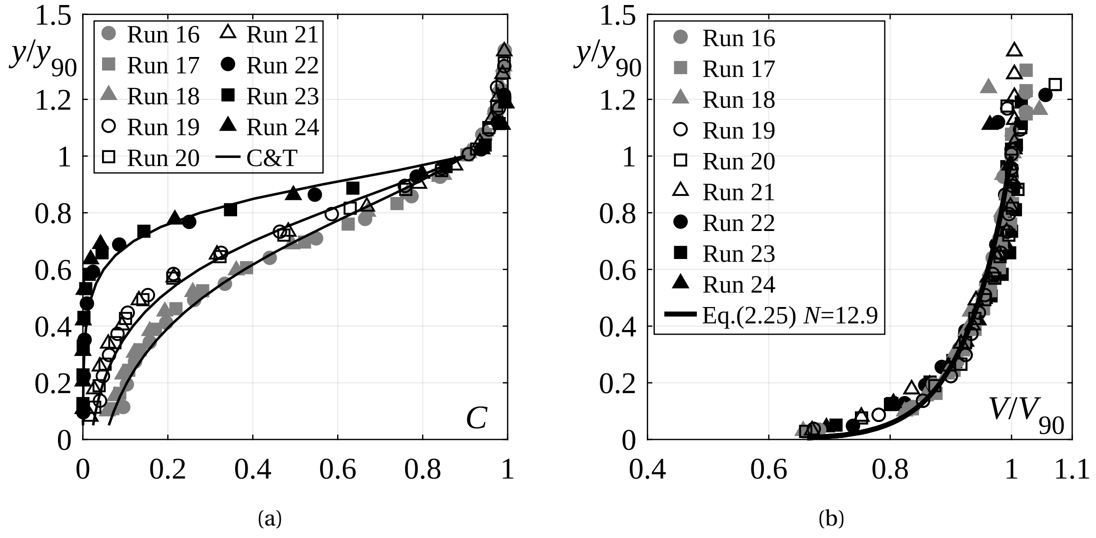

Figure 6.2 – (a) Air concentration profiles at the inflow section for 50° smooth chute test runs (Runs 16-24, Table 6.1) and comparison with (——) advective diffusion model of Chanson and Toombes (2002) with C_1=0.16, 0.29 and 0.36, and (b) Dimensionless velocity V/V_{90} profiles at the inflow section for 50° smooth chute test runs (Runs 16-24, Table 6.1) and comparison with (——) Eq. (2.25).

6.2.2 50° sloping stepped chute

The 50° sloping *stepped chute* test series included skimming flow conditions for a unit discharge range of 0.205 $m^2/s \leq q \leq 0.364\ m^2/s$ (Table 6.1). Two step heights were tested, namely s=0.03 and 0.06 m. The depth-averaged air-concentration C_1 values at the inflow section varied between $0.46 \leq C_1 \leq 0.55$. The air concentration profiles measured at the inflow section for all 50° stepped chute test runs are presented in Figure 6.3a, whereas a typical downstream view of the 50° stepped chute flow is shown in Figure 6.4 (Run 26, Table 6.1).

Although air concentration profiles measured at the various step edges close to the chute end (i.e. step edge 3,4 and 5, Figure 3.2) are found to be quasi-similar (see Appendix B), the measured range of C_1 and the shape of air concentration profiles for different test runs at the inflow section (Figure 6.3a) suggest that the quasi-uniform flow conditions were not attained at the stepped chute end for all test runs. This is shown in Figure 6.5, where measured values of C_1 are compared to the quasi-uniform mean air concentration values C_u of Takahashi and Ohtsu (2012) (i.e. Eq. (2.11)) for the same chute slope and range of relative critical depths, i.e. $2.71 \leq h_c/s \leq 7.94$. For lower relative critical depths, i.e. h_c/s=2.71 and 3.4 (Runs 25 and 26, Table 6.1), the flow conditions at the chute end were practically quasi-uniform with $C_1/C_u \approx 0.95$ (Figure 6.5). On the other hand, for higher relative critical depths, i.e. for $3.97 \leq h_c/s \leq 7.94$ (Runs 27-30), gradually varied flow conditions were attained at the stepped chute end.

The air concentration profiles at the inflow section are further compared with the advective diffusion model of Chanson and Toombes (2002) in Figure 6.3a and show overall good agreement, with overestimation in the mid part and underestimation in the lower part of the profile. The dimensionless velocity V/V_{90} profiles at the 50° stepped chute inflow section (Figure 6.3b) tend to follow the power law equation, i.e. Eq. (2.25) with $N = 4.9$ resulting in R^2=0.92. As expected, a lower value of N was obtained as compared to 30° sloping stepped chutes (i.e. $N = 5.5$, Figure 4.4b).

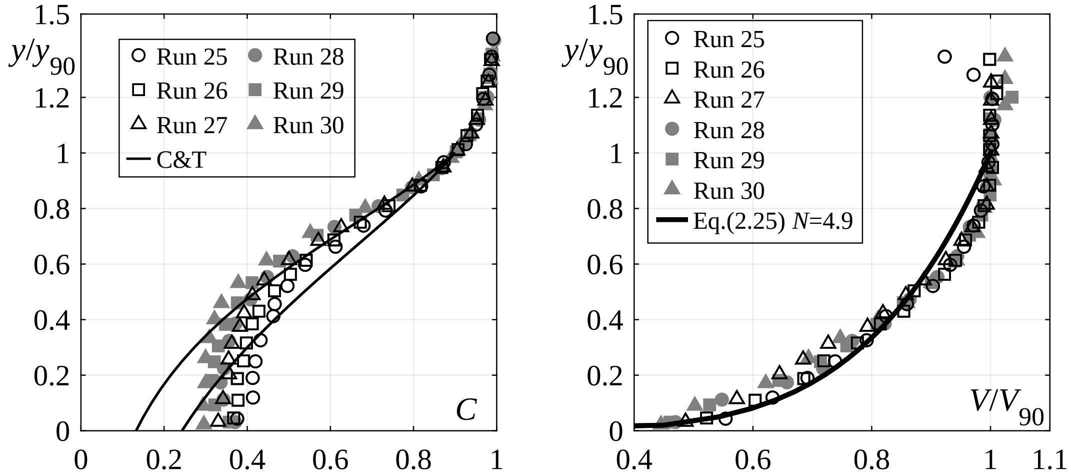

(a)

(b)

Figure 6.3 – (a) Air concentration profiles at the inflow section for 50° stepped chute test runs and comparison with (——) advective diffusion model of Chanson and Toombes (2002) with C_1=0.55 and 0.46, and (b) Dimensionless velocity V/V_{90} profiles at the inflow section for 50° stepped chute test runs and comparison with (——) Eq. (2.25).

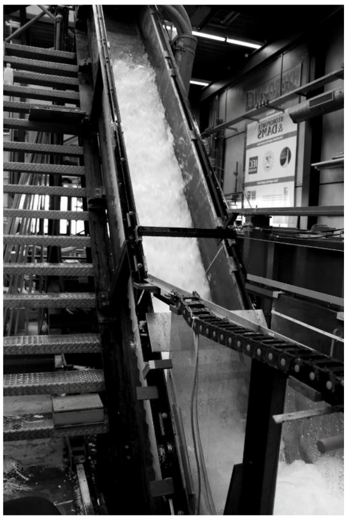

Figure 6.4 – 50° stepped chute flow characteristics seen from downstream for Run 26 (Table 6.1).

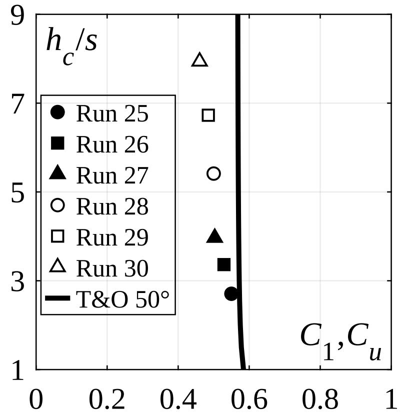

Figure 6.5 – Comparison between measured mean air concentration values C_1 at 50° stepped chute inflow section and quasi-uniform values C_u of Takahashi and Ohtsu (2012). Note: T&O stands for Takahashi and Ohtsu (2012).

6.3 Free surface characteristics

6.3.1 Mean flow depths

A typical streamwise development of the mean (time-averaged) flow depth η (derived from US measurements) along the stilling basin for 50° sloping smooth (Run 22) and stepped (Run 25) chute approach flows are shown in Figure 6.6, and compared to the mean flow depth development for 30° sloping smooth (Run 7) and stepped (Run 10) approach flows for similar unit discharge q, step size s and smooth chute approach flow aeration C_1. The mean flow depths increase in streamwise direction reaching a maximum value in the boiling zone of the flow, herein defined as the roller length $L_{R,\eta}$ (Figure 6.6). Downstream of the roller end, i.e. $x > L_{R,\eta}$, the flow depths decrease reaching quasi-constant tailwater depth h_2. As expected, the higher approach flow Froude numbers F_1 at the 50° smooth and stepped chute end (as compared to 30° sloping chutes) results in higher mean flow depths η and longer jump rollers $L_{R,\eta}$ for quasi-similar unit discharge q .

In Figure 6.7 the measured sequent depth ratio h_2/h_1 is plotted against F_1, including the values for 30° chutes. They are compared to the solution of momentum conservation equation for classical hydraulic jumps, i.e. Eq.(2.38), showing a good agreement. Accordingly, for a given F_1, the sequent depth ratio is practically independent of the approach flow conditions or chute slope φ. These results further strengthen the conclusions made in Chapter 4, that using equivalent clear water parameters at the chute end leads to accurate prediction of the sequent depth ratio using classical momentum principle. Furthermore, as mentioned in Chapter 4, these results indicate that Eq. (2.38) is applicable even if the flow enters at a significant angle to the horizontal, which is not physically sound as Eq. (2.38) was derived for horizontal approach flows. Nevertheless, these results are in line with observations of Peterka (1958) for smooth chute approach flows. The tailwater depth data is reported in Table A.1.

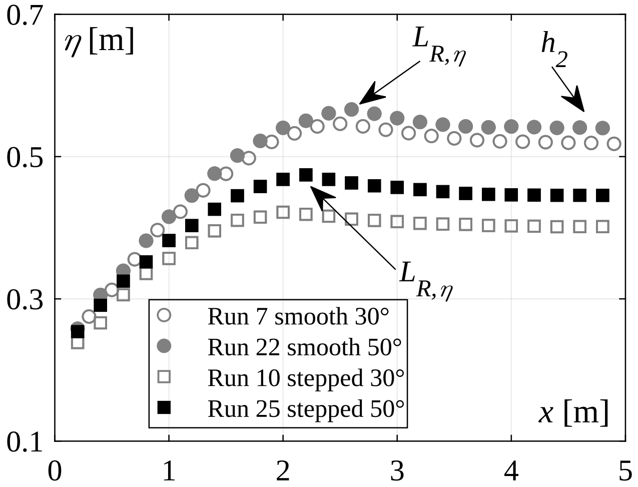

Figure 6.6 – Streamwise mean flow depths η along the stilling basin for Runs 7, 10, 22 and 25 (Table 6.1). $L_{R,\eta}$=roller length based on flow depth measurements; h_2=tailwater depth; x=streamwise coordinate starting at the intersection of chute (pseudo) bottom and stilling basin invert.

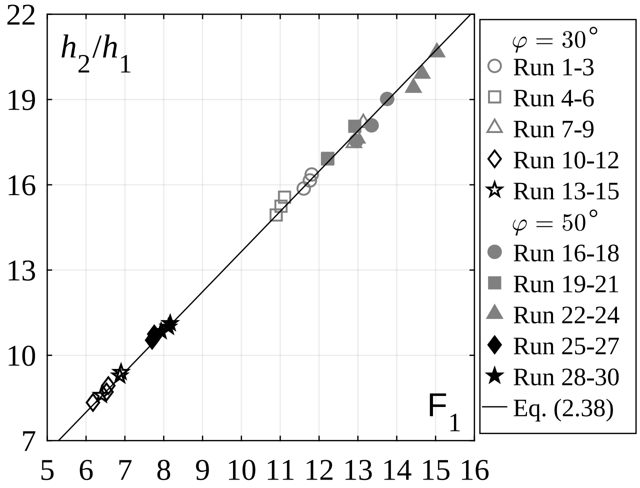

Figure 6.7 – Sequent depth ratio h_2/h_1 as a function of approach Froude number F_1; (——) Eq. (2.38); [Runs 1-9: 30° smooth chute, Runs 10-15: 30° stepped chute, Runs 16-24: 50° smooth chute, Runs 25-30: 50° stepped chute].

The dimensionless mean flow depths $Z = (\eta - h_1)/(h_2 - h_1)$ over the jump roller for 50° smooth and stepped chute approach flows (full symbols) are shown in Figures 6.8a and 6.8b, respectively, and compared to dimensionless flow depth data obtained with 30° smooth and stepped chute (open symbols) approach flows (Figure 4.8). It can be seen that no major effect of the chute slope φ on the development of the mean flow depths Z occur. Similarly to the 30° chutes, the dimensionless mean flow depths for 50° chutes are found to be higher in magnitudes after stepped chutes within the first half of the roller, i.e. $x/L_{R,\eta}\leq 0.5$, as compared to smooth chutes, which is attributed to the relatively higher approach flow depth after stepped chutes. As such, the mean flow depths over the jump roller can be described with the self-similar function introduced in the Chapter 4 (i.e. Eq. (4.1)):

$$Z = \frac{\eta - h_1}{h_2 - h_1} = a\left(\frac{x}{L_{R,\eta}}\right)^b$$

with coefficients a=1.07 and b=0.39 for smooth chute approach flows and a=1.07 and b=0.32 for stepped chute approach flows, irrespective of the chute slope.

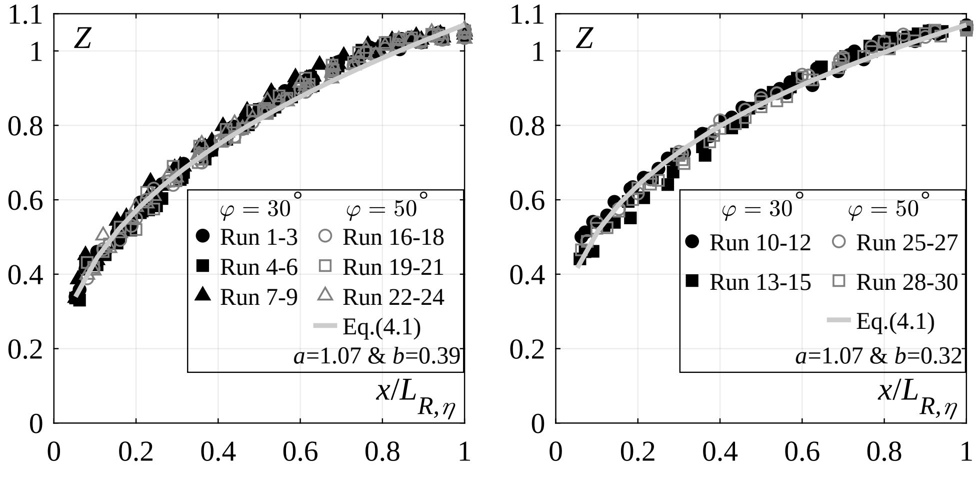

(a) (b)

Figure 6.8 – Dimensionless flow depths Z along the jump roller for 30° and 50° sloping: (a) smooth and (b) stepped chute approach flows; (——) Eq. (4.1); [Runs 1-9: 30° smooth chute, Runs 10-15: 30° stepped chute, Runs 16-24: 50° smooth chute, Runs 25-30: 50° stepped chute].

6.3.2 Roller length

The dimensionless roller lengths L_R/h_2 for 50° (black symbols) smooth (Runs 16-24) and stepped (Runs 25-30) chute approach flows, obtained from flow depths measurements $L_{R,\eta}$ and visual observations $L_{R,D}$ (Figure 3.15), are plotted against the F_1 on Figure 6.9a and compared to the dimensionless roller lengths obtained with 30° (gray symbols) smooth (Runs 1-9) and stepped (Runs 10-15) chute approach flows. One can notice that the dimensionless roller lengths $L_{R,\eta}/h_2$ (full symbols) are practically independent of the approach flow conditions or chute slope with a typical values of $L_{R,\eta} \approx 5.0 h_2$. Similarly to the 30° chute test series, the visually observed roller lengths (open symbols) are consistently shorter, with typical value of the $L_{R,\eta} \approx 4.6 h_2$.

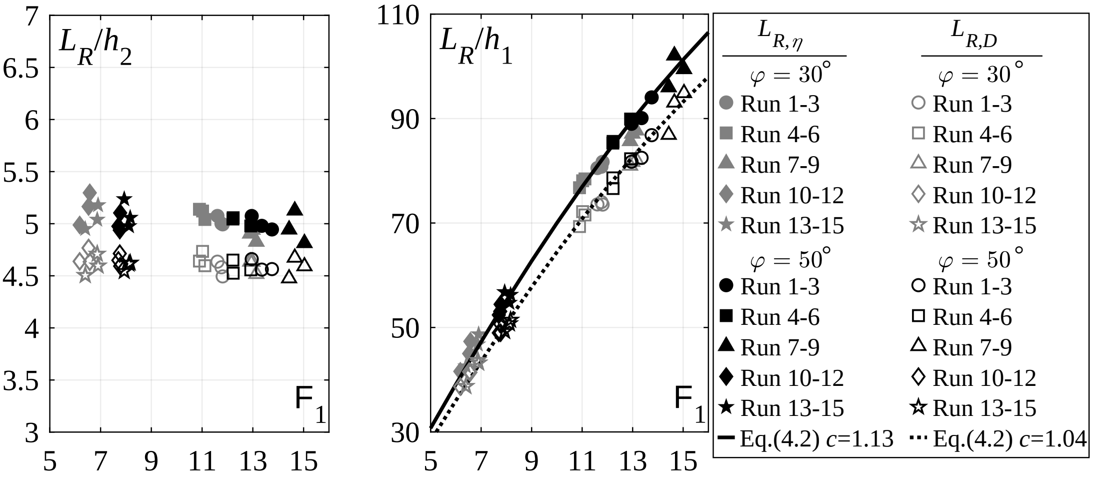

(a) (b)

Figure 6.9 – Roller lengths obtained from measurements $L_{R,\eta}$ and visual observation $L_{R,D}$ plotted against F_1 in dimensionless form as: (a) L_R/h_1 and (b) L_R/h_2; (——) Eq. (4.2); [Runs 1-9: 30° smooth chute, Runs 10-15: 30° stepped chute, Runs 16-24: 50° smooth chute, Runs 25-30: 50° stepped chute].

In Figure 6.9b the roller lengths are plotted in dimensionless forms as L_R/h_1 and compared with Eq. (4.2), showing an excellent agreement. The resulting coefficient of determination for measured $L_{R,\eta}$ and visually observed $L_{R,D}$ roller length are R^2=0.92 and R^2=0.99, respectively. The roller length data are reported in Table A.1.

6.3.3 Flow depth fluctuations and jump length

A typical streamwise development of flow depth fluctuations η' (characterized by standard deviation of US readings) along the stilling basin for 50° sloping smooth (Run 22) and stepped (Run 25) approach flows are shown in Figure 6.10, and compared to the flow depth fluctuation development with 30° sloping smooth (Run 7) and stepped (Run 10) approach flows for similar unit discharge q, step size s and smooth chute approach flow aeration C_1. Similarly to the 30° chute, the surface fluctuations along the hydraulic jump for 50° chute show a monotonic decrease in streamwise direction. As expected, the higher approach F_1 at the 50° chute end results in higher flow depths fluctuation magnitudes.

The hydraulic jump length with respect to the surface fluctuations $L_{J,\eta'}$ was deduced using the criteria introduced in Chapter 4, namely as a distance from the jump toe to the section where the surface fluctuations η' are 1.1 times those measured in the tailwater zone. The resulting dimensionless jump lengths $L_{J,\eta'}/h_2$ downstream of 50° (black symbols) smooth and stepped chutes are plotted in Figure 6.11 against F_1, and compared with dimensionless jump length values obtained downstream of 30° (gray symbols) smooth and stepped chutes and jump length prediction of Peterka (1958). The jump lengths after 50° smooth chutes are

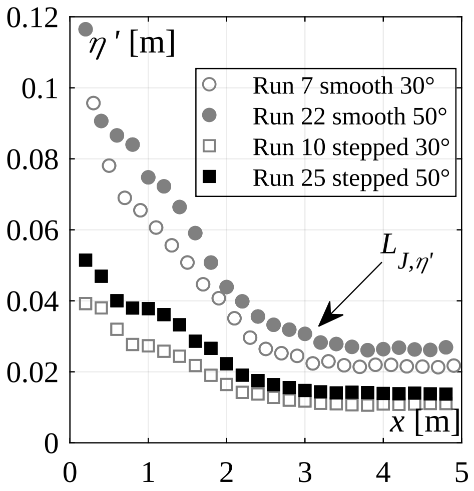

Figure 6.10 – Streamwise flow depth fluctuations η' along the stilling basin for Runs 7, 10, 22 and 25 (Table 6.1).

between 5.50≤ $L_{J,\eta'}/h_2$ ≤6.1 with an overall average value of L_J=5.78h_2, in agreement with the recommendations of Peterka (1958). The hydraulic jumps formed after 50° stepped chutes consistently require an increased flow length x/h_2, namely 6.53≤ $L_{J,\eta'}/h_2$ ≤6.85 with an overall average value of $L_{J,\eta'}$=6.68h_2. One can notice that the chute slope has no major effect on the dimensionless jump lengths $L_{J,\eta'}/h_2$. The detailed jump length results are reported in Appendix A.1.

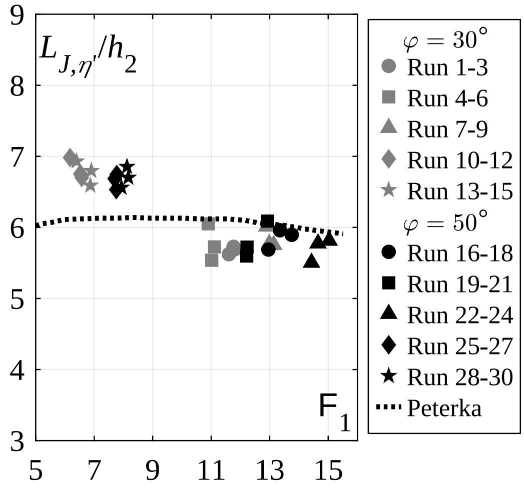

Figure 6.11 – Dimensionless jump lengths $L_{J,\eta'}$ obtained from flow depth fluctuations η' as a function of inflow Froude number F_1, compared to jump length prediction of Peterka (1958); [Runs 1-9: 30° smooth chute, Runs 10-15: 30° stepped chute, Runs 16-24: 50° smooth chute, Runs 25-30: 50° stepped chute].

Figure 6.12a shows the streamwise development of surface fluctuation coefficient $C_H{}' = \eta'/H_k$ ($H_K = \alpha V_1{}^2/(2g)$), plotted against the normalized streamwise coordinate $x/L_{J,\eta'}$ for all 50°

chute test runs. Similarly to the $C_H{}'$ development for 30° chutes (Figure 4.10b), the maximum fluctuation coefficients are observed in the vicinity of the jump toe, caused by the intense splashing of the flow. Further downstream the surface fluctuations coefficients tend to rapidly reduce, attaining quasi-constant values of $C_H{}' \approx 0.01$ in the tailwater zone. No major effect of approach flow conditions on the streamwise development of $C_H{}'$ occurs. In Figure 6.12b the experimental data for 30° chutes was added, showing that no considerable effect of the chute slope φ on the streamwise development of $C_H{}'$ occurs. These results thus suggest that the surface fluctuations are mainly governed by the approach flow kinetic energy H_K. As such the streamwise development of $C_H{}'$ for 50° chutes can be described using the same equations used for 30° sloping chute approach flows, i.e. Eqs. (4.3) and (4.4):

$$C_H{}' = -0.059\frac{x}{L_{J,\eta'}} + 0.042 \qquad 30° \le \varphi \le 50° \qquad 0 < \frac{x}{L_{J,\eta'}} \le 0.25$$

$$C_H{}' = 1.009 - \tanh\left(2.8\frac{x}{L_{J,\eta'}}\right)^{0.26\frac{x}{L_{J,\eta'}}-0.028} \qquad 30° \le \varphi \le 50° \qquad \frac{x}{L_{J,\eta'}} > 0.25$$

resulting in R^2=0.57 and 0.97, respectively.

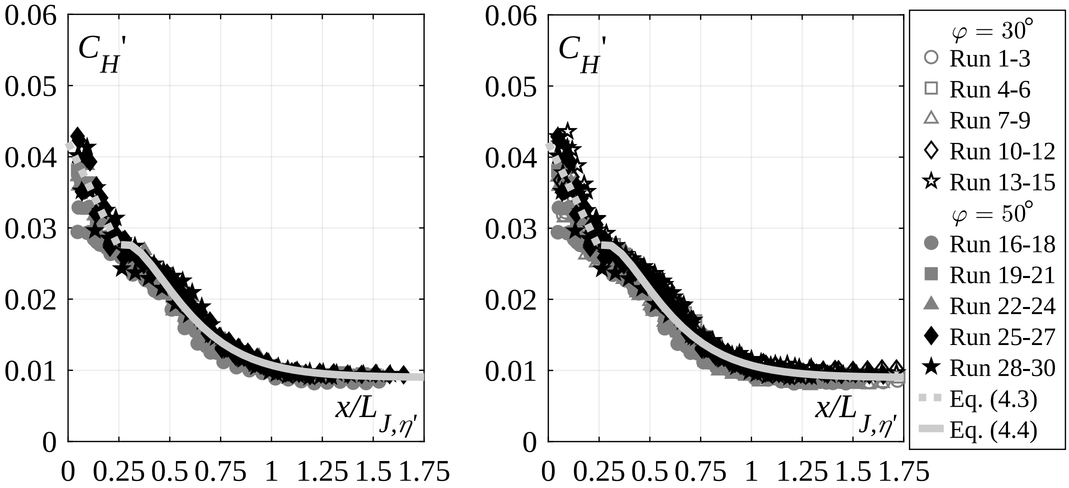

(a) (b)

Figure 6.12 – Streamwise development of flow depth fluctuation coefficient $C_H{}'$ versus normalized streamwise coordinate $x/L_{J,\eta'}$ for: (a) 50° smooth and stepped chute test runs (b) 30° and 50° smooth and stepped chute test runs; (– – –) Eq. (4.3), (——) Eq. (4.4); [Runs 1-9: 30° smooth chute, Runs 10-15: 30° stepped chute, Runs 16-24: 50° smooth chute, Runs 25-30: 50° stepped chute].

6.4 Bottom pressure characteristics

6.4.1 Jump length

Based on the simultaneous pressure measurements conducted at 16 points (Figure 3.2, Table 3.1), the relevant dynamic pressure parameters, used for assessment of hydrodynamic loads acting on the stilling basin invert (introduced in Chapter 2), were derived. A typical streamwise bottom pressure development for 50° sloping chutes are shown in Figure 6.13 (Run 22, smooth chute).

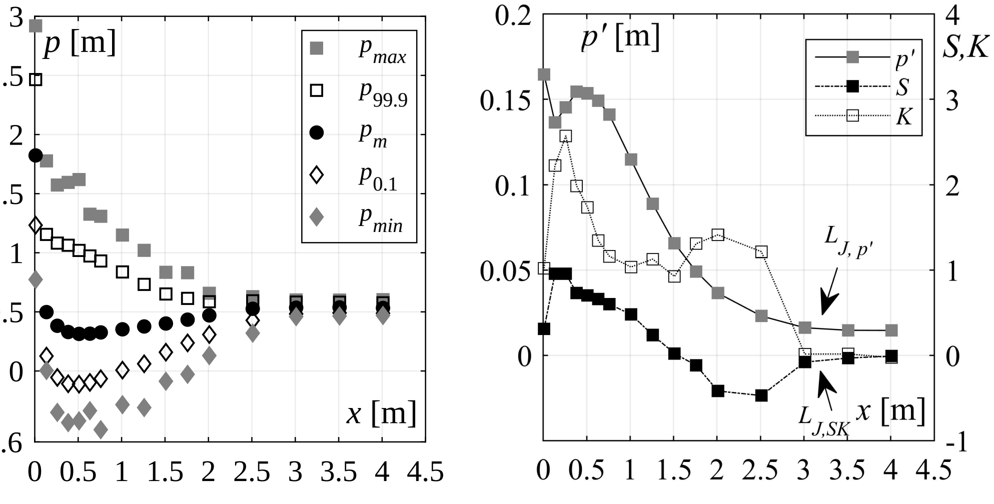

(a) (b)

Figure 6.13 – Streamwise pressure distribution (Run 22, smooth chutes, Table 6.1) of: (a) extreme maximum p_{max}, 99.9% probability $p_{99.9}$, mean p_m, 0.1% probability $p_{0.1}$, and extreme minimum pressure p_{min}, and (b) fluctuating pressure p', skewness S and kurtosis K.

Based on criteria established in Chapter 4, the hydraulic jump lengths L_J for 50° chutes with respect to bottom pressures $L_{J,p'}$ and $L_{J,SK}$ were derived, namely as: (1) $L_{J,p'}$ distance from the jump toe to the section where pressure fluctuations p' are 1.1 times those measured in the tailwater zone, and (2) $L_{J,SK}$ as a distance from the jump toe to the section where the pressure distribution followed a normal probability density function with skewness S and excess kurtosis K tending to zero (e.g. Figure 6.13b). The jump length results are reported in Table A.1. The obtained jump lengths downstream of 50° smooth (gray full symbols) and stepped chutes (black full symbols) are plotted as L_J/h_2 in Figure 6.14 against F_1, along with jump lengths obtained with flow depth measurements $L_{J,\eta'}/h_2$ (Figure 6.11) and jump lengths downstream of 30° smooth (gray open symbols) and stepped (black open symbols) chutes.

The pressure measurements after 50° chutes indicate similar range of dimensionless jump lengths as the flow depth measurements. The overall average values for 50° smooth and stepped chutes are L_J/h_2=5.77h_2 and L_J/h_2=6.73h_2, respectively. Moreover, comparing the dimensionless jump lengths downstream of 30° and 50° chutes (Figure 6.14), it is readily noticeable that no major effect of chute slope φ on the dimensionless jump length occurs. These results undoubtedly show that hydraulic jumps initiated after stepped chutes require an increased length x/h_2, as compared to those after smooth chutes.

In Figure 6.15a to 6.15h, the streamwise development of bottom pressure coefficients $C_P{}'$, $C_P{}^{max}$, $C_P{}^{99.9}$, $C_P{}^{min}$, $C_P{}^{0.1}$, S and K (introduced in Chapter 2) downstream of 50° smooth and stepped chutes are plotted against the normalized streamwise coordinate $X_J = x/L_J$. An overall average value of hydraulic jump length L_J is used, namely L_J/h_2=5.77h_2 and L_J/h_2=6.73h_2 for smooth and stepped chute approach flows, respectively. In following sub-chapters, the effect of chute slope on the streamwise development of each pressure coefficient will be detailed.

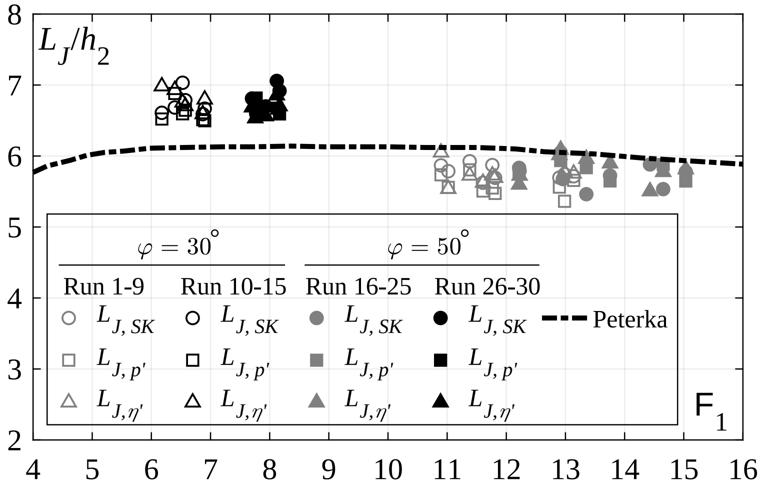

Figure 6.14 – Dimensionless jump lengths L_J/h_2 downstream of 30° and 50° smooth and stepped chutes from pressure ($L_{J,SK}$ and $L_{J,p'}$) and flow depth ($L_{J,\eta'}$) measurements against the inflow Froude number F_1; (– – –) Peterka (1958); [Runs 1-9: 30° smooth chute, Runs 10-15: 30° stepped chute, Runs 16-24: 50° smooth chute, Runs 25-30: 50° stepped chute].

6.4.2 Streamwise distribution of mean pressure

The streamwise development of dimensionless mean pressure P_m downstream of the 50° sloping chutes, similarly to the 30° sloping chutes (Figure 4.13a), indicate the following flow zones (Figure 6.15a):

I. *deflection zone* along $0 \leq X_J \leq 0.18$,

II. *transition zone* along $0.18 < X_J < 1$,

III. *tailwater zone* along $X_J \geq 1$.

The development of mean pressure coefficients P_m for 30° and 50° smooth and stepped chutes are compared in Figure 6.16a and 6.16b, respectively.

Comparing the mean pressure development for *smooth chute* approach flows (Figure 6.16a), a clear effect of chute slope φ within the flow *deflection zone* is visible. At the flow deflection point, i.e. at the jump toe $X_J \approx 0$, up to 60% higher dimensionless mean pressures P_m are observed downstream of 50° chute, as compared to those downstream of 30° chute. Further downstream, within $0 \leq X_J \leq 0.18$, the mean pressures with 50° chute decreases in a similar manner as with 30° chute, however, with slightly higher magnitudes caused by stronger flow curvature due to the more abrupt slope change. The local minimum after 50° chute is observed at $X_J \approx 0.18$, where flow curvature greatly reduce, and beyond which the dimensionless mean pressure magnitudes coincide with those of 30° sloping chute along the remaining part of the stilling basin, i.e. in *transition* and *tailwater zone*. The influence reach of the flow curvature is thus somewhat longer after 50° chute, i.e. $0 \leq X_J \leq 0.18$, as compared to those after 30° chute, i.e. $0 \leq X_J \leq 0.15$.

The effect of chute slope within the *flow deflection zone* is even more pronounced downstream of *stepped chute* approach flows (Figure 6.16b). The streamwise position of the maximum mean pressures downstream of 50° stepped chute is observed further downstream, i.e. at $X_J \approx 0.04$, as compared to 30° stepped chute approach flow at $X_J \approx 0$. The maximum P_m magnitudes downstream of 50° chute are up to 60% higher than maximum P_m magnitudes observed downstream of 30° sloping chute or two times higher for the similar streamwise position, i.e. $X_J \approx 0.04$.

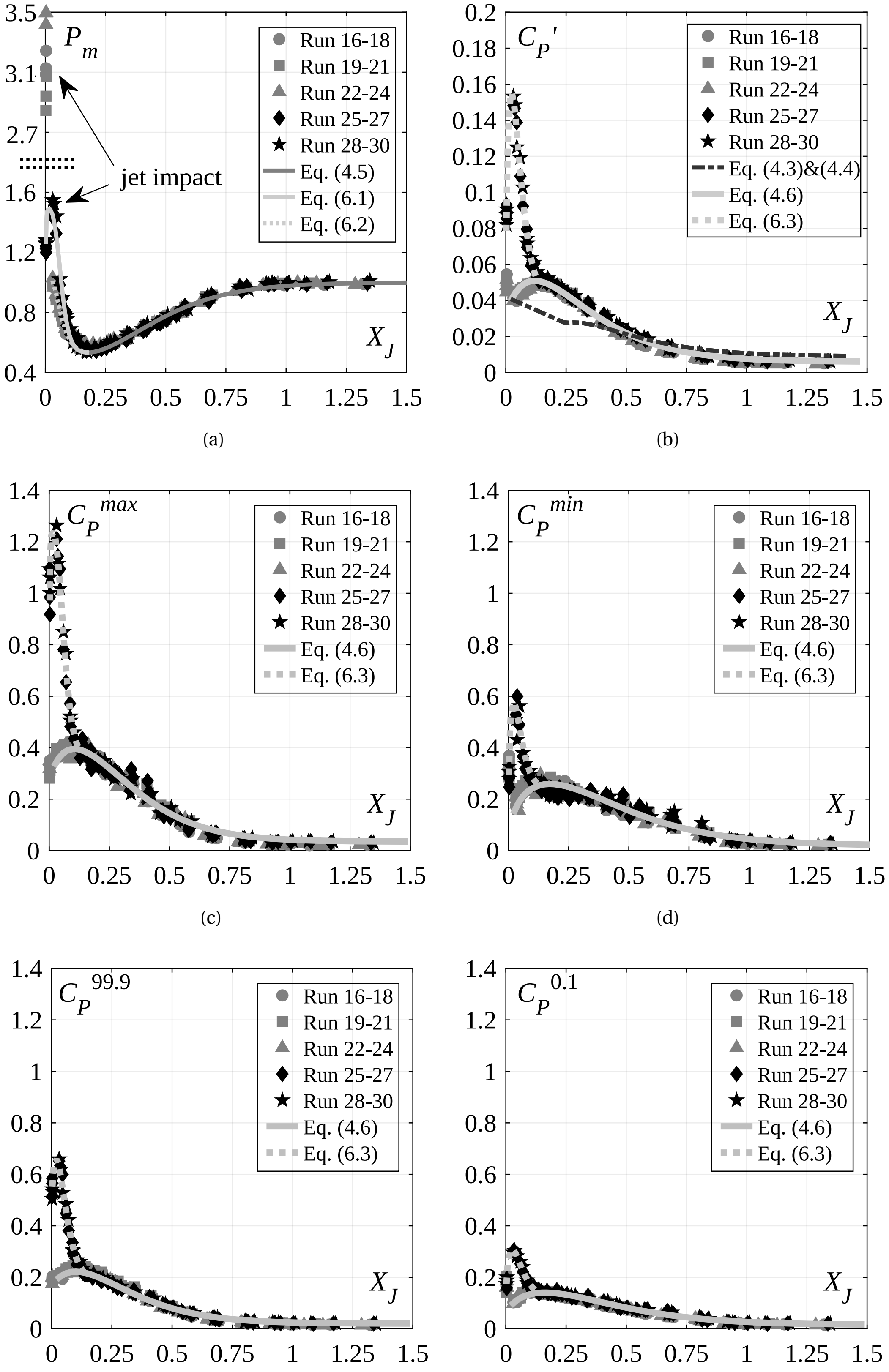
P_m
jet impact
C_P'
C_P^max
C_P^min
C_P^99.9
C_P^0.1
X_J
Run 16-18
Run 19-21
Run 22-24
Run 25-27
Run 28-30
Eq. (4.5)
Eq. (6.1)
Eq. (6.2)
Eq. (4.3)&(4.4)
Eq. (4.6)
Eq. (6.3)
0
0.25
0.5
0.75
1
1.25
1.5

(a) (b)

(c) (d)

(e) (f)

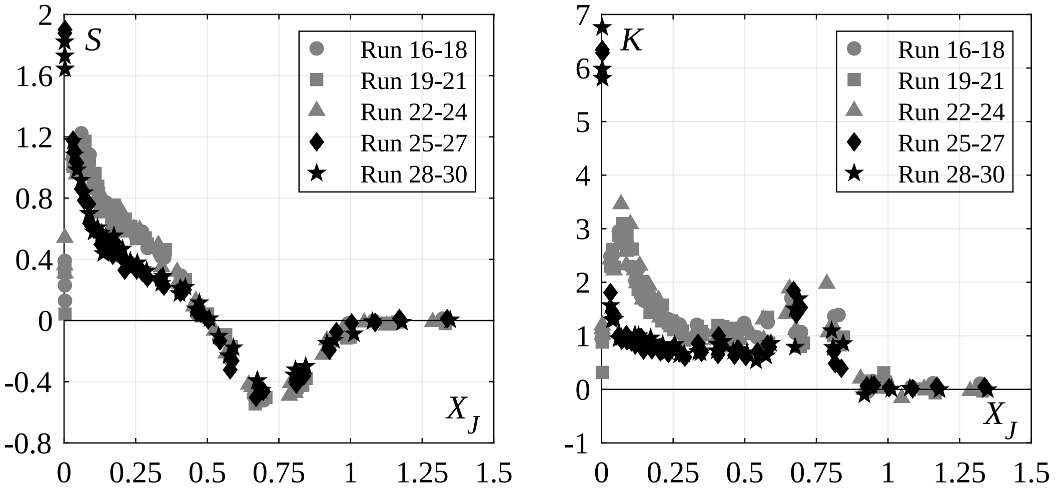

(g) (h)

Figure 6.15 – Streamwise distribution of: (a) mean pressure coefficient P_m, (b) pressure fluctuation coefficient $C_P{}'$, (c) maximum pressure coefficient $C_P{}^{max}$, (d) 99.9th percentile $C_P{}^{99.9}$, (e) minimum pressure coefficient $C_P{}^{min}$, (f) 0.1th percentile $C_P{}^{0.1}$, (g) skewness S, and (h) excess kurtosis K; (——) Eqs. (4.5), Eqs. (4.6) and (6.1); (– – –) Eqs. (4.3), (4.4), (6.2) and (6.3) ; [Runs 16-24: smooth chute; Runs 25-30: stepped chute].

The relative downstream shift of the maximum mean pressure position after 50° stepped chute can be explained by the smaller impact area of the *internal jet* (typical of stepped chute flows, see Figure 2.7) close to the jump toe. As observed by Takahashi and Ohtsu (2012), the impact region of the internal jet decreases with increasing chute slope. Therefore, in case of the 30° chute, a major portion of the incoming flow is "deflected" towards the inner part of the last step cavity (i.e. upstream of the first pressure sensor P1, see Figure 3.2) resulting in a more concentrated flow impact at the jump toe, i.e. at $X_J \approx 0$. On the other hand, in case of the 50° chute, only a small portion of the flow impacts near the jump toe (i.e. fictitious step edge) resulting in the more concentrated impact further downstream, i.e. at $X_J \approx 0.04$. This can be further observed by two times higher skewness and kurtosis values at the jump toe after 50° chute (Figure 6.15g), as compared to the 30° chute (Figure 4.13f). Moreover, these values are similar if comparing streamwise positions $X_J \approx 0.04$ and $X_J \approx 0$ for 50° and 30° chutes, respectively. Downstream of the flow deflection point, within $0.04 < X_J \leq 0.18$, the mean pressures after 50° stepped chute decreases in a similar manner as after 30° chute, however with higher magnitudes caused by stronger flow curvature. The mean pressure coefficients reach a local minimum at $X_J \approx 0.18$, after which they coincide with 30° stepped chute approach flows along the entire remaining stilling basin reach.

Comparing the maximum mean pressures coefficients downstream of 50° chute (i.e. at $X_J \approx 0$ for smooth and $X_J \approx 0.04$ for stepped chutes), one can notice up to 2.5 times higher magnitudes after smooth chute as compared to those after stepped chute (Figure 6.15a).

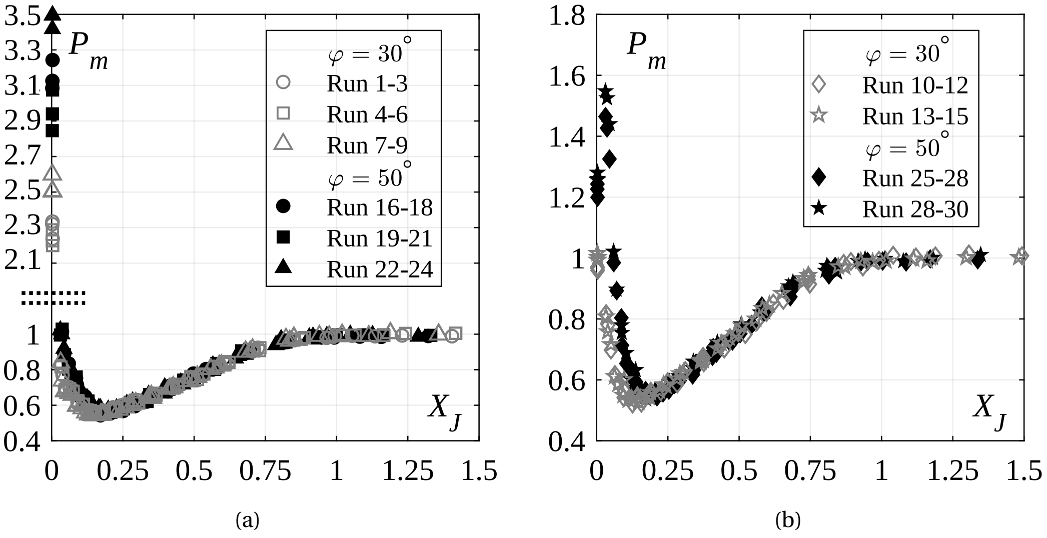

(a) (b)

Figure 6.16 – Streamwise distribution of mean pressure coefficients P_m downstream of 30° and 50° sloping: (a) smooth chute, and (b) stepped chute; [Runs 1-9: 30° smooth chute, Runs 10-15: 30° stepped chute, Runs 16-24: 50° smooth chute, Runs 25-30: 50° stepped chute].

As the mean pressure at this point is mainly governed by the approach flow kinetic energy, the mean pressure at the flow deflection point p_{def} was normalized with approach flow kinetic energy H_k. The resulting mean pressure coefficients ${C_P}^{def}$ are shown in Figure 6.17, along with ${C_P}^{def}$ values for 30° chute. In case of 50° chute, the mean pressures at the flow deflection point are, on average, 41% and 58% of the corresponding approach flow kinetic energy for smooth and stepped chutes, respectively. As described in Chapter 4, the higher magnitudes downstream of smooth chutes are caused by its lower approach flow depth, resulting in a more concentrated impact. Furthermore, the pressure coefficients ${C_P}^{def}$ are approximately 20% higher after 50° smooth and stepped chutes, as compared to the corresponding ones for 30° chute (Figure 6.17). This is clearly caused by the "sharper" angle of the flow impact.

As a result of a slightly shifted flow deflection point, the 50° stepped chute exhibit slightly higher P_m magnitudes within $0.05 \leq X_J < 0.12$, as compared to 50° smooth chute (Figure 6.15a). Further downstream, i.e. $X_J \geq 0.12$, the mean pressure coefficients are practically independent of the approach flow conditions. The pronounced mean pressures in the *flow deflection zone* after 50° stepped ($R^2 = 0.97$) and smooth ($R^2 = 0.95$) chutes can be described as (Figure 6.15a):

$$P_m = 1.53 - \tanh\left(30X_J\right)^{260X_J - 0.15} \qquad \varphi = 50° \text{ stepped chute} \qquad X_J \leq 0.18 \tag{6.1}$$

$$P_m = 1.53 - \tanh\left(22X_J\right)^{40X_J} \qquad \varphi = 50° \text{ smooth chute} \qquad 0.03 \leq X_J \leq 0.18 \tag{6.2}$$

Further downstream, in the *transition* and *tailwater zone*, the streamwise distribution of mean pressures for 50° sloping smooth and stepped chutes can be estimated using the same equation used for 30° sloping smooth and stepped chutes, i.e. Eq. (4.5) (Figure 6.15a):

$$P_m = \tanh\left(3.1X_J\right)^{5.9X_J-0.14} \qquad 30° \leq \varphi \leq 50° \qquad \text{smooth/stepped} \qquad X_J > 0.18$$

Accordingly, no major effect of step size s or smooth chute approach flow aeration C_1 on the streamwise mean pressure distribution occurs.

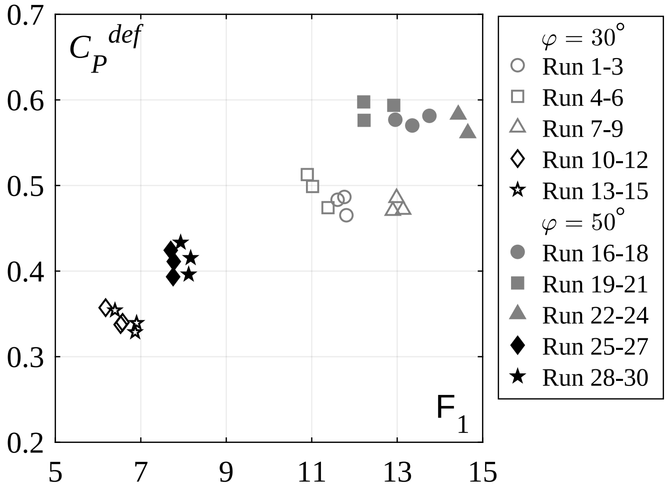

Figure 6.17 – Mean pressure coefficients $C_P{}^{def}$ against inflow Froude number F_1; [Runs 1-9: 30° smooth chute, Runs 10-15: 30° stepped chute, Runs 16-24: 50° smooth chute, Runs 25-30: 50° stepped chute].

6.4.3 Streamwise distribution of pressure fluctuation

The 50° sloping *smooth chute* approach flows (Figure 6.15b) show a typical streamwise pressure fluctuation $C_P{}'$ development (e.g. Abdul Khader and Elango (1974), Fiorotto and Rinaldo (1992b), Lopardo et al. (1982), Lopardo and Romagnoli (2009) and Toso and Bowers (1988)). The pressure fluctuations increase downstream of the jump toe reaching maximum values of $C_P{}' \approx 0.05$ at $X_J \approx 0.12$. Further downstream, they monotonically decrease towards quasi-constant tailwater magnitudes. Due to the flow deviation, at the jump toe ($X_J = 0$), the pressure fluctuations reach or exceed the magnitudes observed at $X_J \approx 0.12$. No major effect of approach flow aeration C_1 on the streamwise development of $C_P{}'$ occurs.

The streamwise development of pressure fluctuation coefficients $C_P{}'$ for 50° and 30° *smooth chutes* are compared in Figure 6.18a. As it can be observed from the latter figure, overall, no considerable effect of the chute slope φ on the pressure fluctuation development occurs.

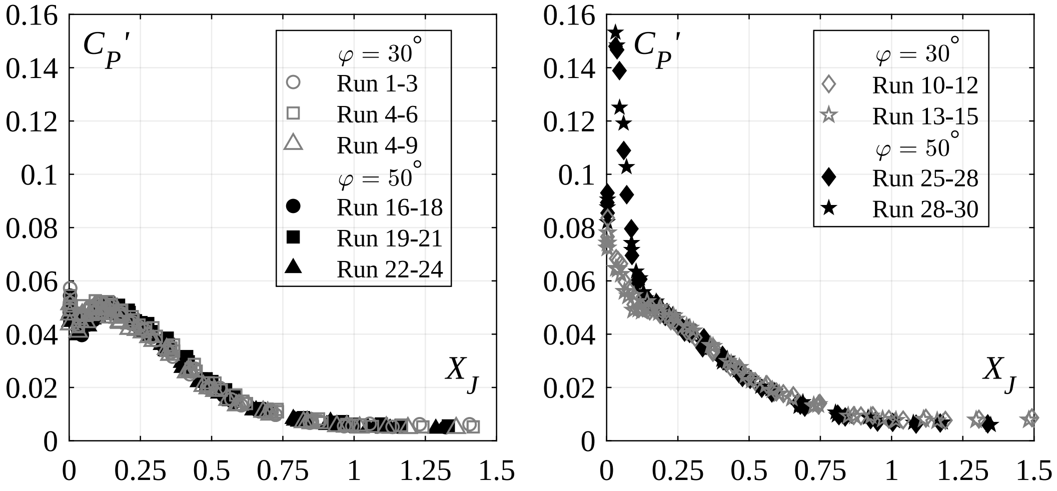

(a) (b)

Figure 6.18 – Streamwise development of pressure fluctuation coefficient C_P' for 30° and 50° sloping: (a) smooth chute, and (b) stepped chute; [Runs 1-9: 30° smooth chute, Runs 10-15: 30° stepped chute, Runs 16-24: 50° smooth chute, Runs 25-30: 50° stepped chute].

Comparing the pressure fluctuation development (Figure 6.15b), the effect of *stepped chute* approach flows is evident. At the jump toe, up to 40% higher magnitudes pressure fluctuation coefficients can be observed, as compared to 50° smooth chute approach flows, reaching up to C_P'=0.09 (Figure 6.19). Downstream of the jump toe, the fluctuation magnitudes sharply increase reaching maximum values of C_P'=0.15 at $X_J \approx 0.04$. These values are up to 3 times higher compared to the maximum values observed for smooth chute approach flows (Figure 6.15b and 6.19). To further illustrate the severeness of pressure fluctuations downstream of stepped chute at this point, in Figure 6.20 the absolute values of the pressure fluctuations p' are compared for smooth (Run 24) and stepped chute (Run 30) approach flows with similar unit discharge of $q \approx$0.360. Despite the significantly higher approach flow Froude number F_1 with the smooth chute approach flows (i.e. $F_1 \approx$14), as compared to stepped chute approach flows (i.e. $F_1 \approx$8), the absolute values of pressure fluctuations p' downstream of stepped chute are about 50% higher at the flow deflection point, as compared to the maximum values observed with smooth chute approach flows (i.e. in the zone of maximum turbulent intensity at $X_J \approx 0.12$). This clearly shows that pronounced pressure fluctuations downstream of stepped chute are caused by the higher turbulence levels of the approaching flow, as compared to smooth chute approach flows. Downstream of the flow deflection point, i.e. $X_J > 0.04$, the pressure fluctuation coefficients monotonically decrease up to $X_J \approx 0.13$, after which they coincide with smooth chute approach flows magnitudes over the entire stilling basin reach. No considerable effect of step size s occurs.

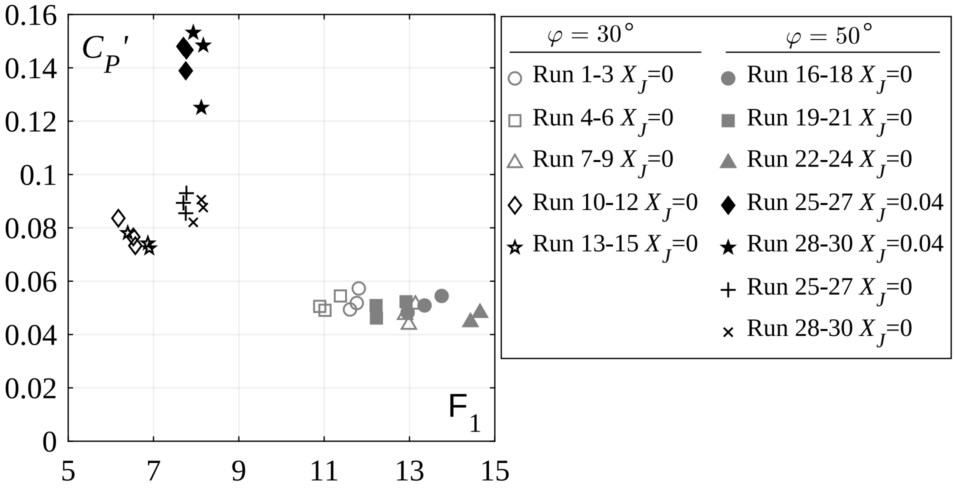

Figure 6.19 – Pressure fluctuation coefficients C_P' at the flow deflection point and the jump toe against inflow Froude number F_1; [Runs 1-9: 30° smooth chute, Runs 10-15: 30° stepped chute, Runs 16-24: 50° smooth chute, Runs 25-30: 50° stepped chute].

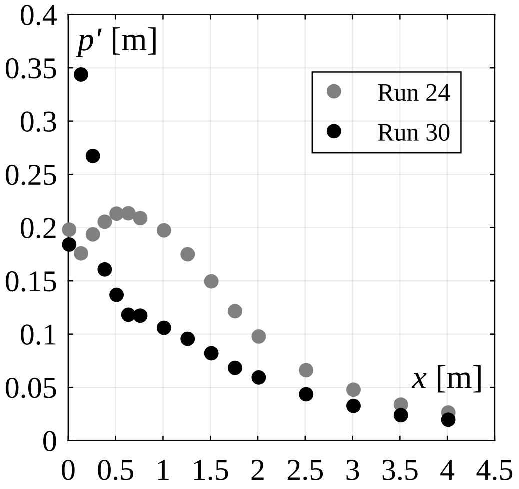

Figure 6.20 – Streamwise development of bottom pressure fluctuations p' for Run 24 (50° smooth chute) and Run 30 (50° stepped chute chute).

The streamwise development of C_P' for 50° and 30° sloping *stepped chute* approach flows are compared in Figure 6.18b. A major effect of the chute slope can be noticed. As a result of the relative downstream shift of the flow deflection point, the maximum pressure fluctuations for 50° chute occurs further downstream ($X_J \approx$0.04), as compared to the 30° sloping chutes ($X_J \approx 0$). At this point, up to 2 times higher C_P' magnitudes are observed, as compared to those of 30° chute at the flow deflection point ($X_J \approx$0) (Figure 6.18b and 6.19). Apart from the flow deflection point, the 50° chute tend to increase the pressure fluctuations at the jump toe as well, with up to 30% higher C_P' magnitudes (Figure 6.18b and 6.19). Downstream of the flow deflection point ($X_J \approx 0.04$), as previously mentioned, the pressure fluctuations monotonically decrease and reach the 30° chute magnitudes at $X_J \approx 0.13$, beyond which they coincide along the remaining downstream reach of the stilling basin.

The pressure $C_P{}'$ and surface fluctuation $C_H{}'$ are also compared in Figure 6.15b (only Eqs. (4.3) and (4.4) are included for clarity). As expected, the surface fluctuations are lower than the corresponding pressure fluctuations within the first half of the hydraulic jump, i.e. X_J<0.5. Similarly to the 30° chute, they are similar at $X_J \approx 0.5$. At this point skewness values of pressure readings reach negative values indicating the detachment of the bottom jet flow, as explained in Chapter 4 (Figure 6.15g). The skewness values reach minimal values at $X_J \approx 0.75$, beyond which they increase towards the zero values in the tailwater zone.

6.4.4 Streamwise distribution of extreme pressures

The extreme pressure coefficients $C_P{}^{max}$ and $C_P{}^{min}$ downstream of 50° chute show a similar streamwise distribution as the previously described pressure fluctuations (Figure 6.15c and 6.15d).

The 50° sloping *smooth chute* approach flows exhibit an increase of extreme pressure coefficients downstream of the jump toe, reaching maximum magnitudes of $C_P{}^{max}$=0.42 and $C_P{}^{min}$=0.29 at $X_J \approx 0.12$ and $X_J \approx 0.18$, respectively. Further downstream, they decrease attaining quasi-constant tailwater magnitudes. As a result of the flow deflection, the extreme pressure coefficients are the same order of magnitudes at the jump toe, i.e. $C_P{}^{max} \approx C_P{}^{min} \approx 0.32$ (Figure 6.15c and 6.22a). In Figure 6.21a and 6.21c the streamwise development of extreme pressure coefficients for 30° and 50° smooth chutes are compared, showing that the chute slope φ has a considerable effect.

The 50° *stepped chute* approach flows produce up to three times higher extreme maximum pressure coefficients $C_P{}^{max}$ at the flow deflection point (i.e. $X_J \approx 0.04$, Figure 6.15c), as compared to 50° smooth chute, or up to two times higher compared to 30° stepped chute (Figure 6.21b). These values reach up to $C_P{}^{max} \approx 1.26$ (Figure 6.15c and 6.22a). Similarly to the pressure fluctuation coefficients, pronounced values are also observed at the jump toe, where they reach up to $C_P{}^{max} \approx 1.1$ (Figure 6.15c and 6.22a). The peak in extreme negative pressures $C_P{}^{min}$ is also observed at the flow deflection point, where they reach up $C_P{}^{min} \approx 0.6$ (Figure 6.15d and 6.22b). These values are up to 2 times higher as compared to 50° smooth or 30° stepped chutes (Figure 6.15d, 6.21d and 6.22b). At the jump toe, the extreme negative pressures are similar as for 50° smooth or 30° stepped chutes (Figure 6.15c, 6.21b and 6.22b). Downstream of the flow deflection point, i.e. $X_J > 0.04$, the extreme pressure coefficients for 50° stepped chutes decrease and are similar to 50° smooth chute approach flow magnitudes for $X_J > 0.13$.

Similar conclusions can be drawn for extreme pressure coefficients with 99.9% and 0.1% percentiles, but with typically two times lower magnitudes (Figure 6.15e and 6.15f).

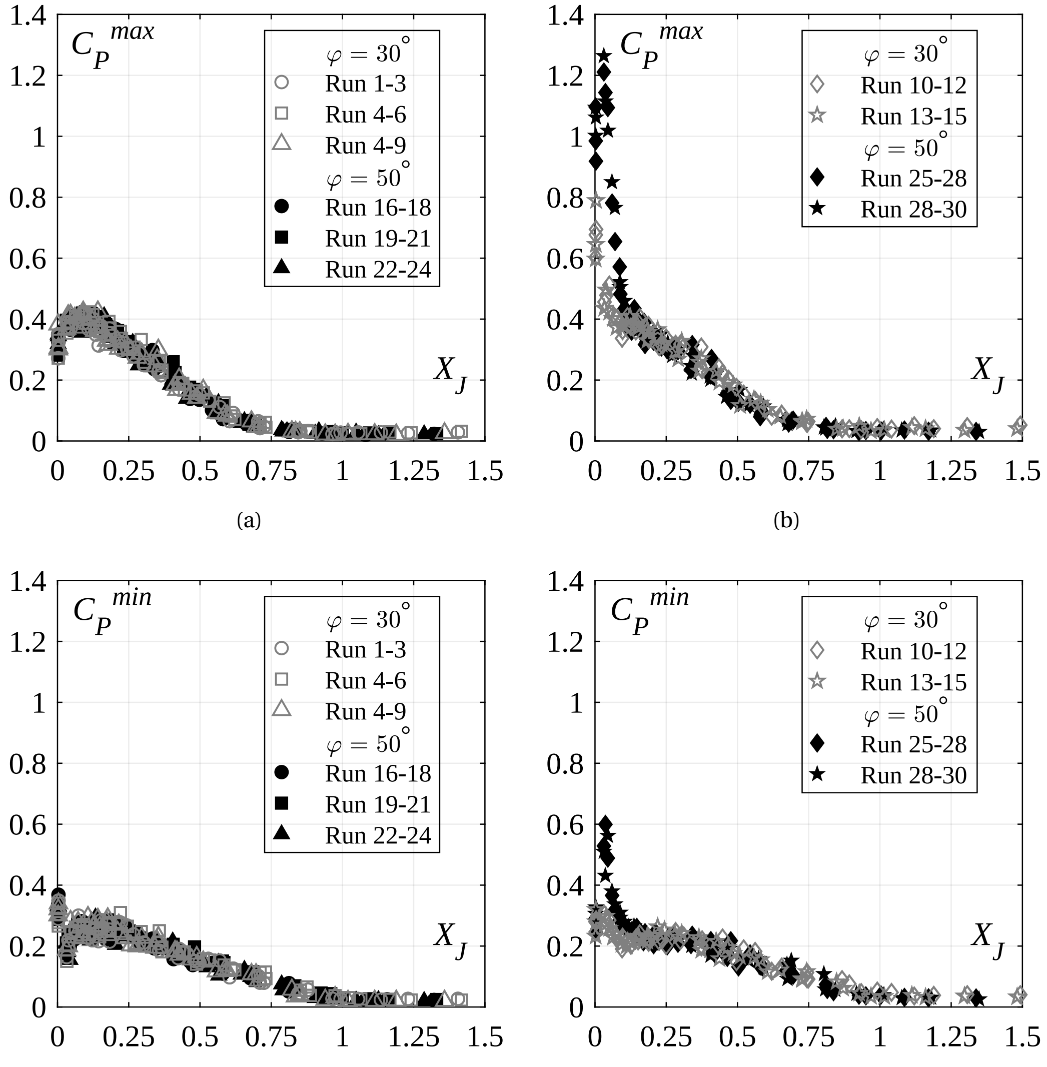

(a) (b)

(c) (d)

Figure 6.21 – Streamwise development of extreme pressure coefficients: (a) $C_P{}^{max}$ for 30° and 50° smooth chutes, (b) $C_P{}^{max}$ for 30° and 50° stepped chutes, (c) $C_P{}^{min}$ for 30° and 50° smooth chutes, and (d) $C_P{}^{min}$ for 30° and 50° stepped chutes; [Runs 1-9: 30° smooth chute, Runs 10-15: 30° stepped chute, Runs 16-24: 50° smooth chute, Runs 25-30: 50° stepped chute].

The fluctuation and extreme pressure coefficients for 50° sloping *smooth chute* approach flows can be described with the same relationship used for 30° chute, i.e. Eq. (4.6) (Figure 6.15c, 6.15d, 6.15e and 6.15f):

$$C_P = d - \tanh\left(eX_J\right)^{jX_J - k} \qquad 30^\circ \le \varphi \le 50^\circ \qquad X_J \geq 0.03$$

where the coefficients d, e, j and k are listed in Table 4.2. The same equation can be used for

50° sloping *stepped chutes* for X_J >0.13. The pronounced pressure coefficients for 50° sloping *stepped chute* approach flows within $X_J \leq 0.13$ are described as:

$$C_P = A - \tanh\left(DX_J\right)^{GX_J+I} \qquad \varphi = 50° \qquad X_J \leq 0.13 \tag{6.3}$$

where coefficients A, D, G and I are listed in Table 6.2.

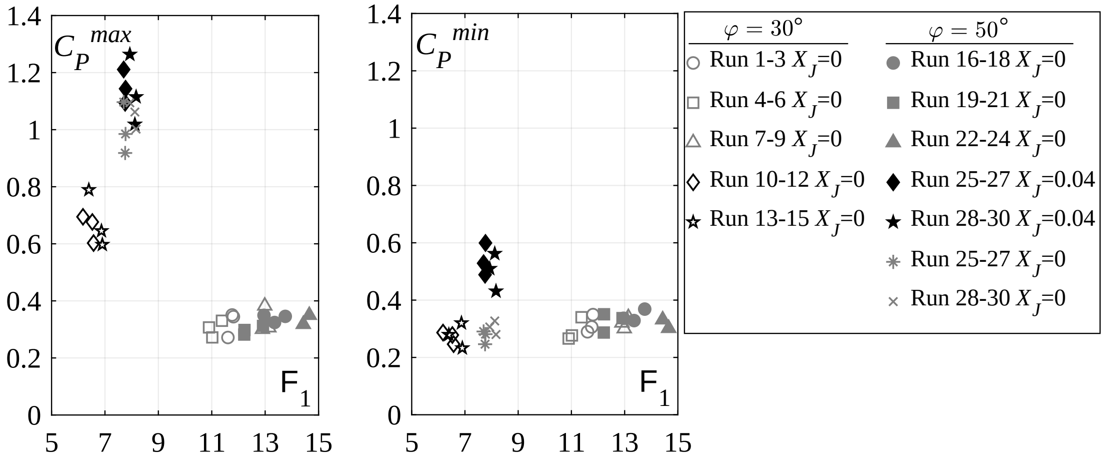

(a) (b)

Figure 6.22 – Extreme pressure coefficients: (a) $C_P{}^{max}$ and (b) $C_P{}^{min}$ at the flow deflection point and jump toe; [Runs 1-9: 30° smooth chute, Runs 10-15: 30° stepped chute, Runs 16-24: 50° smooth chute, Runs 25-30: 50° stepped chute].

Table 6.2 – Coefficients of Eq. (6.3).

Coefficient	A	D	G	I	R^2
C_P'	1.04	19	6	0.000	0.98
$C_P{}^{max}$	1.36	28	154	0.020	0.96
$C_P{}^{min}$	1.24	24	28	-0.050	0.86
$C_P{}^{99.9}$	1.19	21	31	0.070	0.97
$C_P{}^{0.1}$	1.12	18	10	-0.007	0.96

6.4.5 Frequency domain analysis

Figure 6.23 shows power spectrum densities (PSDs) of pressure readings for Run 20 (Figure 6.23a to 6.23c) and Run 29 (Figure 6.23d to 6.23f) being representative examples for 50° sloping smooth and stepped chute approach flows, respectively.

50° sloping *smooth chute* approach flows (Figure 6.23a to 6.23c) exhibit very similar PSD development as the 30° sloping smooth chute approach flows (Figure 4.14a to 4.14c). They reveal:

- Sudden reduction of the spectral energy within energy-containing scales (i.e. low frequency range) between $X_J \approx 0$ and $X_J \approx 0.04$, due to intense energy dissipation (Figure 6.23a),
- Turbulent energy production at low frequency ranges within $0.04 \leq X_J \leq 0.11$ (Figure 6.23a),
- Reduction of spectral content for all range of scales (i.e. frequencies) within $0.11 \leq X_J \leq 0.42$, due to the energy dissipation (Figure 6.23a and 6.23b),
- Detachment of the bottom jet flow at $X_J \approx 0.48$ (Figure 6.23c),
- Pronounced decrease of spectral energy in the downstream half of the jump as the influence of the bottom jet flow is reduced (Figure 6.23c),
- PSD concentrated in a narrow frequency range of 0 to 1.3 Hz in the *tailwater zone*, caused by propagating surface waves.
- Decay rate of $f^{-5/3}$ for inertial range of scales.

Similar conclusions can be made for all experimental runs involving 50° sloping smooth chute approach flows. Dominant frequencies range between 1.3 to 18 Hz in the upstream half of the jump and 0.5 to 0.9 Hz in the downstream half. No significant effect of approach flow aeration C_1 on the PSD development occurs. Overall, no major effect of chute slope φ on the PSD development is found.

Globally looking, the 50° sloping *stepped chute approach flows* exhibit similar PSD streamwise development as 50° sloping smooth chute approach flows (Figure 6.23d to 6.23f). However, similarly to the 30° sloping stepped chute approach flows (Figure 4.14), a major effect of stepped chute inflows within $X_J \leq 0.13$ (Figure 6.23d) can be observed.

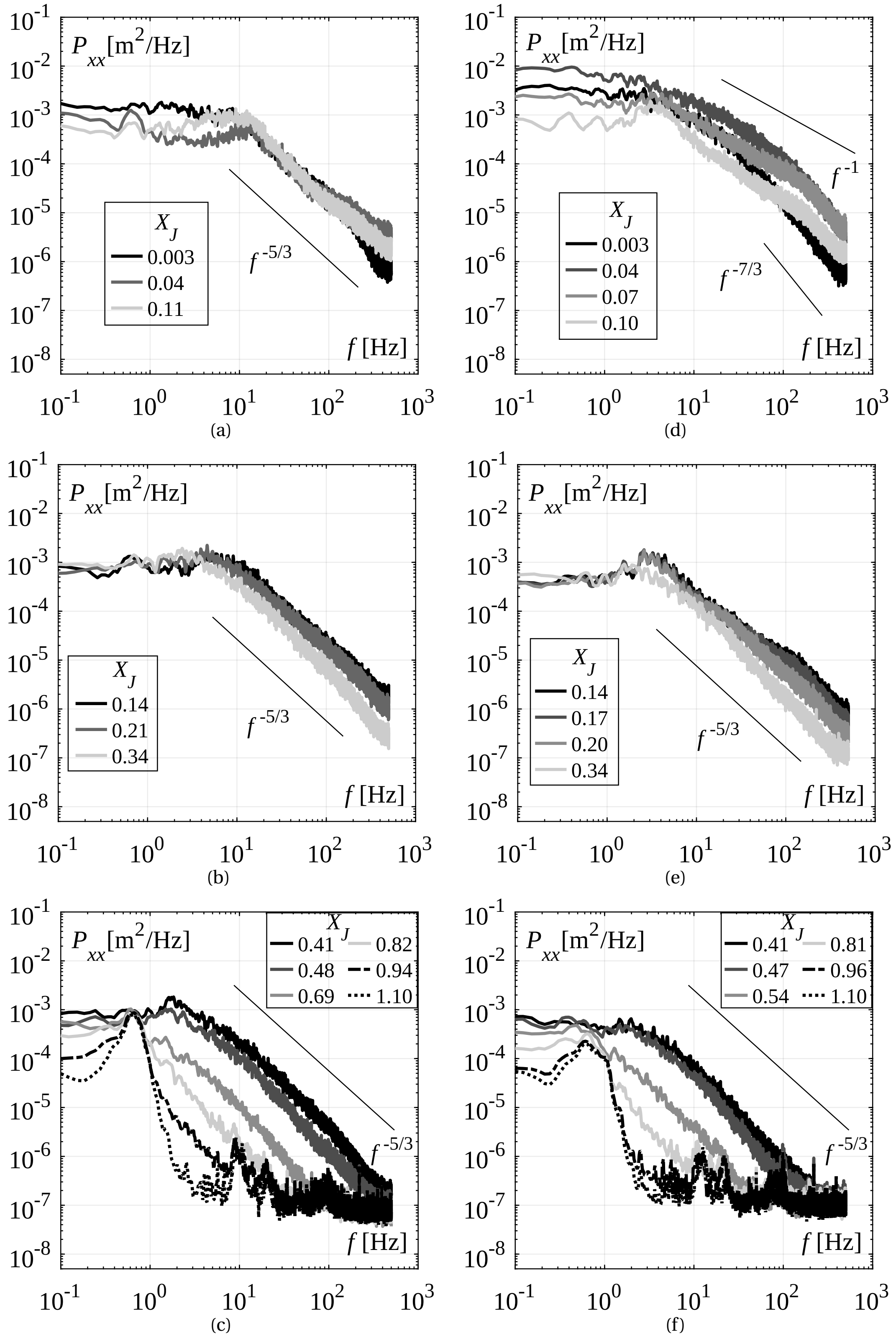

(a) (d) (b) (e) (c) (f)

Figure 6.23 – Power spectral densities of the pressure fluctuations at selected flow distances along the stilling basin invert, for (a-c) Run 20 (50° smooth chute), and (d-f) Run 29 (50° stepped chute).

Contrary to the 30° and 50° smooth chute approach flows, 50° stepped chute approach flows have an increase of spectral content within $0.003 \leq X_J \leq 0.04$, which is attributed to the downstream shift of the flow deflection point (Figure 6.23d). Despite the significantly lower approach Froude number F_1 (Table 6.1), the stepped chute approach flow have a higher spectral content across all range of frequencies within $X_J \leq 0.04$. This is further shown in Figure 6.24a, where PSDs for 50° smooth and stepped chute approach flows are compared at flow deflection point (i.e. X_J=0.003 for smooth and X_J=0.04 for stepped chute). Moreover, similarly to the 30° stepped chute (Figure 4.14), the higher participation of energy content at the high frequency range with stepped chute approach flows is observed, as compared to smooth chute approach flows. This can be clearly seen in Figure 6.24b, where PSDs at X_J=0.07 are compared. These results further strengthen the conclusions made in Chapter 4, that increased pressure coefficients with stepped chute approach flows in the zone $X_J \leq 0.13$ are due to the higher, step induced, turbulence levels of the incoming flow, as compared to smooth chute approach flows.

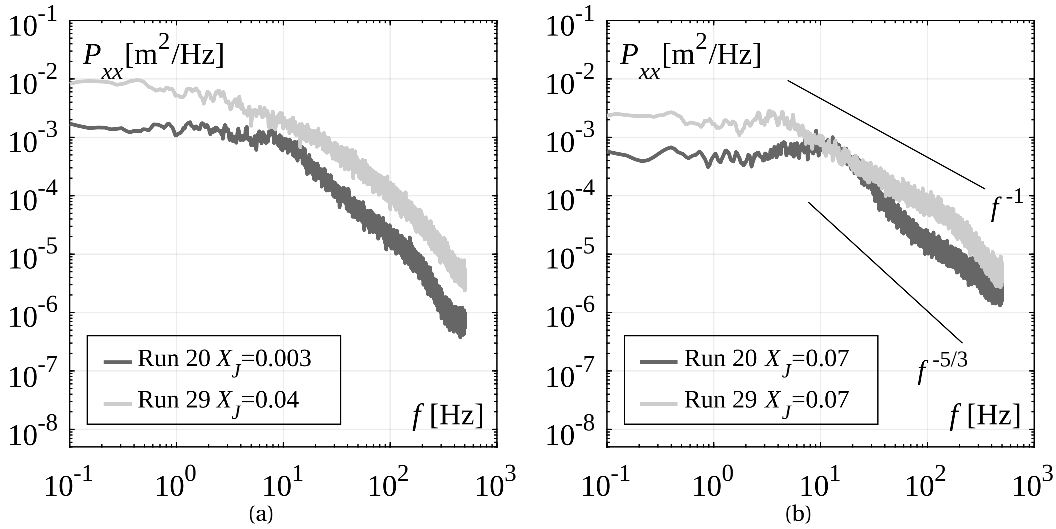

Figure 6.24 – Comparison of power spectral densities for 50° smooth (Run 20) and stepped chute (Run 29) approach flows at (a) flow deflection point, and (b) X_J = 0.07.

The PSDs for 30° and 50° stepped chute approach flows within the zone of pronounced pressure magnitudes, i.e. $X_J \leq 0.13$, are compared in Figure 6.25, namely at the flow deflection point (Figure 6.25a) and at $X_J \approx 0.07$ (Figure 6.25b). Overall, the PSDs have very similar shape, however significantly higher spectral content is observed with 50° stepped chute approach flows, as compared to 30° stepped chute approach flows. Moreover, at the flow deflection point, the decay of f^{-1} tend to expand to higher frequency ranges after 50° chute (some 100 Hz), as compared to those after 30° chute (some 50 Hz). This may be caused by the higher turbulence levels of the 50° sloping stepped approach flows, increasing the pressure coefficients within $X_J \leq 0.13$ (as compared to 30° stepped chutes). Typical dominant frequencies for 50° stepped chute approach flows range between 1 to 7 Hz for $X_J \leq 0.5$, and 0.4 to 0.8 Hz for $X_J \geq 0.5$.

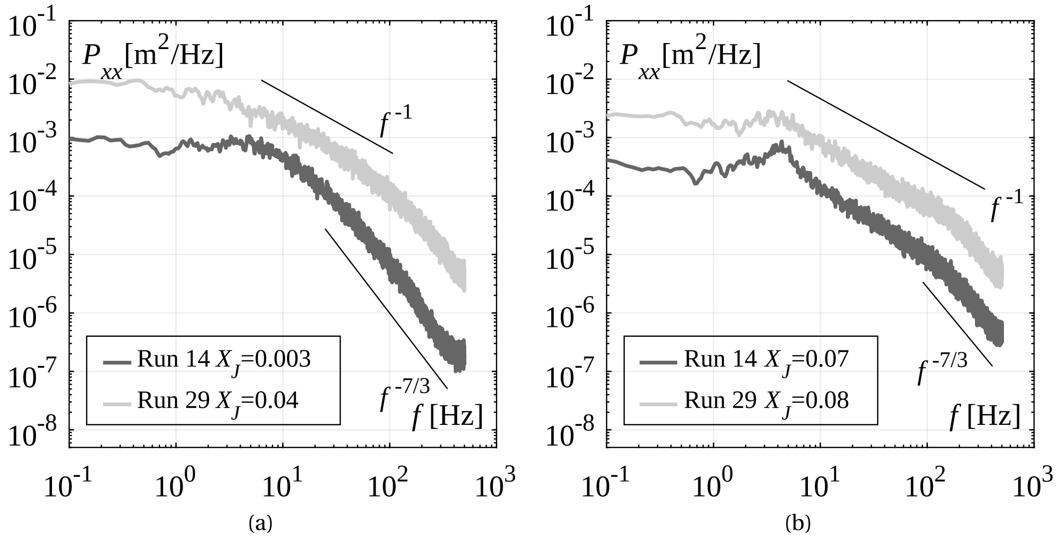

(a) (b)

Figure 6.25 – Comparison of power spectral densities for 30° (Run 14) and 50° (Run 29) stepped chute approach flows at (a) flow deflection point, and (b) $X_J \approx 0.07$.

6.5 Air-water flow properties

6.5.1 Air concentration, air-phase frequency distributions and representative flow depths

Air concentration and air-phase frequency profiles for 50° sloping chutes

Figure 6.26 and 6.27 shows typical development of air concentration and air phase frequency profiles along the hydraulic jump plotted against the dimensionless vertical coordinate $z/(h_2 - h_1)$ for Run 22 (Figure 6.26a, b and Figure 6.27a) and Run 25 (Figure 6.26c, d and Figure 6.27b), being representative examples for 50° sloping smooth and stepped chute approach flows, respectively. The profiles highlight two flow zones identified in Chapter 4, namely: *advective diffusive zone* along $x/L_{R,\eta} \leq 0.8$ and *air release zone* further downstream, i.e. $x/L_{R,\eta} \geq 0.9$.

The *advective diffusive zone* is characterized by two flow regions, namely a shear layer region between the bottom and the elevation of the local minimum air concentration z_{min}, and a recirculation region above. In the shear layer region the air concentration distribution has a typical bell shaped profile with a local maximum C_{max} at the vertical distance from the bottom z_{max} (Figure 6.26). This flow region further show a maximum air-phase frequency F_{max} at the elevation z_{Fmax} which, similarly to the 30° sloping chute approach flows, is consistently observed to be lower than the corresponding z_{max} (Figure 6.27). In the recirculation region, i.e. $z > z_{min}$, the air concentration rapidly increase to unity (Figure 6.26), whereas the air-phase frequency show a secondary peak F_{sec} and decrease to zero (Figure 6.27).In the *air release zone*, i.e. $x/L_{R,\eta}$≥0.9, the shear layer region disappears (Figure 6.26), and air concentrations monotonically increase from the channel invert, due to intense flow deaeration driven by buoyancy. In this flow zone, the air phase frequency profiles first tend to transform into a more "uniform" distribution ($x/L_{R,\eta}$=1.0 in Figure 6.27), where the F_{max} and F_{sec} are of same order of magnitude, and then into a monotonically increasing profile ($x/L_{R,\eta}$=1.2 in Figure 6.27) with a single peak in the upper part of the flow, i.e. F_{sec}. Similarly to the 30° sloping approach flows (Figure 5.10), this transformation is longer for stepped chute approach flows, i.e. $0.8 \leq x/L_{R,\eta} \leq 1.2$ (Figure 6.27b), as compared to smooth chute approach flows, i.e. $0.8 < x/L_{R,\eta} \leq 1.1$ (Figure 6.27a).

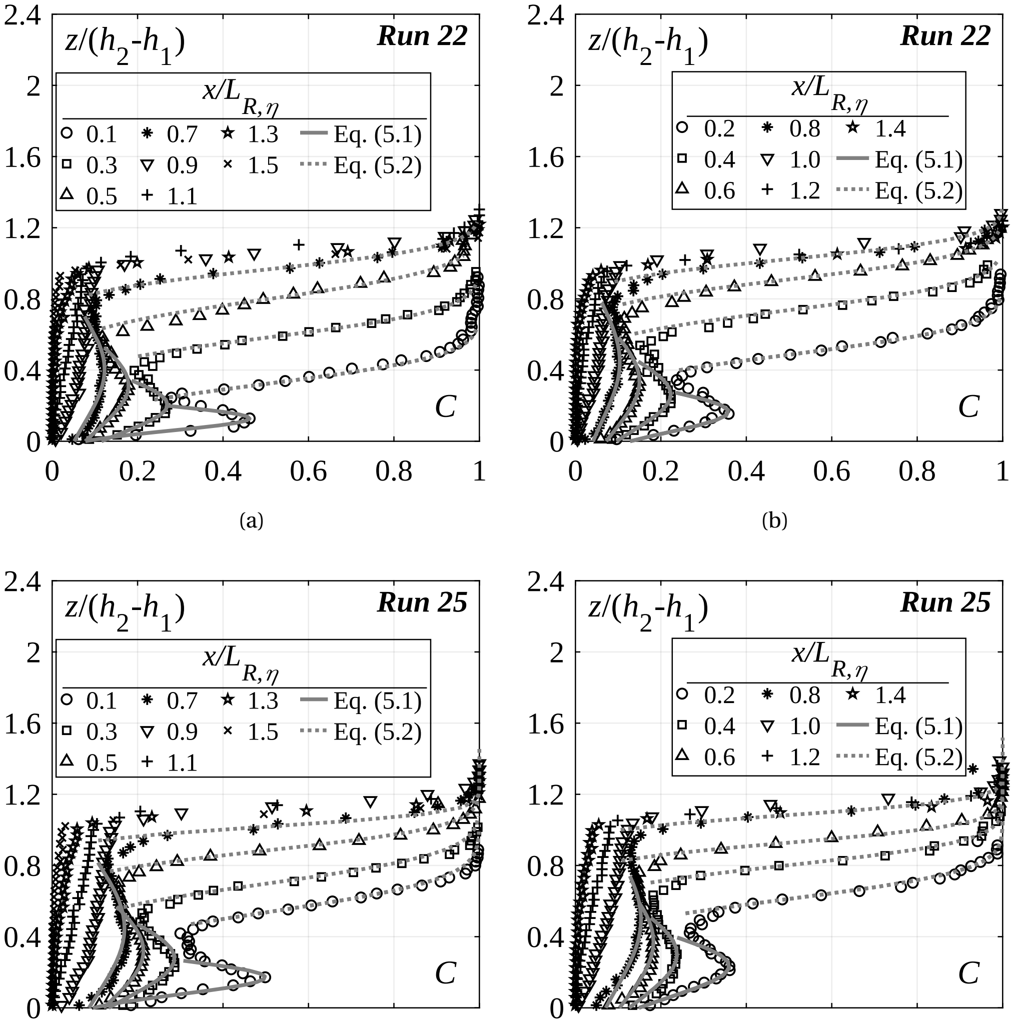

(a) (b)

(c) (d)

Figure 6.26 – Air concentration profiles along the stilling basin for: (a-b) Run 22 (50° smooth chute), and (c-d) Run 25 (50° stepped chute); (——) Eq. 5.1; (- - -) Eq. 5.2.

In Figure 6.26, the air concentration profiles in the advective diffusive zone are compared to the analytical solutions developed by Chanson (1995), i.e. Eqs. (5.1) and (5.2), showing a good agreement. The obtained dimensionless diffusivity ${D_t}^s (V_1 h_1)^{-1}$ and ${D_t}^r (V_1 h_1)^{-1}$ are plotted

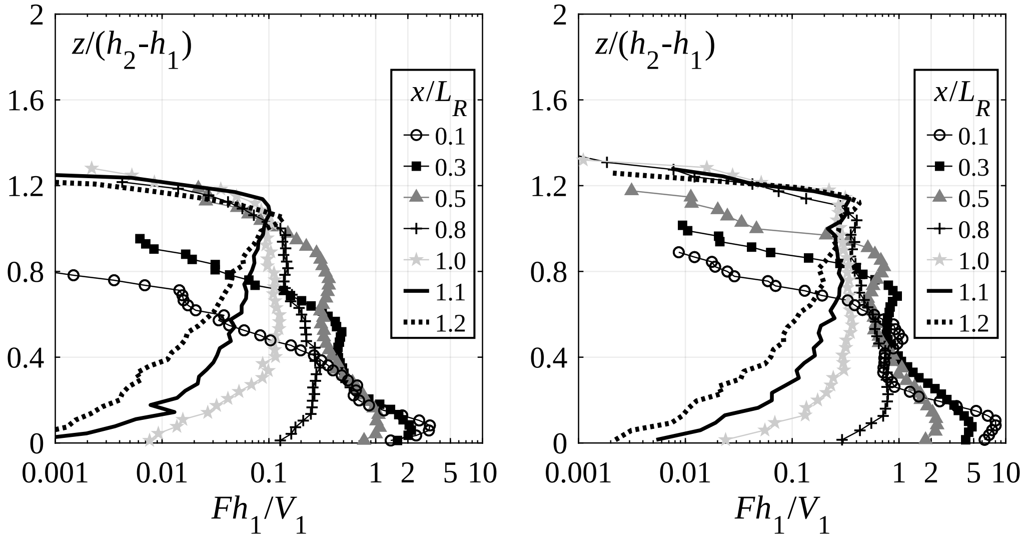

(a) (b)

Figure 6.27 – Dimensionless vertical air-phase frequency Fh_1/V_1 profiles at the selected flow distances $x/L_{R,\eta}$ for: (a) Run 22 (50° smooth chute) and (b) Run 25 (50° stepped chute).

against the normalized streamwise coordinate $x/L_{R,\eta}$ in Figure 6.28a and b, respectively, including the values obtained for 30° sloping chutes. The 50° chutes has the same range of dimensionless turbulent diffusivity as the 30° chutes, showing that no major effect of chute slope φ on the dimensionless turbulent diffusivity ${D_t}^s(V_1h_1)^{-1}$ and ${D_t}^r(V_1h_1)^{-1}$ values occurs.

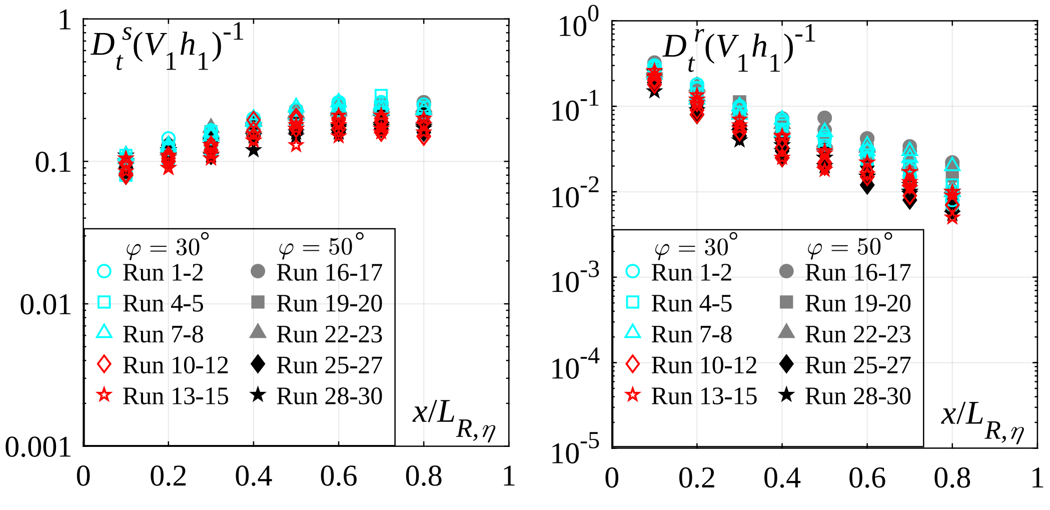

(a) (b)

Figure 6.28 – Streamwise variation of dimensionless turbulent diffusivity in a: (a) shear region ${D_t}^s$ and (b) recirculation region ${D_t}^r$; [Runs 1-9: 30° smooth chute, Runs 10-15: 30° stepped chute, Runs 16-24: 50° smooth chute, Runs 25-30: 50° stepped chute].

Comparison of air concentration distribution between 50° smooth and stepped chute approach flows

Air concentration profiles along the stilling basin for 50° sloping smooth chute approach flow with various C_1 (Runs 16,19 and 28, Table 6.1) and 50° sloping stepped chute approach flow with different s (Runs 25 and 28, Table 6.1) are compared in Figure 6.29 at selected flow distances $x/L_{R,\eta}$ for unit discharges of $q \approx 0.200$ m^2/s. Similarly to the 30° smooth and stepped chutes, the air concentration profiles after 50° smooth and stepped chutes within $0.1 \leq x/L_{R,\eta} \leq 0.3$ are mostly independent of the approach flow conditions (Figure 6.29a and b). The main differences occur close to the stilling basin invert, where significantly higher air concentration values are observed after stepped chute, as compared to those after smooth chute. Further downstream, i.e. $x/L_{R,\eta} > 0.3$, 50° stepped chute approach flow consistently has a lower de-aeration rate along the stilling basin in terms of $x/L_{R,\eta}$ (Figure 6.29c to f). These results, similarly to the 30° chutes, show that longer normalized hydraulic jumps L_J/h_2 occurs after 50° stepped chute, as compared to 50° smooth chute, thus confirming the jump length measurements based on bottom pressure and flow depth characteristics (Figure 6.14). The same conclusions can be made for other test runs.

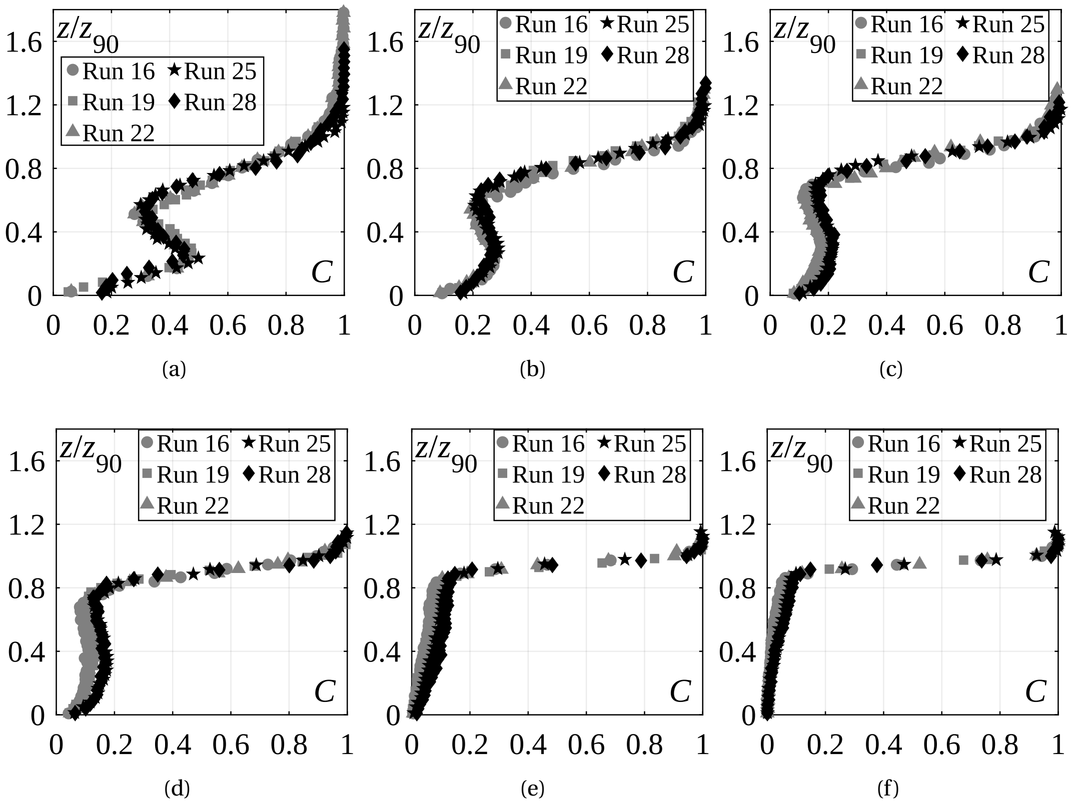

(a) (b) (c)

(d) (e) (f)

Figure 6.29 – Comparison between air concentration profiles in the stilling basin for Runs 16, 19 and 22 (smooth chute approach flows), and Runs 25 and 28 (stepped chute approach flows) at $x/L_{R,\eta}$=: (a) 0.1, (b) 0.3, (c) 0.5, (d) 0.7, (e) 1.0 and (f) 1.2.

Comparison of air concentration distribution between 30° and 50° sloping chutes

Air concentration profiles along the stilling basin for 30° (Run 1, 4, 7) and 50° (Run 16, 19, 22) *smooth chute* approach flows with various C_1 are compared in Figure 6.30a-c at selected flow distances $x/L_{R,\eta}$ for unit discharges of $q \approx 0.200\ \mathrm{m^2/s}$. Observing these figures, no major effect of chute slope φ or approach flow aeration C_1 on the air concentration distribution can be noticed in the stilling basin downstream of smooth chutes. In Figure 6.30d-f, the air concentration profiles for 30° (Run 10 and 13) and 50° (Run 25 and 28) *stepped chute* approach flows are compared at selected flow distances $x/L_{R,\eta}$ for different step heights s and similar unit discharge of $q \approx 0.200\ \mathrm{m^2/s}$. Observing these figures, it can be clearly seen that the air concentration distribution in the stilling basin downstream of stepped chutes is mostly independent of the chute slope φ. The main differences occur in the vicinity of the bottom within $x/L_{R,\eta} \leq 0.4$, where slightly higher air concentration values are observed downstream of 50° stepped chute, as compared to 30° stepped chute (Figure 6.30d and e). Accordingly, no major effect of step size s is observed. The same conclusions can be made for other test runs.

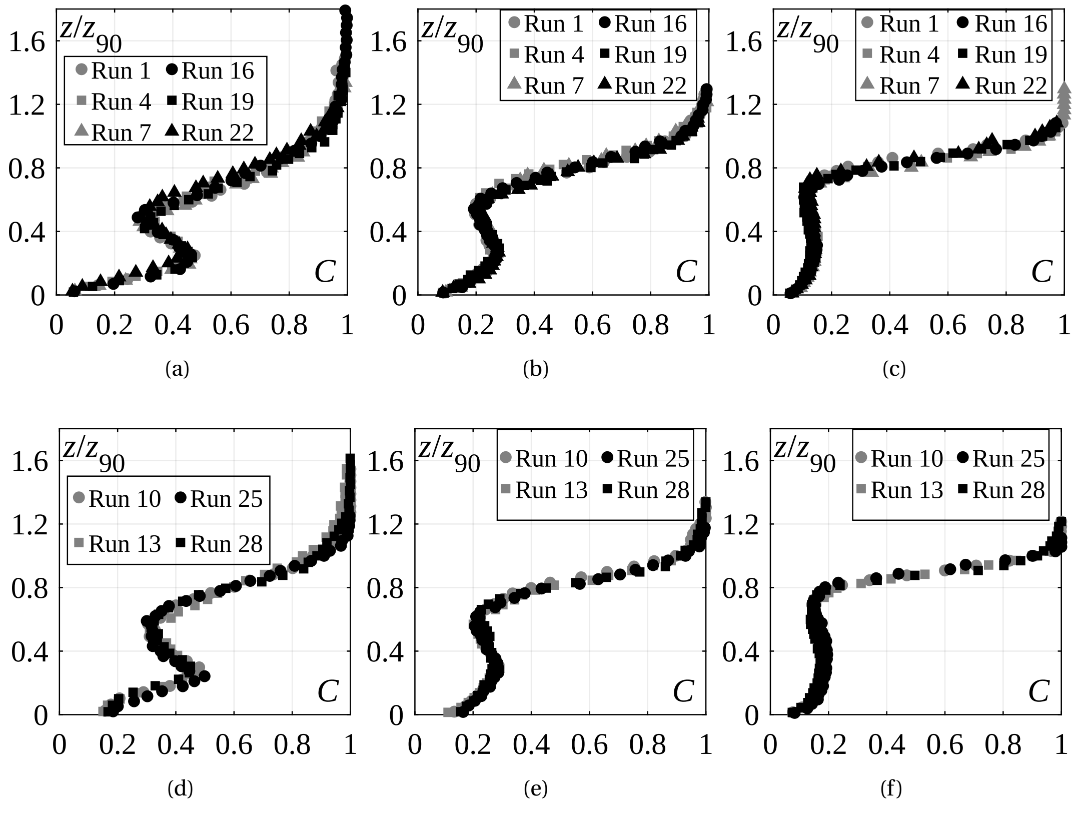

Figure 6.30 – Comparison between air concentration profiles in the stilling basin at distances $x/L_{R,\eta}$=0.1, 0.3 and 0.6 for 50° and 30°: (a-c) smooth chute approach flows (30° chutes: Run 1, 4, 7; 50° chutes:16, 19 and 22) and (d-f) stepped chute approach flows (30° chutes: Run 10, 13; 50° chutes: Run 25 and 28).

Streamwise development of maximum C_{max}, minimum C_{min} and depth-averaged C_a air concentration

In Figures 6.31, 6.32 and 6.33 the streamwise development of maximum air concentration C_{max} (Figure 6.31a), minimum air concentation C_{min} (Figure 6.31b), dimensionless elevation of maximum air concentration Z_{max} (Figure 6.32a), dimensionless elevation of minimum air concentration Z_{min} (Figure 6.32b) and mean air concentration C_a (Figure 6.33) after 50° smooth and stepped chutes are compared to those after 30° smooth and stepped chutes, presented in Chapter 5.

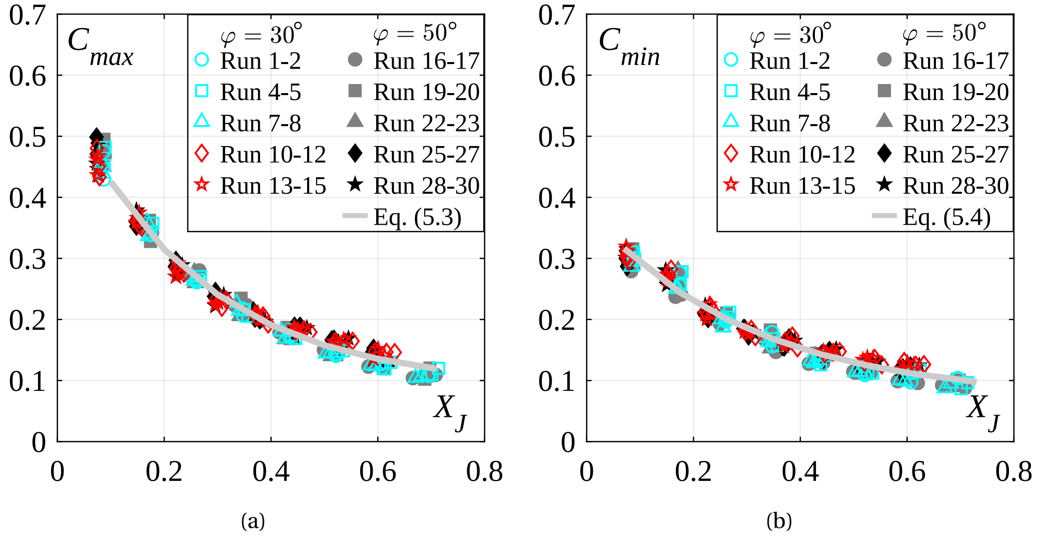

(a) (b)

Figure 6.31 – Streamwise development of (a) maximum air concentration C_{max} and (b) minimum air concentration C_{min}; [Runs 1-9: 30° smooth chute, Runs 10-15: 30° stepped chute, Runs 16-24: 50° smooth chute, Runs 25-30: 50° stepped chute].

Overall, no considerable effect of approach flow conditions or chute slope φ can be seen, further highlighting that air concentration distribution in the stilling basin is mostly independent of the chute slope φ. As such, these parameters can be described using the relations developed for 30° sloping chutes, i.e. Eqs. (5.3), (5.4), (5.5), (5.6) and (5.10) for C_{max}, C_{min}, Z_{max}, Z_{min} and C_a, respectively (Figures 6.31, 6.32 and 6.33):

$$\begin{aligned}
&C_{max} = 0.5\exp\left(-4X_J\right) + 0.09 && 30° \le \varphi \le 50° && 0.07 \le X_J \le 0.7\\
&C_{min} = 0.3\exp\left(-3.1X_J\right) + 0.07 && 30° \le \varphi \le 50° && 0.07 \le X_J \le 0.7\\
&Z_{max} = 0.49\frac{x}{L_{R,\eta}} + 0.018 && 30° \le \varphi \le 50° && 0.1 \le \frac{x}{L_{R,\eta}} \le 0.8\\
&Z_{min} = a\frac{x}{L_{R,\eta}} + b && 30° \le \varphi \le 50° && 0.1 \le \frac{x}{L_{R,\eta}} \le 0.8\\
&C_a = 0.54\exp\left(-1.84X_J\right) && 30° \le \varphi \le 50° && 0.08 \le X_J \le 1.34
\end{aligned}$$

with a=0.91 and b=0.092 for smooth chute approach flows, and a=0.8 and b=0.17 for stepped chute approach flows.

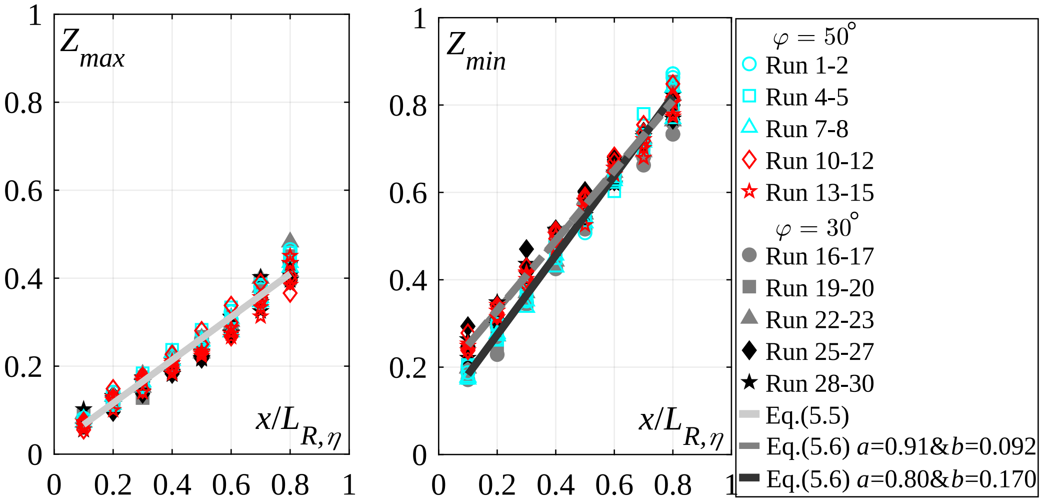

(a) (b)

Figure 6.32 – Streamwise development of (a) dimensionless elevation of maximum air concentration Z_{max} and (b) dimensionless elevation of minimum air concentration Z_{min}; [Runs 1-9: 30° smooth chute, Runs 10-15: 30° stepped chute, Runs 16-24: 50° smooth chute, Runs 25-30: 50° stepped chute].

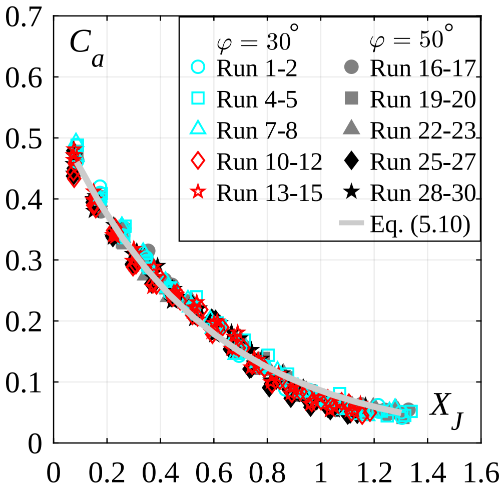

(a)

Figure 6.33 – Streamwise development of depth-averaged air concentration C_a; [Runs 1-9: 30° smooth chute, Runs 10-15: 30° stepped chute, Runs 16-24: 50° smooth chute, Runs 25-30: 50° stepped chute].

Streamwise development of bottom air concentration C_b

In Figure 6.34 the streamwise development of bottom air concentration C_b downstream of 30° and 50° smooth and stepped chutes are compared, including the values of the bottom air concentration at the chute end, i.e. $C_{b,ce}$, illustrated at $X_J = -0.3$.

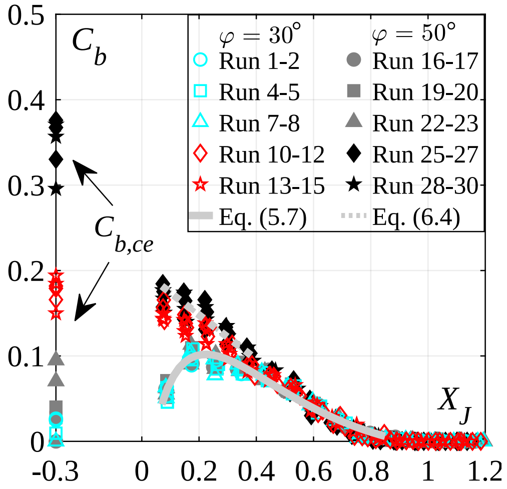

(a)

Figure 6.34 – Streamwise development of bottom air concentration C_b; [Runs 1-9: 30° smooth chute, Runs 10-15: 30° stepped chute, Runs 16-24: 50° smooth chute, Runs 25-30: 50° stepped chute].

Observing the Figure 6.34, it can be noticed that the bottom air concentration development for *smooth chute* approach flows is practically independent of approach flow conditions or chute slope φ. The bottom air concentration development remains virtually unaltered, despite the increased bottom air concentration at the 50° smooth chute end, i.e. $C_{b,ce}$ values. This further strengthens the conclusion made in Chapter 5 that the bottom air concentration values downstream of smooth chutes are not influenced by approach flow aeration C_1 due to the flow deviation at the jump toe, that generates high pressures (Figure 6.16b) and thus promotes de-aeration of the flow at the basin entrance.

The 50° sloping *stepped chute* approach flows has significantly higher bottom air concentration values within $X_J \leq 0.4$, as compared to 50° sloping *smooth chute* approach flows, with values reaching up to $C_b = 0.18$ at $X_J = 0.08$ (Figure 6.34). The increased values after 50° stepped chute approach flows, similarly to those after 30° stepped chutes, can be attributed to the significantly higher $C_{b,ce}$ values and comparatively lower pressure magnitudes at the flow deviation point (Figure 6.15a). Moreover, within $X_J \leq 0.4$, the 50° stepped chute have a slightly higher air concentration values (on average 2% higher) , as compared to 30° stepped chute, despite the significantly higher bottom air concentration values at the 50° stepped chute end (on average 18% higher). This is clearly caused by the higher pressure magnitudes at the flow deviation point downstream of 50° stepped chute (Figure 6.15a), which leads to higher de-aeration rate at the basin entrance.

The streamwise development of bottom air concentration C_b for 50° *smooth chute* approach flows can be described using the same equation developed for 30° smooth chute approach flows, i.e. Eq. 5.7 (Figure 6.34):

$$C_b = 0.98 - \tanh\left(2.4X_J\right)^{0.95X_J-0.03} \qquad 30° \leq \varphi \leq 50° \qquad \text{smooth chute} \qquad 0.08 \leq X_J \leq 0.9$$

The same equation can be used for 50° sloping *stepped chute* approach flows at X_J >0.4. The pronounced bottom air concentrations for 50° sloping stepped chute approach flows can be approximated as ($R^2 = 0.8$, Figure 6.34):

$$C_b = -0.26X_J + 0.2 \qquad \varphi = 50° \qquad \text{stepped chute} \qquad 0.08 \leq X_J \leq 0.4 \qquad (6.4)$$

In terms of the cavitation potential, stilling basins downstream of 50° chutes share the same cavitation protection length with respect to bottom air concentration as 30° chutes, namely: (1) smooth chute approach flows within $0.1 \leq X_J \leq 0.5$ and $0.15 \leq X_J \leq 0.4$ for 5% and 8% bottom air concentration limit, respectively, and (2) stepped chute approach flows within $0 \leq X_J \leq 0.5$ and $0 \leq X_J \leq 0.4$ for 5% and 8% bottom air concentration limit, respectively. As such the pronounced extreme pressures downstream of 50° sloping stepped chutes within $X_J \leq 0.13$ are expected not to pose danger in terms of cavitation.

Streamwise development of maximum F_{max} and secondary F_{sec} air-phase frequency

In Figure 6.35, the streamwise development of the dimensionless maximum air-phase frequency $F_{max}h_1/V_1$ (Figure 6.35a), dimensionless secondary air-phase frequency $F_{sec}h_1/V_1$ (Figure 6.35b), dimensionless elevation of maximum air-phase frequency Z_{Fmax} (Figure 6.35c) and dimensionless elevation of secondary air-phase frequency Z_{Fsec} (Figure 6.35d) downstream of 30° and 50° sloping smooth and stepped chutes are compared. The magnitudes and the development of dimensionless maximum $F_{max}h_1/V_1$ and secondary $F_{sec}h_1/V_1$ air-phase frequency with 50° smooth and stepped chute approach flow are similar to the corresponding ones with 30° smooth and stepped chute approach flows. Furthermore, the streamwise development of dimensionless elevations of maximum Z_{Fmax} and secondary Z_{Fsec} for 50° smooth and stepped chute approach flows are similar to those with 30° sloping smooth and stepped chute approach flows. Therefore, no significant effect of chute slope φ on the development of air-phase frequency along the stilling basin can be observed.

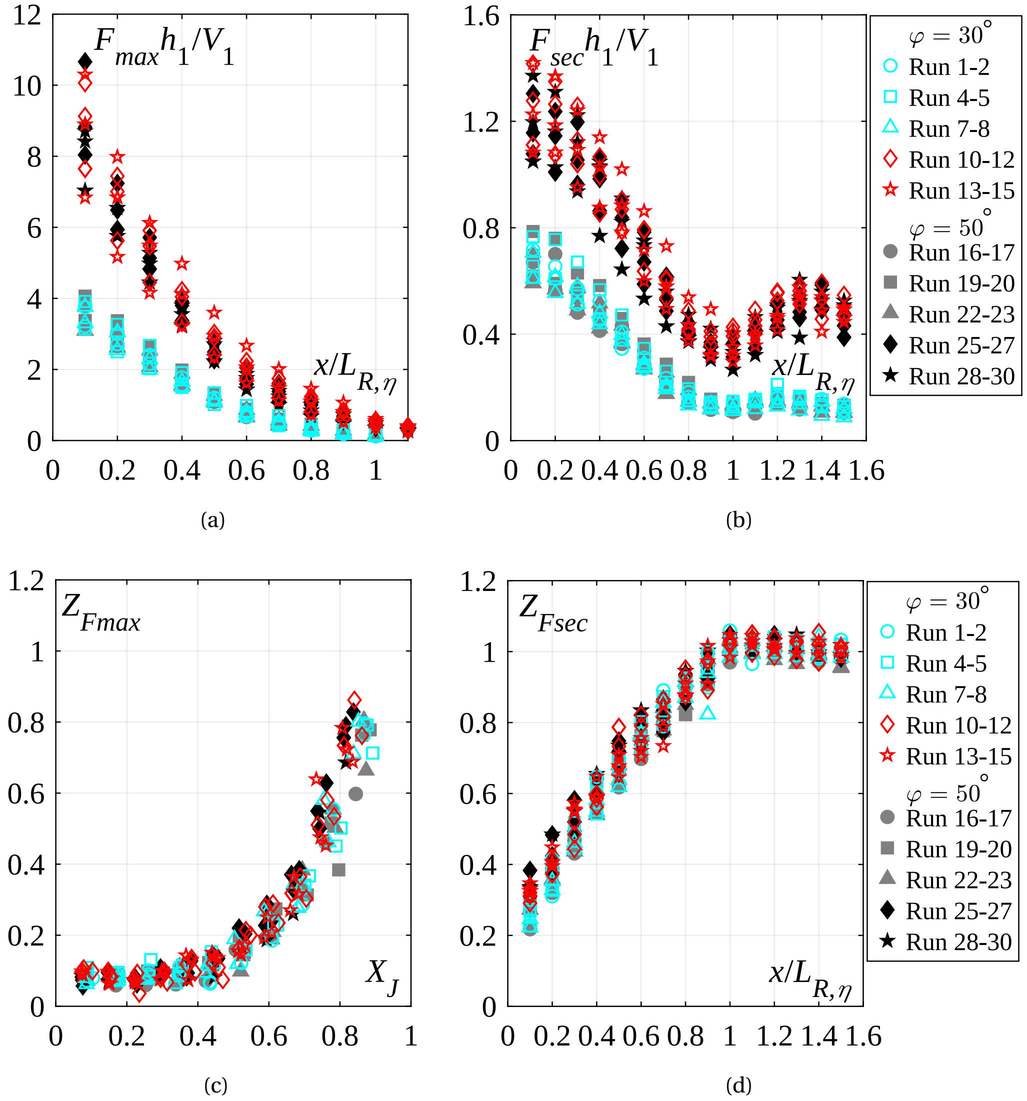

(a) (b)

(c) (d)

Figure 6.35 – Streamwise development of (a) dimensionless maximum air-phase frequency $F_{max}h_1/V_1$, (b) dimensionless secondary air-phase frequency $F_{sec}h_1/V_1$, (c) dimensionless vertical position of maximum air-phase frequency Z_{Fmax}, (d) dimensionless vertical position of secondary air-phase frequency Z_{Fsec}; [Runs 1-9: 30° smooth chute, Runs 10-15: 30° stepped chute, Runs 16-24: 50° smooth chute, Runs 25-30: 50° stepped chute].

Characteristic air-water flow depths

In Figure 6.36, the streamwise development of the dimensionless characteristic flow depth Z_{90} (Figure 6.36a) and dimensionless equivalent clear water depth Z_{cw} (Figure 6.36b) downstream of 30° and 50° smooth and stepped chutes are compared. Observing the latter figures, it can be clearly seen that chute slope φ has no major effect on the development of Z_{90} and Z_{cw}. As such, their streamwise development can be described with the relations developed for

30° smooth and stepped chute approach flows, i.e. Eqs. (5.17) and (5.18) for Z_{90} and Z_{cw}, respectively:

$$Z_{90} = 1.12\left(\frac{x}{L_{R,\eta}}\right)^{c} \qquad 30° \le \varphi \le 50° \qquad 0.1 \le \frac{x}{L_{R,\eta}} \le 1$$

$$Z_{cw} = \tanh\left(3X_J\right)^{4.4X_J - 0.65} \qquad 30° \le \varphi \le 50° \qquad 0.08 \le X_J \le 1.34$$

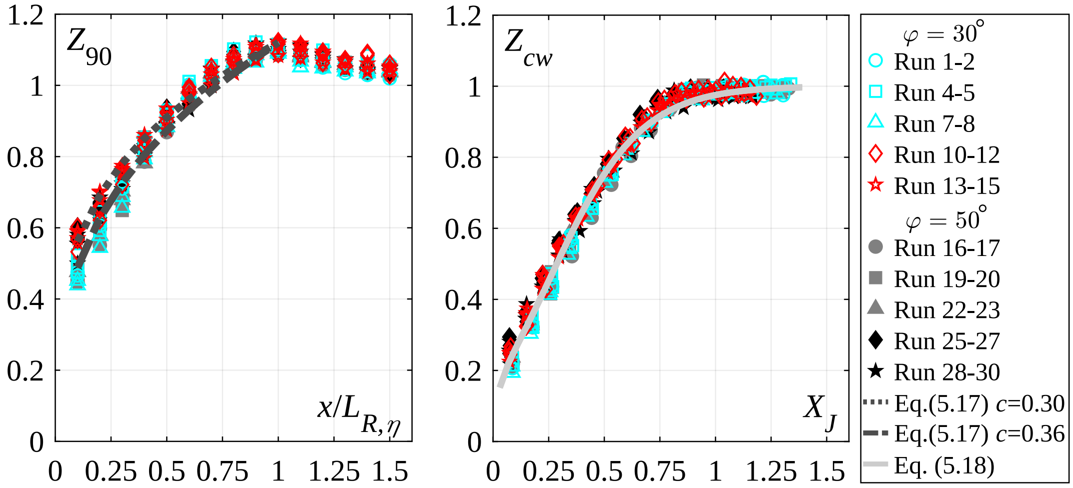

(a) (b)

Figure 6.36 – Streamwise development of (a) dimensionless characteristic flow depth Z_{90} and (b) dimensionless clear-water depth Z_{cw}; [Runs 1-9: 30° smooth chute, Runs 10-15: 30° stepped chute, Runs 16-24: 50° smooth chute, Runs 25-30: 50° stepped chute].

6.5.2 Vertical distribution of air-water flow velocity

Figure 6.37 shows typical streamwise development of dimensionless vertical velocity profiles V/V_1 along the stilling basin for 50° smooth chute (Run 22, Figure 6.37a) and stepped chute approach flows (Run 25, Figure 6.37b).

Within the *advective diffusive zone*, i.e. $x/L_{R,\eta} \le 0.8$, the velocity profiles have a self-similar shape, similar to wall jet flow (Rajaratnam 1965), including the high velocity boundary layer flow in the lower part of the flow, i.e. within $z < z_{V0}$, and flow reversal in the upper part of the flow within $z \ge z_{V0}$. The flow reversal is observed within $0 < x/L_{R,\eta} \le 0.8$, irrespective of the approach flow conditions. Further downstream, in the *air release zone* within $0.9 \le x/L_{R,\eta} \le 1.0$, the velocity profiles, similarly to the 30° chute approach flows (Figure 5.14), still tend to have a wall jet type profile. With the further increase in $x/L_{R,\eta}$, towards the tailwater zone, the velocity profiles transform into an open channel velocity distribution.

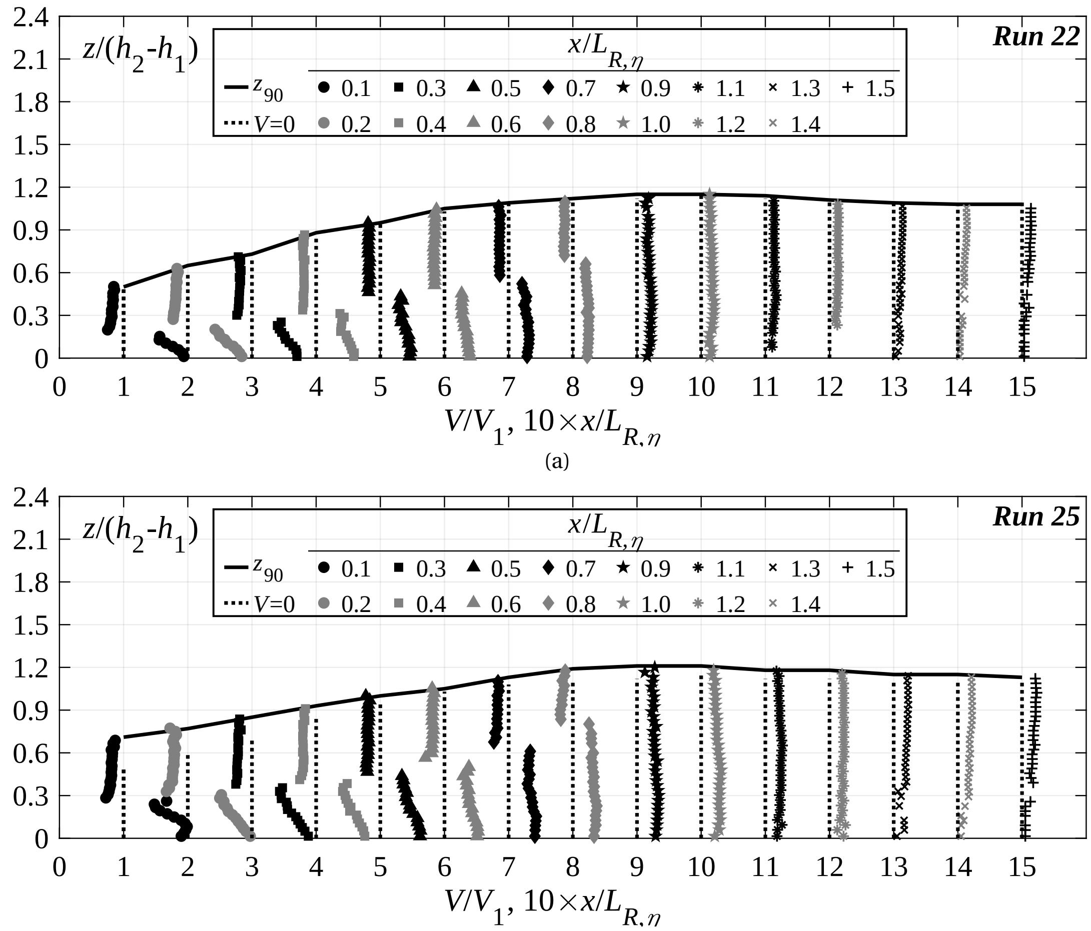

(a)

(b)

Figure 6.37 – Dimensionless vertical velocity distributions V/V_1 along the stilling basin for: (a) Run 22 (50° smooth chute) and (b) Run 25 (50° stepped chute).

In Figure 6.38a and b, the measured velocity profiles for 50° smooth and stepped chute approach flows in the advective diffusive zone are compared to the modified wall jet expressions of Chanson (2010) (i.e. Eqs. (5.11) and (5.12)), respectively. The measured velocity profiles show a good agreement with the latter equations. The exponent M in Eq. (5.11) is typically between 7 to 12. As such, no considerable effect of approach flow conditions or chute slope φ on the shape of the velocity profiles occurs.

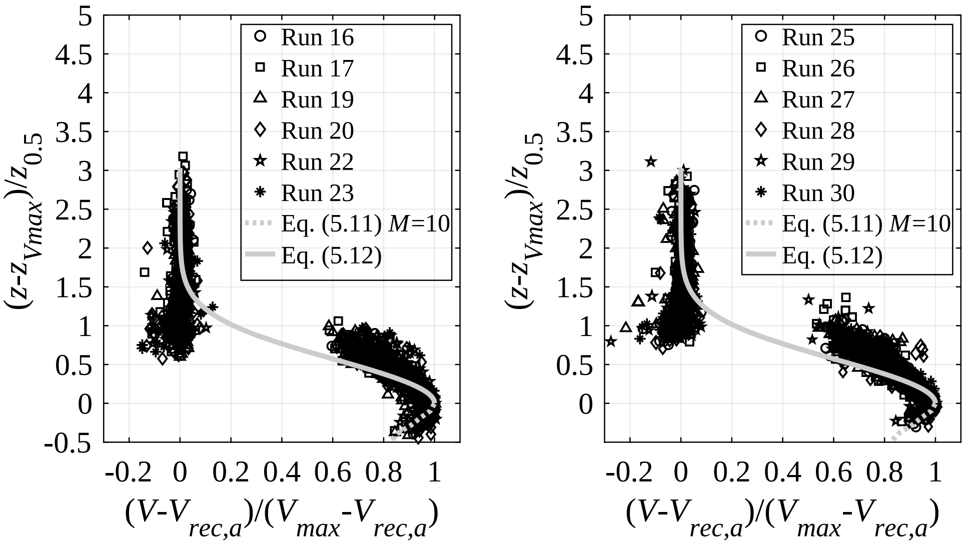

(a) (b)

Figure 6.38 – [Dimensionless vertical velocity distributions $(V - V_{rec})/(V_{max} - V_{rec})$ within advective diffusive zone for 50°: (a) smooth chute and (b) stepped chute approach flows; [Runs 16-24: 50° smooth chute, Runs 25-30: 50° stepped chute].

In Figure 6.39c to f, the streamwise development of dimensionless maximum velocity $(V_{max} - V_2)/(V_2 - V_1)$ (Figure 6.39c), elevation of maximum velocity Z_{Vmax} (Figure 6.39d), mean recirculation velocity $(|V_{rec,a}| - V_2)/(V_1 - V_2)$ (Figure 6.39e) and elevation of flow reversal onset Z_{V0} (Figure 6.39f) downstream of 30° and 50° smooth and stepped chutes are compared. It can concluded that the approach flow conditions or chute slope φ have no major effect. As such, the velocity distribution in the stilling basin is practically independent of the approaching chute slope φ. Therefore, the previously listed dimensionless parameters can be described with the equations developed for 30° sloping chutes, namely Eqs. (5.13), (5.14), (5.15) and (5.16) for dimensionless maximum velocity $(V_{max} - V_2)/(V_2 - V_1)$, elevation of maximum velocity Z_{Vmax}, mean recirculation velocity $(|V_{rec,a}| - V_2)/(V_1 - V_2)$ and elevation of flow reversal onset Z_{V0}, respectively:

$$\frac{V_{max} - V_2}{V_1 - V_2} = 1.1 - \tanh\left(2.5X_J\right)^{1.5} \qquad 30° \le \varphi \le 50° \qquad 0.08 \le X_J \le 1.34$$

$$Z_{Vmax} = 0.021 - \sin\left(1.33X_J\right)^{5.7+X_J} \qquad 30° \le \varphi \le 50° \qquad 0.08 \le X_J \le 1.1$$

$$\frac{|V_{rec,a}| - V_2}{V_2 - V_1} = 1.05 - \tanh\left(2.54\frac{x}{L_{R,\eta}}\right)^{x/L_{R,\eta}-0.02} \qquad 30° \le \varphi \le 50° \qquad 0.1 \le \frac{x}{L_{R,\eta}} \le 0.8$$

$$Z_{V0} = 0.15\exp\left(1.96\frac{x}{L_{R,\eta}}\right) \qquad 30° \le \varphi \le 50° \qquad 0.1 \le \frac{x}{L_{R,\eta}} \le 0.8$$

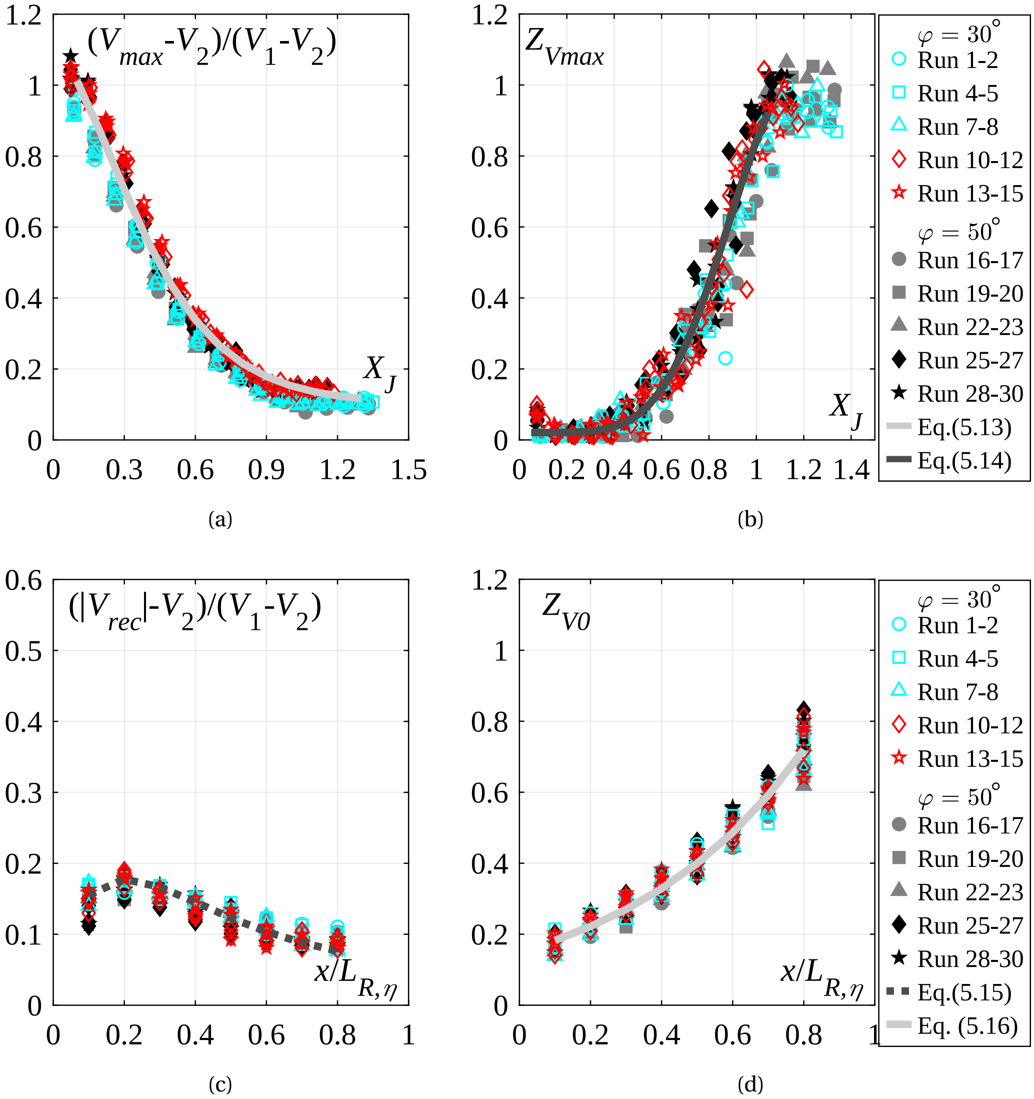

(a) (b)

(c) (d)

Figure 6.39 – Streamwise development of dimensionless: (a) maximum velocity $(V_{max} - V_2)/(V_2 - V_1)$, (b) elevation of maximum velocity Z_{Vmax}, (c) mean recirculation velocity $(|V_{rec,a}| - V_2)/(V_1 - V_2)$, and (d) elevation of flow reversal onset Z_{V0}; [Runs 1-9: 30° smooth chute, Runs 10-15: 30° stepped chute, Runs 16-24: 50° smooth chute, Runs 25-30: 50° stepped chute].

6.6 Conclusions

The effect of the chute slope on the performance and flow characteristics of a plain stilling basin downstream of smooth and stepped chutes is addressed in the present chapter. The following conclusions may be drawn:

Flow depths

- The sequent depth ratio and thus the required tailwater depth, can be estimated with the momentum principle by using the clear water parameters at the chute end, irrespective of the chute slope (i.e. φ=30° or 50°).
- The dimensionless mean flow depths Z over the jump roller are practically independent of the chute slope φ. Dimensionless flow depths Z downstream of stepped chutes are higher in magnitudes within first half of the roller, as compared to those downstream of smooth chutes.
- The streamwise development of surface fluctuation coefficient C_H' is mostly not influenced by the approach flow conditions or chute slope φ, indicating that the surface fluctuations η' are mainly governed by the approach flow kinetic energy.

Length characteristics

- The dimensionless roller lengths L_R/h_2 are virtually independent of the approach flow conditions or chute slope φ. Depending on definition, they can be estimated as L_R=4.6h_2 (stagnation point) or L_R=5.0h_2 (surface maximum).
- The dimensionless hydraulic jump lengths L_J/h_2, deduced based on criteria established in Chapter 4, are not dependent on the chute slope φ. These results undoubtedly show that hydraulic jumps initiated with stepped chute approach flows require an increased distance x/h_2, namely L_J=6.73h_2 and L_J=5.77h_2 for 50° sloping stepped and smooth chute approach flows, respectively.

Bottom pressure characteristics

- Steeper chute slopes pronounce mean pressure magnitudes within the flow deflection zone due to the stronger flow curvature.
- The effect of chute slope φ on the mean bottom pressure distribution is more pronounced downstream of stepped chute approach flows, as compared to smooth chute approach flows. The streamwise position of the maximum mean pressures after 50° stepped chutes is observed further downstream, i.e. at $X_J \approx$0.04, as compared to 30° stepped chute approach flow at $X_J \approx$0. This is caused by the smaller impact area of

the internal jet close to the jump toe. Further downstream, within $0.04 < X_J \leq 0.18$, the mean pressures after 50° sloping stepped chutes decrease in a similar manner as after 30° chute, however with higher magnitudes caused by stronger flow curvature. The mean pressures reach a local minimum at $X_J \approx 0.18$, beyond which they coincide with 30° sloping stepped chute approach flow magnitudes. The pronounced mean pressure magnitudes P_m within $X_J \leq 0.18$ for 50° sloping stepped chute approach flows can be estimated using Eq. (6.1), whereas further downstream, i.e. $X_J > 0.18$, the equation developed for 30° sloping chutes can be used, i.e. Eq. (4.5).

- The fluctuation C_P', extreme maximum $C_P{}^{max}$ and extreme minimum $C_P{}^{min}$ pressure coefficients for smooth chute approach flows are independent of the approach flow conditions or chute slope φ.

- 50° stepped chute approach flows exhibit higher extreme and fluctuating pressure coefficients within $X_J \leq 0.13$, as compared to both 30° stepped and 50° smooth chute approach flows. As a results of a relative downstream shift of the flow deflection point, the maximum extreme and pressure fluctuations for 50° chute occurs further downstream ($X_J \approx 0.04$), as compared to the 30° chute ($X_J \approx 0$). At this point, up to 2 times higher $C_P{}'$ magnitudes are observed, as compared to those of 30° chute at the flow deflection point ($X_J \approx 0$), reaching up to $C_P{}'=0.15$. Furthermore, the extreme positive and negative pressure coefficients are up to two times higher, with values reaching up to $C_P{}^{max}=1.26$ and $C_P{}^{min}=0.6$. These values are up to 3 times higher, when compared to smooth chute approach flows. Apart from the flow deflection point, the 50° sloping stepped chutes tend to increase the extreme positive and pressure fluctuation coefficients at the jump toe as well, with up to 30% higher $C_P{}'$ and 40% higher $C_P{}^{max}$ magnitudes. The pressure coefficient $C_P{}^{min}$ at the jump toe is similar for 30° stepped and 50° smooth chute approach flows. Downstream of the flow deflection point ($X_J \approx 0.04$), the extreme and fluctuation coefficients monotonically decrease and reach the 30° sloping chutes magnitudes at $X_J \approx 0.13$, beyond which they coincide along the remaining downstream reach of the stilling basin.

- Pressure coefficients with 99.9% $C_P{}^{99.9}$ and 0.1 % $C_P{}^{0.1}$ probability exhibit similar streamwise development as the extreme pressures, but with typically two times lower magnitudes than the corresponding extreme maximum $C_P{}^{max}$ and minimum $C_P{}^{min}$ coefficients.

- The pronounced extreme $C_P{}^{max}$, $C_P{}^{99.9}$, $C_P{}^{min}$, $C_P{}^{0.1}$ and fluctuating $C_P{}'$ pressure coefficients within $X_J \leq 0.13$ for 50° stepped chute approach flows can be estimated using Eq. (6.3), whereas further downstream, i.e. $X_J > 0.13$, the equation developed for 30° smooth chute approach flows can be used, i.e. Eq. (4.6).

- The 50° smooth chute approach flows exhibit similar power spectrum density development as 30° smooth chute approach flows.

- Contrary to the 30° and 50° smooth chute approach flows, 50° stepped chute approach flows exhibit an increase of spectral content within $0.003 \leq X_J \leq 0.04$, which is caused by the downstream shift of the flow deflection point. Despite the significantly lower approach Froude number F_1, the stepped chute approach flow exhibit higher spectral content across all range of frequencies within $X_J \leq 0.04$, when compared to the 50° smooth chute approach flows. Similarly to the 30° stepped chutes, the higher participation of energy content at the high frequency range with stepped chute approach flows is observed, as compared to smooth chute approach flows. These results further strengthens the conclusions made in Chapter 4, that pronounced pressure magnitudes with stepped chute approach flows in the zone $X_J \leq 0.12$ are due to the higher, step induced, turbulence levels of the incoming flow, as compared to smooth chute approach flows. Significantly higher spectral content was observed with 50° stepped chute approach flows, as compared to 30° stepped chute approach flows. Moreover, at the flow deflection point, the decay of f^{-1} tend to expand to higher frequency ranges after 50° chutes (some 100 Hz), as compared to those after 30° chutes (some 50 Hz). This may be caused by the higher turbulence levels of the 50° stepped approach flows, pronouncing the pressure fluctuation coefficients within $X_J \leq 0.13$, as compared to 30° stepped chutes.

Air-water flow properties

- Air-water flow properties of the hydraulic jumps are mostly not affected by the chute slope φ. The main differences are observed with 50° stepped chute approach flows, for which slightly higher bottom air concentration values (on average 2%) are observed within $X_J \leq 0.4$, as compared to 30° sloping stepped chute approach flows. The pronounced bottom air concentration values with 50° sloping stepped chutes can be estimated using the Eq. (6.4).
- In terms of cavitation potential, stilling basins after 50° chutes share the same cavitation protection length with respect to bottom air concentration as 30° chutes. As such the pronounced extreme pressure magnitudes downstream of 50° sloping stepped chutes within $X_J \leq 0.13$ are expected not to pose danger in terms of cavitation.

7 Conclusions

In the last decades stepped spillways became engineering practice, mainly due to the advances in dam construction technology and extensive hydraulic investigations on stepped chute flows. Stepped chutes act as a continuous energy dissipater leading to a reduced residual energy at its end. Nevertheless, a properly designed energy dissipater is usually needed at their toe to govern safely the remaining energy. The stepped surface significantly alters the structure of the flow leading to higher turbulence levels, as compared to those of smooth chute flows (Amador et al. 2006). Despite the differences in the approach flow conditions, stilling basin designs developed for smooth chute approach flows are still used for stepped chute approach flows. To date, only a few studies tested the hydraulic behavior and performance of stilling basins in combination with stepped chutes. As such, the knowledge of the stilling basin performance downstream of stepped chutes is limited.

This research investigated the effect of stepped chute approach flows on the hydraulic performance of a plain stilling basin. Physical modeling was conducted using a relatively large-scale experimental facility of a smooth and stepped chute terminating in a plain stilling basin. The experimental campaign included both smooth and stepped chute approaches, allowing direct comparison of the basin performance. To address the influence of aerated inflows, approach flow aeration for smooth chute test runs was varied ($0.15 \leq C_1 \leq 0.37$). Furthermore, the chute angle was varied ($30° \leq \varphi \leq 50°$) to study its effect on the hydraulic behavior of the stilling basin. Experiments were conducted for various discharges ($0.198\text{m}^2/\text{s} \leq q \leq 0.364\text{m}^2/\text{s}$) and two step sizes, namely $s = 0.03$ and $s = 0.06$ m. The measuring campaign included collection of flow conditions at the chute end, dynamic bottom pressure and flow depths along the basin, and internal air-water flow properties of the hydraulic jump.

In what follows, the main findings of this research project are summarized and an outline for the future work on stilling basins downstream of stepped chutes is presented. Finally, a practical design example of a plain stilling basin downstream of a stepped chute is presented.

7.1 Results

The main conclusions of the preset research project are:

Flow depths

- The use of equivalent clear water parameters at the smooth or stepped chute end leads to a correct prediction of the sequent depth ratio h_2/h_1 using the momentum principle, irrespective of the chute slope φ. As such, the sequent depth ratio is independent of the approach flow conditions, for identical F_1.
- The flow depths η along the jump roller are self-similar in shape following Eq. (4.1). Dimensionless flow depths Z downstream of stepped chutes are higher in magnitudes within the first half of the roller, as compared to smooth chutes. They are independent of the chute slope φ.
- The flow depth fluctuations η' decrease in the streamwise direction with the maximum magnitudes close to the jump toe caused by intense splashing of the flow. The streamwise development of the flow depth fluctuation coefficient $C_H{}'$ along the hydraulic jump is independent of the approach flow conditions or chute slope φ, indicating that the surface fluctuations η' are mainly governed by the approach flow kinetic energy.

Length characteristics

- The dimensionless surface roller length L_R/h_2 is independent of the approach flow conditions or chute slope φ. Depending on the definition, the roller length can be estimated as L_R=4.6h_2 (stagnation point) or L_R=5.0h_2 (maximum flow depth).
- Novel criteria for the hydraulic jump length L_J are proposed based on (1) $L_{J,\eta'}$ reduction of flow depth fluctuations η', (2) $L_{J,p'}$ reduction of bottom pressure fluctuations p' and (3) $L_{J,SK}$ Gaussian-shaped pressure distribution with $S \approx 0$ and $K \approx 0$. The results show that the hydraulic jumps initiated after stepped chutes require an increased distance, namely L_J=6.7h_2, as compared to L_J =5.8h_2 after smooth chutes. No significant effect of chute slope on the dimensionless jump length occurs.

Bottom pressure characteristics

- The streamwise bottom mean pressure p_m distribution along the stilling basin is characterized by increased magnitudes within $X_J \leq 0.15$ and $X_J \leq 0.18$ for 30° and 50° sloping chutes, respectively. The increased magnitudes are caused by the jet impact and flow curvature and they are magnified with increasing chute slope. The streamwise position of the maximum mean pressures after 50° sloping stepped chutes is observed further downstream, i.e. at $X_J \approx 0.04$, as compared to 30° sloping stepped chute or 30° and

50° sloping smooth chute approach flows. The mean pressure distribution with 30° sloping smooth or stepped chutes can be estimated using the Eq. (4.5). The pronounced mean pressure magnitudes within $X_J \leq 0.18$ for 50° sloping stepped and smooth chute approach flows can be estimated using Eq. (6.1) and (6.2), respectively.

- Smooth chute approach flows exhibit typical bottom pressure fluctuation p' distribution downstream of the jump toe with maximum fluctuation coefficients of $C_P{}'$=0.05 at X_J=0.12. At the toe, pronounced magnitudes are observed, caused by the flow deflection, which tend to exceed the latter value. The streamwise distribution of extreme pressure coefficients $C_P{}^{max}$ and $C_P{}^{min}$ exhibit similar patterns. The maximum magnitudes downstream of the jump toe are $C_P{}^{max}$ =0.42 and $C_P{}^{min}$ =0.30 at $X_J \approx$0.12 and $X_J \approx$0.18, respectively. The coefficients are not influenced by inflow aeration or chute slope φ.

- Stepped chute approach flows exhibit pronounced extreme and fluctuating pressure coefficients in the upstream part of the stilling basin, as compared to smooth chute approach flows. The areal extent of the pronounced magnitudes increase with increasing chute slope, i.e. $X_J \leq$0.1 and $X_J \leq$0.13 for 30° and 50° stepped chute approach flows, respectively. Their magnitudes increase with increasing chute slope, as well. Within this zone, the pressure fluctuation coefficients $C_P{}'$ are up to 3 times higher, as compared to smooth chute approach flows, reaching up to $C_P{}'$=0.15. The extreme positive and negative pressures are also up to three times higher, with values reaching up to $C_P{}^{max}$=1.26 and $C_P{}^{min}$=0.6. The pressure coefficients are independent of the relative critical depth ($2.7 \leq h_c/s \leq 7.94$).

- Pressure coefficients with 99.9% $C_P{}^{99.9}$ and 0.1% $C_P{}^{0.1}$ probability exhibit similar streamwise development as the extreme pressures, but with typically two times lower magnitudes than the corresponding extreme maximum $C_P{}^{max}$ and minimum $C_P{}^{min}$ coefficients.

- The streamwise distribution of fluctuating and extreme pressure coefficients for smooth chute approach flows can be estimated with Eq. (4.6) for $X_J \geq$0.03. The same equation can be used for stepped chute approach flows for X_J>0.1 and X_J>0.13 with 30° and 50° sloping stepped chutes, respectively. The pronounced magnitudes with 30° ($X_J \leq$0.1) and 50° ($X_J \leq$0.13) sloping stepped chute approach flows can be estimated with Eqs. (4.7) and (6.3), respectively.

- The spectral analysis of the pressure fluctuations provided additional information on the flow features. Dominant frequencies are in range of 0.5-18 Hz and 0.4-7 Hz with smooth and stepped chute approach flows, respectively. Higher spectral energy participation at high frequency ranges is found for stepped chute approach flows within $X_J \leq$0.10 and $X_J \leq$0.13 for 30° and 50° stepped chute approach flow, respectively, indicating that the pronounced pressure coefficients in this zone are likely caused by the higher, step induced, turbulence levels of the incoming flow, as compared to smooth chute approach flows. The latter is more pronounced with 50° sloping stepped chute approach flows, suggesting that the increased pressure magnitudes with 50° sloping stepped chutes are caused by relatively higher turbulence levels of the approaching flow, as compared to 30° sloping stepped chutes.

Air-water flow properties

- The air-water flow measurements indicate two main flow zones, namely advective diffusive zone along $0.1 \leq x/L_{R,\eta} \leq 0.8$, and air release zone along $x/L_{R,\eta} \geq 0.9$, irrespective of the chute slope or approach flow conditions.
- The advective diffusion model of Chanson (1995) for classical hydraulic jumps well reproduce the air concentration profiles in the advective diffusive zone. However, the obtained dimensionless turbulent diffusivities $D_t{}^s(V_1 h_1)^{-1}$ and $D_t{}^r(V_1 h_1)^{-1}$ are considerably higher than those reported for classical hydraulic jumps with partially developed approach flows.
- Air concentration profiles are mostly independent of the approach flow conditions within $0.1 \leq x/L_{R,\eta} \leq 0.3$. The major differences occur in the vicinity of the bottom, where significantly higher air concentration values occur after stepped chutes, as compared to those after smooth chutes. Moreover, smooth chute approach flows show a slightly higher de-aeration rate in the shear layer region. Further downstream, i.e. $x/L_{R,\eta} \geq 0.4$ smooth chute approach flows exhibit significantly higher de-aeration rate, confirming the jump length measurements. The air concentration profiles are independent of the chute slope φ, approach flow aeration C_1 for smooth chute approach flows or step size s $(2.7 \leq h_c/s \leq 7.94)$ for stepped chute approach flow.
- Inclined (30° or 50° chute) approach flows induce significantly higher flow aeration in the lower part of the shear layer region and close to the bottom, i.e. $z < z_{max}$, compared to classical hydraulic jumps.
- Smooth chute approach flows are characterized by a sharp rise of the bottom air concentration with maximum values of C_b=0.11 at $X_J \approx 0.17$, followed by a gradual decrease towards zero values at $X_J \geq 0.9$. The bottom air concentrations are not influenced by the chute slope φ or approach flow aeration C_1 and can be estimated using Eq. (5.7).
- Stepped chute approach flows exhibit pronounced increased air concentration values within $X_J \leq 0.4$, as compared to smooth chute approach flow. The bottom air concentrations are up to 3.5 times higher in the vicinity of the toe, i.e. $X_J \approx 0.08$, reaching values up to C_b=0.18. Further downstream, they decrease in a linear manner and coincide with smooth chute approach flow values at $X_J \geq 0.4$. Slightly higher bottom air concentration values within $X_J \leq 0.4$ are observed with 50° sloping chutes (on average 2%) as compared to 30° sloping chutes. The bottom air concentrations values are not influenced by the step size s. Within $X_J \leq 0.4$ they can be estimated using Eqs. (5.8) and (6.4) for 30° and 50° stepped chutes, respectively. Further downstream, they can be estimated using Eq. (5.7).

- The present experimental results suggest that plain stilling basins with smooth chute approach flows are expected to be exempted from cavitation damage within $0.1 \leq X_J \leq 0.4$ and $0.15 \leq X_J \leq 0.5$ for 5% and 8% bottom air concentration limits to avoid cavitation damage, respectively. In these terms, stepped chute approach flows provide additional air and the plain stilling basins are expected to be protected from cavitation damage within $0 \leq X_J \leq 0.4$ and $0 \leq X_J \leq 0.5$ for 5% and 8% bottom air concentration limits, respectively. As such the increased extreme pressure coefficients with stepped chute approach flows within $X_J \leq 0.13$ are expected not to pose danger in terms of cavitation damage.

- The air-phase frequency profiles in the advective diffusive zone exhibit a typical shape with a major peak F_{max} in the shear layer region and a secondary peak F_{sec} in recirculation region. Further downstream, in the air release zone, the profiles tend to transform into monotonically increasing profiles from the channel invert, where F_{max} disappears.

- The magnitudes of the air-phase frequency are mainly affected by stepped chute approach flows. Similar magnitudes are observed for 30° and 50° sloping chutes.

- Velocity profiles in the advective diffusive zone exhibit a self-similar shape including a high velocity boundary layer flow in the lower part of the flow and flow reversal in the upper part of the flow. The flow reversal occurs within $0.1 \leq x/L_{R,\eta} \leq 0.8$ irrespective of the approach flow conditions or chute slope φ. The modified wall jet expressions of Chanson (2010) describe well the velocity profiles in the advective diffusive region for both approach flow conditions and chute slopes.

- In the air release zone, within $0.9 \leq x/L_{R,\eta} \leq 1.0$, the velocity profiles still tend to exhibit a wall jet type profile. Further downstream, towards the tailwater, they transform into open channel flow velocity distribution.

- The maximum velocities V_{max} decay in an exponential manner and are practically independent of the approach flow conditions or chute slope. They can be estimated using Eq. (5.13).

- The streamwise development of depth averaged recirculation velocities $V_{rec,a}$ show a slight increase within $0.1 \leq x/L_{R,\eta} \leq 0.2$, followed by a gradual decrease towards the end of the advective diffusive zone, where flow reversal disappears. They can be estimated using Eq. (5.15), irrespective of the approach flow conditions or chute slope.

- The characteristic flow depths z_{90} along the jump roller are self-similar in shape following Eq. (5.17). The mean flow depths η recorded with a US sensor corresponds to a range of characteristic flow depths between $z_{70} \leq \eta \leq z_{90}$ for $0.1 \leq x/L_{R,\eta} \leq 0.6$, and $z_{50} \leq \eta \leq z_{70}$ for $x/L_{R,\eta} \geq 0.6$.

- The development of the equivalent clear-water depth z_{cw} show a monotonic increase in the streamwise direction, reaching quasi-constant values in the tailwater zone. They coincide with the mean pressure heads p_m at $X_J \approx 0.5$, showing that the influence of the highly turbulent bottom jet flow is greatly diminished. The streamwise development of the dimensionless equivalent clear-water depth Z_{cw} can be estimated using Eq. (5.18), irrespective of the approach flow conditions or chute angle φ.

7.2 Design recommendations

The following recommendation should be considered in the design of stilling basins downstream of stepped chutes:

- Longer dimensionless "classical" (plain) stilling basin lengths are required downstream stepped chutes, as compared to the basins preceded by smooth chute invert approach. Considering some uncertainties, a minimum basin length of $7h_2$ is recommended for the design flood downstream of stepped chutes. Nevertheless, to ensure appropriate performance for the safety flood, a safety factor has to be applied for the design flood.
- Special care should be taken when designing stilling basin slabs and joints in the zone of $X_J \leq 0.13$, as stepped chute approach flows significantly pronounce the fluctuating and extreme pressures compared to smooth chute approach flows.
- Empirical formulae for predicting flow depth, bottom pressure and air-water flow characteristics along the stilling basin downstream of both smooth and stepped chute approach flows, were developed (i.e. Eqs. (4.1), (4.2), (4.3), (4.4), (4.5), (4.6), (4.7), (5.3), (5.4), (5.5), (5.6), (5.7), (5.8), (5.10), (5.13), (5.14), (5.15), (5.16), (5.17), (5.18), (6.1), (6.2), (6.3) and (6.4)). These empirical relations can be used for the design of plain stilling basin downstream of stepped chutes for a range of relative critical depths $2.7 \leq h_c/s \leq 7.94$ (i.e. for $6.45\ \mathrm{m}^2/\mathrm{s} \leq q \leq 11.51\mathrm{m}^2/\mathrm{s}$ considering a scale factor of 1:10) and chute angles $30° \leq \varphi \leq 50°$.

7.3 Outlook

The following topics could be addressed in future research to further expand the knowledge on stilling basin performance downstream of stepped chutes:

- The present research project investigated two chute angles, namely $\varphi = 30°$ and $\varphi = 50°$ which are typical for the downstream face of embankment and RCC dams, respectively. The tested range of relative critical depth was $2.7 \leq h_c/s \leq 7.94$, corresponding to prototype unit discharge range of $6.45\ \mathrm{m}^2/\mathrm{s} \leq q \leq 11.51\ \mathrm{m}^2/\mathrm{s}$ when considering a scale factor of 1:10. Future research projects could investigate milder slopes, a broader range of relative critical depths and unit discharges.
- The present study focused on aerated stepped chute approach flow conditions. Future investigations could investigate the performance of stilling basins with non-aerated,

developing approach flow conditions, typically encountered at the end of embankment dams with very mild slope or small RCC dams.

- The present study focused only on a plain stilling basin. Other standardized stilling basin types, such as USBR type II and III or a stilling basin with an end sill, could be addressed in future investigations.
- The pressure measurements in the present study were only performed in the stilling basin centerline. Spatial pressure measurements, especially in the zone of the pronounced pressure magnitudes, would be of great interest to asses the areal extent of pressure pulses, needed for the computation of the hydrodynamic loading acting on the slabs.

7.4 Design example

To demonstrate the obtained results, a practical design example of a plain, prismatic and rectangular stilling basin downstream of a smooth and stepped chute is presented. The stilling basin is designed downstream of a 50 m high dam spillway equipped with a standard ogee crest and a 200 m wide prismatic and rectangular smooth or stepped chute integrated into its downstream face (Figure 7.1). The spillway is designed for a design discharge of Q_d=2500 m^3/s. In the case of a stepped chute, a step height of s=0.90 m is considered.

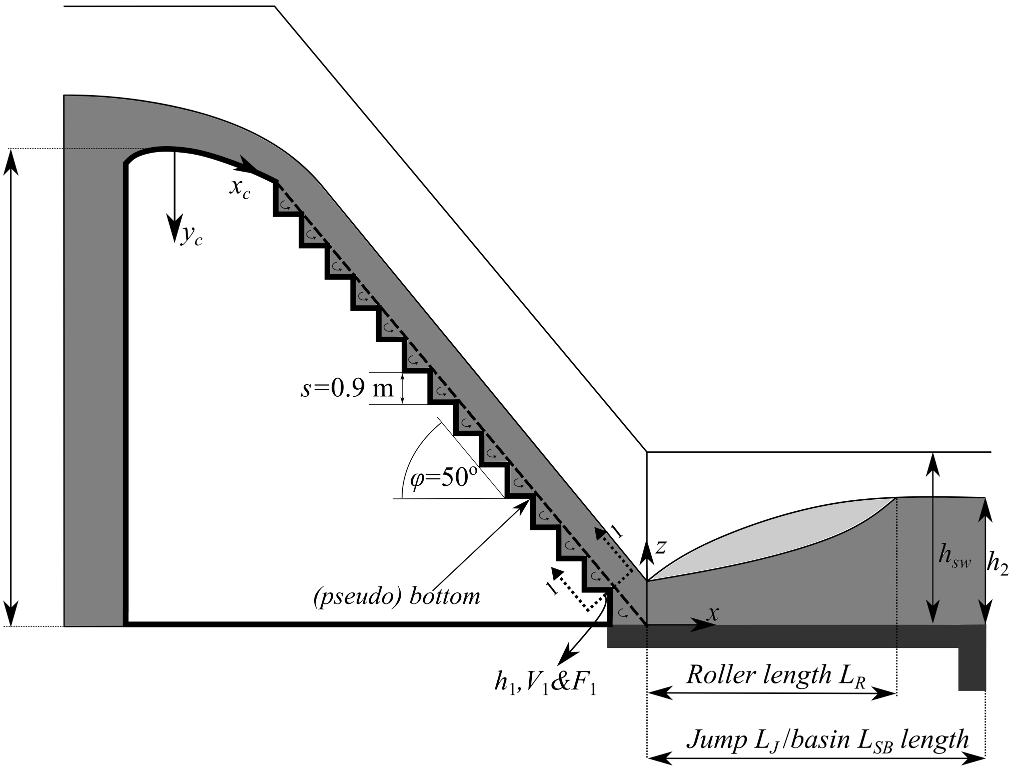

Figure 7.1 – General definition scheme of the design example.

7.4.1 Approach flow conditions

In order to design the stilling basin, the approach flow conditions (i.e. flow conditions at the chute end), have to be first calculated. In the following, the flow conditions at smooth and stepped chute end for a design unit discharge of $q_d = Q_d/B = 12.5\text{m}^2/\text{s}$ are calculated.

Stepped chute

First, the flow regime that is expected to occur over the stepped chute has to be identified. For the given unit discharge $q_d = 12.5\text{m}^2/\text{s}$, considering a rectangular and prismatic channel, the critical flow depth is:

$$h_c = (q_d^2/g)^{1/3} = 2.52 \text{ m}.$$

Considering the step high of s=0.90 m, the relative critical depth is then $h_c/s = 2.80$. This value is roughly 3.5 larger than the relative critical depth for the onset of skimming flow regime $(h_c/s)_s$ according to Chanson (2015b):

$$(h_c/s)_s = \frac{0.881}{s/l + 0.149^{0.317}} = 0.80 \tag{7.1}$$

where $l = s/\tan\varphi = 0.76$ m is the step length. As such the stepped chute will operate in the ***skimming flow regime***.

As skimming flow will occur over the stepped chute, the flow region that will take place at the chute end has to be then identified in order to calculate the inflow conditions. The distance between the stepped spillway crest and the inception point of air entrainment L_i can be obtained from Meireles et al. (2012):

$$L_i = 6.75 s\cos\varphi \left(\frac{q_d}{\sqrt{g \sin\varphi \left(s\cos\varphi\right)^3}} \right)^{0.76} = 23.09 \text{ m}. \tag{7.2}$$

As the dam spillway height H_{dam}=50 m is significantly larger than the vertical distance between the spillway crest and the inception point of air entrainment $y_{c,i} \approx L_i \sin\varphi$=17.68 m, aerated flow conditions will occur at the stepped chute end.

The vertical distance between the spillway crest and the location where quasi uniform flow conditions are attained can be obtained from Boes and Hager (2003a), i.e. Eq. (2.5):

$$H_{dam,u} \approx 24 h_c (\sin\varphi)^{2/3} \approx 50.55 \text{ m}$$

which is approximately equal to the dam spillway height of H_{dam}=50 m. Therefore, ***quasi-uniform flow conditions*** will be attained at the stepped chute end.

The equivalent clear-water depth at the stepped chute end for quasi-uniform flow conditions, i.e. the approach flow depth h_1, can be thus obtained from Boes and Hager (2003a):

$$h_1 = h_c 0.215 (\sin\varphi)^{-1/3} = 0.59 \text{ m} \tag{7.3}$$

yielding the inflow mean water velocity of $V_1 = q_d / h_1 = 21.14$ m/s and inflow Froude number of $F_1 = q_d / (g h_1)^{0.5} = 8.78$.

Smooth chute

In order to calculate the approach flow conditions, the flow region that is expected to occur at the smooth chute end has to be first identified. The distance between the smooth spillway crest and the inception point of air entrainment L_i can be obtained from Wood et al. (1983):

$$L_i = 13.6 k_s \sin\varphi^{0.0796} \left(\frac{q_d}{\sqrt{g \sin\varphi {k_s}^3}} \right)^{0.713} = 63.48 \text{ m}. \tag{7.4}$$

where k_s =0.001 m is the concrete surface roughness. The vertical distance between the spillway crest and the inception point of air entrainment is then $y_{c,i} \approx L_i \sin\varphi = 48.1$ m. As the dam spillway height is H_{dam}=50 m, the inception point of air entrainment will occur approximately at the smooth chute end. Therefore the approach flow depth h_1, i.e. the flow depth at the inception point, can be obtained from Wood et al. (1983):

$$h_1 = k_s \frac{0.223}{\sin\varphi^{0.04}} \left(\frac{q}{\sqrt{g \sin\varphi {k_s}^3}} \right)^{0.643} = 0.46 \text{ m}. \tag{7.5}$$

giving the inflow mean water velocity of $V_1 = q_d / h_1 = 27.29$ m/s and inflow Froude number of $F_1 = q_d / (g h_1)^{0.5} = 12.88$.

7.4.2 Tailwater depth

The required tailwater depth h_2, to maintain the hydraulic jump within the stilling basin perimeter, can be calculated with Bélanger's equation, i.e. Eq. (2.38):

$$\frac{h_2}{h_1} = 0.5\left(\sqrt{1+8{F_1}^2}-1\right)$$

using the clear-water parameters at the chute end. The required tailwater depths are:

- h_2=6.76 m for the ***stepped chute***, and
- h_2=7.88 m for the ***smooth chute***.

Due to the significantly lower approach flow Froude number F_1 at the stepped chute end (i.e. lower approach flow kinetic energy), the required tailwater depth h_2 is lower downstream of a stepped chute, as compared to that downstream of a smooth chute, for the same unit discharge q_d, chute slope φ and dam spillway height H_{dam}.

In practice the required tailwater depth may not be available and a pooled stilling basin would have to be chosen.

7.4.3 Hydraulic jump, stilling basin and roller length

The hydraulic jump length L_J downstream of a ***stepped chute*** is calculated as:

$$L_J = 6.7h_2 = 45.25 \text{ m}$$

On the other hand, the hydraulic jump L_J length downstream of a ***smooth chute*** can be obtained from Peterka (1958), i.e. Figure (2.12):

$$L_J = 6.05h_2 = 47.70 \text{ m}.$$

Although hydraulic jumps downstream of a stepped chute require longer normalized distance L_J/h_2, due to the lower approach flow kinetic energy at the stepped chute end, the absolute value of the hydraulic jump length and thus the stilling basin length is smaller downstream of a stepped chute, as compared to that after a smooth chute, for the same unit discharge q_d, chute slope φ and dam spillway height H_{dam}.

Considering a safety factor of 1.2 for the design flood, the stilling basin lengths L_{SB} are:

- L_{SB}=1.2×L_J=54.3 m for the ***stepped chute***, and
- L_{SB}=1.2×L_J=57.2 m for the ***smooth chute***.

The roller length L_R can be calculated as:

$$L_R = 5.0h_2$$

resulting in:

- L_R=33.78 m for the ***stepped chute***, and
- L_R=39.42 m for the ***smooth chute***.

7.4.4 Flow depth development and sidewall height

The mean flow depth η development along the hydraulic jump roller $x \leq L_R$ (i.e. $x \leq 33.78$ m for stepped and $x \leq 39.42$ for smooth chute) can be obtained from Eq. (4.1):

$$\eta(x) = 1.07\left(\frac{x}{L_R}\right)^{0.32}(h_2 - h_1) + h_1 \qquad \textbf{\textit{for the stepped chute}}$$

$$\eta(x) = 1.07\left(\frac{x}{L_R}\right)^{0.39}(h_2 - h_1) + h_1 \qquad \textbf{\textit{for the smooth chute}}$$

The resulting developments of η are shown in Figures 7.2a and b for stepped and smooth chute, respectively.

They reach maximum values at the roller end of:

- η_{max}=7.19 m for the ***stepped chute***,
- η_{max}=8.40 m for the ***smooth chute***.

Further downstream, between the roller and the hydraulic jump end $L_R < x \leq L_J$ (i.e. $33.78 < x \leq 45.25$ m for stepped chute and $39.42 < x \leq 47.70$ m for smooth chute), the mean flow depths decrease and can be linearly interpolated between the maximum flow depth η_{max} at $x = L_R$ and tailwater depth h_2 at $x = L_J$ (Figures 7.2a and b).

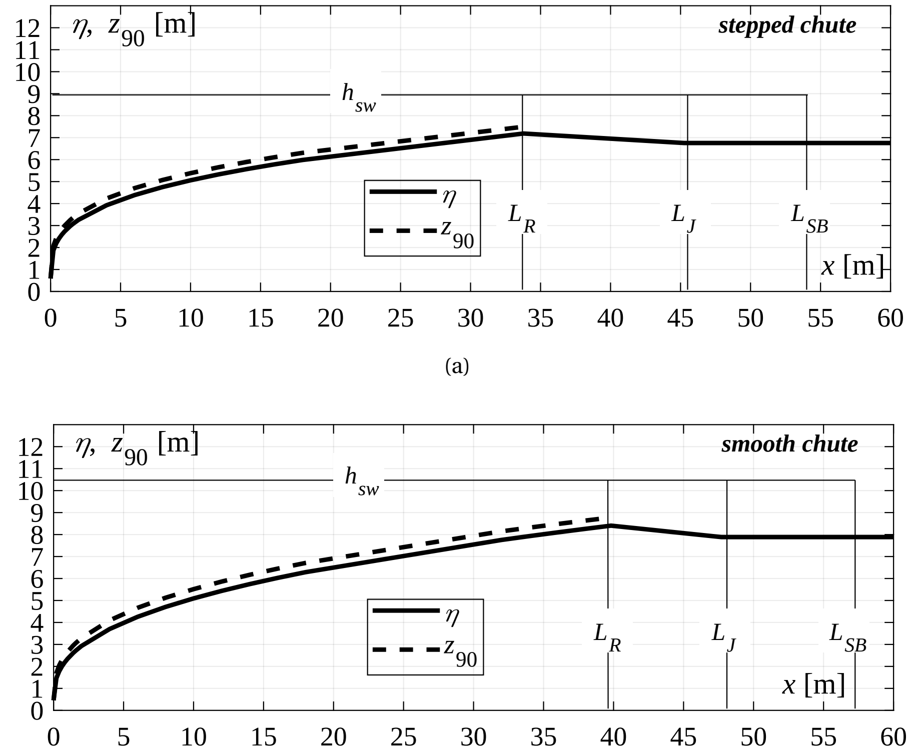

(a)

(b)

Figure 7.2 – Streamwise development of mean flow depth η and characteristic flow depth z_{90} along the stilling basin downstream of a: (a) stepped, and (b) smooth chute; q=12.5 m^2/s, $\varphi = 50°$ and $H_{dam} = 50$ m.

The development of characteristic flow depth z_{90} along the hydraulic jump roller, i.e. $x \leq L_R$, can be obtained from Eq. (5.17):

$$z_{90}(x) = 1.12\left(\frac{x}{L_R}\right)^{0.30}(h_2 - h_1) + h_1 \qquad \textbf{\textit{for the stepped chute}}$$

$$z_{90}(x) = 1.12\left(\frac{x}{L_R}\right)^{0.36}(h_2 - h_1) + h_1 \qquad \textbf{\textit{for the smooth chute}}$$

The resulting developments of the characteristic flow depth z_{90} is shown in Figures 7.2a and b for stepped and smooth chute, respectively. They reach maximum values at the roller end of:

- $z_{90,max}$=7.49 m for the ***stepped chute***,
- $z_{90,max}$=8.78 m for the ***smooth chute***.

Considering a safety factor of 1.2 for freeboard for spray development , the sidewall heights are then (Figures 7.2a and b):

- $h_{sw} = 1.2 \times z_{90,max}$=9.0 m for the ***stepped chute***,
- $h_{sw} = 1.2 \times z_{90,max}$=10.5 m for the ***smooth chute***.

7.4.5 Bottom pressure characteristics

The streamwise development of bottom mean pressure p_m, fluctuating pressure p', extreme maximum pressure p_{max}, pressure with 99.9% probability $p_{99.9}$, extreme minimum pressure p_{min} and pressure with 0.1% probability $p_{0.1}$ along the stilling basin downstream of a ***smooth chute*** can be obtained using Eqs. (4.5), (4.6) and (6.2):

$$
\begin{aligned}
p_m(x) &= \left(1.53 - \tanh\left(22\frac{x}{L_J}\right)^{40\frac{x}{L_J}}\right)(h_2 - h_1) + h_1 && 0.03 \le \frac{x}{L_J} \le 0.18\\
p_m(x) &= \left(\tanh\left(3.1\frac{x}{L_J}\right)^{5.9\frac{x}{L_J}-0.14}\right)(h_2 - h_1) + h_1 && \frac{x}{L_J} > 0.18\\
p'(x) &= \alpha\frac{V_1^2}{2g}\left(1.006 - \tanh\left(3.0\frac{x}{L_J}\right)^{0.31\frac{x}{L_J}+0.006}\right) && \frac{x}{L_J} \ge 0.03\\
p_{max}(x) &= p_m(x) + \alpha\frac{V_1^2}{2g}\left(1.035 - \tanh\left(3.41\frac{x}{L_J}\right)^{3.41\frac{x}{L_J}+0.06}\right) && \frac{x}{L_J} \ge 0.03\\
p_{99.9}(x) &= p_m(x) + \alpha\frac{V_1^2}{2g}\left(1.020 - \tanh\left(3.31\frac{x}{L_J}\right)^{1.60\frac{x}{L_J}+0.037}\right) && \frac{x}{L_J} \ge 0.03\\
p_{min}(x) &= p_m(x) - \alpha\frac{V_1^2}{2g}\left(1.020 - \tanh\left(2.52\frac{x}{L_J}\right)^{1.80\frac{x}{L_J}+0.01}\right) && \frac{x}{L_J} \ge 0.03\\
p_{0.1}(x) &= p_m(x) - \alpha\frac{V_1^2}{2g}\left(1.015 - \tanh\left(2.46\frac{x}{L_J}\right)^{0.79\frac{x}{L_J}+0.01}\right) && \frac{x}{L_J} \ge 0.03
\end{aligned}
$$

with energy correction coefficient of $\alpha = 1.08$. At the jump toe, i.e. $x = 0$, the bottom pressures for ***smooth chute*** are:

- the mean pressure $p_m(0) = 0.58\alpha\frac{V_1^2}{2g}$,
- the fluctuating pressure $p'(0) = 0.05\alpha\frac{V_1^2}{2g}$,
- the extreme maximum pressure $p_{max}(0) = p_m(0) + 0.32\alpha\frac{V_1^2}{2g} = 0.90\alpha\frac{V_1^2}{2g}$,
- the pressure with 99.9% probability $p_{99.9}(0) = p_m(0) + 0.16\alpha\frac{V_1^2}{2g} = 0.74\alpha\frac{V_1^2}{2g}$,

- the extreme minimum pressure $p_{min}(0) = p_m(0) - 0.32\alpha\frac{V_1^2}{2g} = 0.26\alpha\frac{V_1^2}{2g}$,
- the pressure with 0.1% probability $p_{min}(0) = p_m(0) - 0.16\alpha\frac{V_1^2}{2g} = 0.42\alpha\frac{V_1^2}{2g}$.

On the other hand, the streamwise development of bottom pressures along the basin downstream of a ***stepped chute*** can be obtained using Eqs. (4.5), (4.6), (6.1) and (6.3):

$$
\begin{aligned}
p_m(x) &= \left(1.53 - \tanh\left(30\frac{x}{L_J}\right)^{260\frac{x}{L_J}} - 0.15\right)(h_2 - h_1) + h_1 && \frac{x}{L_J} \leq 0.18\\
p_m(x) &= \left(\tanh\left(3.1\frac{x}{L_J}\right)^{5.9\frac{x}{L_J}-0.14}\right)(h_2 - h_1) + h_1 && \frac{x}{L_J} > 0.18\\
p'(x) &= \alpha\frac{V_1^2}{2g}\left(1.04 - \tanh\left(19\frac{x}{L_J}\right)^{6\frac{x}{L_J}}\right) && \frac{x}{L_J} \leq 0.13\\
p'(x) &= \alpha\frac{V_1^2}{2g}\left(1.006 - \tanh\left(3.0\frac{x}{L_J}\right)^{0.31\frac{x}{L_J}+0.006}\right) && \frac{x}{L_J} > 0.13\\
p_{max}(x) &= p_m(x) + \alpha\frac{V_1^2}{2g}\left(1.36 - \tanh\left(28\frac{x}{L_J}\right)^{154\frac{x}{L_J}+0.02}\right) && \frac{x}{L_J} \leq 0.13\\
p_{max}(x) &= p_m(x) + \alpha\frac{V_1^2}{2g}\left(1.035 - \tanh\left(3.41\frac{x}{L_J}\right)^{3.41\frac{x}{L_J}+0.06}\right) && \frac{x}{L_J} > 0.13\\
p_{99.9}(x) &= p_m(x) + \alpha\frac{V_1^2}{2g}\left(1.19 - \tanh\left(21\frac{x}{L_J}\right)^{31\frac{x}{L_J}+0.07}\right) && \frac{x}{L_J} \leq 0.13\\
p_{99.9}(x) &= p_m(x) + \alpha\frac{V_1^2}{2g}\left(1.020 - \tanh\left(3.31\frac{x}{L_J}\right)^{1.60\frac{x}{L_J}+0.037}\right) && \frac{x}{L_J} > 0.13\\
p_{min}(x) &= p_m(x) - \alpha\frac{V_1^2}{2g}\left(1.24 - \tanh\left(24\frac{x}{L_J}\right)^{28\frac{x}{L_J}-0.05}\right) && \frac{x}{L_J} \leq 0.13\\
p_{min}(x) &= p_m(x) - \alpha\frac{V_1^2}{2g}\left(1.020 - \tanh\left(2.52\frac{x}{L_J}\right)^{1.80\frac{x}{L_J}+0.01}\right) && \frac{x}{L_J} > 0.13\\
p_{0.1}(x) &= p_m(x) - \alpha\frac{V_1^2}{2g}\left(1.12 - \tanh\left(18\frac{x}{L_J}\right)^{10\frac{x}{L_J}-0.007}\right) && \frac{x}{L_J} \leq 0.13\\
p_{0.1}(x) &= p_m(x) - \alpha\frac{V_1^2}{2g}\left(1.015 - \tanh\left(2.46\frac{x}{L_J}\right)^{0.79\frac{x}{L_J}+0.01}\right) && \frac{x}{L_J} > 0.13
\end{aligned}
$$

with energy correction coefficient of $\alpha = 1.20$. The resulting streamwise development of bottom pressures are shown in Figures 7.3a and c for ***smooth chute*** and Figures 7.3b and d for ***stepped chute***.

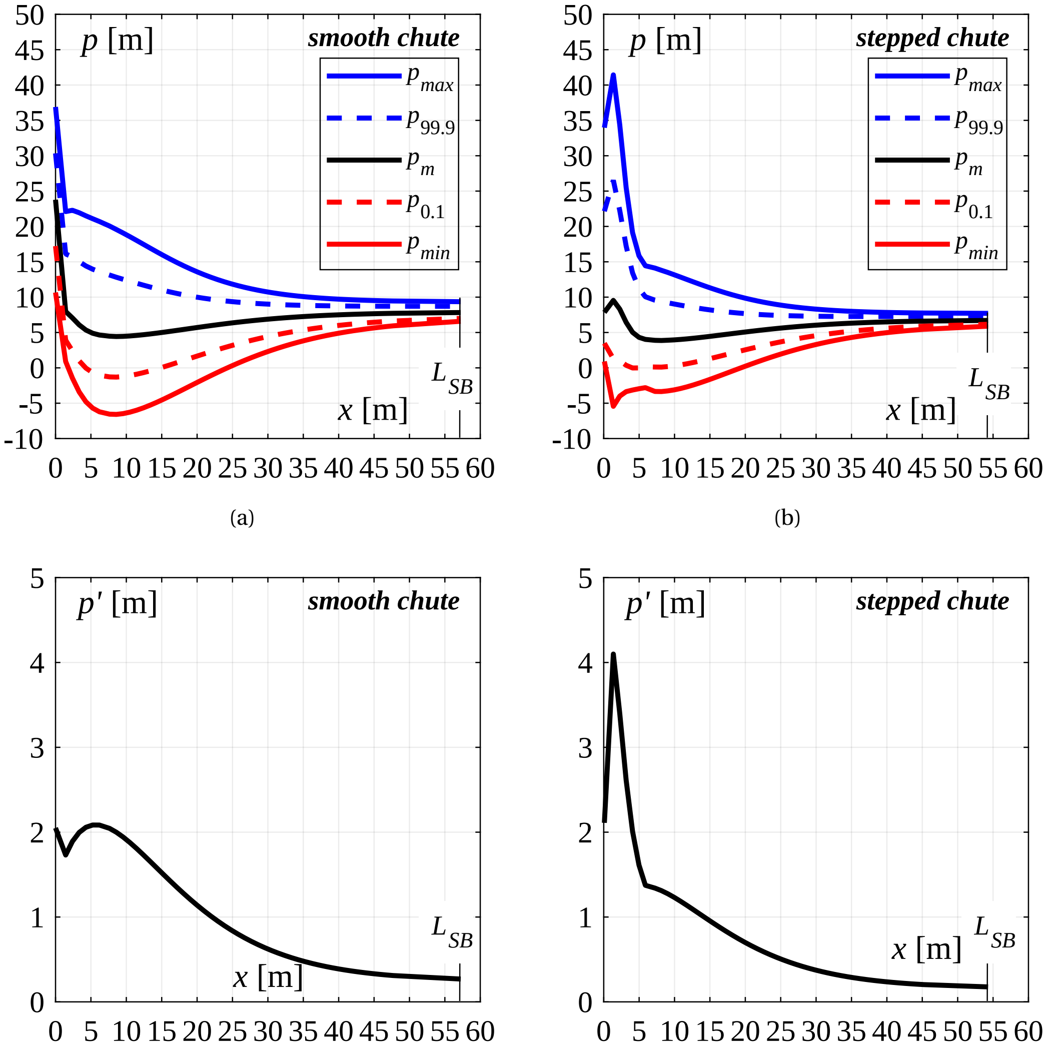

(a) (b) (c) (d)

Figure 7.3 – Streamwise development of bottom: (a) mean pressure p_m, extreme maximum pressure p_{max}, pressure with 99.9% probability p_{99}, extreme minimum pressure p_{min} and pressure with 0.1% probability $p_{0.1}$ for smooth chute, (b) mean pressure p_m, extreme maximum pressure p_{max}, pressure with 99.9% probability p_{99}, extreme minimum pressure p_{min} and pressure with 0.1% probability $p_{0.1}$ for stepped chute, (c) fluctuating pressure p' for smooth chute, and (d) fluctuating pressure p' for stepped chute; q=12.5 m^2/s, $\varphi = 50°$ and $H_{dam} = 50$ m.

Due to the significantly lower approach flow Froude number F_1 at the stepped chute end (i.e. lower approach flow kinetic energy), the bottom pressure magnitudes are mostly lower downstream of a stepped chute, as compared to that downstream of a smooth chute, for the same unit discharge q_d, chute slope φ and dam spillway height H_{dam} (Figure 7.3). As a result of increased turbulence at the stepped chute end, extreme and fluctuating pressures are higher downstream of a stepped chute within $x \leq 4.0$m. Nevertheless, minimum pressures are significantly higher than the vapor pressure $p_{vap} \approx -10$m, irrespective of the chute geometry (i.e. smooth or stepped chute). As such, stilling basins should not endangered by cavitation.

The streamwise developments of bottom pressure characteristics shown in Figure 7.3 can serve as an input for the design of stilling basin slabs and joints. The detailed procedure for the design of stilling basin slabs can be found in Fiorotto and Rinaldo (1992a), Pinheiro (1995), Fiorotto and Salandin (2000), Barjastehmaleki et al. (2016a) and Barjastehmaleki et al. (2016b).

A Recorded tailwater depth, roller and jump lengths

In the following table, all recorded tailwater depth h_2, measured $L_{R,\eta}$ and visually $L_{R,D}$ estimated roller length, and jump lengths from flow depth $L_{J,\eta'}$ and pressure measurements $L_{J,SK}$, $L_{J,p'}$ for are reported.

Table A.1 – Data of recorded tailwater depths h_2, roller lengths from flow depth measurements $L_{R,\eta}$ and visual observation $L_{R,D}$, jump lengths from flow depths $L_{J,\eta'}$, pressure measurements $L_{J,p'}$, and $L_{J,SK}$.

Test run	h_2 [m]	$L_{R,\eta}$ [m]	$L_{R,D}$ [m]	$L_{J,\eta'}$ [m]	$L_{J,p'}$ [m]	$L_{J,SK}$ [m]
1	0.501	2.500	2.250	2.850	2.740	2.850
2	0.620	3.100	2.840	3.550	3.440	3.640
3	0.729	3.700	3.380	4.100	4.010	4.100
4	0.496	2.500	2.280	2.840	2.880	2.940
5	0.603	3.100	2.800	3.650	3.460	3.540
6	0.722	3.700	3.420	4.000	4.010	4.180
7	0.518	2.500	2.340	2.980	2.930	2.960
8	0.632	3.100	2.930	3.800	3.515	3.600
9	0.748	3.700	3.470	4.320	4.010	4.300
10	0.401	2.000	1.860	2.800	2.615	2.650
11	0.503	2.600	2.400	3.400	3.320	3.540
12	0.604	3.200	2.800	4.050	4.010	4.100
13	0.404	2.000	1.820	2.800	2.780	2.700
14	0.516	2.600	2.430	3.400	3.360	3.400
15	0.618	3.200	2.840	4.200	4.010	4.120
16	0.526	2.600	2.400	3.100	2.970	3.010
17	0.643	3.200	2.930	3.830	3.750	3.510
18	0.749	3.800	3.490	4.260	-	4.250
19	0.522	2.600	2.380	3.180	3.100	3.160
20	0.634	3.200	2.950	3.550	3.650	3.700

Test run	h_2 [m]	$L_{R,\eta}$ [m]	$L_{R,D}$ [m]	$L_{J,\eta'}$ [m]	$L_{J,p'}$ [m]	$L_{R,SK}$ [m]
21	0.751	3.800	3.400	4.300	-	4.350
22	0.540	2.600	2.480	3.140	3.050	3.120
23	0.663	3.400	3.100	3.830	3.900	3.670
24	0.769	3.800	3.440	4.230	-	4.520
25	0.446	2.200	2.100	2.910	3.010	3.010
26	0.549	2.800	2.520	3.700	3.740	3.620
27	0.643	3.200	2.990	4.300	-	4.380
28	0.442	2.200	2.040	3.030	2.950	3.120
29	0.554	2.800	2.560	3.710	3.650	3.830
30	0.649	3.400	2.950	4.260	-	4.350

B Test-sheets

The main results of each experimental run are summarized in the following test-sheets. The deduced clear water parameters along with the characteristic flow depth y_{90} and velocity V_{90} are given in a table at the beginning of each test-sheet. The flow depth, bottom pressure and air-water flow data are presented graphically.

Test Run 1

φ = 30°
q=0.198 m^2/s
Configuration: Smooth R+PA

w [m]	C_1 [-]	y_{90} [m]	V_{90} [m/s]	h_1 [m]	V_1 [m/s]	α [-]	F_1 [-]	$R_1\times10^5$ [-]	W_1 [-]
0.26	0.32	0.045	7.02	0.031	6.47	1.09	11.8	1.98	133
0.46	0.31	0.044	6.95	0.031	6.45	1.09	11.8	1.98	133
0.66	0.31	0.045	6.76	0.031	6.34	1.09	11.4	1.98	131

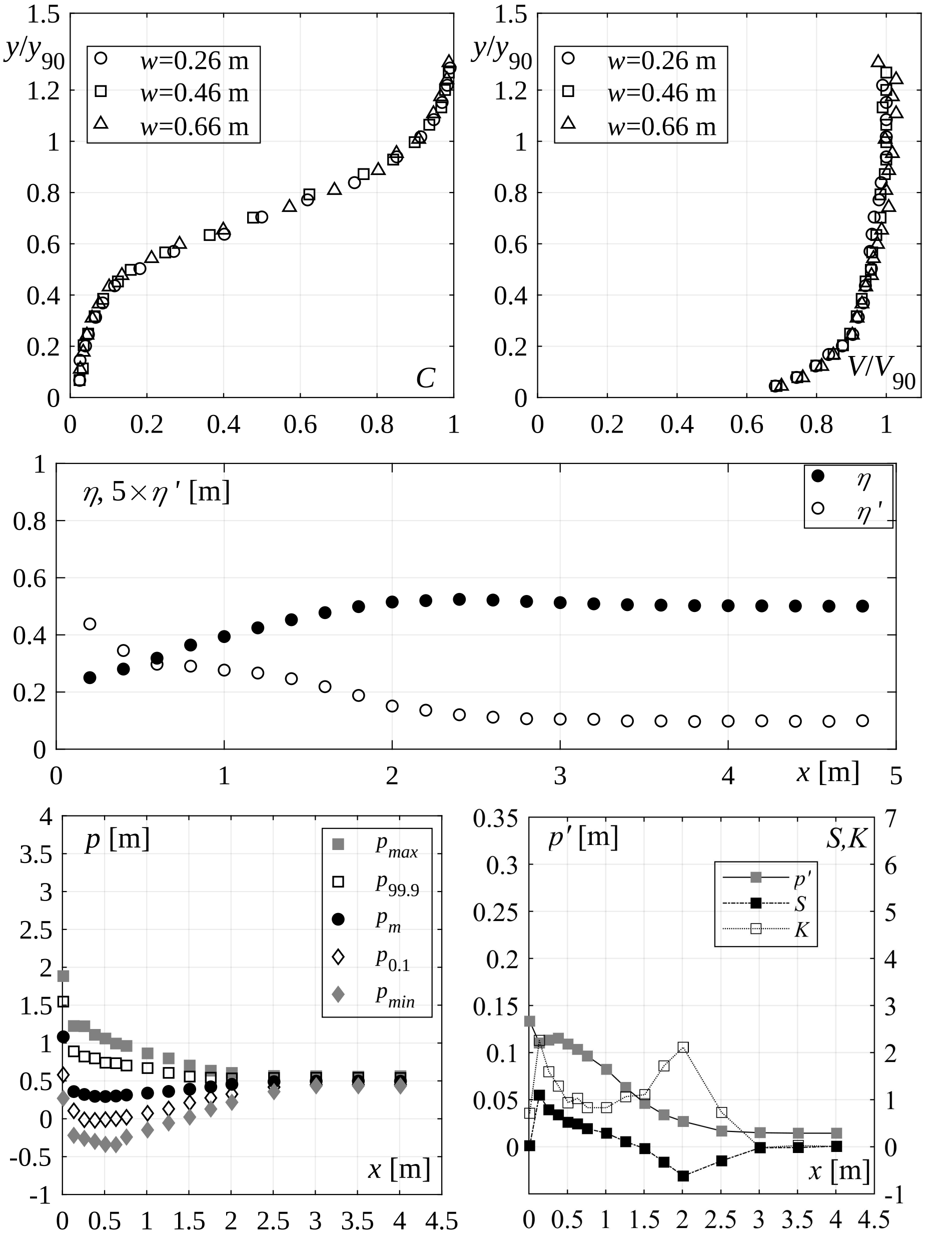

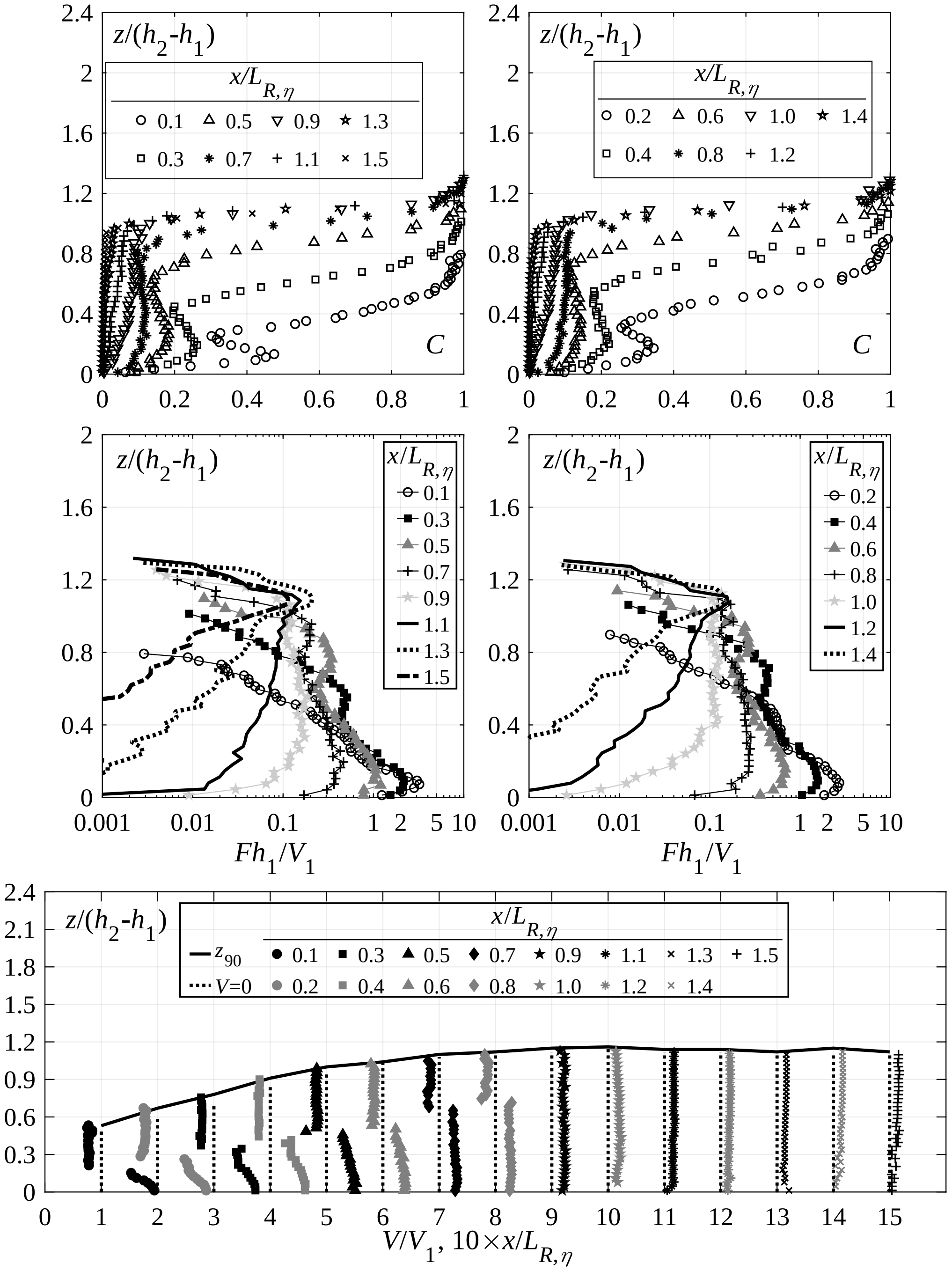
z/(h2-h1)
x/L_R,η
0.1 0.5 0.9 1.3
0.3 0.7 1.1 1.5
C
0 0.2 0.4 0.6 0.8 1
0 0.4 0.8 1.2 1.6 2 2.4
z/(h2-h1)
x/L_R,η
0.2 0.6 1.0 1.4
0.4 0.8 1.2
C
z/(h2-h1)
x/L_R,η
0.1
0.3
0.5
0.7
0.9
1.1
1.3
1.5
0.001 0.01 0.1 1 2 5 10
Fh1/V1
z/(h2-h1)
x/L_R,η
0.2
0.4
0.6
0.8
1.0
1.2
1.4
0.001 0.01 0.1 1 2 5 10
Fh1/V1
z/(h2-h1)
x/L_R,η
z90 0.1 0.3 0.5 0.7 0.9 1.1 1.3 1.5
V=0 0.2 0.4 0.6 0.8 1.0 1.2 1.4
0 0.3 0.6 0.9 1.2 1.5 1.8 2.1 2.4
0 1 2 3 4 5 6 7 8 9 10 11 12 13 14 15
V/V1, 10×x/L_R,η

Test Run 2

φ = 30°
q=0.277 m^2/s
Configuration: Smooth R+PA

w [m]	C_1 [-]	y_{90} [m]	V_{90} [m/s]	h_1 [m]	V_1 [m/s]	α [-]	F_1 [-]	$R_1\times10^5$ [-]	W_1 [-]
0.26	0.32	0.056	7.77	0.038	7.22	1.08	11.8	2.77	166
0.46	0.31	0.056	7.83	0.039	7.13	1.08	11.5	2.77	165
0.66	0.31	0.057	7.68	0.039	7.04	1.08	11.3	2.77	164

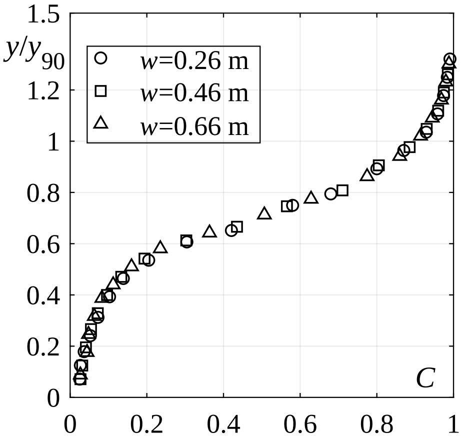

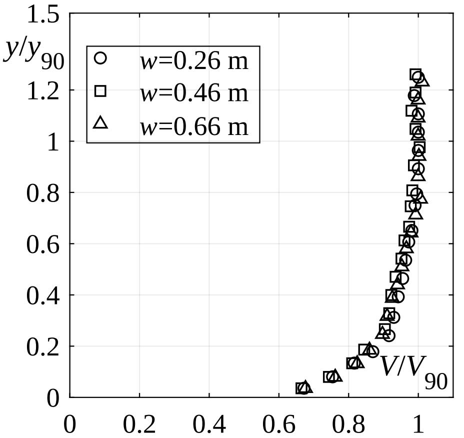

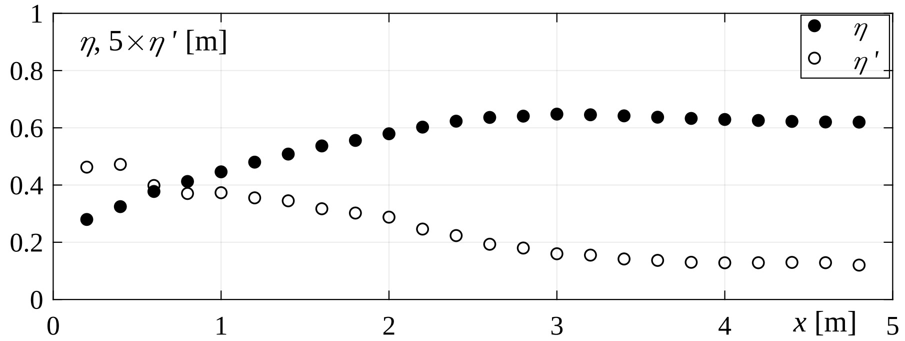

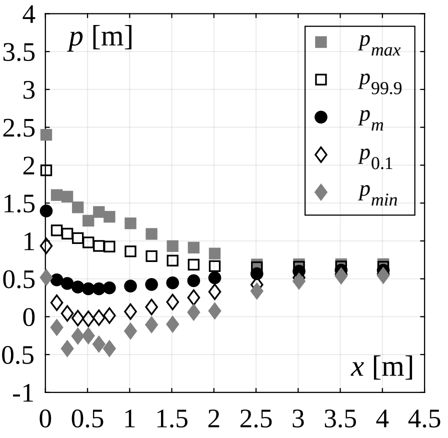

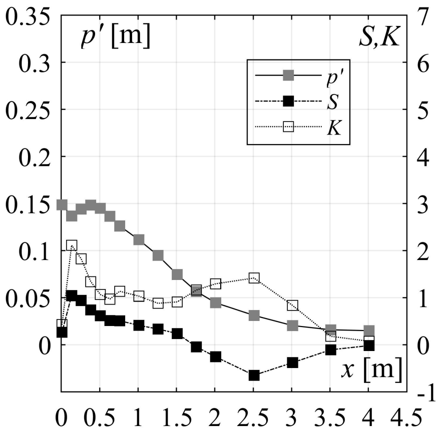

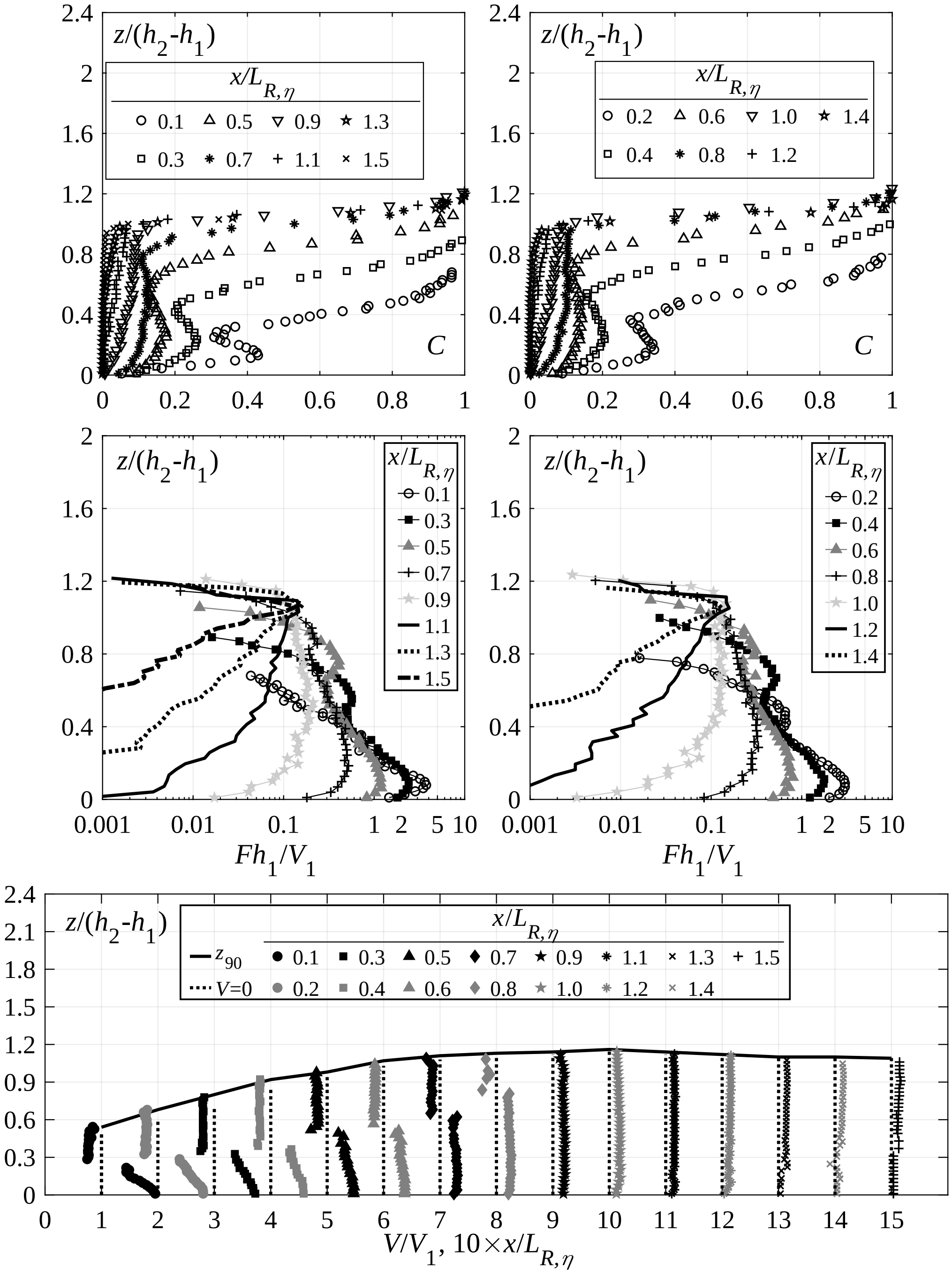
z/(h2-h1)
x/LR,η
0.1
0.3
0.5
0.7
0.9
1.1
1.3
1.5
C
0.2
0.4
0.6
0.8
1.0
1.2
1.4
Fh1/V1
0.001
0.01
0.1
1
2
5
10
z90
V=0
V/V1, 10×x/LR,η

Test Run 3

φ = 30°
q=0.358 m^2/s
Configuration: Smooth R+PA

w [m]	C_1 [-]	y_{90} [m]	V_{90} [m/s]	h_1 [m]	V_1 [m/s]	α [-]	F_1 [-]	$R_1\times10^5$ [-]	W_1 [-]
0.26	0.32	0.068	8.25	0.046	7.79	1.09	11.6	3.58	196
0.46	0.31	0.067	8.25	0.046	7.73	1.09	11.5	3.58	195
0.66	0.31	0.067	8.07	0.046	7.76	1.09	11.5	3.58	195

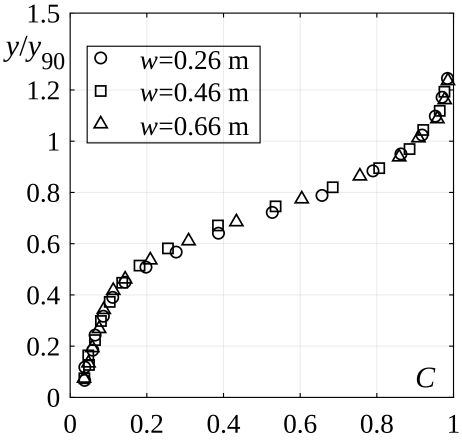

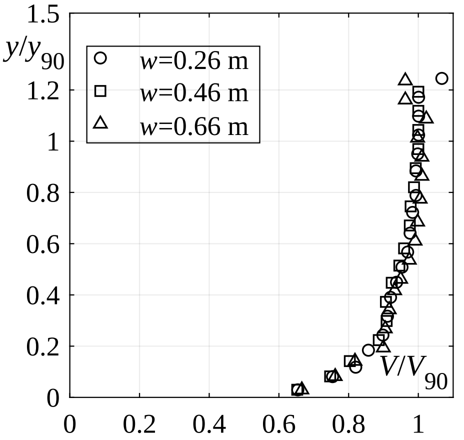

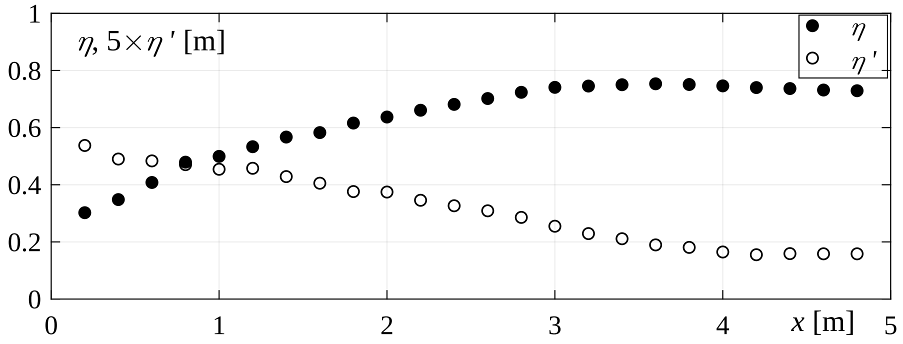

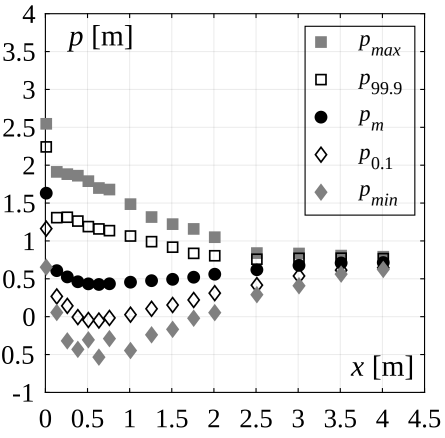

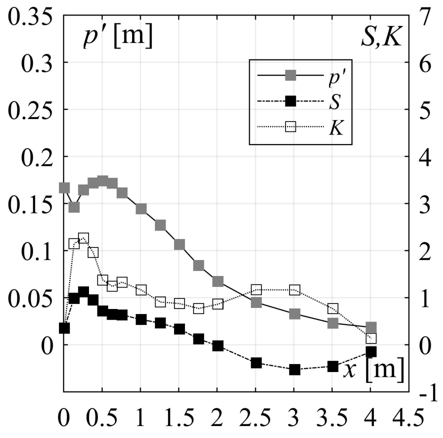

Test Run 4

φ = 30°

q=0.198 m^2/s

Configuration: Smooth R

w [m]	C_1 [-]	y_{90} [m]	V_{90} [m/s]	h_1 [m]	V_1 [m/s]	α [-]	F_1 [-]	$R_1 \times 10^5$ [-]	W_1 [-]
0.26	0.25	0.042	6.74	0.032	6.21	1.09	11.1	1.98	130
0.46	0.24	0.042	6.74	0.032	6.14	1.09	10.9	1.98	129
0.66	0.25	0.043	6.60	0.032	6.18	1.09	11.0	1.98	130

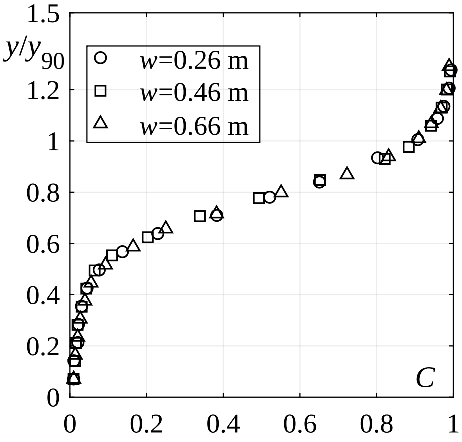

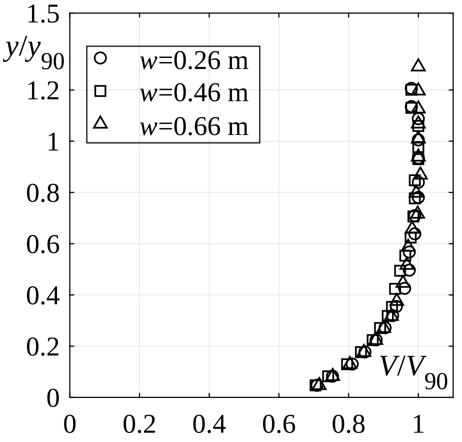

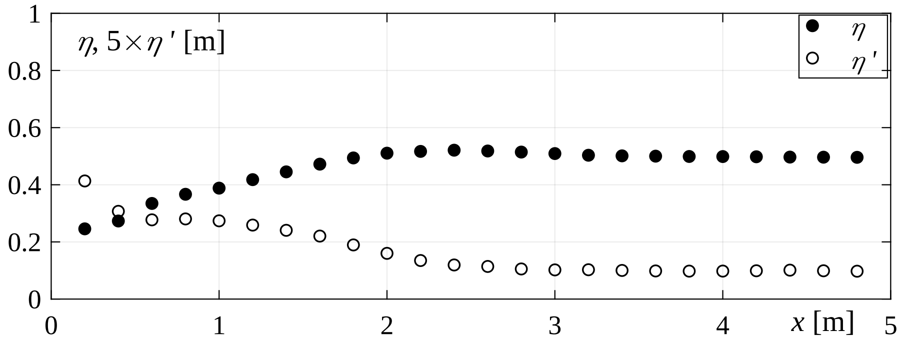

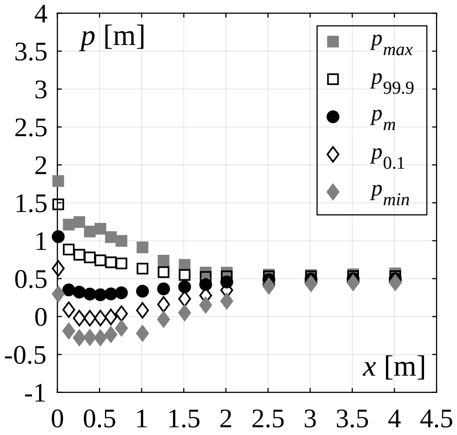

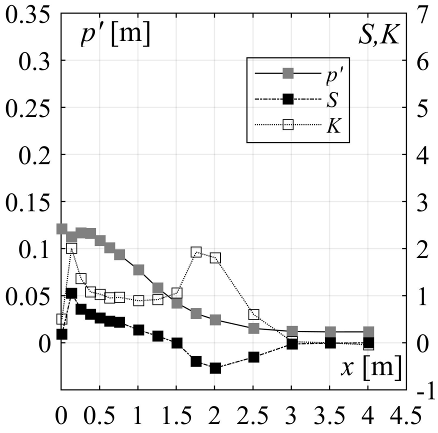

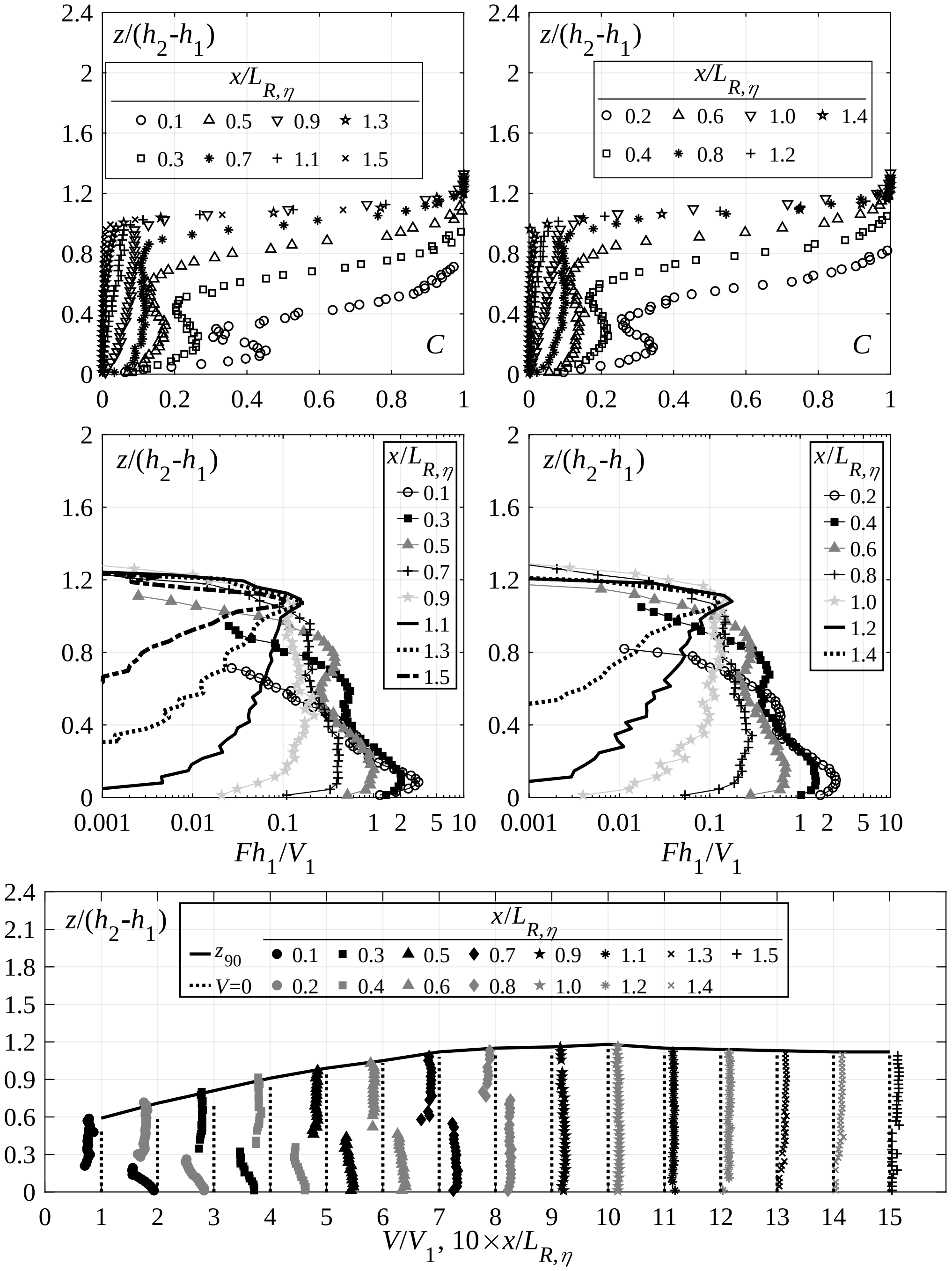
z/(h2-h1)
x/LR,η
0.1
0.3
0.5
0.7
0.9
1.1
1.3
1.5
C
0.2
0.4
0.6
0.8
1.0
1.2
1.4
C
Fh1/V1
Fh1/V1
z90
V=0
V/V1, 10×x/LR,η

Test Run 5

φ = 30°
q=0.277 m^2/s
Configuration: Smooth R

w [m]	C_1 [-]	y_{90} [m]	V_{90} [m/s]	h_1 [m]	V_1 [m/s]	α [-]	F_1 [-]	$R_1 \times 10^5$ [-]	W_1 [-]
0.26	0.26	0.055	7.49	0.040	6.86	1.08	10.9	2.77	162
0.46	0.26	0.055	7.34	0.041	6.81	1.08	10.8	2.77	161
0.66	0.26	0.055	7.34	0.041	6.82	1.08	10.8	2.77	161

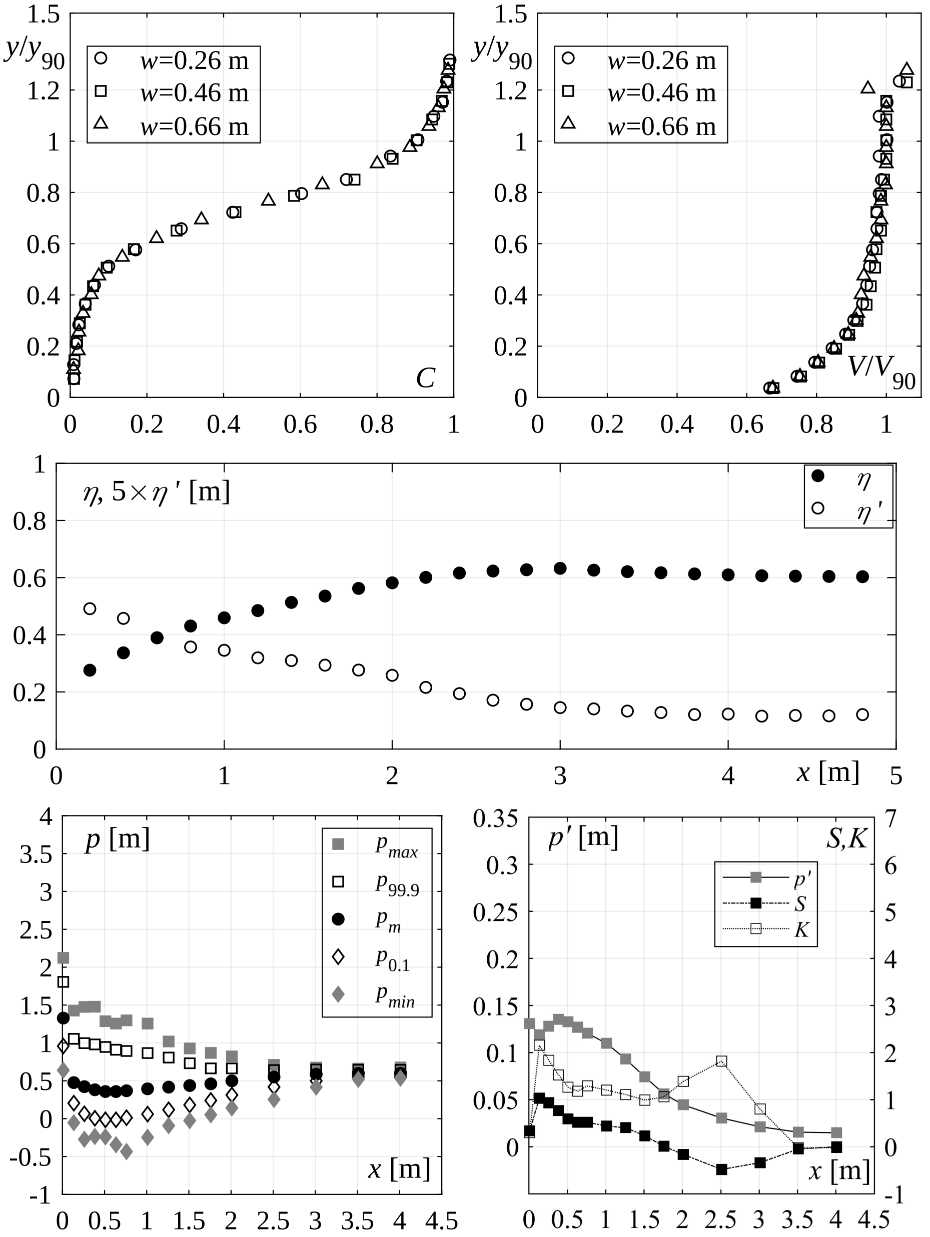

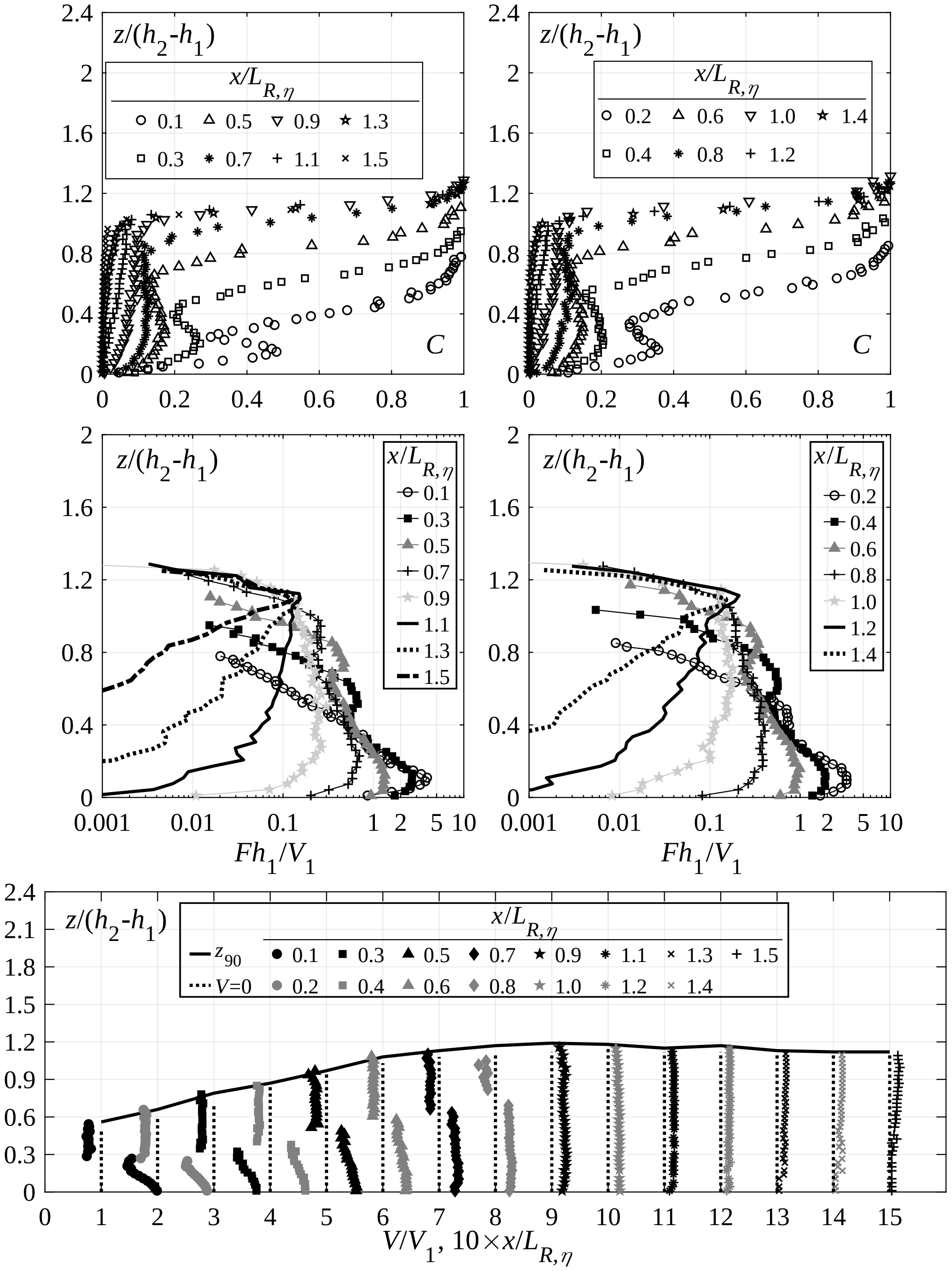
z/(h2-h1)
x/LR,η
0.1 0.5 0.9 1.3
0.3 0.7 1.1 1.5
0.2 0.6 1.0 1.4
0.4 0.8 1.2
C
0 0.2 0.4 0.6 0.8 1
0 0.4 0.8 1.2 1.6 2 2.4
0.1 0.3 0.5 0.7 0.9 1.1 1.3 1.5
0.2 0.4 0.6 0.8 1.0 1.2 1.4
0.001 0.01 0.1 1 2 5 10
Fh1/V1
z90
V=0
0 0.3 0.6 0.9 1.2 1.5 1.8 2.1 2.4
0 1 2 3 4 5 6 7 8 9 10 11 12 13 14 15
V/V1, 10×x/LR,η

Test Run 6

$\varphi = 30°$
q=0.356 m^2/s
Configuration: Smooth R

w [m]	C_1 [-]	y_{90} [m]	V_{90} [m/s]	h_1 [m]	V_1 [m/s]	α [-]	F_1 [-]	$R_1 \times 10^5$ [-]	W_1 [-]
0.26	0.26	0.064	7.91	0.047	7.51	1.08	11.0	3.56	192
0.46	0.26	0.064	7.86	0.047	7.61	1.07	11.2	3.56	193
0.66	0.26	0.063	7.86	0.047	7.57	1.07	11.1	3.56	192

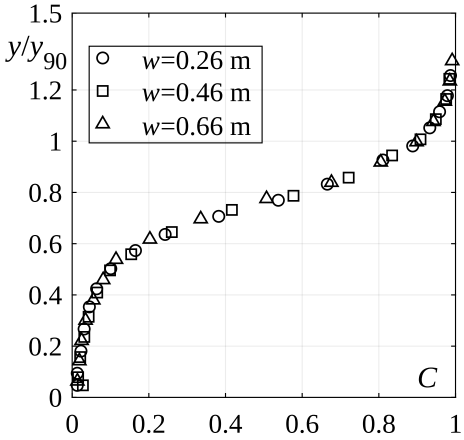

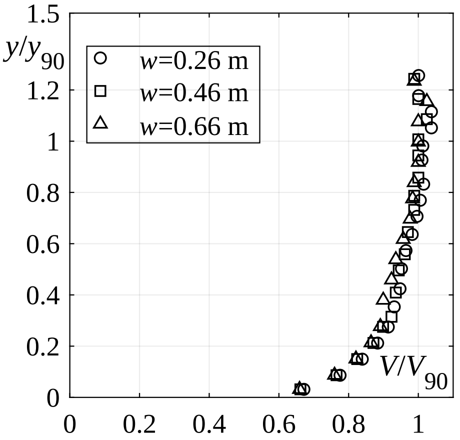

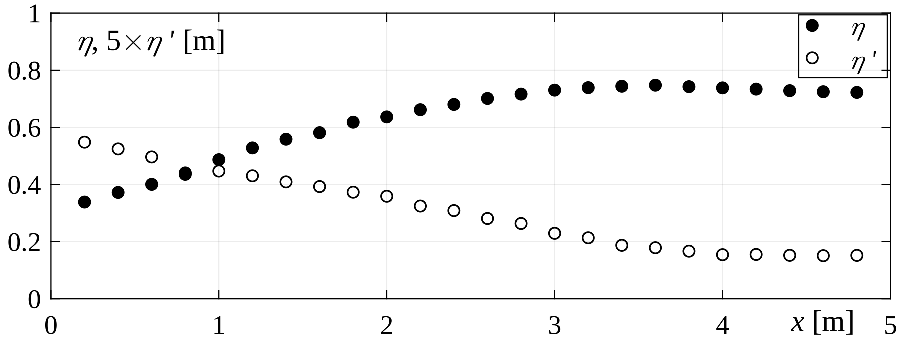

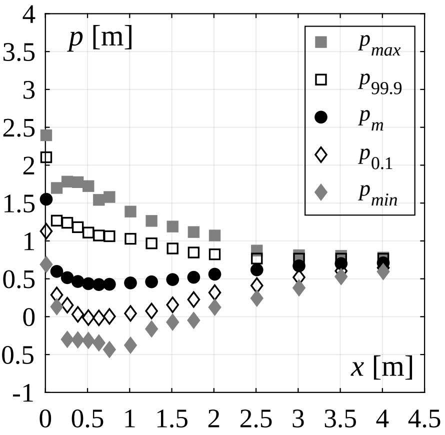

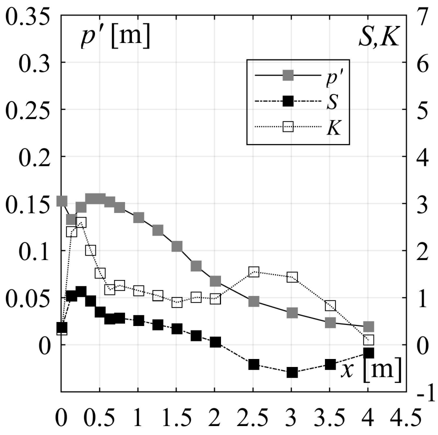

Test Run 7

φ = 30°
q=0.198 m^2/s
Configuration: Smooth SM

w [m]	C_1 [-]	y_{90} [m]	V_{90} [m/s]	h_1 [m]	V_1 [m/s]	α [-]	F_1 [-]	$R_1 \times 10^5$ [-]	W_1 [-]
0.26	0.16	0.034	7.50	0.029	6.95	1.08	13.1	1.98	137
0.46	0.15	0.034	7.34	0.029	6.93	1.09	13.1	1.98	137
0.66	0.15	0.035	7.39	0.029	6.74	1.09	12.5	1.98	137

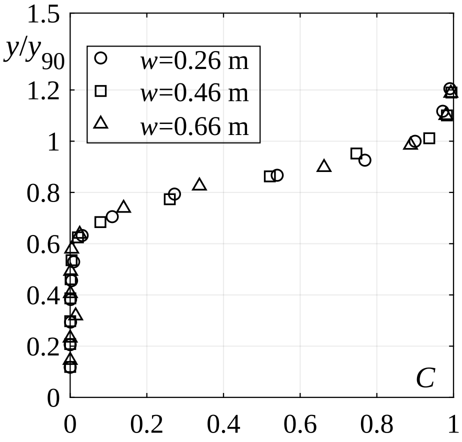

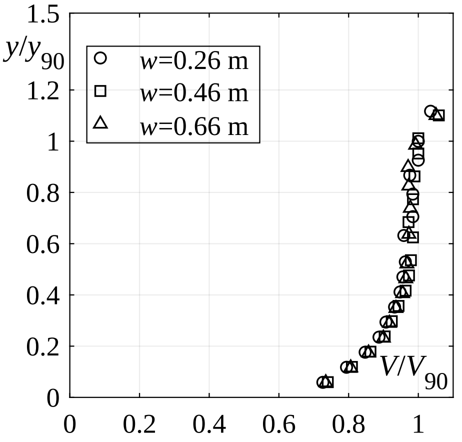

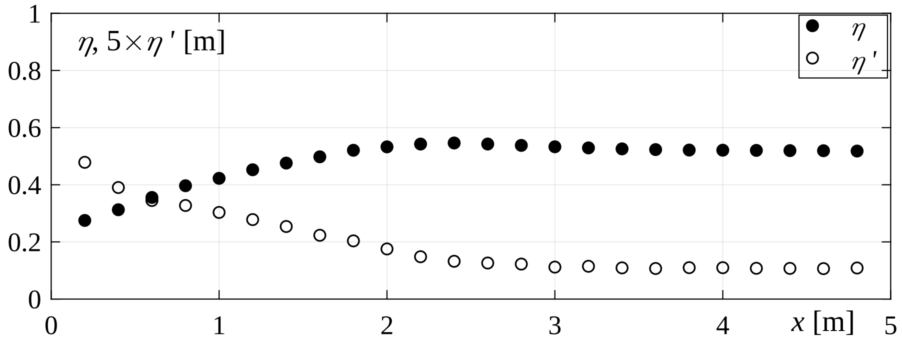

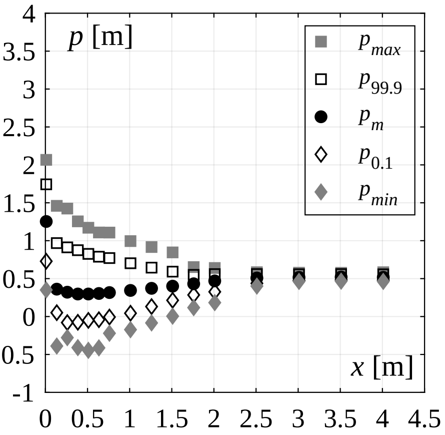

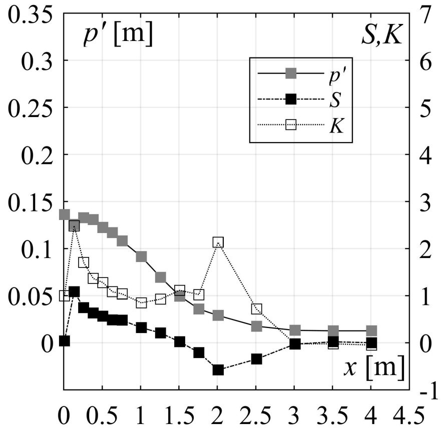

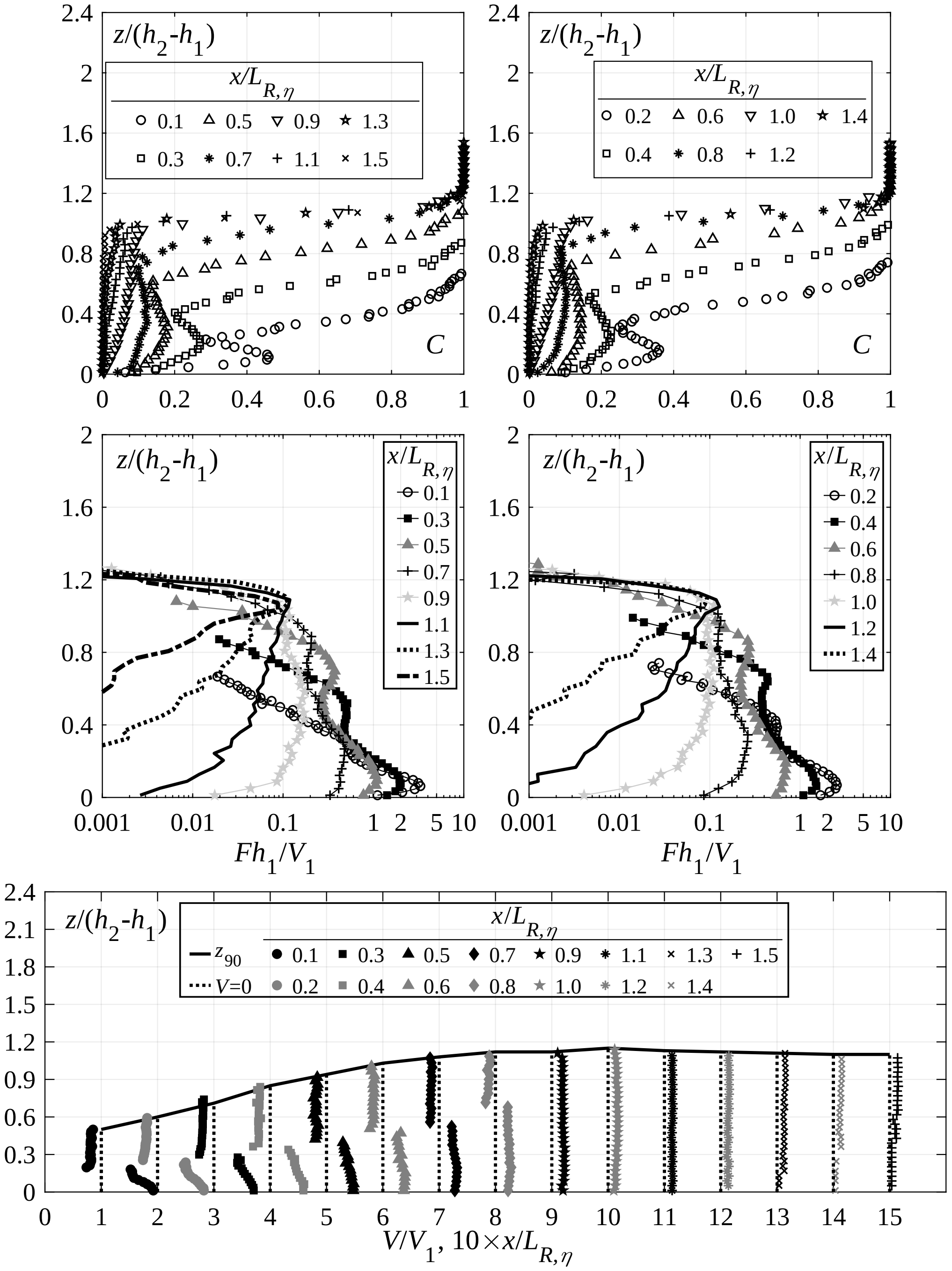
z/(h2-h1)
x/LR,η
0.1 0.5 0.9 1.3
0.3 0.7 1.1 1.5
0.2 0.6 1.0 1.4
0.4 0.8 1.2
C
C
Fh1/V1
0.001 0.01 0.1 1 2 5 10
0 0.2 0.4 0.6 0.8 1
0 0.4 0.8 1.2 1.6 2 2.4
z90
V=0
0 0.3 0.6 0.9 1.2 1.5 1.8 2.1 2.4
0 1 2 3 4 5 6 7 8 9 10 11 12 13 14 15
V/V1, 10×x/LR,η

Test Run 8

φ = 30°
q=0.278 m^2/s
Configuration: Smooth SM

w	C_1	y_{90}	V_{90}	h_1	V_1	α	F_1	$R_1\times10^5$	W_1
[m]	[-]	[m]	[m/s]	[m]	[m/s]	[-]	[-]	[-]	[-]
0.26	0.15	0.043	8.05	0.036	7.68	1.08	12.9	2.78	171
0.46	0.15	0.042	7.86	0.036	7.71	1.08	13.0	2.78	172
0.66	0.15	0.043	8.05	0.036	7.62	1.08	12.7	2.78	171

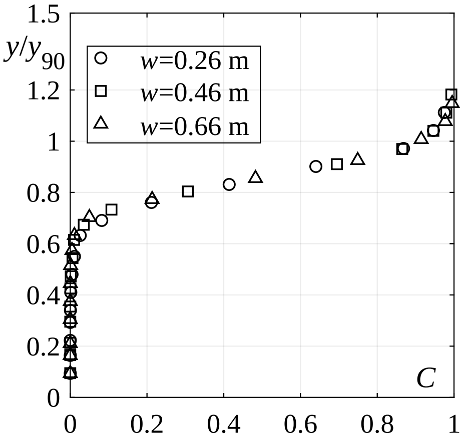

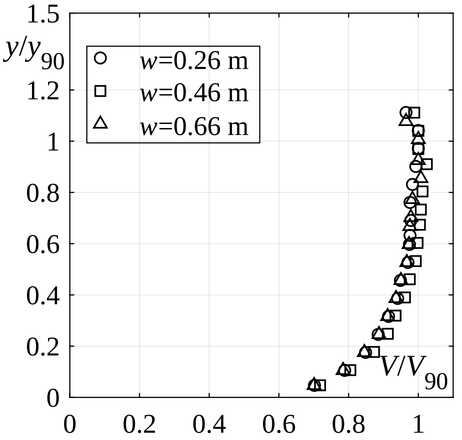

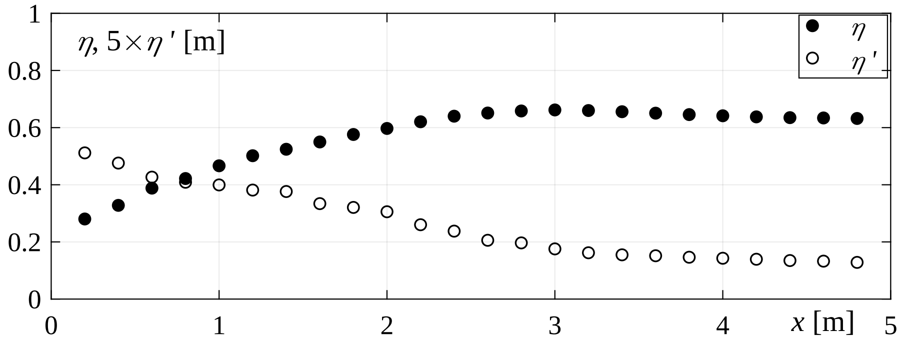

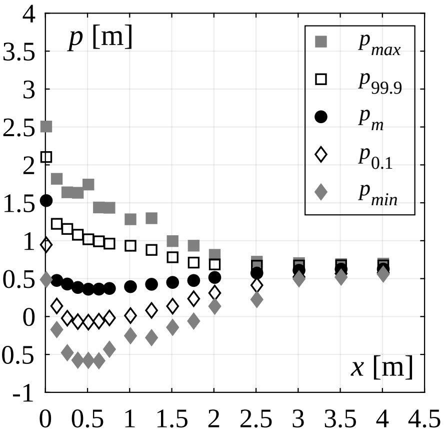

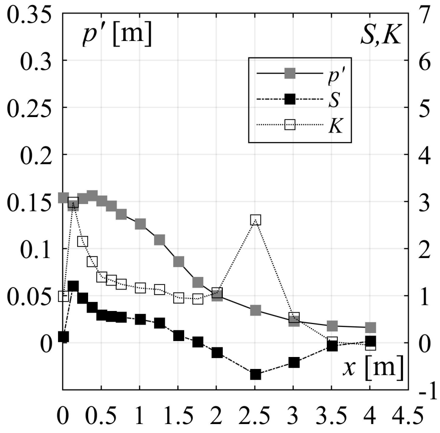

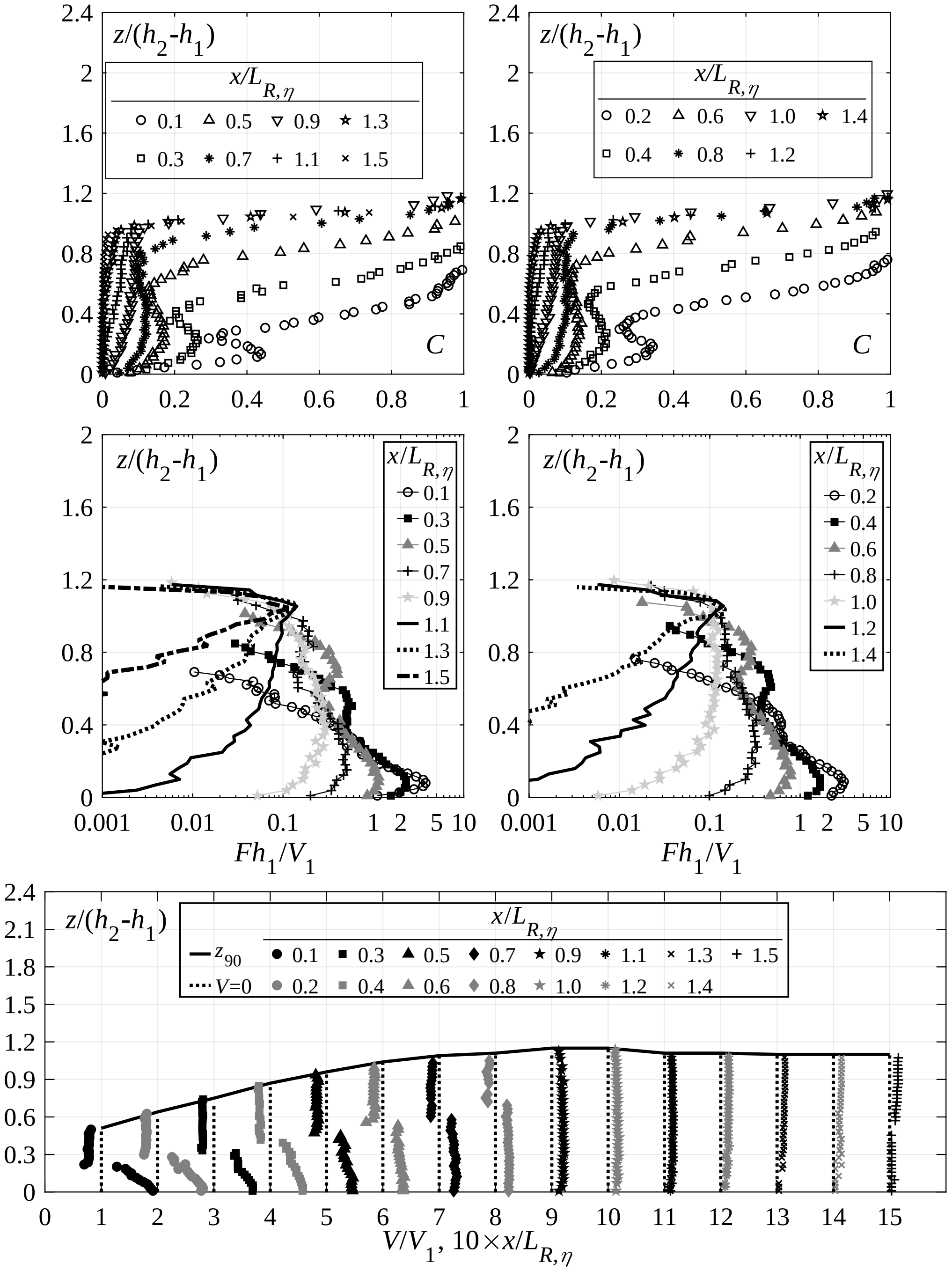
z/(h2-h1)
x/LR,η
0.1 0.3 0.5 0.7 0.9 1.1 1.3 1.5
C
z/(h2-h1)
x/LR,η
0.2 0.4 0.6 0.8 1.0 1.2 1.4
C
0 0.2 0.4 0.6 0.8 1
0 0.4 0.8 1.2 1.6 2 2.4
z/(h2-h1)
x/LR,η
0.1 0.3 0.5 0.7 0.9 1.1 1.3 1.5
Fh1/V1
0.001 0.01 0.1 1 2 5 10
0 0.4 0.8 1.2 1.6 2
z/(h2-h1)
x/LR,η
0.2 0.4 0.6 0.8 1.0 1.2 1.4
Fh1/V1
z/(h2-h1)
x/LR,η
z90
V=0
0.1 0.3 0.5 0.7 0.9 1.1 1.3 1.5
0.2 0.4 0.6 0.8 1.0 1.2 1.4
0 0.3 0.6 0.9 1.2 1.5 1.8 2.1 2.4
0 1 2 3 4 5 6 7 8 9 10 11 12 13 14 15
V/V1, 10×x/LR,η

Test Run 9

φ = 30°
q=0.356 m^2/s
Configuration: Smooth SM

w [m]	C_1 [-]	y_{90} [m]	V_{90} [m/s]	h_1 [m]	V_1 [m/s]	α [-]	F_1 [-]	$R_1 \times 10^5$ [-]	W_1 [-]
0.24	0.15	0.050	8.75	0.042	8.38	1.08	13.0	3.56	202
0.36	0.14	0.050	8.46	0.042	8.38	1.08	13.0	3.56	202
0.48	0.14	0.049	8.46	0.042	8.48	1.08	13.2	3.56	204

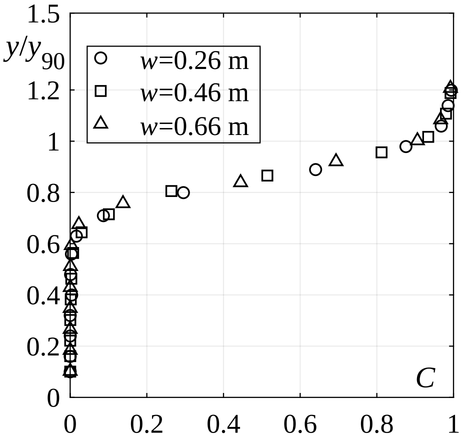

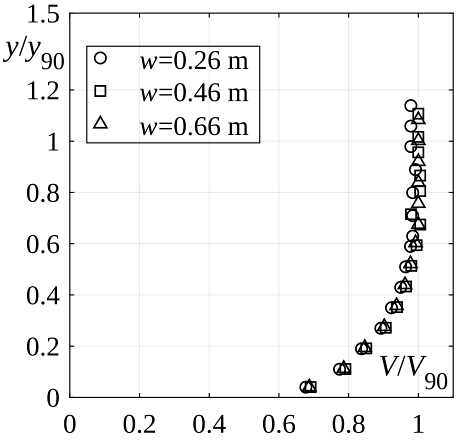

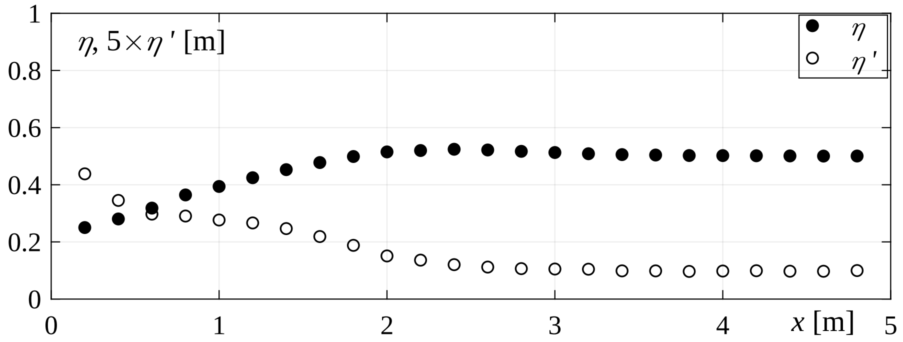

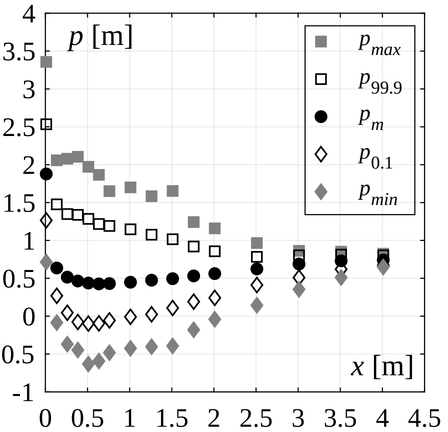

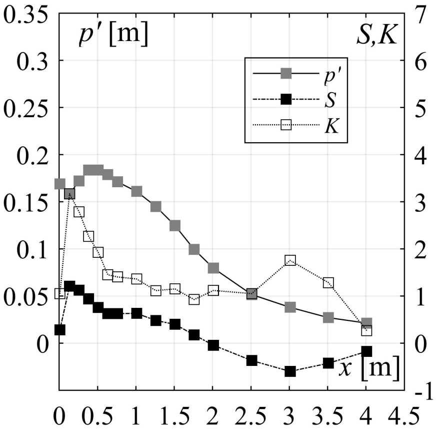

Test Run 10

φ = 30°
q=0.204 m^2/s
Configuration: Stepped s=0.06 m

w [m]	C_1 [-]	y_{90} [m]	V_{90} [m/s]	h_1 [m]	V_1 [m/s]	α [-]	F_1 [-]	$R_1 \times 10^5$ [-]	W_1 [-]
0.24	0.42	0.083	5.68	0.048	4.24	1.18	6.2	2.04	109
0.36	0.42	0.084	5.68	0.048	4.21	1.16	6.1	2.04	109
0.48	0.42	0.084	5.68	0.048	4.22	1.18	6.1	2.04	109

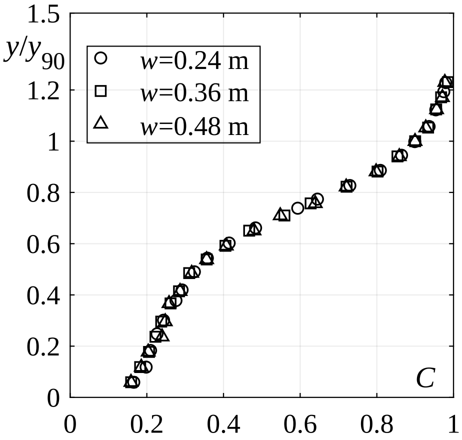

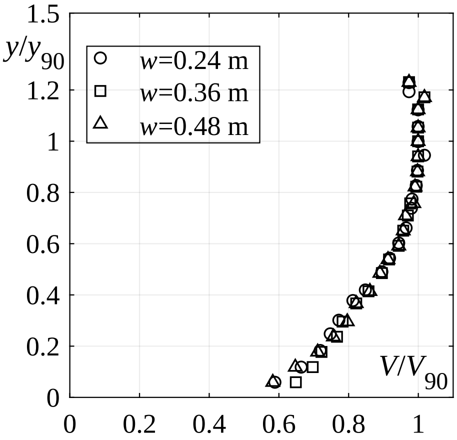

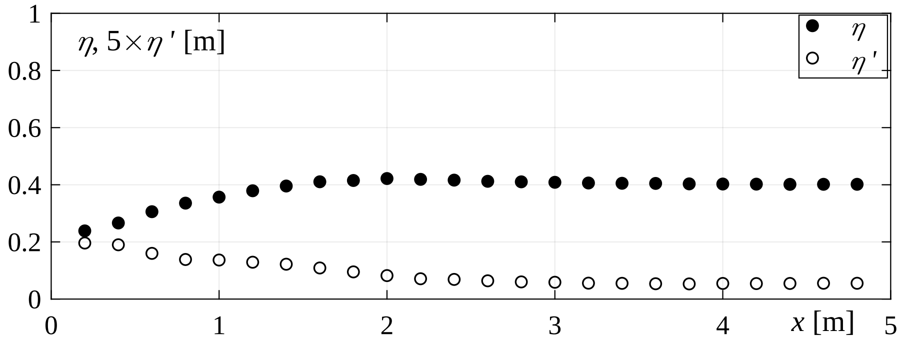

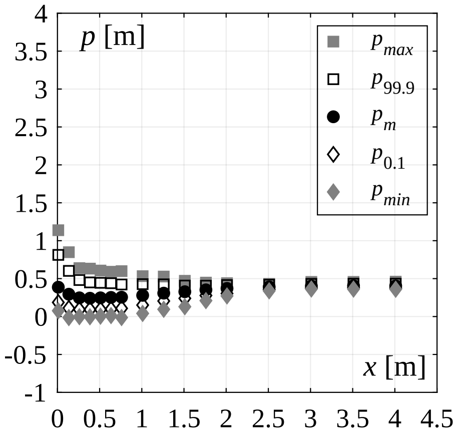

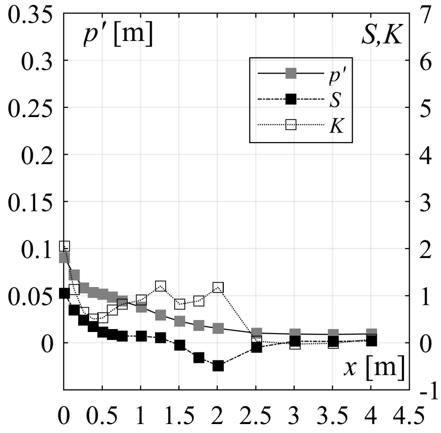

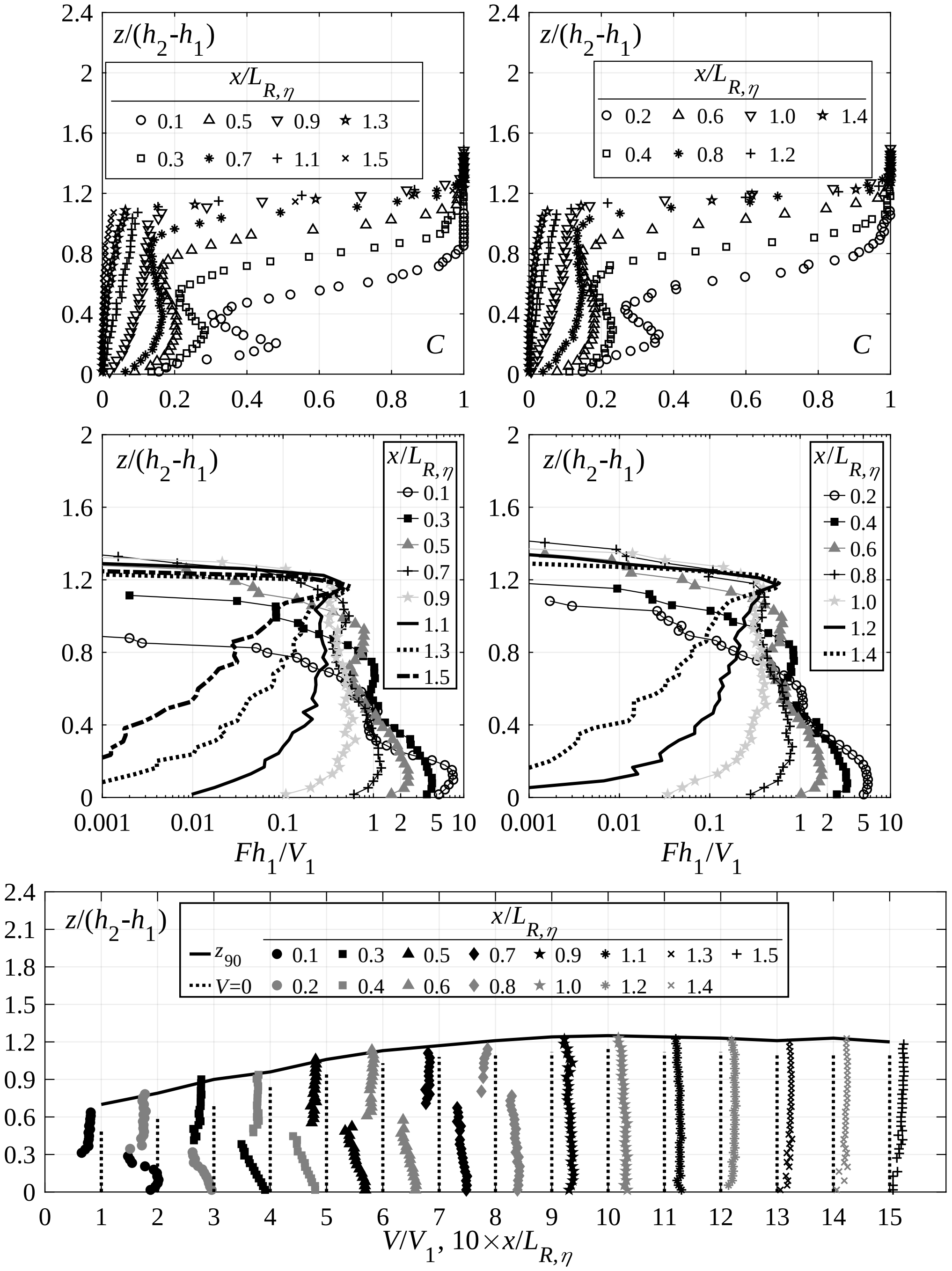

$z/(h_2\text{-}h_1)$
$x/L_{R,\eta}$
○ 0.1 △ 0.5 ▽ 0.9 ★ 1.3
□ 0.3 ✱ 0.7 + 1.1 × 1.5
C
2.4
2
1.6
1.2
0.8
0.4
0
0
0.2
0.4
0.6
0.8
1
$z/(h_2\text{-}h_1)$
$x/L_{R,\eta}$
○ 0.2 △ 0.6 ▽ 1.0 ★ 1.4
□ 0.4 ✱ 0.8 + 1.2
C
$z/(h_2\text{-}h_1)$
$x/L_{R,\eta}$
0.1
0.3
0.5
0.7
0.9
1.1
1.3
1.5
0.001
0.01
0.1
1 2 5 10
Fh_1/V_1
$z/(h_2\text{-}h_1)$
$x/L_{R,\eta}$
0.2
0.4
0.6
0.8
1.0
1.2
1.4
Fh_1/V_1
$z/(h_2\text{-}h_1)$
$x/L_{R,\eta}$
z_{90} ● 0.1 ■ 0.3 ▲ 0.5 ◆ 0.7 ★ 0.9 ✱ 1.1 × 1.3 + 1.5
V=0 ● 0.2 ■ 0.4 ▲ 0.6 ◆ 0.8 ★ 1.0 ✱ 1.2 × 1.4
2.4
2.1
1.8
1.5
1.2
0.9
0.6
0.3
0
0 1 2 3 4 5 6 7 8 9 10 11 12 13 14 15
V/V_1, $10\times x/L_{R,\eta}$

Test Run 11

$\varphi = 30°$

q=0.284 m^2/s

Configuration: Stepped s=0.06 m

w [m]	C_1 [-]	y_{90} [m]	V_{90} [m/s]	h_1 [m]	V_1 [m/s]	α [-]	F_1 [-]	$R_1\times10^5$ [-]	W_1 [-]
0.24	0.42	0.100	0.058	0.058	4.91	1.18	6.5	2.84	138
0.36	0.42	0.100	0.057	0.057	4.95	1.15	6.6	2.84	139
0.48	0.42	0.099	0.057	0.057	4.94	1.17	6.6	2.84	139

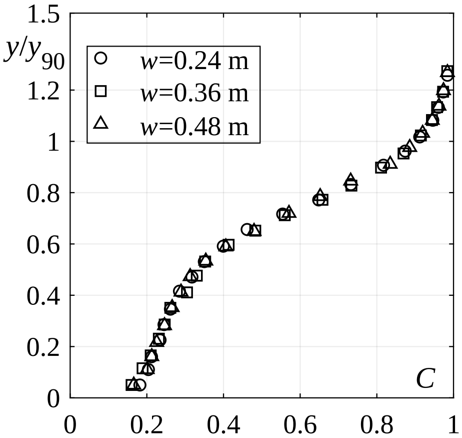

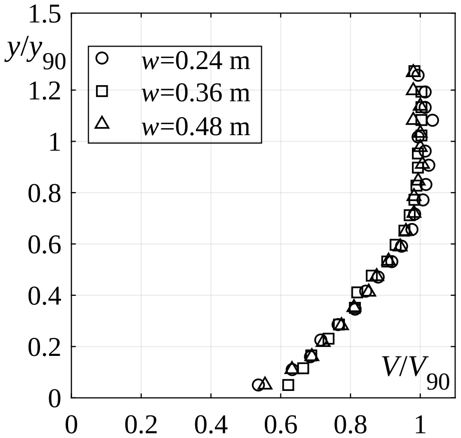

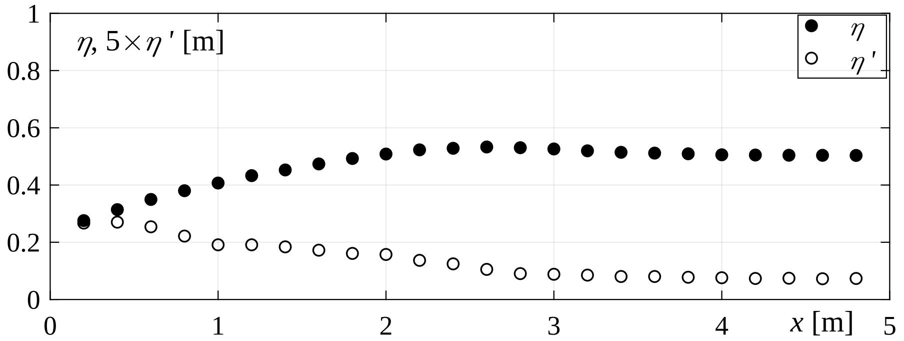

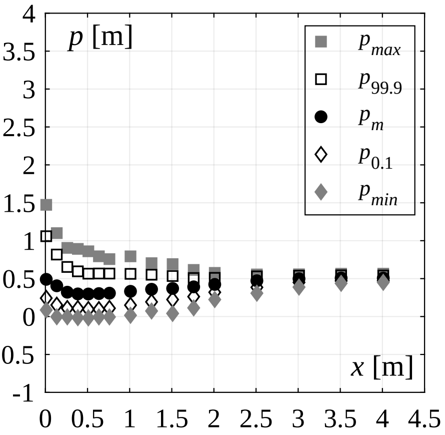

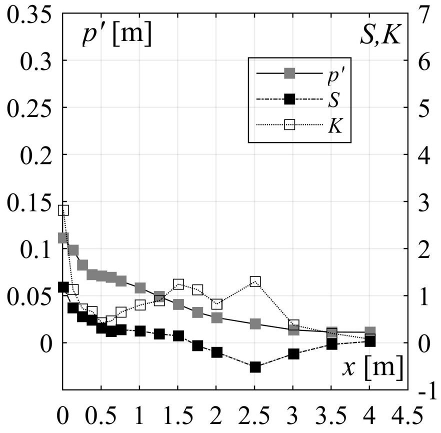

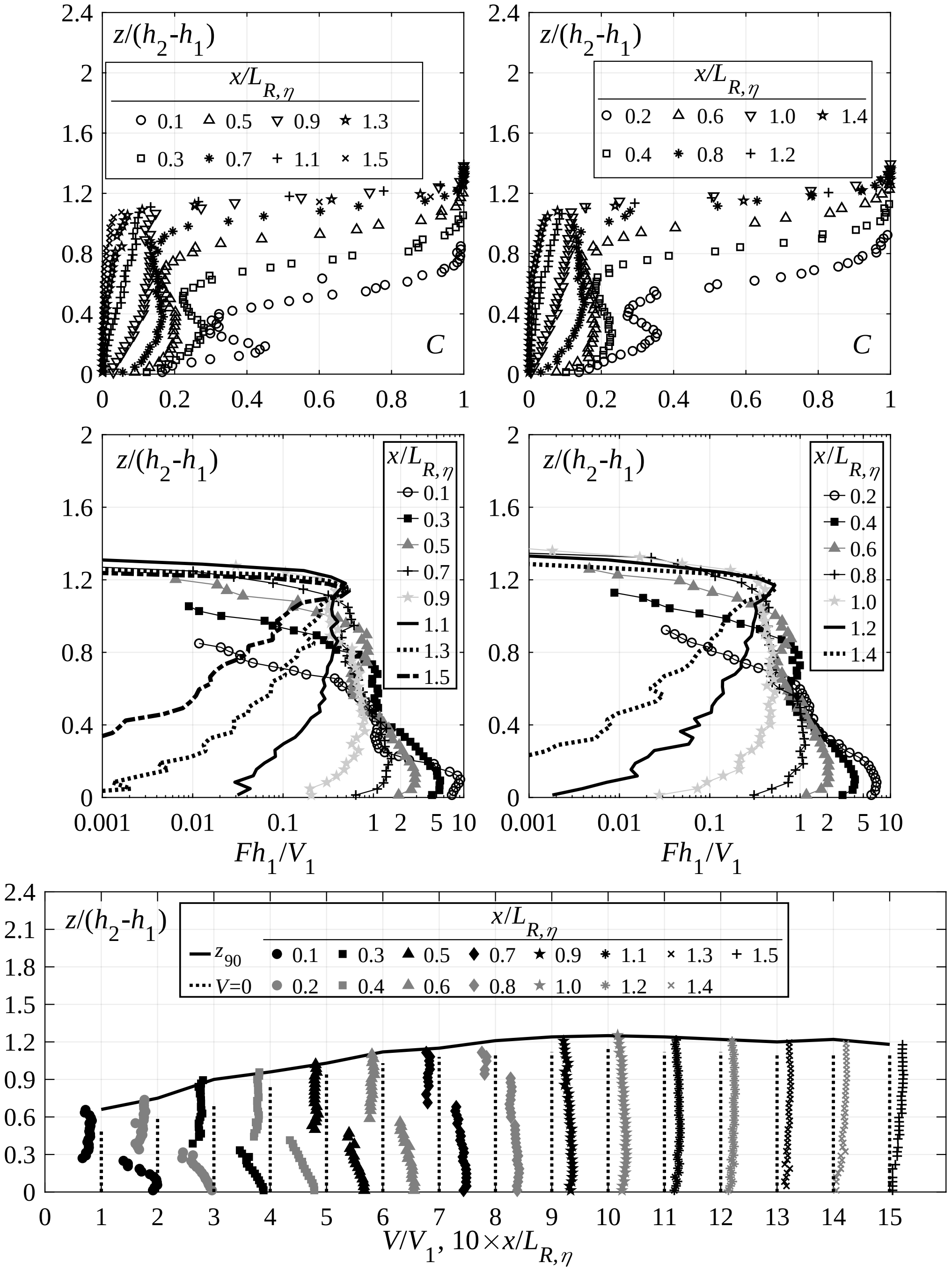
z/(h2-h1)
x/LR,η
○ 0.1 △ 0.5 ▽ 0.9 ★ 1.3
□ 0.3 ✱ 0.7 + 1.1 × 1.5
○ 0.2 △ 0.6 ▽ 1.0 ★ 1.4
□ 0.4 ✱ 0.8 + 1.2
C
C
0 0.2 0.4 0.6 0.8 1
0 0.4 0.8 1.2 1.6 2 2.4
0.1 0.3 0.5 0.7 0.9 1.1 1.3 1.5
0.2 0.4 0.6 0.8 1.0 1.2 1.4
0.001 0.01 0.1 1 2 5 10
Fh1/V1
z90
V=0
0 0.3 0.6 0.9 1.2 1.5 1.8 2.1 2.4
0 1 2 3 4 5 6 7 8 9 10 11 12 13 14 15
V/V1, 10×x/LR,η

Test Run 12

$\varphi = 30°$
q=0.362 m^2/s
Configuration: Stepped s=0.06 m

w [m]	C_1 [-]	y_{90} [m]	V_{90} [m/s]	h_1 [m]	V_1 [m/s]	α [-]	F_1 [-]	$R_1 \times 10^5$ [-]	W_1 [-]
0.24	0.41	0.114	7.06	0.068	5.35	1.18	6.6	3.62	163
0.36	0.41	0.114	7.04	0.067	5.40	1.15	6.7	3.62	164
0.48	0.41	0.114	7.03	0.067	5.41	1.17	6.7	3.62	164

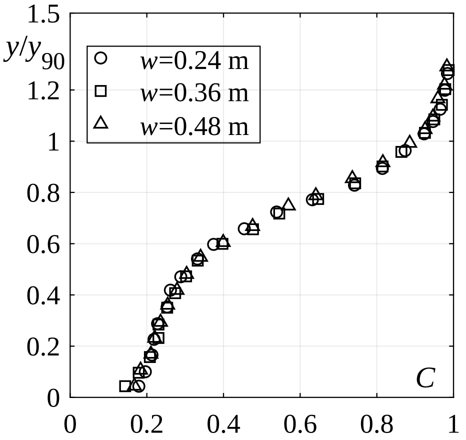

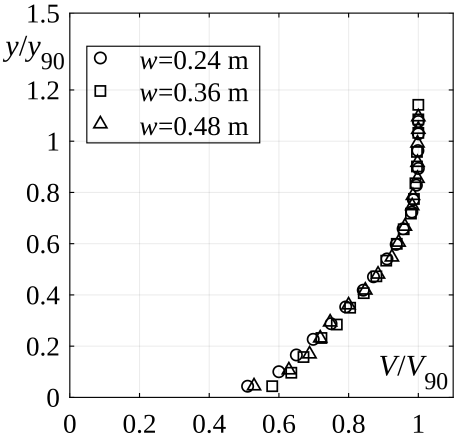

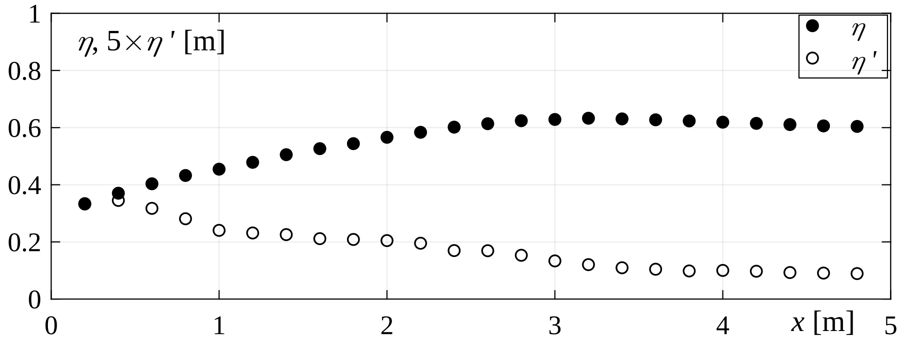

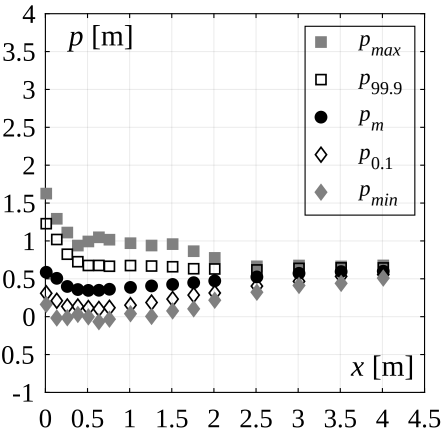

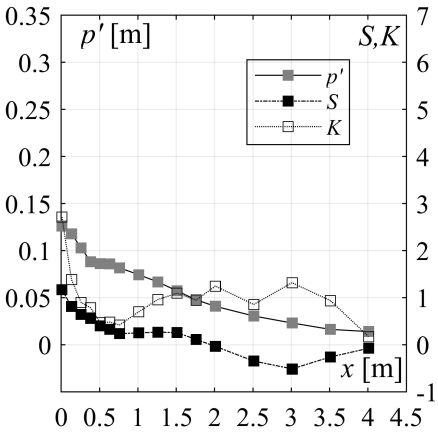

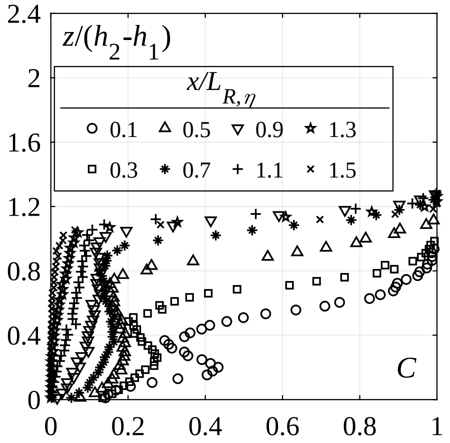
$z/(h_2\text{-}h_1)$
$x/L_{R,\eta}$
○ 0.1 △ 0.5 ▽ 0.9 ★ 1.3
□ 0.3 ✱ 0.7 + 1.1 × 1.5
C
2.4 2 1.6 1.2 0.8 0.4 0
0 0.2 0.4 0.6 0.8 1

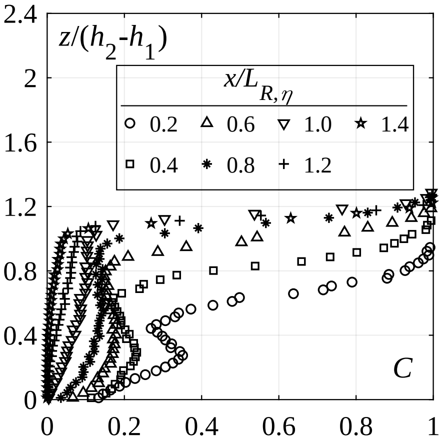
$z/(h_2\text{-}h_1)$
$x/L_{R,\eta}$
○ 0.2 △ 0.6 ▽ 1.0 ★ 1.4
□ 0.4 ✱ 0.8 + 1.2
C
2.4 2 1.6 1.2 0.8 0.4 0
0 0.2 0.4 0.6 0.8 1

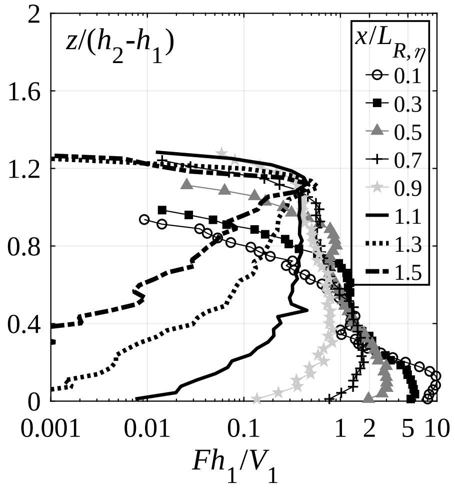
$z/(h_2\text{-}h_1)$
$x/L_{R,\eta}$
0.1
0.3
0.5
0.7
0.9
1.1
1.3
1.5
2 1.6 1.2 0.8 0.4 0
0.001 0.01 0.1 1 2 5 10
Fh_1/V_1

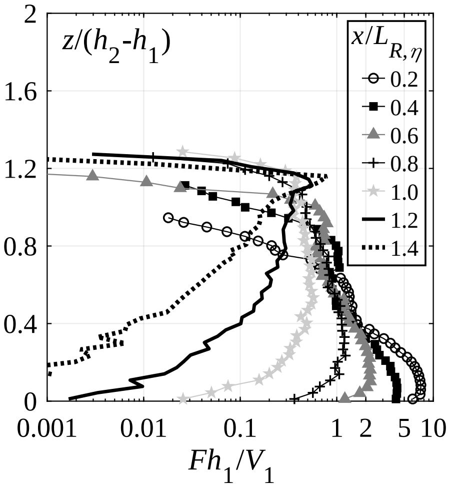
$z/(h_2\text{-}h_1)$
$x/L_{R,\eta}$
0.2
0.4
0.6
0.8
1.0
1.2
1.4
2 1.6 1.2 0.8 0.4 0
0.001 0.01 0.1 1 2 5 10
Fh_1/V_1

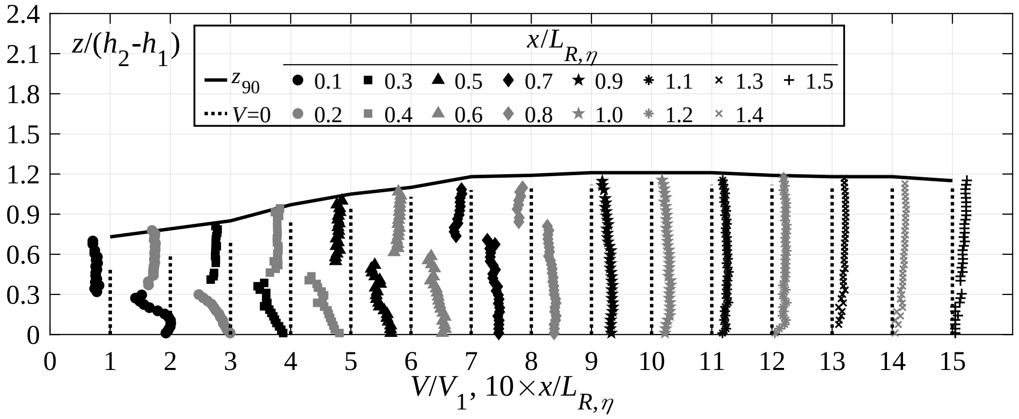
$z/(h_2\text{-}h_1)$
$x/L_{R,\eta}$
z_{90}
V=0
● 0.1 ■ 0.3 ▲ 0.5 ◆ 0.7 ★ 0.9 ✱ 1.1 × 1.3 + 1.5
● 0.2 ■ 0.4 ▲ 0.6 ◆ 0.8 ★ 1.0 ✱ 1.2 × 1.4
2.4 2.1 1.8 1.5 1.2 0.9 0.6 0.3 0
0 1 2 3 4 5 6 7 8 9 10 11 12 13 14 15
V/V_1, $10\times x/L_{R,\eta}$

Test Run 13

$\varphi = 30°$
q=0.204 m^2/s
Configuration: Stepped s=0.03 m

w [m]	C_1 [-]	y_{90} [m]	V_{90} [m/s]	h_1 [m]	V_1 [m/s]	α [-]	F_1 [-]	$R_1 \times 10^5$ [-]	W_1 [-]
0.24	0.41	0.079	5.81	0.047	4.34	1.19	6.4	2.04	110
0.36	0.41	0.079	5.89	0.047	4.36	1.20	6.4	2.04	111
0.48	0.41	0.079	5.78	0.047	4.34	1.21	6.4	2.04	110

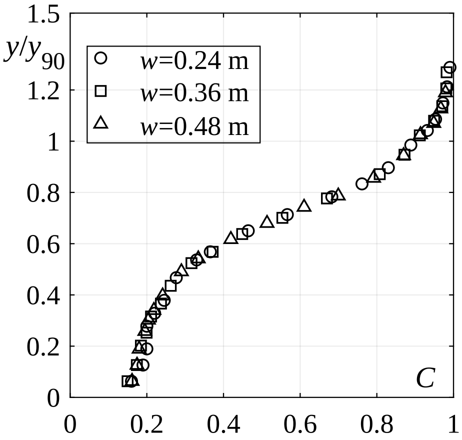

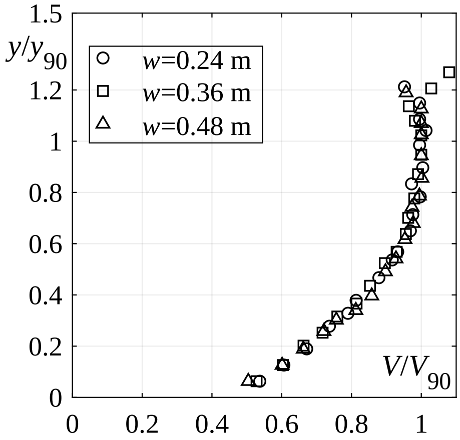

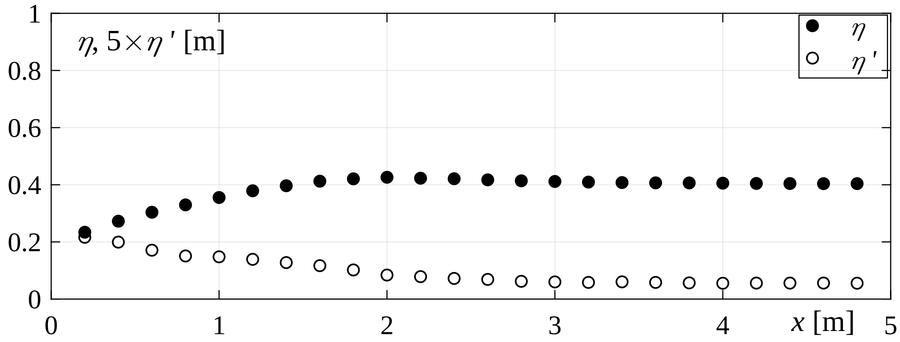

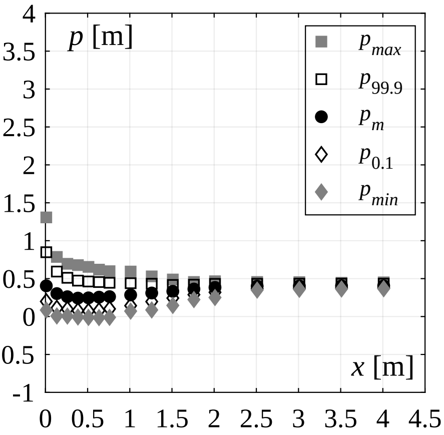

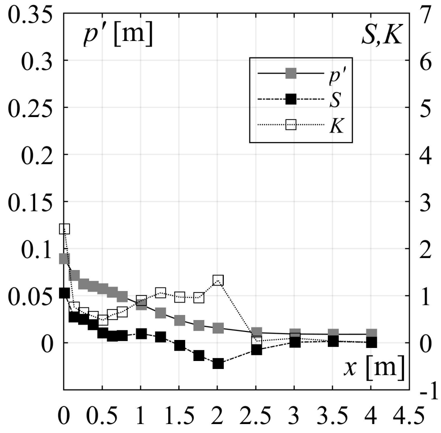

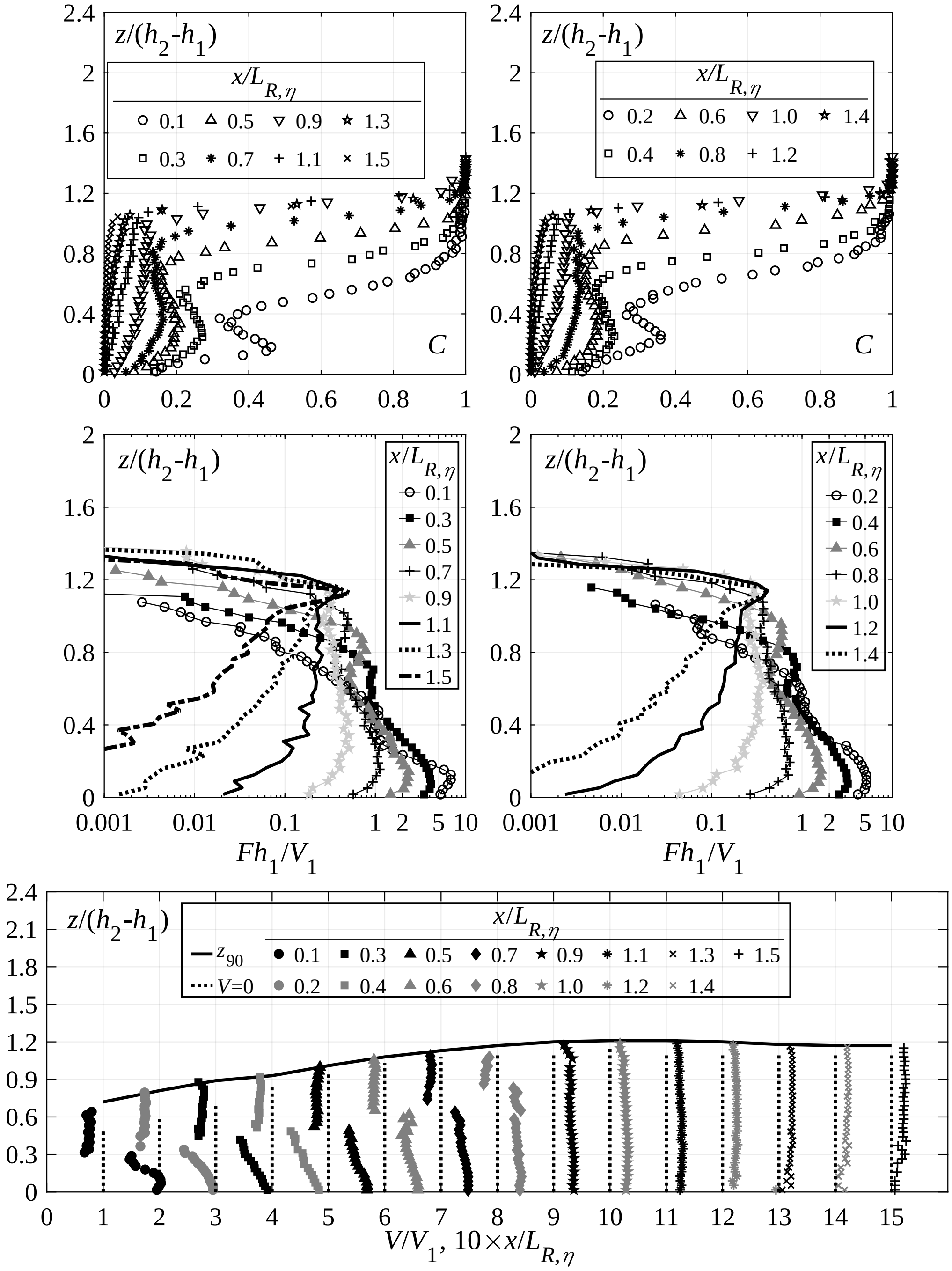
z/(h2-h1)
x/LR,η
○ 0.1 △ 0.5 ▽ 0.9 ★ 1.3
□ 0.3 ✱ 0.7 + 1.1 × 1.5
○ 0.2 △ 0.6 ▽ 1.0 ★ 1.4
□ 0.4 ✱ 0.8 + 1.2
C
2.4
2
1.6
1.2
0.8
0.4
0
0.2
0.4
0.6
0.8
1
0.1 0.3 0.5 0.7 0.9 1.1 1.3 1.5
0.2 0.4 0.6 0.8 1.0 1.2 1.4
0.001
0.01
0.1
1 2 5 10
Fh1/V1
z90
V=0
0.1 0.3 0.5 0.7 0.9 1.1 1.3 1.5
0.2 0.4 0.6 0.8 1.0 1.2 1.4
2.1
1.8
1.5
0.9
0.6
0.3
0 1 2 3 4 5 6 7 8 9 10 11 12 13 14 15
V/V1, 10×x/LR,η

Test Run 14

φ = 30°
q=0.282 m^2/s
Configuration: Stepped s=0.03 m

w [m]	C_1 [-]	y_{90} [m]	V_{90} [m/s]	h_1 [m]	V_1 [m/s]	α [-]	F_1 [-]	$R_1\times10^5$ [-]	W_1 [-]
0.24	0.41	0.093	6.70	0.056	5.07	1.19	6.9	2.82	140
0.36	0.41	0.093	6.72	0.055	5.10	1.19	6.9	2.82	141
0.48	0.41	0.094	6.70	0.056	5.08	1.18	6.9	2.82	140

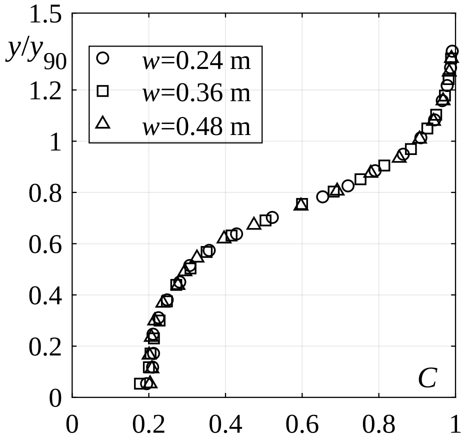

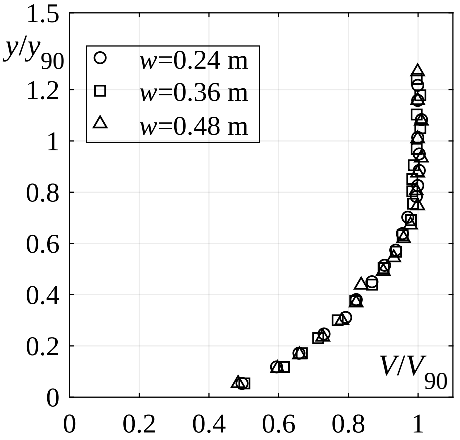

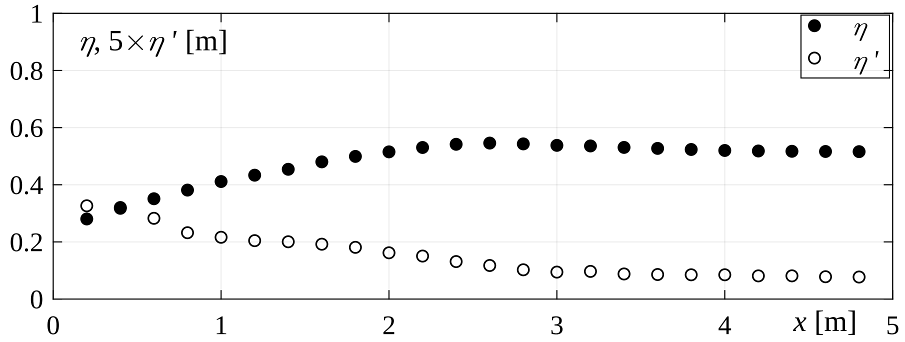

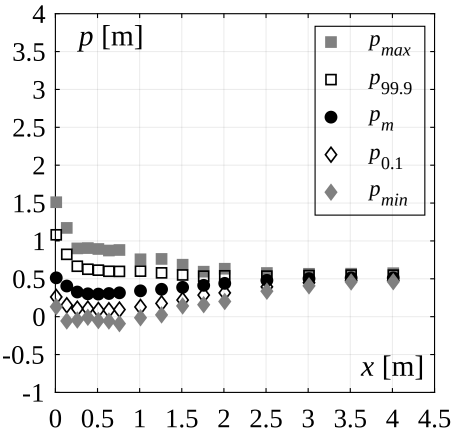

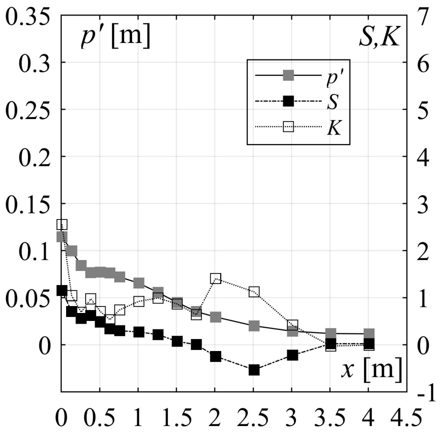

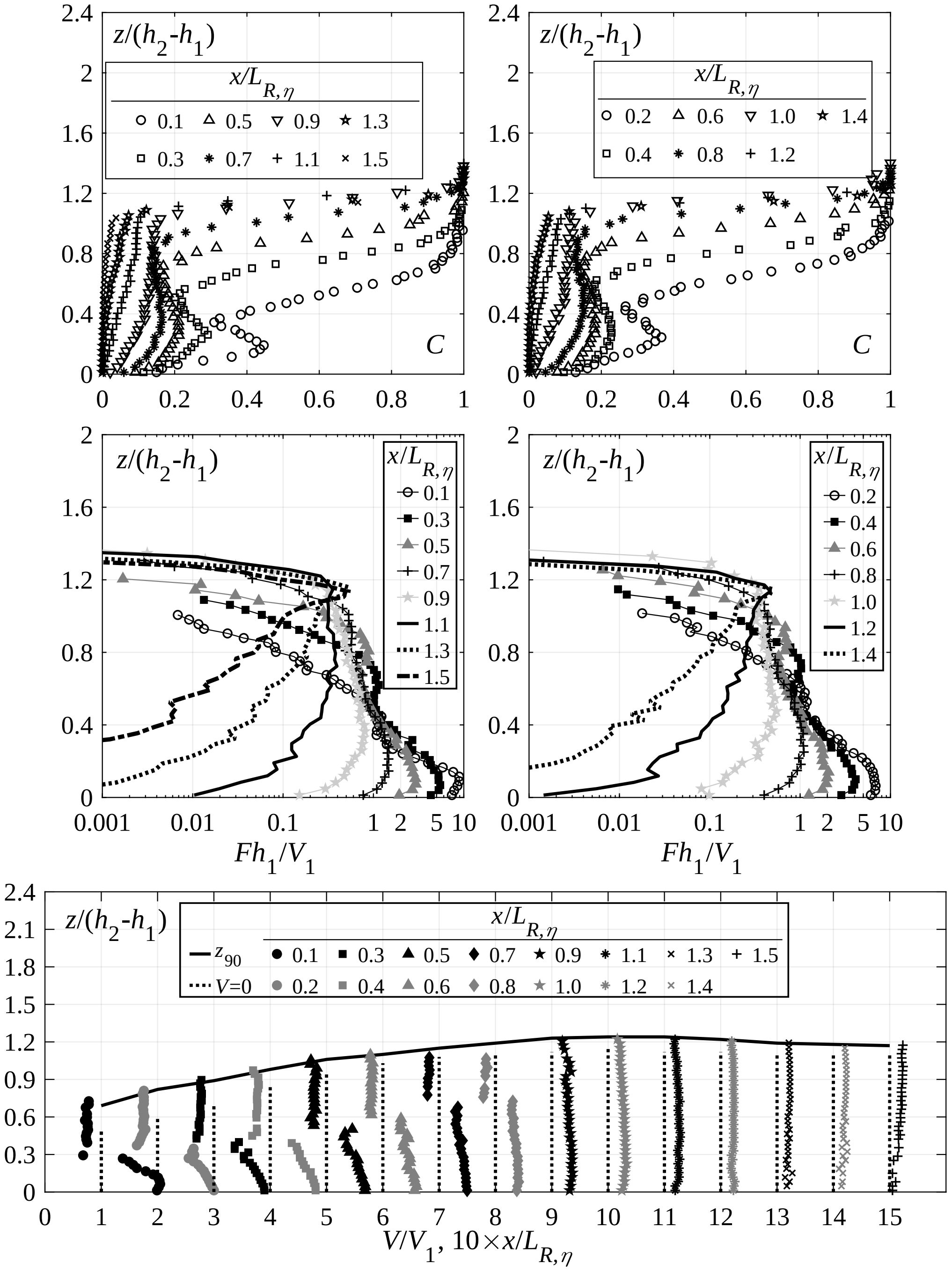
z/(h2-h1)
x/LR,η
0.1
0.3
0.5
0.7
0.9
1.1
1.3
1.5
0.2
0.4
0.6
0.8
1.0
1.2
1.4
C
0
0.4
0.8
1.2
1.6
2
2.4
0.2
0.4
0.6
0.8
1
0.001
0.01
0.1
1
2
5
10
Fh1/V1
z90
V=0
0.3
0.6
0.9
1.2
1.5
1.8
2.1
2.4
0
1
2
3
4
5
6
7
8
9
10
11
12
13
14
15
V/V1, 10×x/LR,η

Test Run 15

φ = 30°
q=0.364 m^2/s
Configuration: Stepped s=0.03 m

w [m]	C_1 [-]	y_{90} [m]	V_{90} [m/s]	h_1 [m]	V_1 [m/s]	α [-]	F_1 [-]	$R_1\times10^5$ [-]	W_1 [-]
0.24	0.41	0.111	7.22	0.066	5.54	1.18	6.9	3.64	166
0.36	0.41	0.110	7.22	0.066	5.55	1.18	6.9	3.64	167
0.48	0.40	0.111	7.23	0.066	5.52	1.17	6.9	3.64	166

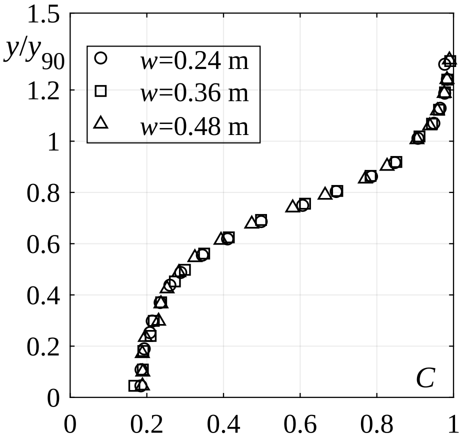

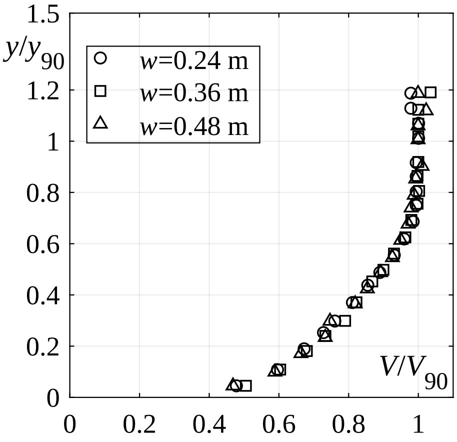

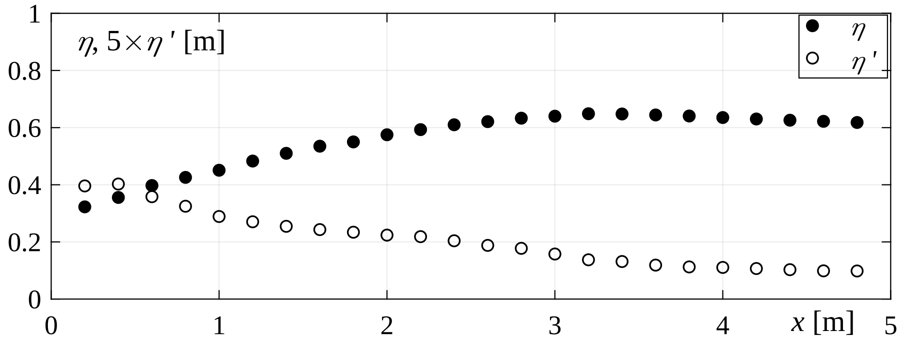

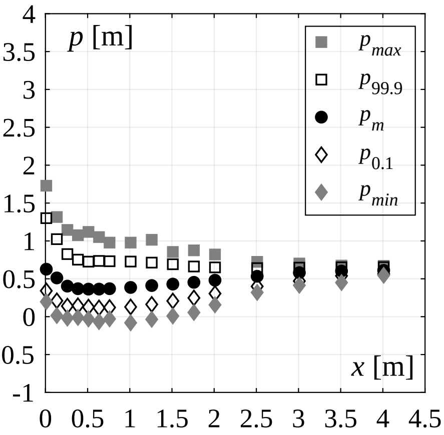

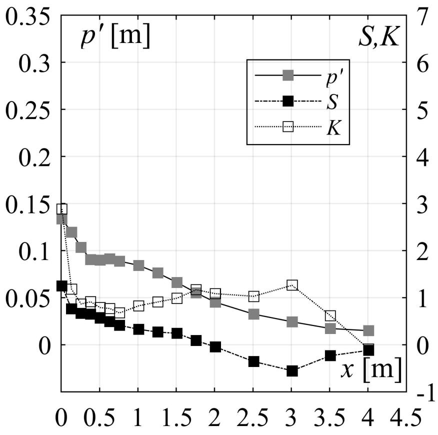

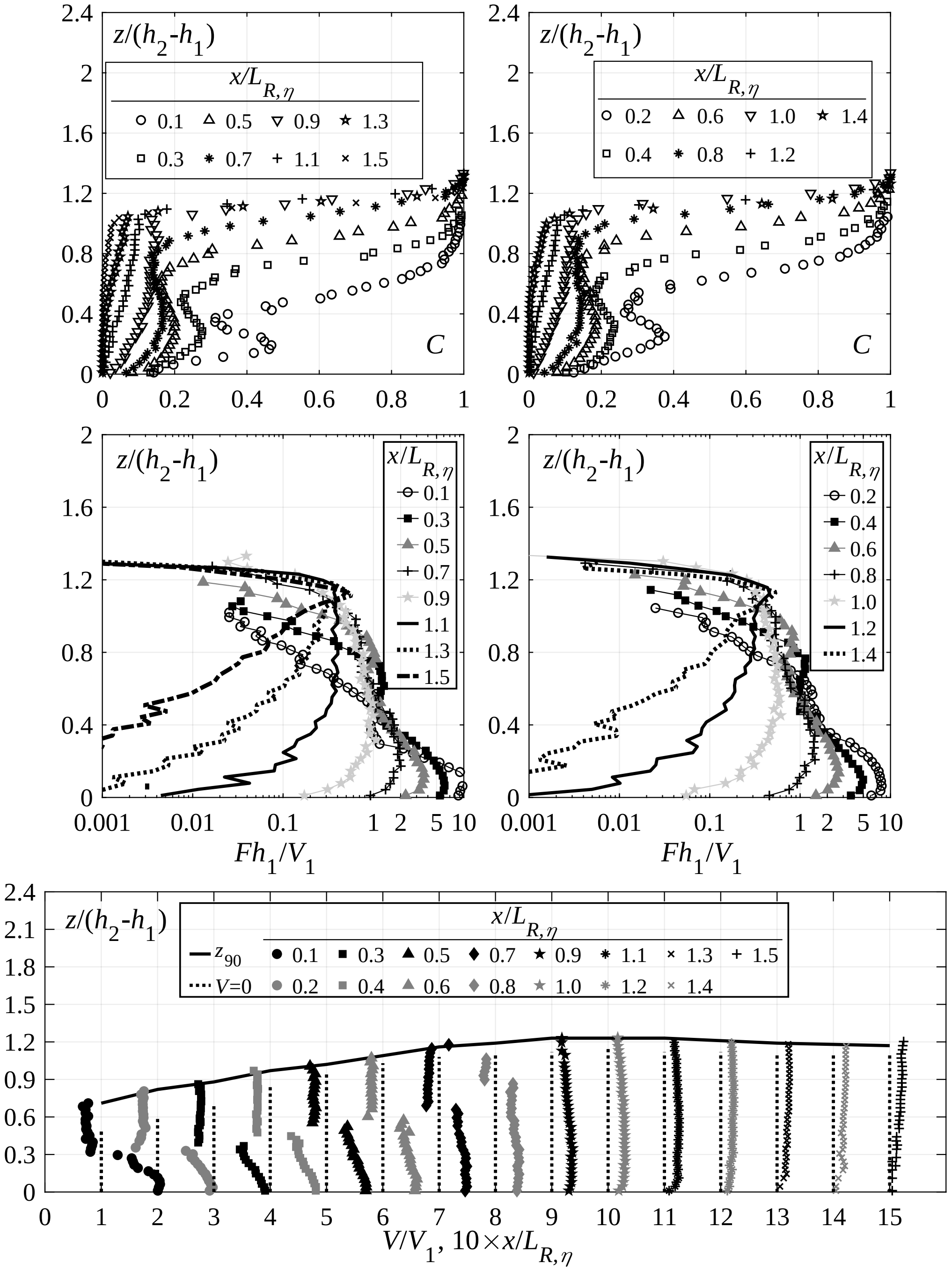
z/(h2-h1)
x/L_{R,η}
0.1 0.5 0.9 1.3
0.3 0.7 1.1 1.5
C
0.2 0.6 1.0 1.4
0.4 0.8 1.2
0 0.2 0.4 0.6 0.8 1
0 0.4 0.8 1.2 1.6 2 2.4
0.001 0.01 0.1 1 2 5 10
Fh1/V1
0.1 0.3 0.5 0.7 0.9 1.1 1.3 1.5
0.2 0.4 0.6 0.8 1.0 1.2 1.4
z90
V=0
0 0.3 0.6 0.9 1.2 1.5 1.8 2.1 2.4
0 1 2 3 4 5 6 7 8 9 10 11 12 13 14 15
V/V1, 10×x/L_{R,η}

Test Run 16

$\varphi = 50°$
q=0.198 m^2/s
Configuration: Smooth R+PA

w [m]	C_1 [-]	y_{90} [m]	V_{90} [m/s]	h_1 [m]	V_1 [m/s]	α [-]	F_1 [-]	$R_1 \times 10^5$ [-]	W_1 [-]
0.26	0.37	0.044	8.42	0.028	7.16	1.08	13.8	1.98	140
0.46	0.37	0.045	8.31	0.028	7.01	1.08	13.3	1.98	138
0.66	0.36	0.046	8.20	0.029	6.83	1.08	12.8	1.98	136

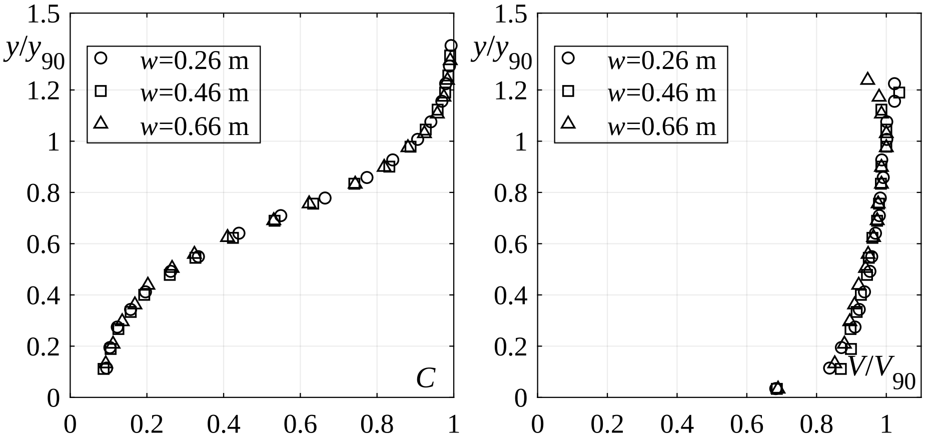

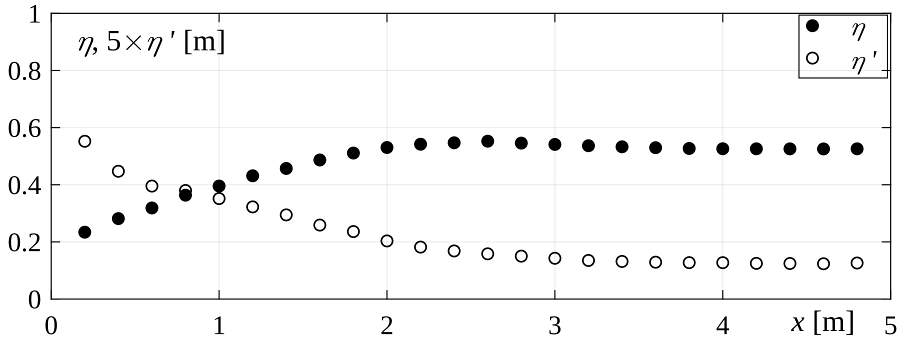

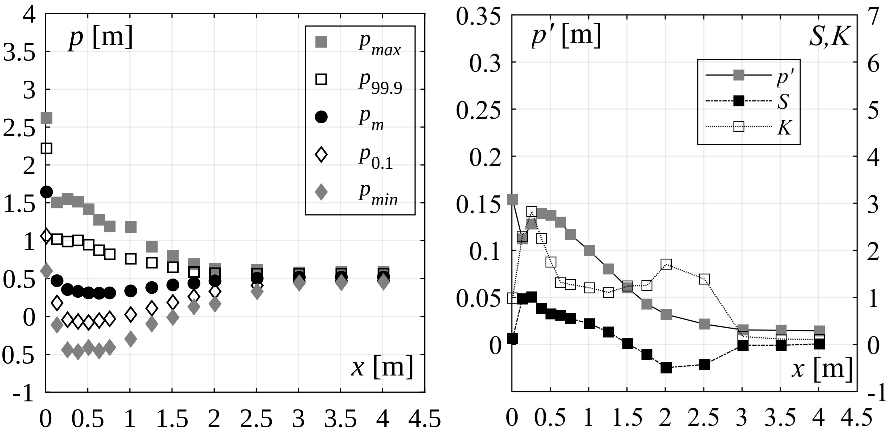

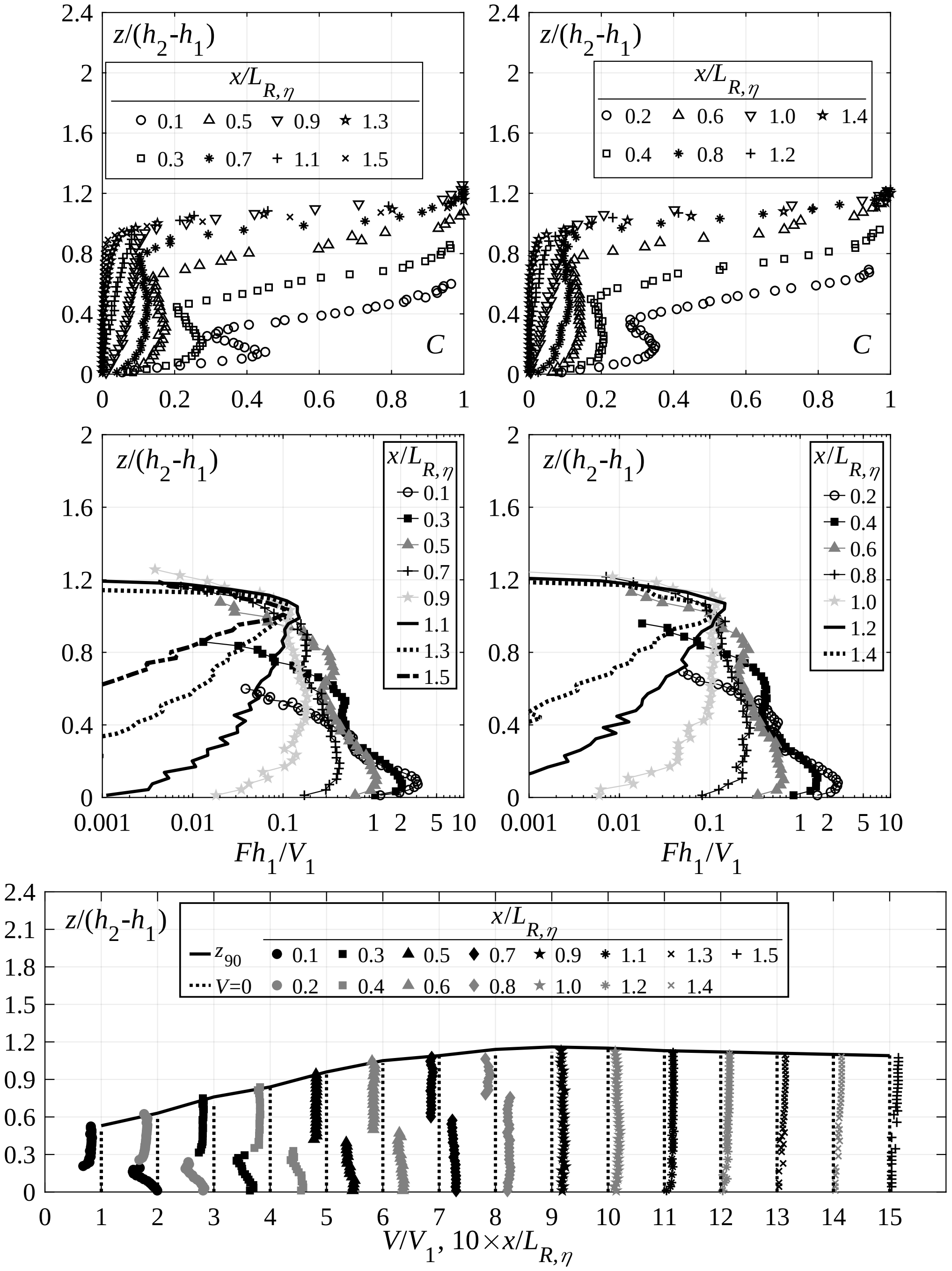
z/(h2-h1)
x/LR,η
0.1 0.5 0.9 1.3
0.3 0.7 1.1 1.5
C
0.2 0.6 1.0 1.4
0.4 0.8 1.2
0 0.2 0.4 0.6 0.8 1
0 0.4 0.8 1.2 1.6 2 2.4
0.1 0.3 0.5 0.7 0.9 1.1 1.3 1.5
0.2 0.4 0.6 0.8 1.0 1.2 1.4
0.001 0.01 0.1 1 2 5 10
Fh1/V1
z90
V=0
0 1 2 3 4 5 6 7 8 9 10 11 12 13 14 15
0 0.3 0.6 0.9 1.2 1.5 1.8 2.1 2.4
V/V1, 10×x/LR,η

Test Run 17

φ = 50°
q=0.280 m^2/s
Configuration: Smooth R+PA

w [m]	C_1 [-]	y_{90} [m]	V_{90} [m/s]	h_1 [m]	V_1 [m/s]	α [-]	F_1 [-]	$R_1 \times 10^5$ [-]	W_1 [-]
0.26	0.36	0.055	9.09	0.036	7.88	1.07	13.4	2.80	174
0.46	0.35	0.056	9.09	0.036	7.76	1.06	13.0	2.80	173
0.66	0.34	0.056	8.95	0.037	7.62	1.06	12.7	2.80	171

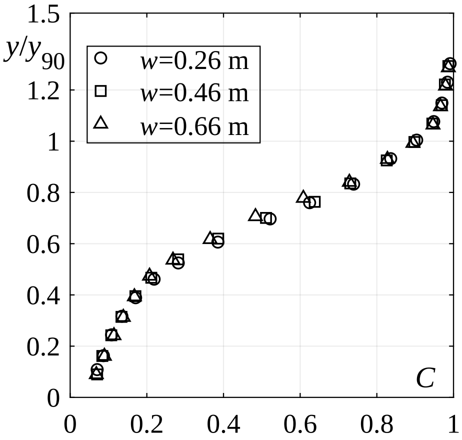

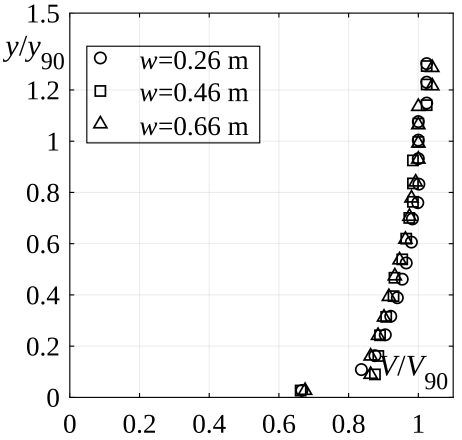

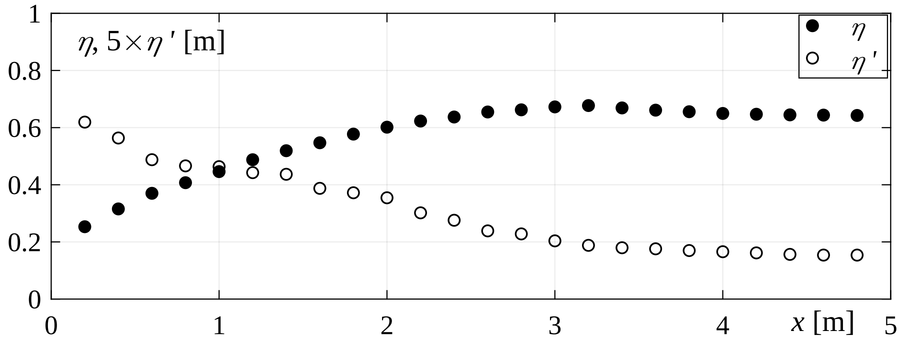

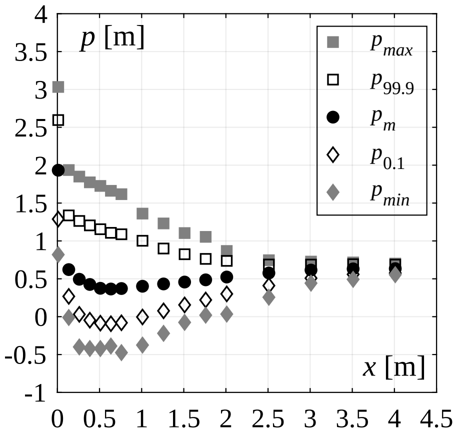

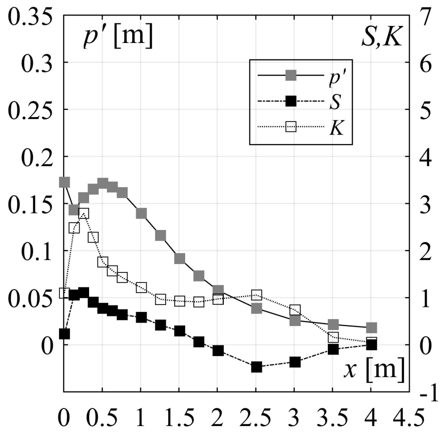

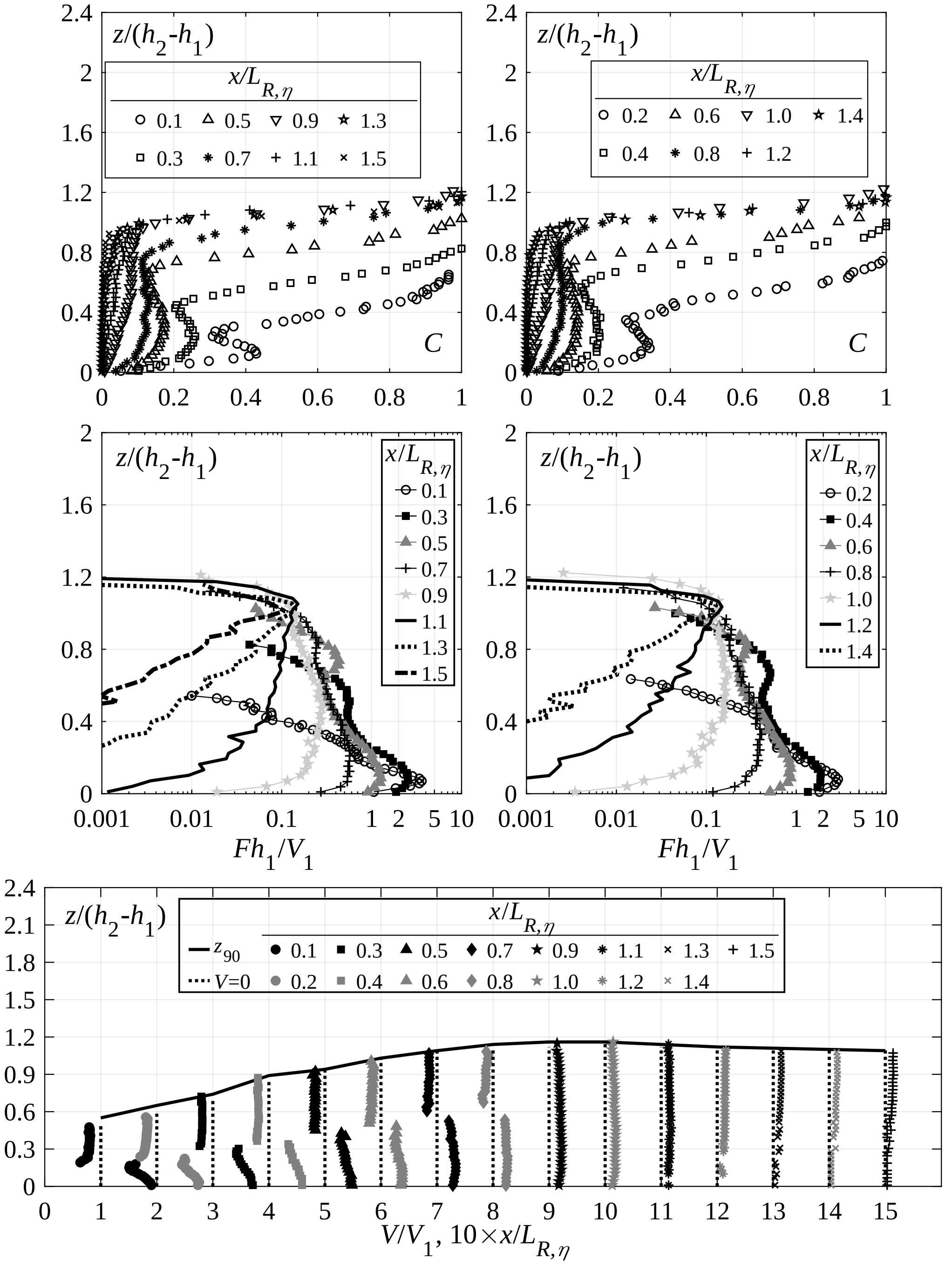
z/(h2-h1)
x/LR,η
0.1
0.3
0.5
0.7
0.9
1.1
1.3
1.5
C
z/(h2-h1)
x/LR,η
0.2
0.4
0.6
0.8
1.0
1.2
1.4
C
0
0.2
0.4
0.6
0.8
1
0
0.4
0.8
1.2
1.6
2
2.4
z/(h2-h1)
x/LR,η
0.1
0.3
0.5
0.7
0.9
1.1
1.3
1.5
Fh1/V1
z/(h2-h1)
x/LR,η
0.2
0.4
0.6
0.8
1.0
1.2
1.4
Fh1/V1
0.001
0.01
0.1
1
2
5
10
0
0.4
0.8
1.2
1.6
2
z/(h2-h1)
x/LR,η
z90
V=0
0.1
0.2
0.3
0.4
0.5
0.6
0.7
0.8
0.9
1.0
1.1
1.2
1.3
1.4
1.5
V/V1, 10×x/LR,η
0
1
2
3
4
5
6
7
8
9
10
11
12
13
14
15
0
0.3
0.6
0.9
1.2
1.5
1.8
2.1
2.4

Test Run 18

φ = 50°
q=0.358 m^2/s
Configuration: Smooth R+PA

w [m]	C_1 [-]	y_{90} [m]	V_{90} [m/s]	h_1 [m]	V_1 [m/s]	α [-]	F_1 [-]	$R_1\times10^5$ [-]	W_1 [-]
0.26	0.35	0.065	9.68	0.043	8.38	1.07	13.0	3.58	203
0.46	0.34	0.066	9.54	0.043	8.24	1.07	12.6	3.58	201
0.66	0.34	0.066	9.54	0.044	8.19	1.07	12.5	3.58	201

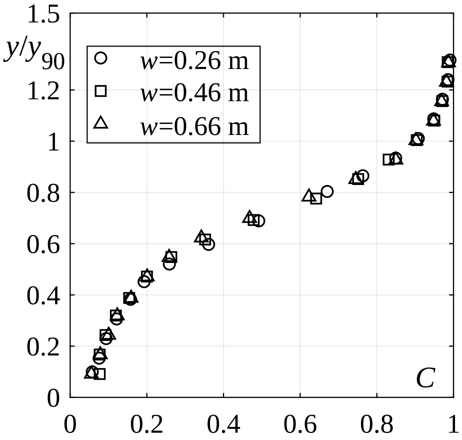

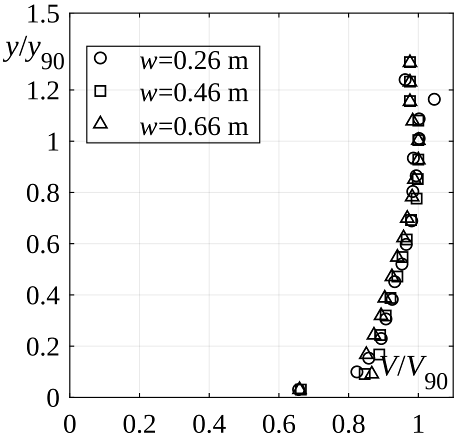

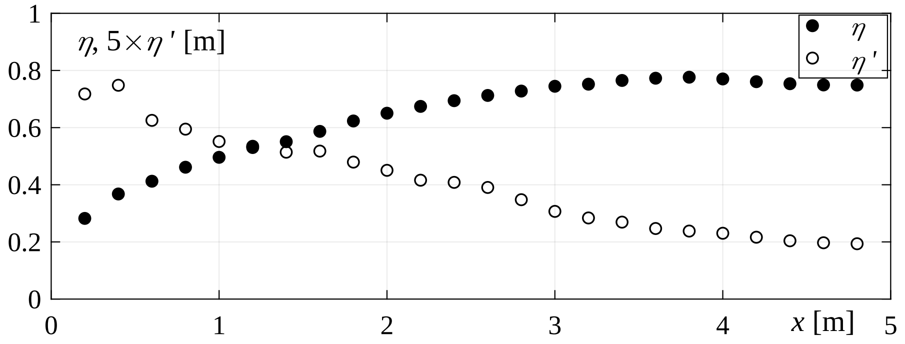

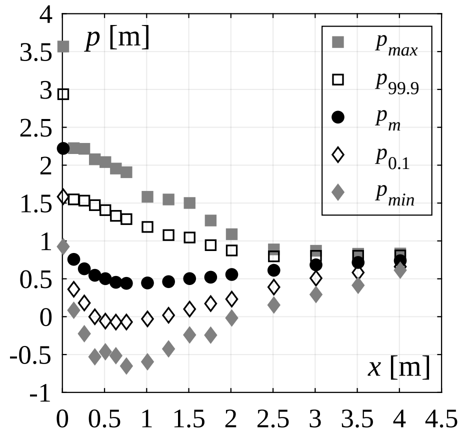

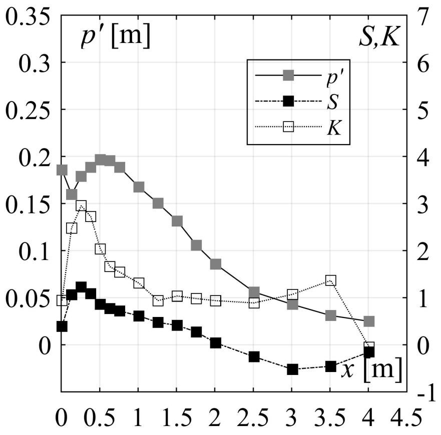

Test Run 19

φ = 50°
q=0.199 m^2/s
Configuration: Smooth R

w [m]	C_1 [-]	y_{90} [m]	V_{90} [m/s]	h_1 [m]	V_1 [m/s]	α [-]	F_1 [-]	$R_1\times10^5$ [-]	W_1 [-]
0.26	0.28	0.040	8.08	0.029	6.88	1.08	12.9	1.99	137
0.46	0.29	0.040	8.01	0.029	6.95	1.08	13.1	1.99	138
0.66	0.28	0.040	7.86	0.029	6.87	1.08	12.9	1.99	137

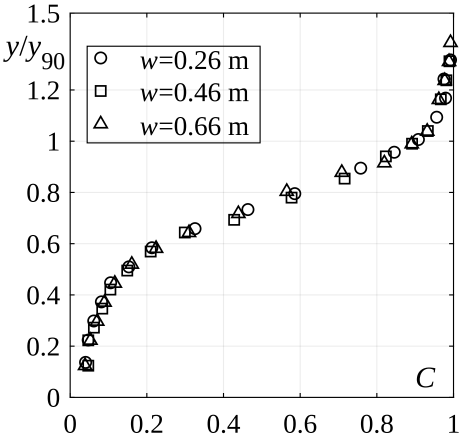

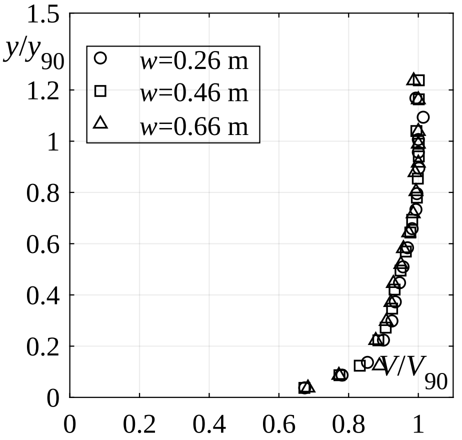

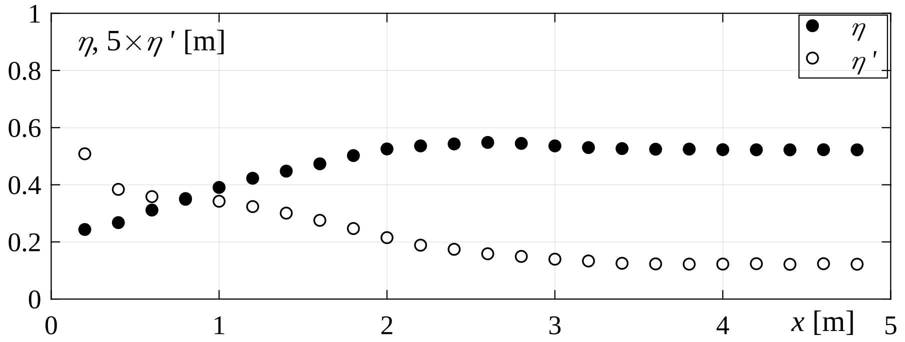

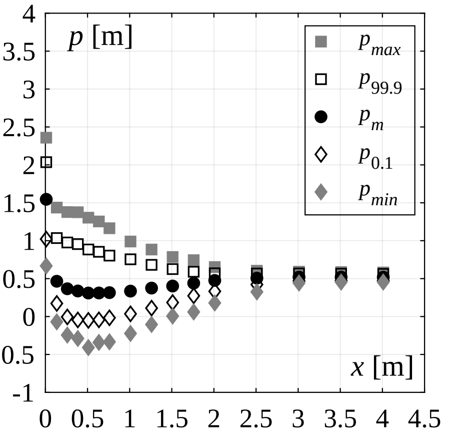

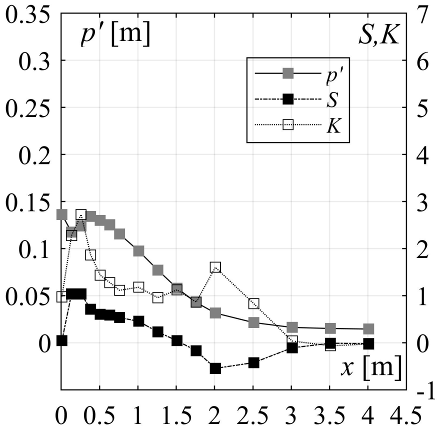

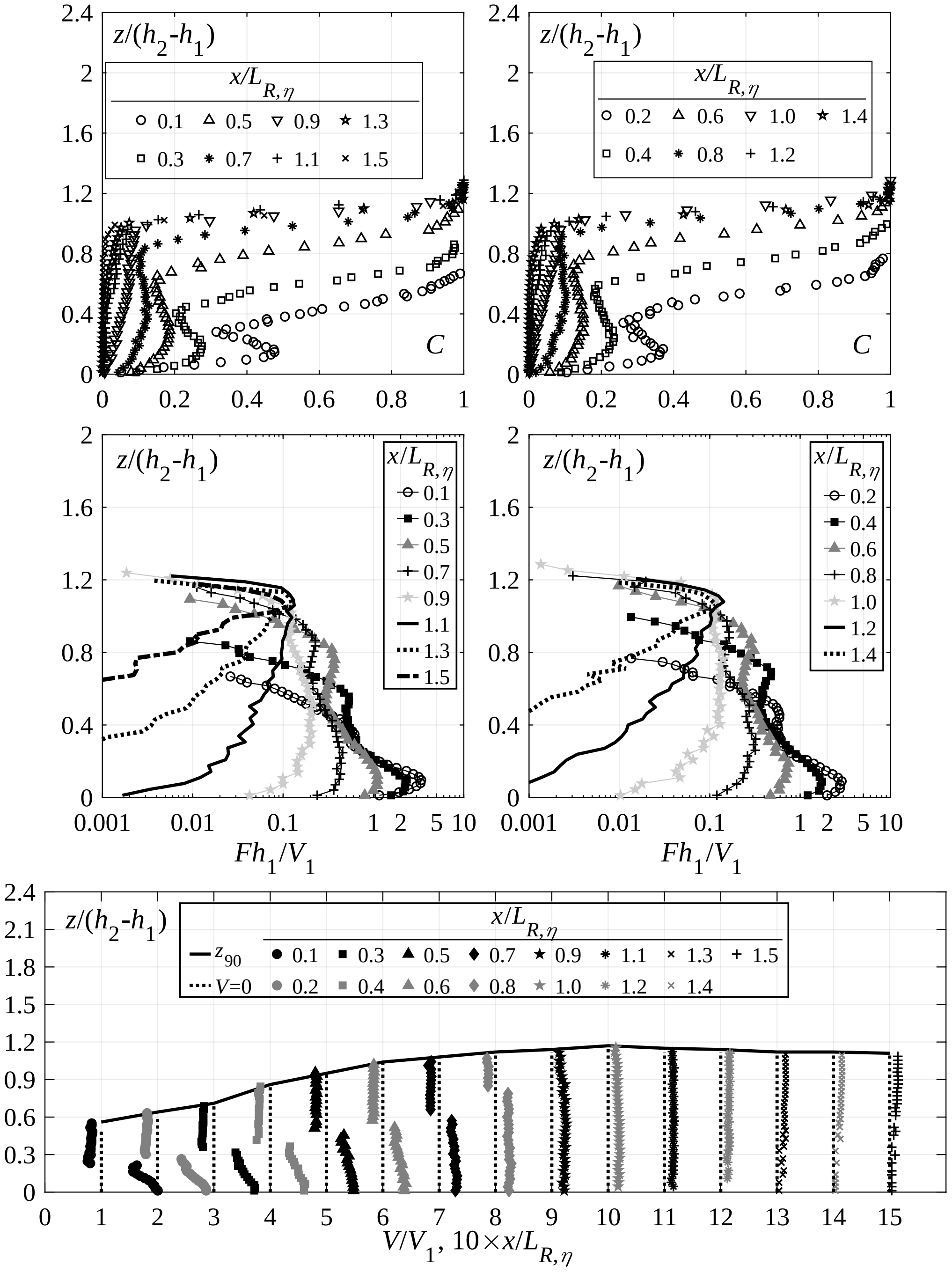

$z/(h_2-h_1)$
$x/L_{R,\eta}$
○ 0.1 △ 0.5 ▽ 0.9 ★ 1.3
□ 0.3 ✱ 0.7 + 1.1 × 1.5
C
○ 0.2 △ 0.6 ▽ 1.0 ★ 1.4
□ 0.4 ✱ 0.8 + 1.2
0 0.2 0.4 0.6 0.8 1
0 0.4 0.8 1.2 1.6 2 2.4
0.1 0.3 0.5 0.7 0.9 1.1 1.3 1.5
0.2 0.4 0.6 0.8 1.0 1.2 1.4
0.001 0.01 0.1 1 2 5 10
Fh_1/V_1
z_{90}
V=0
0 0.3 0.6 0.9 1.2 1.5 1.8 2.1 2.4
0 1 2 3 4 5 6 7 8 9 10 11 12 13 14 15
V/V_1, $10\times x/L_{R,\eta}$

Test Run 20

$\varphi = 50°$
q=0.278 m^2/s
Configuration: Smooth R

w [m]	C_1 [-]	y_{90} [m]	V_{90} [m/s]	h_1 [m]	V_1 [m/s]	α [-]	F_1 [-]	$R_1 \times 10^5$ [-]	W_1 [-]
0.26	0.29	0.053	8.68	0.038	7.41	1.07	12.2	2.78	168
0.46	0.28	0.052	8.62	0.038	7.38	1.08	12.1	2.78	168
0.66	0.28	0.052	8.56	0.038	7.40	1.08	12.2	2.78	168

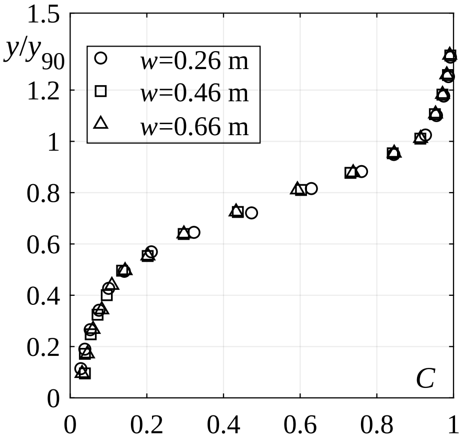

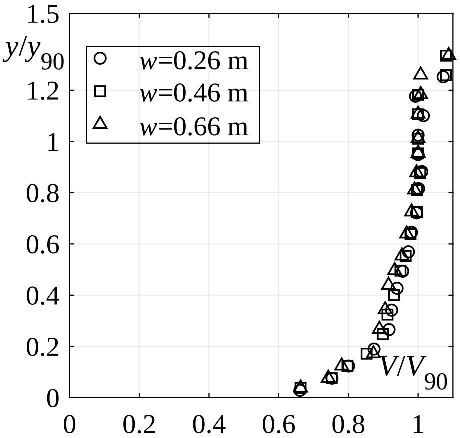

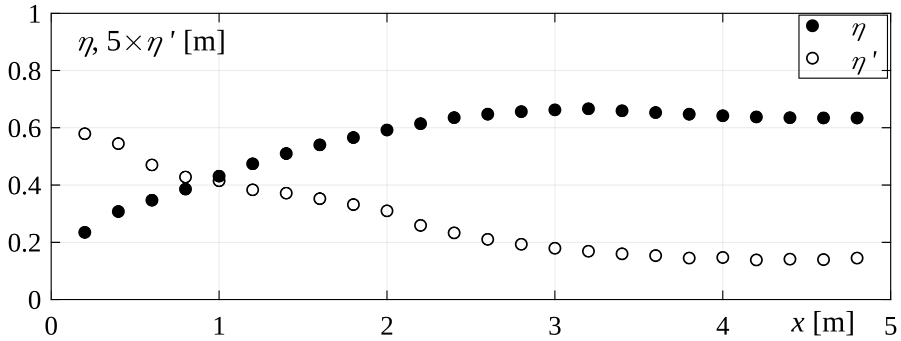

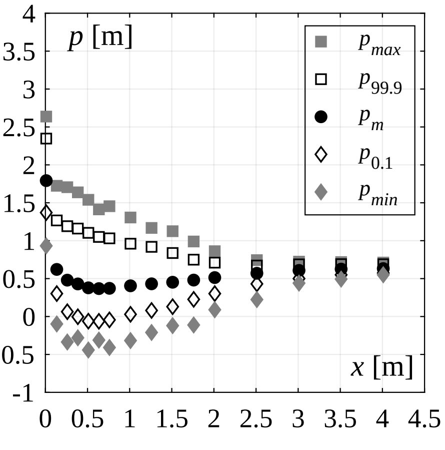

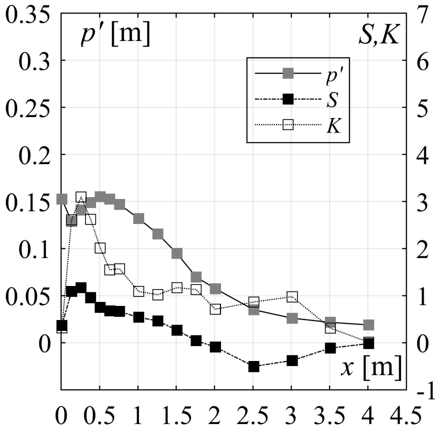

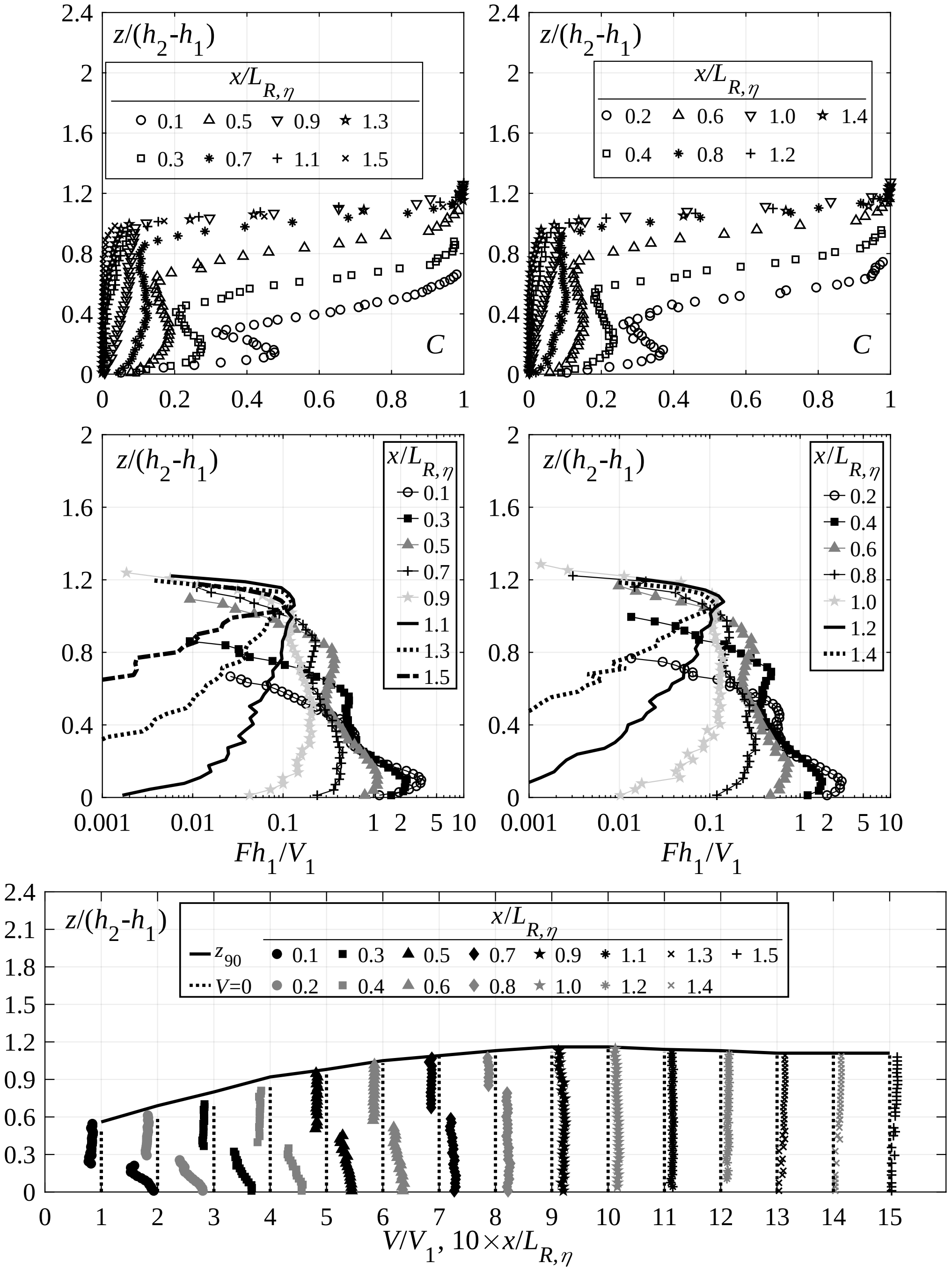
z/(h2-h1)
x/LR,η
0.1 0.5 0.9 1.3
0.3 0.7 1.1 1.5
C
0.2 0.6 1.0 1.4
0.4 0.8 1.2
0 0.2 0.4 0.6 0.8 1
0 0.4 0.8 1.2 1.6 2 2.4
0.1 0.3 0.5 0.7 0.9 1.1 1.3 1.5
0.2 0.4 0.6 0.8 1.0 1.2 1.4
0.001 0.01 0.1 1 2 5 10
Fh1/V1
z90
V=0
0 1 2 3 4 5 6 7 8 9 10 11 12 13 14 15
0 0.3 0.6 0.9 1.2 1.5 1.8 2.1 2.4
V/V1, 10×x/LR,η

Test Run 21

φ = 50°
q=0.358 m^2/s
Configuration: Smooth R

w [m]	C_1 [-]	y_{90} [m]	V_{90} [m/s]	h_1 [m]	V_1 [m/s]	α [-]	F_1 [-]	$R_1\times10^5$ [-]	W_1 [-]
0.26	0.16	0.031	8.82	0.026	7.61	1.08	15.0	1.99	144
0.46	0.16	0.031	8.64	0.026	7.67	1.08	15.2	1.99	145
0.66	0.17	0.031	8.43	0.026	7.64	1.08	15.1	1.99	145

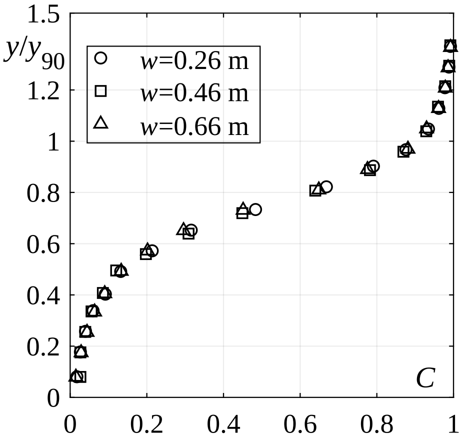

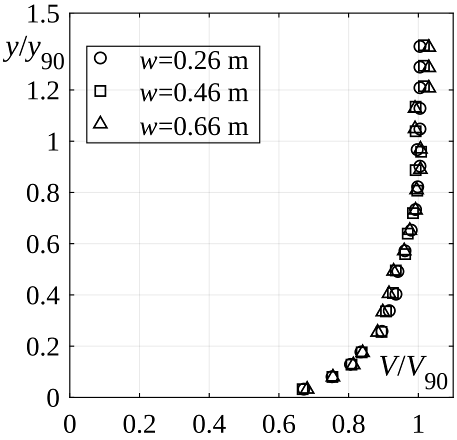

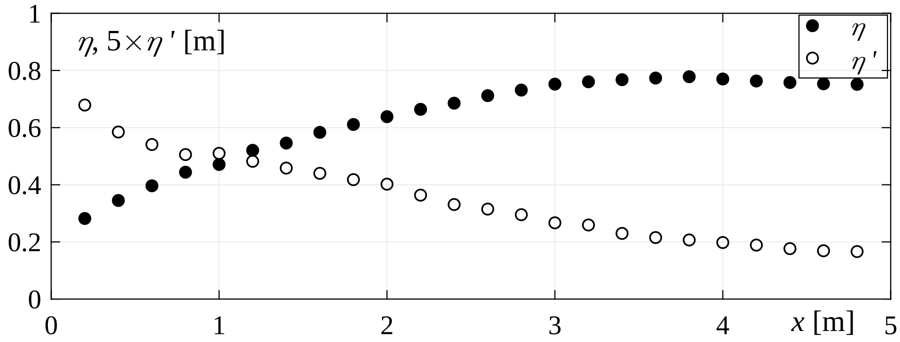

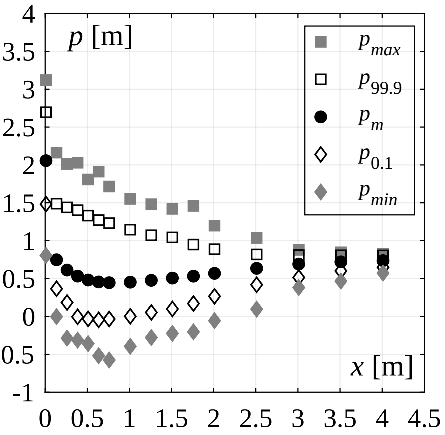

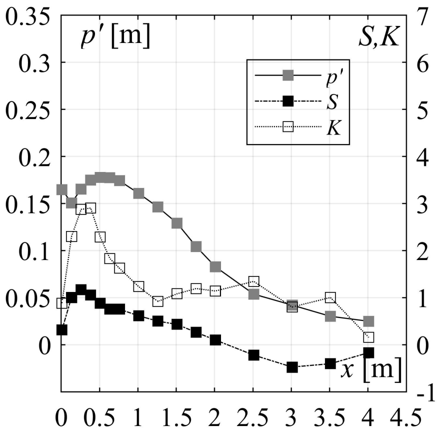

Test Run 22

$\varphi = 50°$
q=0.199 m^2/s
Configuration: Smooth SM

w [m]	C_1 [-]	y_{90} [m]	V_{90} [m/s]	h_1 [m]	V_1 [m/s]	α [-]	F_1 [-]	$R_1\times10^5$ [-]	W_1 [-]
0.26	0.16	0.031	8.82	0.026	7.61	1.08	15.0	1.99	144
0.46	0.16	0.031	8.64	0.026	7.67	1.08	15.2	1.99	145
0.66	0.17	0.031	8.43	0.026	7.64	1.08	15.1	1.99	145

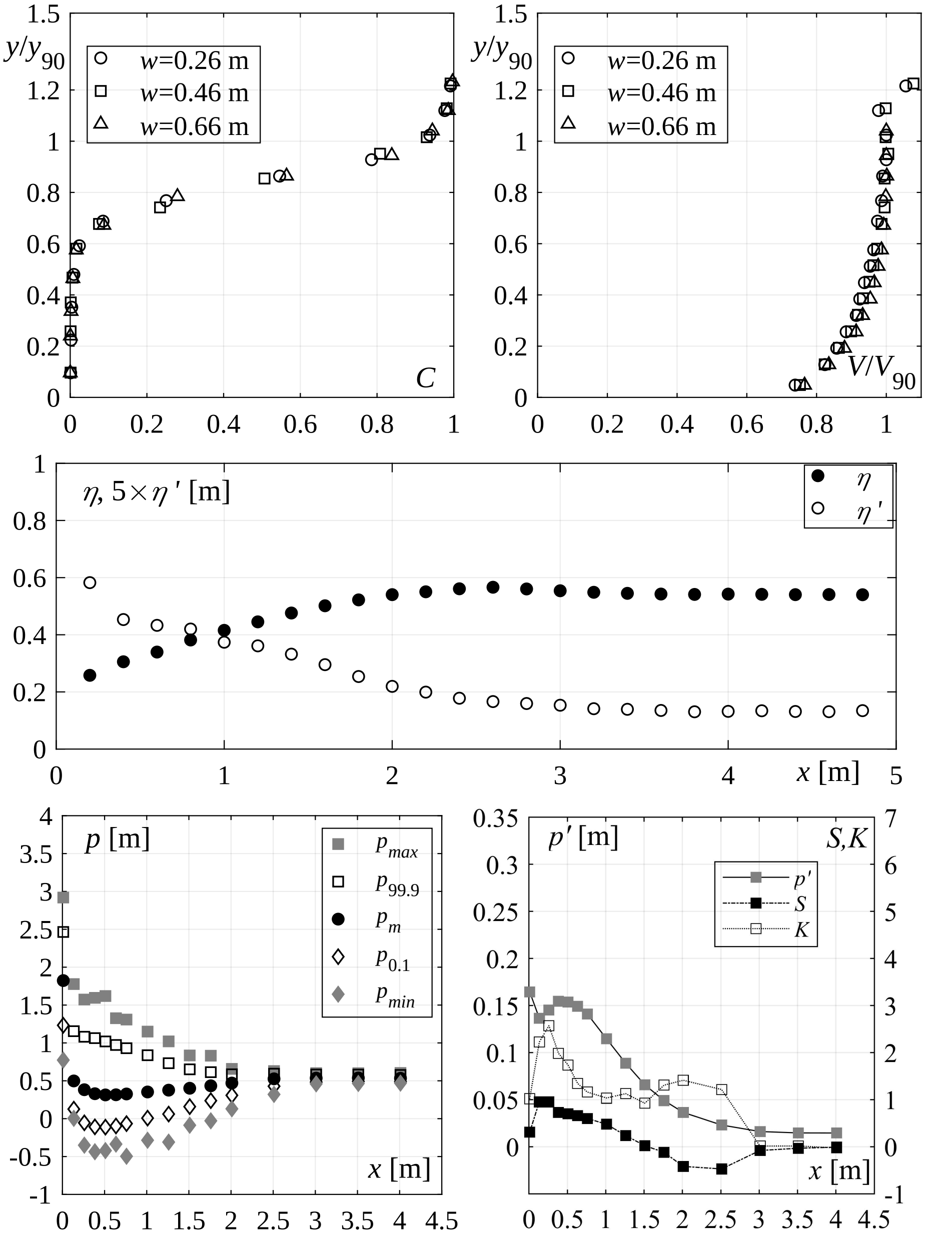

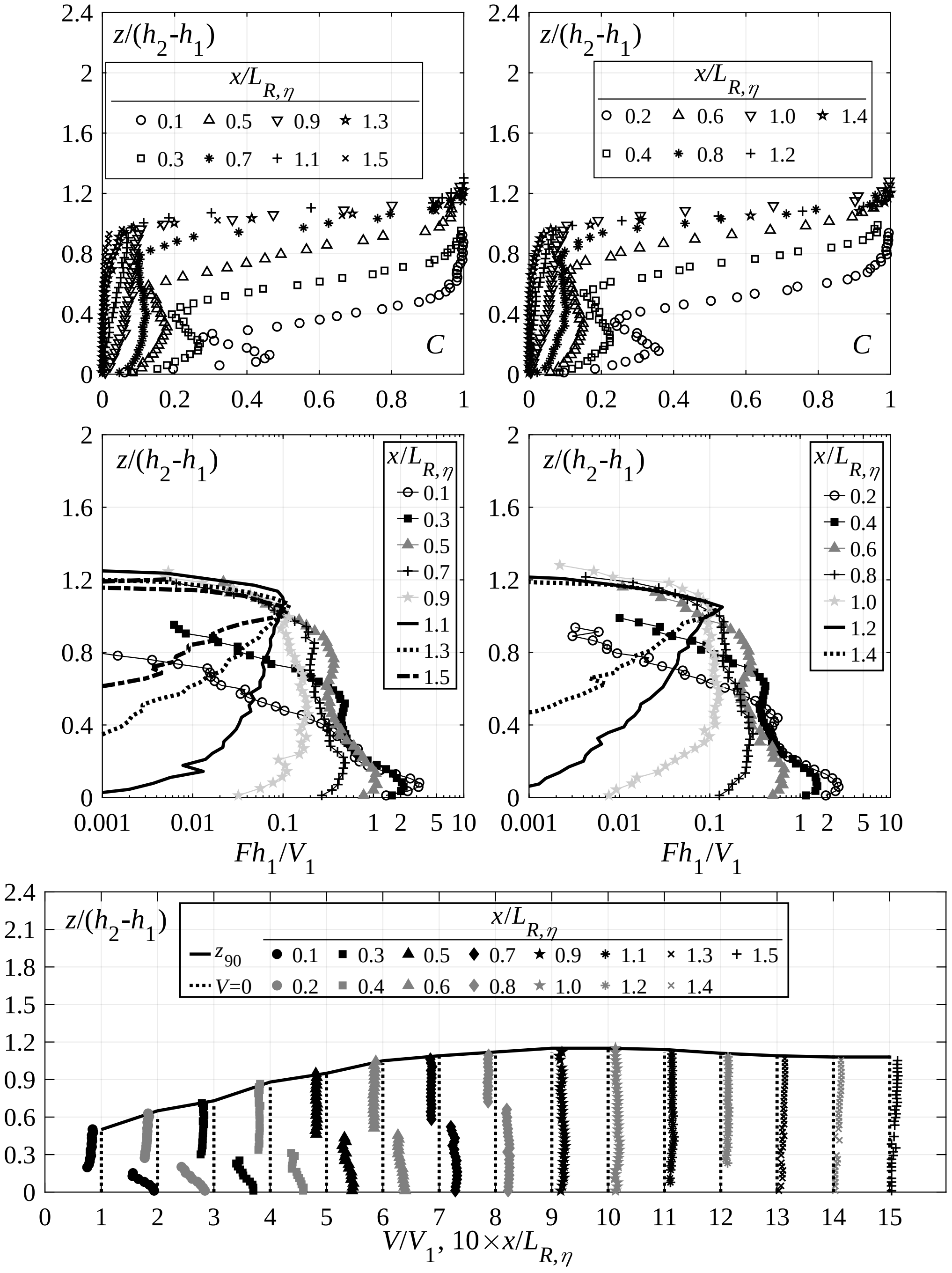
$z/(h_2\text{-}h_1)$
$x/L_{R,\eta}$
0.1 0.5 0.9 1.3
0.3 0.7 1.1 1.5
C
0.2 0.6 1.0 1.4
0.4 0.8 1.2
C
Fh_1/V_1
0.001 0.01 0.1 1 2 5 10
z_{90}
V=0
V/V_1, $10\times x/L_{R,\eta}$
0 1 2 3 4 5 6 7 8 9 10 11 12 13 14 15
0 0.3 0.6 0.9 1.2 1.5 1.8 2.1 2.4

Test Run 23

$\varphi = 50°$
q=0.279 m^2/s
Configuration: Smooth SM

w [m]	C_1 [-]	y_{90} [m]	V_{90} [m/s]	h_1 [m]	V_1 [m/s]	α [-]	F_1 [-]	$R_1 \times 10^5$ [-]	W_1 [-]
0.26	0.16	0.039	9.16	0.033	8.38	1.09	14.7	2.79	179
0.46	0.15	0.039	9.09	0.033	8.38	1.09	14.7	2.79	179
0.66	0.15	0.039	8.89	0.033	8.37	1.08	14.6	2.79	179

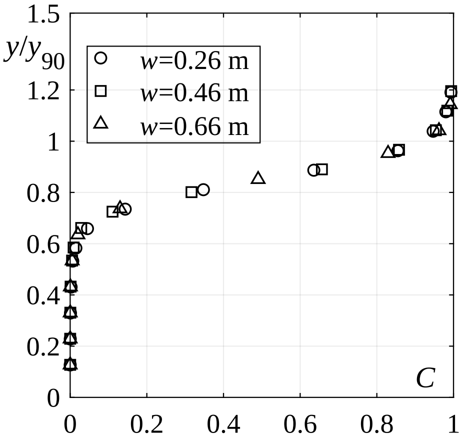

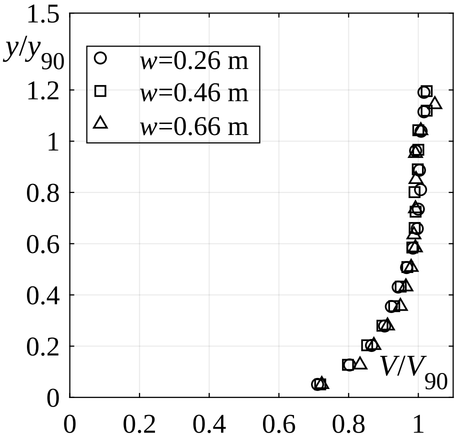

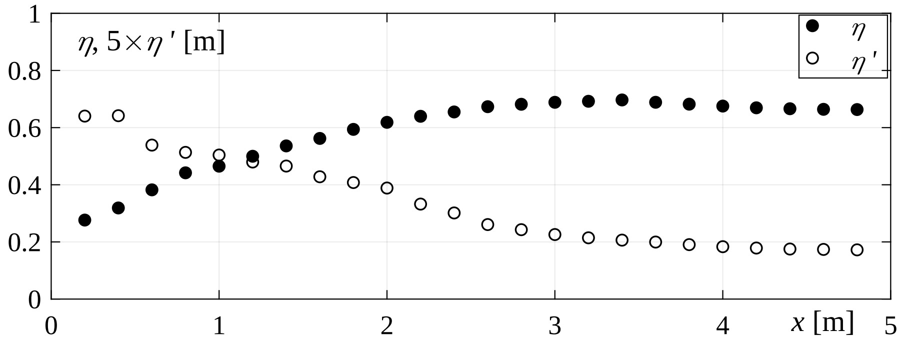

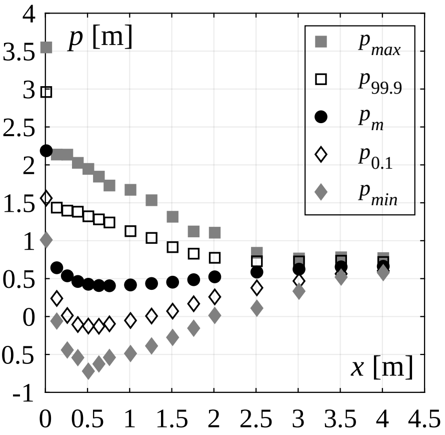

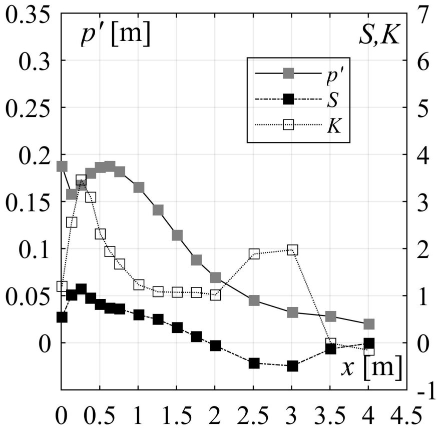

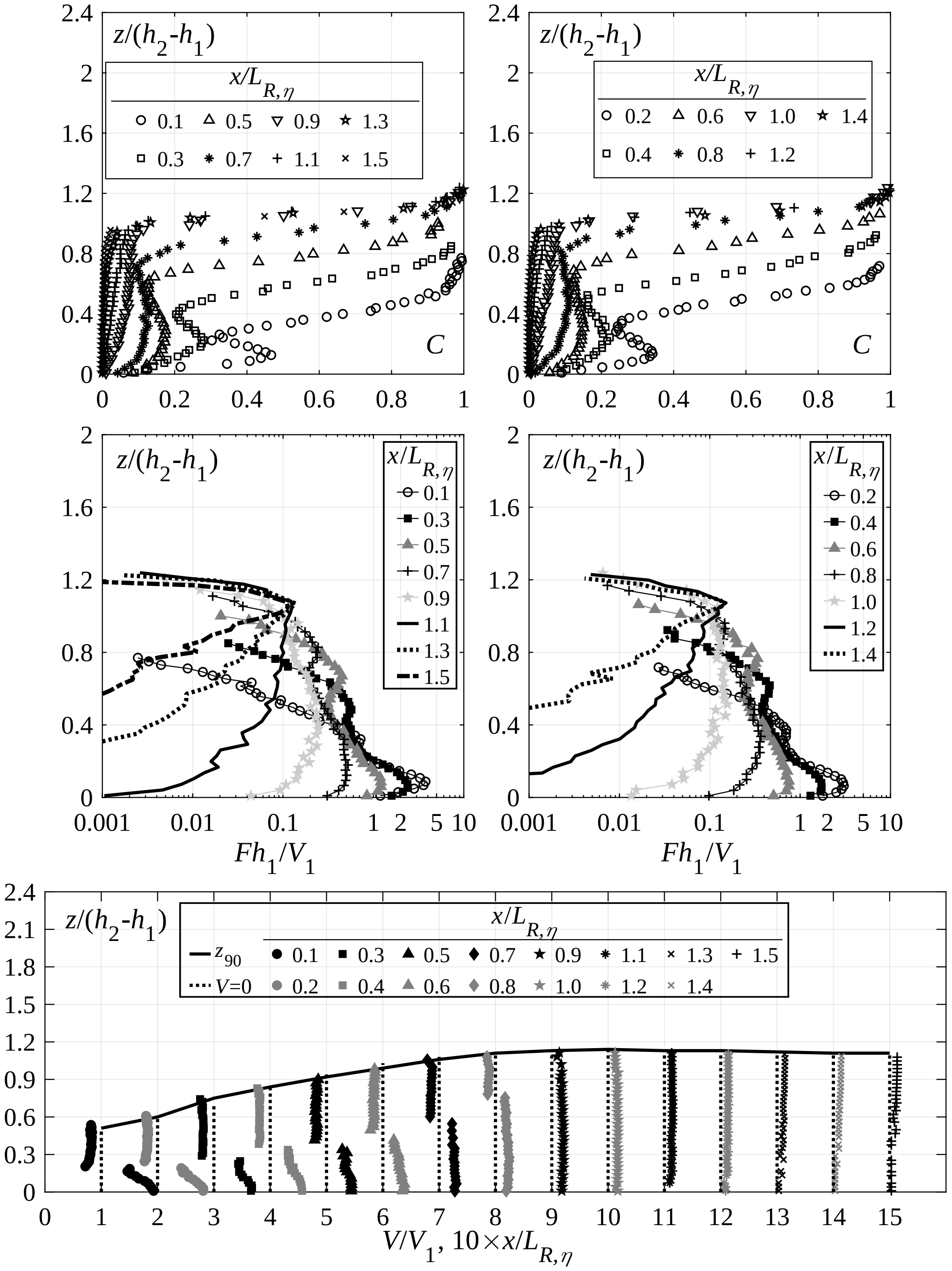
z/(h2-h1)
x/LR,η
○ 0.1 △ 0.5 ▽ 0.9 ★ 1.3
□ 0.3 ✱ 0.7 + 1.1 × 1.5
C
○ 0.2 △ 0.6 ▽ 1.0 ★ 1.4
□ 0.4 ✱ 0.8 + 1.2
0 0.2 0.4 0.6 0.8 1
0 0.4 0.8 1.2 1.6 2 2.4
0.1 0.3 0.5 0.7 0.9 1.1 1.3 1.5
0.2 0.4 0.6 0.8 1.0 1.2 1.4
0.001 0.01 0.1 1 2 5 10
Fh1/V1
z90
V=0
0.1 0.3 0.5 0.7 0.9 1.1 1.3 1.5
0.2 0.4 0.6 0.8 1.0 1.2 1.4
0 0.3 0.6 0.9 1.2 1.5 1.8 2.1 2.4
0 1 2 3 4 5 6 7 8 9 10 11 12 13 14 15
V/V1, 10×x/LR,η

Test Run 24

φ = 50°
q=0.356 m^2/s
Configuration: Smooth SM

w [m]	C_1 [-]	y_{90} [m]	V_{90} [m/s]	h_1 [m]	V_1 [m/s]	α [-]	F_1 [-]	$R_1\times10^5$ [-]	W_1 [-]
0.26	0.15	0.046	9.65	0.040	8.99	1.08	14.4	3.56	210
0.46	0.15	0.046	9.50	0.040	8.99	1.07	14.4	3.56	210
0.66	0.15	0.047	9.31	0.040	8.97	1.07	14.4	3.56	210

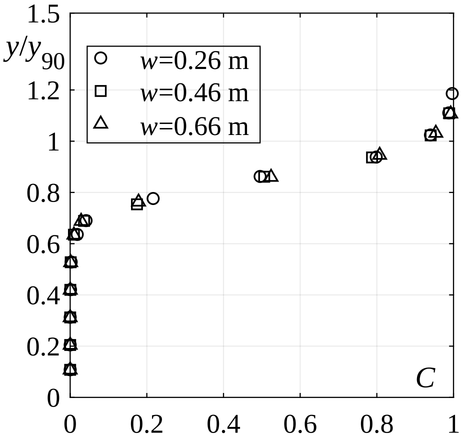

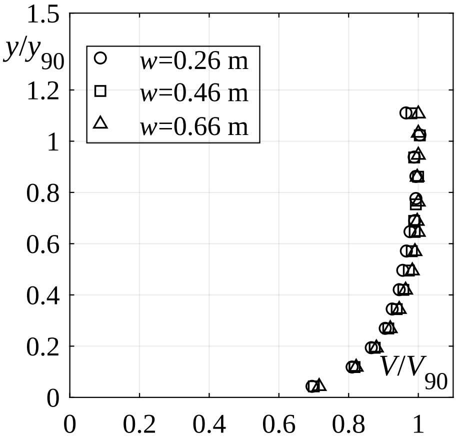

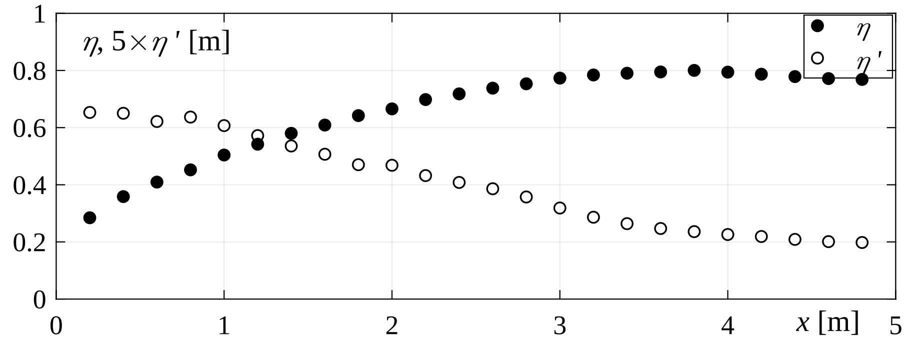

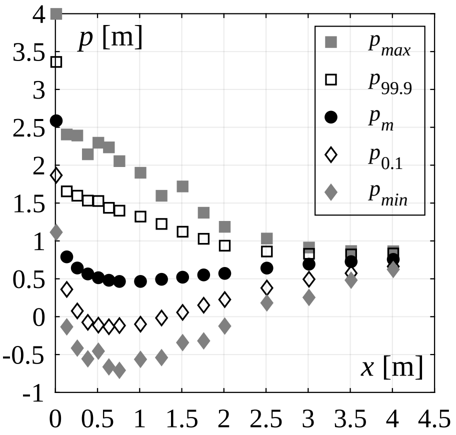

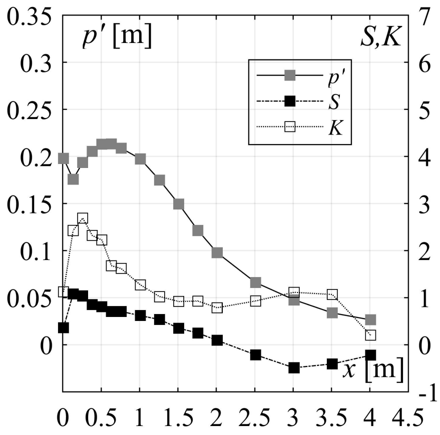

Test Run 25

φ = 50°
q=0.205 m^2/s
Configuration: Stepped s=0.06 m

w	C_1	y_{90}	V_{90}	h_1	V_1	α	F_1	R_1x10^5	W_1
[m]	[-]	[m]	[m/s]	[m]	[m/s]	[-]	[-]	[-]	[-]
0.235	0.55	0.092	6.89	0.041	4.95	1.18	7.8	2.05	118
0.313	0.53	0.090	6.86	0.042	4.87	1.18	7.6	2.05	117
0.391	0.54	0.090	6.84	0.042	4.91	1.18	7.7	2.05	118

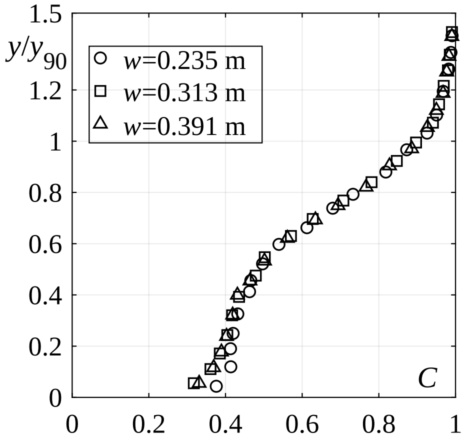

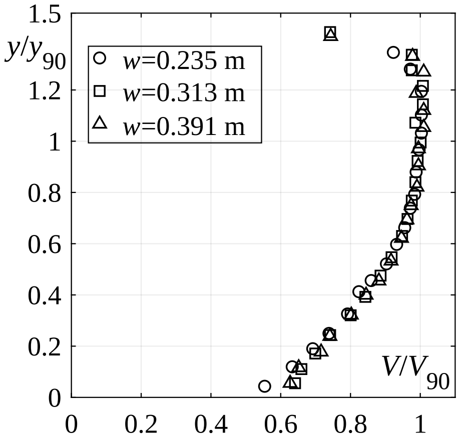

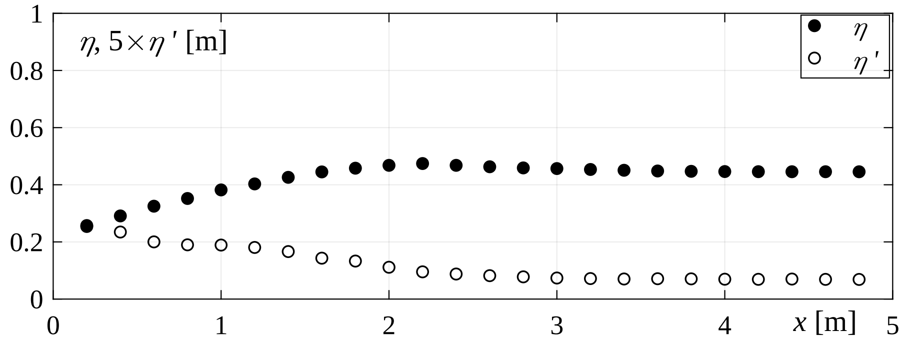

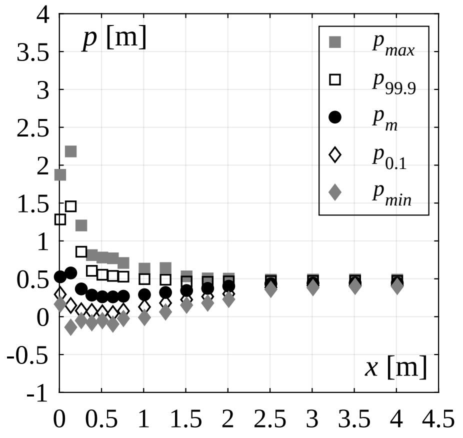

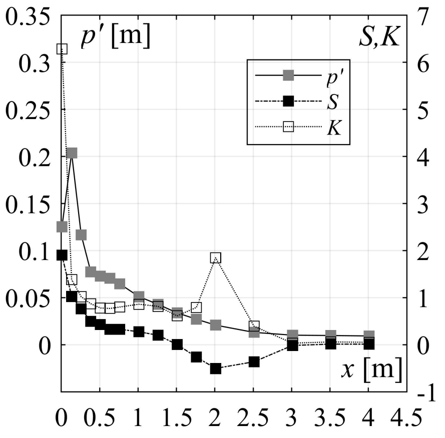

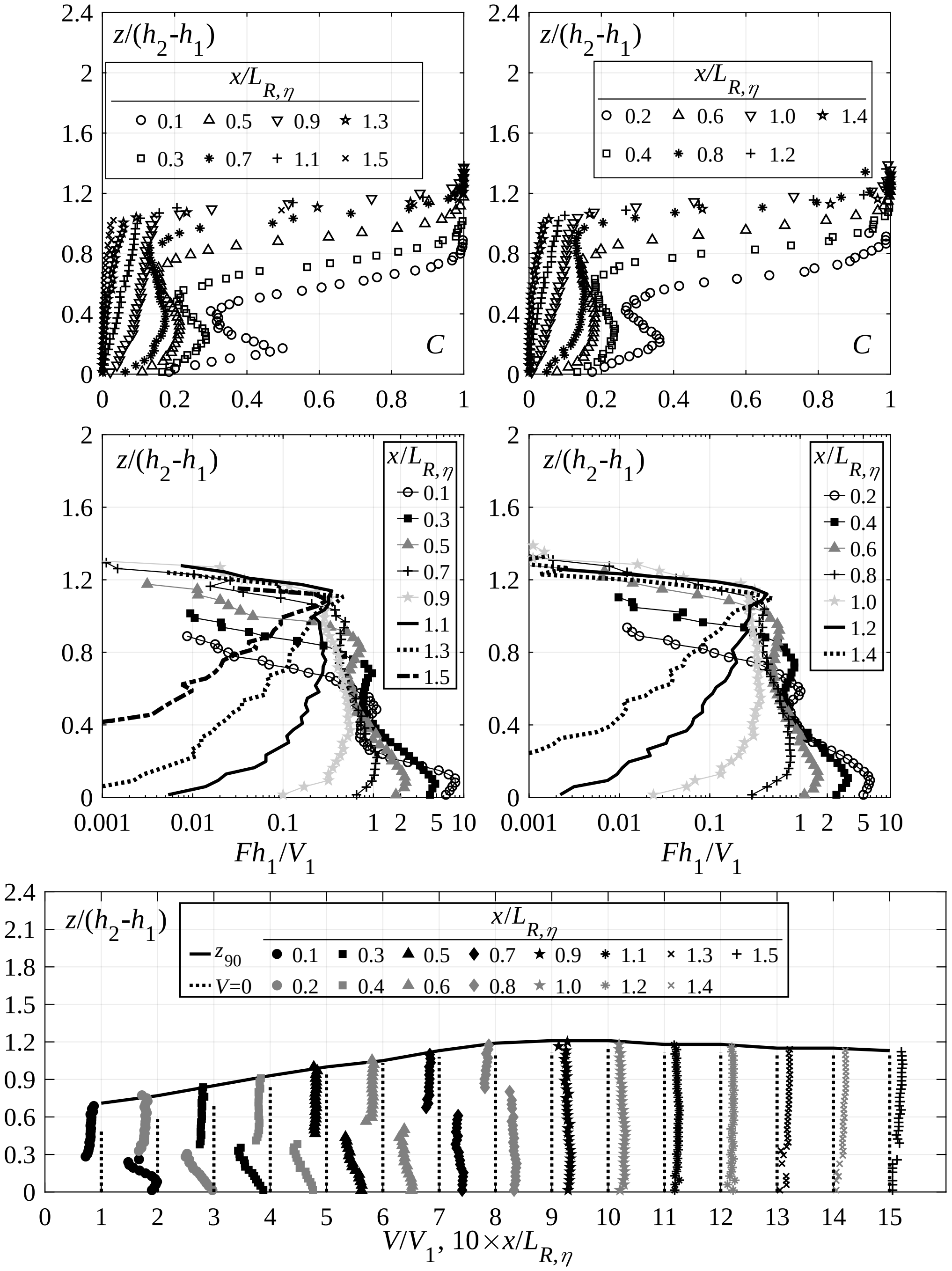
z/(h2-h1)
x/LR,η
0.1
0.3
0.5
0.7
0.9
1.1
1.3
1.5
0.2
0.4
0.6
0.8
1.0
1.2
1.4
C
0
0.2
0.4
0.6
0.8
1
1.2
1.6
2
2.4
Fh1/V1
0.001
0.01
0.1
1
2
5
10
z90
V=0
0.3
0.9
1.5
1.8
2.1
V/V1, 10×x/LR,η
3
4
6
7
8
9
11
12
13
14
15

Test Run 26

φ = 50°

q=0.284 m^2/s

Configuration: Stepped s=0.06 m

w [m]	C_1 [-]	y_{90} [m]	V_{90} [m/s]	h_1 [m]	V_1 [m/s]	α [-]	F_1 [-]	$R_1 \times 10^5$ [-]	W_1 [-]
0.235	0.53	0.109	7.49	0.051	5.52	1.19	7.8	2.84	147
0.313	0.52	0.108	7.48	0.052	5.48	1.19	7.7	2.84	146
0.391	0.52	0.108	7.44	0.052	5.49	1.18	7.7	2.84	146

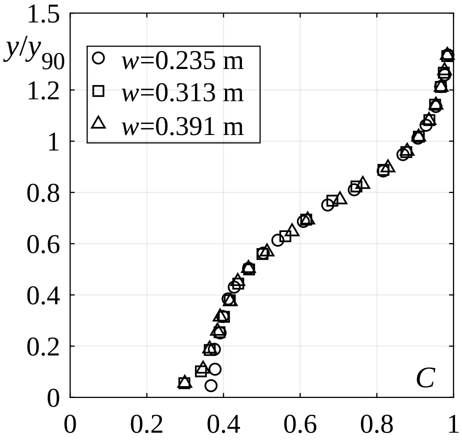

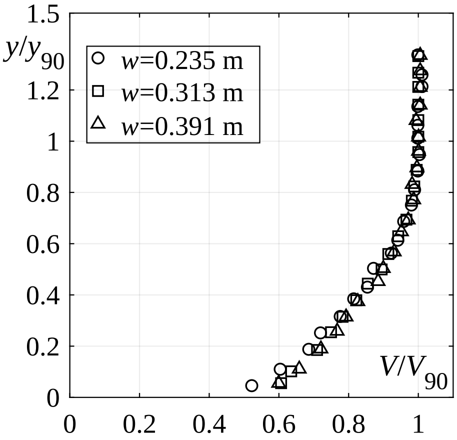

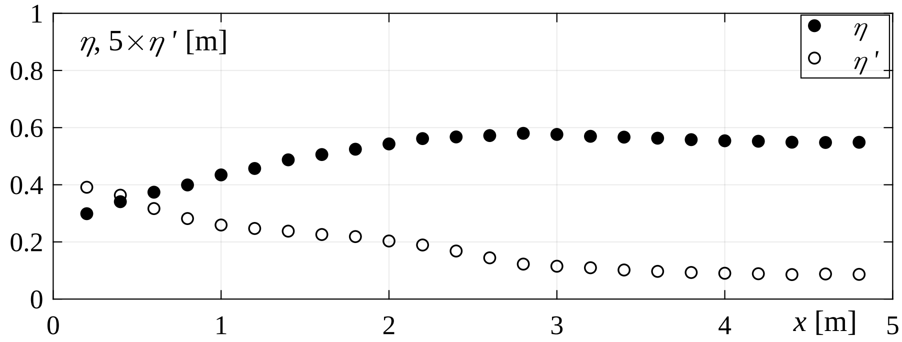

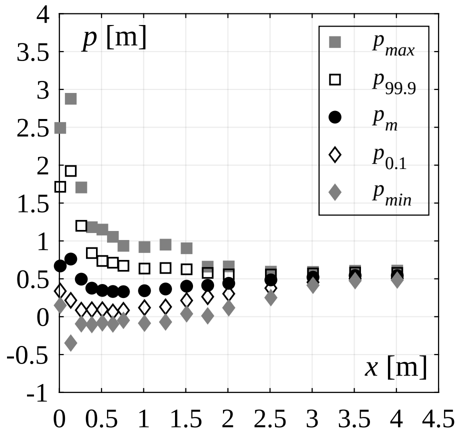

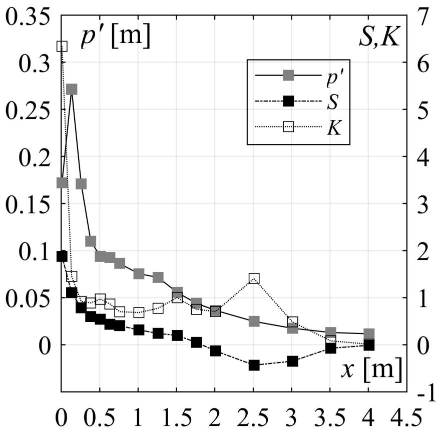

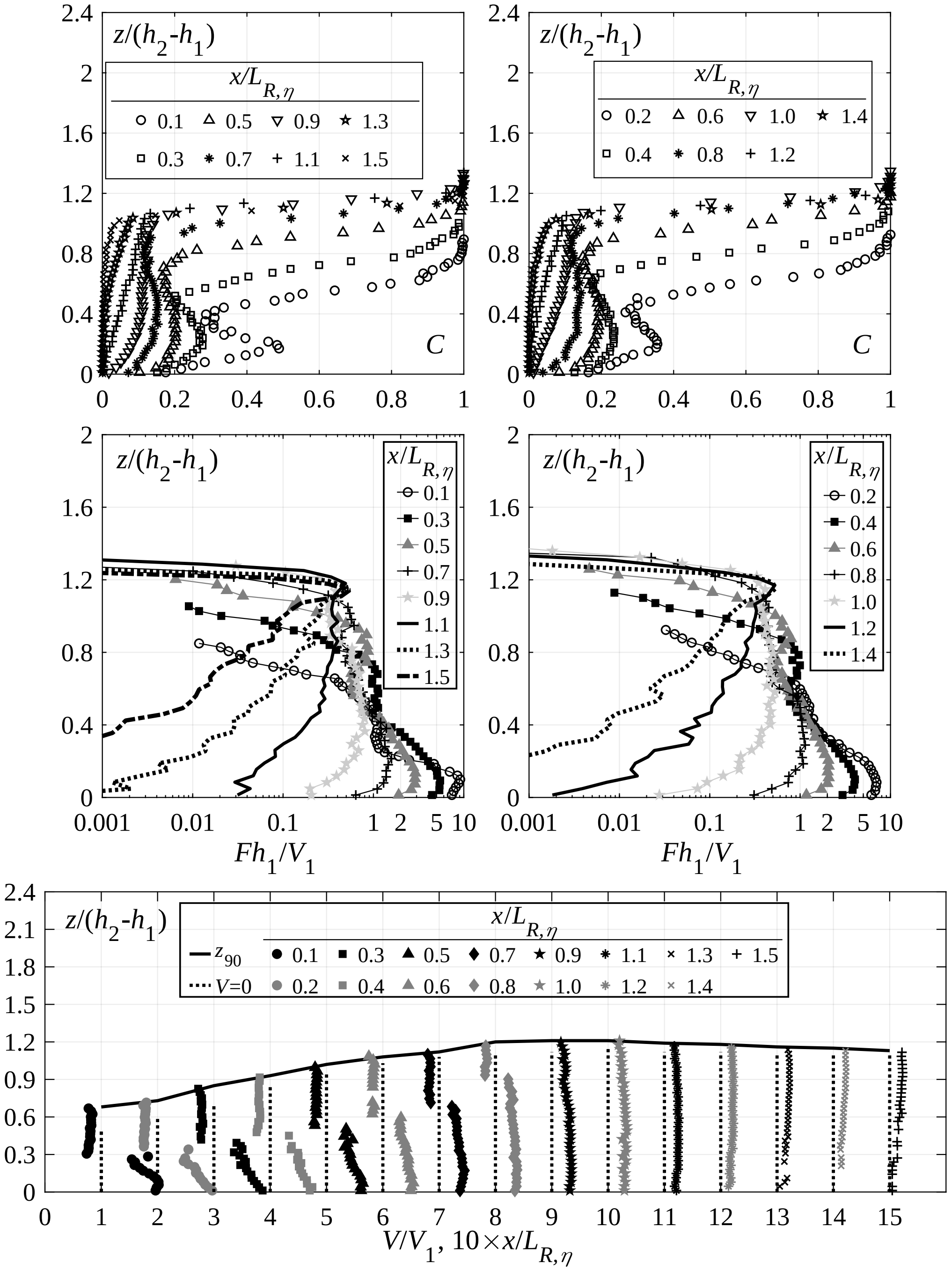
z/(h2-h1)
x/LR,η
0.1 0.5 0.9 1.3
0.3 0.7 1.1 1.5
C
0.2 0.6 1.0 1.4
0.4 0.8 1.2
C
x/LR,η
0.1 0.3 0.5 0.7 0.9 1.1 1.3 1.5
0.2 0.4 0.6 0.8 1.0 1.2 1.4
Fh1/V1
z90
V=0
V/V1, 10×x/LR,η
0 0.2 0.4 0.6 0.8 1
0.001 0.01 0.1 1 2 5 10
0 1 2 3 4 5 6 7 8 9 10 11 12 13 14 15
0 0.3 0.6 0.9 1.2 1.5 1.8 2.1 2.4
0 0.4 0.8 1.2 1.6 2 2.4

Test Run 27

φ = 50°
q=0.364 m^2/s
Configuration: Stepped s=0.06 m

w [m]	C_1 [-]	y_{90} [m]	V_{90} [m/s]	h_1 [m]	V_1 [m/s]	α [-]	F_1 [-]	$R_1 \times 10^5$ [-]	W_1 [-]
0.235	0.50	0.123	7.79	0.061	5.96	1.19	7.7	3.64	173
0.313	0.50	0.120	7.81	0.061	6.02	1.17	7.8	3.64	173
0.391	0.49	0.120	7.68	0.060	6.02	1.18	7.8	3.64	174

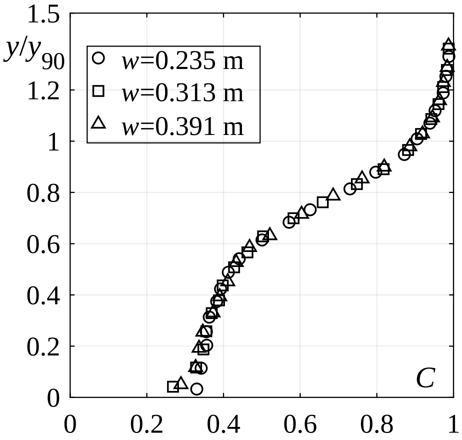

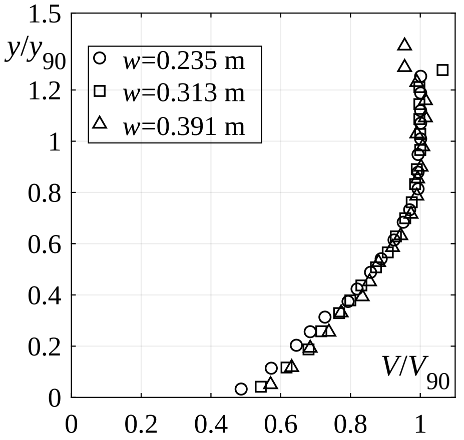

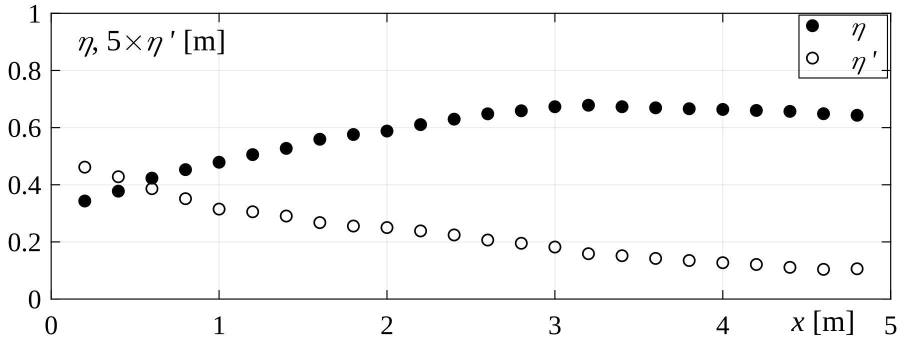

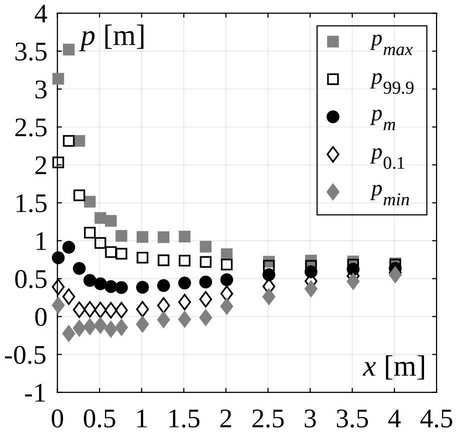

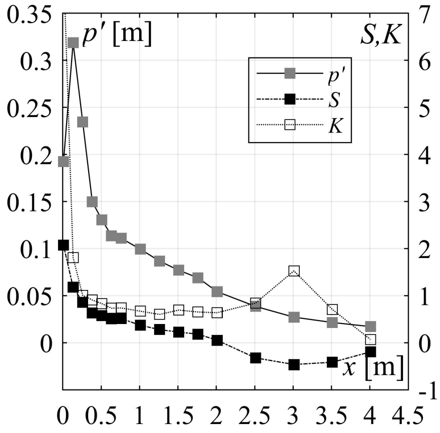

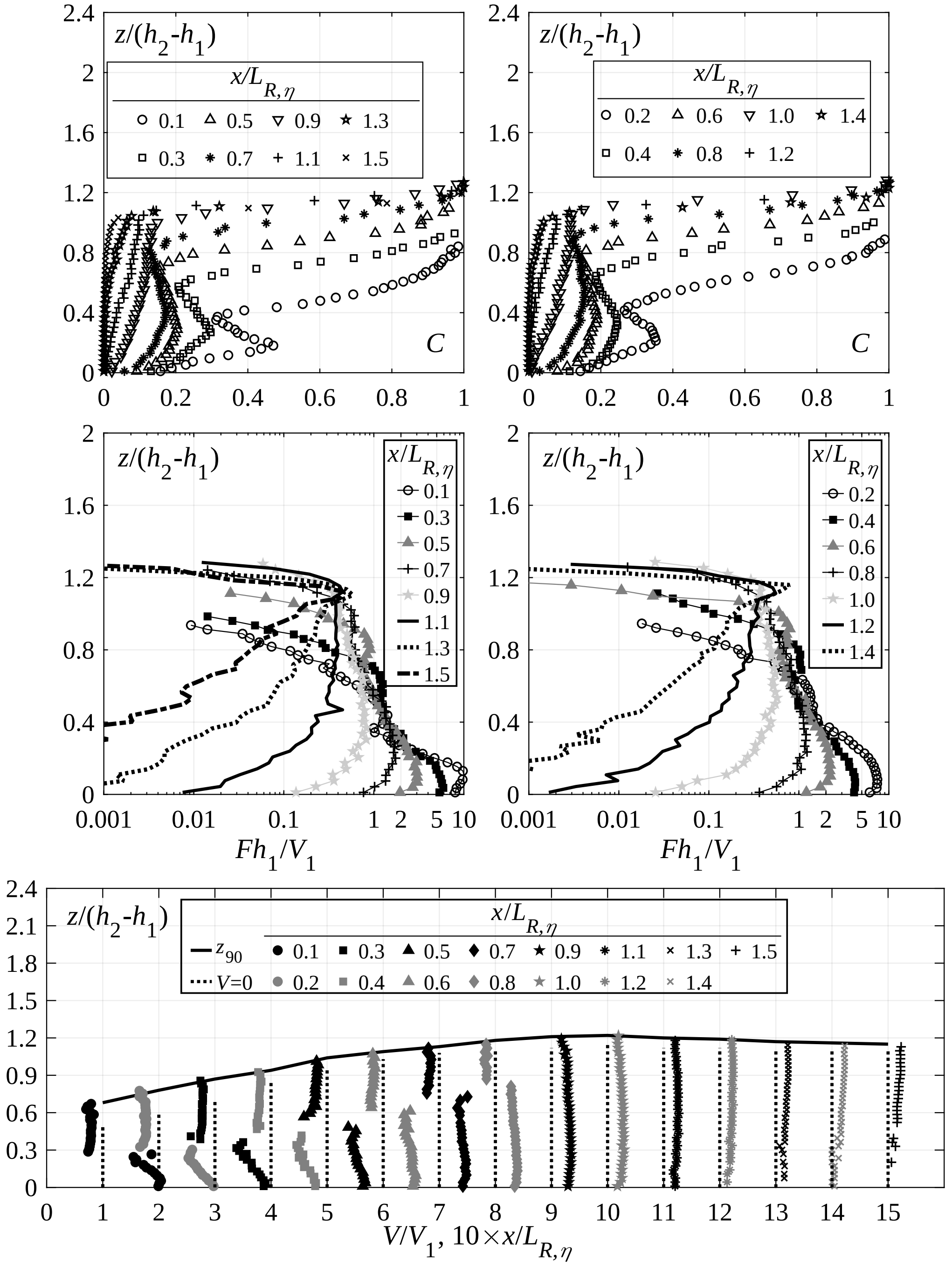
$z/(h_2\text{-}h_1)$
$x/L_{R,\eta}$
0.1 0.5 0.9 1.3
0.3 0.7 1.1 1.5
0.2 0.6 1.0 1.4
0.4 0.8 1.2
C
Fh_1/V_1
0.001 0.01 0.1 1 2 5 10
z_{90}
V=0
V/V_1, $10\times x/L_{R,\eta}$
0 1 2 3 4 5 6 7 8 9 10 11 12 13 14 15
0 0.3 0.6 0.9 1.2 1.5 1.8 2.1 2.4
0 0.4 0.8 1.2 1.6 2 2.4
0 0.2 0.4 0.6 0.8 1

Test Run 28

$\varphi = 50°$

q=0.205 m^2/s

Configuration: Stepped *s*=0.03 m

w	C_1	y_{90}	V_{90}	h_1	V_1	α	F_1	$R_1 \times 10^5$	W_1
[m]	[-]	[m]	[m/s]	[m]	[m/s]	[-]	[-]	[-]	[-]
0.235	0.50	0.080	7.11	0.040	5.10	1.18	8.1	2.05	120
0.313	0.49	0.079	7.07	0.040	5.12	1.20	8.2	2.05	120
0.391	0.49	0.078	7.06	0.040	5.12	1.18	8.2	2.05	120

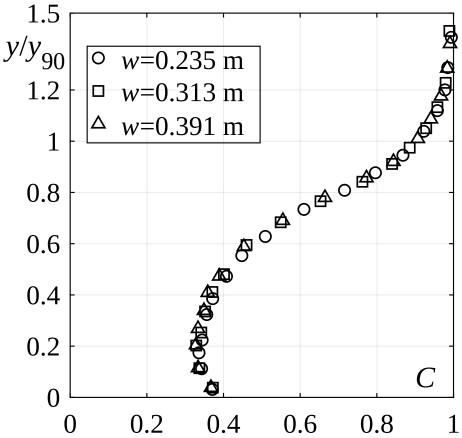

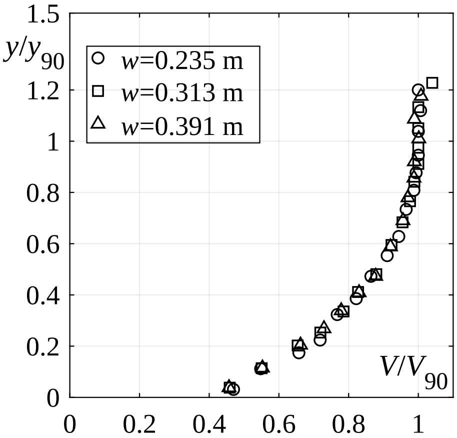

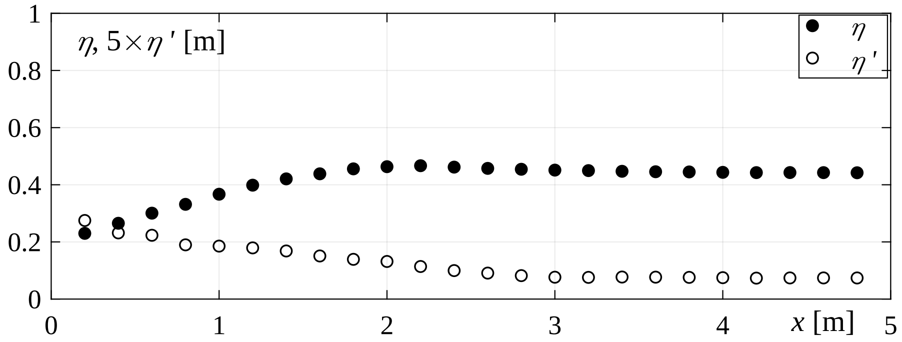

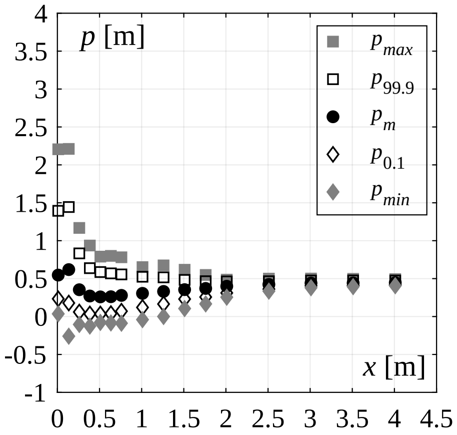

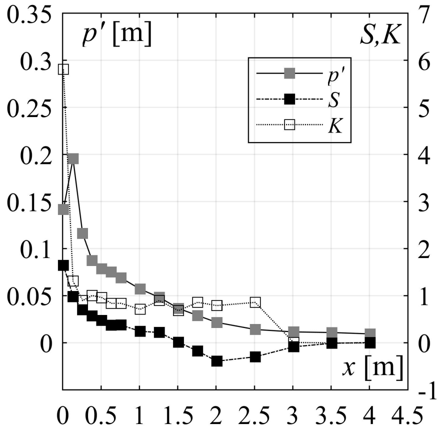

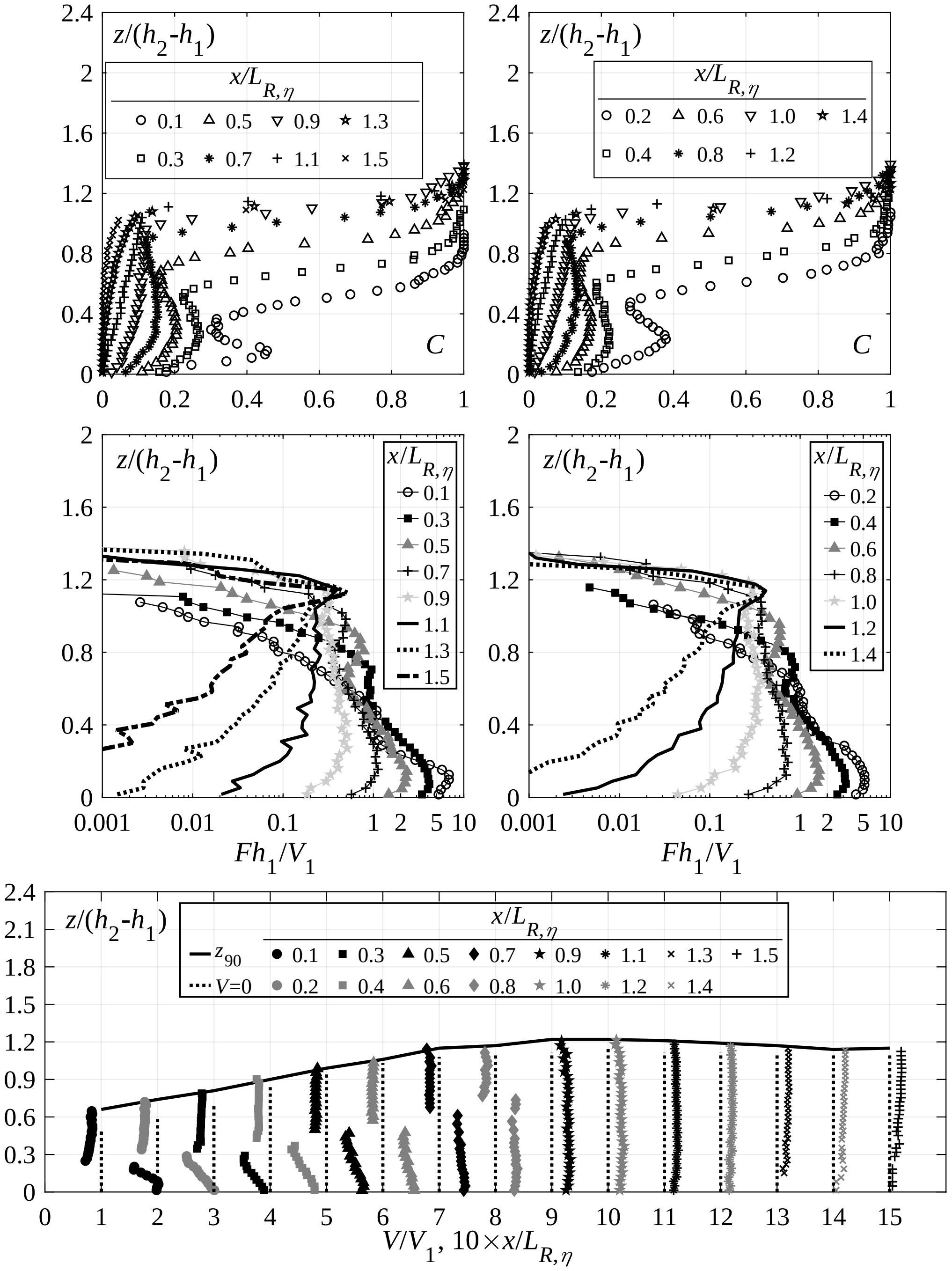
2.4
2
1.6
1.2
0.8
0.4
0
$z/(h_2\text{-}h_1)$
$x/L_{R,\eta}$
○ 0.1 △ 0.5 ▽ 0.9 ★ 1.3
□ 0.3 ✱ 0.7 + 1.1 × 1.5
○ 0.2 △ 0.6 ▽ 1.0 ★ 1.4
□ 0.4 ✱ 0.8 + 1.2
C
0 0.2 0.4 0.6 0.8 1
0.001 0.01 0.1 1 2 5 10
Fh_1/V_1
0.1 0.3 0.5 0.7 0.9 1.1 1.3 1.5
0.2 0.4 0.6 0.8 1.0 1.2 1.4
2.1 1.8 1.5 1.2 0.9 0.6 0.3
z_{90}
V=0
● 0.1 ■ 0.3 ▲ 0.5 ♦ 0.7 ★ 0.9 ✱ 1.1 × 1.3 + 1.5
● 0.2 ■ 0.4 ▲ 0.6 ♦ 0.8 ★ 1.0 ✱ 1.2 × 1.4
0 1 2 3 4 5 6 7 8 9 10 11 12 13 14 15
V/V_1, $10\times x/L_{R,\eta}$

Test Run 29

φ = 50°
q=0.284 m^2/s
Configuration: Stepped s=0.03 m

w [m]	C_1 [-]	y_{90} [m]	V_{90} [m/s]	h_1 [m]	V_1 [m/s]	α [-]	F_1 [-]	$R_1\times10^5$ [-]	W_1 [-]
0.235	0.48	0.097	7.88	0.050	5.71	1.19	8.2	2.84	149
0.313	0.48	0.096	7.88	0.050	5.68	1.20	8.1	2.84	149
0.391	0.47	0.096	7.88	0.050	5.65	1.19	8.0	2.84	148

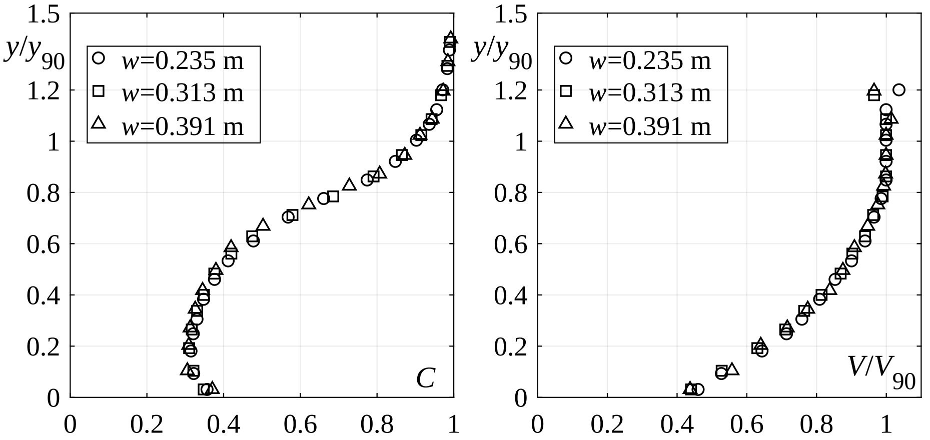

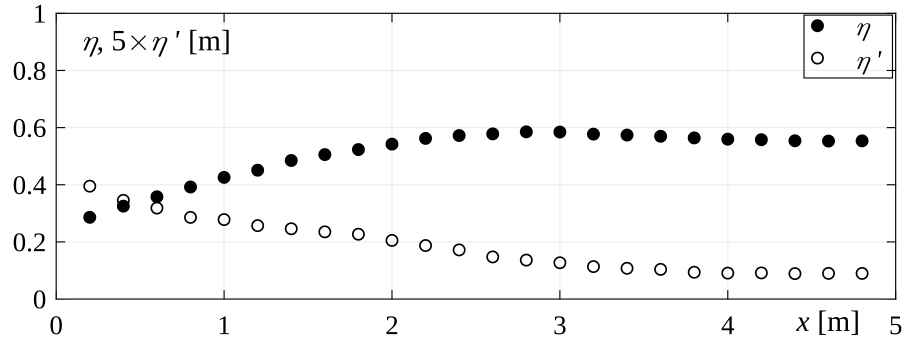

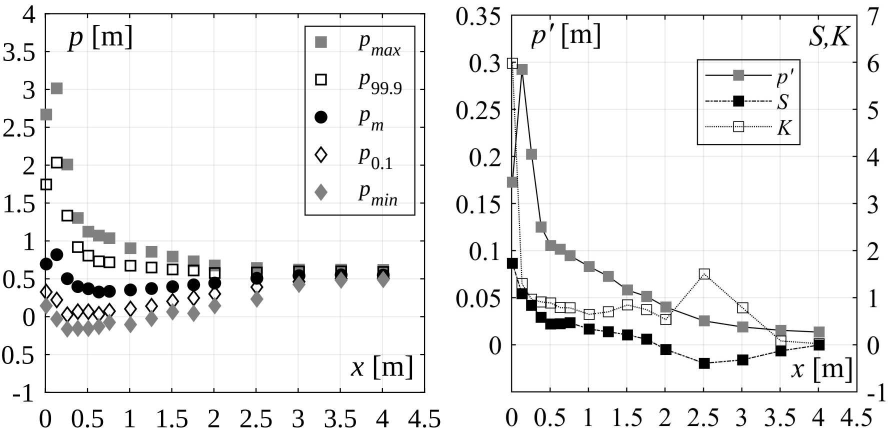

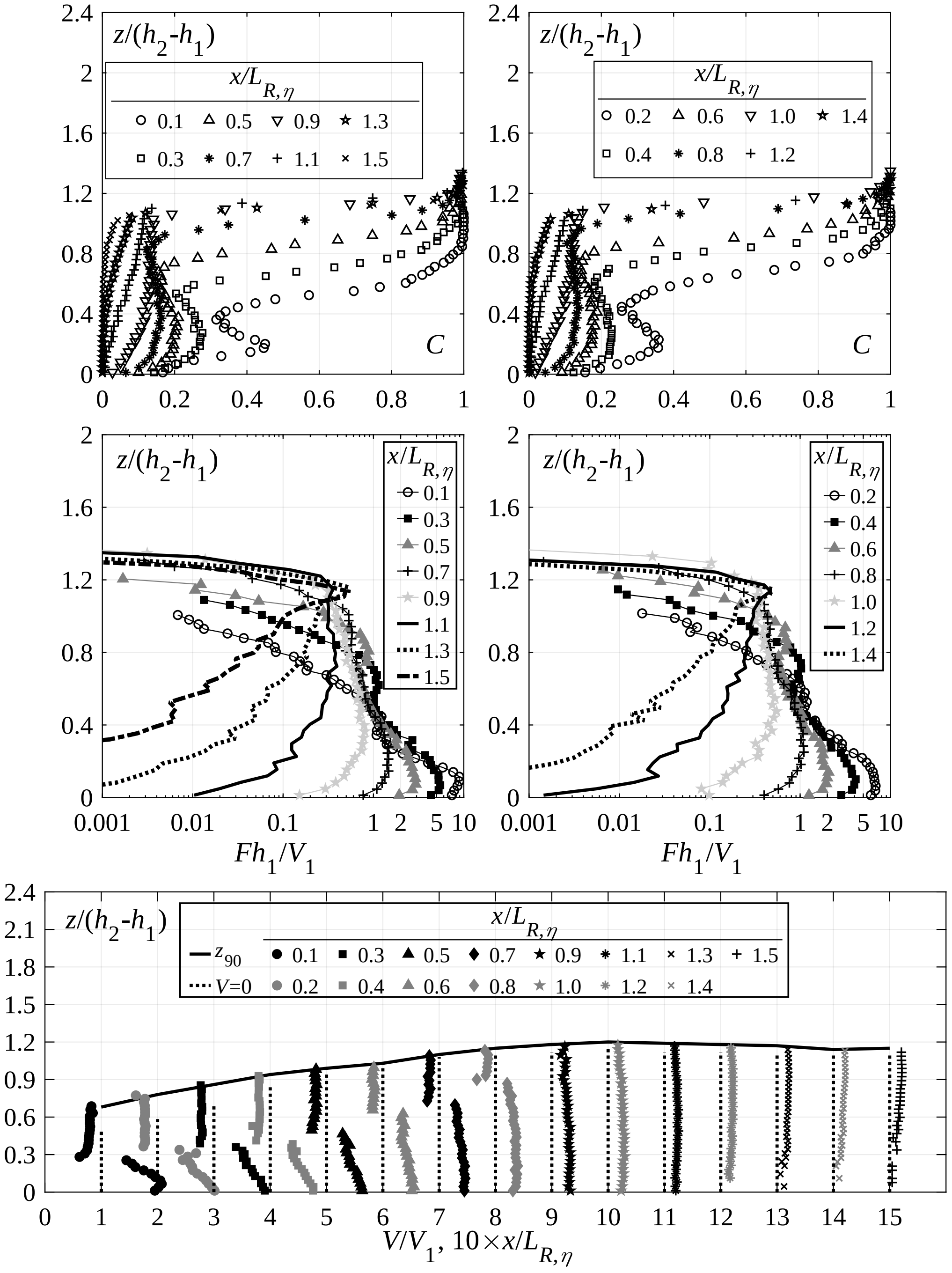
z/(h2-h1)
x/LR,η
0.1 0.5 0.9 1.3
0.3 0.7 1.1 1.5
C
0.2 0.6 1.0 1.4
0.4 0.8 1.2
C
0 0.2 0.4 0.6 0.8 1
0 0.4 0.8 1.2 1.6 2 2.4
z/(h2-h1)
x/LR,η
0.1 0.3 0.5 0.7 0.9 1.1 1.3 1.5
0.2 0.4 0.6 0.8 1.0 1.2 1.4
0 0.4 0.8 1.2 1.6 2
0.001 0.01 0.1 1 2 5 10
Fh1/V1
z/(h2-h1)
x/LR,η
z90
V=0
0.1 0.3 0.5 0.7 0.9 1.1 1.3 1.5
0.2 0.4 0.6 0.8 1.0 1.2 1.4
0 0.3 0.6 0.9 1.2 1.5 1.8 2.1 2.4
0 1 2 3 4 5 6 7 8 9 10 11 12 13 14 15
V/V1, 10×x/LR,η

Test Run 30

$\varphi = 50°$
q=0.364 m^2/s
Configuration: Stepped s=0.03 m

w [m]	C_1 [-]	y_{90} [m]	V_{90} [m/s]	h_1 [m]	V_1 [m/s]	α [-]	F_1 [-]	$R_1 \times 10^5$ [-]	W_1 [-]
0.235	0.46	0.111	8.61	0.060	6.08	1.19	7.9	3.64	174
0.315	0.46	0.110	8.61	0.059	6.12	1.19	8.0	3.64	175
0.391	0.45	0.108	8.61	0.059	6.16	1.19	8.1	3.64	176

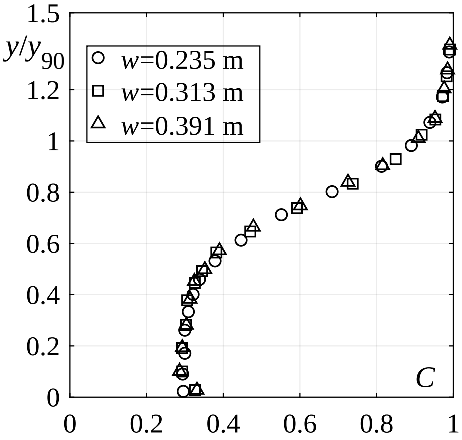

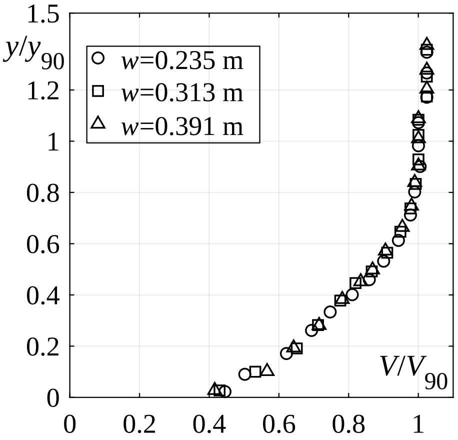

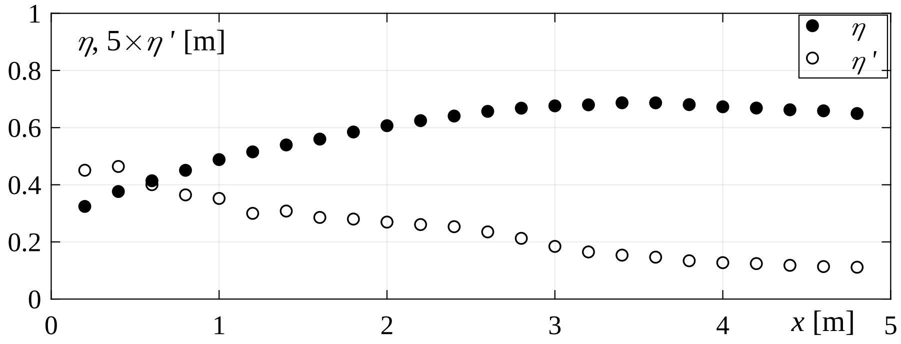

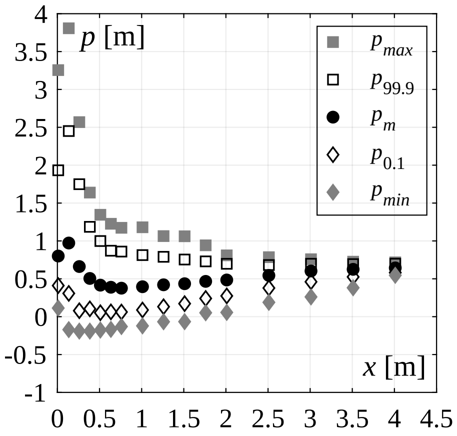

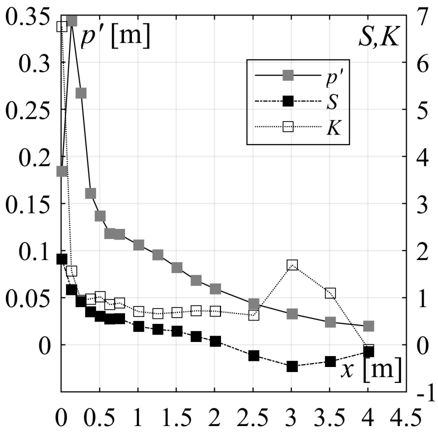

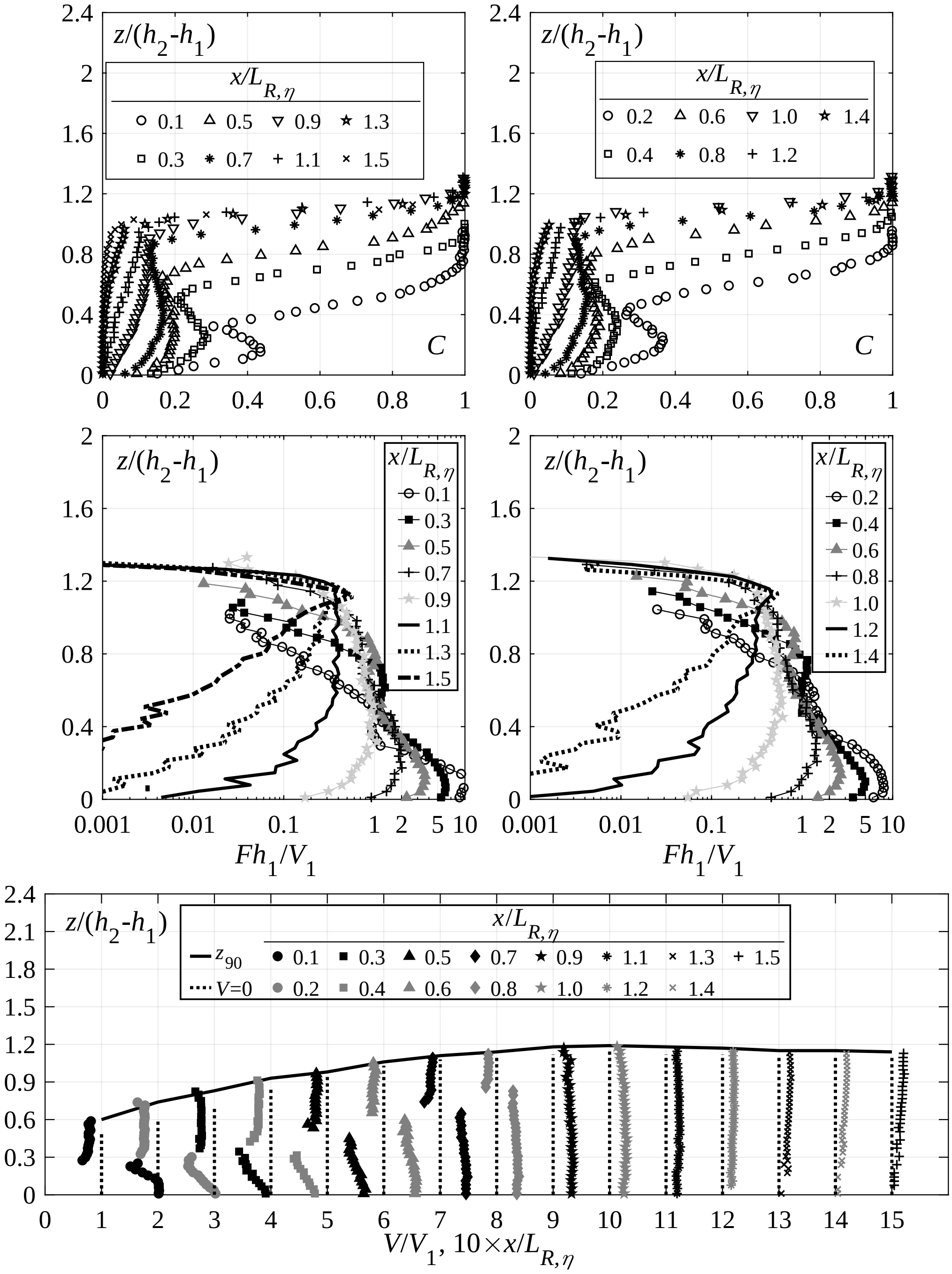
z/(h2-h1)
x/LR,η
0.1
0.3
0.5
0.7
0.9
1.1
1.3
1.5
C
0.2
0.4
0.6
0.8
1.0
1.2
1.4
C
0
0.2
0.4
0.6
0.8
1
0
0.4
0.8
1.2
1.6
2
2.4
z/(h2-h1)
x/LR,η
0.1
0.3
0.5
0.7
0.9
1.1
1.3
1.5
0.2
0.4
0.6
0.8
1.0
1.2
1.4
0.001
0.01
0.1
1
2
5
10
Fh1/V1
Fh1/V1
z/(h2-h1)
x/LR,η
z90
V=0
0.1
0.3
0.5
0.7
0.9
1.1
1.3
1.5
0.2
0.4
0.6
0.8
1.0
1.2
1.4
0
0.3
0.6
0.9
1.2
1.5
1.8
2.1
2.4
0
1
2
3
4
5
6
7
8
9
10
11
12
13
14
15
V/V1, 10×x/LR,η

Bibliography

Abdul Khader, M. H. and Elango, K. (1974). Turbulent pressure field beneath a hydraulic jump. *Journal of Hydraulic Research*, 12(4):469–489.

Akbari, M. E., Mittal, M. K., and Pande, P. K. (1982). Pressure fluctuations on the floor of free and forced hydraulic jumps. In Stephenson, H. S. and Stapleton, C. A., editors, *Proc. Intl. Conf. on the Hydraulic Modelling of Civil Engineering Structure*, 87–96, Conventry, England.

Amador, A., Sánchez-Juny, M., and Dolz, J. (2006). Characterization of the nonaerated flow region in a stepped spillway by PIV. *Journal of Fluids Engineering*, 128(6):1266–1273.

Amador, A., Sánchez-Juny, M., and Dolz, J. (2009). Developing flow region and pressure fluctuations on steeply sloping stepped spillways. *Journal of Hydraulic Engineering*, 135(12):1092–1100.

André, S. (2004). *High velocity aerated flows on stepped chutes with macro-roughness elements.* In Schleiss, A., editor. Communication LCH 20. École Polytechnique Fédérale de Lausanne.

André, S., Boillat, J.-L., and Schleiss, A. J. (2005). Discussion of "Two-Phase flow characteristics of stepped spillways". *Journal of Hydraulic Engineering*, 131(5):423–427.

André, S., Boillat, J.-L., and Schleiss, A. J. (2008). Ecoulements aérés sur évacuateurs en marches d'escalier équipées de macro-rugosités - Partie I: Caractéristiques hydrauliques. *Houille Blanche*, 2008(1):91–100.

André, S. and Schleiss, A. J. (2008). Discussion of "Pressure on a stepped spillway" by Sánchez-Juny, M., Bladé, E. and Dolz, J. *Journal of Hydraulic Research*, 46(4):574–576.

Bakhmeteff, B. A. and Matzke, A. E. (1936). The hydraulic jump in terms of dynamic similarity. *Proceedings of the American Society of Civil Engineers*, 61(2):145–162.

Barjastehmaleki, S., Fiorotto, V., and Caroni, E. (2016a). Design of stilling basin linings with sealed and unsealed joints. *Journal of Hydraulic Engineering*, 142(12):04016064 1–10.

Barjastehmaleki, S., Fiorotto, V., and Caroni, E. (2016b). Spillway stilling basins lining design via Taylor hypothesis. *Journal of Hydraulic Engineering*, 142(6):04016010 1–11.

Bauer, W. J. (1953). Turbulent boundary layer on steep slopes. *ASCE Transactions*, 119(9):1212–1233.

Baumann, A., Arefi, F., and Schleiss, A. J. (2006). Design of two stepped spillways for a pumped storage scheme in Iran. In *Proc. Intl. Conf. Hydro 2006 -Maximising the Benefits of Hydropower*, (CD–ROM), Porto Carras, Greece.

Bélanger, J. B. C. J. (1828). Essai sur la solution numérique de quelques problèmes relatifs au mouvement permanent des eaux courantes. (Essay on the numerical solution of some problems relative to steady flow of water.).

Bidone, G. (1820). *Le Remou et sur la Propagation des Ondes*. Turin : de l'Imprimerie Royale.

Boes, R. M. (2000a). Discussion of "Characteristics of skimming flow over stepped spillways". *Journal of Hydraulic Engineering*, 126(11):860–862.

Boes, R. M. (2000b). Scale effects in modelling two-phase stepped spillway flow. In Minor, H.-E. and Hager, W. H., editors, *Hydraulics of stepped spillways*, 53–60, Zürich, Switzerland. Balkema, Rotterdam.

Boes, R. M. (2000c). *Zweiphasenströmung und Energieumsetzung an Grosskaskaden*. In Minor, H.-E., editor. VAW Mitteilungen 166. ETH Zürich.

Boes, R. M. and Hager, W. H. (2003a). Hydraulic design of stepped spillways. *Journal of Hydraulic Engineering*, 129(9):671–679.

Boes, R. M. and Hager, W. H. (2003b). Two-phase flow characteristics of stepped spillways. *Journal of Hydraulic Engineering*, 129(9):661–670.

Bollaert, E., Lesleighter, E., McComber, S., Bozorgmehr, P., Fahey, L., and Scriven, D. (2016). Rock scour in Australia: some latest Queensland experiences. In Harris, J., Whitehouse, R., and Moxon, S., editors, *Proc. 8th Intl. Conf. on Scour and Erosion*, Online: http://eprints.hrwallingford.co.uk/1631/, Oxford, UK.

Bowers, C. E. and Tsai, F. Y. (1969). Fluctuating pressures in spillway stilling basins. *Journal of Hydraulics Division*, 95(6):2071–2080.

Bribesca, J. L. S. and Mariles, O. A. F. (1979). Experimental analysis of macroturbulence effects on the lining of stilling basins. In *Proc. 13th ICOLD Congress*, 85–103, New Delhi, India.

Bukreev, V. I. (1966). Statistical characteristics of the pressure fluctuation in a hydraulic jump. *Journal of Applied Mechanics and Technical Physics*, 7(5):97–99.

Bung, D. B. (2011). Developing flow in skimming flow regime on embankment stepped spillways. *Journal of Hydraulic Research*, 49(5):639–648.

Bung, D. B., Sun, Q., Meireles, I., Viseu, T., and Matos, J. S. (2012). USBR type III stilling basin performance for steep stepped spillways. In Matos, J., Pagliara, S., and Meireles, I., editors, *Proc. 4th Intl. IAHR Symposium on Hydraulic Structures*, (CD–ROM), Porto, Portugal.

Cain, P. and Wood, I. (1981). Measurements of self-aerated flow on a spillway. *Journal of the Hydraulics Division*, 107(11):1425–1444.

Cardoso, G., Meireles, I., and Matos, J. (2007). Pressure head along baffle stilling basins donwstream of steeply sloping stepped chutes. In Di Silvio, G. and Lanzoni, S., editors, *Proc. 32nd IAHR World Congress*, (CD–ROM), Venice, Italy.

Chachereau, Y. and Chanson, H. (2011a). Bubbly flow measurements in hydraulic jumps with small inflow Froude numbers. *International Journal of Multiphase Flow*, 37(6):555–564.

Chachereau, Y. and Chanson, H. (2011b). Free-surface fluctuations and turbulence in hydraulic jumps. *Experimental Thermal and Fluid Science*, 35(6):896–909.

Chamani, M. (2000). Air inception in skimming flow regime over stepped spillways. In Minor, H.-E. and Hager, W. H., editors, *Hydraulics of stepped spillways*, 61–67, Zürich, Switzerland. Balkema.

Chamani, M. R. and Rajaratnam, N. (1994). Jet flow on stepped spillways. *Journal of Hydraulic Engineering*, 120(2):254–259.

Chamani, M. R. and Rajaratnam, N. (1999). Characteristics of skimming flow over stepped spillways. *Journal of Hydraulic Engineering*, 125(4):361–368.

Chanson, H. (1994). *Hydraulic design of stepped cascades, channels, weirs and spillways.* Pergamon, Oxford, UK.

Chanson, H. (1995). Air-water gas transfer at hydraulic jump with partially developed inflow. *Water Research*, 29(10):2247–2254.

Chanson, H. (1997). *Air bubble entrainment in free-surface turbulent shear flows.* Academic Press, London, UK.

Chanson, H. (2001). Transition flow regime on stepped spillways. The facts. In *Proc. 29th IAHR Congress*, 490–497, Beijing, China.

Chanson, H. (2002). *The hydraulics of stepped chutes and spillways.* Balkema, Lisse, The Netherlands.

Chanson, H. (2006). Hydraulics of skimming flows on stepped chutes: the effects of inflow conditions? *Journal of Hydraulic Engineering*, 44(1):51–60.

Chanson, H. (2007). Bubbly flow structure in hydraulic jump. *European Journal of Mechanics, B/Fluids*, 26(3):367–384.

Chanson, H. (2009a). *Advective diffusion of air bubbles in hydraulic Jump with large Froude numbers: an experimental study.* Report CH75/09. University of Queensland, Australia.

Chanson, H. (2009b). Current knowledge in hydraulic jumps and related phenomena. A survey of experimental results. *European Journal of Mechanics - B/Fluids*, 28(2):191–210.

Chanson, H. (2009c). Turbulent air-water flows in hydraulic structures: dynamic similarity and scale effects. *Environmental Fluid Mechanics*, 9(2):125–142.

Chanson, H. (2010). Convective transport of air bubbles in strong hydraulic jumps. *International Journal of Multiphase Flow*, 36(10):798–814.

Chanson, H. (2011). Hydraulic jumps: turbulence and air bubble entrainment. *La Houille Blanche*, 2011(3):5–16.

Chanson, H. (2015a). Discussion of "Cavitation potential of flow on stepped spillways" by Frizell, K.W., Renna, F.M., and Matos, J. *Journal of Hydraulic Engineering*, 141(5):1–2.

Chanson, H. (2015b). *Energy dissipation in hydraulic structures.* CRC Press.

Chanson, H. and Brattberg, T. (2000). Experimental study of the air–water shear flow in a hydraulic jump. *International Journal of Multiphase Flow*, 26(4):583–607.

Chanson, H. and Chachereau, Y. (2013). Scale effects affecting two-phase flow properties in hydraulic jump with small inflow Froude number. *Experimental Thermal and Fluid Science*, 45:234–242.

Chanson, H. and Gualtieri, C. (2008). Similitude and scale effects of air entrainment in hydraulic jumps. *Journal of Hydraulic Research*, 46(1):35–44.

Chanson, H. and Toombes, L. (2001). *Experimental investigations of air entrainment in transition and skimming flows down a stepped chute. Application to embankment overflow stepped spillways.* Research Report No. CE158. The University of Queensland, Brisbane, Australia, asdasd edition.

Chanson, H. and Toombes, L. (2002). Air–water flows down stepped chutes: turbulence and flow structure observations. *International Journal of Multiphase Flow*, 28(11):1737–1761.

Chanson, H. and Toombes, L. (2004). Hydraulics of stepped chutes : the transition flow. *Journal of Hydraulic Engineering*, 42(1):43–54.

Chanson, H., Yasuda, Y., and Ohtsu, I. (2002). Flow resistance in skimming flows in stepped spillways and its modelling. *Canadian Journal of Civil Engineering*, 29(6):809–819.

Christodoulou, G. (1999). Design of stepped spillways for optimal energy dissipation. *Hydropower & Dams*, 1999(5):90–93.

Elviro, V. and Mateos, C. (1995). Spanish research into stepped spillways. *International Journal of Hydropower and Dams,*, 2(5):61–65.

Essery, I. T. S. and Horner, M. W. (1978). *The hydraulic design of stepped spillways.* CIRIA, 33, London, UK.

Felder, S. and Chanson, H. (2009a). Energy dissipation, flow resistance and gas-liquid interfacial area in skimming flows on moderate-slope stepped spillways. *Environmental Fluid Mechanics*, 9(4):427–441.

Felder, S. and Chanson, H. (2009b). Turbulence, dynamic similarity and scale effects in high-velocity free-surface flows above a stepped chute. *Experiments in Fluids*, 47(1):1–18.

Felder, S. and Chanson, H. (2011). Air-water flow properties in step cavity down a stepped chute. *International Journal of Multiphase Flow*, 37(7):732–745.

Felder, S. and Chanson, H. (2016). Air–water flow characteristics in high-velocity free-surface flows with 50% void fraction. *International Journal of Multiphase Flow*, 85(2016):186–195.

Felder, S. and Pfister, M. (2017). Comparative analyses of phase-detective intrusive probes in high-velocity air–water flows. *International Journal of Multiphase Flow*, 90:88–101.

Fiorotto, V. and Rinaldo, A. (1992a). Fluctuating uplift and lining design in spillway stilling basins. *Journal of Hydraulic Engineering*, 118(4):578–596.

Fiorotto, V. and Rinaldo, A. (1992b). Turbulent pressure fluctuations under hydraulic jumps. *Journal of Hydraulic Research*, 30(4):499–520.

Fiorotto, V. and Salandin, P. (2000). Design of anchored slabs in spillway stilling basins. *Journal of Hydraulic Engineering*, 126(7):502–512.

Frisch, U. (1995). *Turbulence*. Cambridge University Press, Cambridge, UK.

Frizell, K., Kubitschek, J. P., and Matos, J. (2009). Stilling basin performance for stepped spillways of mild slopes – Type III basins. In *Proc. 33rd IAHR World Congress, Vancouver, Canada*, (CD–ROM).

Frizell, K., Renna, F., and Matos, J. (2013). Cavitation potential of flow on stepped spillways. *Journal of Hydraulic Engineering*, 139(6):630–636.

Frizell, K. and Svoboda, C. (2012). Performance of type III stilling basins – stepped spillway studies. Technical report, U.S. Bureau of Reclamation, U.S. Bureau of Reclamation, Denver, Colorado.

Frizell, K., Svoboda, C., and Matos, J. (2016). Performance of type III stilling basins for stepped spillways. In *Proc. 2nd Intl. Seminar on Dam Protection Against Overtopping*, Online: https://mountainscholar.org/handle/10217/1, Ft. Collins, Colorado.

Frizell, K. H. (1990). Hydraulic model study of Mc Clure dam existing and proposed RCC stepped spillways. Technical report, US Bureau of Reclamation, U.S. Bureau of Reclamation, Denver, Colorado.

Frizell, K. H. (2006). Research state-of-the-art and needs for hydraulic design of stepped spillways. Technical report, US Bureau of Reclamation, U.S. Bureau of Reclamation, Denver, Colorado.

Gomes, J., Marques, M., and Matos, J. (2007). Predicting cavitation inception on steeply sloping stepped spillways. In Di Silvio, G. and Lanzoni, S., editors, *Proc. 32nd IAHR World Congress,* (CD–ROM), Venice, Italy.

Gomes, J. F., Amador, A., Marques, M., Matos, J., and Sánchez-Juny, M. (2006). Hydrodynamic pressure field on steeply sloping stepped spillways. In Chanson, H., editor, *Proc. Intl. Junior Researcher and Engineer Workshop on Hydraulic Structures,* 71–80. The University of Queensland, Brisbane, Australia.

Gonzalez, C. (2005). *An experimental study of free-surface aeration on embankment stepped chutes.* PhD Thesis. University of Queensland, Brisbane, Australia.

Gonzalez, C. and Chanson, H. (2007). Hydraulic design of stepped spillways and downstream energy dissipators for embankment dams. *Dam Engineering,* 17(4):223–244.

Gualtieri, C. and Chanson, H. (2007). Experimental analysis of Froude number effect on air entrainment in the hydraulic jump. *Environmental Fluid Mechanics,* 7(3):217–238.

Hager, W. H. (1991). Uniform aerated chute flow. *Journal of Hydraulic Engineering,* 117(4):528–533.

Hager, W. H. (1992). *Energy dissipators and hydraulic jump.* Dordrecht, Netherlands.

Hager, W. H. (1993). Classical hydraulic jump: free surface profile. *Canadian Journal of Civil Engineering,* 20(3):536–539.

Hager, W. H. and Bremen, R. (1989). Classical hydraulic jump: sequent depths. *Journal of Hydraulic Research,* 27(5):565–585.

Hager, W. H., Bremen, R., and Kawagoshi, N. (1990). Classical hydraulic jump: length of roller. *Journal of Hydraulic Research,* 28(5):591–608.

Hager, W. H. and Pfister, M. (2013). Stepped spillways : technical advance from 1900. In *Proc. 35th IAHR World Congress,* 7379 – 7386, Chengdu, China.

Hager, W. H. and Sinniger, R. (1985). Flow characteristics of the hydraulic jump in a stilling basin with an abrupt bottom rise. *Journal of Hydraulic Research,* 23(2):101–113.

Henry, H. (1950). *A study of flow below a submerged sluice gate.* M.Sc. thesis. State University of Iowa, Iowa City, Iowa.

Horner, M. W. (1969). *An analysis of flow on cascades of steps.* University of Birmingham, Birmingham, UK.

Houston, K. (1987). Hydraulic model studies of Upper Stillwater dam stepped spillway and outlet works. Technical report, US Bureau of Reclamation, U.S. Bureau of Reclamation, Denver, Colorado.

Hunt, S. L. and Kadavy, K. C. (2011). Inception point relationship for flat-sloped stepped spillways. *Journal of Hydraulic Engineering*, 137(2):262–266.

Hunt, S. L. and Kadavy, K. C. (2013). Inception point for embankment dam stepped spillways. *Journal of Hydraulic Engineering*, 139(1):60–64.

Hunt, S. L. and Kadavy, K. C. (2014). Flow depth and energy coefficient relationships for stepped spillways. In *Proc. 5th IAHR Intl. Symp. on Hydraulic Structures*, 1–9, Brisbane, Australia. University of Queensland.

Khatsuria, R. M. (2005). *Hydraulics of spillways and energy dissipators.* Marcel Dekker, New York, USA.

Khatsuria, R. M., Deolalikar, P. B., and Bhosekar, V. V. (1992). Pull out forces on a concrete lined training wall in a stilling basin. In *8th APD-IAHR Congress*, Pune, India.

Kobus, H. (1984). Local air entrainment and detrainment. In Kobus, H., editor, *Scale Effects in Modelling Hydraulic Structures*, 4.10, 1–10, Esslingen am Neckar, Germany.

Kramer, K. (2004). *Development of aerated chute flow.* In Minor, H.-E., editor, VAW Mitteilungen 183. Laboratory of Hydraulics, Hydrology and Glaciology, ETH Zürich, Zürich, Switzerland.

Kramer, M. and Chanson, H. (2018). Transition flow regime on stepped spillways: air–water flow characteristics and step-cavity fluctuations. *Environmental Fluid Mechanics*, 18(4):947–965.

Kucukali, S. and Chanson, H. (2008). Turbulence measurements in hydraulic jumps with partially-developed inflow conditions. *Experimental Thermal and Fluid Science*, 33(1):41–53.

Kucukali, S. and Chanson, H. (2009). Turbulent length–time scales distributions in hydraulic jumps. *Proceedings of the Institution of Civil Engineers - Water Management*, 162(4):269–277.

Leutheusser, H. J. and Kartha, V. C. (1972). Effects of inflow condition on hydraulic jump. *Journal of Hydraulics Division*, 98(8):1367–1385.

Long, D., Rajaratnam, N., Steffler, P. M., and Smy, P. R. (1991). Structure of flow in hydraulic jumps. *Journal of Hydraulic Research*, 29(2):207–218.

Lopardo, R. A., De Lio, J. C., and Vernet, G. F. (1982). Physical modelling on cavitation tendency for macroturbulence of hydraulic jump. In Stephenson, H. S. and Stapleton, C. A., editors, *Proc. Intl. Conf. on the Hydraulic Modelling of Civil Engineering Structure*, 109–121, Conventry, England.

Lopardo, R. A. and Henning, R. E. (1985). Experimental advances on pressure fluctuation beneath hydraulic jumps. In *Proc. 21st IAHR World Congress*, 634–638, Melbourne, Australia.

Lopardo, R. A. and Romagnoli, M. (2009). Pressure and velocity fluctuations in stilling basins. In *Advances in Water Resources and Hydraulic Engineering*, 2093–2098. Berlin, Germany.

Lueker, M. L., Mohseni, O., Gulliver, J. S., Schulz, H., and Christopher, R. A. (2008). *The physical model study of the Folsom dam auxiliary spillway system.* Project Report 511. St. Anthony Falls Laboratory, University of Minnesota, Minneapolis, Minnesota.

Madsen, P. A. and Svendsen, I. A. (1983). Turbulent bores and hydraulic jumps. *Journal of Fluid Mechanics*, 129(1983):1–25.

Matos, J. (1999). *Emulsionamento de ar e dissipação de energia do escoamento em descarregadores em degraus.* Ph.D. thesis, IST, Lisbon, Portugal (in Portuguese).

Matos, J. (2000). Hydraulic design of stepped spillways over RCC dams. In Minor, H.-E. and Hager, W. H., editors, *Proc. Intl. Workshop on Hydraulics of Stepped Spillways*, 187–194, Zürich, Switzerland. Balkema.

Matos, J. (2001). Discussion of "Onset of skimming flow on stepped spillways" by Chamani, M. R. *Journal of Hydraulic Research*, 127(6):519–521.

Matos, J. (2005). Discussion of "Hydraulic design of stepped spillways" by R. M. Boes and W. H. Hager. *Journal of Hydraulic Engineering*, 131(6):525–527.

Matos, J. and Meireles, I. (2014). Hydraulics of stepped weirs and dam spillways: engineering challenges, labyrinths of research. In Chanson, H. and Toombes, L., editors, *Proc. 5th IAHR Intl. Symp. on Hydraulic Structures*, Brisbane, Australia.

Matos, J., Pinheiro, A. N., Quintela, A., and Frizell, K. H. (2001). On the role of stepped overlays to increase spillway capacity of embankment dams. In *Proc. ICOLD European Symposium (NNCOLD)*, 473–483, Geiranger, Norway.

Matos, J., Sánchez-Juny, M., Quintela, A., and Dolz, J. (2000). Air entrainment and safety against cavitation damage in stepped spillways over RCC dams. In Minor, H.-E. and Hager, W. H., editors, *Proc. Intl .Workshop on Hydraulics of Stepped Spillways*, 69–76, Rotterdam, Nederlands.

McCorquodale, J. A. and Khalifa, A. (1983). Internal flow in hydraulic jumps. *Journal of Hydraulic Engineering*, 109(5):684–701.

McDonald, L. (2013). *Paradise dam review.* Report No. DC 13127. Queensland Government, Department of Energy and Water Supply, Queensland, Australia.

Meireles, I. (2011). *Hydraulics of stepped chutes: experimental-numerical-theoretical study.* PhD thesis. University of Aveiro, Aveiro, Portugal.

Meireles, I. and Matos, J. (2009). Skimming flow in the nonaerated region of stepped spillways over embankment dams. *Journal of Hydraulic Engineering*, 135(8):685–689.

Meireles, I., Matos, J., and Melo, J. F. (2005). Pressure head and residual energy in skimming flow on steeply sloping stepped spillways. In Jun, B.-H., editor, *Proc. 31st IAHR World Congress*, 2654–2663, Seoul, Korea.

Meireles, I., Matos, J., and Silva Afonso, A. (2010). Flow characteristics along a USBR type III stilling basin downstream of steep stepped spillways. In Janssen, R. and Chanson, H., editors, *Proc. 3rd Int. Junior Researcher and Engineer Workshop on Hydraulic Structures,*, 57–64, Brisbane, Australia.

Meireles, I., Renna, F., Matos, J., and Bombardelli, F. (2012). Skimming, nonaerated flow on stepped spillways over roller compacted concrete dams. *Journal of Hydraulic Engineering*, 138(10):870–877.

Monin, A. S. and Yanglom, A. M. (1975). *Statistical fluid mechanics, Vol. 2.* MIT Press, Cambridge, Massachusetts.

Montano, L. and Felder, S. (2018). Effect of inflow conditions on the air-water flow properties in hydraulic jumps. In Lau, T. C. W. and Kelso, R. M., editors, *Proc. 21st Australasian Fluid Mechanics Conference*, Adelaide, Australia.

Montano, L., Li, R., and Felder, S. (2018). Continuous measurements of time-varying free-surface profiles in aerated hydraulic jumps with a LIDAR. *Experimental Thermal and Fluid Science*, 93:379–397.

Moore, W. I. (1943). Energy loss at the base of a free overfall. *Transactions American. Society of Civil Engineers*, 108(1):1343–1360.

Mossa, M. and Tolve, U. (1998). Flow visualization in bubbly two-phase hydraulic jump. *Journal of Fluids Engineering*, 120(1):160–165.

Mouaze, D., Murzyn, F., and Chaplin, J. R. (2005). Free surface length scale estimation in hydraulic jumps. *Journal of Fluids Engineering*, 127(6):1191–1193.

Murzyn, F. and Chanson, H. (2008). Experimental assessment of scale effects affecting two-phase flow properties in hydraulic jumps. *Experiments in Fluids*, 45(3):513–521.

Murzyn, F. and Chanson, H. (2009a). Experimental investigation of bubbly flow and turbulence in hydraulic jumps. *Environmental Fluid Mechanics*, 9(2):143–159.

Murzyn, F. and Chanson, H. (2009b). Free-surface fluctuations in hydraulic jumps: experimental observations. *Experimental Thermal and Fluid Science*, 33(7):1055–1064.

Murzyn, F., Mouaze, D., and Chaplin, J. (2005). Optical fibre probe measurements of bubbly flow in hydraulic jumps. *International Journal of Multiphase Flow*, 31(1):141–154.

Murzyn, F., Mouazé, D., and Chaplin, J. (2007). Air–water interface dynamic and free surface features in hydraulic jumps. *Journal of Hydraulic Research*, 45(5):679–685.

Novakoski, C. K., Conterato, E., Marques, M., Teixeira, E. D., Lima, G. A., and Mees, A. (2017a). Macro-turbulent characteristcs of pressures in hydraulic jump formed downstream of a stepped spillway. *RBRH (Brazilian Journal of Water Resources)*, 22(22).

Novakoski, C. K., Hampe, R. F., Conterato, E., Marques, M. G., and Teixeira, E. D. (2017b). Longitudinal distribution of extreme pressures in a hydraulic jump downstream of a stepped spillway. *RBRH (Brazilian Journal of Water Resources)*, 22(42).

Ohtsu, I. and Yasuda, Y. (1997). Characteristics of flow conditions on stepped channels. In *Proc. 27th IAHR Congress*, San Francisco, USA.

Ohtsu, I., Yasuda, Y., and Awazu, S. (1990). *Free and submerged hydraulic jumps in rectangular channels.* Report of Research Inst. of Science and Technology, No. 35 35. Nihon University, Japan.

Ohtsu, I., Yasuda, Y., and Takahashi, M. (2004). Flow characteristics of skimming flows in stepped channels. *Journal of Hydraulic Engineering*, 130(9):860–869.

Ostad Mirza, M. J. (2016). *Experimental study on the influence of abrupt slope changes on flow characteristics over stepped spillways.* In Schleiss, A. and de Saldanha Gonçalves Matos, J., editors, Communication LCH 64. École Polytechnique Fédérale de Lausanne.

Peterka, A. J. (1958). *Hydraulic design of stilling basins and energy dissipators.* United States Department of the Interior, Denver, Colorado.

Peyras, L., Royet, P., and Degoutte, G. (1992). Flow and energy dissipation over stepped gabion weirs. *Journal of Hydraulic Engineering*, 118(5):707–717.

Pfister, M. (2008). *Schussrinnenbelüfter-Lufttransport ausgelöst durch interne Abflussstruktur.* In Minor, H.-E., editor, VAW Mitteilungen 203. ETH Zürich.

Pfister, M. and Boes, R. M. (2014). Discussion of "Skimming, nonaerated flow on stepped spillways over roller compacted concrete dams". *Journal of Hydraulic Engineering*, 140(10):07014012.

Pfister, M. and Chanson, H. (2014). Two-phase air-water flows: scale effects in physical modeling. *Journal of Hydrodynamics*, 26(2):291–298.

Pfister, M. and Hager, W. H. (2011). Self-entrainment of air on stepped spillways. *International Journal of Multiphase Flow*, 37(2):99–107.

Pinheiro, A. N. (1995). *Acções hidrodinâmicas em soleiras de bacias de dissipação de energia por ressalto.* Ph.D. Thesis. IST, Lisbon (in Portuguese).

Rajaratnam, N. (1962a). An experimental study of air entrainment characteristics of the hydraulic jump. *Journal of the Institution of Engineers India*, 42:247–273.

Rajaratnam, N. (1962b). Profile equation for the hydraulic jump. *Water Power*, 13(8):324–327.

Rajaratnam, N. (1965). The hydraulic jump as a wall jet. *Journal of the Hydraulics Division*, 91(5):107–132.

Rajaratnam, N. and Chamani, M. (1995). Energy loss at drops. *Journal of Hydraulic Research*, 33(3):373–384.

Rajaratnam, N. and Subramanya, K. (1968). Profile of the hydraulic jump. *ASCE Journal of the Hydraulics Division*, 94((3)):663–673.

Rasmussen, R. E. H. (1956). Some experiments on cavitation erosion in water mixed with air. In *International Symposium on Cavitation in Hydrodynamics*, 1–25, National Physical Laboratory, London.

Resch, F. J., Leutheusser, H. J., and Alemu, S. (1974). Bubbly two-phase flow in hydraulic jump. *Journal of the Hydraulics Division*, 100(1):137–149.

Richard, G. I. and Gavrilyuk, S. I. (2013). The classical hydraulic jump in a model of shear shallow-water flows. *Journal of Fluid Mechanics*, 725(2013):492–521.

Russell, S. O. and Sheehan, G. J. (1974). Effect of entrained air on cavitation damage. *Canadian Journal of Civil Engineering*, 1(1):97–107.

Sanchez-Juny, M., Bladé, E., and Dolz, J. (2007). Pressures on a stepped spillway. *Journal of Hydraulic Research*, 45(4):505–511.

Sánchez-Juny, M., Blade, E., and Dolz, J. (2008). Analysis of pressure on a stepped spillway. *Journal of Hydraulic Research*, 46(3):410–414.

Sánchez-Juny, M. and Dolz, J. (2005). Experimental study of transition and skimming flows on stepped spillways in RCC dams: qualitative analysis and pressure measurements. *Journal of Hydraulic Research*, 43(5):540–548.

Sánchez-Juny, M., Pomares, J., and Dolz, J. (2000). Pressure field in skimming flow over a stepped spillway. In Minor, H.-E. and Hager, W. H., editors, *Proc. Intl. Workshop on Hydraulics of Stepped Spillways*, 137–145, Rotterdam, Nederlands. VAW, ETH Zurich.

Schiebe, F. and Bowers, C. E. (1971). Boundary pressure fluctuations due to macroturbulence in hydraulic jumps. In *Symposia on Turbulence in Liquids 84*, 134–139, Rolla, Missouri.

Schröder, R. (1963). Die turbulente Strömung im freien Wechselsprung (the turbulent flow in the classical hydraulic jump). Habilitation-Thesis, Mitteilung 59. Institut für Wasserbau und Wasserwirtschaft, Technische Universitat Berlin, Berlin.

Schwalt, M. and Hager, W. H. (1992). Die Strahlbox (the jetbox). *Schweizer Ingenieur und Architekt*, 110(27/28):547–549 (in German).

Spoljaric, A. (1984). Dynamic characteristics of the load on the bottom plate under hydraulic jump. In Stephenson, H. S. and Stapleton, C. A., editors, *Hydrosoft '84*, 129–141, Protoroz, Serbia.

Straub, L. G. and Anderson, A. G. (1958). Experiments on self-aerated flow in open channels. *Journal of the Hydraulics Division*, 84(7):1–35.

Takahashi, M. and Ohtsu, I. (2012). Aerated flow characteristics of skimming flow over stepped chutes. *Journal of Hydraulic Research*, 50(4):427–434.

Takahashi, M. and Ohtsu, I. (2014). Analysis of nonuniform aerated skimming flows on stepped channels. In *Proc. 5th IAHR Intl. Symp. on Hydraulic Structures*, 1–9, Brisbane, Australia. University of Queensland.

Takahashi, M. and Ohtsu, I. (2017). Effects of inflows on air entrainment in hydraulic jumps below a gate. *Journal of Hydraulic Research*, 55(2):259–268.

Takahashi, M., Yasuda, Y., and Ohtsu, I. (2005). Effect of Reynolds number on characteristics of skimming flows in stepped channels. In *Proc. 31st IAHR World Congress*, 2880–2889, Seoul, Korea.

Terrier, S. (2006). *Hydraulic performance of stepped spillway aerators and related downstream flow features.* In Schleiss, A., editor, Communication LCH 64. École Polytechnique Fédérale de Lausanne.

Thandaveswara, B. S. (1974). *Self aerated flow characteristics in developing zones and in hydraulic jumps.* PhD thesis. Indian Institute of Science Department of Civil Engineering Bangalore, India.

Toombes, L. (2002). *Experimental study of air-water flow properties on low-gradient stepped cascades.* PhD thesis. University of Queensland, Australia.

Toombes, L. and Chanson, H. (2000). Air-water flow and gas transfer at aeration cascades: a comparative study of smooth and stepped chutes. In Minor, H.-E. and Hager, W. H., editors, *International Workshop on Hydraulics of Stepped Spillways*, 77–88, Rotterdam, Netherlands. Balkema.

Toso, J. W. and Bowers, C. E. (1988). Extreme pressures in hydraulic-jump stilling basins. *Journal of Hydraulic Engineering*, 114(8):829–843.

Tozzi, M. J. (1992). *Caracterização comportamento de escoamentos em vertedouros com paramento em degraus.* Ph.D. thesis. Escola Politécnica da Universidade de S. Paulo, Brazil (in Portuguese).

Tullis, J. and Rahmeyer, W. J. (1982). Spillway models. In Stephenson, H. S. and Stapleton, C. A., editors, *Proc. Intl. Conf. on the Hydraulic Modelling of Civil Engineering Structure*, Conventry, England.

Valero, D., Bung, D. B., and Crookston, B. M. (2018). Energy dissipation of a type III basin under design and adverse conditions for stepped and smooth spillways. *Journal of Hydraulic Engineering*, 144(7):04018036.

Valero, D., Bung, D. B., Crookston, B. M., and Matos, J. (2016). Numerical investigation of USBR type III stilling basin performance downstream of smooth and stepped spillways. In Crookston, B. M. and Tullis, B., editors, *Proc. 6th IAHR Intl. Symp. on Hydraulic Structures and Water System Management*, 652–663, Portland, Oregon, USA.

Vasiliev, O. F. and Bukreyev, V. I. (1967). Statistical characteristics of pressure fluctuations in the region of hydrailic jump. In *Proc. 12th IAHR World Congress*, 1–8, Fort Collins.

Vischer, D. L. and Hager, W. H. (1998). *Dam hydraulics.* John Wiley & Sons, Ltd, West Sussex, England.

Wang, H. (2014). *Turbulence and air entrainment in hydraulic jumps.* PhD thesis. The University of Queensland, Australia.

Wang, H. and Chanson, H. (2015a). Air entrainment and turbulent fluctuations in hydraulic jumps. *Urban Water Journal*, 12(6):502–518.

Wang, H. and Chanson, H. (2015b). Experimental study of turbulent fluctuations in hydraulic jumps. *Journal of Hydraulic Engineering*, 141(7):4015010.

Wang, H. and Chanson, H. (2017). Estimate of void fraction and air entrainment flux in hydraulic jump using Froude number. *Canadian Journal of Civil Engineering*, 45(2):105–116.

Wang, H. and Chanson, H. (2019). Characterisation of transverse turbulent motion in quasi-two-dimensional aerated flow: application of four-point air-water flow measurements in hydraulic jump. *Experimental Thermal and Fluid Science*, 100:222–232.

Wang, H., Hu, Z., and Chanson, H. (2015a). Two-dimensional bubble clustering in hydraulic jumps. *Experimental Thermal and Fluid Science*, 68:711–721.

Wang, H., Murzyn, F., and Chanson, H. (2014). Total pressure fluctuations and two-phase flow turbulence in hydraulic jumps. *Experiments in Fluids*, 55(11):1847.

Wang, H., Murzyn, F., and Chanson, H. (2015b). Interaction between free-surface, two-phase flow and total pressure in hydraulic jump. *Experimental Thermal and Fluid Science*, 64:30–41.

Wilhelms, S. C. and Gulliver, J. S. (2005). Bubbles and waves description of self-aerated spillway flow. *Journal of Hydraulic Research*, 43(5):522–531.

Wood, I. (1983). Uniform region of self-aerated flow. *Journal of Hydraulic Engineering*, 109(2):447–461.

Wood, I. (1991). *Air entrainment in free-surface flows.* IAHR Hydraulic Structures Design Manuals 4. Balkema, Rotterdam, Netherlands.

Wood, R. I., Ackers, P., and Loveless, J. (1983). General method for critical point on spillways. *Journal of Hydraulic Engineering*, 109(2):308–312.

Yasuda, Y. and Ohtsu, I. (1999). Flow resistance of skimming flow in stepped channels. In *Proc. 28th IAHR Congress*, (CD-ROM), Graz, Austria.

Zhang, G. and Chanson, H. (2017). Self-aeration in the rapidly- and gradually-varying flow regions of steep smooth and stepped spillways. *Environmental Fluid Mechanics*, 17(1):27–46.

Zhang, G., Wang, H., and Chanson, H. (2013). Turbulence and aeration in hydraulic jumps: free-surface fluctuation and integral turbulent scale measurements. *Environmental Fluid Mechanics*, 13(2):189–204.

Zhang, J. M., Chen, J. G., and Wang, Y. (2012). Experimental study on time-averaged pressure in stepped spillway. *Journal of Hydraulic Research*, 50(2):236–240.

Ivan Stojnic

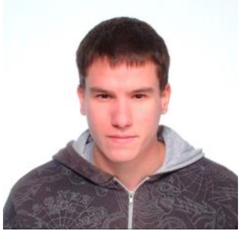

Birth	27 October 1990
Nationality	Serbian
Contact	ivan.stojnic@.epfl.ch

Education

2015 - 2019	**PhD in Hydraulic Engineering**, École polytechnique fédérale de Lausanne (EPFL), Lausanne, Switzerland Instituto Superior Técnico (IST), Lisbon, Portugal
2013 - 2014	**Master of Science (MSc) in Civil Engineering**, Faculty of Civil Engineering, University of Belgrade, Belgrade, Serbia Focus: Hydraulic engineering
2009 – 2013	**Bachelor of Science (BSc) in Civil Engineering**, Faculty of Civil Engineering, University of Belgrade, Belgrade, Serbia Focus: Hydraulic engineering

Professional experience

2016 - 2019	**Laboratory of Hydraulic Constructions, EPFL** Research assistant and PhD student (since 2016) Project engineer for Kariba dam plunge pool rehabilitation
2014	**Directorate for Inland Waterways “Plovput”, Ministry of Transportation and Civil Engineering**, Belgrade, Serbia Internship Hydrographic survey and data analysis Design and maintenance of waterways Design of electronic navigation charts
2013	**Energoprojekt Visokogradnja**, Belgrade, Serbia Internship Design of water supply and sewer networks

Computer skills

Software	MS Office, AutoCAD, Inventor, LabView, ArcGis, Photoshop, CorelDraw, HEC-RAS
Programming	VBA, Matlab, Java, C++, Pascal

Languages

Serbian	Native
English	Fluent
Russian	Intermediate
Portuguese	Basic
French	Basic
German	Basic

Teaching

Follow-up of 2 Master theses, as well as numerous semester projects and exercises of graduate students in the courses of hydraulic structures and dams of the School of Architecture, Civil and Environmental Engineering (ENAC) of EPFL.

Publications

Stojnic, I., Pfister, M., Matos J., Schleiss, A. J. (2019). Hydraulic jump downstream of a stepped chute: an experimental study. *Proc. 38th IAHR World Congress*, Panama City, Panama.

Noseda, M., Stojnic, I., Pfister, M. and Schleiss, A. J. (2019). Upstream erosion and sediment passage at Piano Key Weirs. *Journal Of Hydraulic Engineering*, 145(8), 04019029.

Stojnic, I., Ylla, C., Amini, A. De Cesare, G., Schleiss, A. J. (2018). Kariba plunge pool rehabilitation. *Proc. HYDRO 2018,* Gdansk, Poland.

Stojnic, I., Bron, C., Amini, A. De Cesare, G. (2018). Effect of spilling from adjacent orifices on the velocity field and pressures in front of needle stop-logs, *Proc. 11th International Symposium on Ultrasonic Doppler Methods for Fluid Mechanics and Fluid Engineering,* Berlin, Germany.